THEORY AND APPLICATIONS OF TRANSPORT IN POROUS MEDIA

Emerging Topics in Heat and Mass Transfer in Porous Media

From Bioengineering and Microelectronics to Nanotechnology

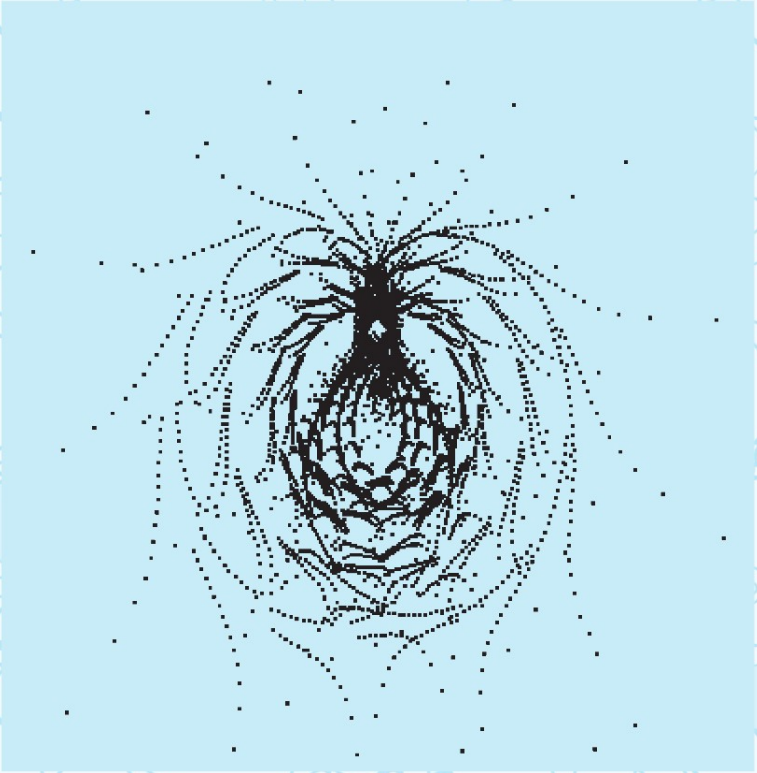

Peter Vadász (Ed.)

Emerging Topics in Heat and Mass Transfer in Porous Media

Theory and Applications of Transport in Porous Media

Series Editor:
Jacob Bear, *Technion – Israel Institute of Technology, Haifa, Isreal*

Volume 22

The titles published in this series are listed at the end of the volume.

Emerging Topics in Heat and Mass Transfer in Porous Media

From Bioengineering and Microelectronics to Nanotechnology

Peter Vadász
Editor

Department of Mechanical Engineering,
Northern Arizona University, Flagstaff, AZ, U.S.A.

Springer

Editor
Peter Vadász
Department of Mechanical Engineering
Northern Arizona University
Flagstaff, AZ, U.S.A.
peter.vadasz@nau.edu

ISBN: 978-1-4020-8177-4 e-ISBN: 978-1-4020-8178-1

Library of Congress Control Number: 2008921941

© 2008 Springer Science+Business Media B.V.
No part of this work may be reproduced, stored in a retrieval system, or transmitted
in any form or by any means, electronic, mechanical, photocopying, microfilming, recording
or otherwise, without written permission from the Publisher, with the exception
of any material supplied specifically for the purpose of being entered
and executed on a computer system, for exclusive use by the purchaser of the work.

Cover illustration: A fractal resulting from evaluating the projection of the trajectory of differences between numerical solutions of natural convection in porous media within the weak turbulent (chaotic) regime window at different accuracy levels (see pages 128–129). Figure 6d (modified) was published in P. Vadász and S. Olek, Convergence and Accuracy of Adomian's Decomposition Method for the Solution of Lorenz Equations, International Journal of Heat and Mass Transfer, Vol. 43(10), pp. 1715–1734, 2000.

Printed on acid-free paper

9 8 7 6 5 4 3 2 1

springer.com

Preface

This book is a synthesis of emerging topics in heat and mass transfer in porous media. It brings together some of the world leaders in research on transport phenomena in porous media to present the state of the art of its theory as well as the application of the theory in emerging fields such as bioengineering, microelectronics and nanotechnology. The well renowned scientists presenting their findings in the review chapters presented are not only among the best world leaders in their field, they also capture the research that is undertaken in all the parts of the globe, from the Far East (Hong-Kong), the Southern Hemisphere (New Zealand and South Africa) to Europe and America.

The book is separated into two parts. The first presents the state of the art of the theory of heat and mass transfer in porous media and can be used in both the traditional (underground flow, filtering and reservoir engineering) as well as in the more recent emerging applications. The second part deals with emerging topics and applications of the theory to bioengineering, microelectronics, and nanotechnology.

Traditionally, the topic of transport phenomena in porous media was almost exclusively reserved to the field of underground flow (water, oil, gas, etc.) and filtering. With some singular exceptions on applications to drying processes of fabric, the development of the theory of transport phenomena in porous media was historically driven by the needs of technologies linked to reservoir engineering or civil engineering. A turning point in this development was reached in the early part of the second half in the twenty century when special attention to heat transfer in porous media yielded an exceeding expansion of interest. This development continued in the twenty first century and reached recently such an impressive use in a diverse collection of technological applications that created the motivation behind the preparation of this book.

The book starts with introducing the theoretical aspects of heat transfer in porous media by introducing the state of the art on the topic. It begins by introducing the topic of conduction in porous media subject to Lack of Local Thermal Equilibrium – LaLotheq (or Local Thermal Non-Equilibrium – LTNE) and its link to Dual-Phase-Lagging (DuPhlag), the latter having a wider range of applications. It follows into heat convection effects in porous media, extending the existing knowledge to generalized heterogeneity effects, instability of unsteady boundary layers, transition to weak turbulence and chaos, gravity-modulated convection and thermal-vibrational porous media convection.

This state of the art theoretical background is followed by chapters dealing with its application to emerging fields such as bioengineering, microelectronics, and nanotechnology. Bio- convection effects in porous media are presented in detail followed by the porous media application to macromolecular transport in arterial walls in particular, and to flow and heat transfer in biological tissues in general. The emerging application of metal foams as passive thermal control systems in cooling of microelectronics introduces another interesting aspect of heat transfer in porous media. The book concludes with the introduction of modeling of heat conduction in nanofluid suspensions as a derivative of interface heat transfer modeling in porous media.

The book should be of interest to scientists, researchers, engineers and graduate students that intend pursuing an application of transport phenomena in porous media or intend working on one of the emerging technologies covered in the book. In addition industry leaders that want to engage their teams in a deeper understanding of the concepts underlying the new emerging technologies should also be interested in the work reported in this book. Finally, since the topics covered are truly interdisciplinary and cross-disciplinary the disciplines that should find an interest are quite diverse, all engineering fields, biological sciences and physical sciences are just examples.

September 2007 Peter Vadász
Flagstaff, AZ, USA

Contents

Contributors

Abdalla AlAmiri
Mechanical Engineering Department, United Arab Emirates University, P.O. Box 17555 Al-Ain, UAE, alamiri@uaeu.ac.ae

Joseph L. Bull
Vascular Mechanics Lab, Biomedical Engineering Department, University of Michigan, Ann Arbor, MI 48109, USA, joebull@umich.edu

Marie-Catherine Charrier-Mojtabi
Laboratoire P.H.A.SE., UFR PCA, Université Paul Sabatier,118 route de Narbonne, 31062 Toulouse cedex, France, cmojtabi@cict.fr

J.P. Ennis-King
Cooperative Research Centre for Greenhouse Gas Technologies, CSIRO Petroleum, Private Bag 10, Clayton South, VIC 3169, Australia

Suresh V. Garimella
Cooling Technologies Research Center, School of Mechanical Engineering, Purdue University, West Lafayette, IN 47907-2088 USA, sureshg@ecn.purdue.edu

Saneshan Govender
University of Kwa-Zulu Natal, School of Mechanical Engineering, King George V Avenue, Durban 4001 South Africa, govenders65@ukzn.ac.za

A. Haji-Sheikh
Department of Mechanical and Aerospace Engineering, The University of Texas at Arlington, Arlington, TX 76019-0023, USA, haji@mae.uta.edu

Khalil Khanafer
Vascular Mechanics Lab, Biomedical Engineering Department, University of Michigan, Ann Arbor, MI 48109, USA, khanafer@umich.edu

Shankar Krishnan
Bell Laboratories, Alcatel-Lucent, Blanchardstown Industrial Park, Dublin-15, Ireland, skrishnan@alcatel-lucent.com

A.V. Kuznetsov
North Carolina State University, Mechanical & Aerospace Engineering, Box 7910, Raleigh, NC 27695, USA, avkuznet@eos.ncsu.edu

W.J. Minkowycz
Department of Mechanical and Industrial Engineering, University of Illinois at Chicago, Chicago, IL 60607-7022, USA, WJM@uic.edu

Abdelkader Mojtabi
Institut de mécanique des Fluides, UMR CNRS-INP-UPS N°5502, Université Paul Sabatier, 118 route de Narbonne, 31062 Toulouse cedex, France, mojtabi@imft.fr

Jayathi Y. Murthy
Cooling Technologies Research Center, School of Mechanical Engineering, Purdue University, West Lafayette, IN 47907-2088 USA, jmurthy@ecn.purdue.edu

D.A. Nield
Department of Engineering Science, University of Auckland, Private Bag 92019, Auckland 1142, New Zealand, d.nield@auckland.ac.nz

Yazdan Pedramrazi
Reservoir Engineering Research Institute(RERI), 385 Sherman Ave, Suite 5, Palo Alto, CA 94036, USA, yazdan@rerinst.org

Ioan Pop
Faculty of Mathematics, University of Cluj, R-3400 Cluj, Romania,
pop-ioan@yahoo.co.uk; popi@math.ubbcluj.ro

D.A.S. Ress
Department of Mechanical Engineering, University of Bath, Claverton Down, Bath BA2 7AY, UK, D.A.S.Ress@bath.ac.uk

A. Selim
Department of Mechanical Engineering, University of Bath, Claverton Down, Bath BA2 7AY, UK

Peter Vadász
Department of Mechanical Engineering, Northern Arizona University,
P.O. Box 15600, Flagstaff, AZ 86011-5600, USA, peter.vadasz@nau.edu

K. Vafai
Mechanical Engineering Department, University of California, Riverside, CA 92505, USA, vafai@engr.ucr.edu

Liqiu Wang
Department of Mechanical Engineering, The University of Hong Kong, Pokfulam Road, Hong Kong, lqwang@hku.hk

Xiaohao Wei
Department of Mechanical Engineering, The University of Hong Kong, Pokfulam Road, Hong Kong

Mingtian Xu
Institute of Thermal Science and Technology, Shandong University, Jinan 250061, China

Dual-Phase-Lagging and Porous-Medium Heat Conduction Processes

Liqiu Wang, Mingtian Xu, and Xiaohao Wei

Abstract We review some major progresses on dual-phase-lagging heat conduction and its intrinsic application in porous-medium heat conduction. The topics include well-posedness, solution structure, thermal wave and resonance, and intrinsic equivalence between the dual-phase-lagging heat conduction and the Fourier heat conduction in porous media subject to lack of local thermal equilibrium.

1 Introduction

By lumping microstructural effects into delayed temporal responses in the macroscopic formulation, Tzou (1995a) proposed a dual-phase-lagging constitutive equation for heat conduction, relating the temperature gradient $\bigtriangledown T$ at a material point $\vec{x}$ and time $t + \tau_T$ to the heat flux density vector $\mathbf{q}$ at $\vec{x}$ and time $t + \tau_q$ through material thermal conductivity k,

$$\mathbf{q}(\vec{x}, t + \tau_q) = -k \bigtriangledown T(\vec{x}, t + \tau_T). \tag{1}$$

Two delay times τ_T and τ_q are regarded as intrinsic thermal or structural properties of the material. The former is due to the microstructural interactions such as phonon–electron interaction or phonon scattering, and is termed as the phase-lag of the temperature gradient. The latter is, on the other hand, interpreted as the relaxation time accounting for the fast-transient effects of thermal inertia, and is named as the phase-lag of the heat flux.

Xu and Wang (2005) developed the relation between the constitutive model (1) and the Boltzmann transport equation. With the constitutive model (1), the first law

Liqiu Wang
The University of Hong Kong, Hong Kong
e-mail: lqwang@hku.hk

Mingtian Xu
Institute of Thermal Science and Technology, Shandong University, Jinan, China

Xiaohao Wei
The University of Hong Kong, Hong Kong

P. Vadász (ed.), *Emerging Topics in Heat and Mass Transfer in Porous Media*,
© Springer Science+Business Media B.V. 2008

of thermodynamics leads to delay/advanced dual-phase-lagging heat-conduction equations (Xu and Wang 2005). Xu and Wang (2005) discussed proper initial and boundary conditions and developed analytical solutions of such equations. Also obtained by Xu and Wang (2005) were the conditions under which the thermal oscillation occurs.

Expanding $\bigtriangledown T$ and $\mathbf{q}$ with respect to time t by Taylor series and retaining only the first-order terms in τ_T and τ_q, we obtain a linear version of (1) at point $\vec{x}$ and time t (Tzou 1995a, 1997),

$$\mathbf{q} + \tau_q \frac{\partial \mathbf{q}}{\partial t} = -k[\bigtriangledown T + \tau_T \frac{\partial}{\partial t}(\bigtriangledown T)], \tag{2}$$

which is known as the Jeffreys-type constitutive equation of heat flux (Joseph and Preziosi 1989). Eliminating $\mathbf{q}$ from (2) and the classical energy equation leads to the dual-phase-lagging heat conduction equation that reads, if all thermophysical material properties are assumed to be constant,

$$\frac{1}{\alpha}\frac{\partial T}{\partial t} + \frac{\tau_q}{\alpha}\frac{\partial^2 T}{\partial t^2} = \triangle T + \tau_T \frac{\partial}{\partial t}(\triangle T) + f(\vec{x}, t), \tag{3}$$

where α is the thermal diffusivity of the material, $\triangle$ is the Laplacian, and f stands for internal heat sources.

The dual-phase-lagging heat-conduction equation forms a generalized, unified equation that reduces to the classical parabolic heat-conduction equation when $\tau_T = \tau_q$, the hyperbolic heat-conduction equation when $\tau_T = 0$ and $\tau_q = \tau$ with τ as the relaxation time defined by Chester (1963), the energy equation in the phonon scattering model (Joseph and Preziosi 1989, Guyer and Krumhansi 1966) when $\alpha = \frac{\tau_R c^2}{3}$, $\tau_T = \frac{9}{5}\tau_N$ and $\tau_q = \tau_R$, and the energy equation in the phonon–electron interaction model (Kaganov et al. 1957, Anisimòv et al. 1974, Qiu and Tien 1993) when $\alpha = \frac{k}{c_e + c_l}$, $\tau_T = \frac{c_l}{G}$ and $\tau_q = \frac{1}{G}[\frac{1}{c_e} + \frac{1}{c_l}]^{-1}$. In the phonon scattering model, c is the average speed of phonons (sound speed), τ_R is the relaxation time for the umklapp process in which momentum is lost from the phonon system, and τ_N is the relaxation time for normal processes in which momentum is conserved in the phonon system. In the phonon–electron interaction model, k is the thermal conductivity of the electron gas, G is the phonon–electron coupling factor, and c_e and c_l are the heat capacity of the electron gas and the metal lattice, respectively. This, with its success in describing and predicting phenomena such as ultrafast pulse-laser heating, propagating of temperature pulses in superfluid liquid helium, nonhomogeneous lagging response in porous media, thermal lagging in amorphous materials, and effects of material defects and thermomechanical coupling (Tzou and Zhang 1995), has given rise to the research effort on various aspects of dual-phase-lagging heat conduction.

The dual-phase-lagging heat conduction was shown to be admissible by the second law of the extended irreversible thermodynamics (Tzou 1997) and by the Boltzmann transport equation (Xu and Wang 2005). It was also proven to be well-posed in a finite region of n–dimensions ($n \geq 1$) under any linear boundary

conditions including Dirichlet, Neumann and Robin types (Wang and Xu 2002, Wang et al. 2001). Solutions of one-dimensional (1D) heat conduction were obtained for some specific initial and boundary conditions by Antaki (1998), Dai and Nassar (1999), Lin et al. (1997), Tang and Araki (1999), Tzou (1995a, b, 1997), Tzou and Zhang (1995). Wang and Zhou (2000, 2001) and Wang et al. (2008) developed methods of measuring the phase-lags of the heat flux and the temperature gradient and obtained analytical solutions for regular 1D, 2D and 3D heat-conduction domains under essentially arbitrary initial and boundary conditions. The solution structure theorems were also developed for both mixed and Cauchy problems of dual-phase-lagging heat-conduction equations (Wang and Zhou 2000, Wang et al. 2001, 2008) by extending those for the hyperbolic heat conduction (Wang 2000a). These theorems build relationships among the contributions (to the temperature field) by the initial temperature distribution, the source term and the initial time-rate change of the temperature, uncover the structure of temperature field and considerably simplify the development of solutions. Xu and Wang (2002) addressed thermal features of the dual-phase-lagging heat-conduction, conditions and features of thermal oscillation and resonance and their difference with those in the classical and in particular. Tzou (1997) and Vadász (2005a, b, 2006a, b) developed an *approximate* equivalence between the heat conduction in porous media and the dual-phase-lagging heat conduction, and applied the latter to examine features of the former. An *exact* equivalence between these two processes has also recently discovered by Wang and Wei (2008).

The present review focuses on four aspects of dual-phase-lagging heat conduction: the well-posedness, the solution structure, the thermal oscillation and resonance, and the equivalence with the Fourier heat conduction in porous media. The readers are refereed to Tzou (1997), Wang and Zhou (2000, 2001) and Wang et al. (2008) for the other aspects of the dual-phase-lagging heat conduction.

2 Well-Posedness

Wang et al. (2001) and Wang and Xu (2002) examine the existence, uniqueness and stability of the solution with respect to initial conditions for the following initial-boundary value problem

$$\begin{cases} \frac{1}{\alpha} T_t(\vec{x}, t) + \frac{\tau_q}{\alpha} T_{tt}(\vec{x}, t) = \triangle T(\vec{x}, t) + \tau_T \frac{\partial}{\partial t} \triangle T(\vec{x}, t), & \Omega \times (0, +\infty), \\ k \frac{\partial T(\vec{x}, t)}{\partial n} + hT(\vec{x}, t)|_{\partial\Omega} = 0, & (0, +\infty), \\ T(\vec{x}, 0) = \phi(\vec{x}, t),\ T_t(\vec{x}, 0) = \psi(\vec{x}, t), & \Omega. \end{cases} \tag{4}$$

Here t is the time, T is the temperature, α is the thermal diffusivity, τ_T and τ_q are the phase-lag of the temperature gradient and the heat flux, respectively, $\vec{x}$ denotes a point in the space domain Ω of n–dimensions with the boundary $\partial\Omega$, $\triangle$ is the Laplacian, ϕ and ψ are known functions, $\partial T/\partial n$ is the normal derivative of T,

$T_t = \partial T/\partial t$, $T_{tt} = \partial^2 T/\partial t^2$, k and h are nonnegative real constants and satisfy $k + h \neq 0$.

Note that (4) covers the Dirichlet, Neumann and Robin boundary conditions by different combinations of k and h. Physical implications and limitations of these three boundary conditions have been well discussed by Tzou (1997) and Fournier and Boccara (1989). For the heat conduction involving heat flux-specified boundary conditions, it is more convenient to use the dual-phase-lagging heat conduction equation in terms of the heat flux $\mathbf{q}$ or the heat flux potential Φ defined by $\mathbf{q} = \bigtriangledown\Phi$. The Φ-version heat conduction equation has exactly the same structure as its T-version. The 1D $\mathbf{q}$-version heat conduction equation is also of the same structure as its T-version. A mixed formulation for both $\mathbf{q}$ and T directly by two coupled energy and constitutive equations is more general in view of applications of the dual-phase-lagging model. The readers are referred to Tzou (1997) for the details.

2.1 Existence

Wang and Xu (2002) examine the existence of (4) by using the separation of the variables to find its solution in the form

$$T(\vec{x}, t) = X(\vec{x})\Gamma(t). \tag{5}$$

This involves a prior assumption of existence. The existence can also be proven without this prior assumption but with more mathematics involved (Wang and Zhou, 2000, 2001, Wang et al. 2008). In the interest of clarity and briefness, we fellow Wang and Xu (2002) here in proving the existence.

A substitution of (5) into (4) leads to

$$X(\vec{x})[\frac{1}{\alpha}\Gamma_t(t) + \frac{\tau_q}{\alpha}\Gamma_{tt}(t)] = \triangle X(\vec{x})[\Gamma(t) + \tau_T\Gamma_t(t)]$$

which becomes, after dividing by $X(\vec{x})[\Gamma(t) + \tau_T\Gamma_t(t)]$,

$$\frac{\frac{1}{\alpha}\Gamma_t(t) + \frac{\tau_q}{\alpha}\Gamma_{tt}(t)}{\Gamma(t) + \tau_T\Gamma_t(t)} = \frac{\triangle X(\vec{x})}{X(\vec{x})}. \tag{6}$$

Therefore, Wang and Xu (2002) obtain the separation equation for the temporal variable $\Gamma_t(t)$

$$\tau_q\Gamma_{tt}(t) + (1 + \alpha\tau_T\lambda)\Gamma_t(t) + \alpha\lambda\Gamma(t) = 0, \tag{7}$$

and the homogeneous system for the spatial variable $X(\vec{x})$

$$\triangle X(\vec{x}) + \lambda X(\vec{x}) = 0, \vec{x} \in \Omega, \tag{8}$$

$$k\frac{\partial X}{\partial n} + hX = 0, \vec{x} \in \partial\Omega, \tag{9}$$

where λ is the separation constant.

Integrating (8) over Ω after multiplying $X(\vec{x})$ yields

$$\int_\Omega X \triangle X d\Omega + \lambda \int_\Omega X^2 d\Omega = 0 \tag{10}$$

which is, by applying the Green identity to $\int_\Omega X \triangle X d\Omega$,

$$\int_{\partial\Omega} X\frac{\partial X}{\partial n} d(\partial\Omega) - \int_\Omega \triangledown X \cdot \triangledown X d\Omega + \lambda \int_\Omega X^2 d\Omega = 0. \tag{11}$$

By (9), if $k \neq 0$, we obtain

$$\frac{\partial X}{\partial n}|_{\partial\Omega} = -\frac{h}{k} X|_{\partial\Omega}.$$

Therefore, (11) becomes

$$\lambda \int_\Omega X^2 d\Omega = \int_\Omega \triangledown X \cdot \triangledown X d\Omega + \frac{h}{k} \int_{\partial\Omega} X^2 d(\partial\Omega) \geq 0,$$

which implies

$$\lambda \geq 0. \tag{12}$$

For the case of $k = 0$, a similar analysis also leads to (12).

Using the solution of (7)–(9) available in Wang and Zhou (2000, 2001) and Wang et al. (2001, 2008) for various Ω, we have a solution of (4)

$$\begin{cases} T(\vec{x}, t) = \sum_{m=1}^{\infty} e^{\nu_m t}[A_m cos\mu_m t + B_m \underline{sin}(\mu_m t)]X_m(\vec{x}), \\ A_m = \frac{1}{M_m} \int_\Omega \phi(\vec{x}) X_m(\vec{x}) d\Omega, \\ B_m = \frac{1}{M_m \underline{\mu_m}} \int_\Omega \psi(\vec{x}) X(\vec{x}) d\Omega - \frac{\nu_m}{M_m \underline{\mu_m}} \int_\Omega \phi(\vec{x}) X_m(\vec{x}) d\Omega, \end{cases} \tag{13}$$

where,

$$\nu_m = -\frac{1 + \alpha\tau_T\lambda_m}{2\tau_q}, \tag{14}$$

$$\mu_m = \frac{\sqrt{4\alpha\tau_q\lambda_m - (1 + \alpha\tau_T\lambda_m)^2}}{2\tau_q}, \tag{15}$$

$$\underline{\mu}_m = \begin{cases} \mu_m \text{ if } \mu_m \neq 0 \\ 1 \quad \text{if } \mu_m = 0, \end{cases} \tag{16}$$

$$\underline{sin}(\mu_m t) = \begin{cases} sin(\mu_m t) & \text{if } \mu_m \neq 0 \\ t & \text{if } \mu_m = 0, \end{cases} \tag{17}$$

and

$$M_m = \int_\Omega X_m^2(\vec{x}) d\Omega. \tag{18}$$

Here, λ_m and $X_m(\vec{x})$ are eigenvalues and eigenfunctions of (8) and (9), respectively. They are Ω-dependent and available in Wang and Zhou (2000), (2001) and Wang et al. (2008) for various Ω. Therefore, (4) has at least one solution.

2.2 Inequality

For the uniqueness and stability, Wang and Xu (2002) first develop an important inequality for (4). Note that

$$\frac{\partial}{\partial t}(T + \tau_q T_t)^2 = 2(T + \tau_q T_t)(T_t + \tau_q T_{tt}) = 2\alpha(T + \tau_q T_t)(\triangle T + \tau_T \triangle T_t), \tag{19}$$

in which the heat-conduction equation in (4) has been used. Integrating (19) with respect to $\vec{x}$ over Ω yields

$$\int_\Omega \frac{\partial}{\partial t}(T+\tau_q T_t)^2 d\Omega = 2\alpha \int_\Omega (T \triangle T + \tau_T T \triangle T_t + \tau_q T_t \triangle T + \tau_q \tau_T T_t \triangle T_t) d\Omega. \tag{20}$$

By the Green identity,

$$\int_\Omega T \triangle T d\Omega = \int_{\partial\Omega} T \frac{\partial T}{\partial n} d(\partial\Omega) - \int_\Omega \nabla T \cdot \nabla T d\Omega,$$

$$\int_\Omega T \triangle T_t d\Omega = \int_{\partial\Omega} T \frac{\partial T_t}{\partial n} d(\partial\Omega) - \int_\Omega \nabla T \cdot \nabla T_t d\Omega,$$

$$\int_\Omega T_t \triangle T d\Omega = \int_{\partial\Omega} T_t \frac{\partial T}{\partial n} d(\partial\Omega) - \int_\Omega \nabla T_t \cdot \nabla T d\Omega,$$

$$\int_\Omega T_t \triangle T_t d\Omega = \int_{\partial\Omega} T_t \frac{\partial T_t}{\partial n} d(\partial\Omega) - \int_\Omega \nabla T_t \cdot \nabla T_t d\Omega.$$

Also note that,

$$\int_\Omega \nabla T \cdot \nabla T_t d\Omega = \int_\Omega \nabla T_t \cdot \nabla T d\Omega = \frac{1}{2} \int_\Omega \frac{\partial}{\partial t}(\nabla T \cdot \nabla T) d\Omega.$$

Therefore, (20) can be re-written as

$$\int_{\Omega} \frac{\partial}{\partial t}(T + \tau_q T_t)^2 d\Omega + \alpha(\tau_T + \tau_q) \int_{\Omega} \frac{\partial}{\partial t}(\nabla T \cdot \nabla T) d\Omega =$$
$$2\alpha \int_{\partial\Omega} T \frac{\partial T}{\partial n} d(\partial\Omega) - 2\alpha \int_{\Omega} \nabla T \cdot \nabla T d\Omega + 2\alpha\tau_T \int_{\partial\Omega} T \frac{\partial T_t}{\partial n} d(\partial\Omega)$$
$$+2\alpha\tau_q \int_{\partial\Omega} T_t \frac{\partial T}{\partial n} d(\partial\Omega) + 2\alpha\tau_q\tau_T \int_{\partial\Omega} T_t \frac{\partial T_t}{\partial n} d(\partial\Omega) - 2\alpha\tau_q\tau_T \int_{\Omega} \nabla T_t \cdot \nabla T_t d\Omega. \tag{21}$$

For the case of $k \neq 0$, the boundary condition in (4) becomes

$$\frac{\partial T}{\partial n}|_{\partial\Omega} = -\frac{h}{k} T|_{\partial\Omega}. \tag{22}$$

Substituting (22) into (21) and defining

$$g(t) = \alpha(\tau_T + \tau_q) \int_{\Omega} \nabla T \cdot \nabla T d\Omega + \frac{\alpha h}{k}(\tau_T + \tau_q) \int_{\partial\Omega} T^2 d(\partial\Omega) + \int_{\Omega} (T + \tau_q T_t)^2 d\Omega, \tag{23}$$

yield

$$\frac{\partial g(t)}{\partial t} = -\frac{2\alpha h}{k} \int_{\partial\Omega} T^2 d(\partial\Omega) - 2\alpha \int_{\Omega} \nabla T \cdot \nabla T d\Omega - 2\alpha\tau_q\tau_T \frac{h}{k} \int_{\partial\Omega} T_t^2 d(\partial\Omega)$$
$$- 2\alpha\tau_q\tau_T \int_{\Omega} \nabla T_t \cdot \nabla T_t d\Omega \tag{24}$$

which is negative semi-definite because $\alpha, \tau_T, \tau_q, h$ and k are not negative. Therefore,

$$g(t_1) \leq g(t_0), \forall t_1 \geq t_0. \tag{25}$$

The inequality for the case of $k = 0$ can also be written in the form of (25). However, the definition of $g(t)$ should be

$$g(t) = \alpha(\tau_T + \tau_q) \int_{\Omega} \nabla T \cdot \nabla T d\Omega + \int_{\Omega} (T + \tau_q T_t)^2 d\Omega. \tag{26}$$

2.3 Uniqueness

Suppose that $T_1(\vec{x}, t)$ and $T_2(\vec{x}, t)$ are two solutions of (4). The difference between them

$$w(\vec{x}, t) = T_1(\vec{x}, t) - T_2(\vec{x}, t),$$

must satisfy the following initial-boundary value problem (Wang and Xu 2002)

$$\begin{cases} \dfrac{1}{\alpha} w_t + \dfrac{\tau_q}{\alpha} w_{tt} = \triangle w + \tau_T \dfrac{\partial}{\partial t} \triangle w, \ \Omega \times (0, \infty), \\ k \dfrac{\partial w}{\partial n} + h w|_{\partial \Omega} = 0, \\ w|_{t=0} = 0, \ w_t|_{t=0} = 0. \end{cases} \tag{27}$$

For the case of $k \neq 0$, an application of (25)–(27) yields, with $t_1 = t > 0$ and $t_0 = 0$,

$$\begin{aligned} &\alpha(\tau_T + \tau_q) \int_\Omega \triangledown w(\vec{x}, t) \cdot \triangledown w(\vec{x}, t) d\Omega + \frac{\alpha h}{k} (\tau_T + \tau_q) \int_{\partial \Omega} w^2(\vec{x}, t) d(\partial \Omega) \\ &+ \int_\Omega [w(\vec{x}, t) + \tau_q w_t(\vec{x}, t)]^2 d\Omega \leq \alpha(\tau_T + \tau_q) \int_\Omega \triangledown w(\vec{x}, 0) \cdot \triangledown w(\vec{x}, 0) d\Omega \\ &+ \frac{\alpha h}{k} (\tau_T + \tau_q) \int_{\partial \Omega} w^2(\vec{x}, 0) d(\partial \Omega) + \int_\Omega [w(\vec{x}, 0) + \tau_q w_t(\vec{x}, 0)]^2 d\Omega = 0. \end{aligned} \tag{28}$$

This requires,

$$\triangledown w(\vec{x}, t) = 0, \tag{29}$$

and,

$$w(\vec{x}, t) + \tau_q w_t(\vec{x}, t) = 0. \tag{30}$$

Therefore, w is independent of $\vec{x}$ (29). The general solution of (30) is thus

$$w(\vec{x}, t) = c e^{-\frac{t}{\tau_q}} \tag{31}$$

with c as a constant. Applying the initial condition $w(\vec{x}, 0) = 0$ yields

$$c = 0. \tag{32}$$

Therefore

$$w(\vec{x}, t) = 0, \tag{33}$$

i.e.,

$$T_1(\vec{x}, t) = T_2(\vec{x}, t). \tag{34}$$

However, T_1 and T_2 are any two solutions of (4) so that the solution of (4) is unique. Similarly, the uniqueness can also be established for the case of $k = 0$ (Wang and Xu 2002).

2.4 Stability

Wang and Xu (2002) establish the stability with respect to the initial conditions by the following stability theorem.

Theorem 1. *If*

$$|\phi(\vec{x})| \leq \varepsilon, \tag{35}$$

$$|\psi(\vec{x})| \leq \varepsilon, \tag{36}$$

and

$$|\bigtriangledown \phi(\vec{x})| \leq \varepsilon, \tag{37}$$

the solution $T(\vec{x}, t)$ *of (4) satisfies*

$$|T(\vec{x}, t)| \leq c\varepsilon. \tag{38}$$

Here ε *is a small positive constant, and* c *is a nonnegative constant.*

Proof. For the case of $k \neq 0$, (25) yields, for (4) when $t > 0$ and $t_0 = 0$,

$$\begin{aligned}
&\alpha(\tau_T + \tau_q)\int_\Omega \bigtriangledown T \cdot \bigtriangledown T d\Omega + \frac{\alpha h}{k}(\tau_T + \tau_q)\int_{\partial\Omega} T^2 d(\partial\Omega) + \int_\Omega (T + \tau_q T_t)^2 d\Omega \\
&\leq \alpha(\tau_T + \tau_q)\int_\Omega |\bigtriangledown \phi|^2 d\Omega + \frac{\alpha h}{k}(\tau_T + \tau_q)\int_{\partial\Omega} \phi^2 d(\partial\Omega) + \int_\Omega (\phi + \tau_q \psi)^2 d\Omega, \\
&\leq \alpha(\tau_T + \tau_q)\varepsilon^2 V + \frac{\alpha h}{k}(\tau_T + \tau_q)\varepsilon^2 S + (1 + \tau_q)^2 \varepsilon^2 V \\
&= [(\alpha V + \frac{\alpha h}{k} S)(\tau_T + \tau_q) + (1 + \tau_q)^2 V]\varepsilon^2 = M\varepsilon^2,
\end{aligned} \tag{39}$$

where (35)–(37) have been used,

$$M = \left(\alpha V + \frac{2\alpha h}{k} S\right)\left(\tau_T + \tau_q\right) + (1 + \tau_q)^2 V, \tag{40}$$

V is the volume of Ω, and S is the area of $\partial\Omega$. Equation (39) implies

$$\alpha(\tau_T + \tau_q)\int_\Omega |\bigtriangledown T|^2 d\Omega \leq M\varepsilon^2, \tag{41}$$

$$\frac{\alpha h(\tau_T + \tau_q)}{k}\int_{\partial\Omega} T^2 d(\partial\Omega) \leq M\varepsilon^2, \tag{42}$$

which are equivalent to,

$$\int_{\Omega} |\bigtriangledown T|^2 d\Omega \leq M_1 \varepsilon^2, \tag{43}$$

$$\int_{\partial\Omega} T^2 d(\partial\Omega) \leq M_2 \varepsilon^2. \tag{44}$$

Here

$$M_1 = \frac{M}{\alpha(\tau_T + \tau_q)}, M_2 = \frac{Mk}{\alpha h(\tau_T + \tau_q)}.$$

Since, for any two square-integrable functions f_1 and f_2,

$$\int_{\Omega} |f_1||f_2| d\Omega \leq \sqrt{\int_{\Omega} f_1^2 d\Omega} \sqrt{\int_{\Omega} f_2^2 d\Omega},$$

$$\int_{\partial\Omega} |f_1||f_2| d(\partial\Omega) \leq \sqrt{\int_{\partial\Omega} f_1^2 d(\partial\Omega)} \sqrt{\int_{\partial\Omega} f_2^2 d(\partial\Omega)},$$

Wang and Xu (2002) obtain

$$\int_{\Omega} |\bigtriangledown T| d\Omega \leq \sqrt{\int_{\Omega} |\bigtriangledown T|^2 d\Omega} \sqrt{\int_{\Omega} d\Omega} \leq \sqrt{M_1 V}\varepsilon, \tag{45}$$

and

$$\int_{\partial\Omega} |T| d(\partial\Omega) \leq \sqrt{\int_{\partial\Omega} T^2 d(\partial\Omega)} \sqrt{\int_{\partial\Omega} d(\partial\Omega)} \leq \sqrt{M_2 S}\varepsilon, \tag{46}$$

in which (43) and (44) have been used. Equations (45) and (46) can be rewritten into

$$\int_{\Omega} \eta_1(\vec{x}, t) d\Omega \leq 0, \forall\Omega, \tag{47}$$

and

$$\int_{\partial\Omega} \eta_2(\vec{x}, t) d(\partial\Omega) \leq 0, \forall\partial\Omega, \tag{48}$$

where

$$\eta_1(\vec{x}, t) = | \bigtriangledown T(\vec{x}, t) | - \sqrt{\frac{M_1}{V}}\varepsilon, \eta_2(\vec{x}, t) = | T(\vec{x}, t) | - \sqrt{\frac{M_2}{S}}\varepsilon.$$

To obtain a local form of (47) and (48), Wang and Xu (2002) consider a subregion $\Omega_{\triangle v}$ of volume $\triangle v$ around point $\vec{x_1}$ in Ω at arbitrary time instant τ, and a subsurface $\partial\Omega_{\triangle s}$ of area $\triangle s$ around point $\vec{x_2}$ on $\partial\Omega$ at arbitrary time instant τ. Let

$$I_{\triangle v} = \mid \eta_1(\vec{x_1}, t) - \tfrac{1}{\triangle v} \int_{\Omega_{\triangle v}} \eta_1(\vec{x}, t) d\Omega_{\triangle v} \mid, \tag{49}$$

$$I_{\triangle s} = \mid \eta_2(\vec{x_2}, t) - \tfrac{1}{\triangle s} \int_{\partial\Omega_{\triangle s}} \eta_2(\vec{x}, t) d\partial\Omega_{\triangle s} \mid . \tag{50}$$

Then,

$$I_{\triangle v} \geq 0, \tag{51}$$

$$I_{\triangle s} \geq 0. \tag{52}$$

Also,

$$I_{\triangle v} = \mid \tfrac{1}{\triangle v} \int_{\Omega_{\triangle v}} [\eta_1(\vec{x_1}, t) - \eta_1(\vec{x}, t)] d\Omega_{\triangle v} \mid$$
$$\leq \tfrac{1}{\triangle v} \int_{\Omega_{\triangle v}} \max_{\vec{x} \in \Omega_{\triangle v}} \mid [\eta_1(\vec{x_1}, t) - \eta_1(\vec{x}, t)] \mid d\Omega_{\triangle v} = \max_{\vec{x} \in \Omega_{\triangle v}} \mid [\eta_1(\vec{x_1}, t) - \eta_1(\vec{x}, t)] \mid,$$
$$I_{\triangle s} = \mid \tfrac{1}{\triangle s} \int_{\partial\Omega_{\triangle s}} [\eta_2(\vec{x_2}, t) - \eta_2(\vec{x}, t)] d\partial\Omega_{\triangle s} \mid$$
$$\leq \tfrac{1}{\triangle s} \int_{\Omega_{\triangle s}} \max_{\vec{x} \in \partial\Omega_{\triangle s}} \mid [\eta_2(\vec{x_2}, t) - \eta_2(\vec{x}, t)] \mid d\partial\Omega_{\triangle s} = \max_{\vec{x} \in \partial\Omega_{\triangle v}} \mid [\eta_2(\vec{x_2}, t) - \eta_2(\vec{x}, t)] \mid,$$

which tend to zero as $\triangle v \to 0$ or $\triangle s \to 0$. Hence Wang and Xu (2002) obtain

$$I_{\triangle v} \leq 0, \text{as } \triangle v \to 0, \tag{53}$$

$$I_{\triangle s} \leq 0, \text{as } \triangle s \to 0. \tag{54}$$

To satisfy (51)–(54), Wang and Xu (2002) conclude that

$$\eta_1(\vec{x_1}, \tau) = \lim_{\triangle v \to 0} \frac{1}{\triangle v} \int_{\Omega_{\triangle v}} \eta_1(\vec{x}, t) d\Omega_{\triangle v}, \tag{55}$$

and

$$\eta_2(\vec{x_2}, \tau) = \lim_{\triangle s \to 0} \frac{1}{\triangle s} \int_{\partial\Omega_{\triangle s}} \eta_2(\vec{x}, t) d\partial\Omega_{\triangle s}, \tag{56}$$

which yield, after using (47) and (48),

$$\eta_1(\vec{x_1}, \tau) \leq 0, \tag{57}$$

$$\eta_2(\vec{x_2}, \tau) \leq 0. \tag{58}$$

Since $\vec{x_1}$, $\vec{x_2}$ and τ are arbitrary, Wang and Xu (2002) obtain

$$\eta_1(\vec{x}, t) \leq 0, \tag{59}$$

$$\eta_2(\vec{x}, t) \leq 0, \tag{60}$$

i.e.,

$$| \bigtriangledown T(\vec{x}, t) | \leq \sqrt{\frac{M_1}{V}}\varepsilon, \vec{x} \in \Omega, \tag{61}$$

$$| T(\vec{x}, t) | \leq \sqrt{\frac{M_2}{S}}\varepsilon, \vec{x} \in \partial\Omega. \tag{62}$$

Therefore, as $\varepsilon \to 0$,

$$| \bigtriangledown T(\vec{x}, t) | \to 0, \forall \vec{x} \in \Omega, \tag{63}$$

and

$$| T(\vec{x}, t) | \to 0, \forall \vec{x} \in \partial\Omega. \tag{64}$$

Let $\vec{x}$ be an arbitrary point in Ω, $\vec{x_0}$ be a point on $\partial\Omega$. There exists a point $\vec{y}$ in Ω between $\vec{x}$ and $\vec{x_0}$, by the Lagrange mean-value theorem, such that

$$T(\vec{x}, t) = T(\vec{x_0}, t) + \bigtriangledown T(\vec{y}, t) \cdot (\vec{x} - \vec{x_0}). \tag{65}$$

Therefore

$$|T(\vec{x}, t)| \leq |T(\vec{x_0}, t)| + | \bigtriangledown T(\vec{y}, t)|| \vec{x} - \vec{x_0} |, \tag{66}$$

which, with (63) and (64), leads to

$$|T(\vec{x}, t)| \to 0, \forall \vec{x} \in \Omega, \text{ as } \varepsilon \to 0. \tag{67}$$

Equations (64) and (67) lead Wang and Xu (2006) to conclude that there exists a positive constant c such that

$$|T(\vec{x}, t)| \leq c\varepsilon, \forall \vec{x} \in \Omega, \text{ and } \forall \vec{x} \in \partial\Omega. \tag{68}$$

Therefore, the solution of (4) is stable with respect to the initial conditions.

3 Solution Structure

The temperature field in dual-phase-lagging heat conduction comes from the combined contribution of three sources: the initial time-rate change of the temperature, the initial temperature distribution and the source term. Wang and Zhou (2000, 2001) and Wang et al. (2001, 2008) show that these three contributions are inter-expressible. The relations among the three contributions are termed as the solution structure theorems. These theorems uncover the solution structure, simplify the development of solutions of dual-phase-lagging heat-conduction equations significantly, and are with various forms (Wang and Zhou 2000, 2001; Wang et al. 2001, 2008). Here we follow Wang et al. 2001 in developing two of them expressing solutions of

$$\begin{cases} \frac{1}{\alpha} T_t(\vec{x}, t) + \frac{\tau_q}{\alpha} T_{tt}(\vec{x}, t) = \triangle T(\vec{x}, t) + \tau_T \frac{\partial}{\partial t} \triangle T(\vec{x}, t), \ \Omega \times (0, +\infty) \\ L(T, T_n)|_{\partial\Omega} = 0, \\ T(M, 0) = \phi(p), \ T_t(\vec{x}, 0) = 0, \end{cases} \tag{69}$$

and

$$\begin{cases} \frac{1}{\alpha} T_t(\vec{x}, t) + \frac{\tau_q}{\alpha} T_{tt}(\vec{x}, t) = \triangle T(\vec{x}, t) + \tau_T \frac{\partial}{\partial t} \triangle T(\vec{x}, t) + f(\vec{x}, t), \ \Omega \times (0, +\infty) \\ L(T, T_n)|_{\partial\Omega} = 0, \\ T(\vec{x}, 0) = 0, \ T_t(\vec{x}, 0) = 0, \end{cases} \tag{70}$$

in terms of the solution of

$$\begin{cases} \frac{1}{\alpha} T_t(\vec{x}, t) + \frac{\tau_q}{\alpha} T_{tt}(\vec{x}, t) = \triangle T(\vec{x}, t) + \tau_T \frac{\partial}{\partial t} \triangle T(\vec{x}, t), \ \Omega \times (0, +\infty) \\ L(T, T_n)|_{\partial\Omega} = 0, \\ T(\vec{x}, 0) = 0, \ T_t(\vec{x}, 0) = \psi(p). \end{cases} \tag{71}$$

Here $\vec{x}$ denotes a point in the space domain Ω with the boundary $\partial\Omega$, $\triangle$ is the Laplacian, T_n is the normal derivative of T, $L(T, T_n)$ represents linear functions of T and T_n, and $L(T, T_n)|_{\partial\Omega} = 0$ denotes homogeneous boundary conditions. Note that commonly-used Dirichlet, Neumann and Robin boundary conditions are the special cases of the linear function L. Wang et al. (2001) limit the discussion to the case that f, ϕ and ψ satisfy conditions for well-posedness and that the order of differentiation is interchangeable for some high-order partial derivatives of T with respect to the time and spatial coordinates.

Theorem 2. *Let $W(\psi, \vec{x}, t)$ denote the solution of (71). The solution of (69) can be written as*

$$T_1(\vec{x}, t) = \frac{1}{\tau_q} \left[W(\phi, \vec{x}, t) + \tau_q \frac{\partial W(\phi, \vec{x}, t)}{\partial t} + W(\phi_1, \vec{x}, t) \right], \tag{72}$$

where

$$\phi_1 \equiv -\alpha\tau_T \triangle \phi(p). \tag{73}$$

Proof. As $W(\psi, \vec{x}, t)$ is the solution of (71), we have

$$\begin{cases} \frac{1}{\alpha}\frac{\partial}{\partial t}W(\phi, \vec{x}, t) + \frac{\tau_q}{\alpha}\frac{\partial^2}{\partial t^2}W(\phi, \vec{x}, t) & \Omega \times (0, +\infty) \\ - \triangle W(\phi, \vec{x}, t) - \tau_T \frac{\partial}{\partial t} \triangle W(\phi, \vec{x}, t) = 0, \\ L[W(\phi, \vec{x}, t), \frac{\partial}{\partial n}W(\phi, \vec{x}, t)] \mid_{\partial\Omega} = 0, \\ W(\phi, \vec{x}, 0) = 0, \frac{\partial}{\partial t}W(\phi, \vec{x}, 0) = \phi(p), \end{cases} \tag{74}$$

and

$$\begin{cases} \frac{1}{\alpha}\frac{\partial}{\partial t}W(\phi_1, \vec{x}, t) + \frac{\tau_q}{\alpha}\frac{\partial^2}{\partial t^2}W(\phi_1, \vec{x}, t) & \Omega \times (0, +\infty) \\ - \triangle W(\phi_1, \vec{x}, t) - \tau_T \frac{\partial}{\partial t} \triangle W(\phi_1, \vec{x}, t) = 0, \\ L[W(\phi_1, \vec{x}, t), \frac{\partial}{\partial n}W(\phi_1, \vec{x}, t)] \mid_{\partial\Omega} = 0, \\ W(\phi_1, \vec{x}, 0) = 0, \frac{\partial}{\partial t}W(\phi_1, \vec{x}, 0) = \phi_1(p). \end{cases} \tag{75}$$

Hence

$$\begin{aligned} &\frac{1}{\alpha}\frac{\partial}{\partial t}T_1 + \frac{\tau_q}{\alpha}\frac{\partial^2}{\partial t^2}T_1 - \triangle T_1 - \tau_T\frac{\partial}{\partial t} \triangle T_1 \\ &= \frac{1}{\tau_q}\left[\frac{1}{\alpha}\frac{\partial W(\phi, \vec{x}, t)}{\partial t} + \frac{\tau_T}{\alpha}\frac{\partial^2 W(\phi, \vec{x}, t)}{\partial t^2} - \triangle W(\phi, \vec{x}, t) - \tau_T\frac{\partial}{\partial t} \triangle W(\phi, \vec{x}, t)\right] \\ &\quad + \frac{\partial}{\partial t}\left[\frac{1}{\alpha}\frac{\partial W(\phi, \vec{x}, t)}{\partial t} + \frac{\tau_q}{\alpha}\frac{\partial^2 W(\phi, \vec{x}, t)}{\partial t^2} - \triangle W(\phi, \vec{x}, t) - \tau_T\frac{\partial}{\partial t} \triangle W(\phi, \vec{x}, t)\right] \\ &\quad + \frac{1}{\tau_q}\left[\frac{1}{\alpha}\frac{\partial W(\phi_1, \vec{x}, t)}{\partial t} + \frac{\tau_q}{\alpha}\frac{\partial^2 W(\phi_1, \vec{x}, t)}{\partial t^2} - \triangle W(\phi_1, \vec{x}, t) - \tau_T\frac{\partial}{\partial t} \triangle W(\phi_1, \vec{x}, t)\right] \\ &\quad = 0 \end{aligned}$$

which indicates that the T_1 in (72) satisfies the equation in (69).

Also,

$$\begin{aligned} L(T_1, \frac{\partial}{\partial n}T_1) = L\Bigg\{ &\frac{1}{\tau_q}\left[W(\phi, \vec{x}, t) + \tau_q\frac{\partial W(\phi, \vec{x}, t)}{\partial t} + W(\phi_1, \vec{x}, t)\right], \\ &\frac{1}{\tau_q}\frac{\partial}{\partial n}\left[W(\phi, \vec{x}, t) + \tau_q\frac{\partial W(\phi, \vec{x}, t)}{\partial t} + W(\phi_1, \vec{x}, t)\right]\Bigg\} \\ = &\frac{1}{\tau_q}L\left[W(\phi, \vec{x}, t), \frac{\partial}{\partial n}W(\phi, \vec{x}, t)\right] \end{aligned}$$

$$+\frac{\partial}{\partial t}L\left[W(\phi,\vec{x},t),\frac{\partial}{\partial n}W(\phi,\vec{x},t)\right]$$
$$+\frac{1}{\tau_q}L\left[W(\phi_1,\vec{x},t),\frac{\partial}{\partial n}W(\phi_1,\vec{x},t)\right],$$

and

$$\begin{aligned}L(T_1,\frac{\partial}{\partial n}T_1)\mid_{\partial\Omega}=&\ \frac{1}{\tau_q}L\left[W(\phi,\vec{x},t),\frac{\partial}{\partial n}W(\phi,\vec{x},t)\right]\mid_{\partial\Omega}\\&+\frac{\partial}{\partial t}L\left[W(\phi,\vec{x},t),\frac{\partial}{\partial n}W(\phi,\vec{x},t)\right]\mid_{\partial\Omega}\\&+\frac{1}{\tau_q}L\left[W(\phi_1,\vec{x},t),\frac{\partial}{\partial n}W(\phi_1,\vec{x},t)\right]\mid_{\partial\Omega}=0\end{aligned}$$

in which boundary conditions in (74) and (75) have been used. This indicates that the T_1 in (72) satisfies the boundary condition in (69).

Finally, by (74) and (75),

$$\begin{aligned}T_1(\vec{x},0)&=\tfrac{1}{\tau_q}\left[W(\phi,\vec{x},t)+\tau_q\tfrac{\partial W(\phi,\vec{x},t)}{\partial t}+W(\phi_1,\vec{x},t)\right]\mid_{t=0}\\&=\tfrac{1}{\tau_q}\left[W(\phi,\vec{x},0)+\tau_q\tfrac{\partial W(\phi,\vec{x},0)}{\partial t}+W(\phi_1,\vec{x},0)\right]\\&=\tfrac{\partial W(\phi,\vec{x},0)}{\partial t}=\phi\end{aligned}$$

and

$$\begin{aligned}\tfrac{\partial}{\partial t}T_1(\vec{x},t)\mid_{t=0}&=\tfrac{1}{\tau_q}\tfrac{\partial}{\partial t}\left[W(\phi,\vec{x},t)+\tau_q\tfrac{\partial W(\phi,\vec{x},t)}{\partial t}+W(\phi_1,\vec{x},t)\right]\mid_{t=0}\\&=\tfrac{1}{\tau_q}\tfrac{\partial}{\partial t}\left[W(\phi,\vec{x},t)+\tau_q\tfrac{\partial W(\phi,\vec{x},t)}{\partial t}\right]\mid_{t=0}+\tfrac{\phi_1(p)}{\tau_q}\\&=\tfrac{\alpha}{\tau_q}\left[\triangle W(\phi,\vec{x},t)+\tau_T\tfrac{\partial}{\partial t}(\triangle W(\phi,\vec{x},t))\right]\mid_{t=0}+\tfrac{\phi_1(p)}{\tau_q}\\&=\alpha\tfrac{\tau_T}{\tau_q}\triangle\phi(p)+\tfrac{1}{\tau_q}\phi_1(p)=0.\end{aligned}$$

Therefore, the T_1 in (72) also satisfies initial conditions in (69).

Theorem 3. *Let $W(\psi,\vec{x},t)$ denote the solution of (71). The solution of (70) can be written as*

$$T_2(\vec{x},t)=\int_0^t W(f_\tau,\vec{x},t-\tau)d\tau, \tag{76}$$

where

$$f_\tau=\frac{\alpha}{\tau_q}f(\vec{x},\tau). \tag{77}$$

Proof. As $W(\psi,\vec{x},t)$ is the solution of (71), we have

$$\begin{cases} \frac{1}{\alpha}\frac{\partial}{\partial t}W(f_\tau, \vec{x}, t-\tau) + \frac{\tau_q}{\alpha}\frac{\partial^2}{\partial t^2}W(f_\tau, \vec{x}, t-\tau) & \Omega \times (0, +\infty) \\ -\triangle W(f_\tau, \vec{x}, t-\tau) - \tau_T \frac{\partial}{\partial t}\triangle W(f_\tau, \vec{x}, t-\tau) = 0; \\ L\left[W(f_\tau, \vec{x}, t-\tau), \frac{\partial}{\partial n}W(f_\tau, \vec{x}, t-\tau)\right]|_{\partial\Omega} = 0, \\ W(f_\tau, \vec{x}, t-\tau)|_{t=\tau} = 0, \frac{\partial}{\partial t}W(f_\tau, \vec{x}, t-\tau)|_{t=\tau} = \frac{\alpha}{\tau_q} f(\vec{x}, \tau). \end{cases} \tag{78}$$

Therefore,

$$\begin{aligned} & \frac{1}{\alpha}\frac{\partial}{\partial t}T_2 + \frac{\tau_q}{\alpha}\frac{\partial^2}{\partial t^2}T_2 - \triangle T_2 - \tau_T \frac{\partial}{\partial t}\triangle T_2 \\ = & \frac{1}{\alpha}\frac{\partial}{\partial t}\int_0^t W(f_\tau, \vec{x}, t-\tau)d\tau + \frac{\tau_q}{\alpha}\frac{\partial^2}{\partial t^2}\int_0^t W(f_\tau, \vec{x}, t-\tau)d\tau \\ & - \triangle \int_0^t W(f_\tau, \vec{x}, t-\tau)d\tau - \tau_T \frac{\partial}{\partial t}\triangle \int_0^t W(f_\tau, \vec{x}, t-\tau)d\tau \\ = & \frac{1}{\alpha}\left[\int_0^t \frac{\partial W(f_\tau, \vec{x}, t-\tau)}{\partial t}d\tau + W(f_\tau, \vec{x}, t-\tau)|_{\tau=t}\right] \\ & + \frac{\tau_q}{\alpha}\left[\int_0^t \frac{\partial^2 W(f_\tau, \vec{x}, t-\tau)}{\partial t^2} + \frac{\partial W(f_\tau, \vec{x}, t-\tau)}{\partial t}|_{\tau=t}\right] \\ & - \triangle \int_0^t W(f_\tau, \vec{x}, t-\tau)d\tau - \tau_T \triangle \frac{\partial}{\partial t}\int_0^t W(f_\tau, \vec{x}, t-\tau)d\tau \\ = & \int_0^t \frac{1}{\alpha}\frac{\partial W(f_\tau, \vec{x}, t-\tau)}{\partial t}d\tau + \int_0^t \frac{\tau_q}{\alpha}\frac{\partial^2 W(f_\tau, \vec{x}, t-\tau)}{\partial t^2}d\tau + f(\vec{x}, t) \\ & - \int_0^t \triangle W(f_\tau, \vec{x}, t-\tau)d\tau - \int_0^t \tau_T \triangle \frac{\partial W(f_\tau, \vec{x}, t-\tau)}{\partial t}d\tau = f(\vec{x}, t) \end{aligned}$$

which indicates that the T_2 in (76) satisfies the equation in (70).

Also,

$$\begin{aligned} L(T_2, \tfrac{\partial}{\partial n}T_2)|_{\partial\Omega} &= L\left[\textstyle\int_0^t W(f_\tau, \vec{x}, t-\tau)d\tau, \frac{\partial}{\partial n}\int_0^t W(f_\tau, \vec{x}, t-\tau)d\tau\right]|_{\partial\Omega} \\ &= L\left[\textstyle\int_0^t W(f_\tau, \vec{x}, t-\tau)d\tau, \int_0^t \frac{\partial}{\partial n}W(f_\tau, \vec{x}, t-\tau)d\tau\right]|_{\partial\Omega} \\ &= \textstyle\int_0^t L\left[W(f_\tau, \vec{x}, t-\tau), \frac{\partial}{\partial n}W(f_\tau, \vec{x}, t-\tau)\right]|_{\partial\Omega}\, d\tau = 0, \end{aligned}$$

in which the boundary condition in (78) has been used. Therefore, the T_2 in (76) satisfies the boundary condition in (70).

Finally,

$$T_2(\vec{x}, 0) = \int_0^0 W(f_\tau, \vec{x}, t-\tau)d\tau = 0,$$

and, by (78),

$$\frac{\partial}{\partial t}T_2(\vec{x},t)\mid_{t=0}=\left[\int_0^t\frac{\partial}{\partial t}W(f_\tau,\vec{x},t-\tau)d\tau+W(f_\tau,\vec{x},t-\tau)\mid_{\tau=t}\right]\mid_{t=0}=0.$$

Therefore, the T_2 in (76) also satisfies initial conditions in (70).

By Theorems 2 and 3 and the principle of superposition, we can express the solution $T(\vec{x},t)$ of

$$\begin{cases}\frac{1}{\alpha}T_t(\vec{x},t)+\frac{\tau_q}{\alpha}T_{tt}(\vec{x},t)=\triangle T(\vec{x},t)+\tau_T\frac{\partial}{\partial t}\triangle T(\vec{x},t)+f(\vec{x},t),\ \Omega\times(0,+\infty)\\ L(T,T_n)|_{\partial\Omega}=0,\\ T(\vec{x},0)=\phi(p),\ T_t(\vec{x},0)=\psi(p)\end{cases}\tag{79}$$

in term of W as

$$\begin{aligned}T(\vec{x},t)=\ & W(\psi,\vec{x},t)+\frac{1}{\tau_q}\left[W(\phi,\vec{x},t)+\tau_q\frac{\partial W(\phi,\vec{x},t)}{\partial t}+W(\phi_1,\vec{x},t)\right]\\ &+\int_0^t W(f_\tau,\vec{x},t-\tau)d\tau\end{aligned}\tag{80}$$

with ϕ_1 and f_τ defined by (73) and (77). The details of W depend on Ω and boundary conditions, and are available in Wang and Zhou (2000, 2001) and Wang et al. (2008).

4 Thermal Oscillation and Resonance

Thermal features of the dual-phase-lagging heat conduction have been and still are the object of intense investigations due to its intrinsic interest and its relevance to the emerging technologies involving ultrafast pulse-laser heating, superfluid liquid helium, porous media, bio-transport and amorphous materials. The readers are refereed to Wang et al. (2008) for a comprehensive list of the references. Here we follow Xu and Wang (2002) in studying conditions and features of thermal oscillation and resonance and in comparing with those in the classical and hyperbolic heat conduction.

4.1 Thermal Oscillation

Without losing the generality, Xu and Wang (2002) consider the one-dimensional initial-boundary value problem of dual-phase-lagging heat conduction

$$\begin{cases}\frac{1}{\alpha}(\frac{\partial T}{\partial t}+\tau_q\frac{\partial^2 T}{\partial t^2})=\frac{\partial^2 T}{\partial x^2}+\tau_T\frac{\partial^3 T}{\partial t\partial x^2}+\frac{1}{k}(S+\tau_q\frac{\partial S}{\partial t}),\ (0,l)\times(0,+\infty),\\ T(0,t)=T(l,t)=0,\\ T(x,0)=\phi(x),\ T_t(x,0)=\psi(x),\end{cases}\tag{81}$$

whose solution represents the temperature distribution in an infinitely-wide slab of thickness l. Here t is the time, T is the temperature, α is the thermal diffusivity of the medium, S is the volumetric heat source, ϕ and ψ are two given functions, τ_T and τ_q are the phase lags of the temperature gradient and heat flux vector, respectively.

For a free thermal oscillation, $S = 0$. By taking the boundary conditions into account, let

$$T(x,t) = \sum_{m=1}^{\infty} \Gamma_m(t) sin\beta_m x, \tag{82}$$

where

$$\beta_m = \frac{m\pi}{l}.$$

Using the Fourier sine series to express ϕ and ψ as

$$\phi(x) = \sum_{m=1}^{\infty} \phi_m sin\beta_m x, \tag{83}$$

and

$$\psi(x) = \sum_{m=1}^{\infty} \psi_m sin\beta_m x, \tag{84}$$

where

$$\phi_m = \frac{2}{l}\int_0^l \phi(\xi) sin\beta_m \xi d\xi,$$

and

$$\psi_m = \frac{2}{l}\int_0^l \psi(\xi) sin\beta_m \xi d\xi.$$

A substitution of (82), (83) and (84) into (81) yields, by making use of the orthogonality of $sin(\beta_m X)(m = 1, 2, \cdots)$,

$$\tau_q \ddot{\Gamma}_m + (1 + \alpha\tau_T\beta_m^2)\dot{\Gamma}_m + \beta_m^2 \alpha \Gamma_m = 0, \tag{85}$$

$$\Gamma_m(0) = \phi_m, \dot{\Gamma}_m(0) = \psi_m. \tag{86}$$

Introduce the damping coefficient f_m by

$$f_m = \frac{1}{\tau_q} + \tau_T \omega_m^2$$

and the natural frequency coefficient ω_m by

$$\omega_m^2 = \frac{\alpha\beta_m^2}{\tau_q}.$$

Equation (85) reduces to

$$\ddot{\Gamma}_m + f_m\,\dot{\Gamma}_m + \omega_m^2\Gamma_m = 0. \tag{87}$$

The solution of (87) can be readily obtained by the method of undetermined coefficients as

$$\Gamma_m(t) = be^{\lambda t} \tag{88}$$

with λ as a coefficient to be determined. Substituting (88) into (87) leads to

$$\lambda^2 + f_m\lambda + \omega_m^2 = 0, \tag{89}$$

which has solutions λ_1, λ_2

$$\lambda_{1,2} = -\frac{f_m}{2} \pm \sqrt{\Lambda}. \tag{90}$$

Here Λ is the discriminate of (89) and is defined by

$$\Lambda = \left(\frac{f_m}{2}\right)^2 - \omega_m^2.$$

Therefore, a positive, negative and vanished discriminate yields two distinct real λ_1, λ_2, two complex conjugate λ_1, λ_2, and two equal real λ_1, λ_2, respectively. The critical damping coefficient f_{mc} is referred to the damping coefficient at a fixed ω_m and $\Lambda = 0$. Therefore,

$$f_{mc} = 2\omega_m. \tag{91}$$

The nondimensional damping ratio, ζ_m, is defined as the ratio of f_m over f_{mc},

$$\zeta_m = \frac{f_m}{f_{mc}} = \frac{f_m}{2\omega_m} = \frac{1}{2\tau_q\omega_m} + \frac{\tau_T\omega_m}{2}. \tag{92}$$

The system is at underdamped oscillation, critically-damped oscillation or overdamped oscillation, respectively when $\zeta_m < 1$, $\zeta_m = 1$ or $\zeta_m > 1$. By (90) and (92), Xu and Wang (2002) obtain an expression of $\lambda_{1,2}$ in terms of ζ_m and ω_m,

$$\lambda_{1,2} = \omega_m\left(-\zeta_m \pm \sqrt{\zeta_m^2 - 1}\right). \tag{93}$$

Underdamped Oscillation

For this case ($\zeta_m < 1$), there are two complex conjugate λ_1, λ_2,

$$\lambda_{1,2} = \omega_m \left(-\zeta_m \pm i\sqrt{1-\zeta_m^2} \right). \tag{94}$$

Therefore

$$\Gamma_m(t) = e^{-\zeta_m \omega_m t} \left(a_m cos\omega_m t\sqrt{1-\zeta_m^2} + b_m sin\omega_m t\sqrt{1-\zeta_m^2} \right). \tag{95}$$

After the determination of integration constants a_m and b_m by the initial conditions (86), Xu and Wang (2002) obtain

$$\Gamma_m(t) = e^{-\zeta_m \omega_m t} \left(\phi_m cos\omega_m t\sqrt{1-\zeta_m^2} + \frac{\psi_m + \zeta_m \omega_m \phi_m}{\omega_m \sqrt{1-\zeta_m^2}} sin\omega_m t\sqrt{1-\zeta_m^2} \right) \tag{96}$$

which may be rewritten as

$$\Gamma_m(t) = A_m e^{-\zeta_m \omega_m t} sin(\omega_{dm} t + \varphi_{dm}). \tag{97}$$

Here,

$$A_m = \sqrt{\phi_m^2 + \left(\frac{\psi_m + \zeta_m \omega_m \phi_m}{\omega_{dm}} \right)^2}, \tag{98}$$

$$\omega_{dm} = \omega_m \sqrt{1-\zeta_m^2}, \tag{99}$$

$$\varphi_{dm} = tan^{-1} \left(\frac{\phi_m \omega_{dm}}{\psi_m + \zeta_m \omega_m \phi_m} \right). \tag{100}$$

Therefore, the system is oscillating with the frequency ω_{dm} and an exponentially decaying amplitude $A_m e^{-\zeta_m \omega_m t}$. Figure 1 typifies the oscillatory pattern, for $\zeta_m = 0.1$, $\phi_m = 1.0$, $\psi_m = 0.0$ and $\omega_m = 1.0$. The wave behavior is still observed in the

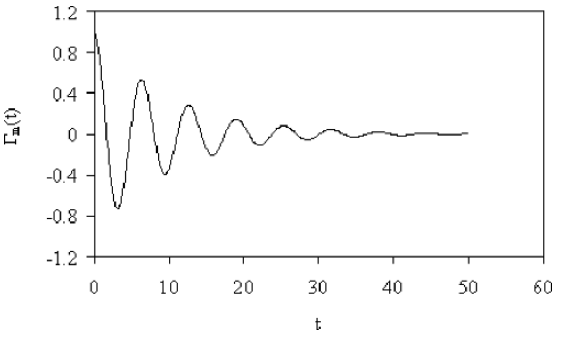

Fig. 1 Variation of $\Gamma_m(t)$ with the time t: $\zeta_m = 0.1$, $\phi_m = 1.0$, $\psi_m = 0.0$, $\omega_m = 1.0$ (after Xu and Wang 2002)

dual-phase-lagging heat conduction. However, the amplitude decays exponentially due to the damping of thermal diffusion. This differs very much from the classical heat conduction. $\zeta_m < 1$ forms the condition for the thermal oscillation of this kind.

Figure 2 illustrates the variation of $\Gamma_m(t)$ with the time t when ψ_m is changed to 1.0 from 0. Γ_m is observed to be able of surpassing ϕ_m at some instants. Such phenomenon is caused by the no-vanishing initial time-rate change of the temperature and cannot appear in the classical heat conduction. The classical maximum and minimum principle is, therefore, not valid in the dual-phase-lagging heat conduction.

While $\Gamma_m(t)$ is oscillatory, it is not periodic because of the decaying amplitude. $\Gamma_m(t)$ oscillates in time with a fixed damped period T_{dm} given by

$$T_{dm} = \frac{2\pi}{\omega_{dm}}. \tag{101}$$

4.1.1 Critically-Damped Oscillation

For this case, $\zeta_m = 1$. This requires, by (92),

$$\omega_m = \frac{1 \pm \sqrt{1 - \frac{\tau_T}{\tau_q}}}{\tau_T}. \tag{102}$$

Therefore, the critically damped oscillation appears only when $\tau_T \leq \tau_q$. When the system is in the critically damped oscillation, there are two equal λ_1, λ_2. Therefore,

$$\Gamma_m(t) = a_m e^{-\omega_m t} + b_m t e^{-\omega_m t},$$

which becomes after determining the integration constants a_m and b_m by the initial conditions (86),

$$\Gamma_m(t) = e^{-\omega_m t}[\phi_m + (\psi_m + \omega_m \phi_m)t]. \tag{103}$$

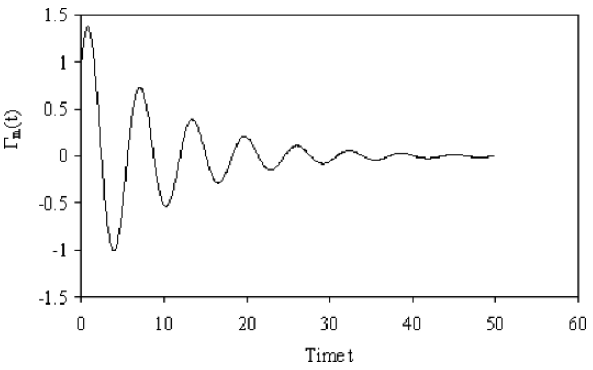

Fig. 2 Variation of $\Gamma_m(t)$ with the time t: $\zeta_m = 0.1$, $\phi_m = 1.0$, $\psi_m = 1.0$, $\omega_m = 1.0$ (after Xu and Wang 2002)

By letting $\frac{d|\Gamma_m(t)|}{dt} = 0$ and analyzing the sign of $\frac{d^2|\Gamma_m(t)|}{dt^2}$, Xu and Wang (2002) obtain the maximal value of $|\ \Gamma_m(t)\ |$

$$Max[|\ \Gamma_m(t)\ |] = e^{-\frac{\psi_m}{\psi_m + \omega_m \phi_m}} \left| \phi_m + \frac{\psi_m}{\omega_m} \right| \tag{104}$$

at

$$t_m = \frac{\psi_m}{\omega_m(\psi_m + \omega_m \phi_m)}, \tag{105}$$

that is positive if

$$\psi_m^2 > -\omega_m \phi_m \psi_m.$$

This clearly requires that $\psi_m \neq 0$. Therefore, $|\ \Gamma_m(t)\ |$ decreases monotonically as t increases from 0 when

$$\psi_m^2 \leq -\omega_m \phi_m \psi_m.$$

This is very similar to that in the classical heat-conduction equation. When

$$\psi_m^2 > -\omega_m \phi_m \psi_m,$$

however, $|\ \Gamma_m(t)\ |$ first increases from ϕ_m to $Max[|\ \Gamma_m(t)\ |]$ as t increases from 0 to t_m and then decreases monotonically (Fig. 3). Therefore, although the temperature field does not oscillate, its absolute value reaches the maximum value at $t = t_m > 0$ rather than at the initial time instant $t = 0$.

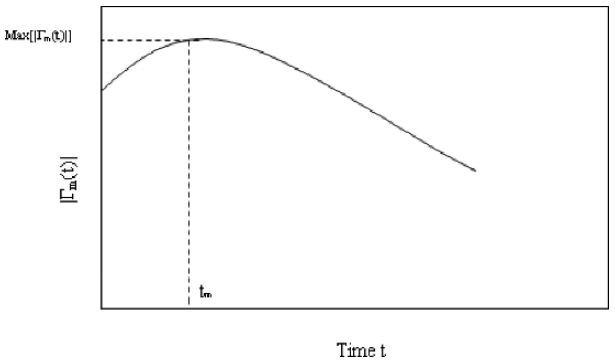

Fig. 3 $|\ \Gamma_m(t)\ |$ at the critically damped oscillation and $\psi_m^2 > -\omega_m \phi_m \psi_m$ (after Xu and Wang 2002)

4.1.2 Overdamped Oscillation

For this case ($\zeta_m > 1$),

$$\lambda_{1,2} = \omega_m \left(-\zeta_m \pm \sqrt{\zeta_m^2 - 1} \right). \tag{106}$$

The solution of (87) is, thus, subject to the condition (86),

$$\begin{aligned} \Gamma_m(t) = \frac{e^{-\zeta_m \omega_m t}}{2\sqrt{\zeta_m^2 - 1}} \left[\left(\frac{\psi_m}{\omega_m} + \phi_m \left(\zeta_m + \sqrt{\zeta_m^2 - 1} \right) \right) e^{\omega_m t \sqrt{\zeta_m^2 - 1}} + \right. \\ \left. \left(-\frac{\psi_m}{\omega_m} + \phi_m \left(-\zeta_m + \sqrt{\zeta_m^2 - 1} \right) \right) e^{-\omega_m t \sqrt{\zeta_m^2 - 1}} \right]. \end{aligned} \tag{107}$$

Letting $\frac{d|\Gamma_m(t)|}{dt} = 0$ leads to two extreme points,

$$t_{m1} = 0 \tag{108}$$

and

$$t_{m2} = -\frac{1}{2\omega_m \sqrt{\zeta_m^2 - 1}} ln \left[\frac{\zeta_m - \sqrt{\zeta_m^2 - 1}}{\zeta_m + \sqrt{\zeta_m^2 - 1}} \frac{\frac{\psi_m}{\omega_m} + \phi_m \left(\zeta_m + \sqrt{\zeta_m^2 - 1} \right)}{\frac{\psi_m}{\omega_m} + \phi_m \left(\zeta_m - \sqrt{\zeta_m^2 - 1} \right)} \right], \tag{109}$$

with Max1$[|\Gamma_m(t)|] = |\phi_m|$ and Max2$[|\Gamma_m(t)|]$=$|\Gamma_m(t_{m2})|$, respectively. Therefore, $|\Gamma_m(t)|$ decreases monotonically from $t = 0$ when $t_{m2} = 0$ (very like that in classical heat conduction). When $t_{m2} > 0$, however, $|\Gamma_m(t)|$ first increases from $|\phi_m|$ to a maximal value Max2$[|\Gamma_m(t)|]$ as t increases from 0 to t_{m2} and then decreases for $t \geq t_m$ (Fig. 4). There is no oscillation if $\zeta_m > 1$.

When $\tau_T > \tau_q$,

$$1 + \alpha \tau_T \frac{m^2 \pi^2}{l^2} > 1 + \alpha \tau_q \frac{m^2 \pi^2}{l^2} \geq 2\sqrt{\alpha \tau_q} \frac{m\pi}{l}.$$

This, with (92), yields

$$\zeta_m = \frac{1 + \tau_T \alpha \frac{m^2 \pi^2}{l^2}}{2\sqrt{\alpha \tau_q} \frac{m\pi}{l}} > 1.$$

Therefore the system is always at the overdamped oscillation if $\tau_T > \tau_q$. Consequently, there is no thermal oscillation.

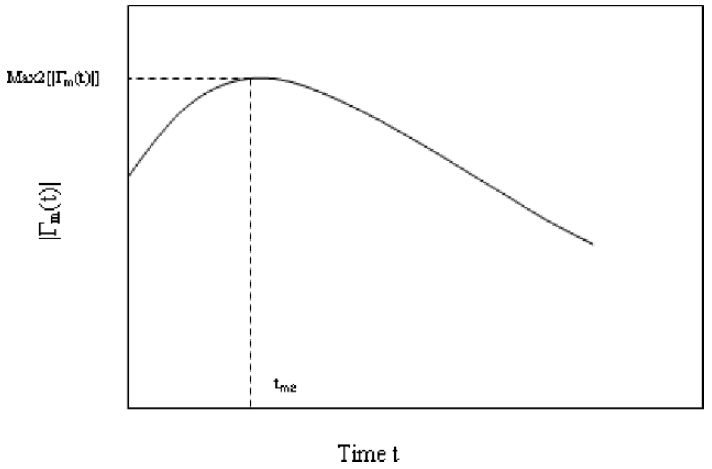

Fig. 4 | $\Gamma_m(t)$ | at the overdamped oscillation and $t_{m2} > 0$ (after Xu and Wang 2002)

$\zeta_m = 1.0$ separates the underdamped modes from the overdamped modes. Applying $\zeta_m < 1$ in (92) yields the region of m where the underdamped modes can occur:

$$\begin{array}{ll} \frac{l}{\pi C_1} < m < \frac{l}{\pi C_2}, & \text{if } \tau_q > \tau_T > 0; \\ m > \frac{l}{\pi C}, & \text{if } \tau_q > \tau_T = 0. \end{array} \tag{110}$$

Here C_1 and C_2 are the relaxation distances defined by Tzou (1992)

$$C_1 = \sqrt{\alpha\tau_T}\left(\sqrt{\frac{\tau_q}{\tau_T}} + \sqrt{\frac{\tau_q}{\tau_T} - 1}\right),$$

$$C_2 = \sqrt{\alpha\tau_T}\left(\sqrt{\frac{\tau_q}{\tau_T}} - \sqrt{\frac{\tau_q}{\tau_T} - 1}\right),$$

$$C = 2\sqrt{\alpha\tau_q}.$$

Therefore, the thermal oscillation occurs only for the modes between $\frac{l}{\pi C_1}$ and $\frac{l}{\pi C_2}$ for the case of $\tau_q > \tau_T > 0$. This is different from the thermal wave in the hyperbolic heat conduction where the oscillation appears always for the high order modes (Tzou 1992).

The behavior of an individual temperature mode discussed above also represents the entire thermal response if $\phi(x) = A\sin\frac{m\pi x}{l}$ and $\psi(x) = B\sin\frac{m\pi x}{l}$ with A and B as constants. For the general case, a change $\triangle\Gamma_m(t)$ in the $m-$th mode would lead to a change $\triangle\Gamma_m(t)\sin\frac{m\pi x}{l}$ in $T(x,t)$ because

$$T(x,t) = \sum_{m=1}^{\infty} \Gamma_m(t)\sin\frac{m\pi x}{l}.$$

4.2 Resonance

For the dual-phase-lagging heat conduction, the amplitude of the thermal wave may become exaggerated if the oscillating frequency of an externally applied heat source is at the resonance frequency.

Consider a heat source in the system (81) in the form of

$$S(x,t) = Qg(x)e^{i\Omega t}.$$

Here Q, independent of x and t, is the strength, $g(x)$ is the spanwise distribution, and Ω is the oscillating frequency. Expand $T(x,t)$ and $g(x)$ by the Fourier sine series,

$$T(x,t) = \sum_{m=1}^{\infty} \Gamma_m(t) sin(\beta_m x), \tag{111}$$

$$g(x) = \sum_{m=1}^{\infty} D_m sin(\beta_m x), \tag{112}$$

where $\Gamma_m(t)$ and β_m are defined in the last subsection, and

$$D_m = \frac{2}{l}\int_0^l g(x) sin(\beta_m x) dx. \tag{113}$$

Such a $T(x,t)$ in (111) automatically satisfies the boundary conditions in (81). Substituting (111) and (112) into the equation in (81) and making use of the orthogonality of the set $sin(\beta_m x)$ yield

$$\ddot{\Gamma}_m(t) + 2\zeta_m\omega_m\dot{\Gamma}_m(t) + \omega_m^2\Gamma_m(t) = \frac{QD_m\alpha}{k\tau_q}(1 + i\Omega\tau_q)e^{i\Omega t}, \tag{114}$$

whose solution is readily obtained as

$$\Gamma_m(t) = B_m e^{(\Omega t + \varphi_m)i}. \tag{115}$$

Here,

$$B_m = \frac{QD_m\alpha}{k\omega_m} B_{\Omega^* m}, \tag{116}$$

$$B_{\Omega^* m} = \frac{\eta_m + i\Omega^*{}_m}{\sqrt{(1-\Omega^*{}_m{}^2)^2 + 4\zeta_m^2\Omega^*{}_m{}^2}}, \tag{117}$$

$$tan^{-1}(\varphi_m) = -\frac{2\zeta_m\Omega^*{}_m}{1-\Omega^{*2}_m}, \tag{118}$$

$$\eta_m = \frac{1}{\sqrt{\alpha \tau_q}\beta_m}, \tag{119}$$

$$\Omega^*{}_m = \frac{\Omega}{\omega_m}. \tag{120}$$

For the resonance, $|B_{\Omega^* m}|^2$ reaches its maximum value. Note that, by (117),

$$|B_{\Omega^*{}_m}|^2 = \frac{\eta_m^2 + \Omega^{*2}_m}{\left(1 - \Omega^{*2}_m\right)^2 + 4\zeta_m^2 \Omega^{*2}_m}. \tag{121}$$

Therefore, the resonance requires

$$\frac{\partial |B_{\Omega^*_m}|^2}{\partial \Omega^{*2}_m} = 0,$$

which yields, by noting also that $\Omega^*_m \geq 0$,

$$\Omega^*_{mr}{}^2 = -\eta_m^2 + \sqrt{\left(1 + \eta_m^2\right)^2 - 4\zeta_m^2 \eta_m^2}, \tag{122}$$

where Ω^*_{mr} stands for the external source frequency at resonance. As Ω^*_{mr} must be real, Xu and Wang (2002) obtain another condition for the resonance in addition to (122),

$$(1 + \eta_m^2)^2 - 4\zeta_m^2 \eta_m^2 > \eta_m^4. \tag{123}$$

The variation of Ω^*_{mr} with the ζ_m and η_m is shown in Figs. 5 and 6. It is observed that Ω^*_{mr} decreases as the damping parameter ζ_m and the phase lagging parameter η_m increase. Figure 7 illustrates the variation of $|B_{\Omega^*_m}|$ with Ω^*_m and ζ_m at $\eta_m = 1$. For $\zeta_m = 0.9$, Eq. (123) cannot be satisfied. Therefore, there is no resonance when $\zeta_m = 0.9$ at $\eta_m = 1$ (Fig. 7).

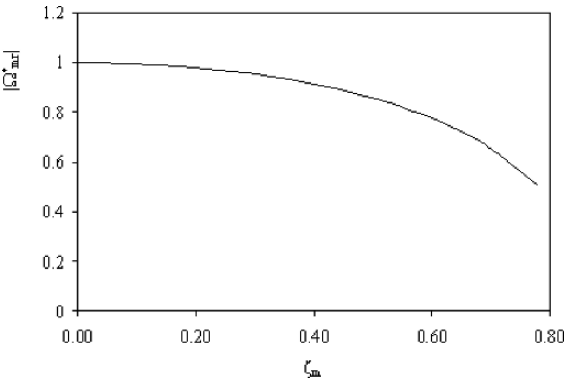

Fig. 5 Variation of $|\Omega^*_{mr}|$ with ζ_m at $\eta_m = 1.0$ (after Xu and Wang 2002)

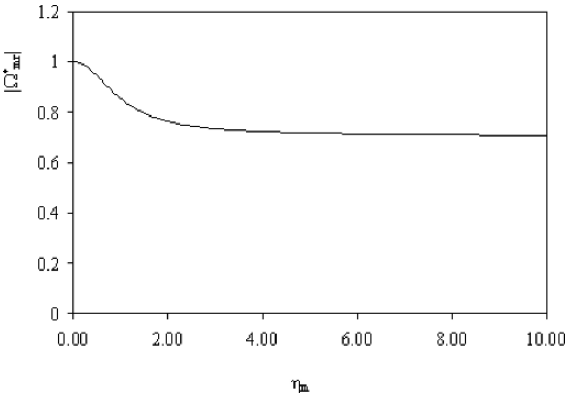

Fig. 6 Variation of $|\ \Omega^*_{mr}\ |$ with η_m at $\zeta_m = 0.5$ (after Xu and Wang 2002)

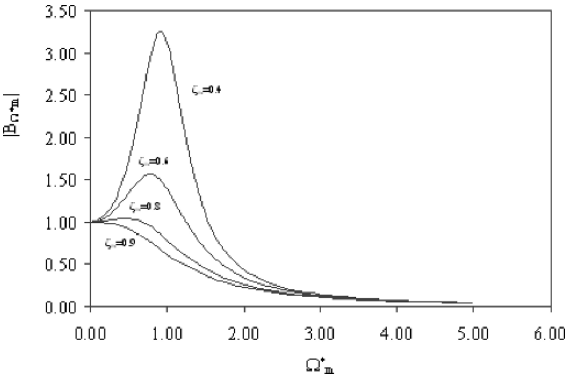

Fig. 7 Variation of $|B_{\Omega^*_m}|$ with Ω^*_m and ζ_m at $\eta_m = 1$ (after Xu and Wang 2002)

5 Equivalence Between Dual-Phase-Lagging and Porous-Medium Heat Conduction Processes

The microscale model for heat conduction in porous media is well-known. It consists of field equation and constitutive equation. The field equation comes from the conservation of energy (the first law of thermodynamics). The commonly-used constitutive equation is the Fourier law of heat conduction for the relation between the temperature gradient ∇T and the heat flux density vector $\mathbf{q}$ (Wang 1994).

For transport in porous media, the macroscale (so-called Darcy scale in the literature) is a phenomenological scale that is much larger than the microscale of pores and grains and much smaller than the system length scale. The interest in the macroscale rather than the microscale comes from the fact that a prediction at the microscale is complicated because of complex microscale geometry of porous media, and that we are usually more interested in large scales of transport for practical applications. Existence of such a macroscale description equivalent to the microscale behavior requires a good separation of length scale and has been well discussed by Auriault (1991).

To develop a macroscale model of transport in porous media, the method of volume averaging starts with a microscale description (Whitaker 1999, Wang 2000b).

Both conservation and constitutive equations are introduced at the microscale. Resulting microscale field equations are then averaged over a representative elementary volume (REV), the smallest differential volume resulting in statistically meaningful local average properties, to obtain macroscale field equations. In the process of averaging, *averaging theorems* are used to convert integrals of gradient, divergence, curl, and partial time derivatives of a function to some combination of gradient, divergence, curl, and partial time derivatives of integrals of the function and integrals over the boundary of the REV (Whitaker 1999, Wang 2000b). The readers are referred to Whitaker (1999) and Wang (2000b) for the details of the method of volume averaging and to Wang (2000b) for the other methods of obtaining macroscale models.

Quintard and Whitaker (1993) use the method of volume averaging to develop one- and two-equation macroscale models for heat conduction in porous media. First, they define the microscale problem by the first law of thermodynamics and the Fourier law of heat conduction (Fig. 8)

$$(\rho c)_f \frac{\partial T_f}{\partial t} = \nabla \cdot (k_f \nabla T_f), \text{ in the fluid phase } f \tag{124}$$

$$(\rho c)_s \frac{\partial T_s}{\partial t} = \nabla \cdot (k_s \nabla T_s), \text{ in the solid phase } s \tag{125}$$

$$T_f = T_s, \text{ at the fluid-solid interface } A_{fs} \tag{126}$$

$$\mathbf{n}_{fs} \cdot k_f \nabla T_f = \mathbf{n}_{fs} \cdot k_s \nabla T_s, \text{ at the fluid-solid interface } A_{fs} \tag{127}$$

Here ρ, c and k are the density, specific heat and thermal conductivity, respectively, subscripts f and s refer to the fluid and solid phases, respectively, A_{fs} represents the area of the fluid-solid interface contained in the REV; $\mathbf{n}_{fs}$ is the outward-directed surface normal from the fluid-phase toward the solid-phase, and $\mathbf{n}_{fs} = -\mathbf{n}_{sf}$ (Fig. 8). To be complete, Quintard and Whitaker (1993) have also specified the initial conditions and the boundary conditions at the entrances and exits of the REV; however, we need not do so for our discussion.

Next Quintard and Whitaker (1993) apply the superficial averaging process to (124) and (125) to obtain,

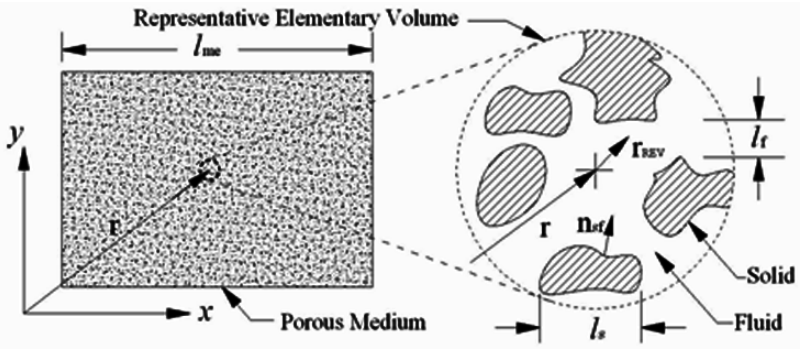

Fig. 8 Rigid porous medium system

$$\frac{1}{V_{\mathrm{REV}}}\int_{V_f}(\rho c)_f\frac{\partial T_f}{\partial t}dV=\frac{1}{V_{\mathrm{REV}}}\int_{V_f}\nabla\cdot(k_f\nabla T_f)dV, \tag{128}$$

and

$$\frac{1}{V_{\mathrm{REV}}}\int_{V_s}(\rho c)_s\frac{\partial T_s}{\partial t}dV=\frac{1}{V_{\mathrm{REV}}}\int_{V_s}\nabla\cdot(k_s\nabla T_s)dV, \tag{129}$$

where V_{REV}, V_f and V_s are the volumes of the REV, fluid phase in REV and solid phase in REV, respectively. We should note that the superficial temperature is evaluated at the centroid of the REV, whereas the phase temperature is evaluated throughout the REV. Neglecting variations of (ρc) within the REV and considering the system to be rigid so that V_f and V_s are not functions of time, the volume-averaged form of (124) and (125) are

$$(\rho c)_f\frac{\partial<T_f>}{\partial t}=<\nabla\cdot(k_f\nabla T_f)>, \tag{130}$$

and

$$(\rho c)_s\frac{\partial<T_s>}{\partial t}=<\nabla\cdot(k_s\nabla T_s)>, \tag{131}$$

where angle brackets indicate superficial quantities such as

$$<T_f>=\frac{1}{V_{\mathrm{REV}}}\int_{V_f}T_f dV,$$

and

$$<T_s>=\frac{1}{V_{\mathrm{REV}}}\int_{V_s}T_s dV.$$

The superficial average is however an unsuitable variable because it can yield erroneous results. For example, if the fluid temperature were a constant, the superficial average would differ from this constant (Quintard and Whitaker 1993). On the other hand, intrinsic phase averages do not have this shortcoming. These averages are defined by

$$<T_f>^f=\frac{1}{V_f}\int_{V_f}T_f dV, \tag{132}$$

and

$$<T_s>^s=\frac{1}{V_s}\int_{V_s}T_s dV. \tag{133}$$

Also, intrinsic averages are related to superficial averages by

$$< T_f >= \epsilon_f < T_f >^f, \tag{134}$$

and

$$< T_s >= \epsilon_s < T_s >^s, \tag{135}$$

where ϵ_f and ϵ_s are the volume fractions of the fluid and solid phases with $\epsilon_f = \varphi$, $\epsilon_s = 1 - \varphi$ and a constant porosity φ for a rigid two-phase system.

Quintard and Whitaker (1993) substitute (134) and (135) into (130) and (131) to obtain

$$\epsilon_f (\rho c)_f \frac{\partial < T_f >^f}{\partial t} =< \nabla \cdot (k_f \nabla T_f) >, \tag{136}$$

and

$$\epsilon_s (\rho c)_s \frac{\partial < T_s >^s}{\partial t} =< \nabla \cdot (k_s \nabla T_s) > . \tag{137}$$

Next Quintard and Whitaker (1993) apply the spatial averaging theorem to (136) and (137) and neglect variations of physical properties within the REV. The result is

$$\underbrace{\epsilon_f (\rho c)_f \frac{\partial < T_f >^f}{\partial t}}_{\text{accumulation}} = \underbrace{\nabla \cdot \left\{ k_f \left[\epsilon_f \nabla < T_f >^f + < T_f >^f \nabla \epsilon_f + \frac{1}{V_{\text{REV}}} \int_{A_{fs}} \mathbf{n}_{fs} T_f dA \right] \right\}}_{\text{conduction}} + \underbrace{\frac{1}{V_{\text{REV}}} \int_{A_{fs}} \mathbf{n}_{fs} \cdot k_f \nabla T_f dA}_{\text{interfacial flux}}, \tag{138}$$

and

$$\underbrace{\epsilon_s (\rho c)_s \frac{\partial < T_s >^s}{\partial t}}_{\text{accumulation}} = \underbrace{\nabla \cdot \left\{ k_s \left[\epsilon_s \nabla < T_s >^s + < T_s >^s \nabla \epsilon_s + \frac{1}{V_{\text{REV}}} \int_{A_{fs}} \mathbf{n}_{fs} T_s dA \right] \right\}}_{\text{conduction}} + \underbrace{\frac{1}{V_{\text{REV}}} \int_{A_{fs}} \mathbf{n}_{fs} \cdot k_s \nabla T_s dA}_{\text{interfacial flux}} . \tag{139}$$

By introducing the spatial decompositions $T_f =< T_f >^f + \tilde{T}_f$ and $T_s =< T_s >^s + \tilde{T}_s$ and by applying scaling arguments and the spatial averaging theorem, (138) and (139) are simplified into

$$\epsilon_f(\rho c)_f \frac{\partial < T_f >^f}{\partial t} = \nabla \cdot \{k_f[\epsilon_f \nabla < T_f >^f + \frac{1}{V_{\text{REV}}} \int_{A_{fs}} \mathbf{n}_{fs} \tilde{T}_f dA]\} + \frac{1}{V_{\text{REV}}} \int_{A_{fs}} \mathbf{n}_{fs} \cdot k_f \nabla < T_f >^f dA + \frac{1}{V_{\text{REV}}} \int_{A_{fs}} \mathbf{n}_{fs} \cdot k_f \nabla \tilde{T}_f dA, \tag{140}$$

and

$$\epsilon_s(\rho c)_s \frac{\partial < T_s >^s}{\partial t} = \nabla \cdot \{k_s[\epsilon_s \nabla < T_s >^s + \frac{1}{V_{\text{REV}}} \int_{A_{fs}} \mathbf{n}_{sf} \tilde{T}_s dA]\} + \frac{1}{V_{\text{REV}}} \int_{A_{fs}} \mathbf{n}_{sf} \cdot k_s \nabla < T_s >^s dA + \frac{1}{V_{\text{REV}}} \int_{A_{fs}} \mathbf{n}_{sf} \cdot k_s \nabla \tilde{T}_s dA. \tag{141}$$

After developing the closure for $\tilde{T}_f$ and $\tilde{T}_s$, Quintard and Whitaker (1993) obtain a two-equation model

$$\epsilon_f(\rho c)_f \frac{\partial < T_f >^f}{\partial t} = \nabla \cdot \{\mathbf{K}_{ff} \cdot \nabla < T_f >^f + \mathbf{K}_{fs} \cdot \nabla < T_s >^s\} + ha_v(< T_s >^s - < T_f >^f), \tag{142}$$

and

$$\epsilon_s(\rho c)_s \frac{\partial < T_s >^s}{\partial t} = \nabla \cdot \{\mathbf{K}_{ss} \cdot \nabla < T_s >^s + \mathbf{K}_{sf} \cdot \nabla < T_f >^f\} - ha_v(< T_s >^s - < T_f >^f), \tag{143}$$

where h and a_v come from modeling of the interfacial flux and are the film heat transfer coefficient and the interfacial area per unit volume, respectively, $\mathbf{K}_{ff}$, $\mathbf{K}_{ss}$, $\mathbf{K}_{fs}$ and $\mathbf{K}_{sf}$ are the effective thermal conductivity tensors, and the coupled thermal conductivity tensors are equal

$$\mathbf{K}_{fs} = \mathbf{K}_{sf}.$$

When porous media are isotropic and physical properties of the two phases are constant, (142) and (143) reduce to

$$\gamma_f \frac{\partial < T_f >^f}{\partial t} = k_f \triangle < T_f >^f + k_{fs} \triangle < T_s >^s + ha_v(< T_s >^s - < T_f >^f), \tag{144}$$

and

$$\gamma_s \frac{\partial < T_s >^s}{\partial t} = k_s \triangle < T_s >^s + k_{sf} \triangle < T_f >^f + ha_v(< T_s >^s - < T_f >^f), \tag{145}$$

where $\gamma_f = \varphi(\rho c)_f$ and $\gamma_s = (1 - \varphi)(\rho c)_s$ are the fluid-phase and solid-phase effective thermal capacities, respectively, φ is the porosity, k_f and k_s are the effective thermal conductivities of the fluid and solid phases, respectively, $k_{fs} = k_{sf}$ is the cross effective thermal conductivity of the two phases.

The one-equation model is valid whenever the two temperatures $< T_f >^f$ and $< T_s >^s$ are sufficiently close to each other so that

$$< T_f >^f = < T_s >^s = < T > . \tag{146}$$

This *local thermal equilibrium* is valid when any one of the following three conditions occurs (Quintard and Whitaker 1993, Whitaker 1999): (1) either ϵ_f or ϵ_s tends to zero, (2) the difference in the liquid-phase and solid-phase physical properties tends to zero, (3) the square of the ratio of length scales $(l_{fs}/L)^2$ tends to zero (e.g. steady, one-dimensional heat conduction). Here $l_{fs}^2 = [\epsilon_f \epsilon_s (\epsilon_f k_s + \epsilon_s k_f)]/(ha_v)$, and $L = L_T L_{T1}$ with L_T and L_{T1} as the characteristic lengths of $\nabla < T >$ and $\nabla\nabla < T >$, respectively, such that $\nabla < T >= O(\triangle < T > /L_T)$ and $\nabla\nabla < T >= O(\triangle < T > /L_{T1} L_T)$.

When the local thermal equilibrium is valid, Quintard and Whitaker (1993) add (142) and (143) to obtain a one-equation model

$$< \rho > C \frac{\partial < T >}{\partial t} = \nabla \cdot [\mathbf{K}_{eff} \cdot \nabla < T >]. \tag{147}$$

Here $< \rho >$ is the spatial average density defined by

$$< \rho >= \epsilon_f \rho_f + \epsilon_s \rho_s, \tag{148}$$

and C is the mass-fraction-weighted thermal capacity given by

$$C = \frac{\epsilon_f (\rho c)_f + \epsilon_s (\rho c)_s}{\epsilon_f \rho_f + \epsilon_s \rho_s}. \tag{149}$$

The effective thermal conductivity tenor is

$$\mathbf{K}_{eff} = \mathbf{K}_{ff} + 2\mathbf{K}_{fs} + \mathbf{K}_{ss}. \tag{150}$$

The choice between the one-equation model and the two-equation model has been well discussed by Quintard and Whitaker (1993) and Whitaker (1999). They have also developed methods of determining the effective thermal conductivity tensor $\mathbf{K}_{eff}$ in the one-equation model and the four coefficients $\mathbf{K}_{ff}$, $\mathbf{K}_{fs} = \mathbf{K}_{sf}$, $\mathbf{K}_{ss}$, and ha_v in the two-equation model. Their studies suggest that the coupling coefficients are on the order of the smaller of $\mathbf{K}_{ff}$ and $\mathbf{K}_{ss}$. Therefore, the coupled conductive terms should not be omitted in any detailed two-equation model of heat conduction processes. When the principle of is not valid, the commonly-used two-equation model in the literature is the one without the coupled conductive terms (Glatzmaier and Ramirez 1988)

$$\epsilon_f (\rho c)_f \frac{\partial < T_f >^f}{\partial t} = \nabla \cdot \left(\mathbf{K}_{ff} \cdot \nabla < T_f >^f \right) + ha_v \left(< T_s >^s - < T_f >^f \right), \tag{151}$$

and

$$\epsilon_s(\rho c)_s \frac{\partial < T_s >^s}{\partial t} = \nabla \cdot \left(\mathbf{K}_{ss} \cdot \nabla < T_s >^s\right) - ha_v \left(< T_s >^s - < T_f >^f\right). \quad (152)$$

On the basis of the analysis by Quintard and Whitaker (1993), we now know that the coupled conductive terms $\mathbf{K}_{fs} \cdot \nabla < T_s >^s$ and $\mathbf{K}_{sf} \cdot \nabla < T_f >^f$ cannot be discarded in the exact representation of the two-equation model. However, we could argue that (151) and (152) represent a reasonable approximation of (142) and (143) for a heat conduction process in which $\nabla < T_f >^f$ and $\nabla < T_s >^s$ are *sufficiently close* to each other. Under these circumstances $\mathbf{K}_{ff}$ in (151) would be given by $\mathbf{K}_{ff} + \mathbf{K}_{fs}$ while $\mathbf{K}_{ss}$ in (152) should be interpreted as $\mathbf{K}_{sf} + \mathbf{K}_{ss}$. This limitation of (151) and (152) is believed to be the reason behind the paradox of heat conduction in porous media subject to lack of local thermal equilibrium well-analyzed by Vadász (2005c, 2007). For isotropic porous media and constant physical properties of the two phases, (151) and (152) reduce to the traditional formulation of heat conduction in porous media (Bejan 2004, Bejan et al. 2004, Nield and Bejan 2006, Vadász 2005c)

$$\gamma_f \frac{\partial < T_f >^f}{\partial t} = k_{ef} \triangle < T_f >^f + ha_v \left(< T_s >^s - < T_f >^f\right), \quad (153)$$

and

$$\gamma_s \frac{\partial < T_s >^s}{\partial t} = k_{es} \triangle < T_s >^f - ha_v \left(< T_s >^s - < T_f >^f\right), \quad (154)$$

where we introduce the *equivalent* effective thermal conductivities $k_{ef} = k_f + k_{fs}$ and $k_{es} = k_s + k_{sf}$ for the fluid and solid phases, respectively, to take the above note into account. To describe the thermal energy exchange between solid and gas phases in casting sand, Tzou (1997) has also directly postulated (153) and (154) (using k_f and k_s rather than k_{ef} and k_{es}) as a two-step model, parallel to the two-step equations in the microscopic phonon-electron interaction model (Kaganov et al. 1957, Anisimòv et al. 1974, Qiu and Tien 1993).

Stimulated by Tzou (1997), Vadász (2005a, b), (2006a, b), Vadász et al. (2005), Wang et al. (2008) develop an equivalence between the dual-phase lagging and two-phase porous-medium heat conduction processes based on (144) and (145). We first rewrite (144) and (145) in their operator form

$$\begin{bmatrix} \gamma_f \dfrac{\partial}{\partial t} - k_f \triangle + ha_v & -k_{fs} \triangle - ha_v \\ -k_{fs} \triangle - ha_v & \gamma_s \dfrac{\partial}{\partial t} - k_s \triangle + ha_v \end{bmatrix} \begin{bmatrix} < T_f >^f \\ < T_s >^s \end{bmatrix} = 0. \quad (155)$$

We then obtain a uncoupled form by evaluating the operator determinant such that

$$\left[\left(\gamma_f \frac{\partial}{\partial t} - k_f \triangle + ha_v\right)\left(\gamma_s \frac{\partial}{\partial t} - k_s \triangle + ha_v\right) - \left(k_{fs} \triangle - ha_v\right)^2\right] < T_i >^i = 0, \tag{156}$$

where the index i can take f or s. Its explicit form reads, after dividing by $ha_v(\gamma_f + \gamma_s)$

$$\frac{\partial \langle T_i \rangle^i}{\partial t} + \tau_q \frac{\partial^2 \langle T_i \rangle^i}{\partial t^2} = \alpha \triangle \langle T_i \rangle^i + \alpha \tau_T \frac{\partial}{\partial t}(\triangle \langle T_i \rangle^i) + \frac{\alpha}{k}[S(\vec{x}, t) + \tau_q \frac{\partial S(\vec{x}, t)}{\partial t}], \tag{157}$$

where

$$\begin{aligned} &\tau_q = \frac{\gamma_f \gamma_s}{ha_v(\gamma_f + \gamma_s)}, && \tau_T = \frac{\gamma_f k_s + \gamma_s k_f}{ha_v(k_f + k_s + 2k_{fs})}, \\ &k = k_f + k_s + 2k_{fs}, && \alpha = \frac{k}{\rho c} = \frac{k_f + k_s + 2k_{fs}}{\gamma_f + \gamma_s}, \\ &S(\vec{x}, t) + \tau_q \frac{\partial S(\vec{x}, t)}{\partial t} = \frac{k_{fs}^2 - k_f k_s}{ha_v} \triangle^2 \langle T_i \rangle^i. \end{aligned} \tag{158}$$

Therefore, $< T_f >^f$ and $< T_s >^s$ satisfy *exactly* the same dual-phase-lagging heat-conduction equation [Eq. (157)]. Note that (144) and (145) are the mathematical representation of the first law of thermodynamics and the Fourier law of heat conduction for heat conduction processes in porous media at macroscale. Therefore, we have the *exact* equivalence between the dual-phase-lagging heat conduction and the heat conduction in porous media. This is significant because all results in these two fields become mutually applicable. In particular, all analytical methods and results in Wang and Zhou (2000, 2001) and Wang et al. (2008) can be applied to study heat conduction in porous media.

By (158), we can readily obtain that, in the porous-medium heat conduction

$$\frac{\tau_T}{\tau_q} = 1 + \frac{\gamma_f^2 k_s + \gamma_s^2 k_f - 2\gamma_f \gamma_s k_{fs}}{\gamma_f \gamma_s (k_f + k_s + 2k_{fs})}. \tag{159}$$

It can be large, equal or smaller than 1 depending on the sign of $\gamma_f^2 k_s + \gamma_s^2 k_f - 2\gamma_f \gamma_s k_{fs}$. Therefore, we may have thermal oscillation and resonance in general for heat conduction in porous media subject to lack of local thermal equilibrium (Xu and Wang 2002). This agrees with the experimental data of casting sand in Tzou (1997). Discarding the coupled conductive terms in (144) and (145) assumes k_{fs}=0 so that τ_T/τ_q is always larger than 1, and exclude the possibility of thermal oscillation and resonance (Vadász 2005a, b, 2006a, b, Vadász et al. 2005). The coupled conductive terms in (144) and (145) are thus responsible for the thermal oscillation and resonance in the porous-medium heat conduction subject to lack of local thermal equilibrium.

Although each of τ_T and τ_q is ha_v-dependent, their ratio τ_T/τ_q is not. This makes its evaluation much simpler as detailed by Vadász (2005a). The readers are also

referred to Vadász (2005a) for the correlations between physical properties in (158) and those in Hays-Stang (1999) and Minkowycz et al. (1999).

6 Concluding Remarks

The dual-phase-lagging heat conduction equation originates from the first law of thermodynamics and the dual-phase-lagging constitutive relation of heat flux density. It is developed in examining energy transport involving the high-rate heating in which the non-equilibrium thermodynamic transition and the microstructural effect become important associated with shortening of the response time. In addition to its application in the ultrafast pulse-laser heating, the dual-phase-lagging heat conduction equation also arises in describing and predicting phenomena such as propagating of temperature pulses in superfluid liquid helium, nonhomogeneous lagging response in porous media, thermal lagging in amorphous materials, and effects of material defects and thermomechanical coupling. Furthermore, The dual-phase-lagging heat conduction equation forms a generalized, unified equation with the classical parabolic heat-conduction equation, the hyperbolic heat-conduction equation, the energy equation in the phonon scattering model, and the energy equation in the phonon-electron interaction model as its special cases. This, with the rapid growth of microscale heat conduction of high-rate heat flux, has attracted the recent research effort on dual-phase-lagging heat conduction: its physical basis and experimental verification, well-posedness, solution structure, analytical and numerical solutions, methods of measuring thermal relaxation times, thermal oscillation and resonance, and equivalence with and application in porous-medium heat conduction.

The dual-phase-lagging heat conduction has been shown to be admissible by the second law of the extended irreversible thermodynamics and by the Boltzmann transport equation. It is also proven to be well-posed in a finite region of $n-$dimension ($n \geq 1$) under any linear boundary conditions including Dirichlet, Neumann and Robin types. The solution structure theorems are developed as well for both mixed and Cauchy problems of dual-phase-lagging heat-conduction equations. These theorems inter-relate contributions (to the temperature field) of the initial temperature distribution, the source term and the initial time-rate change of the temperature, uncover the structure of temperature field and considerably simplify the development of solutions. The thermal oscillation and resonance in the dual-phase-lagging heat conduction have been examined in details. Conditions and features of underdamped, critically-damped and overdamped oscillations have been obtained and compared with those in the classical parabolic heat conduction and the hyperbolic heat conduction. The condition for the thermal resonance is also available. Both the underdamped oscillation and the critically-damped oscillation cannot appear if the phase lag of the temperature gradient τ_T is larger than that of the heat flux τ_q. The modes of underdamped thermal oscillation are limited to a region fixed by two relaxation distances defined by $\sqrt{\alpha\tau_T}(\sqrt{\frac{\tau_q}{\tau_T}} + \sqrt{\frac{\tau_q}{\tau_T} - 1})$ and

$\sqrt{\alpha\tau_T}(\sqrt{\frac{\tau_q}{\tau_T}} - \sqrt{\frac{\tau_q}{\tau_T} - 1})$ for the case of $\tau_T > 0$, and by one relaxation distance $2\sqrt{\alpha\tau_q}$ for the case of $\tau_T = 0$.

An exact equivalence exists between the dual-phase-lagging heat conduction and the Fourier heat conduction in porous media subject to lack of local thermal equilibrium. This has a profound impact on the further development of the two fields. Applying the result regarding thermal waves in shows that the and can occur in porous-medium heat conduction subject to lack of local thermal equilibrium, a phenomenon observed experimentally. Such thermal waves and, possibly resonance come actually from the coupled conductive terms in (144) and (145).

Acknowledgments We benefited immensely from the stimulating work by and discussion with Prof. P. Vadász on equivalence between the dual-phase-lagging heat conduction and the Fourier heat conduction in porous media. The support of our research program by the CRCG of the University of Hong Kong (200607176138) and the Research Grant Council of the Hong Kong Special Administration Region of China (HKU7049/06P) is also greatly appreciated.

References

Anisimòv SI, Kapeliovich BL, Perelman TL (1974) *Sov. Phys. JETP* **39**: 375–377.
Antaki P (1998) *Int. J. Heat Mass Transfer* **41**: 2253–2258.
Auriault JL (1991) *Int. J. Engng Sci.* **29**: 785–795.
Bejan A (2004) *Convection heat transfer* (3rd ed). Wiley, New York.
Bejan A, Dincer I, Lorente S, Miguel AF, Reis AH (2004) *Porous and complex flow structures in modern technologies*. Springer, New York.
Chester M (1963) *Phys. Rev.* **131**: 2013–2015.
Dai W, Nassar R (1999) *Numer. Meth. Part. Di. E.* **15**: 697–708.
Fournier D. Boccara AC (1989) *Physica A* **157**: 587–592.
Glatzmaier GC, Ramirez WF (1988) *Chem. Eng Sci* **43**: 3157–3169.
Guyer RA, Krumhansi JA (1966) *Phys. Rev.* **148**: 766–778.
Hays-Stang KJ, Haji-Sheikh A (1999) *Int J Heat Mass Transfer* **42**: 455–465.
Joseph DD, Preziosi L (1989) *Rev. Mod. Phys.* **61**: 41–73.
Kaganov MI, Lifshitz IM, Tanatarov MV (1957) *Sov. Phys. JETP* **4**: 173–178.
Lin CK, Hwang CC, Chang YP (1997) *Int. J. Heat Mass Tran.* **40**: 1716–1719.
Minkowycz WJ, Haji-Sheikh A, Vafai K (1999) *Int. J. Heat Mass Tran.* **42**: 3373–3385.
Nield DA, Bejan A (2006) *Convection in porous media* (3rd ed). Springer, New York.
Qiu TQ, Tien CL (1993) *J. Heat Tran.* **115**: 835–841.
Quintard M, Whitaker S (1993) *Adv. Heat Tran.* **23**: 369–464.
Tang DW, Araki N (1999) *Int. J. Heat Mass Tran.* **42**: 855–860.
Tzou DY (1992) *J. Appl. Mech.* **59**: 862–866.
Tzou DY (1995a) *J. Heat Tran.* **117**: 8–16.
Tzou DY (1995b) *AIAA J.Thermophys* **9**: 686–693.
Tzou DY (1997) *Macro- to microscale heat transfer: the lagging behavior*. Taylor & Francis, Washington.
Tzou DY, Zhang YS (1995) *Int. J. Engng. Sci.* **33**: 1449–1463.
Vadasz JJ, Govender S, Vadász P (2005) *Int. J. Heat Mass Tran.* **48**: 2673–2683.
Vadász P (2005a) *J. Heat Tran.* **127**: 307–314.
Vadász P (2005b) *Int. J. Heat Mass Tran.* **48**: 2822–2828.

Vadász P (2005c) *Transport Porous Med.* **59**: 341–355.
Vadász P (2006a) *Int. J. Heat Mass Tran.* **49**: 4886–4892.
Vadász P (2006b) *J. Heat Tran.* **128**: 465–477.
Vadász P (2007) *Int. J. Heat Mass Tran.* **50**, 4131–4140.
Wang LQ (1994) *Int. J. Heat Mass Tran.* **37**: 2627–2634.
Wang LQ (2000a) *Int. J. Heat Mass Tran.* **43**: 365–373.
Wang LQ (2000b) *Transport Porous Med.* **39**: 1–24.
Wang LQ, Wei XH (2008) *Int. J. Heat Mass Transfer* **51**: 1751–1756.
Wang LQ, Xu MT (2002) *Int. J. Heat Mass Tran.* **45**: 1165–1171.
Wang LQ, Zhou XS (2000) *Dual-phase-lagging heat-conduction equations*. Shandong University Press, Jinan.
Wang LQ, Zhou XS (2001) *Dual-phase-lagging heat-conduction equations: problems and solutions*. Shandong University Press, Jinan.
Wang LQ, Xu MT, Zhou XS (2001) *Int. J. Heat Mass Tran.* **44**: 1659–1669.
Wang LQ, Zhou XS, Wei XH (2008) *Heat Conduction: mathematical models and analytical solutions.* Springer-Verlag, Berlin.
Whitaker S (1999) *The method of volume averaging*. Kluwer, Dordrecht.
Xu MT, Wang LQ (2002) *Int. J. Heat Mass Tran.* **45**: 1055–1061.
Xu MT, Wang LQ (2005) *Int. J. Heat Mass Tran.* **48**: 5616–5624.

Heat Transfer Analysis Under Local Thermal Non-equilibrium Conditions

A. Haji-Sheikh and W.J. Minkowycz

1 Introduction

The Local Thermal Non-Equilibrium (LTNE) hypothesis emerges when studying a rapid transport of heat in porous media. The non-equilibrium phenomenon is an interesting issue during a rapid heating or a cooling process. This phenomenon occurs in various engineering applications such as nuclear devices, Fichot et al. (2006), fuel cells, Damm and Fedorov (2006), electronic systems, Lage et al. (1996), micro devices, Jiang et al. (2001), and others. Generally, a classical approach is used to determine the materials temperature in the presence of Local Thermal Equilibrium (LTE). In the absence of LTE, the single energy equation needs to be replaced with two energy equations, one for the solid and another for the fluid.

Earlier, Vick and Scott (1998) determined the heat transfer in a matrix with embedded particles using a finite-difference approach. They reported a thermal lag that depends on the property ratio and contact conductance while the temperature response due to an applied heat flux differs from that predicted using the classical heat conduction technique. Lee and Vafai (1999) used a two-equation model and performed an analytical determination of the solid and fluid temperature differential in porous media within a forced convective flow. The studies in Minkowycz et al. (1999) show that the thermal non-equilibrium condition in a fluidized porous bed depends on the structure of solid materials, mean pore size, interstitial heat transfer coefficient, and thermophysical properties. For a porous medium subject to rapid transient heating or cooling, the studies in Minkowycz et al. (1999) established conditions for departure from local thermal equilibrium. Therefore, the occurrence of the LTNE in the presence of a rapidly changing heat source depends on the magnitude of a dimensionless quantity called the Sparrow number in

A. Haji-Sheikh
The University of Texas at Arlington, Arlington, TX, USA
e-mail: haji@mae.uta.edu

W.J. Minkowycz
University of Illinois at Chicago, Chicago, IL, USA
e-mail: WJM@uic.edu

P. Vadász (ed.), *Emerging Topics in Heat and Mass Transfer in Porous Media*,
© Springer Science+Business Media B.V. 2008

Minkowycz et al. (1999). Otherwise, the local thermal equilibrium condition exists and it controls the transport of energy through the porous media.

Parametric studies, reported here, describe the role of a dimensionless quantity that identifies the early departure from local thermal equilibrium in the presence of a rapidly changing heat source. The numerically-obtained data reveal the implication of non-equilibrium thermal phenomena in a fluid-saturated porous medium in the presence of a heat source. This presentation describes early departure from the local thermal equilibrium, as has been reported in various studies of laser heating, in combustors, and in other similar applications.

2 Theoretical Model

The concept of local thermal non-equilibrium emerges in many heat transfer applications involving porous media. During rapid heating or cooling, it is appropriate to use a simplified velocity field obtainable by a classical procedure. This presentation emphasizes the study of energy equation during relatively rapid heating and cooling processes.

2.1 Energy Equation

When the thermophysical properties are independent of temperature, the continuity and momentum equations yield the velocity distribution. The energy equation is obtainable by applying the energy balance concept to a differential element in the flow field that contains both solid and fluid phases. The applied energy balance to a volume element in Figure 1, under locally thermal non-equilibrium condition, leads to the following set of governing equations as recommended in Amiri and Vafai (1994) and Lee and Vafai (1999),

$$\varepsilon C_f \frac{\partial T_f(\boldsymbol{r},t)}{\partial t} + C_f \mathbf{V}\cdot\nabla T_f = -\nabla\cdot\boldsymbol{q}_f(\boldsymbol{r},t) + h a_p (T_s - T_f) \tag{1a}$$

$$(1-\varepsilon) C_s \frac{\partial T_s(\boldsymbol{r},t)}{\partial t} = -\nabla\cdot\boldsymbol{q}_s(\boldsymbol{r},t) - h a_p (T_s - T_f) \tag{1b}$$

In this equation, $\varepsilon = V_f/V$ is the porosity that stands for the fraction of volume a fluid occupies, T_f is the mean fluid temperature, and T_s is the mean temperature of the solid materials, all within a differential element dV. Also, $\boldsymbol{q}_f$ and $\boldsymbol{q}_s$ are the heat flux vectors in the fluid and solid materials, respectively. Other parameters are the heat capacitances C_f and C_s for fluid and solid materials, interstitial heat transfer coefficient h, and the contact area parameter A_p between fluid and solid materials within a differential element dV. Adding Eq. (1a)–(1b) and after replacing $\boldsymbol{q}_f + \boldsymbol{q}_s$ with $\boldsymbol{q}$, the resulting relation is

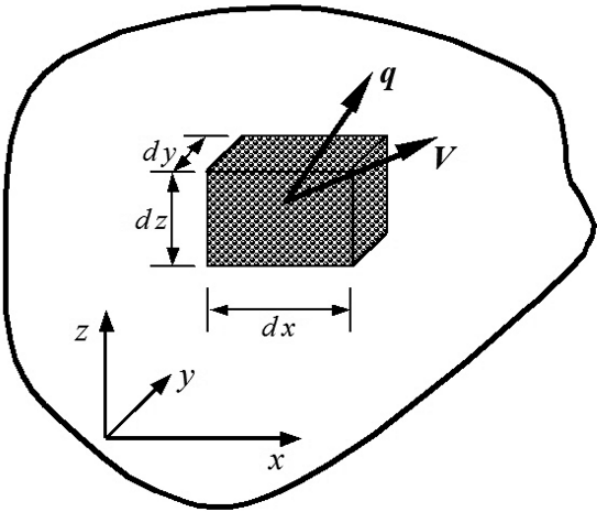

Fig. 1 Schematic of a differential element in a porous region

$$-\nabla \cdot \boldsymbol{q}(\boldsymbol{r},t) = \varepsilon C_f \frac{\partial T_f(\boldsymbol{r},t)}{\partial t} + C_f \boldsymbol{V} \cdot \nabla T_f + (1-\varepsilon) C_s \frac{\partial T_s(\boldsymbol{r},t)}{\partial t} \tag{2}$$

In phase change application, T_f becomes the temperature of the phase change materials as the pores may contain vapor, liquid, solid, or a combination. For the sake of generality, it is appropriate to add a volumetric heat source function $S(\boldsymbol{r},t)$ to Eq. (2) to become

$$-\nabla \cdot \boldsymbol{q}(\boldsymbol{r},t) + S(\boldsymbol{r},t) = \varepsilon C_f \frac{\partial T_f(\boldsymbol{r},t)}{\partial t} + C_f \boldsymbol{V} \cdot \nabla T_f + (1-\varepsilon) C_s \frac{\partial T_s(\boldsymbol{r},t)}{\partial t} \tag{3}$$

Under local thermal equilibrium condition, the solid and the adjacent fluid are at the same temperature, $T_s = T_f$. However, during a rapid heating or cooling, the fluid and solid are not at the same temperature, locally. Therefore, before the onset of equilibrium, there is an energy exchange between the solid phase and the fluid phase within the pores, and temperature undergoes a transient process, as defined by the equation

$$C_f \Delta V_p \frac{\partial T_f}{\partial t} = h \Delta A_p (T_s - T_f) \tag{4}$$

where ΔV_p is the mean pore volume, ΔA_p is its contact surface area with the solid phase, and h is the interstitial heat transfer coefficient. As a shorthand notation, $r_h = \Delta V_p / \Delta A_p$ is considered to be a pore hydraulic radius in Eq. (4) and it becomes

$$T_s(\boldsymbol{r},t) = T_f(\boldsymbol{r},t) + \tau_t \frac{\partial T_f(\boldsymbol{r},t)}{\partial t} \tag{5}$$

where $\tau_t = r_h C_f / h$. In this formulation, the solid matrix plays the primary role of energy transport and reversing it would changer this formulation.

Equation (3) contains the heat flux vector $\boldsymbol{q}$ that depends on temperature. Under the local thermal equilibrium condition, when $T_s = T_f$, the Fourier equation applies,

$$\boldsymbol{q}(\boldsymbol{r}, t) = -k_e \nabla T_f(\boldsymbol{r}, t) \tag{6}$$

where k_e is the effective or equivalent thermal conductivity of the porous medium. It is reported in Fournier and Boccara (1989) that Eq. (6) does not hold under a rapid heating process. In the absence of local thermal equilibrium, when the departures of $\boldsymbol{q}$ and ∇T from local equilibrium are relatively small, it is suggested in Tzou (1997) that the Fourier equation, as given in Eq. (6), needs to be modified to become

$$\boldsymbol{q}(\boldsymbol{r}, t) + \Delta \boldsymbol{q}(\boldsymbol{r}, t) = -k_e \{\nabla T_f(\boldsymbol{r}, t) + \Delta[\nabla T_f(\boldsymbol{r}, t)]\} \tag{7}$$

as time changes. Accordingly, using a two-term Taylor series expansion for the time dependent differential changes on each sides, Eq. (7) can be written as

$$\boldsymbol{q}(\boldsymbol{r}, t) + \tau_q \frac{\partial \boldsymbol{q}(\boldsymbol{r}, t)}{\partial t} = -k_e \{\nabla T_f(\boldsymbol{r}, t) + \tau_x \frac{\partial}{\partial t}[\nabla T_f(\boldsymbol{r}, t)]\} \tag{8}$$

The relaxation time τ_q describes the time delay as heat travels from pore to pore; therefore, it depends on the direction of energy transport between solid and fluid. When the solid structure has a higher local temperature than the materials in a pore, as an approximation, $\tau_q \approx C_s R_c \Delta V_s / \Delta A_s$; the parameter ΔV_s is the differential volume within the solid structure while R_c and ΔA_s are the contact resistance and contact area between individual solid structures, respectively. The relaxation time τ_x describes the time delay as temperature changes in the fluid and solid material. The physical descriptions of these parameters are presented in the net section.

Equations (3), (5), and (8) contain three unknowns, T_f, T_s, and the heat flux vector $\boldsymbol{q}$. One can eliminate T_s and retain T_f using Eq. (5) and eliminate $\boldsymbol{q}$ using Eq. (8). Then, following some simplifications, Eq. (3) takes the form

$$\begin{aligned} \mathsf{L}(T_f) + \tau_q \frac{\partial}{\partial t}[\mathsf{L}(T_f)] + (\tau_x - \tau_q) \frac{\partial [\nabla \cdot (k_e \nabla T_f)]}{\partial t} + \left(S + \tau_q \frac{\partial S}{\partial t} \right) \\ = C \frac{\partial}{\partial t} \left[T_f + (\tau_e + \tau_q) \frac{\partial T_f}{\partial t} + \tau_e \tau_q \frac{\partial^2 T_f}{\partial t^2} \right] \end{aligned} \tag{9}$$

where $T_f = T_f(\boldsymbol{r}, t)$, $S = S(\boldsymbol{r}, t)$, $C = \varepsilon C_f + (1-\varepsilon) C_s$, $\tau_e = (1-\varepsilon) C_s C_f r_h / hC$, and $\mathsf{L}(T_f) = \nabla \cdot (k_e \nabla T_f) - C_f \boldsymbol{V} \cdot \nabla T_f$. An alternative form of τ_e, that is, $\tau_e = (1-\varepsilon)(C_s/C)\tau_t$ indicates that $\tau_e < \tau_t$. The terms within the square brackets on the right side of Eq. (9) include the first two terms of the Taylor series expansion and a third term. This third term is smaller than the third term of this Taylor series $(\tau_e + \tau_q)^2 \left(\partial^2 T / \partial t^2\right) / 2!$ since $\tau_e \tau_q < (\tau_e + \tau_q)^2 / 2!$. As stated earlier, the higher

order terms of the Taylor series expansion in Eq. (8) are eliminated; therefore, for consistency of these formulations, the third term within the square brackets on the right-hand-side of Eq. (9) is small and should be neglected. Then, the reduced form of Eq. (9) is

$$\begin{aligned} \mathsf{L}(T_f) + \tau_q \frac{\partial}{\partial t}[\mathsf{L}(T_f)] + (\tau_x - \tau_q)\frac{\partial[\nabla \cdot (k_e \nabla T_f)]}{\partial t} \\ + \left(S + \tau_q \frac{\partial S}{\partial t}\right) = C\left[\frac{\partial T_f}{\partial t} + (\tau_e + \tau_q)\frac{\partial^2 T_f}{\partial t^2}\right] \end{aligned} \tag{10}$$

For a few special cases, Eq. (10) has exact solutions; however, in general, the solution of Eq. (10) requires a numerical procedure.

2.2 Physical Interpretation of Relaxation Times

The lag time τ_t is a parameter that influences the state of local thermal non-equilibrium phenomena in porous media. The physical nature of the lag time $\tau_t = r_h C_f / h$, in Eq. (5), is well defined and its value is obtainable once h is known. The other parameters, r_h and C_f in the definition of τ_t, are usually available for a well-defined porous system. A relatively large value of τ_t indicates that there will be detectable temperature variations in the presence of a rapidly changing energy input. Large differences between T_f and T_s can be realized when the condition of local thermal equilibrium fails to exist depending on the values of the thermophysical properties including the time delay parameters. For a system with a specified characteristic length L, Minkowycz et al. (1999) introduced a dimensionless quantity called the Sparrow number, where

$$\begin{aligned} Sp &= hL^2/k_e r_h \\ &= Nu_{r_h}(k_f/k_e)(L/r_h)^2 \end{aligned} \tag{11}$$

indicates the presence of local thermal non-equilibrium condition. Alternatively, the parameter τ_t controls the size of the Sparrow number, that can be written as $Sp = (C_f/C)/(\alpha\tau_t/L^2)$. For stationary materials in the pores, the interstitial Nusselt number $Nu_{r_h} = hr_p/k_f$ has a value between 1 and 2 depending on the geometry of the pores. Therefore, according to Eq. (11), in addition to the thermal conductivity ratio, the ratio of a characteristic length L to the hydraulic radius r_h plays a significant role in the determination of Sp. For spherical bodies, cylindrical prisms, and square prisms, the values of $Nu_{r_h} = 1.09$, 1.45, and 1.23 are reported in Minkowycz et al. (1999), respectively.

For a thermally fully developed laminar flow in circular passages, the value of $Nu_{r_h} = hr_h/k_f$ is ≈ 0.92. When the mean cross section area A_c departs from a circular profile, the empirical relation

$$Nu_{r_h} = 0.92/[1 + (A_c - 4\pi r_h^2)/A_c] \tag{12}$$

provides a reasonable estimation of the interstitial Nusselt number for a laminar and thermally fully developed flow, Minkowycz et al. (1999). Also, the value of interstitial heat transfer coefficient h is obtainable from the Wakao and Kaguei (1982); e.g., a correlation for a packed bed of spherical particles is

$$\frac{h}{k_f d} = 2 + 1.1 Re^{0.6} Pr^{1/3} \tag{13}$$

where $Re = \varepsilon u_p d \big/ \nu$, and d is the diameter of the spheres. Equation (13) properly considers the flow in the pores to be thermally fully developed.

Another parameter that enters the analysis is τ_q. Experimental studies are needed to ascertain the proper value of τ_q in Eq. (10). Often, it is possible to provide an estimate of τ_q values using existing information in the literature. According to the Fourier equation, the heat flux across a control volume is related to ∇T. However, prior to onset of LTE, the actual heat flux is larger because additional thermal energy must be supplied to the individual structures across contact surfaces and through constrictions within the differential element. To account for the change in heat flux, one can set $\Delta A_s \Delta q \approx \Delta V_s C_s \partial(\Delta T_s) \big/ \partial t$, where ΔT_s is the temperature difference across a constriction and/or a contact surface. Substituting for $\Delta T_s = q R_c$ results in the relation

$$\Delta q \approx (\Delta V_s \big/ \Delta A_s) C_s R_c (\partial q \big/ \partial t) \tag{14}$$

where R_c is the contact resistance. A comparison of Eq. (14) with Eqs. (7) and (8) suggests that $\tau_q \approx C_s R_c \Delta V_s \big/ \Delta A_s$. The value of R_c depends on various factors including geometry, applied pressure, and the constriction effect; hence, it is difficult to develop an accurate prediction in the absence of experimental data.

The study of physical parameters that control the value of τ_x is the next topic for discussion. Although, the experimental determination of a reasonably accurate value of τ_x is desirable, different theories are cited for its determination. They include taking $\tau_x = \tau_t$ which is a reasonable choice when τ_q is much smaller than τ_t. Nnanna (2002) used a theoretical reasoning for determination of τ_x by viewing the temperature of solid materials T_s and the temperature of pore materials T_p to be different under LTNE condition. In Nnanna (2002) formulation, $T_p \equiv T_f$, since the materials in the pores can be in gaseous, in liquid, or in solid forms. By definition, the heat flux can be viewed as

$$\boldsymbol{q} + \Delta \boldsymbol{q} = -k_e \nabla (T_e + \Delta T_e) \tag{15}$$

wherein T_e is the mean temperature within a differential element defined by the relation

$$T_e = \frac{\varepsilon C_p}{C} T_p + \frac{(1-\varepsilon) C_s}{C} T_s \tag{16}$$

Moreover, by placing T_e from Eq. (16) in Eq. (15), it becomes

$$\begin{aligned} \boldsymbol{q} + \Delta \boldsymbol{q} = & -k_e \left[\frac{\varepsilon C_p}{C} \nabla T_p + \frac{(1-\varepsilon) C_s}{C} \nabla T_s \right] \\ & - k_e \left[\frac{\varepsilon C_p}{C} \nabla (\Delta T_p) + \frac{(1-\varepsilon)\, C_s}{C} \nabla (\Delta T_s) \right]. \end{aligned} \tag{17a}$$

Since by definition, $\Delta T_s \cong \tau_q \, \partial T_s / \partial t$ and $\Delta T_p \cong \tau_t \, \partial T_p / \partial t$, Eq. (17) takes the form

$$\begin{aligned} \boldsymbol{q} + \Delta \boldsymbol{q} = & -k_e \left[\frac{\varepsilon\, C_p}{C} \nabla T_p + \frac{(1-\varepsilon)\, C_s}{C} \nabla T_s \right] \\ & - k_e \left[\frac{\varepsilon\, C_p}{C} \tau_t \frac{\partial (\nabla T_p)}{\partial t} + \frac{(1-\varepsilon)\, C_s}{C} \tau_q \frac{\partial (\nabla T_s)}{\partial t} \right]. \end{aligned} \tag{17b}$$

where $\Delta \boldsymbol{q} = \tau_q \partial \boldsymbol{q} / \partial t$. Next, one can use Eq. (5) to replace T_s with $T_s = T_p + \tau_t \, \partial T_p / \partial t$, use the definition $C = \varepsilon\, C_p + (1-\varepsilon)\, C_s$, and delete the higher order terms to obtain the working relation

$$\boldsymbol{q} + \tau_q \frac{\partial \boldsymbol{q}}{\partial t} = -k_e \left[\nabla T_p + \tau_x \frac{\partial (\nabla T_p)}{\partial t} \right] \tag{18a}$$

wherein

$$\tau_x = \tau_t + \frac{(1-\varepsilon)\, C_s}{C} \tau_q. \tag{18b}$$

In the presence of a moving fluid, the solution of Eq. (10) depends on the functional form of the velocity vector $\mathbf{V}$. Among various possible cases, two different and simple functional forms are examined in the next two sections: one is for a stationary fluid when $\mathbf{V} = 0$, neglecting the $C_f \mathbf{V} \cdot \nabla T_f$ in Eq. (10) and the second one is for a special case when the velocity field is known.

3 Temperature Field with Stationary Fluids

For a stationary fluid in the pores, $V = 0$ and Eq. (10) takes the form

$$\begin{aligned} \nabla \cdot (k_e \nabla T_f) + \tau_x \frac{\partial [\nabla \cdot (k_e \nabla T_f)]}{\partial t} + \left(S + \tau_q \frac{\partial S}{\partial t} \right) \\ = C \left[\frac{\partial T_f}{\partial t} + (\tau_e + \tau_q) \frac{\partial^2 T_f}{\partial t^2} \right] \end{aligned} \tag{19}$$

This form of the energy equation for the temperature field is similar to that for the thermal conduction in microscale systems. Therefore, the solution of Eq. (19) is

similar to that for heat transfer in microscale devices, as given in Hays-Stang and Haji-Sheikh (1999). This solution is applicable to various regular geometries having homogeneous boundary conditions. However, a prescribed heat flux q at the walls can be also accommodated using homogeneous boundary conditions of the second kind while the product of q and a properly selected Dirac delta function serves a volumetric heat source. As a standard procedure, in classical heat conduction, one can introduce an auxiliary equation that satisfies the Laplace equation $\nabla \cdot (k_e \nabla T^*) = 0$ with the specified non-homogeneous boundary conditions to determine $T^*(\boldsymbol{r}, t)$. This would lead to a transformation

$$T_f(\boldsymbol{r}, t) = \theta_f(\boldsymbol{r}, t) + T^*(\boldsymbol{r}, t) \tag{20}$$

Using this transformation, Eq. (19) becomes

$$\begin{aligned} \nabla \cdot (k_e \nabla \theta_f) \; + \; \tau_x \frac{\partial [\nabla \cdot (k_e \nabla \theta_f)]}{\partial t} + \left(S + \tau_q \frac{\partial S}{\partial t} \right) + S_b \\ = C \left[\frac{\partial \theta_f}{\partial t} + (\tau_e + \tau_q) \frac{\partial^2 \theta_f}{\partial t^2} \right] \end{aligned} \tag{21a}$$

where

$$S_b = -C \left[\frac{\partial T^*}{\partial t} + (\tau_e + \tau_q) \frac{\partial^2 T^*}{\partial t^2} \right] \tag{21b}$$

is a known function. The auxiliary term S_b in Eq. (21a) vanishes when the non-homogeneous boundary conditions are independent of time. Following this transformation, the solution of Eq. (21a) for $\theta_f(\boldsymbol{r}, t)$ has two components, and it takes the following form

$$\theta_f(\boldsymbol{r}, t) = \theta_I(\boldsymbol{r}, t) + \theta_S(\boldsymbol{r}, t) \tag{22}$$

The function $\theta_I(\boldsymbol{r}, t)$ represents the contribution from the initial condition while $\theta_S(\boldsymbol{r}, t)$ represents the contribution of the volumetric heat source.

3.1 Temperature Solutions

For constant thermophysical properties, the analytical solution of Eq. (21a) is possible by applying the standard separation of variables technique; in the absence of the volumetric hear source terms. This leads to the following series solution for regular geometries,

$$\theta_f(\boldsymbol{r}, t) = \sum_{n=1}^{\infty} \psi_n(t) F_n(\boldsymbol{r}) e^{-\gamma_n t} \tag{23}$$

The function $F_n(\mathbf{r})$ is the eigenfunction in the diffusion equation under local thermal equilibrium condition; it satisfies the relation

$$\nabla \cdot [K \nabla F_n(\boldsymbol{r})] = -\gamma_n C F_n(\boldsymbol{r}) \tag{24}$$

Furthermore, in accordance with the Sturm-Liouville problem, the eigenfunctions $F_n(\mathbf{r})$ are orthogonal and the orthogonality condition is

$$\int_V F_n(\boldsymbol{r}) F_m(\boldsymbol{r})\, dV = \begin{cases} 0 & \text{when } n \neq m \\ N_n & \text{when } n = m \end{cases} \tag{25}$$

for regular geometries. Placing $\theta_f(\boldsymbol{r}, t)$ from Eq. (23) in Eq. (21a), after using this orthogonality condition, yields the ordinary differential equation for the time parameter ψ_n(t),

$$\frac{d^2\psi_n(t)}{dt^2} - 2\beta_n \frac{d\psi_n(t)}{dt} + \lambda_n^2 \psi_n(t) = S_n^*(t) \tag{26}$$

wherein $S_n^*(t)$ is

$$S_n^*(t) = \frac{e^{\gamma_n t}}{N_n C(\tau_q + \tau_e)} \int_V F_n(\boldsymbol{r}) \left(S_b(\boldsymbol{r}, t) + S(\boldsymbol{r}, t) + \tau_q \frac{\partial S(\boldsymbol{r}, t)}{\partial t} \right) dV \tag{27a}$$

The other parameters in Eq. (26) are

$$\beta_n = \gamma_n \left[1 - \frac{1}{2} \frac{\tau_x}{\tau_q + \tau_e} - \frac{1}{2\gamma_n(\tau_q + \tau_e)} \right] \tag{27b}$$

$$\lambda_n = \gamma_n \left[1 - \frac{\tau_x}{\tau_q + \tau_e} \right]^{1/2} \tag{27c}$$

Equation (26) is an ordinary differential equation whose solution is

$$\begin{aligned} \psi_n(t) = {} & e^{\beta_n t} \left\{ D_{1n} sinh\left[\sqrt{(\beta_n^2 - \lambda_n^2)} t \right] + D_{2n} cosh\left[\sqrt{(\beta_n^2 - \lambda_n^2)}\, t \right] \right\} \\ & + \int_{\tau=0}^{t} \frac{e^{\beta_n(t-\tau)} sinh\left[\sqrt{(\beta_n^2 - \lambda_n^2)}(t - \tau) \right]}{\sqrt{(\beta_n^2 - \lambda_n^2)}} S_n^*(\tau) d\tau \end{aligned} \tag{28}$$

Depending on the relative magnitude of β_n and λ_n, the quantity $\sqrt{\beta_n^2 - \lambda_n^2}$ can be real or imaginary, while $\psi_n(t)$ is always real. The constants D_{1n} and D_{2n} in Eq. (28) depend on the initial temperature $T_i(\boldsymbol{r}) = T(\boldsymbol{r}, 0)$ and its derivative $T_{ii}(\boldsymbol{r}) = [\partial T(\boldsymbol{r}, t)/\partial t]_{t \to 0}$. Once the function $\psi_n(t)$ is known, Eq. (23) provides the function $\theta_f(\boldsymbol{r}, t)$ with homogeneous boundary conditions for insertion in Eq. (20).

The contribution of the initial condition in Eq. (22) is

$$\theta_I(\boldsymbol{r},t)=\sum_{n=1}^{\infty}\frac{F_n(\boldsymbol{r})}{N_n}e^{-(\gamma_n-\beta_n)t}\left\{\frac{sinh\left[\sqrt{(\beta_n^2-\lambda_n^2)}t\right]}{\sqrt{(\beta_n^2-\lambda_n^2)}}\right.$$
$$\times\left[(\gamma_n-\beta_n)\int_V F_n(\boldsymbol{r}')T_i(\boldsymbol{r}')dV'+\int_V F_n(\boldsymbol{r}')T_{ii}(\boldsymbol{r}')dV'\right] \tag{29}$$
$$\left.+\ cosh\left[\sqrt{(\beta_n^2-\lambda_n^2)}t\right]\int_V F_n(\boldsymbol{r}')T_i(\boldsymbol{r}')dV'\right\}$$

while the contribution of the volumetric heat source in Eq. (22) is

$$\theta_S(\mathbf{r},t)=\sum_{n=1}^{\infty}\int_{\tau=0}^{t}\int_V\left(\frac{F_n(\boldsymbol{r})F_n(\boldsymbol{r}')}{CN_n}\right)e^{-\gamma_n(t-\tau)}$$
$$\times\left\{\frac{e^{\beta_n(t-\tau)}sinh\left[\sqrt{(\beta_n^2-\lambda_n^2)}(t-\tau)\right]}{(\tau_q+\tau_e)\sqrt{(\beta_n^2-\lambda_n^2)}}\right\} \tag{30}$$
$$\times\left(S(\boldsymbol{r}',\tau)+\tau_q\frac{\partial S(\boldsymbol{r}',\tau)}{\partial\tau}\right)dV'd\tau$$

Further details related to the method of determination of the alternative Green's function solution, as defined in Beck et al. (1992), are in Sect. 5. Extensive data utilizing Eq. (30) are in Minkowycz et al. (1999)

The following two numerical examples are selected to show the solutions for the temperature field under local thermal equilibrium and non-equilibrium conditions. The first example is for a semi-infinite body with temperature jump at the wall. The second example considers a porous plate with a finite thickness.

Example 1. For a one-dimensional porous system initially at a temperature T_i, the surface temperature increases to temperature T_o when $t > 0$ during a rapid heating process. As a shorthand notation, let $\tau_a = \tau_e + \tau_q$, and then the dimensionless parameters, using a new dimensionless temperature θ_f, are

$$\xi = x/\sqrt{\alpha\tau_a},\ \eta = t/\tau_a, r = \tau_x/\tau_a,\ \text{and}\ \theta_f = (T_f - T_i)/(T_o - T_i). \tag{31}$$

Equation (19), when $S = 0$, reduces and takes the form

$$\frac{\partial^2\theta_f}{\partial\xi^2}+r\frac{\partial^3\theta_f}{\partial\eta\partial\xi^2}=\frac{\partial\theta_f}{\partial\eta}+\frac{\partial^2\theta_f}{\partial\eta^2}\ \text{for}\ 0\le\xi<b \tag{32}$$

wherein b is the medium thickness and it approaches infinity for a semi-infinite body. Because of the definition of η, this equation is valid if, and only if, $\tau_a = \tau_q + \tau_e > 0$; that is, in the presence of the local thermal non-equilibrium condition. Defining the Laplace transform of $\theta_f(\xi,\eta)$ as $\bar{\theta}_f(\xi,S)$, the Laplace transform of

Eq. (32), when $\theta_f(\xi, 0) = 0$ and $(\partial\theta/\partial\eta|_{\eta=0} = 0)$, takes the form

$$(1 + rs)\frac{d^2\bar{\theta}_f}{d\xi^2} - \left(s + s^2\right)\bar{\theta}_f = 0 \text{ for } 0 \leq \xi < b \tag{33}$$

as $b \to \infty$ for a semi-infinite body.

Equation (33) is an ordinary differential equation whose solution that satisfies the condition as $b \to \infty$ is

$$\bar{\theta}_f = De^{-\sqrt{s(s+1)/(rs+1)}\xi} \tag{34}$$

The constant D in Eq. (34) depends on the surface condition, when $\xi = 0$. For the boundary condition of the first kind, consider the solid matrix having a temperature $T_s = T_o$ at $\xi = 0$. In one-dimensional space, Eq. (5) takes the form

$$T_s(x, t) = T_f(x, t) + \tau_t \frac{\partial T_f(x, t)}{\partial t} \tag{35a}$$

Using the parameters in Eq. (31) and $r_t = \tau_t/\tau_a$, Eq. (35a) becomes dimensionless,

$$\theta_s(\xi, \eta) = \theta_f(\xi, \eta) + r_t \frac{\partial\theta_f(\xi, \eta)}{\partial\eta} \tag{35b}$$

since $\theta_f = (T_f - T_i)/(T_o - T_i)$ and $\theta_s = (T_s - T_i)/(T_o - T_i)$. The Laplace transform of Eq. (35b) yields a simple relation between relation $\bar{\theta}_f$ and $\bar{\theta}_s$; that is

$$\begin{aligned} \bar{\theta}_s(\xi, s) &= \bar{\theta}_f(\xi, s) + r_t s\bar{\theta}_f(\xi, s) \\ &= (1 + r_t s)\,\bar{\theta}_f(\xi, s) \end{aligned} \tag{35c}$$

At the $\xi = 0$ surface, Eq. (35c) provides the surface condition,

$$\begin{aligned} (1 + rs)\bar{\theta}_f(0, s) &= \bar{\theta}_s(0, s) \\ &= \frac{1}{s} \end{aligned} \tag{35d}$$

Using this surface condition in Eq. (34) makes $D = \bar{\theta}_f(0, s) = 1/[s(1 + r_t s)]$ and then Eq. (34) takes the following form:

$$\bar{\theta}_f = \frac{e^{-\sqrt{s(s+1)/(rs+1)}\xi}}{s(1 + rs)} \tag{36a}$$

while Eq. (35c) provides the relation

$$\bar{\theta}_s = \frac{1}{s}e^{-\sqrt{s(s+1)/(rs+1)}\xi} \tag{36b}$$

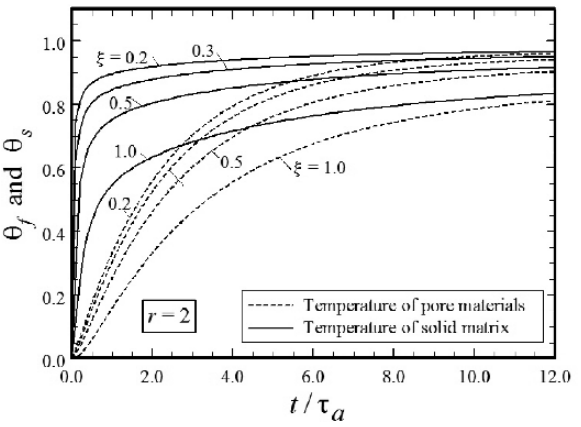

Fig. 2 The variation of temperature with time at selected locations within solids and pores for a semi-infinite body, when $r = \tau_t/\tau_a = 2$

In general, the inverse Laplace transforms of Eqs. (36a,b) are obtainable numerically with ease, using the existing softwares, e.g., see Valkó and Vajda (2002) for programming in Mathematica, Wolfram (1999).

As an illustration of the results, the inverse Laplace transform of $\bar{\theta}_f(\xi, s)$ and $\bar{\theta}_s(\xi, s)$ are obtained numerically at selected values of r and ξ. The data are acquired for a single case when $\tau_x = \tau_t$, that makes $r_t = r$. The acquired data, plotted in Fig. 2, show the local thermal non-equilibrium condition when $r = 2$. The data clearly show relatively large differences between the values of $\theta_f(\xi, s)$ and $\theta_s(\xi, s)$ indicating the existence of LTNE at relatively small times. Reducing the value of τ_t causes r to reduce and; therefore, it reduces the difference between $\theta_f(\xi, s)$ and $\theta_s(\xi, s)$. The data in Fig. 3 are prepared for $r = 0.5$ and they clearly show that the difference between $\theta_f(\xi, s)$ and $\theta_s(\xi, s)$ has been reduced. Furthermore, during a rapid heating, the characteristic length L in a semi-infinite body is the thermal penetration length, defined as $L^2/(\alpha t) = t/(\tau_e + \tau_q)$. This penetration

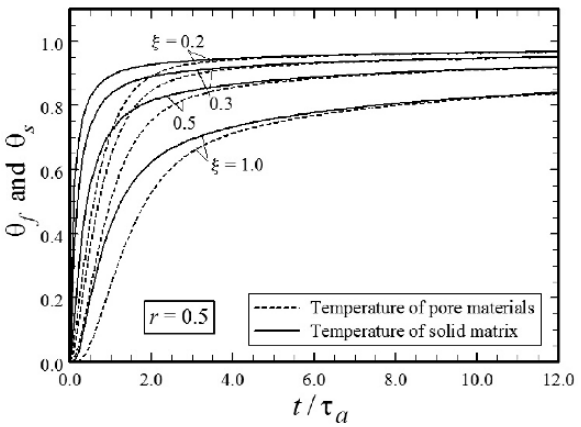

Fig. 3 The variation of temperature with time at selected locations within solids and pores for a semi-infinite body, when $r = \tau_t/\tau_a = 0.5$

length makes the Sp for data in Fig. 2 and 3 to become $Sp = (C_f/C)\eta^2/r$. It is reported in Minkowycz et al. (1999) that the LTE condition exists when $Sp > 100$ while the transition range toward LTNE being within $50 < Sp < 100$. The data in Fig. 3 clearly indicates LTE condition for $Sp = 100$ is located when $\eta^2 = (t/\tau_a)^2$ exceeds 50, depending on the value of C_f/C. A similar trend exists for the data plotted in Fig. 2 and the value of $r = 2$ indicates the LTE condition when $\eta^2 = (t/\tau_a)^2$ exceeds 200.

The mathematical steps in Example 1 reveal a special case, when $r = 1$. This condition reduces Eqs. (36a, b) to take the form

$$\bar{\theta}_s = \frac{1}{s} e^{-\sqrt{s}\xi} \tag{37a}$$

and

$$\bar{\theta}_f = \frac{e^{-\sqrt{s}\xi}}{s(1+s)}. \tag{37b}$$

The inverse Laplace transform of Eq. (37a) is

$$\begin{aligned} \theta_s = \frac{T_s - T_i}{T_o - T_i} &= \text{erfc}\left(\frac{\xi}{\sqrt{4\eta}}\right) \\ &= \text{erfc}\left(\frac{x}{\sqrt{4\alpha t}}\right). \end{aligned} \tag{38a}$$

Utilizing the convolution theorem, Eq. (37b) leads to the functional form of θ_f as

$$\theta_f = \frac{T_f - T_i}{T_o - T_i} = \int_{\tau=0}^{\eta} \text{erfc}\left(\frac{\xi}{\sqrt{4\tau}}\right) e^{-(\eta-\tau)/r} d\tau \tag{38b}$$

while τ is a dummy variable. The solution forms in Eqs. (38a, b) are identical to those obtainable using the classical diffusion equation in semi-infinite bodies. This is expected since Eq. (32) when $r = 1$ can be written as

$$\left(1 + \frac{\partial}{\partial \eta}\right)\left(\frac{\partial^2 \theta_f}{\partial \xi^2} - \frac{\partial \theta_f}{\partial \eta}\right) = 0 \text{ for } 0 \le \xi < \infty \tag{39}$$

and it is satisfied when the diffusion equation $\alpha \partial^2 T_f/\partial x^2 - \partial T_f/\partial t = 0$ is satisfied.

There is another case that emerges when τ_t and τ_x are negligibly small. In this case, Eq. (19) becomes the classical wave equation. For a one-dimensional solution in a semi-infinite solid, Eqs. (39a, b) lead to the relation, Harris et al. (2001),

$$\bar{\theta}_f = \bar{\theta}_s = \frac{1}{S} e^{-\sqrt{s(s+1)}\xi} \tag{40}$$

and the corresponding temperature solution is

$$\theta_f(\xi,\eta)=\left[e^{-\xi/2}+\frac{\xi}{4}\int_{\eta'=0}^{\eta}\frac{e^{-\eta'/2}\,\mathrm{I}_1\left(\frac{1}{2}\sqrt{\eta'^2-\xi^2}\right)}{\sqrt{\eta'^2-\xi^2}}d\eta'\right]H(\eta-\xi) \tag{41}$$

wherein $H(\eta-\xi)=0$ when $\xi>\eta$, otherwise $H(\eta-\xi)=1$. The wave front ξ_o in this limiting wave-like phenomenon is located at $\xi_o=\eta$. Therefore, the transport of energy in a system with a high value of τ_q and a very small value of τ_t approaches that for the thermal wave phenomenon. However, the parameters τ_t and τ_x can produce a dumping effect in porous media that would often eliminate the occurrence of a wave front. This consistent with the statement in Vadasz (2005) that the physical conditions necessary for thermal waves to materialize in dual-phase-lagging porous media conduction are not attainable in a porous slab subject to a combination of constant heat flux and temperature boundary conditions. Also, the data reported in Nnanna et al. (2005) confirm these observations.

Minkowycz et al. (1999) used Eq. (30) to determine the temperature field in the presence of the boundary conditions of the second kind at $x=0$ for bodies with finite thickness. There is a certain singularity that can emerge in the presence of a non-homogeneous boundary condition of the first kind at $x=0$; it is discussed in the next example.

Example 2. The computation of temperature for the materials in the pores requires the solution of equation

$$\frac{\partial^2\theta_f}{\partial x^2}+\tau_x\frac{\partial^3\theta_f}{\partial t\,\partial x^2}=\frac{1}{\alpha}\left[\frac{\partial\theta_f}{\partial t}+\tau_a\frac{\partial^2\theta_f}{\partial t^2}\right] \tag{42a}$$

with $\theta_f=(T_f-T_i)/(T_o-T_i)$. There is an interesting special case when $\tau_x=\tau_a$ while considering the earlier stated hypothesis that $\tau_x=\tau_t$. The solution of this equation in a plate with a thickness of b and with the boundary conditions

$$\begin{cases}\theta_f=\theta_s=0 \text{ when } t=0\\ \theta_s=1 \text{ at } x=0 \text{ and } t>0\\ \partial\theta_f/\partial x=0 \text{ at } x=b\end{cases} \tag{42b}$$

is of interest. The second condition and Eq. (35a) provide the surface temperature for the pore materials; it is

$$\theta_f(0,t)=1-exp(-t/\tau_t) \tag{43}$$

This suggests using a transformation

$$\theta_f(x,t)=\psi(x,t)+1-exp(-t/\tau_t) \tag{44}$$

in order to have a homogeneous boundary condition at $x=0$. Following the use of this transformation, the boundary conditions for ψ are

$$\begin{cases} \psi = 0 \text{ when } t = 0 \\ \psi = 0 \text{ at } x = 0 \\ \partial\psi/\partial x = 0 \text{ at } x = L \end{cases} \tag{45}$$

Note that all the boundary conditions in Eq. (45) are homogeneous. Moreover, in one-dimensional space, the transformation in Eq. (44) makes Eq. (19) to take the following form,

$$\frac{\partial^2\psi}{\partial x^2} + \tau_x \frac{\partial^3\psi}{\partial t \partial x^2} = \frac{1}{\alpha}\left[\frac{\partial\psi}{\partial t} - \frac{1}{\tau_t}e^{-t/\tau_t} + \tau_a \frac{\partial^2\psi}{\partial t^2} + \frac{\tau_a}{(\tau_t)^2}e^{-t/\tau_t}\right]$$

When $\tau_t = \tau_a$, the two exponential terms in this equation have the same magnitudes but with opposite signs; they would drop out and this equation also becomes homogeneous. Therefore, the solution for this equation with the specified boundary conditions for ψ, in Eq. (45), is a trivial one; that is $\psi = 0$. Certainly this is unacceptable because it makes $\theta_f(x, t) = 1 - exp(-t/\tau_t)$, independent of the axial coordinate x. It is possible to eliminate this phenomenon when $\tau_x = \tau_t = \tau_a$. This is expected when using the $\tau_x = \tau_t$ model and the relation $\tau_q = \tau_t(1 - \varepsilon)C_f/C$. Under these conditions, Eq. (42a) takes the form as given by Eq. (39) whose solution is satisfied if the equation

$$\alpha \frac{\partial^2\theta_f}{\partial x^2} - \frac{\partial\theta_f}{\partial t} = 0 \tag{46a}$$

is satisfied; which is the classical diffusion equation. The above transformation, Eq. (44), makes Eq. (46b) to become

$$\alpha \frac{\partial^2\psi}{\partial x^2} - \frac{\partial\psi}{\partial t} + \frac{1}{\tau_t}e^{-t/\tau_t} = 0 \tag{46b}$$

subject to boundary conditions as given by Eq. (45).

In dimensionless space, when $\eta = t/\tau_t$ and $\xi = x/\sqrt{\alpha\tau_t}$, the solution of the function $\psi(\xi, \eta)$, as given in Beck et al. (1992), is

$$\psi(\xi, \eta) = \frac{2}{\xi_b}\sum_{m=1}^{\infty} sin\left[(n - 1/2)\,\pi\xi/\xi_b\right]\frac{e^{-\eta} - e^{-[(m-1)\pi/\xi_b]^2\eta}}{\left[(m-1)\pi/\xi_b\right]^2 - 1} \tag{47}$$

where $\xi_b = b/\sqrt{\alpha\tau_t}$. Following the computation of $\psi(\xi, \eta)$, Eq. (44) provides the values of $\theta_f(\xi, \eta)$, and the values of $\theta_s(\xi, \eta)$ are obtainable using Eq. (35b). These quantities are computed and the data are plotted in Fig. 4 for $x/b = \xi/\xi_b = 0.1$, 0.2, 0.3, 0.5 and 1; the data plotted in Fig. 4 are for $\xi_b = 1$. The solid lines represent the temperatures of the solid matrix and the dash lines are for the materials in pores. It is essential to use an alternative method of analysis for the purpose of verifying the accuracy of this solution. Accordingly, the solution of Eq. (33) with the Laplace transform of boundary conditions, as given by Eqs. (42b), is

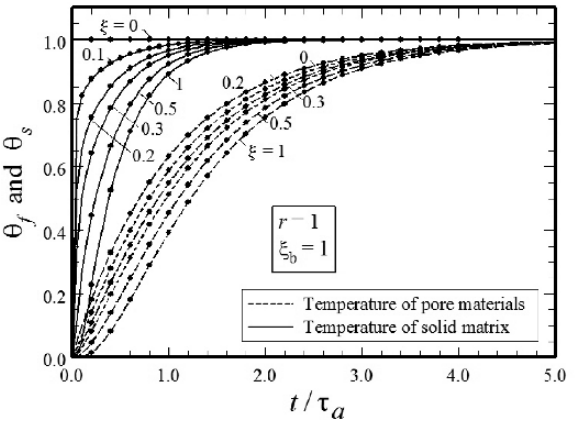

Fig. 4 The variation of temperature with time at selected locations within solid and pore materials in a plate, when $r = \tau_t/\tau_a = 1$

$$\bar{\theta}_f(\xi, s) = \frac{1}{s(1+rs)} \frac{cosh\left[\sqrt{s(s+1)/(1+rs)}(\xi_b - \xi)\right]}{cosh[\sqrt{s(s+1)/(1+rs)}\xi_b]} \tag{48}$$

where $\bar{\theta}_f(\xi, s)$ is the Laplace transform of $\theta_f(\xi, \eta)$ in dimensionless space. The inverse Laplace transform of Eq. (48) is acquired numerically, using the methodology as described earlier. The circular symbols in Fig. 4 depict these numerically computed data. The data equally agree well with both the solid lines and dash lines in Fig. 4. In fact, these numerical computed data from Eqs. (44) and (48) are nearly identical to all six significant figures over the entire range of acquired data plotted in Fig. 4.

It is hypothesized in the aforementioned Example 1 and 2 that τ_t and τ_q are known. Generally, it is possible to determine a reasonably accurate estimate for τ_t. However, it is difficult to develop accurate predictions for τ_q in the absence of experimental data. Because, the value of R_c depends on various factors including geometry, applied pressure, and the constriction effect, thermal conductivity of the fluid, etc. Nnanna et al. (2005) used air as a fluid within packed bed of 3 mm spherical glass beads. Based on Eq. (13) and the definition of τ_t, they reported $\tau_t = 0.036s$. As expected, this value of τ_t is relatively small since the pores are filled air in Nnanna et al. (2005). Additionally, since the thermal conductivity of air is small, R_c in $\tau_q = C_s R_c \Delta V_s / \Delta A_s$ increases and the value of τ_q is expected to increase to a relatively large value, in the neighborhood of 500 seconds. The data show a significant temperature delay due to a large value of τ_q. However, a very small value of τ_t did not indicate a wave-like phenomenon because an inverse estimation procedure showed that τ_x to be of the order of τ_q, which is much larger than τ_t. This is the primary motivation for the development of an alternative functional form for τ_x, Eq. (18b), to be used for different combination values of τ_t and τ_q.

Using 99 percent pure tetracosane within a packed bed of 3 mm glass spheres, Nnanna and Haji-Sheikh (2005) studied the LTNE during a phase change

phenomenon. Using conduction between adjacent spheres as the sole source of thermal resistance, they reported a preliminary estimate of $\tau_q \approx 50\,s$. The phase change phenomenon in the pores required a modified procedure for estimation of τ_t. The reported estimated lag time $\tau_t \approx (\rho L_t)_p r_h[h(T_s - T_m)]$ includes the contribution of the latent heat L_t in the pores and interstitial heat transfer coefficient using the relation $hr_h/k_e = 2/3$. For an estimated value of $T_s - T_m \approx 4$ to $5^\circ C$, this procedure resulted in a reasonable initial value of $\tau_t \sim 60\,s$ for its inverse determination from a set of experimentally acquired temperature data during a phase change phenomenon. There is a remarkably close agreement between these initial estimated values and the computed values of $\tau_q = 47.3\,s$ and $\tau_t = 60.1\,s$, as reported in Nnanna et al. (2004) and in Nnanna and Haji-Sheikh (2005) following an inverse estimation procedure.

4 Temperature Field with Moving Fluid

Various studies related to the effects of local thermal non-equilibrium in porous media are in the archival literature. As an illustration, the studies related to the developing forced convection is reported by Khashan et al. (2005), Hao and Tao (2003a, b Part I and II), Nield et al. (2002), and others. Certainly, in the presence of phase change in the flow field, the condition of LTNE exists and this phenomenon is discussed in Duval et al. (2004) and in Cao et al. (2000).

For a fluid moving with a finite velocity, the computation of temperature, from Eq. (10), is possible by numerical means. Also, analytical solutions are possible for special cases, and these solutions can serve as valuable tools for verification objectives. One special case is when the velocity vector in Eq. (10) has a constant value. Further simplification can be realized when the two parameters τ_x and τ_q have nearly the same value; this latter condition modifies Eq. (10) to become

$$\mathsf{L}(T_f) + \tau_q \frac{\partial}{\partial t}[\mathsf{L}(T_f)] + \left(S + \tau_q \frac{\partial S}{\partial t}\right) = C\left[\frac{\partial T_f}{\partial t} + (\tau_e + \tau_q)\frac{\partial^2 T_f}{\partial t^2}\right] \tag{49a}$$

As before, using a function T^* that satisfies the non-homogeneous boundary conditions and applying Eq. (20) leads to the equation

$$\mathsf{L}(\theta_f) + \tau_q \frac{\partial}{\partial t}[\mathsf{L}(\theta_f)] + \left(S + \tau_q \frac{\partial S}{\partial t}\right) + S_b = C\left[\frac{\partial \theta_f}{\partial t} + (\tau_e + \tau_q)\frac{\partial^2 \theta_f}{\partial t^2}\right] \tag{49b}$$

where S_b depends on the functional form of T^*. For this specific case, when velocity has a constant value, it is often possible to use Eq. (23) and obtain series solutions for regular geometries. However, for this case, the function $F_n(\boldsymbol{r})$ in Eq. (23) can be the solution of equation

$$\mathsf{L}[F_n(\boldsymbol{r})] = -\gamma_n C F_n(\boldsymbol{r}) \tag{50}$$

Therefore, Eqs. (20) and (5) would provide the final temperature solution once the function $\theta_f(r, t)$, the solution for Eq. (49b), is known. It should be stated that it is often possible to find a transformation that produces a partial differential equation without the convection terms for all values of r.

Example 3. To demonstrate the behavior of this solution methodology, consideration is given to a relatively thick porous plate initially at temperature T_i. A fluid is entering or leaving this plate in x-direction and, in the absence of other walls, the velocity u has a constant value. In the presence of heat flux at $x = 0$, this example represents an interesting application of transpiration cooling for surface protection in the presence a suddenly applied large heat flux. The case of a sudden temperature change to T_o at $x = 0$ is included in this example, mainly for comparing the two solutions. When $\theta = (T - T_i)/T_{ref}$ while there is no volumetric heat source, the governing energy equation takes the form

$$k_e\left(\frac{\partial^2\theta_f}{\partial x^2}+\tau_x\frac{\partial^3\theta_f}{\partial x^2\partial t}\right)-C_f u\left(\frac{\partial\theta_f}{\partial x}+\tau_q\frac{\partial^2\theta_f}{\partial x\partial t}\right)=C\left[\frac{\partial\theta_f}{\partial t}+\tau_a\frac{\partial^2\theta_f}{\partial t^2}\right] \tag{51}$$

where τ_a, τ_q, and τ_x are as defined earlier. Using dimensionless variables $\xi = x/\sqrt{\alpha\tau_a}$, $\eta = t/\tau_a$, $r = \tau_x/\tau_a$, $r_q = \tau_q/\tau_a$, $r_t = \tau_t/\tau_a$, Eqs. (51) and (35a) become

$$\frac{\partial^2\theta_f}{\partial\xi^2}+r\frac{\partial^3\theta_f}{\partial\xi^2\partial\eta}-H\left(\frac{\partial\theta_f}{\partial\xi}+r_q\frac{\partial^2\theta_f}{\partial\xi\partial\eta}\right)=\frac{\partial\theta_f}{\partial\eta}+\frac{\partial^2\theta_f}{\partial\eta^2} \tag{52a}$$

$$\theta_s=\theta_f+r_t\frac{\partial\theta_f}{\partial t} \tag{52b}$$

wherein $H = (u/|u|)(C_f/C)\sqrt{C\,|u|^2\,\tau_a/k_e}$. The quantity $(u/|u|) = 1$ when fluid is moving in the positive x-direction and $(u/|u|) = -1$ when fluid is moving in the negative x-direction. Using the definition of θ, the initial conditions are $\theta_f(\xi, 0) = 0$ and $\partial\theta_f(\xi, t)/\partial t|_{t=0} = 0$, while the boundary conditions are to be specified later. Also, the reference temperature T_{ref} depends on the specified boundary condition at $x = 0$ and it will be determined later. By defining the interstitial Peclet number as $Pe = Cur_h/k_e$, it makes the controlling parameter $H = \pm(C_f/C)^{3/2}\,Pe/\sqrt{Nu_{rh}}$. This shows that the value of H strongly depends on Pe, since $C_f/C < 1$ and Nu_{rh} is of the order of 1. It is known that the effect of axial conduction becomes negligible when Pe is larger than 1. Therefore, in the presence of axial conduction in Eq. (52a), the parameter H is generally smaller than 1.

A simple method of finding the solution of Eq. (52a) is by using the Laplace transform method. When $\bar{\theta}(\xi, s)$ is the Laplace transform of $\theta(\xi, \eta)$, the Laplace transform of Eq. (52a) with the specified initial conditions takes the following form:

$$(1+rs)\frac{d^2\bar{\theta}_f}{d\xi^2}-H\left(1+r_q s\right)\frac{d\bar{\theta}_f}{d\xi}=(s+s^2)\bar{\theta}_f \tag{53}$$

This is an ordinary second order differential equation with constant coefficients whose solution is

$$\bar{\theta}_f(\xi, s) = e^{H(1+r_q s)\xi}\left[D_1 e^{-\sqrt{H^2(1+r_q s)^2+4(1+rs)(s+s^2)}\xi} + D_2\, e^{\sqrt{H^2(1+r_q s)^2+4(1+rs)(s+s^2)}\xi}\right] \tag{54}$$

When H is negative, the problem under consideration simulates flow leaving a porous device with insulated sidewalls. Therefore, for a sufficiently thick device, the condition of finite $\bar{\theta}_f(\xi, s)$ as $\xi \to \infty$ makes $D_2 = 0$. The first set of data in Fig. 5(a) is for suddenly applied heat flux q_w at $x = 0$, see the inset of Fig. 5(a) for q_w direction. For the data in this figure, $T_{ref} = q_w\sqrt{\alpha\tau_a}/k_e$, and this makes $\theta_f = k_e(T_f - T_i)/(q_w\sqrt{\alpha\tau_a}\,)$ and $\theta_s = k_e(T_s - T_i)/(q_w\sqrt{\alpha\tau_a}\,)$. The application of boundary condition of the second kind at $x = 0$ requires the use of Eq. (8) with a constant q_w, that is

$$q_w = -k_e\{\nabla T_f(0, t) + \tau_x \frac{\partial}{\partial t}[\nabla T_f(0, t)]\} \tag{55}$$

In dimensionless space, this equation provides the value of D_1 in Eq. (54) and it becomes

$$\bar{\theta}_f(\xi, s) = \frac{exp\left\{\left[H(1 + r_q s) - \sqrt{H^2(1 + r_q s)^2 + 4(1 + rs)(s + s^2)}\right]\xi\right\}}{s(1 + rs)\left[H(1 + r_q s) - \sqrt{H^2(1 + r_q s)^2 + 4(1 + rs)(s + s^2)}\right]} \tag{56}$$

The second set of data in Fig. 5(b) is for the boundary condition of the first kind at $x = 0$. Assuming the reference temperature is $T_{ref} = T_o - T_i$, the porous materials temperature $\theta_s(0, \eta) = 1$ readily provides the value of $D_1 = 1/[s(1 + r_t s)]$, using Eq. (35d). This makes Eq. (54) to become

$$\bar{\theta}_f(\xi, s) = \frac{e^{H(1+r_q s)\xi}}{s(1 + r_t s)} e^{-\sqrt{H^2(1+r_q s)^2+4(1+rs)(s+s^2)}\xi} \tag{57}$$

The inverse Laplace transforms for these two cases, Eqs. (56) and (57), are acquired numerically, see a Mathematica package from Valkó and Vajda (2002). Figures 5 (a-b) are prepared to show this trend when $H = -1/2$ and $\tau_q/\tau_t = (1 - \varepsilon)C_s/C = 1/2$; therefore, the input parameters in Eq. (57) become $r = 1.25$, $r_q = 0.5$, and $r_t = 1$. The data plotted in both figures show the condition of LTNE that becomes LTE at larger times. Of course, as before, LTNE condition exists when r is relatively large. The data in Fig. 5(a) show a gradual increase in the solid materials temperature $\theta_s(0, \eta)$ at $\xi = 0$ location, while $\theta_s(0, \eta)$ undergoes is rapid jump in Fig. 5(b) due to specified boundary condition. At larger values, e.g., $\xi = 2$, the functional variations of temperature within the solid materials and the fluid in the pores become similar.

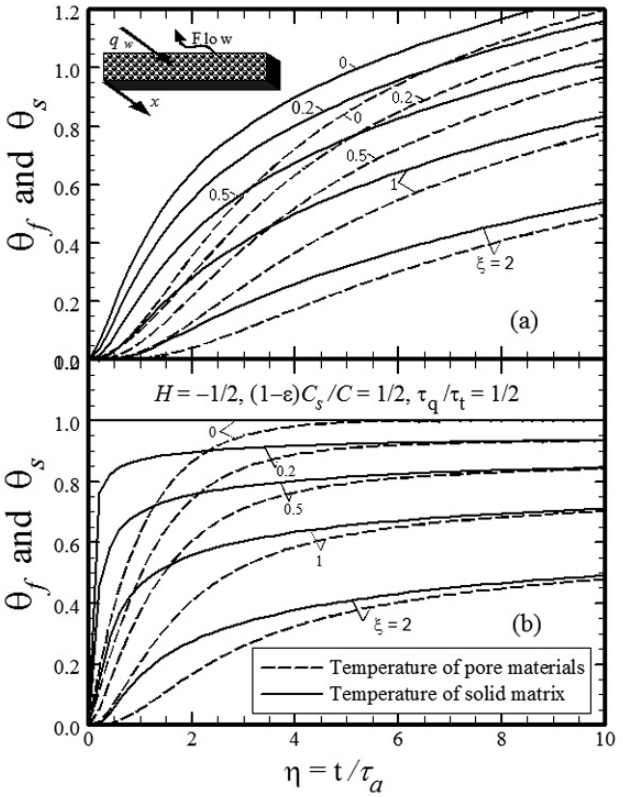

Fig. 5 The variation of temperature with time at selected locations within solid and pore materials in the presence of a flow field, (a) boundary condition of the second kind and (b) boundary condition of the first kind

5 Remarks and Discussions

The formulation of the governing energy equations under LTNE condition shows that the exact temperature solutions in all regular geometries are obtainable when there is no moving fluid. The methodology can be extended to regular geometries with moving fluid for special cases. In general, the eigenfunctions, if available, are those for classical solution under LTE condition while modifications are needed to account for the time as a variable. For a generalized solution, it is appropriate to present a Green's function solution. The Green's function represents the thermal response of the system to a point source of unit strength at location $\boldsymbol{r}'$ occurring at time τ. The functional form of the source is $S = C\delta(\tau-\tau^*)\delta(\boldsymbol{r}'-\boldsymbol{r}^*)$. In the absence of a moving fluid, by placing $S(\boldsymbol{r}', \tau)$ in Eq. (30), following some algebraic steps, the result in terms of Green's function is

$$G(\boldsymbol{r}, t|\boldsymbol{r}', \tau) = G_1(\boldsymbol{r}, t|\boldsymbol{r}', \tau) + \frac{\tau_q}{\tau_e + \tau_q}\left[G_2(\boldsymbol{r}, t|\boldsymbol{r}', \tau) - G_3(\boldsymbol{r}, t|\boldsymbol{r}', \tau)\right] \qquad (58)$$

where

$$G_1(\boldsymbol{r}, t|\boldsymbol{r}', \tau) = \sum_{n=1}^{\infty} \left(\frac{F_n(\boldsymbol{r}) F_n(\boldsymbol{r}')}{N_n} \right) e^{-\gamma_n (t-\tau)} \times \left\{ \frac{e^{\beta_n (t-\tau)} sinh\left[\sqrt{(\beta_n^2 - \lambda_n^2)} (t-\tau) \right]}{(\tau_q + \tau_e) \sqrt{(\beta_n^2 - \lambda_n^2)}} \right\}, \tag{59}$$

$$G_2(\boldsymbol{r}, t|\boldsymbol{r}', \tau) = \sum_{n=1}^{\infty} \left(\frac{F_n(\boldsymbol{r}) F_n(\boldsymbol{r}')}{N_n} \right) e^{-\gamma_n (t-\tau)} \times \left\{ e^{\beta_n (t-\tau)} cosh\left[\sqrt{(\beta_n^2 - \lambda_n^2)}\, (t-\tau) \right] \right\} \tag{60}$$

and

$$G_3(\boldsymbol{r}, t|\boldsymbol{r}', \tau) = \sum_{n=1}^{\infty} \left(\frac{F_n(\boldsymbol{r}) F_n(\boldsymbol{r}')}{N_n} \right) e^{-\gamma_n (t-\tau)} \times \left\{ (\gamma_n - \beta_n) \frac{e^{\beta_n (t-\tau)} sinh\left[\sqrt{(\beta_n^2 - \lambda_n^2)} (t-\tau) \right]}{\sqrt{(\beta_n^2 - \lambda_n^2)}} \right\} \tag{61}$$

The Green's function solution that describes Eq. (29) is

$$T_I(\boldsymbol{r}, t) = \int_V G_3(\boldsymbol{r}, t|\boldsymbol{r}', \tau) T_i(\boldsymbol{r}') dV' + (\tau_q + \tau_e) \int_V G_1(\boldsymbol{r}, t|\boldsymbol{r}', \tau) T_{ii}(\boldsymbol{r}') dV' + \int_V G_2(\boldsymbol{r}, t|\boldsymbol{r}', \tau) T_i(\boldsymbol{r}') dV' \tag{62}$$

and Eq. (30) for the volumetric heat source effect is

$$T_S(\boldsymbol{r}, t) = \frac{1}{C} \int_{\tau=0}^{t} d\tau \int_V G_1(\boldsymbol{r}, t|\boldsymbol{r}', \tau) \left(S(\boldsymbol{r}', \tau) + \tau_q \frac{\partial S(\boldsymbol{r}', \tau)}{\partial \tau} \right) dV' \tag{63}$$

Therefore, the temperature solutions for variety of systems are readily available by modifying the available Green's functions and Green's function solutions for classical Fourier type heat conduction. This methodology can be extended to systems with moving fluids but with limitations as presented earlier, e.g., in Sect. 4.

This presentation confirms that in the presence of a rapidly changing local temperature in a porous medium, the condition of LTNE is expected. The acquired data for LTNE in porous media indicate that the assumption of LTE is valid when t/τ_t is relatively large. However, it is not universally valid since the temperature information under LTNE condition differs from those with LTE condition in a number of applications depending on time, specified thermophysical properties, and imposed heating conditions.

Nomenclature

A	area, m^2
A_p	pore area parameter $\Delta A_p/\Delta V$, m^{-1}
b	plate thichness, m
C	$\varepsilon C_f + (1-\varepsilon)C_s$
C_f, C_p	capacitance for pore materials, $Jm^{-3}K^{-1}$
C_s	capacitance for solid martix, $Jm^{-3}K^{-1}$
$F_n(\boldsymbol{r})$	eigenfunction, Eq. (23)
h	interstitial heat transfer coefficient, $Wm^{-2}K^{-1}$
k_e	equivalent thermal conductivity, $Wm^{-2}K^{-1}$
L	characteristic lenght, m
$\mathrm{L}(T_f)$	operator, $\nabla\cdot(k_e\nabla T_f) - C_f V\cdot\nabla T_f$
LTE	local thermal equilibrium
LTNE	local thermal non-equilibrium
m, n	indices
N_n	norms
Nu_{rh}	hr_h/k_e
Pe	Cur_h/k_e
q	heat flux, W/m^2
r	τ_x/τ_a
r_h	$\Delta V_p/\Delta A_p$, m
r_q, r_t	τ_q/τ_a and τ_t/τ_a
R_c	contact resistance, m^2KW^{-1}
S	volumetric heat source, Wm^{-3}
S_n^*	see equation (27a)
Sp	Sparrow number, $hL^2/k_e r_p$
T	temperature, K
T_o	T_s at $x=0$, K
T_{ref}	$q_w\sqrt{\alpha\tau_a}/k_e$ or $T_o - T_i$
t	time, s
u	x-component of velocity, m/s
$\boldsymbol{V}$	velocity vector
V_p	pore volume, m^3
x	coordinate, m

Greek Symbols

α	thermal diffusivity, m^2s^{-1}
β_n	parameter related to γ_n, equation (27b)
γ_n	eigenvalue
ε	V_f/V
η	t/τ_a
θ	transformed temperature, Eq. (20) or $(T_f - T_i)/T_{ref}$

λ_n	parameter related to γ_n, equation (27c)
ν	kinematic viscosity, m^2/s
ξ	$x/\sqrt{\alpha\tau_a}$
τ	dummy variable and Green's function parameter
τ_a	lag time $\tau_e + \tau_q$, s
τ_e	$(1-\varepsilon)(C_s/C)\tau_t$, s
τ_q	lag time in Eq. (8), s
τ_t	lag time for pore temperature, s
τ_x	in Eq. (8), s
ψ	transformed dimensionless temperature, Eq. (44)
ψ_n	time parameter, Eq. (23)

Subscripts

i	initial
f	fluid
p	pore
s	solid
w	wall

References

Amiri A and Vafai K (1994), Analysis of dispersion effects and non-thermal equilibrium, non-Darcian, variable porosity incompressible flow through porous media, *International Journal of Heat and Mass Transfer*, Vol. 37, pp. 939–954.

Beck J V, Cole K D, Haji-Sheikh A, and Litkouhi B (1992), *Heat Conduction Using Green's Functions,* Hemisphere Publishing Corp., Washington, D. C.

Cao L, Kakaç S, Liu H T, and Sarma P K (2000), The effects of thermal non-equilibrium and inlet temperature on two-phase flow pressure drop type instabilities in an upflow boiling system, *International Journal of Thermal Sciences*, Vol. 39, No. 9–11, pp. 886–895.

Damm D L and Fedorov A G (2006), Local thermal non-equilibrium effects in porous electrodes of the hydrogen-fueled SOFC, *Journal of Power Sources*, Vol. 159, No. 2, pp. 1153–1157.

Duval F, Fichot F, and Quintard M (2004), A local thermal non-equilibrium model for two-phase flows with phase-change in porous media, *International Journal of Heat and Mass Transfer*, Vol. 47, No. 3, pp. 613–639.

Fichot F, Duval F, Trégourès N, Béchaud C, and Quintard M (2006), The impact of thermal non-equilibrium and large-scale 2D/3D effects on debris bed reflooding and coolability, *Nuclear Engineering and Design*, Vol. 236, No. 19–21, pp. 2144–2163.

Fournier D and Boccara A C (1989), Heterogeneous media and rough surfaces: A fractal approach for heat diffusion studies, *Physica A: Statistical and Theoretical Physics*, Vol. 157, No. 1, pp. 587–592.

Hao Y L and Tao Y-X (2003a), Non-thermal equilibrium melting of granular packed bed in horizontal forced convection. Part I: experiment, *International Journal of Heat and Mass Transfer*, Vol. 46, No. 26, pp. 5017–5030.

Hao Y L and Tao Y-X (2003b), Non-thermal equilibrium melting of granular packed bed in horizontal forced convection. Part II: numerical simulation, *International Journal of Heat and Mass Transfer*, Vol. 46, No. 26, pp. 5031–5044

Harris K T, Haji-Sheikh A, and Nnanna A G A (2001), Phase change phenomena in porous media—A non-local thermal equilibrium model, *International Journal of Heat and Mass Transfer*, Vol. 44, pp. 1619–1625.

Hays-Stang K J and Haji-Sheikh A (1999), A unified solution for heat conduction in thin films, *International Journal of Heat and mass Transfer* Vol. 42, pp. 455–465.

Jiang P-X, Fan M-H, Si G-S, and Ren Z (2001), Thermal-hydraulic performance of small scale micro-channel and porous-media heat-exchangers, *International Journal of Heat and Mass Transfer*, Vol. 44, pp. 1039–1051.

Khashan S A, Al-Amiri A M, and Al-Nimr M A (2005), Assessment of the local thermal non-equilibrium condition in developing forced convection flows through fluid-saturated porous tubes, *Applied Thermal Engineering*, Vol. 25, No. 10, pp. 1429–1445.

Lage J L, Weinert A K, Price D C, and Weber, R M (1996), Numerical study of low permeability micorporous heat sink for coiling phased-array radar systems, *International Journal of Heat Mass Transfer*, Vol. 39, No. 17, pp. 3633–3647.

Lee D-Y and Vafai K (1999), Analytical characterization and conceptual assessment of solid and fluid temperature differentials in porous media, *International Journal of Heat and Mass Transfer*, Vol. 42, No. 3, pp. 423–435.

Minkowycz W J, Haji-Sheikh A, and Vafai K (1999), On departure from local thermal equilibrium in porous media due to a rapidly changing heat source. The Sparrow Number, *International Journal of Heat and Mass Transfer*, Vol. 42, No. 18, pp. 3373–3385.

Nield D A, Kuznetsov A V, and Xiong M (2002), Effect of local thermal non-equilibrium on thermally developing forced convection in a porous medium, *International Journal of Heat and Mass Transfer*, Vol. 45, No. 25, pp. 4949–4955.

Nnanna A G A (2002), Phase change phenomena in porous media: A local thermal non-equilibrium study. Ph.D. Dissertation, The University of Texas at Arlington, Arlington, Texas.

Nnanna A G A and Haji-Sheikh A (2005), Sensitivity coefficients for experimental estimation of interstitial properties during phase change in porous media, *Inverse Problem in Science and Engineering*, Vol. 13, No. 6, pp. 595–616.

Nnanna A G A, Haji-Sheikh A, and Harris K T (2004), Experimental study of local thermal non-equilibrium phenomena during phase change in porous media, *International Journal of Heat and Mass Transfer*, Vol. 47, No. 19-20, pp. 4365–4375.

Nnanna A G A, Harris K T, and Haji-Sheikh A (2005), An experimental study of non-Fourier thermal response in porous media, *Journal of Porous Media*., Vol. 8, No. 1, pp 31–44.

Tzou D Y (1997), *Macro- to Microscale Heat Transfer: The Lagging Behavior*, Taylor and Francis, New York.

Vadasz P (2005), Lack of oscillations in dual-phase-lagging heat conduction for a porous slab subject to imposed heat flux and temperature, *International Journal of Heat and Mass Transfer*, Vol. 48, No. 14, pp. 2822–2828.

Valkó P P and Vajda S (2002), Inversion of noise-free Laplace transforms: Towards a standardized set of test problems, *Inverse Problems in Engineering*, Vol. 10, pp. 467–483.

Vick B and Scott E P (1998), Heat transfer in a matrix with embedded particles, *ASME*, *HTD*, Vol. 361–4, No. 0272–5673, pp. 193–198.

Wakao N and Kaguei S (1982), *Heat and Mass Transfer in Packed Beds*, Gordon and Breach Science Publication, Cambridge.

Wolfram, S (1999), *The Mathematica Book*, Fourth edition, Cambridge University press, Cambridge, UK.

General Heterogeneity Effects on the Onset of Convection in a Porous Medium

D.A. Nield

1 Introduction

The classical Horton–Rogers–Lapwood problem, for the onset of convection in a horizontal layer of a saturated porous medium uniformly heated from below, has been extensively studied. Studies of the effects of heterogeneity in this situation are surveyed in Nield and Bejan (2006). The pioneering study was that of Gheorghitza (1961). Particularly notable are the studies of vertical heterogeneity (especially the case of horizontal layers) by McKibbin and O'Sullivan (1980, 1981), McKibbin and Tyvand (1982, 1983, 1984), Nield (1994) and Leong and Lai (2001, 2004), and the studies of horizontal heterogeneity by McKibbin (1986), Nield (1987) and Gounot and Caltagirone (1989). Some more general aspects of conductivity heterogeneity have been discussed by Vadasz (1990), Braester and Vadasz (1993) and Rees and Riley (1990). Until recently one set of questions has been left unanswered: namely in what respects, if any, does the effect of vertical heterogeneity (by this is meant variation in the vertical direction and this includes horizontal layering) differ from the effect of horizontal heterogeneity for each of the permeability (hydrodynamic) and conductivity (thermal) types, and how do these two types interact with each other? This chapter surveys attempts to answer those questions and related matters.

The topic of permeability heterogeneity is currently of interest for an additional reason. Simmons et al. (2001) and Prasad and Simmons (2003) have pointed out that in many heterogeneous geologic systems, hydraulic properties such as the hydraulic conductivity of the system under consideration can vary by many orders of magnitude and sometimes rapidly over small spatial scales. They also pointed out that the onset of instability in transient, sharp interface problems is controlled by very local conditions in the vicinity of the evolving boundary layer and not by the global layer properties or indeed some average property of that macroscopic layer. They also pointed out that any averaging process would remove the very structural controls

D.A. Nield
University of Auckland, Auckland, New Zealand
e-mail: d.nield@auckland.ac.nz

P. Vadász (ed.), *Emerging Topics in Heat and Mass Transfer in Porous Media*,

© Springer Science+Business Media B.V. 2008

and physics that are expected to be important in controlling the onset, growth, and/or decay of instabilities in a highly heterogeneous system. In particular, in the case of dense plume migration in highly heterogeneous environments the application of an average global Rayleigh number based upon average hydraulic conductivity of the medium is problematic. In these cases, an average Rayleigh number is unable to predict the onset of instability accurately because the system is characterized by unsteady flows and large amplitude perturbations.

Nield and Simmons (2007) have emphasized the need to distinguish between weak heterogeneity and strong heterogeneity. For the case of weak heterogeneity (properties varying by a factor not greater than 3 or so) the introduction of an equivalent Rayleigh number is useful. The extent to which an equivalent Rayleigh number (based on averaged permeability and averaged conductivity) might work was investigated by Nield (1994) for the case of vertical heterogeneity. He concluded that provided the variation of each of the various parameters lies within one order of magnitude, a rough and ready estimate of an effective Rayleigh number can be made that is useful as a criterion for Rayleigh–Bénard convection. This effective Rayleigh number is based on the arithmetic mean quantities (such as the permeability) that appear in the numerator, and the harmonic mean of quantities (such as the viscosity) that appear in the denominator of the defining expression. Similar conclusions were drawn by Leong and Lai (2001, 2004). In the case of strong heterogeneity the concept of an effective Rayleigh number loses validity as a criterion for the onset of instability.

In this chapter we first look at the case of weak heterogeneity for the general case involving both vertical heterogeneity and horizontal heterogeneity. For this complicated situation no exact analytical solution can be expected to exist, but it is reasonable to seek an approximate analytical solution, based on the expectation that for weak heterogeneity the solution would not differ dramatically from the solution for the homogeneous case. Following this approach, we utilize an extension of the Galerkin approximate method that has been widely employed (see, for example, Finlayson (1972)). In the context of the onset of convection, the Galerkin method commonly used involves trial functions of the vertical coordinate only. The analysis described below employs a Galerkin method involving trial functions of both the vertical and horizontal coordinates and chosen to be the known exact solutions for the homogeneous case.

The problem studied is two-dimensional convection in a rectangular box with impervious thermally insulated side walls. In Section 2 an analysis is presented based on the Brinkman model for the momentum equation and for the double-diffusive situation. In Section 3 some illustrative results are presented. In Section 4 the discussion is extended to include the situation where the basic vertical gradient in nonuniform. This situation is treated as a heterogeneity of that gradient. In Section 5 results are given for the case of a bidisperse porous medium. As a special case this covers local thermal non-equilibrium in a regular porous medium. In Section 6 it is shown how an enclosure of non-uniform width can be considered as case of heterogeneity of width. In Section 7 strong heterogeneity is discussed. Some concluding remarks are made in Section 8.

2 Analysis

Single-phase flow in a saturated porous medium is considered. Asterisks are used to denote dimensional variables. We consider a rectangular box, $0 \leq x^* \leq L$, $0 \leq y^* \leq H$, where the y^*-axis is in the upward vertical direction. The side walls are taken as insulated, and uniform temperatures T_u and T_l are imposed at the upper and lower boundaries, respectively. Likewise the sidewalls are taken to be impermeable to concentration flux and uniform concentrations C_u and C_l are imposed at the upper and lower boundaries, respectively.

Within this box the permeability is $K^*(x^*, y^*)$ and the overall (effective) thermal conductivity is $k^*(x^*, y^*)$. The Darcy velocity is denoted by $\mathbf{u}^* = (u^*, v^*)$. The Oberbeck–Boussinesq approximation is invoked.

The equations of continuity (expressing conservation of mass) for the velocity components are

$$\frac{\partial u^*}{\partial x^*} + \frac{\partial v^*}{\partial y^*} = 0. \tag{1}$$

We write the momentum equations as

$$\frac{\partial P^*}{\partial x^*} = -\frac{\mu}{K^*}u^* + \tilde{\mu}\nabla^2 u^*, \tag{2}$$

$$\frac{\partial P^*}{\partial y^*} = -\frac{\mu}{K^*}v^* + \tilde{\mu}\nabla^2 v^* + \rho_f g[\beta_T(T^* - T_0+)\,\beta_C(C^* - C_0)] \tag{3}$$

Here ρ_f is the density of the fluid, β_T and β_C are the volumetric thermal and solutal expansion coefficients of the fluid, and T_0 and C_0 are the reference temperature and concentration, respectively.

The thermal energy and solutal equations are taken as

$$(\rho c)_m \frac{\partial T^*}{\partial t^*} + (\rho c)_f \mathbf{v}^* \cdot \nabla T^* = {k^*}_f \nabla^2 T^*, \tag{4}$$

$$\phi \frac{\partial C^*}{\partial t^*} + \mathbf{v}^* \cdot \nabla C^* = {D^*}_m \nabla^2 C^*. \tag{5}$$

Here c denotes the specific heat at constant pressure, k denotes the thermal conductivity, and ${D^*}_m = \phi D^*$ where D^* is the diffusivity of the solute in a fluid clear of solid material.

In order to simplify the following analysis, on the right-hand side of Eq. (4) the terms involving the partial derivatives of ${k^*}_f$ with respect to the spatial coordinates have been dropped. In accordance with the assumption of weak heterogeneity, it is assumed that the variation of ${k^*}_f$ over the enclosure is small compared with the mean value of ${k^*}_f$. It can be shown that this approximation has no effect on the results presented below provided that ${k^*}_f$ is a linear function of the spatial variables considered separately. A similar approximation involving ${D^*}_m$ has been made in Eq. (5). A similar assumption about the variation of the permeability is made below.

We define K_0, k_o and D_{m0} as the mean values of K^*, k^* and ${D^*}_m$, respectively, and write

$$K = K^*/K_0, \quad k_f = {k^*}_f/k_{f0}, \quad D_m = {D^*}_m/D_{m0}. \tag{6}$$

We introduce dimensionless variables as follows:

$$x^* = Lx,\ y^* = Hy,\ t^* = \frac{(\rho c)_f}{k_{f0}} d^2 t,\ P^* = \frac{k_{f0}\mu}{(\rho c)_f K_0} P, \tag{7}$$

$$u^* = \frac{\phi k_{f0}}{(\rho c)_f L} u,\ v^* = \frac{\phi k_{f0}}{(\rho c)_f H} v, \tag{8}$$

$${T_f}^* = (T_l - T_u)\theta + T_u,\ C^* = (C_l - C_u)\gamma + C_u. \tag{9}$$

We take the reference temperature T_0 as $T_l - T_u$ and the reference concentration C_0 as $C_l - C_u$.

We define a thermal Rayleigh number Ra_T, a solutal Rayleigh number Ra_C, a Darcy number Da , and a heat capacity ratio σ, by

$$\mathrm{Ra}_T = \frac{\rho_f g \beta_T (T_l - T_u) K_0 H}{\mu k_{f0}/(\rho c)_f}, \qquad \mathrm{Ra}_C = \frac{\rho_f g \beta_C (C_l - C_u) K_0 H}{\mu D_{m0}},$$
$$\mathrm{Da} = \frac{\tilde{\mu}}{\mu}\frac{K_0}{H^2}, \quad \sigma = \frac{(\rho \mathrm{c})_m}{(\rho c)_f}. \tag{10}$$

We also introduce the height-to-depth aspect ratio A defined by

$$A = H/L. \tag{11}$$

The continuity equation becomes

$$A^2 \frac{\partial u}{\partial x} + \frac{\partial v}{\partial y} = 0. \tag{12}$$

The streamfunction ψ is according defined by

$$u = \frac{1}{A^2}\frac{\partial \psi}{\partial y}, v = -\frac{\partial \psi}{\partial x}. \tag{13}$$

Elimination of the pressure from Eqs. (2) and (3), on the assumption that the maximum variation of permeability in the box is a small fraction of the mean permeability so that derivatives of the permeability are small, gives

$$\left[A^2 \frac{\partial^2}{\partial x^2} + \frac{\partial^2}{\partial y^2} - DaK(x, y)\left(A^2 \frac{\partial^2}{\partial x^2} + \frac{\partial^2}{\partial y^2}\right)^2\right]\psi = -K(x, y)A^2$$
$$\times \left(\mathrm{Ra}_T \frac{\partial \theta}{\partial x} + \mathrm{Ra}_C \frac{\partial \gamma}{\partial x}\right), \tag{14}$$

Also, the thermal energy Eqs (4) and (5) become

$$\frac{\partial\theta}{\partial t}+\left(\frac{\partial\psi}{\partial y}\frac{\partial\theta}{\partial x}-\frac{\partial\psi}{\partial x}\frac{\partial\theta}{\partial y}\right)=k(x,y)\left(A^2\frac{\partial^2}{\partial x^2}+\frac{\partial^2}{\partial y^2}\right)\theta, \tag{15}$$

$$\phi\frac{\partial\gamma}{\partial t}+\left(\frac{\partial\psi}{\partial y}\frac{\partial\gamma}{\partial x}-\frac{\partial\psi}{\partial x}\frac{\partial\gamma}{\partial y}\right)=D(x,y)\left(A^2\frac{\partial^2}{\partial x^2}+\frac{\partial^2}{\partial y^2}\right)\gamma. \tag{16}$$

The conduction steady state solution is

$$\psi=0,\ \theta=\gamma=1-y. \tag{17}$$

We now perturb this solution and write

$$\psi=\Psi,\ \theta=1-y+\Theta,\ \gamma=1-y+\Gamma. \tag{18}$$

Substitution in Eqs. (14)–(16) and linearization gives

$$\left[-\left(A^2\frac{\partial^2}{\partial x^2}+\frac{\partial^2}{\partial y^2}\right)+\mathrm{Da}K(x,y)\left(A^2\frac{\partial^2}{\partial x^2}+\frac{\partial^2}{\partial y^2}\right)^2\right]\Psi$$
$$-K(x,y)A^2\left(\mathrm{Ra}_T\frac{\partial\Theta}{\partial x}+\mathrm{Ra}_C\frac{\partial\Gamma}{\partial x}\right)=0 \tag{19}$$

$$\frac{\partial\Theta}{\partial t}+\frac{\partial\Psi}{\partial x}-k(x,y)\left(A^2\frac{\partial^2}{\partial x^2}+\frac{\partial^2}{\partial y^2}\right)\Theta=0, \tag{20}$$

$$\phi\frac{\partial\Gamma}{\partial t}+\frac{\partial\Psi}{\partial x}-D(x,y)\left(A^2\frac{\partial^2}{\partial x^2}+\frac{\partial^2}{\partial y^2}\right)\Gamma=0. \tag{21}$$

We consider just the case in which the thermal and solutal gradient are both destabilizing (Ra_T and Ra_C both positive). We then invoke the principle of exchange of stabilities. The differential equations take the matrix form

$$\mathbf{LY}=0, \tag{22}$$

where

$$\mathbf{Y}=(\Psi,\Theta,\Gamma)^T, \tag{23}$$

$$L_{11}=-\left(A^2\frac{\partial^2}{\partial x^2}+\frac{\partial^2}{\partial y^2}\right)+\mathrm{Da}K(x,y)\left(A^2\frac{\partial^2}{\partial x^2}+\frac{\partial^2}{\partial y^2}\right)^2,$$

$$L_{12}=-K(x,y)A^2\,\mathrm{Ra_T}\frac{\partial}{\partial x},$$

$$L_{13}=-K(x,y)A^2\,\mathrm{Ra_C}\frac{\partial}{\partial x},$$

$$
\begin{aligned}
L_{21} &= \frac{\partial}{\partial x}, \\
L_{22} &= -k(x, y)\left(A^2\frac{\partial^2}{\partial x^2} + \frac{\partial^2}{\partial y^2}\right), \\
L_{23} &= 0, \\
L_{31} &= \frac{\partial}{\partial x}, \\
L_{32} &= 0, \\
L_{33} &= -D(x, y)\left(A^2\frac{\partial^2}{\partial x^2} + \frac{\partial^2}{\partial y^2}\right).
\end{aligned} \tag{24}
$$

For conducting, isosolutal stress-free top and bottom boundaries and insulating, impermeable, stress-free side walls, the boundary conditions are

$$
\begin{aligned}
&\Psi = \frac{\partial^2\Psi}{\partial x^2} = \frac{\partial\Theta}{\partial x} = \frac{\partial\Gamma}{\partial x} = 0 \text{ at } x = 0 \text{ and at } x = 1, \\
&\Psi = \frac{\partial^2\Psi}{\partial y^2} = \Theta = \Gamma = 0 \text{ at } y = 0 \text{ and at } y = 1.
\end{aligned} \tag{25}
$$

This set of boundary conditions is satisfied by

$$\Psi_{mn} = \sin m\pi x \sin n\pi y, \ \ m, n = 1, 2, 3, \ldots. \tag{26}$$

$$\Theta_{pq} = \Gamma_{pq} = \cos p\pi x \sin q\pi y, \ \ p, q = 1, 2, 3, \ldots. \tag{27}$$

We can take this set of functions (that are exact eigenfunctions for the homogeneous case) as trial functions for an approximate solution of the heterogeneous case. For example, working at second order, we can try

$$\Psi = A_{11}\Psi_{11} + A_{12}\Psi_{12} + A_{21}\Psi_{21} + A_{22}\Psi_{22}, \tag{28}$$

$$\Theta = B_{11}\Theta_{11} + B_{12}\Theta_{12} + B_{21}\Theta_{21} + B_{22}\Theta_{22}, \tag{29}$$

$$\Gamma = C_{11}\Gamma_{11} + C_{12}\Gamma_{12} + C_{21}\Gamma_{21} + C_{22}\Gamma_{22}. \tag{30}$$

Let R_1, R_2, R_3 be the residuals when the expressions (28)–(30) are substituted in the left-hand sides of the 3 differential equations (22). In turn, R_1 and R_2 are made orthogonal to Θ_{11}, Θ_{12}, Θ_{21}, Θ_{22} and R_3 is made orthogonal to Ψ_{11}, Ψ_{12}, Ψ_{21}, Ψ_{22}.

The result is 12 linear homogeneous equations in the 12 constants $A_{11}, \ldots, C_{22}$ whose solution requires the vanishing of the determinant of coefficients, namely

$$\det \mathbf{M} = 0, \tag{31}$$

where $\mathbf{M}$ is a 12 by 12 matrix.

The full algebraic details are omitted here but may be found in Kuznetsov and Nield (2007).

A typical element is $M_{1,1} =< \Psi_{11} L_{11} \Psi_{11} >$, where the angle brackets denote an average over the square:

$$< f(x, y) >= \int_0^1 \int_0^1 f(x, y)\, \mathrm{d}x \mathrm{d}y \tag{32}$$

In a general case the integrals could be obtained by quadrature but in simple cases they can be found analytically. The eigenvalue equation, Eq. (31) can then be solved to give the critical Rayleigh number Ra.

For illustrative purposes we consider a quartered square in which each slowly varying quantity is approximated by a piecewise-constant distribution. The mean value of the quantity is approximated by its value at centre of the main square: $\bar{f} = f(0.5, 0.5)$. In each quarter, the function is approximated by its value at the centre of that quarter, and a truncated Taylor series expansion is used to approximate this quantity. For example, in the region $1/2 < x < 1, 1/2 < y < 1$, $f(x, y)$ is approximated by f(0.75,0.75) and then by

$$f(0.5, 0.5) + 0.25 f_x(0.5, 0.5) + 0.25 f_y(0.5, 0.5).$$

Hence we consider the following case.

$$\begin{array}{l}
\text{For } 0 < x < 1/2, 0 < y < 1/2, \\
K(x, y) = 1 - \delta_H - \delta_V, k(x, y) = 1 - \varepsilon_{TH} - \varepsilon_{TV}, D(x, y) = 1 - \varepsilon_{CH} - \varepsilon_{CV}; \\
\text{for } 1/2 < x < 1, 0 < y < 1/2, \\
K(x, y) = 1 + \delta_H - \delta_V, k(x, y) = 1 + \varepsilon_{TH} - \varepsilon_{TV}, D(x, y) = 1 + \varepsilon_{CH} - \varepsilon_{CV}; \\
\text{for } 0 < x < 1/2, 1/2 < y < 1, \\
K(x, y) = 1 - \delta_H + \delta_V, k(x, y) = 1 - \varepsilon_{TH} + \varepsilon_{TV}, D(x, y) = 1 - \varepsilon_{CH} + \varepsilon_{CV}; \\
\text{for } 1/2 < x < 1, 1/2 < y < 1, \\
K(x, y) = 1 + \delta_H + \delta_V, k(x, y) = 1 + \varepsilon_{TH} + \varepsilon_{TV}, D(x, y) = 1 + \varepsilon_{CH} + \varepsilon_{CV}.
\end{array} \tag{33}$$

Here, for example,

$$\delta_H = \frac{1}{4}\left[\frac{\partial K/\partial x}{K}\right]_{x=1/2, y=1/2}, \quad \delta_V = \frac{1}{4}\left[\frac{\partial K/\partial y}{K}\right]_{x=1/2, y=1/2}. \tag{34}$$

We have ensured that the requirements $< K(x, y) >= 1$, $< k(x, y) >= 1$, and $< D(x, y) >= 1$ are satisfied.

The solution for the homogeneous case (which is also given by a single term Galerkin approximation) is given by

$$\mathrm{Ra}_T + \mathrm{Ra}_C = \mathrm{Ra}_0, \tag{35}$$

where

$$\mathrm{Ra}_0 = \frac{(A^2 + 1)^2 \pi^2 [\mathrm{Da}(\mathrm{A}^2 + 1)\pi^2 + 1]}{A^2}. \tag{36}$$

One can now perturb this solution using the double term Galerkin approximation and the assumption that the heterogeneity quantities $\delta_H, \delta_V, \varepsilon_{TH}, \varepsilon_{TV}, \varepsilon_{CH}, \varepsilon_{CV}$ are small compared with unity and are of the same order of smallness, ε. This assumption allows the twelfth-order determinant to be expanded algebraically. (It is possible to put use elementary row and column transformations to put the determinant in quasi-diagonal form (where all the terms off the principle diagonal are of order ε) and use a special algorithm for the expansion to order ε^2.)

In the expression thus obtained, we set

$$\mathrm{Ra}_T = \mathrm{Ra}_0(1+S) - \mathrm{Ra}_C, \tag{37}$$

substitute in the eigenvalue equation, and solve for S to order ε^2, in terms of the parameter Ra_C and the other parameters, namely Da , A and the heterogeneity parameters. In this way we obtain an expression of the form

$$\begin{aligned} S = {} & C_{11H}{\delta_H}^2 + C_{22H}{\varepsilon_{TH}}^2 + C_{33H}{\varepsilon_{CH}}^2 + C_{23H}\varepsilon_{TH}\varepsilon_{CH} + C_{13H}\delta_H\varepsilon_{CH} \\ & + C_{12H}\delta_H\varepsilon_{TH} + C_{11V}{\delta_V}^2 + C_{22V}{\varepsilon_{TV}}^2 + C_{33V}{\varepsilon_{CV}}^2 + C_{23V}\varepsilon_{TV}\varepsilon_{CV} \\ & + C_{13V}\delta_V\varepsilon_{CV} + C_{12V}\delta_V\varepsilon_{TV}, \end{aligned} \tag{38}$$

where each of the coefficients is a function Da, A, and Ra_C . For example, in the purely thermal case where $\mathrm{Ra}_C = 0$, and for a square enclosure ($A = 1$), one finds that

$$\begin{aligned} \mathrm{Ra} &= 4\pi^2\left\{1 - \frac{64}{567\pi^2}\left[7(4\delta_H - 2.5\varepsilon_{TH})^2 + 3(2\delta_V - 5\varepsilon_{TV})^2\right]\right\}. \\ &\approx 40\{1 - 1.281(\delta_H - 0.625\varepsilon_{TH})^2 - 0.137(\delta_V - 2.5\varepsilon_{TV})^2\} \end{aligned} \tag{39}$$

Thus here

$$\begin{aligned} S &= -1.281(\delta_H - 0.625\varepsilon_{TH})^2 - 0.137(\delta_V - 2.5\varepsilon_{TV})^2 \\ &= -1.281{\delta_H}^2 - 0.500{\varepsilon_{TH}}^2 + 1.601\delta_H\varepsilon_{TH}. - 0.137{\delta_V}^2 - 0.858{\varepsilon_{TV}}^2 \\ &\quad + 0.686\delta_V\varepsilon_{TV} \end{aligned} \tag{40}$$

3 Results and Discussion

3.1 Thermal Convection in a Square Enclosure

First, looking at the monodiffusive case for a square, Eq. (39), a number of conclusions can be drawn. The effects of weak horizontal heterogeneity and vertical heterogeneity are each of second order in the property deviations. Their combined contribution is of the order of the variances of the distributions for permeability and conductivity (which are here equal to ${\delta_H}^2 + {\delta_V}^2$ and ${\varepsilon_H}^2 + {\varepsilon_V}^2$, respectively.)

One should note that the effects of the horizontal and vertical contributions are immediately comparable only if one uses the total amount of variation across the box as the measure of heterogeneity. If one uses the rate of variation with distance as the criterion, one has to take account of the fact that the x- and y-coordinates have been differently scaled, by a factor A. For example, in terms of quantities evaluated at the centre of the box,

$$\frac{\delta_V}{\delta_H} = \frac{\partial K/\partial y}{\partial K/\partial x} = \frac{H}{L}\frac{\partial K^*/\partial y^*}{\partial K^*/\partial x^*} = A\frac{\partial K^*/\partial y^*}{\partial K^*/\partial x^*}. \tag{41}$$

Thus if A is large then the vertical heterogeneity has a greater impact than the horizontal heterogeneity, other things being equal. Allowing for the aspect ratio effect, we see that the effect of vertical heterogeneity is somewhat greater than that of horizontal heterogeneity.

Further, the two effects act independently at this order of approximation. Product terms like $\delta_H\delta_V$ are absent in Eq. (39). Since the expression in square brackets in Eq. (39) is positive definite, the heterogeneities lead to a reduction in the critical value of Ra for all combinations of horizontal and vertical heterogeneities and all combinations of permeability and conductivity heterogeneities. (The reduction is zero for the very special case where $\delta_H = 0.625\,\varepsilon_H$ and $\delta_V = 2.5\,\varepsilon_V$.) The effects of the horizontal permeability heterogeneity and the horizontal conductivity heterogeneity are subtractive at the first combination step (and similarly with horizontal replaced by vertical), as one might expect since the permeability appears in the numerator in the definition of Ra whereas the conductivity appears in the denominator.

3.2 Thermal Convection in a Tall Rectangular Enclosure

One finds that in the limit as the height-to-depth aspect ratio A becomes large,

$$\begin{aligned}\mathrm{Ra} &= 4\pi^2A^2\left\{1 + \frac{16}{135\pi^2}\left[5(4\delta_H - \varepsilon_H)^2 + 4(16\delta_V - \varepsilon_V)(\delta_V - \varepsilon_V)\right]\right\} \\ &\approx 40A^2\{1 + 0.060(4\delta_H - \varepsilon_H)^2 + 0.192(16\delta_V - \varepsilon_V)(\delta_V - \varepsilon_V)\}.\end{aligned} \tag{42}$$

Comparison with Eq. (39) shows that the homogeneous case value of Ra is increased by the factor horizontal heterogeneity leads to an increase in Ra and the vertical heterogeneity produces either an increase or decrease depending on the value of δ_V/ε_V.

Further details may be found in Nield and Kuznetsov (2007a).

3.3 Double Diffusive Convection in a Square Enclosure

Returning to the more general double-diffusive case, one general result can be observed at the outset. For the case $\varepsilon_{CH} = \varepsilon_{TH}$ and $\varepsilon_{CV} = \varepsilon_{TV}$ the large determinant $\mathbf{M}$ factorizes, and the eigenvalue equation reduces to a form in which the Rayleigh numbers Ra_T and Ra_C appear only in the combination $(\mathrm{Ra}_T + \mathrm{Ra}_C)$. This means

that in this case the thermal and solutal effects are perfectly coupled, a result of the fact that the separate thermal and solutal eigenvalue problems are identical so that the streamline patterns for the two problems are identical. Thus in this special case the double-diffusive problem reduces to the thermal problem. In the general case this does not occur, and a detailed investigation is needed.

As examples we here consider two special cases, approximating a Darcy porous medium and a fluid clear of solid material.

Table 1 presents the results for the low Darcy number limit. The value $A = 1$ is known to give the minimum Rayleigh number as A (which can be interpreted as a horizontal wavenumber) varies. The general trends are clear. Each of the three agencies (hydrodynamic, thermal, solutal) acting alone is destabilizing. The purely hydrodynamic (permeability) effect is independent of the value of the thermal and solutal Rayleigh numbers. The hydrodynamic–thermal and hydrodynamic–solutal coupling leads to stabilization. As expected, the thermal effects decrease as the solutal Rayleigh number increases, and the solutal effects increase as the solutal Rayleigh number increases. There is a thermal–solutal symmetry and a symmetry about the value $\mathrm{Ra}_C / \mathrm{Ra}_0 = 1/2$ (i.e. about the $\mathrm{Ra}_T = \mathrm{Ra}_C$ situation). The thermal–solutal coupling has a maximum value when $\mathrm{Ra}_C/\mathrm{Ra}_0 = 1/2$.

Table 2 presents results for a case involving a large Darcy number (approximating a fluid clear of solid material). Here $\mathrm{Ra}_0/\mathrm{Da}$ represents the usual Rayleigh number

Table 1 Heterogeneity coefficients (see Eq. (38)) for the case $\mathrm{Da} = 0$, $A = 1$ ($\mathrm{Ra}_0 = 4\pi^2 = 39.48$)

Ra_C /Ra_0	C_{11H}	C_{22H}	C_{33H}	C_{23H}	C_{13H}	C_{12H}
0	−1.281	−0.500	0	0	0	1.601
0.1	−1.281	−0.422	−0.021	−0.058	0.160	1.441
0.2	−1.281	−0.349	−0.049	−0.102	0.320	1.281
0.3	−1.281	−0.283	−0.083	−0.134	0.480	1.121
0.4	−1.281	−0.223	−0.123	−0.154	0.640	0.960
0.5	−1.281	−0.170	−0.170	−0.160	0.800	0.800
0.6	−1.281	−0.123	−0.223	−0.154	0.960	0.640
0.7	−1.281	−0.083	−0.283	−0.134	1.121	0.480
0.8	−1.281	−0.049	−0.349	−0.102	1.281	0.320
0.9	−1.281	−0.021	−0.422	−0.058	1.441	0.160
1.0	−1.281	0	−0.500	0	1.601	0
$\mathrm{Ra}_C/\mathrm{Ra}_0$	C_{11V}	C_{22V}	C_{33V}	C_{23V}	C_{13V}	C_{12V}
0	−0.137	−0.858	0	0	0	0.686
0.1	−0.137	−0.760	−0.073	−0.025	0.068	0.618
0.2	−0.137	−0.664	−0.150	−0.044	0.137	0.549
0.3	−0.137	−0.571	−0.229	−0.058	0.206	0.480
0.4	−0.137	−0.482	−0.310	−0.066	0.274	0.441
0.5	−0.137	−0.395	−0.395	−0.069	0.343	0.343
0.6	−0.137	−0.310	−0.482	−0.066	0.412	0.274
0.7	−0.137	−0.228	−0.572	−0.057	0.480	0.206
0.8	−0.137	−0.150	−0.664	−0.044	0.549	0.137
0.9	−0.137	−0.073	−0.760	−0.025	0.618	0.068
1.0	−0.137	0	−0.858	0	0.686	0

Table 2 Heterogeneity coefficients for the case Da = 100, $A = 1/\sqrt{2}$ ($\mathrm{Ra}_0/\mathrm{Da} = 27\pi^4/4 = 657.51$)

$\mathrm{Ra}_C/\mathrm{Ra}_0$	C_{11H}	C_{22H}	C_{33H}	C_{23H}	C_{13H}	C_{12H}
0	1.441	−0.360	0	0	0	0.0005
0.1	1.441	−0.308	−0.020	−0.032	0.0001	0.0005
0.2	1.441	−0.260	−0.043	−0.058	0.0001	0.0004
0.3	1.441	−0.214	−0.070	−0.076	0.0002	0.0004
0.4	1.441	−0.173	−0.101	−0.086	0.0002	0.0003
0.5	1.441	−0.135	−0.135	−0.090	0.0003	0.0003
0.6	1.441	−0.101	−0.173	−0.086	0.0003	0.0002
0.7	1.441	−0.070	−0.214	−0.076	0.0004	0.0002
0.8	1.441	−0.043	−0.260	−0.058	0.0004	0.0001
0.9	1.441	−0.020	−0.308	−0.032	0.0005	0.0001
1.0	1.441	0	−0.360	0	0.0005	0
$\mathrm{Ra}_C/\mathrm{Ra}_0$	C_{11V}	C_{22V}	C_{33V}	C_{23V}	C_{13V}	C_{12V}
0	0.748	−0.748	0	0	0	0.0001
0.1	0.748	−0.671	−0.072	−0.005	0.00001	0.0001
0.2	0.748	−0.594	−0.145	−0.009	0.00002	0.00009
0.3	0.748	−0.518	−0.219	−0.012	0.00003	0.00008
0.4	0.748	−0.442	−0.293	−0.013	0.00004	0.00007
0.5	0.748	−0.367	−0.367	−0.014	0.00006	0.00006
0.6	0.748	−0.293	−0.442	−0.013	0.00007	0.00004
0.7	0.748	−0.219	−0.518	−0.012	0.00008	0.00003
0.8	0.748	−0.145	−0.594	−0.009	0.00009	0.00002
0.9	0.748	−0.072	−0.671	−0.005	0.0001	0.00001
1.0	0.748	0	−0.748	0	0.0001	0

for a fluid, and it is known that this attains its minimum when $A = 1/\sqrt{2}$ in the clear fluid limit. The trends shown in Table 2 are similar to those shown previously in Table 1, with two notable exceptions. Now the purely hydrodynamic effect is stabilizing, and the amount of hydrodynamic–thermal and hydrodynamic–solutal coupling is very small. The latter effect is not unexpected, because for a clear fluid a change in permeability is a nebulous concept.

4 Non-Uniform Basic Temperature Gradient

We suppose that the vertical temperature gradient in the basic state (quasi-static) is a function of the vertical coordinate,

$$\frac{\mathrm{d}T_0^*}{\mathrm{d}y^*} = \frac{T_1 - T_0}{L} F(y^*/L), \tag{43}$$

where F has unit mean,

$$\int_0^1 F(y)\mathrm{d}y = 1. \tag{44}$$

The conduction solution is given by

$$\psi = 0, \quad \theta = 1 - \int_0^y F(\eta)\mathrm{d}\eta. \tag{45a,b}$$

For the quartered square example one now has

$$\begin{aligned}
&K(x, y) = 1 - \delta_H - \delta_V, k(x, y) = 1 - \varepsilon_H - \varepsilon_V, F(y) = 1 - \eta,\\
&\text{for } 0 < x < 1/2, 0 < y < 1/2;\\
&K(x, y) = 1 + \delta_H - \delta_V, k(x, y) = 1 + \varepsilon_H - \varepsilon_V, F(y) = 1 - \eta,\\
&\text{for } 1/2 < x < 1, 0 < y < 1/2;\\
&K(x, y) = 1 - \delta_H + \delta_V, k(x, y) = 1 - \varepsilon_H + \varepsilon_V, F(y) = 1 + \eta,\\
&\text{for } 0 < x < 1/2, 1/2 < y < 1;\\
&K(x, y) = 1 + \delta_H + \delta_V, k(x, y) = 1 + \varepsilon_H + \varepsilon_V, F(y) = 1 + \eta,\\
&\text{for } 1/2 < x < 1, 1/2 < y < 1.
\end{aligned} \tag{46}$$

$$\begin{aligned}
\delta_H &= \frac{1}{4}\left[\frac{1}{K}\frac{\partial K}{\partial x}\right]_{(1/2,1/2)}, \quad \delta_V = \frac{1}{4}\left[\frac{1}{K}\frac{\partial K}{\partial y}\right]_{(1/2,1/2)},\\
\varepsilon_H &= \frac{1}{4}\left[\frac{1}{k}\frac{\partial k}{\partial x}\right]_{(1/2,1/2)}, \quad \varepsilon_V = \frac{1}{4}\left[\frac{1}{k}\frac{\partial k}{\partial y}\right]_{(1/2,1/2)},\\
\eta &= \frac{1}{4}\left[\frac{1}{F}\frac{\mathrm{d}F}{\mathrm{d}y}\right]_{(1/2)}.
\end{aligned} \tag{47}$$

In terms of the shorthand notation

$$\begin{aligned}
&\Delta_H = (8/3\pi)\delta_H,\ \Delta_V = (8/3\pi)\delta_V,\ \mathrm{E}_H = (4/3\pi)\varepsilon_H,\ \mathrm{E}_V = (8/3\pi)\varepsilon_V,\\
&\mathrm{H} = (8/3\pi)\eta
\end{aligned} \tag{48}$$

this leads to the critical value

$$\begin{aligned}
\mathrm{Ra} &= 4\pi^2\left\{1 - \frac{64}{567\pi^2}\left[7(4\delta_H - 2.5\varepsilon_H)^2 + 3(2\delta_V - 5\varepsilon_V)^2\right.\right.\\
&\quad \left.\left. + \eta(60\delta_V - 87\varepsilon_V) + 12\eta^2\right]\right\}\\
&\approx 40\{1 - 1.281(\delta_H - 1.25\varepsilon_H)^2 - 0.137(\delta_V - 1.25\varepsilon_V)^2\\
&\quad - 0.686\eta(\delta_V - 1.45\varepsilon_V) - 0.137\eta^2\}
\end{aligned} \tag{49}$$

For the case of a tall box, in the limit as $A \to \infty$, one finds that

$$R/A^2 = 1 + S, \tag{50}$$

where

$$S = \frac{1}{15}\left[5(2\Delta_H - \mathrm{E}_H)^2 + (16\Delta_V - \mathrm{E}_V)(\Delta_V - \mathrm{E}_V) + 2\mathrm{H}(\Delta_V - \mathrm{E}_V) + \mathrm{H}^2\right] \tag{51}$$

This leads to

$$\begin{aligned}\mathrm{Ra} &= 4\pi^2 A^2 \left\{1 + \frac{64}{135\pi^2}\left[(16\delta_H - \varepsilon_H)(\delta_H - \varepsilon_H) + 5(2\delta_V - \varepsilon_V)^2\right.\right. \\ &\quad \left.\left. + 5\eta(4\delta_V - \varepsilon_V) + 20\eta^2\right]\right\} \\ &\approx 40A^2\{1 + 0.048(16\delta_H - \varepsilon_H)(\delta_H - \varepsilon_H) + 0.240(2\delta_V - \varepsilon_V)^2 \\ &\quad + 0.240\eta(4\delta_V - \varepsilon_V) + 1.201\eta^2\}.\end{aligned} \tag{52}$$

Further details may be found in Nield and Kuznetsov (2007d).

5 Bidisperse Porous Medium

A bidisperse medium differs from a regular one in that the solid phase is replaced by a porous medium. The equations of continuity (expressing conservation of mass) for the velocity components in the two phases are

$$\frac{\partial {u_f}^*}{\partial x^*} + \frac{\partial {v_f}^*}{\partial y^*} = 0, \tag{53}$$

$$\frac{\partial {u_p}^*}{\partial x^*} + \frac{\partial {v_p}^*}{\partial y^*} = 0. \tag{54}$$

We note that in the traditional Darcy formulation the pressure is an intrinsic quantity, i.e. it is the pressure in the fluid. We recognize that in a BDPM the fluid occupies all of the f-phase (the macropore portion) and a fraction of the p-phase (the micropore portion of the porous phase). We denote the volume fraction of the f-phase by ϕ (something that in a regular porous medium would be called the porosity) and the porosity in the p-phase by ε. Thus $1-\phi$ is the volume fraction of the p-phase, and the volume fraction of the BDPM occupied by the fluid is $\phi + (1-\phi)\varepsilon$. The volume average of the temperature over the fluid is

$$T_F{}^* = \frac{\phi {T_f}^* + (1-\phi)\varepsilon {T_p}^*}{\phi + (1-\phi)\varepsilon}. \tag{55}$$

The drag force (per unit volume) balances the gradient of the excess pressure over hydrostatic. Our basic hypothesis is that in a BDPM the drag is increased by an amount $\zeta(\mathbf{v}_f{}^* - \mathbf{v}_p{}^*)$ for the f-phase and decreased by the same amount for the p-phase.

Within the enclosure the permeability is $K^*(x^*, y^*)$ and the overall (effective) thermal conductivity is $k^*(x^*, y^*)$. Accordingly, we write the momentum equations as

$$\frac{\partial p^*}{\partial x^*} = -\frac{\mu}{{K^*}_f}{u_f}^* - \zeta({u_f}^* - {u_p}^*) + \tilde{\mu}\nabla^2 {u_f}^*, \tag{56}$$

$$\frac{\partial p^*}{\partial x^*} = -\frac{\mu}{{K^*}_p} {u_p}^* - \zeta({u_p}^* - {u_f}^*) + \tilde{\mu}\nabla^2 {u_p}^*, \tag{57}$$

$$\frac{\partial p^*}{\partial y^*} = -\frac{\mu}{{K^*}_f} {v_f}^* - \zeta({v_f}^* - {v_p}^*) + \tilde{\mu}\nabla^2 {v_f}^* + \rho_F g\hat{\beta}({T_F}^* - T_0), \tag{58}$$

$$\frac{\partial p^*}{\partial y^*} = -\frac{\mu}{{K^*}_p} {v_p}^* - \zeta({v_p}^* - {v_f}^*) + \tilde{\mu}\nabla^2 {v_p}^* + \rho_F g\hat{\beta}({T_F}^* - T_0). \tag{59}$$

We have simplified the equations by assuming that the effective viscosities in the two phases are identical. Here ρ_F is the density of the fluid, $\hat{\beta}$ is the volumetric thermal expansion coefficient of the fluid, and T_0 is a reference temperature.

The thermal energy equations are taken as

$$\phi(\rho c)_f \frac{\partial {T_f}^*}{\partial t^*} + \phi(\rho c)_f {\mathbf{v}_f}^* \cdot \nabla {T_f}^* = \phi {k^*}_f \nabla^2 {T_f}^* + h({T_p}^* - {T_f}^*), \tag{60}$$

$$(1-\phi)(\rho c)_p \frac{\partial {T_p}^*}{\partial t^*} + (1-\phi)(\rho c)_p {\mathbf{v}_p}^* \cdot \nabla {T_p}^* = (1-\phi){k^*}_p \nabla^2 {T_p}^* + h({T_f}^* - {T_p}^*). \tag{61}$$

Here c denotes the specific heat at constant pressure, k^* denotes the thermal conductivity, and h is an inter-phase heat transfer coefficient (incorporating the specific area).

We define K_{f0}, K_{p0}, k_{f0} and k_{p0} as the mean values of ${K^*}_f$, ${K^*}_p$, ${k^*}_f$ and ${k^*}_p$, respectively, and write

$$\hat{K}_f = {K^*}_f / K_{f0},\ \hat{K}_p = {K^*}_p / K_{p0},\ \hat{k}_f = {k^*}_f / k_{f0},\ \hat{k}_p = {k^*}_p / k_{p0}. \tag{62}$$

Then Eqs. (56)–(59) lead to

$$\left[\left(1+\sigma_f \hat{K}_f\right)\nabla^2 - \mathrm{Da}_f \hat{K}_f \nabla^4\right]\psi_f - \beta\sigma_f \hat{K}_f \nabla^2 \psi_p = \mathrm{Ra}_f \hat{K}_f \frac{\partial \theta_F}{\partial x}, \tag{63}$$

$$-\sigma_f \hat{K}_p \nabla^2 \psi_f + \beta\left[\left(\frac{1}{K_r} + \sigma_f \hat{K}_p\right)\nabla^2 - \mathrm{Da}_f \hat{K}_p \nabla^4\right]\psi_p = \mathrm{Ra}_f \hat{K}_p \frac{\partial \theta_F}{\partial x}, \tag{64}$$

where

$$\frac{\partial \theta_F}{\partial x} = \frac{\phi \frac{\partial \theta_f}{\partial y} + (1-\phi)\varepsilon \frac{\partial \theta_p}{\partial x}}{\phi + (1-\phi)\varepsilon}. \tag{65}$$

Here we have introduced the dimensionless parameters

$$\sigma_f = \frac{\zeta K_{f0}}{\mu}, \quad \beta = \frac{(1-\phi)k_{p0}(\rho c)_f}{\phi k_{f0}(\rho c)_p}, \quad K_r = \frac{K_{p0}}{K_{f0}} \tag{66}$$

Thus σ_f is an inter-phase momentum transfer parameter, while β is a modified thermal diffusivity ratio.

Also, the thermal energy equations (60) and (61) become

$$\frac{\partial \theta_f}{\partial t} - \frac{\partial \psi_f}{\partial y}\frac{\partial \theta_f}{\partial x} + \frac{\partial \psi_f}{\partial x}\frac{\partial \theta_f}{\partial y} = \hat{k}_f \nabla^2 \theta_f + H(\theta_p - \theta_f), \tag{67}$$

$$\alpha \frac{\partial \theta_p}{\partial t} - \frac{\partial \psi_p}{\partial y}\frac{\partial \theta_p}{\partial x} + \frac{\partial \psi_f}{\partial x}\frac{\partial \theta_p}{\partial y} = \hat{k}_p \nabla^2 \theta_p + \gamma H(\theta_f - \theta_p), \tag{68}$$

where

$$\alpha = \frac{k_{f0}}{k_{p0}}\frac{(\rho c)_p}{(\rho c)_f}, \quad \gamma = \frac{\phi k_{f0}}{(1-\phi)k_{p0}}, \quad H = \frac{hd^2}{\phi k_{f0}}. \tag{69}$$

Thus α is a thermal diffusivity ratio, γ is a modified thermal conductivity ratio, and H is an inter-phase heat transfer parameter. The procedure in Section 2 now leads to

$$\begin{aligned} \mathrm{Ra} = \mathrm{Ra}_0(1 &+ C_{11H}{\delta_{fH}}^2 + C_{22H}{\delta_{pH}}^2 + C_{33H}{\varepsilon_{fH}}^2 + C_{44H}{\varepsilon_{pH}}^2 + C_{12H}\delta_{fH}\delta_{pH} \\ &+ C_{34H}\varepsilon_{fH}\varepsilon_{pH} + C_{13H}\delta_{fH}\varepsilon_{fH} + C_{24H}\delta_{pH}\varepsilon_{pH} + C_{14H}\delta_{fH}\varepsilon_{pH} \\ &+ C_{23H}\delta_{pH}\varepsilon_{fH} + C_{11V}{\delta_{fV}}^2 + C_{22V}{\delta_{pV}}^2 + C_{33V}{\varepsilon_{fV}}^2 + C_{44V}{\varepsilon_{pV}}^2 \\ &+ C_{12V}\delta_{fV}\delta_{pV} + C_{34V}\varepsilon_{fV}\varepsilon_{pV} + C_{13V}\delta_{fV}\varepsilon_{fV} + C_{24V}\delta_{pV}\varepsilon_{pV} + C_{14V}\delta_{fV}\varepsilon_{pV} \\ &+ C_{23V}\delta_{pV}\varepsilon_{fV}). \end{aligned} \tag{70}$$

For example, for the case $\phi = 0.4$, $\varepsilon = 0.4$, $A = 1$, $\mathrm{Da}_f = 1$, $K_r = 1$, $\sigma_f = 1$, $\beta = 10$, $\gamma = 1$, $H = 1$, one finds that $\mathrm{Ra}_0 = 1255.46$, and $C_{11H} = 0.031$, $C_{22H} = 0.003$, $C_{33H} = -0.180$, $C_{44H} = -0.024$, $C_{12H} = 0.000$, $C_{34H} = 0.002$, $C_{13H} = 0.110$, $C_{24H} = 0.001$, $C_{14H} = 0.006$, $C_{23H} = 0.010$; $C_{11V} = 0.031$, $C_{22V} = 0.003$, $C_{33V} = -0.660$, $C_{44V} = -0.093$, $C_{12V} = 0.000$, $C_{34V} = 0.019$, $C_{13V} = 0.108$, $C_{24V} = 0.001$, $C_{14H} = 0.006$ and $C_{23V} = 0.009$. The results for this and other cases show that certain coefficients are generally small, and for practical purposes may be set equal to zero. These are c_{22H}, c_{12H}, c_{24H}, c_{22V}, c_{12V}, c_{24V} and c_{14}. Also c_{23H}, and c_{23V}, are relatively small. The conclusion is that the effect of the hydrodynamic heterogeneity of the p-phase is generally small. This result could be expected. On the other hand, the thermal heterogeneity of the p-phase can be quite significant when the thermal diffusivity of the p-phase is relatively large.

Further details can be found in Nield and Kuznetsov (2007f).

6 Enclosure of Variable Width

We consider an almost rectangular box, $0 \le x^* \le L + \delta^*(y^*)$, $0 \le y^* \le H$, where the y^* axis is in the upward vertical direction and $|\delta^*(y^*)/L| << 1$, and it is assumed that $\delta^*(y^*)$ has zero mean. We now introduce a transformation of coordinates,

$$\xi = x/g(y), \eta = y, \tag{71}$$

where

$$g(y) = 1 + \frac{\delta^*(y^*)}{L}. \tag{72}$$

Thus the mean value of $g(y)$ is 1.

It is now assumed that

$$\frac{\mathrm{d}\delta^*}{\mathrm{d}y^*} << \frac{L}{H} \tag{73}$$

so that

$$\left| \frac{1}{g(\eta)} \frac{\mathrm{d}g(\eta)}{\mathrm{d}\eta} \right| << 1. \tag{74}$$

The equations analogous to Eqs. (19) and (20) are

$$A^2 \frac{\partial^2 \psi}{\partial \xi^2} + [g(\eta)]^2 \frac{\partial^2 \psi}{\partial \eta^2} + g(\eta) A \frac{\partial \theta}{\partial \xi} = 0, \tag{75}$$

$$\mathrm{Ra} g(\eta) A \frac{\partial \psi}{\partial \xi} - \left[A^2 \frac{\partial^2 \theta}{\partial \xi^2} + [g(\eta)]^2 \frac{\partial^2 \theta}{\partial \eta^2} \right] = 0. \tag{76}$$

The boundary conditions are taken to be

$$\psi = 0 \text{ and } \theta = 0 \text{ on } \eta = 0, \tag{77a,b}$$

$$\psi = 0 \text{ and } \theta = 0 \text{ on } \eta = 1, \tag{78a,b}$$

$$\psi = 0 \text{ and } \partial\theta/\partial\xi = 0 \text{ on } \xi = 0, \tag{79a,b}$$

$$\psi = 0 \text{ and } \partial\theta/\partial\xi = 0 \text{ on } \xi = 1. \tag{80a,b}$$

We have used the assumption in Eq. (74) to approximate the normal derivative on the boundary by the horizontal derivative.

In terms of the notation

$$I_{mn} = 2 < g(\eta) \sin m\pi\eta \sin n\pi\eta >, \tag{81}$$

$$J_{mn} = 2 < [g(\eta)]^2 \sin m\pi\eta \sin n\pi\eta >, \tag{82}$$

one finds that now

$$\mathbf{M} = \begin{bmatrix} \pi^2(A^2 + J_{11}) & 4\pi^2 J_{12} & \pi I_{11} & \pi I_{12} \\ \pi^2 J_{12} & \pi^2(A^2 + 4J_{22}) & \pi I_{12} & \pi I_{22} \\ \mathrm{Ra}\pi I_{11} & \mathrm{Ra}\pi I_{12} & \pi^2(A^2 + J_{11}) & 4\pi^2 J_{12} \\ \mathrm{Ra}\pi I_{12} & \mathrm{Ra}\pi I_{22} & \pi^2 J_{12} & \pi^2(A^2 + 4J_{22}) \end{bmatrix} \tag{83}$$

for the case of general A and defining S by

$$\mathrm{Ra} = \mathrm{Ra}_0(1 + S), \tag{84}$$

one finds that to first order in small quantities,

$$S = 2\left[\frac{J_{11} - 1}{A^2 + 1} - (I_{11} - 1)\right]. \tag{85}$$

We now consider some special cases.

Case 1. For a linear variation in the enclosure width, necessarily antisymmetric about the horizontal midline, modeled by $g = g_1$ where

$$g_1(\eta) = 1 + \alpha(2\eta - 1), \tag{86}$$

one finds that

$$I_{11} = 1 \text{ and } J_{11} = 1 + \alpha^2\left(\frac{1}{3} - \frac{2}{\pi^2}\right) \approx 1 + 0.131\alpha^2, \tag{87a,b}$$

$$S = \frac{\alpha^2}{A^2 + 1}\left(\frac{2}{3} - \frac{4}{\pi^2}\right) \approx 0.261\frac{\alpha^2}{A^2 + 1}. \tag{88}$$

This implies that $\mathrm{Ra} > \mathrm{Ra}_0$ when α is non-zero, for all values of A, i.e. a small departure from the exact rectangular shape is stabilizing.

Case 2. For a quadratic variation of enclosure width, symmetric about the horizontal midline, modeled by $g = g_2$ where

$$g_2(\eta) = 1 + \beta(6\eta^2 - 6\eta + 1), \tag{89}$$

one finds that

$$\begin{aligned} I_{11} &= 1 - \frac{3\beta}{\pi^2} \approx 1 - 0.304\beta \\ J_{11} &= 1 - \frac{6\beta}{\pi^2} + \beta^2\left(\frac{1}{5} - \frac{6}{\pi^2} + \frac{54}{\pi^4}\right) \approx 1 - 0.608\beta + 0.146\beta^2. \end{aligned} \tag{90a,b}$$

$$\begin{aligned} S &= \frac{1}{A^2 + 1}\left[-\frac{12\beta}{\pi^2} + \beta^2\left(\frac{2}{5} - \frac{12}{\pi^2} + \frac{108}{\pi^4}\right)\right] + \frac{6\beta}{\pi^2} \\ &\approx \frac{-1.216\beta + 0.293\beta^2}{A^2 + 1} + 0.608\beta. \end{aligned} \tag{91}$$

One finds that the departure from a rectangular shape is stabilizing for all values of β under the assumption that $A \geq 1$.

Case 3. For a sinusoidal variation of enclosure width, symmetric about the horizontal midline, modeled by $g = g_3$ where

$$g_3(\eta) = 1 + \sigma \sin \pi \eta, \tag{92}$$

one finds that

$$\begin{aligned} I_{11} &= 1 + \frac{2\sigma}{3\pi} \approx 1 + 0.212\sigma, \\ J_{11} &= 1 + \frac{4\sigma}{3\pi} + \sigma^2 \left(\frac{3}{4} - \frac{20}{3\pi^2} \right) \approx 1 + 0.424\sigma + 0.074\sigma^2. \end{aligned} \tag{93a,b}$$

$$S = \frac{1}{A^2+1} \left[\frac{8\sigma}{3\pi} + \sigma^2 \left(\frac{3}{2} - \frac{10}{3\pi^2} \right) \right] - \frac{4\beta}{3\pi} \approx \frac{0.849\sigma + 0.149\sigma^2}{A^2+1} - 0.424\sigma. \tag{94}$$

Thus the departure from a rectangular shape is stabilizing for all values of σ when $A \geq 1$.

In cases 2 and 3 the profiles have a similar shape, so the similarity in the results is as expected.

Case 4. For a sinusoidal variation of enclosure width, antisymmetric about the horizontal midline, modeled by $g = g_4$ where

$$g_4(\eta) = 1 + \tau \sin 2\pi \eta, \tag{95}$$

one finds that

$$\begin{aligned} I_{11} &= 1, \\ J_{11} &= 1 + \frac{\tau^2}{2}. \end{aligned} \tag{96a,b}$$

$$S = \frac{\tau^2}{A^2+1}. \tag{97}$$

Thus for this case the departure from a rectangular shape is stabilizing for all values of τ and for all values of A. This case is similar to case 1.

We also have a general result: for a square enclosure $A = 1$, $\mathrm{Ra} \geq \mathrm{Ra}_0$ for any function $g(\eta)$ with unit mean. This follows quickly from the identity

$$1 + J_{11} \pm 2I_{11} = 2 \int_0^1 (g \pm 1)^2 \sin^2 \pi \eta \, d\eta \geq 0 \tag{98}$$

which implies that

$$\mathrm{Ra} - \mathrm{Ra}_0 = \frac{\pi^2}{{I_{11}}^2} \left[(1 + J_{11})^2 - 4{I_{11}}^2 \right] \geq 0. \tag{99}$$

Further details can be found in Nield and Kuznetsov (2007e).

7 Strong Heterogeneity

The topic of strong heterogeneity remains open for future research, but some suggestions have been made.

Nield and Simmons (2007) observed that the reciprocal of the permeability is a measure to the resistance to motion, and they invoked an analogy with electrical resistance. In the case of convection induced by buoyancy the primary flow is vertical and the net heat flow is vertical, and for horizontal layering the contributions of the individual layers are in series for the flow of mass and heat. In particular, the resultant of two resistances of magnitudes 1 and ε is $1 + \varepsilon$, and if ε is small then the resultant differs little from unity. In contrast, for the case of vertical layering the resistances are in parallel. Then the resultant of two resistances of magnitudes 1 and ε is $\varepsilon/(1 + \varepsilon)$, a quantity that differs greatly from unity when ε is small.

Further, Nield and Simmons (2007) have proposed a rough-and-ready criterion for the onset of convection in this situation. This criterion is not restricted to the two-dimensional situation. It is based on the famous Figs. 2 and 3 of Beck (1972) that have been reproduced many times, for example as Figs. 6.22 and 6.23 in Nield and Bejan (2006). These show the variation of the critical Rayleigh number, and the preferred cellular mode, as functions of the aspect ratios $A_x = H/L_x$ and $A_y = H/L_y$ for a three-dimensional box with height H and horizontal dimensions L_x and L_y.

(Actually Beck worked with the reciprocals of those aspect ratios.) The figures apply to a box with impermeable conducting top and bottom and impermeable insulating sidewalls, and occupied by a porous medium for which the Darcy model is applicable. Beck showed that the critical Rayleigh number for a homogeneous medium is given by

$$\mathrm{Ra} = \pi^2 \min \left(b + \frac{1}{b} \right)^2 \tag{100}$$

where

$$b = \left[(pA_x)^2 + (qA_y)^2 \right]^{1/2} \tag{101}$$

and the minimum is take over the set of nonnegative integers p and q. Beck's figures show that in the region $A_x < 1$, $A_y < 1$, the value of Ra does not exceed 40.7. Also, in the region $A_x > A_y > 1$, the critical mode is $p = 1$, $q = 0$, so that

$$\mathrm{Ra} = \pi^2 \left(A_x + {A_x}^{-1} \right)^2 . \tag{102}$$

Furthermore, when $A_x > 1$ and $A_y < 1$ the value of Ra does not exceed the value given by the expression in Eq. (102).

Similarly, in the region $A_y > A_x > 1$, the critical mode is $p = 0$, $q = 1$, so that

$$\mathrm{Ra} = \pi^2 \left(A_y + {A_y}^{-1} \right)^2 , \tag{103}$$

and when $A_y > 1$ and $A_x < 1$ the value of Ra does not exceed the value given by the expression in Eq. (103).

One can now construct a generalized Rayleigh number for a heterogeneous box in the following way. The basic idea is that if at any stage one finds instability in any part of the enclosure at any time, then the whole system can be considered to be unstable. One starts with a domain consisting of the box and considers subdomains. Each subdomain is taken to be a rectangular box, of arbitrary size and with arbitrary aspect ratios, bounded by planes $x = x_1, x = x_2, y = y_1, y = y_2, z = z_1, z = z_2$. Nield and Simmons call these things sub-boxes. Then for each sub-box one can calculate the aspect ratios and a local Rayleigh number Ra_l based on the height of the sub-box and with other properties given the mean value over the sub-box. In particular, the sub-box mean of the basic temperature gradient at a particular time is employed here. One can then define a geometrically adjusted Rayleigh number Ra_g defined by

$$\mathrm{Ra}_g = \begin{cases} \mathrm{Ra}_l & \text{if } A_x < 1 \text{ and } A_y < 1, \\ \frac{4\mathrm{Ra}_l}{\left(\mathrm{A}_x + A_x{}^{-1}\right)^2} & \text{if } A_x > 1 \text{ and } A_x > A_y, \\ \frac{4\mathrm{Ra}_l}{\left(\mathrm{A}_y + A_y{}^{-1}\right)^2} & \text{if } A_y > 1 \text{ and } A_y > A_x. \end{cases} \tag{104}$$

Finally, one can define an overall Rayleigh number Ra_O by

$$\mathrm{Ra}_O = \max\ \mathrm{Ra}_g \tag{105}$$

where the maximum is taken over all the subdomains and all times.

One then expects that if $\mathrm{Ra}_O > 41$ then instability will occur. The criterion for instability will be met in at least one sub-box, and hence the whole system will be unstable. If $\mathrm{Ra}_O << 41$ then it is unlikely that instability will occur. If Ra_O is only slightly less than 41 then a closer examination of the particular situation is needed to determine whether or not instability will occur.

The expectation that $\mathrm{Ra}_O > 41$ is a sufficient condition for instability is based on the fact that the impermeable conducting boundaries are the most restrictive boundaries pertaining to the Darcy model. The boundary conditions on the top and bottom of the sub-boxes are undetermined, but one can be sure that the present criterion is conservative.

(Specifying the value of a variable on the boundary is more restrictive than, for example, specifying the value of the derivative of that variable. In an eigenvalue problem with a given differential equation, the more restrictive the boundary conditions then the greater the eigenvalue. In Table 6.1 of Nield and Bejan (2006), which gives the values of the critical Rayleigh number for various boundary conditions, the largest entry for Ra_c corresponds to the impermeable conducting boundaries.)

One can also incorporate the effect of anisotropy, at the sub-box level, by defining a local Rayleigh number with K/α_m replaced by the square of the harmonic mean of the square root of K_V/α_{mV} and K_H/α_{mH}, where the subscripts V and H refer to the vertical and horizontal values. (Here $\alpha_m = k_m/(\rho \mathrm{c})_f$, where k_m is the effective thermal conductivity of the medium.)

8 Concluding Remarks

The analysis presented in this chapter shows that in the case of weak heterogeneity the Rayleigh number based on mean properties is correct, as a criterion for the onset of convection, to first order in the small heterogeneities. The second order corrections have been made for heterogeneity of permeability, thermal diffusivity, solutal diffusivity, basic vertical temperature gradient, and enclosure width, and extensions to two-temperature and two-velocity models have been presented. Two further extensions of the analysis are now mentioned.

The above results are all for the case of conducting thermal boundary conditions on the top and bottom walls. The case of insulating conditions (constant heat flux) was considered by Nield and Kuznetsov (2007b). This is of interest because in an infinite layer the critical wave number is zero (corresponding to $A \to \infty$). It was found that the dramatic change of convection pattern does not greatly change the effect of the heterogeneity, once account has been made of the change in aspect ratio. Some minor differences showed up. For the case of conducting boundaries, it was found that the heterogeneities lead to a reduction in the critical value of Ra for all combinations of horizontal and vertical heterogeneities and all combinations of permeability and conductivity heterogeneities. For the case of constant flux boundaries, the situation is more complicated. Now the combination of vertical heterogeneity and horizontal heterogeneity can be either stabilizing or destabilizing, and there are differences between the effects of permeability heterogeneity and conductivity heterogeneity. A further extension has been made by Nield and Kuznetsov (2007c) to include the effect of anisotropy, both of permeability and conductivity. One finds that there is now an interaction between the horizontal heterogeneities of horizontal permeability and vertical permeability, for example, but again horizontal and vertical heterogeneities of each property remain independent, to second order. It is found that when the aspect ratio and the permeability and conductivity anisotropy ratios are optimized to produce the minimum Rayleigh number, all the heterogeneity terms lead to a reduction in the Rayleigh number.

References

Beck JL (1972) Convection in a box of porous material saturated with fluid. Physics of Fluids 15:1377–1383

Braester C, Vadasz P (1993) The effect of a weak heterogeneity of a porous medium on natural convection. Journal of Fluid Mechanics 254:345–362

Gheorghitza SI (1961) The marginal stability in porous inhomogeneous media. Proceedings of the Cambridge Philosophical Society 57:871–877

Finlayson BA (1972) The method of weighted residuals and variational principles. Academic Press, New York

Gounot J, Caltagirone JP (1989) Stabilité et convection naturelle au sein d'une couche poreuse non homogène. International Journal of Heat and Mass Transfer 32:1131–1140

Kuznetsov AV, Nield DA (2007) The effects of combined horizontal and vertical heterogeneity on the onset of convection in a porous medium: Double diffusive case. Transport in Porous Media, to appear

Leong JC, Lai FC (2001) Effective permeability of a layered porous cavity. ASME Journal of Heat Transfer 123:512–519

Leong JC, Lai FC (2004) Natural convection in rectangular layers porous cavities. Journal of Thermophysics and Heat Transfer 18:457–463

McKibbin R (1986) Heat transfer in a vertically-layered porous medium heated from below. Transport in Porous Media 1:361–370

McKibbin R, O'Sullivan MJ (1980) Onset of convection in a layered porous medium heated from below. Journal of Fluid Mechanics 96:375–393

McKibbin R, O'Sullivan MJ (1981) Heat transfer in a layered porous medium heated from below. Journal of Fluid Mechanics 111:141–173

McKibbin R, Tyvand PA (1982) Anisotropic modelling of thermal convection in multilayered porous media. Journal of Fluid Mechanics 118:315–319

McKibbin R, Tyvand PA (1983) Thermal convection in a porous medium composed of alternating thick and thin layers. International Journal of Heat and Mass Transfer 26:761–780

McKibbin R, Tyvand PA (1984) Thermal convection in a porous medium with horizontal cracks. International Journal of Heat and Mass Transfer 27:1007–1023

Nield DA (1987) Convective heat transfer in porous media with columnar structure. Transport in Porous Media 2:177–185

Nield DA (1994) Estimation of an effective Rayleigh number for convection in a vertically inhomogeneous porous medium or clear fluid. International Journal of Heat and Fluid Flow 15: 337–340

Nield DA, Bejan A (2006) Convection in porous media, 3rd edition. Springer, New York

Nield DA, Simmons CT (2007) A discussion on the effect of heterogeneity on the onset of convection in a porous medium. Transport in Porous Media 68:413–421

Nield DA, Kuznetsov AV (2007a) The effects of combined horizontal and vertical heterogeneity on the onset of convection in a porous medium. International Journal of Heat and Mass Transfer 50:1909–1915; erratum 4512–4512

Nield DA, Kuznetsov AV (2007b) The onset of convection in a shallow box occupied by a heterogeneous porous medium with constant flux boundaries. Transport in Porous Media 67:441–451

Nield DA, Kuznetsov AV (2007c) The effects of combined horizontal and vertical heterogeneity and anisotropy on the onset of convection in a porous medium. International Journal of Thermal Sciences 46:1211–1218

Nield DA, Kuznetsov AV (2007d) The effects of combined horizontal and vertical heterogeneity on the onset of transient convection in a porous medium. Journal of Porous Media to appear

Nield DA, Kuznetsov AV (2007e) The onset of convection in a porous medium occupying an enclosure of variable width. ASME Journal of Heat Transfer to appear

Nield DA, Kuznetsov AV (2007f) The effects of combined horizontal and vertical heterogeneity on the onset of convection in a bidisperse porous medium. International Journal of Heat and Mass Transfer 50:3329–3339

Prasad A, Simmons CT (2003) Unstable density-driven flow in heterogeneous porous media: A stochastic study of the Elder [1967b] "short heater" problem, Water Resources Research 39 (1): #1007

Rees DAS, Riley DS (1990) The three-dimensionality of finite-amplitude convection in a layered porous medium heated from below. Journal of Fluid Mechanics 211:437–461

Simmons CT, Fenstemaker TR, Sharp JM (2001) Variable-density flow and solute transport in heterogeneous porous media: Approaches, resolutions and future challenges. Journal of Contaminant Hydrology 52:245–275

Vadasz P (1990) Bifurcation phenomena in natural convection in porous media. In: Heat Transfer, vol 5, Hemisphere, Washington, DC, pp 147–152

The Instability of Unsteady Boundary Layers in Porous Media

D.A.S. Rees, A. Selim, and J.P. Ennis-King

1 Introduction

The aim of this Chapter is to summarise the state-of-the-art in the study of the instability of unsteady diffusive boundary layers in porous media. We shall focus on the boundary layer which is formed when the temperature or solute concentration at a plane boundary is changed instantaneously to a new level. Such an idealised system may be applied in a variety of contexts, such as in the subsurface storage of carbon dioxide which is expanded upon below, and it shall be regarded as the standard problem in this Chapter. The thermal/solutal field which then forms is unsteady and it spreads outwards uniformly by diffusion. When the evolving system is unstably stratified, i.e. less dense fluid lies below more dense fluid, it is stable at first but eventually becomes unstable. It is therefore necessary to determine the critical time after which the system is deemed unstable. Many methods have been used to do this and much of the attention here will be focused on describing and comparing these methods. It is hoped that such a discussion will inform and guide future work on the stability of unsteady basic states. We also summarise modifications to this standard problem: isolated disturbances, anisotropy, ramped heating, internal heat sources and local thermal nonequilibrium. Thereafter, we discuss the present

D.A.S. Rees
University of Bath, Bath, UK
e-mail: D.A.S.Rees@bath.ac.uk

A. Selim
University of Bath, Bath, UK

J.P. Ennis-King
Cooperative Research Centre for Greenhouse Gas Technologies,
CSIRO Petroleum, Clayton South,
VIC, Australia

P. Vadász (ed.), *Emerging Topics in Heat and Mass Transfer in Porous Media*,

© Springer Science+Business Media B.V. 2008

knowledge on how the growing disturbances are modified when they become large and enter the nonlinear regime. The Chapter ends with a checklist of topics which could usefully be pursued.

2 Background

Although the thermal version of the problem has often been the focus of application e.g. to porous insulation or geothermal systems, there is increasing interest in the unsteady boundary layer due to solute diffusion in the subsurface. For example a fertilizer or a pollutant can dissolve in the water near the ground surface and increase its density. When convection begins, the dissolved substance is carried downwards. A similar phenomenon can occur in the groundwater beneath saline lakes, where evaporation at the surface increases brine density. The migration of brine due to convection has implications for the possible use of salt lakes as disposal sites for pumped saline groundwater (Wooding et al. 1997).

A more recent area of application has arisen from proposals for the large scale subsurface storage of carbon dioxide in order to reduce atmospheric emissions and so limit the effects of hydrocarbon usage on global climate. Typical storage locations would be deeper than 800–1000 m, and at these subsurface conditions the carbon dioxide-rich phase is about half to two-thirds the density of the formation water. After injection into permeable rock beneath a suitable low permeability sealing rock, some of the carbon dioxide will rise due to buoyancy and accumulate beneath the seal. At the same time carbon dioxide dissolves in the formation water (typical solubility is 2–5% by weight depending on salinity). Unusually for a gas, the dissolved carbon dioxide increases the fluid density, and thus the system becomes unstably stratified (Ennis-King and Paterson 2005). The onset of convection significantly accelerates the further dissolution of carbon dioxide, and is important for assessing the security of storage over hundreds or thousands of years.

In these examples of solutal convection, the mapping onto the simplified problem of an instantaneous rise in concentration at a sharp boundary assumes that the initial transport process (e.g. the migration of the gas-phase carbon dioxide) is fast compared with the evolution of the boundary layer. In the carbon dioxide example, there is the additional complication of a two-phase region at the top boundary, which is simplified into a boundary condition of constant solute concentration for a single phase system. The transport properties of typical rocks are neither homogeneous nor isotropic, and indeed the inhomogeneity is present across a wide range of length scales. Thus the standard problem, based on an homogeneous and isotropic porous medium, is only the first step to a theory that can make useful predictions in real contexts.

As a further complication, in many cases the solute can react with the minerals in the rock, altering both permeability and fluid density. This is true of carbon dioxide, which forms a weak acid when dissolved. These alterations can act to either oppose or strengthen convection, depending on whether the geochemical reactions lead to net precipitation or net dissolution. Such coupling goes well beyond the standard problem, but again needs to be assessed in practical applications (Ennis-King and Paterson 2007).

3 Governing Equations

Darcy's law and the Boussinesq approximation are assumed to be valid, the porous medium is taken to be isotropic and rigid, and the fluid and solid phases are taken to be in local thermal equilibrium. Subject to these constraints, the dimensional equations governing flow and the transport of one diffusing species (taken as temperature here) are

$$\frac{\partial \overline{u}}{\partial \overline{x}} + \frac{\partial \overline{v}}{\partial \overline{y}} = 0, \tag{1a}$$

$$\overline{u} = -\frac{K}{\mu}\frac{\partial \overline{P}}{\partial \overline{x}}, \tag{1b}$$

$$\overline{v} = -\frac{K}{\mu}\frac{\partial \overline{P}}{\partial \overline{y}} + \frac{\rho g \beta K}{\mu}(T - T_\infty), \tag{1c}$$

$$\frac{\partial T}{\partial \overline{t}} + \overline{u}\frac{\partial T}{\partial \overline{x}} + \overline{v}\frac{\partial T}{\partial \overline{y}} = \alpha\Big(\frac{\partial^2 T}{\partial \overline{x}^2} + \frac{\partial^2 T}{\partial \overline{y}^2}\Big). \tag{1d}$$

In these equations $\overline{x}$ is the coordinate in the horizontal direction while $\overline{y}$ is vertically upward. The corresponding velocities are $\overline{u}$ and $\overline{v}$, respectively. All the other terms have their usual meaning for porous medium convection: K is the permeability, μ is the dynamic viscosity, ρ is the density of the fluid at the ambient temperature, T_∞. The heated horizontal surface is held at the temperature T_w, where $T_w > T_\infty$. Finally, the quantities g, β and α are gravity, the coefficient of cubical expansion and the thermal diffusivity of the saturated medium, respectively.

Two possible nondimensionalisations may be made depending on whether convection is to take place in a deep-pool system (i.e. a semi-infinite domain) or in a layer of uniform thickness. The former has no natural physical lengthscale while the latter does. In the former case nondimensionalisation takes place using

$$L = \frac{\mu\alpha}{\rho g \beta K (T_w - T_\infty)} \tag{2}$$

as a natural lengthscale based on the properties of the porous medium and the saturating fluid, while, in the latter case, the depth of the layer is taken. Thus there is no Darcy–Rayleigh number for deep pool systems, but there is for the finite thickness layer. Indeed, (2) is equivalent to setting $\mathrm{Ra} = 1$, where $\mathrm{Ra} = \rho g \beta K (T_w - T_\infty) L/\mu\alpha$ is the Darcy–Rayleigh number, and rearranging for L. In this Chapter we consider the deep-pool system as representing our standard system.

On using the scalings,

$$\overline{t} = \frac{L^2}{\alpha}t, \qquad (\overline{x}, \overline{y}) = L(x, y), \qquad (\overline{u}, \overline{v}) = \frac{\alpha}{L}(u, v),$$
$$\overline{P} = \frac{\alpha\mu}{K}p, \qquad T = T_\infty + (T_w - T_\infty)\theta, \tag{3}$$

Equations (1a, b, c, d) become,

$$\frac{\partial u}{\partial x} + \frac{\partial v}{\partial y} = 0, \tag{4a}$$

$$u = -\frac{\partial p}{\partial x}, \tag{4b}$$

$$v = -\frac{\partial p}{\partial y} + \theta, \tag{4c}$$

$$\frac{\partial \theta}{\partial t} + u\frac{\partial \theta}{\partial x} + v\frac{\partial \theta}{\partial y} = \frac{\partial^2 \theta}{\partial x^2} + \frac{\partial^2 \theta}{\partial y^2}. \tag{4d}$$

The boundary conditions corresponding to a sudden change in the boundary temperature are:

$$y = 0: \quad v = 0, \quad \theta = 1 \qquad \text{and} \qquad y \to \infty: \quad v, \theta \to 0, \tag{4e}$$

while $\theta = 0$ everywhere for $t < 0$.

For simplicity we shall treat the problem as two dimensional and adopt the streamfunction in place of the velocities and pressure; we set

$$u = -\frac{\partial \psi}{\partial y} \qquad \text{and} \qquad v = \frac{\partial \psi}{\partial x}, \tag{5}$$

and eliminate pressure by cross-differentiation. Equations (4) reduce to

$$\frac{\partial^2 \psi}{\partial x^2} + \frac{\partial^2 \psi}{\partial y^2} = \frac{\partial \theta}{\partial x}, \tag{6a}$$

$$\frac{\partial \theta}{\partial t} + \frac{\partial \psi}{\partial x}\frac{\partial \theta}{\partial y} - \frac{\partial \psi}{\partial y}\frac{\partial \theta}{\partial x} = \frac{\partial^2 \theta}{\partial x^2} + \frac{\partial^2 \theta}{\partial y^2}, \tag{6b}$$

which are to be solved subject to the boundary conditions,

$$y = 0: \quad \psi = 0, \quad \theta = 1 \qquad \text{and} \qquad y \to \infty: \quad \psi, \theta \to 0, \tag{6c}$$

and the initial condition that

$$\psi = \theta = 0 \quad \text{at} \quad t = 0. \tag{6d}$$

The basic state which we analyse for stability is given by $\psi = 0$, i.e. no flow, and

$$\theta = \operatorname{erfc}(\eta) = \frac{2}{\sqrt{\pi}} \int_{\eta}^{\infty} e^{-\xi^2}\, d\xi, \tag{7}$$

where

$$\eta = \frac{y}{2\sqrt{t}}. \tag{8}$$

Thus the basic state is one where the temperature field expands with time, but otherwise keeps the same shape, i.e. it is self-similar.

4 Linearised Stability Equations

Given that the basic thermal profile has uniform thickness in terms of η, it is very reasonable to make a coordinate transformation to take advantage of that fact, and it means that computational grids may then be used efficiently. It is also convenient to modify the time coordinate. Therefore we shall change from an (x, y, t) system to an (x, η, τ) system where

$$\tau = t^{1/2}. \tag{9}$$

In addition, we shall introduce perturbations with amplitude, ϵ, according to

$$\psi = \epsilon\hat{\psi}, \qquad \theta = \operatorname{erfc}\eta + \epsilon\hat{\theta}, \tag{10}$$

where linearised theory is obtained when $\epsilon \ll 1$, while the fully nonlinear perturbation equations are obtained when $\epsilon = 1$. The perturbation equations are, therefore,

$$4\tau\frac{\partial^2\hat{\psi}}{\partial x^2} + \frac{1}{\tau}\frac{\partial^2\hat{\psi}}{\partial\eta^2} = 4\tau\frac{\partial\hat{\theta}}{\partial x}, \tag{11a}$$

$$2\tau\frac{\partial\hat{\theta}}{\partial\tau} + 2\epsilon\tau\left(\frac{\partial\hat{\psi}}{\partial x}\frac{\partial\hat{\theta}}{\partial\eta} - \frac{\partial\hat{\psi}}{\partial\eta}\frac{\partial\hat{\theta}}{\partial x}\right) = 4\tau^2\frac{\partial^2\hat{\theta}}{\partial x^2} + \frac{\partial^2\hat{\theta}}{\partial\eta^2} + 2\eta\frac{\partial\hat{\theta}}{\partial\eta} + \frac{4}{\sqrt{\pi}}\tau e^{-\eta^2}\frac{\partial\hat{\psi}}{\partial x}. \tag{11b}$$

Small-amplitude roll cell perturbations may be analysed by setting $\epsilon = 0$ in (11) and by substituting,

$$\hat{\psi}(\eta, x, \tau) = \left[i\Psi(\eta, \tau)e^{ikx} - \text{c.c.}\right], \tag{12a}$$

$$\hat{\theta}(\eta, x, \tau) = \left[\Theta(\eta, \tau)e^{ikx} + \text{c.c.}\right], \tag{12b}$$

where c.c. denotes complex conjugate. The wavenumber of the rolls is k, and therefore their wavelength is $2\pi/k$. The resulting equations for Ψ and Θ are,

$$\Psi'' - 4\tau^2k^2\Psi = 4\tau^2k\Theta, \tag{13a}$$

$$2\tau\Theta_\tau = \Theta'' + 2\eta\Theta' - 4\tau^2k^2\Theta - \frac{4}{\sqrt{\pi}}\tau k e^{-\eta^2}\Psi, \tag{13b}$$

where primes denote derivatives with respect to η. The boundary conditions to be satisfied by these disturbances are that

$$\eta = 0: \quad \Psi = \Theta = 0 \qquad \text{and} \qquad \eta \to \infty: \quad \Psi, \Theta \to 0. \tag{13c}$$

5 Comparison of the Methods Used

The overall system given by (13) is parabolic in time which implies that the most natural method of solution is to follow the evolution of disturbances. The other commonly used ways of assessing the stability characteristics are (i) by reducing (13) to an ordinary differential eigenvalue problem for the critical time, (ii) using a local Rayleigh number method which compares the system with the Darcy–Bénard problem and (iii) using an energy method to find the earliest time for which a fully nonlinear disturbance suffers no growth. In this section we shall discuss the merits and demerits of each approach.

5.1 Quasi-Static Analyses

Generally, within the context of boundary layer stability theory, the earliest works reduce the linearised stability equations to ordinary differential form in some way, and then the critical parameter (e.g. Rayleigh number, Reynolds number, time) is obtained as an eigenvalue. More specifically, in the present context, such ordinary differential eigenvalue problems arise by assuming that all time-derivatives are zero—this may be called a quasi-static assumption. Whilst this assumption seems reasonable, it is essential to note that the critical time depends on whether the quasi-static assumption is made before the coordinate transformation (8,9) or afterwards. When it is made beforehand, (13) yield,

$$\Psi'' - 4\tau^2 k^2 \Psi = 4\tau^2 k \Theta, \tag{14a}$$

$$\Theta'' + 2\eta\Theta' - 4\tau^2 k^2 \Theta - \frac{4}{\sqrt{\pi}}\tau k e^{-\eta^2}\Psi = 0. \tag{14b}$$

When it is made afterwards, (14a) remains the same, but (14b) is modified by the removal of the $2\eta\Theta'$ term to give,

$$\Theta'' - 4\tau^2 k^2 \Theta - \frac{4}{\sqrt{\pi}}\tau k e^{-\eta^2}\Psi = 0. \tag{14c}$$

We name these quasi-static cases QS1 and QS2 respectively, and they are known as propagation theory and the frozen time method. Our computed critical values of τ and k are shown in Table 1; these values correspond to the minimum value on the neutral curve.

Table 1 Critical times and wavenumbers for the different methods. QS quasi-static; LR local Rayleigh number; ES energy stability; AT amplitude theory. Results marked with an asterisk are extrapolated from finite thickness calculations

Case	τ_c	t_c	k_c	Reference
QS1	12.9439	167.544	0.06963	Selim and Rees (2007a)
QS2	7.4559	55.590	0.05834	Present chapter
QS3	12.43	154.5	0.0736	Yoon and Choi (1989)
QS4	7.27	52.85	0.07428	Kim et al. (2003)
LR1	46.5520	2261.2	0.06607	Tan et al. (2003)
LR2	9.8696	97.409	0.07958	Present chapter
ES1 *	~ 9.6	~ 93		Caltagirone (1980)
ES2 *	~ 5.5	~ 30		Ennis-King et al. (2005)
AT1	8.9018	79.242	0.07807	Selim and Rees (2007a)
AT2 *	~ 8.9	~ 80		Caltagirone (1980)
AT3a *	8.7	75	0.066	Ennis-King et al. (2005)
AT3b	10.56	111.5	0.0752	Ennis-King et al. (2005)
AT4	12.1	147	0.07	Riaz et al. (2006)
AT5 *	8.671	75.19	0.06529	Xu et al. (2006)
AT6 *	7.75	60	0.05	Hassanzadeh et al. (2006)

It is clear from Table 1 that there is a very substantial difference between the critical times and wavenumbers for cases QS1 and QS2. We believe that it is not at all useful to discuss which case is the correct one, for both are the result of making strong assumptions which are essentially arbitrary. There is no reason to believe that the setting of the time derivative to zero corresponds to the behaviour of a real disturbance. Indeed, it could be argued quite strongly that a zero time derivative is a very strong constraint. The work of Selim and Rees (2007a) shows that disturbances which evolve in time have profiles which vary in shape, and, in particular, they become thinner in terms of η (but thicker, in terms of y) with time. Therefore the magnitude of Θ at any chosen value of η (or y) evolves at a different rate from the value of Θ at any other chosen value of the coordinate. Thus the quasi-static method puts a strong constraint on which disturbances are allowable.

In addition to the critical values differing greatly, the onset profiles (not shown due to the need for brevity) are also very different. The presence of the $2\eta\Theta'$ term for the QS1 case causes a superexponential decay in the temperature field, as opposed to an exponential one for the QS2 case. The QS1 disturbance is much narrower than the QS2 disturbance.

Two other papers offer quasi-static results for the identical problem. Yoon and Choi (1989) consider a finite layer, and when the Rayleigh number is large, the deep-pool results are obtained. They approximated the complementary error function solution given in (7) by a fourth order polynomial in η, and employ propagation theory. Their critical data are labelled as QS3 in Table 1 and they are close to those of QS1, which is also a propagation theory analysis, but one which is based on the precise basic temperature profile. The second paper is by Kim et al. (2003); these authors employ a propagation theory using v and θ as the dependent variables. However, they apply the boundary condition, $\partial v/\partial y = 0$, on the lower surface and it is termed a stress-free condition. Given the equation of continuity, (4a), this implies

that $\partial u/\partial x = 0$ on $x = 0$, and hence that u is a constant. It is not clear how such a condition may be interpreted, but certainly their critical data, labelled QS4, are very different from those of cases QS1 and QS3 as the boundary condition used is quite different.

Finally, we mention the use of a subtle technical detail in the papers by Yoon and Choi (1989) and Kim et al. (2002, 2003). In these papers the disturbances are assigned particular forms of variation with time prior to the setting of all time derivatives to zero. All three of these papers develop their linearised stability equations using the vertical velocity instead of the streamfunction. On scaling grounds they set the vertical velocity to be proportional to t, but the equation for the vertical velocity has a similar form to (13a) above by having no time derivative. Therefore such a rescaling has no effect on the computed critical values, and their propagation theory stability criteria are identical to that which would be obtained without using the scaling. But we note that, should an analogous clear fluid problem be considered, or even a porous medium system where the velocity time derivative is not negligible, then such scalings will alter the stability criteria.

5.2 Local Rayleigh Number Analysis

This is a 'quick and easy' approach to finding the rough values of the critical parameters. Therefore it may be used to provide a rapid estimate prior to using more sophisticated techniques. In essence the method derives an expression for a time-dependent Rayleigh number and compares this with the classical value of $4\pi^2$, which corresponds to Darcy–Bénard convection in a horizontal layer of uniform thickness (see Lapwood 1948, Horton and Rogers 1945). In addition, the nondimensional wavenumber is set equal to π, which is the critical Darcy–Bénard wavenumber.

The thickness of the thermal layer we are considering grows in time, and therefore a Rayleigh number which is based upon that thickness will also increase. The chief issue, then, is how to define the thickness of the thermal layer. Tan et al. (2003) used the following as the local Rayleigh number,

$$\mathrm{Ra}_{\mathrm{Tan}} = -\frac{\rho g \beta K}{\mu \alpha}\left(\hat{y}^2 \frac{\partial T}{\partial \hat{y}}\right), \tag{15}$$

so that this function depends on both $\hat{y}$ and $\hat{t}$, which, we note, are dimensional quantities. After the expression for the dimensional basic temperature field is substituted into (15), $\mathrm{Ra}_{\mathrm{Tan}}$ is maximised over $\hat{y}$ to find its largest value at any point in time. The maximising value of $\hat{y}$ is then taken as the thickness of the layer: $\hat{y}_c = 2\sqrt{\alpha \hat{t}}$. In terms of the present nondimensionalisation, we obtain

$$\mathrm{Ra}_{\mathrm{Tan,max}} = \frac{\rho g \beta K (T_w - T_\infty)}{\mu \alpha} \frac{4\sqrt{\alpha \hat{t}}}{e\sqrt{\pi}} = \left(\frac{4}{e\sqrt{\pi}}\right)\tau. \tag{16}$$

On setting this equal to $4\pi^2$ we obtain the critical time,

$$\tau_c = \pi^{5/2} e, \tag{17}$$

which is given numerically in Table 1 as case LR1. This value is very different from the quasi-static values, being roughly a factor of 4 times as large as for the other methods. On the other hand, the dimensional wavelength of the cells may be taken as being $2\hat{y}_c$, since Darcy–Bénard convection has cells of square cross-section as its most unstable mode, and this translates into

$$k_c = \frac{2\pi L}{2\hat{y}_c} = \frac{1}{\pi^{3/2} e}, \tag{18}$$

which is also given in Table 1. This value is quite close to those obtained by other methods.

An alternative and less complicated approach would be to say that the boundary layer thickness in terms of η is 2, and that a local Rayleigh number could be defined according to

$$\mathrm{Ra}_{\mathrm{local}} = \frac{\rho g \beta K (T_w - T_\infty) \hat{y}_{\mathrm{bl}}}{\mu \alpha}, \tag{19}$$

which varies only in time. The boundary layer thickness in terms of $\hat{y}$ is given by

$$\eta_{\mathrm{bl}} = \frac{\hat{y}_{\mathrm{bl}}}{2\sqrt{\alpha \hat{t}}} = 2, \tag{20}$$

and therefore $\hat{y}_{\mathrm{bl}} = 4\sqrt{\alpha \hat{t}}$. The setting of the Rayleigh number given in (19) to $4\pi^2$ for this value of y_{bl} yields,

$$\tau_c = \pi^2. \tag{21}$$

The corresponding wavenumber becomes,

$$k_c = \frac{1}{4\pi}. \tag{22}$$

These values are also placed in Table 1 for comparison, and are denoted as case LR2.

Admittedly, these are only two possible choices, but they seem to indicate that the critical wavenumber is not so highly affected by different ways of defining the boundary layer thickness or the way in which a local Rayleigh number number is chosen. However, the critical time is affected strongly. Given that there is no definitive way of choosing an expression for the local Rayleigh number, we would conclude that this method is only capable of providing a very rough ball-park estimate of the critical time and wavenumber prior to the use of more accurate methods.

5.3 Energy Stability Analysis

The idea behind this method is to find a time before which no disturbances grow. An energy functional is defined:

$$\bar{\Theta} = \langle \Theta^2 \rangle^{1/2} = \left[\int_0^\infty \Theta^2 \, dy \right]^{1/2}, \tag{23}$$

and variational methods are used to determine the earliest time for which

$$\frac{\mathrm{d}\bar{\Theta}}{\mathrm{d}t} = 0. \tag{24}$$

Caltagirone (1980) applied this technique to the finite layer. His result for the deep-pool system, which may be extrapolated from his large-Rayleigh number result, is given in Table 1 and labelled as case ES1. A second analysis of this type, extending Caltagirone's work to anisotropic media, was undertaken by Ennis-King et al. (2005), but their isotropic results (labelled ES2 in Table 1) are somewhat at variance with those of Caltagirone by suggesting a much earlier critical time. An independent third study by Xu et al. (2006) undertakes an identical anisotropic analysis to that of Ennis-King et al. (2005) and they present a graph for the critical Rayleigh number against time. However, there is insufficent information within that paper to allow us to determine which, if either, of the energy stability analyses of Caltagirone (1980) and Ennis-King et al. (2005) is correct.

There is a widely held belief that energy methods always yield the definitive smallest parameter. In the present context Caltagirone's critical time is much closer to those using an accurate amplitude theory (described in the next subsection), but his computed critical time using amplitude theory is lower than that for energy stability theory. The critical times obtained by Ennis-King et al. (2005) are such that the energy stability analysis yields a earlier critical time than their amplitude theory. Therefore it is clear that the energy stability analysis must be revisited in order to clarify the situation. Some further comments are made on this towards the end of the next subsection.

5.4 Amplitude Theory

This method utilises solutions of the full parabolic disturbance equations, such as those given by (13). As the temperature equation has a single time derivative, it is necessary to provide an initial condition, which is the initial perturbation whose evolution will then be determined. Generally this has been undertaken using either Galerkin methods for a finite thickness layer (Caltagirone 1980, Ennis-King et al. 2005, Xu et al. 2006), or in the deep-pool system by Galerkin methods (Ennis-King et al. 2005) or by finite difference methods (Selim and Rees 2007a). A means of determining the amplitude of the evolving perturbation also has to be defined, and this is not easy to resolve *a priori*. The options which have been used in the literature

are the following: (i) the maximum value of Θ, (ii) the rate of heat transfer at the surface, (iii) a thermal energy content integral, $\langle\Theta\rangle$, and (iv) an 'energy' integral similar to that given in (23). In all cases the chosen measure is evaluated at each timestep and the times at which time-derivative is zero are noted together with the wavenumber, k.

The evolution of $E = \langle\Theta\rangle$ (measure (iii)) for a set of wavenumbers, k, is shown in Fig. 1. These curves are typical of the other measures of the amplitude of the disturbance, which show only quantitative differences. The initial disturbance profile is $\Theta = \eta e^{-3\eta}$ and it was introduced at $\tau = 1$, which is well before the critical time. It is clear that the disturbance decays substantially at first, followed by growth. At later times, the disturbance eventually decays once more, indicating that there is only a finite interval during which growth may take place.

After a suitable number of simulations, a neutral curve may be constructed showing how the onset time varies with wavenumber. This is illustrated in Fig. 2, which displays the neutral curves obtained by Selim and Rees (2007a) corresponding to the first three of the above measures, and to the quasi-static theory. Of the various measures displayed there, the one with the lowest critical time is the thermal energy content measure, which, given that it is an integral, is a global quantity, rather than a local one as represented by the surface rate of heat transfer. This minimum is given in Table 1 and is denoted as case AT1.

The aforementioned paper by Caltagirone (1980) also presents the results of a full unsteady simulation, the critical values for which are given in Table 1 and denoted by AT2. Apart from the numerical method used, the only difference between his simulation and that of Selim and Rees (2007a) is that his critical values are based on the evolution of $\bar{\Theta} = \langle\Theta^2\rangle^{1/2}$. Despite this difference, the agreement is very good indeed.

Ennis-King et al. (2005) apply Caltagirone's method to both the finite thickness and deep-pool systems, using different sets of basis functions in each case. These result are respectively denoted as case AT3a and AT3b in Table 1 (the AT3b results were not explicitly given in the paper, but are provided here for comparison). Again

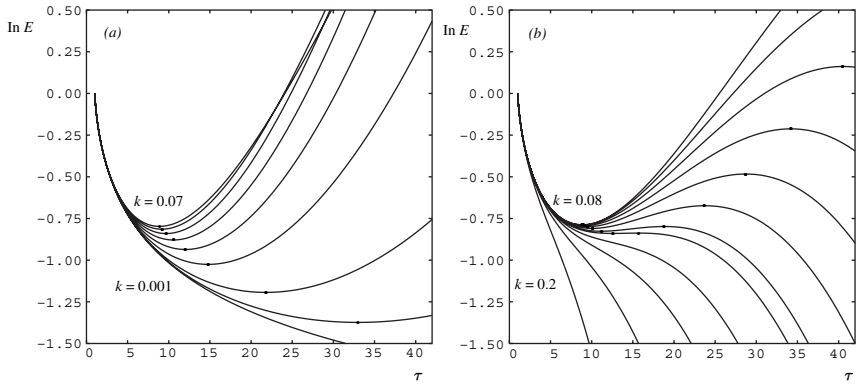

Fig. 1 Variation of ln E against τ for different values of k

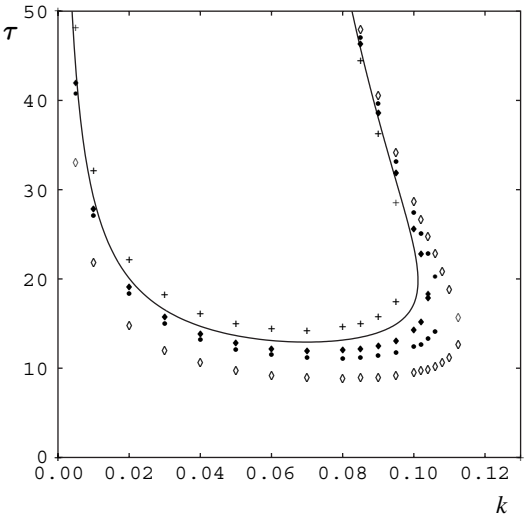

Fig. 2 *Neutral curves*: The continuous curve represents quasi-static theory. The symbol ◇ represents the thermal energy content. The symbols • and + represent the surface heat flux criterion in terms of η and y respectively. The symbol ♦ represents the maximum temperature criterion

for AT3a there is an extrapolation of the finite depth results to the deep-pool limit, which causes some loss of precision. The AT3b deep-pool results are only weakly dependent on the initial conditions as long as the starting disturbance is within the diffusion layer. The difference between the results in AT3a and AT3b appears to originate from the choice of basis functions and the form of the initial disturbance in each case.

On the other hand, Riaz et al. (2006) used a different set of Galerkin expansion functions in η to obtain a critical time and wavenumber (case AT4) which are quite close to the QS1 case of Selim and Rees (2007a). The analysis of Xu et al. (2006), denoted as case AT5, follows the methodology of Ennis-King et al. (2005) and is an extrapolation of finite thickness results. Thus AT3a and AT5 agree, and give results that are very similar to case AT1 of Selim and Rees (2007a).

The work of Hassanzadeh et al. (2006) (case AT6) uses the same methodology as Ennis-King et al. (2005) and Xu et al. (2006) for the finite thickness case, but varies the type of initial conditions (white noise, or one of two Fourier modes) and the boundary conditions. The lower bound given for the instability corresponds to the zero time derivative condition. The value for t_c is somewhat lower than the corresponding AT3a and AT5 results using a similar approach—the difference may relate to the variation of initial conditions.

5.4.1 Comment on Stability Criteria

Caltagirone (1980), together with many later authors including Kim and Kim (2005) and Kim et al. (2002) who look at slightly different impulsive problems, presents

two different stability criteria using amplification theory. One of these is the zero time derivative criterion, $\mathrm{d}\bar{\Theta}/\mathrm{d}t = 0$, while the other is the time taken for the disturbance to achieve its original value of $\bar{\Theta}$. Kim et al. (2003) go further and say that experimental considerations should be heeded to determine the level of amplification required for marginal stability to be declared. Although Fig. 1 shows the variation of $\langle \Theta \rangle$, it is clear that the latter criterion will yield greatly different critical times depending on when the disturbance is seeded into the boundary layer. Therefore we regard the former criterion as being more intuitive.

5.4.2 Comment on the Choice of Initial Disturbance Profile

The manner in which the initial perturbation profile for the numerical simulations is chosen has been questioned by Kim et al. (2002) who state, quite reasonably, that it is arbitrary. Indeed, it was this fact that motivated the general analysis of Green (1990) who developed a method involving a series expansion about the critical time, where the mode calculated was the result of minimising the critical time over mode shapes (using a Fourier expansion) and the wavenumber, and is such that the growth rate is zero. His method was applied to a problem of ramp heating, and to date it is unknown how good it is for the problem being discussed in this section. However, one of the important conclusions of the work of Selim and Rees (2007a) is that the profile of the initial disturbance generally has very little effect on the critical time whenever the time at which it is introduced into the system is sufficiently early. In other words, all disturbances appear to be attracted towards a common evolutionary path, as shown in Fig. 3, and if the introduction time is sufficiently early, then this process is essentially complete by the time marginal instability occurs.

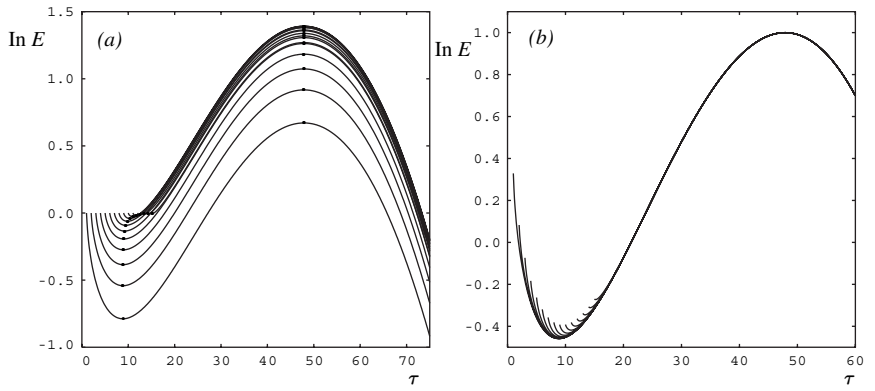

Fig. 3 Variation of $\ln E$ against τ, for disturbances introduced at various values of τ, for $k = 0.085$. (**a**) Computed $\ln E$ curves; (**b**) Normalised $\ln E$ curves

5.5 Discussion

What is to be made of the widely differing values of the critical times quoted in Table 1? Energy methods are generally held in high esteem, especially for problems where the basic state whose stability characteristics are being sought is steady. Here we have two sets of results which are very different from one another, and without considering the results obtained by other methods, we are not in a position to decide between them. Both the local Rayleigh number and the quasi-static theories are very definitely approximate, the former more so than the latter. It is certainly possible to calibrate the local Rayleigh number method *a posteriori* to get an exact match with almost any result we wish, but ideally we need to obtain good results independently of such calibration. The amplitude theory results should be excellent in the sense that the exact linearised equations are being solved. But one also has to consider which is the best way to measure the amplitude of the evolving disturbance—Fig. 2 depicts the different neutral curves corresponding to four such measures, and no doubt the use of $\bar{\Theta}$, defined in (23), would provide a fifth. The numerical results of Ennis-King et al. (2005) for amplitude theory and finite thickness use between 8 and 16 terms in the Galerkin expansion to the full profile of the evolving disturbances, and the comparable results of Xu et al. (2006) have similar accuracy; both are close to those of Caltagirone (1980) and Selim and Rees (2007a). The amplitude results of Ennis-King et al. (2005) for the semi-infinite case, using at least 10 terms in a Galerkin expansion, are close to Selim and Rees (2007a) for k_c but give a larger value for t_c, while the one-term approximation of Riaz et al. (2006) gives a still higher value of t_c.

We would tentatively suggest, therefore, that Caltagirone (1980) and Selim and Rees (2007a) presently give the benchmark critical values for situations where the evolution of disturbances is undertaken. We await confirmation of a further study using energy methods in order to decide between the quoted results of Caltagirone (1980) and Ennis-King et al. (2005). Although we think it likely that such an analysis will provide an earlier critical time than does amplitude theory, it is our belief that the critical profile will not be one that is on the attracting solution path mentioned earlier.

Finally, if we consider the shape of the various neutral curves in Fig. 2, it is worthy of note that each one is quite flat near its minimum, and therefore it is perhaps not surprising that the various methods have yielded quite different critical wavenumbers.

6 Isolated Small-Amplitude Disturbances

In all of the above considerations it has been assumed that the disturbances have been characterised by a single wavenumber in the x-direction and are therefore monochromatic. Should a spatially non-periodic initial disturbance need to be considered, then it is possible to Fourier-transform the disturbance, compute as many single-wavenumber solutions as is required, then apply the inverse Fourier

Transform formula to obtain the resulting evolution of the time-dependent system. Thus it would appear that little else needs to be said about the linear stability problem.

However, there is much interest in the published literature on how localised disturbances evolve. Despite the above statement that a sufficiently early introduction of a disturbance causes the stability criterion to be independent of the disturbance profile, this is true only in terms of its profile in the η-direction. When the disturbance is localised in the x-direction, then it takes time for the disturbance to diffuse horizontally and generate new cells either side of itself.

This process is illustrated in Fig. 4. A full two-dimensional finite difference scheme was used to investigate the evolution of a narrow isolated disturbance placed at $x = 0$. Suitable symmetry conditions were applied at $x = 0$ to mimic correctly the solution in $x < 0$. The Figure shows the boundaries between the thermal cells, i.e. it indicates where there is zero rate of heat transfer. As each boundary is crossed, the sign of the rate of heat transfer changes. The Figure does not indicate the variation of the amplitude of the disturbance, but successive maxima and minima reduce in size as x increases for any chosen τ.

The chief interest here lies in the fact that the wavelength of cells is not uniform. Each new cell that is generated tends to have a larger width than the cell immediately next to it, and each cell tends to grow in width as τ increases. This behaviour is different from that obtained in the analogous situation in Darcy-Bénard convection where unpublished computations undertaken by one of the authors show that cells remain of constant wavelength as they spread into the external undisturbed regions. In the present case, the fastest growing disturbance at any point in time

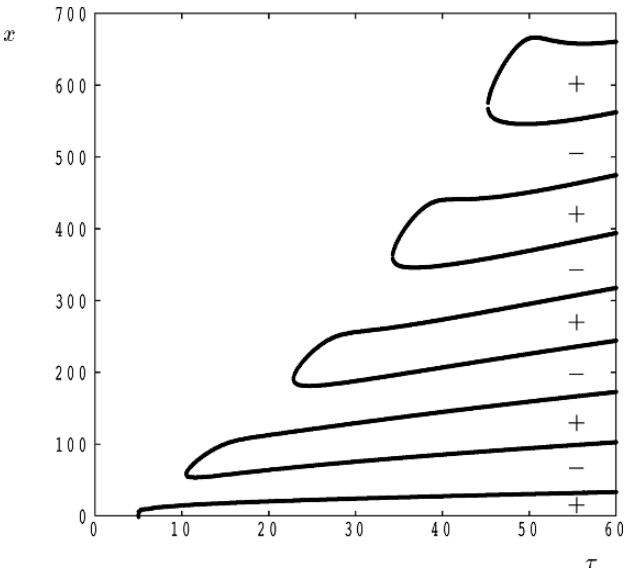

Fig. 4 Depicting the evolution and spread of thermal cell boundaries as τ increases

has a wavenumber which decreases as time progresses. Therefore we think that the increase in the wavelength is very likely to be related to the fact that smaller wavenumbers grow faster.

7 Other Linear Systems

We now give a quick overview of similar systems considered by various authors. In all cases they will have used one or more of the methods discussed above.

7.1 Anisotropy

Ennis-King et al. (2005) have extended the standard case to include anisotropy in the permeability. The permeability tensor remains diagonal, and so the principle axes remain in the coordinate directions. These authors consider both finite layers and semi-infinite deep-pool systems, employing different nondimensionalisations for the two cases. For the finite layer two different boundary conditions are considered on the unsalted boundary. Energy stability theory and amplitude theory are presented. The change in the isotropic results which are obtained when anisotropy is introduced are much as expected, and are qualitatively identical to the isotropic case. Of most interest is the fact that their results are substantially different from those of Caltagirone (1980) when the porous medium is isotropic, as discussed above.

7.2 Ramped Heating

Kim and Kim (2005) considered a finite layer which is at a uniform temperature initially, but where the temperature of the lower boundary increases linearly with time. They use a Galerkin-based amplitude theory, monitoring the rate of growth of disturbances using $\bar{\Theta}$. Neutral curves are presented which correspond to the criteria $\bar{\Theta}_t = 0$ and $\Theta = 1$ (where $\Theta = 1$ is set at the time the disturbance is introduced). The former they call the 'intrinsic' stability criterion, while the latter is termed the 'marginal' stability criterion. The general tenor of other papers, and the view of the present authors, is that the former should be called the marginal stability criterion, while the latter is irrelevant, as discussed earlier. The authors state that disturbances grow superexponentially after the 'marginal' stability time; Fig. 1 shows that this is not true for the present standard problem and quite obviously so for values of k close to 0.1 where there is only a small interval of growth before decay is re-established.

Hassanzadeh et al. (2006) also consider a case in which the solute concentration at the boundary decreases linearly with time. This is relevant to underground storage of carbon dioxide, where the pressure in the gas phase may decline and thus reduce the concentration of dissolved carbon dioxide in the two-phase region (although in practice this reduction would not be linear in the pressure at typical conditions of interest). It is shown that for layers of finite thickness and small Rayleigh numbers,

a fast enough decrease at the boundary may prevent a perturbation from growing and eliminate convection, whereas in the deep pool limit (large Rayleigh numbers) the instability criterion is unaffected.

7.3 Internal Heat Sources

Kim et al. (2002) also considered a finite layer at a uniform temperature initially. At $t = 0$ a uniform internal heat generation is turned on, which forms an unstably stratified boundary layer at the cold upper surface. This configuration eventually tends to a steady state. Therefore all interest is focussed on the onset times for those cases where the Rayleigh number is above the critical value for the steady state situation. The authors use a propagation/quasi-static theory to determine the onset times—this is performed in terms of the η-variable—and use a quasi-static theory in the Cartesian variables (termed a frozen-time theory). The results obtained by means of these theories differ from one another, but are much closer to one another than are those given by QS1 and QS2 in Table 1.

7.4 Local Thermal Nonequilibrium

Nouri-Borujerdi et al. (2007) modified the standard problem by dropping the assumption that the fluid and solid phases are in local thermal equilibrium. The great majority of papers reporting convection in porous media assume that the temperatures of the phases are identical locally, that is, they assume that the heat transfer which takes place between the phases either happens so quickly, or else, the flow rate is sufficiently slow, that, to a good approximation, the two-phase system may be described by a single energy equation. But there are situations when such an assumption is not accurate, and then the temperature fields of the two phases have to be modelled by separate, but coupled, equations. The coupling takes the form of source/sink terms that are proportional to the local difference in temperature between the phases, and which allow the flow of heat between the phases.

These authors followed the methodology of Selim and Rees (2007a) by applying a quasi-static theory and an amplitude theory based on $E = \langle \Theta \rangle$. Generally it was found that the critical time decreases as the degree of local thermal nonequilibrium increases. This may be attributed to the fact that the convecting fluid does not have to impart heat to the solid phase, and therefore it experiences less of what might be termed a thermal drag.

8 Nonlinear Studies

Once an evolving disturbance becomes sufficiently strong, it will interact with itself via the nonlinear terms in the governing equations. This will serve to modify the further development of the disturbance in a wide variety of ways. Moreover, the

effect of having multiple disturbances (which are distinguished by having different wavenumbers) complicates the situation substantially in terms of their nonlinear interaction.

The earliest nonlinear simulations were undertaken by Elder (1967, 1968). He employed a two-dimensional fully numerical scheme to determine the convection in a finite thickness layer subjected to an instantaneous rise in the temperature of the lower surface. In these simulations, the nondimensional lower boundary temperature was set to $\theta = 1 + \epsilon'(x)$, where ϵ' is a random variable with zero mean. This type of boundary condition provides an alternative means of disturbing the evolving thermal boundary layer. His simulations showed the formation of a highly irregular series of cells within the boundary layer. These interact in a complex manner with cell-merging taking place. Eventually the evolving basic state tends towards a steady linear profile, and there follows a long period of adjustment of the cells. He also considered convection in a fully infinite domain where the initial condition for the basic state is that $\theta = 0$ in $y > 0$ and $\theta = 1$ in $y < 0$.

Caltagirone (1980) also employed a nonlinear finite difference model, but this was used to provide confirmation of his energy theory results.

Selim and Rees (2007b) solved the full two-dimensional equations for the disturbances, but used a horizontal Fourier decomposition together with a vertical finite difference method. Thus the following substitutions were made in (11) where $\epsilon = 1$ was chosen:

$$\psi(x, \eta, \tau) = \sum_{n=1}^{N} \psi_n(\eta, \tau) \sin nkx, \tag{25a}$$

$$\theta(x, \eta, \tau) = \tfrac{1}{2}\theta_0(\eta, \tau) + \sum_{n=1}^{N} \theta_n(\eta, \tau) \cos nkx, \tag{25b}$$

where $N = 5$ was generally found to provide excellent accuracy. The resulting unsteady equations were solved using a variant of the Keller box method, and the initial disturbance took the form,

$$\theta_1 = A_1 \eta e^{-3\eta}, \tag{26}$$

with all other terms in (25) set to zero. The chief qualitative result of this paper is that strongly nonlinear disturbances suffer from premature stabilisation. The linear stability curves displayed in Fig. 2 indicate that small-amplitude disturbances have only a finite interval of time over which they can grow. The computations of Selim and Rees (2007b) show that restabilisation often takes place earlier than would be expected from the data represented in Fig. 2. Figure 5 shows the evolution of the surface rate of heat transfer of the primary mode,

$$q_1 = \left.\frac{\partial \theta_1}{\partial \eta}\right|_{\eta=0}, \tag{27}$$

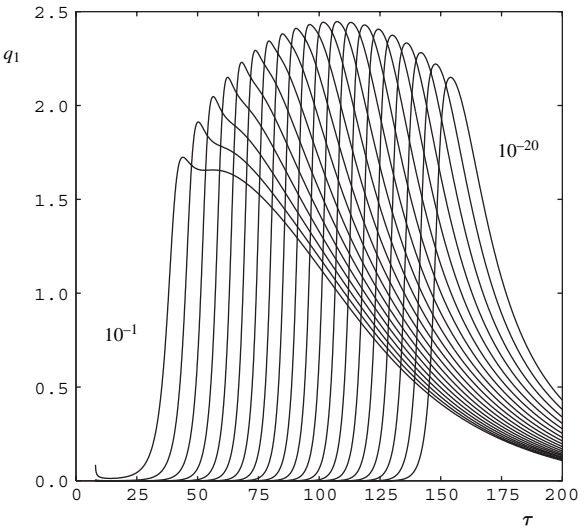

Fig. 5 The variation with τ of q_1 for $k = 0.04$, the disturbance initiation time, $\tau = 8$, and for the amplitudes $A_1 = 10^{-1}, 10^{-2}, \ldots, 10^{-20}$. The curve on the extreme left corresponds to $A_1 = 10^{-1}$ (Selim and Rees 2007b)

for $k = 0.04$ and for a variety of initial amplitudes, A_1. Various features stand out from this Figure. The first is that the time at which restabilisation occurs (defined now as being when q_1 begins to decrease) depends very strongly on the value of A_1. For very small amplitudes the restabilisation time is consistent with linear theory based on a heat transfer criterion. For large amplitudes restabilisation occurs very early indeed. The second feature is that the maximum response does not correspond to the largest initial disturbance amplitude. For this wavenumber, the maximum response occurs when $A_1 \simeq 10^{-12}$.

A third feature is that all disturbances, even in the nonlinear regime, eventually decay towards zero. This is surprising from the point of view that the Rayleigh number based upon the basic boundary layer thickness continues to increase, thereby rendering the boundary layer increasingly unstable. Therefore the solutions shown in Fig. 5 must become unstable to other disturbances. Given that the boundary layer thickens with time, and that convection cells usually tend to a roughly square cross-section, it seems reasonable to attempt to destabilise solutions such as those shown in Fig. 5 using longer wavelength/smaller wavenumber perturbations.

It is this observation which motivated the work contained in Selim and Rees (2008), who consider subharmonic destabilisations. These authors also used (25), but, for a 2:1 subharmonic case, the primary mode is now taken to correspond to $n = 2$, while the subharmonic corresponds to $n = 1$. In addition, a much larger value of N is taken than for the simulations reported in Selim and Rees (2007b). Typically the magnitude of A_1 is much less than that of A_2, so that the primary

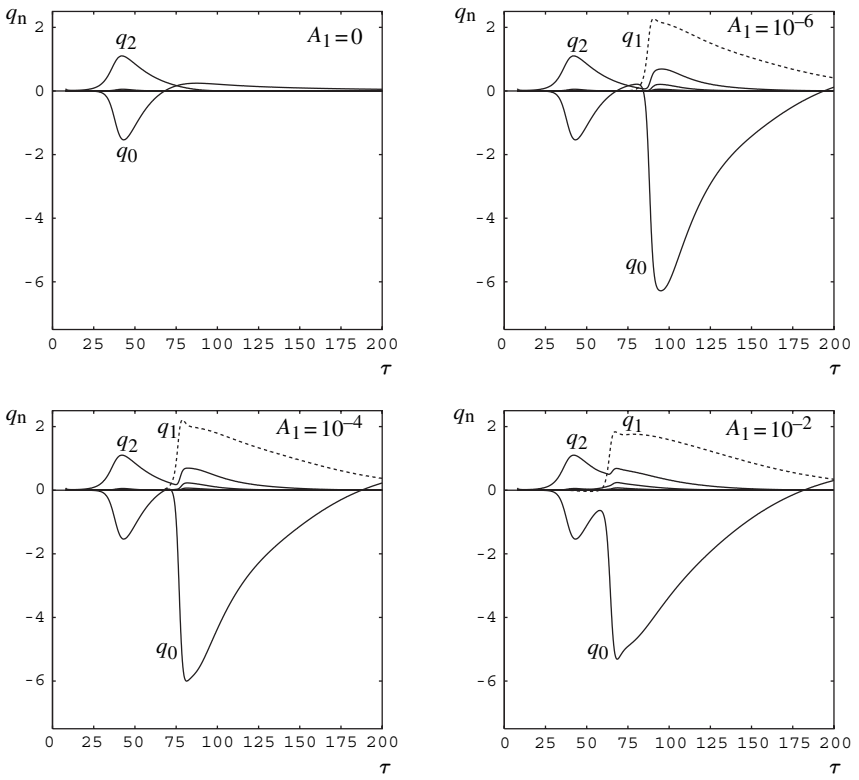

Fig. 6 Variation with τ of the surface rates of heat transfer, q_n, corresponding to the modes, $n = 0, 1, 2, \cdots$. These simulations correspond to $k = 0.035$ and $A_2 = 10^{-1}$. The disturbance was introduced at $\tau = 8$ (from Selim and Rees 2008)

mode may evolve in almost exactly the same way as before, but, soon after the primary begins to decay, the subharmonic begins to grow and eventually takes over as the dominant pattern.

Figure 6 shows the manner in which the surface rates of heat transfer of each mode vary in time where the primary mode has wavenumber 0.07 and $A_2 = 0.1$. The datum case with no subharmonic disturbance corresponds to $A_1 = 0$, and this exhibits a moderate amount of growth prior to eventual decay. Of particular interest in the other subfigures are the times at which the subharmonic, shown by the q_1 curves, takes over as the dominant pattern. As might be expected, the larger the initial value of A_1, the earlier this happens. Once more, it is interesting to note that the largest magnitude in the mean rate of heat transfer, q_0, for the cases we present, is obtained for the smallest value of A_1, rather than for the largest.

Contours of the temperature disturbance field at various times are shown in Fig. 7 to illustrate the manner in which the subharmonic destabilisation takes place. At $\tau = 10$ an apparently uniform set of cells is present. For convenience we shall label

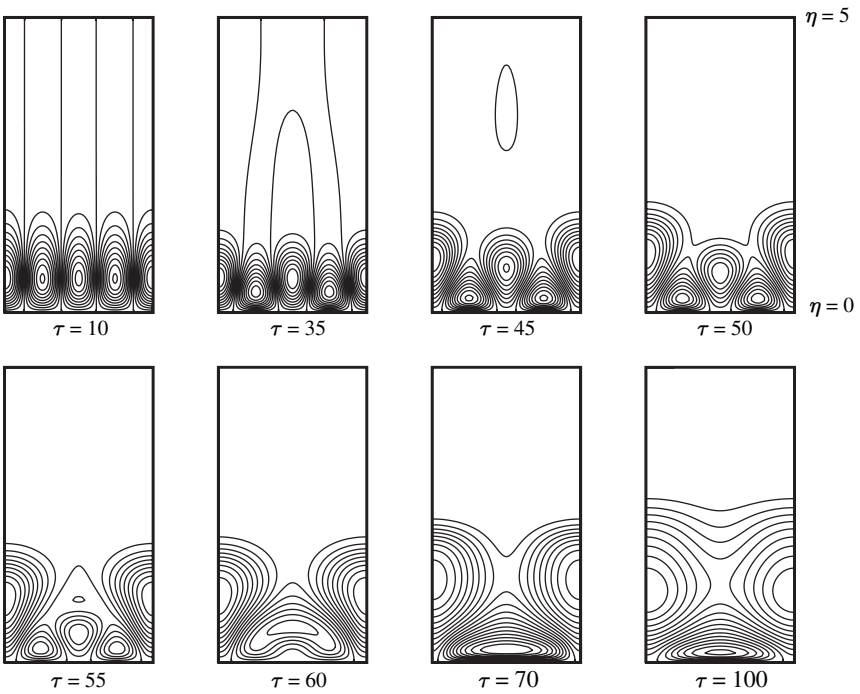

Fig. 7 Contours of the perturbation temperature field at chosen times for the subharmonic instability corresponding to $k = 0.035$, $A_1 = 10^{-2}$ and $A_2 = 10^{-1}$, where the disturbance was introduced at $\tau = 8$ (from Selim and Rees 2008)

these cells 0 through to 4 from left to right, noting that cells 0 and 4 are identical. The subharmonic instability now manifests itself by causing (i) even numbered cells to become stronger and occupy more space in the η-direction than do the odd numbered cells, and (ii) cells 0 and 4 become stronger than cell 2. Once $\tau = 55$ is reached, cells 0 and 4 are now dominant, with the remains of cells 1, 2 and 3 occupying a triangular-shaped region corresponding to the contour $\Theta = 0$. After this point, cells 1 and 3 merge, destroying cell 2 in the process. Thereafter the fully developed nonlinear subharmonic convection is fully established. We note that the final subfigure, which corresponds to $\tau = 100$, has the following features: (i) the middle cell is pushed close to the heated surface due to a strong inflow towards the surface and (ii) the outer cells have expanded substantially due to the fact that the flow is away from the surface.

A full categorisation of the roles played by the sizes of A_1 and A_2 is quite a large task, especially as such a systematic set of computations would need to take place over a set of wavenumbers. Moreover, other subharmonic disturbances may also be considered, such as 1:3, 2:3 and 3:4, where cases of the form $M{:}M+1$ may be regarded as being very much like the well-known Eckhaus instability.

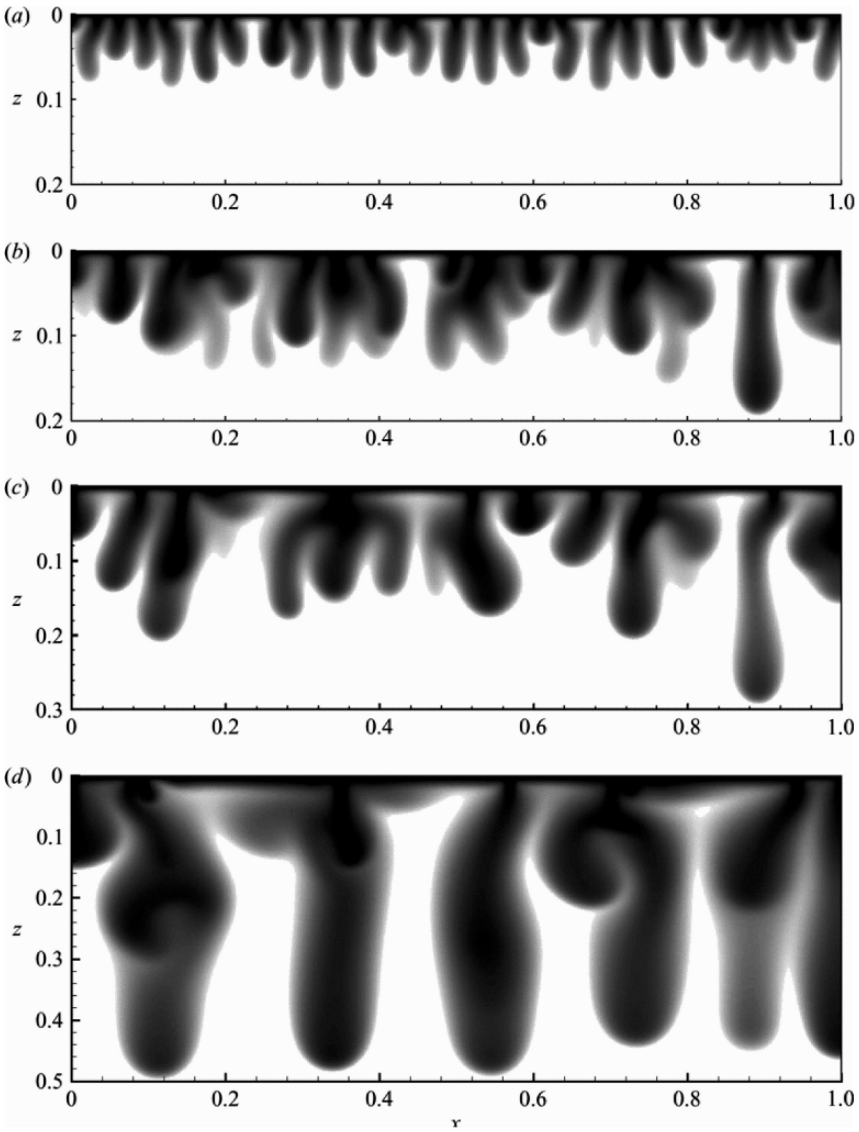

Fig. 8 Contours of concentration showing the change in the wavelength of plumes with time. For unit vertical depth and Ra $= 4000$: (**a**) $t = 1$, (**b**) $t = 1.8$, (**c**) $t = 2.3$ and (**d**) $t = 3.8$ (Riaz et al. 2006)

Given that Fig. 6 also shows that the subharmonic itself decays after a certain time, it suggests the possibility of a further subharmonic destabilisation. However, it is important to realise that the use of a horizontal Fourier expansion by Selim and Rees (2007b, 2008) is a very strong constraint on the overall behaviour of the system. Various papers have appeared which use finite difference methods to solve

systems such as the present one, but with large horizontal physical domains, and whilst the fact that a finite domain is also a constraint, it is nevertheless a very much weaker one. These papers suggest that the true physical behaviour is one where the flow becomes chaotic. The first hint of this is in the FLUENT computations of Tan et al. (2003) who solve the full two-dimensional equations of motion in Cartesian coordinates in a fairly small region. No mention is made of how disturbances are introduced into the system, but waves of uniform wavelength appear. However, one of these is stronger than the others and begins to grow preferentially, which bypasses the subharmonic cascade of Selim and Rees (2008). A similar scenario was found by Riaz et al. (2006) who considered a system with a very much larger aspect ratio.

The work of Riaz et al. (2006) concentrates to a large extent on the postcritical dynamics when the instabilities have become strongly nonlinear. There is too much detailed information in their paper for it to be summarised briefly here, and we restrict attention to the flow shown in Fig. 8. These authors consider convection due to the sudden introduction of a solute at the upper surface of a layer of finite depth. The simulation shown used $\mathrm{Ra} = 4000$ and the snapshots shown are at times which are sufficiently early that the lower surface has not affected the development of the instability. Figure 8 shows an essentially chaotic system where the observed wavelength clearly increases with time. Presumably this is not a continuous increase, but rather it comes about by the nonlinear interactions of embryonic plumes especially the merging of neighbouring plumes. In this regard, the subharmonic cascade of Selim and Rees (2008) could be regarded as providing part of the explanation of this. But equally well, the merging of two plumes could also be regarded as a form of Coandă effect (where a jet of fluid is deflected towards a neighbouring surface). Here, by analogy, the lack of availability of fluid to entrain from one side of a plume causes the deflection of the plume in that direction, and therefore it is natural for two plumes to move toward one another and to coalesce.

Other features arise if the suddenly heated/salted surface is semi-infinite, as the leading edge of the surface then plays a strong role, at least initially. Although the primary aim of the paper by Rees and Bassom (1993) is the description of the instability of a steady thermal boundary layer generated by a semi-infinite heated surface, these authors also presented a computation of the immediate aftermath of the sudden rise of the surface temperature. One snapshot of this process is shown in Fig. 9 where multiple cells have been generated, but which have also been ejected from the developing boundary layer. Therefore a plume is caused which eventually rises away from the boundary layer and, in this case, is advected to the right by the overall flow field generated by the hot surface. A very similar situation is shown in Fig. 10 where a snapshot of a simulation by Wooding et al. (1997) is given. Their situation is a model of an evaporating solar pond where there is a high solute concentration on the left hand two-thirds of the upper surface, and where evaporation causes fluid to leave the system to form a suction surface. The systems studied by Rees and Bassom (1993) and Wooding et al. (1997) would have been mathematically identical without the suction surface. Wooding et al. (1997) attribute this starting plume to a strong perturbation caused by high horizontal density gradients near the leading edge.

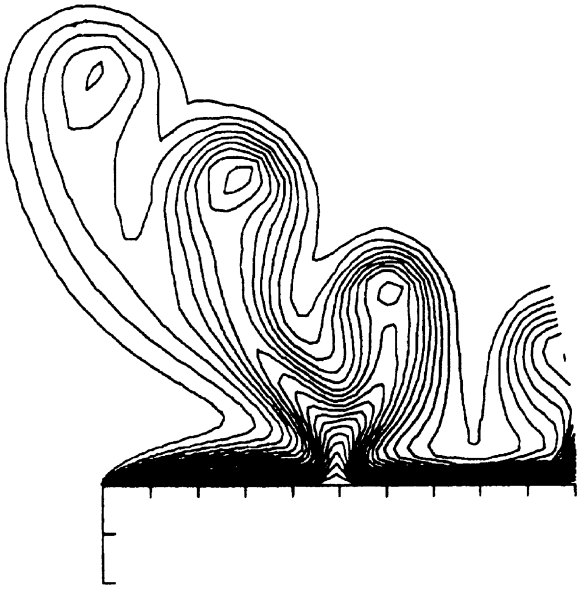

Fig. 9 Depicting the complex plume generated near the leading edge of a suddenly heated semi-infinite surface (Rees and Bassom 1993)

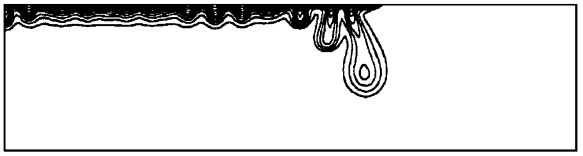

Fig. 10 Depicting the complex plume generated near the leading edge of a suddenly salted semi-infinite surface with suction (Wooding et al. 1997)

9 Conclusion

The study of the instability of unsteady boundary layers is an active topic. Much is known about the behaviour of the small-amplitude disturbances and the results obtained by Caltagirone (1980) and Selim and Rees (2007a) should be regarded as being the definitive instability criterion, at least for amplitude theory. There remain issues to resolve for the application of energy stability theory. No doubt it is possible to extend the linearised theory presented here to more complicated situations, such as systems with (i) discrete horizontal layers, (ii) non-Newtonian fluids and (iii) both heat and salt as diffusing species. It is likely that there could be some qualitative differences as compared with our standard problem. We think that it is possible to contrive layered situations where the neutral stability curve takes more exotic shapes, such as having two turning points—in such situations some disturbances could have two intervals of growth and three intervals of decay. Double diffusive

convection offers parameter ranges where the primary mode at onset for the Darcy–Bénard problem is unsteady; similar ranges might make the development of an onset criterion for unsteady boundary layers somewhat problematical. Likewise viscoelastic fluids can admit highly oscillatory flows.

Of course many of these situations could be extended to the nonlinear domain, but we feel it would also be of some considerable interest to determine the nonlinear development of isolated disturbances.

However, of perhaps more importance is the fact that the basic state that we have studied does not have a linear profile because, in the Darcy–Bénard context, it is well-known that three dimensional convection often ensues in these situations. Therefore we think it highly likely that the preferred nonlinear flow will be three dimensional and possibly chaotic. The next step should therefore be the development of codes which are capable of producing computations such as those of Riaz et al. (2006) in three dimensions.

Finally, there already exist many studies where unsteady boundary layers are formed by boundary conditions which oscillate in time. Space has proved insufficient to give a review of this highly interesting topic.

Acknowledgment The first author would like to record his gratitude to Prof. Andrew Bassom who initiated his interest in studying boundary layer instabilities. He would also like to thank Dr. Aminreza Noghrehabadi who supplied all the calculations in Nouri-Borujerdi et al. (2007) while visiting the University of Bath.

References

Caltagirone J-P (1980) Stability of a saturated porous layer subject to a sudden rise in surface temperature: comparison between the linear and energy methods. Quart J Mech Appl Math 33:47–58.

Elder JW (1967) Transient convection in a porous medium. J Fluid Mech 27:609–623.

Elder JW (1968) The unstable thermal interface. J Fluid Mech 32:69–96.

Ennis-King JP, Paterson L (2005) Role of convective mixing in the long-term storage of carbon dioxide in deep saline formations. SPE J 10(3):349–356.

Ennis-King JP, Paterson L (2007) Coupling of geochemical reactions and convective mixing in the long-term geological storage of carbon dioxide. Int J Greenhouse Gas Control 1:86–93.

Ennis-King JP, Preston I, Paterson L (2005) Onset of convection in anisotropic porous media subject to a rapid change in boundary conditions. Phys Fluids 17:084107.1–084107.15.

Green T (1990) The momentary instability of a saturated porous layer with a time-dependent temperature distribution, and the most unstable disturbance. Water Resour Res 26:2015–2021.

Hassanzadeh H, Pooladi-Darvish M, Keith DW (2006) Stability of a fluid in a horizontal saturated porous layer: effect of non-linear concentration profile, initial, and boundary conditions. Transp Porous Med 65:193–211.

Horton CW, Rogers RT (1945) Convection currents in a porous medium. J Appl Phys 16:367–370.

Kim MC, Kim S (2005) Onset of convective instability in a fluid-saturated porous layer subjected to time-dependent heating. Int J Heat Mass Transfer 32:416–424.

Kim MC, Kim S, Choi CK (2002) Convective instability in fluid-saturated porous layer under uniform volumetric heat sources. Int Comm Heat Mass Transfer 29:919–928.

Kim MC, Kim S, Chung BJ, Choi CK (2003) Convective instability in a horizontal porous layer saturated with oil and a layer of gas underlying it. Int Comm Heat Mass Transfer 30:225–234.

Lapwood ER (1948) Convection of a fluid in a porous medium. Proc Camb Phil Soc 44:508–521.
Nouri-Borujerdi A, Noghrehabadi AR, Rees DAS (2007) The linear stability of a developing thermal front in a porous medium: the effect of local thermal nonequilibrium. Int J Heat Mass Transfer 50:3090–3099.
Rees DAS, Bassom AP (1993) The nonlinear nonparallel wave instability of free convection induced by a horizontal heated surface in fluid-saturated porous media. J Fluid Mech 253:267–296.
Riaz A, Hesse M, Tchelepi HA, Orr FM (2006) Onset of convection in a gravitationally unstable diffusive boundary layer in porous media. J Fluid Mech 548:87–111.
Selim A, Rees DAS (2007a) The stability of a developing thermal front in a porous medium. I. Linear theory. J Porous Med 10:1–15.
Selim A, Rees DAS (2007b) The stability of a developing thermal front in a porous medium. II. Nonlinear theory. J Porous Med 11:17–23.
Selim A, Rees DAS (2008) The stability of a developing thermal front in a porous medium. III. Secondary instabilities. (In preparation).
Tan K-K, Sam T, Jamaludin H (2003) The onset of transient convection in bottom heated porous media. Int J Heat Mass Transfer 46:2857–2873.
Wooding RA, Tyler SW, White I (1997) Convection in groundwater below an evaporating salt lake. I. Onset of instability. Water Resour Res 33:1199–1218.
Xu X, Chen S, Zhang D (2006) Convective stability analysis of the long-term storage of carbon dioxide in deep saline aquifers. Adv Water Resources 29:397–407.
Yoon DY, Choi CK (1989) Thermal convection in a saturated porous medium subjected to isothermal heating. Korean J Chem Eng 6:144–149.

Analytical Transition to Weak Turbulence and Chaotic Natural Convection in Porous Media

Peter Vadász

Abstract A review on the transition to weak turbulence and chaotic natural convection in porous media is presented in this chapter. In particular, the question on how can one obtain the transition point analytically is emphasized and topics such as the hysteresis phenomenon linked to this transition is discussed. Fractal types of results obtained by comparing solutions at different accuracy levels are finally presented to conclude the chapter.

1 Introduction

The wide variety of traditional applications of heat transfer in porous media such as those listed in Nield and Bejan (2006) and Bejan (1995) are insulation of buildings and equipment, energy storage and recovery, geothermal reservoirs, nuclear waste disposal, chemical reactor engineering, and the storage of heat generating materials such as grain and coal. Also, geophysical applications, such as ground water flow (where the heat transfer analogy may apply to the mass transfer equations when considering underground water contamination) and the flow of magma in the earth mantle close to the earth crust serve as additional traditional examples. With the particular development of emerging applications of the theory of heat transfer in porous media, the importance of this topic of research is substantially enhanced. In particular, the problem of estimating the heat flux in convective flows in porous media places a special theoretical challenge, as the raw experimental results are very much dispersed over a wide range, beyond the experimental error (see Fig. 9 in Nield and Bejan, 2006). The reason for this dispersion is associated with a wide variety of possible heat transfer regimes, namely: motionless-conduction, laminar-Darcy, laminar-Forchheimer, weak-turbulent-Darcy (or "temporal chaotic") and strong-turbulent ("spatio-temporal-chaotic"). These regimes can occur depending on the

P. Vadász
Northern Arizona University, Flagstaff, AZ, USA
e-mail: peter.vadasz@nau.edu

P. Vadász (ed.), *Emerging Topics in Heat and Mass Transfer in Porous Media*,

© Springer Science+Business Media B.V. 2008

combination of appropriate values of Rayleigh, Darcy and Prandtl numbers. The present chapter reviews the transitions from a motionless-conduction regime to steady laminar-Darcy convection and further to weak-turbulent-Darcy convection. The accurate definitions of each of these regimes can be introduced by considering a fluid saturated porous layer heated from below and following a procedure of increasing the temperature difference between the bottom and top boundaries. The transition from a motionless-conduction to a steady-convection regime is independent of whether a Darcy or a Forchheimer model is used since this transition is obtained from a linear stability analysis around a motionless solution, hence non-linear effects (such as the Forchheimer terms) vanish. If the porous matrix consists of material that is associated with a very small value of Darcy number ($Da < 10^{-3}$) and the fluid's Prandtl number is of an order of magnitude around $Pr \sim 10$, then the transition from steady to non-steady convection leads to a weak-turbulent regime. This transition is associated with the loss of stability of the steady convection due to the non-linear interactions in the energy equation, while the resulting filtration velocity values are still within the Darcy regime.

Vadasz and Olek (1999a, b, 2000a, b) and Vadasz (1999b, 2001a, d) demonstrated that the transition from steady to chaotic (weak-turbulent) convection in porous media could be recovered from a truncated Galerkin approximation, which yields a system that is equivalent to the familiar Lorenz equations (Lorenz, 1963; Sparrow, 1982) similarly as in a pure fluid (non-porous domain) which was presented by Vadasz (1999a, 2000, 2006). In particular it was noticed that the transition to chaos when the initial conditions are not too far away from any one of the convective steady state solutions passes through a limit cycle at a particular sub-critical value of Rayleigh number. Here the term "sub-critical" is used in the context of the transition from steady convection to a non-periodic state, typically referred to as chaotic. The critical value of the Rayleigh number is the value at which this transition to chaos is predicted by the linear stability analysis of the convective steady state solutions. Vadasz (1999b) used a weak non-linear method of solution to this problem, which revealed a mechanism for the Hysteresis phenomenon.

Nield and Bejan (2006) provide an excellent summary of the analytical as well as the experimental work available so far on the estimation of Nusselt number in porous media convection. For example, for values of Rayleigh number slightly beyond the convection threshold a linear relationship between the Nusselt and Rayleigh numbers is suggested in Nield and Bejan (2006) based on Elder (1967), which fits well with experimental data. Such a linear relationship can be derived analytically via a weak non-linear analysis of the problem using an expansion around the convection threshold (see Braester and Vadasz, 1993; Vadasz and Braester, 1992) and can be expressed in the form $Nu = 1 + 2\ (R - 1)$ where $R = Ra/Ra_{cr}$ is the scaled Rayleigh number and $Ra_{cr} = 4\pi^2$ is the critical value of the Rayleigh number associated with the loss of linear stability of the motionless solution, i.e. on the convection threshold. Vadasz (2001a) has shown that this linear equation represents the first two terms in a Taylor expansion of a more general relationship, that was derived and presented here, and applies to a much wider range of Rayleigh number values.

Bau (1994) indicates that *"One of the hallmarks of chaotic systems is their sensitivity to initial conditions and small perturbations (noise). ... Of course, when one is modelling real systems, the initial conditions are not precisely known and all real systems are subject to perturbations and noise. Hence, ..., no long term prediction of the detailed behavior of a chaotic system is possible. The lack of long-term predictability is a fundamental property of chaotic systems just like the uncertainty principle is a corner stone of quantum mechanics...."* This conclusion is somewhat disappointing as it implies that it is hopeless to attempt modelling real systems within the chaotic regime due to lack of long-term predictability. It is shown in this paper that despite the sensitivity of the post-transient chaotic solution, in terms of its dependent variables, to variations in initial conditions, the dissipative nature of the convective system reduces substantially this sensitivity, when these dependent variables are being averaged over a sufficiently large time range. In this context, Sparrow (1982) indicates that in attempting to provide an explanation about the irregularity of the trajectory in the chaotic regime *"we know we are seeing a portion of a very high period orbit"*. If chaotic solutions are a result of a very large period, it implies that by averaging the results over a period smaller than the largest period of the solution, it might compromise the accuracy of the averaging process. This loss of accuracy may be significant, in which case the high sensitivity of the solution to initial conditions applies to the averaged values as well, or this loss of accuracy may be minor, the latter being expected in dissipative systems. Then, despite the sensitivity of the post-transient solution to variations in initial conditions, the corresponding averaged values over a sufficiently large time interval lack this substantial sensitivity. This paper shows that the mean Nusselt number is just an example of such a case. Its affinity to different initial conditions is very weak, and subject to a minor loss of accuracy, one can predict its value even within the weak-turbulent regime, except for some transition regions where the hysteresis phenomenon may substantially affect it. Actually, it will be shown that the only impact that the transition to chaos causes on the predicted results in terms of the averaged heat flux is a minor loss of accuracy. Since chaos is a result of limited and finite accuracy of the solution, one can not expect to obtain results that within the chaotic regime can be reached up to any desired accuracy. This accuracy is limited also by the fact that we have no way to anticipate a finite number of frequencies (and their corresponding periods) over which to integrate the heat flux in order to yield an accurate average Nusselt number. It will be shown that these effects introduce only a minor error in the estimation of the Nusselt number.

2 Problem Formulation and Reduced Set of Equations

A narrow ($W = W_* / H_* << 1$) fluid saturated porous layer subject to gravity and heated from below, as presented in Fig. 1, is considered. A Cartesian co-ordinate system is used such that the vertical axis z is collinear with gravity, i.e. $\hat{\boldsymbol{e}}_g = -\hat{\boldsymbol{e}}_z$. The time derivative term is not neglected in Darcy's equation, a condition that

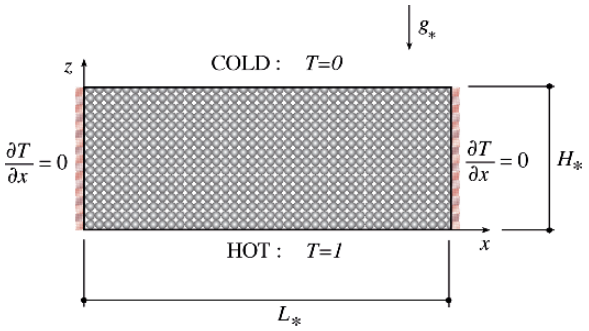

Fig. 1 A fluid saturated porous layer heated from below

was well discussed and substantiated by Vadasz and Olek (1999a, 2000a) and Vadasz (1998, 1999b). Other than that Darcy's law is assumed to govern the fluid flow, while the Boussinesq approximation is applied for the effects of density variations.

Subject to these conditions the following dimensionless set of governing equations is obtained

$$\nabla \cdot \boldsymbol{V} = 0 \tag{1}$$

$$\left[\frac{1}{Va}\frac{\partial}{\partial \hat{t}} + 1\right] \boldsymbol{V} = -\nabla p + RaT\hat{\boldsymbol{e}}_z \tag{2}$$

$$\frac{\partial T}{\partial \hat{t}} + \boldsymbol{V} \cdot \nabla T = \nabla^2 T \tag{3}$$

The values $\alpha_{e*}/H_* M_f$, $\mu_* \alpha_{e*}/k_* M_f$, and $\Delta T_c = (T_H - T_C)$ are used to scale the filtration velocity components (u_*, v_*, w_*) , pressure (p_*), and temperature variations ($T_* - T_C$), respectively, where α_{e*} is the effective thermal diffusivity, μ_* is fluid's viscosity, k_* is the permeability of the porous matrix and M_f is the ratio between the heat capacity of the fluid and the effective heat capacity of the porous domain. The height of the layer H_* was used for scaling the variables x_*, y_*, z_* and H_*^2/α_{e*} for scaling the time t_*. Accordingly, $x = x_*/H_*$, $y = y_*/H_*$ and $z = z_*/H_*$ and $\hat{t} = t_* \alpha_{e*}/H_*^2$. In equation (3) Ra is the gravity related Rayleigh number in porous media defined in the form $Ra = \beta_* \Delta T_c g_* H_* k_* M_f / \alpha_{e*} \nu_*$. The time derivative term was included in Darcy's equation (3), where Va is a dimensionless group which includes the Prandtl and Darcy numbers as well as the porosity of the porous domain and is defined by $Va = \phi\, Pr/Da$. Straughan (2001) suggested to name this dimensionless group the "Vadasz number" and to use the symbol Va. Subsequently, this suggestion was adopted by Lombardo and Mulone (2002), Govender (2003, 2006a,b), Straughan (2004), Mulone, and Straughan (2006), Sheu (2006), Bhadauria (2007) and others. Vadasz and Olek (1999a, 2000a) have shown that when investigating wave phenomena, such as the present case, the time derivative in equation (3) needs to be included irrespective of how large the value of Va is. Without including this term the possibility of oscillatory convection is wiped out, and subsequently the transition to turbulence by using the present model becomes impossible. Including

the time derivative term in equation (2) is equivalent to maintaining the highest derivative in an equation in order to satisfy all boundary (or initial) conditions, as it is typically applied for investigating boundary layers.

As all the boundaries are rigid the solution must follow the impermeability conditions there, i.e. $\boldsymbol{V} \bullet \hat{\boldsymbol{e}}_{\boldsymbol{n}} = 0$ on the boundaries, where $\hat{\boldsymbol{e}}_{\boldsymbol{n}}$ is a unit vector normal to the boundary. The temperature boundary conditions are: $T = 1$ at $z = 0$, $T = 0$ at $z = 1$ and $\nabla T \bullet \hat{\boldsymbol{e}}_{\boldsymbol{n}} = 0$ on all other walls representing the insulation condition on these walls.

For convective rolls having axes parallel to the shorter dimension (i.e. y) $v = 0$, and the governing equations can be presented in terms of a stream function defined by $u = \partial\psi/\partial z$ and $w = -\partial\psi/\partial x$, which upon applying the curl ($\nabla\times$) operator on equation (2) yields the following system of partial differential equations from equations (1), (2) and (3)

$$\left[\frac{1}{Va}\frac{\partial}{\partial\hat{t}} + 1\right]\left[\frac{\partial^2\psi}{\partial x^2} + \frac{\partial^2\psi}{\partial z^2}\right] = -Ra\frac{\partial T}{\partial x} \tag{4}$$

$$\frac{\partial T}{\partial\hat{t}} + \frac{\partial\psi}{\partial z}\frac{\partial T}{\partial x} - \frac{\partial\psi}{\partial x}\frac{\partial T}{\partial z} = \frac{\partial^2 T}{\partial x^2} + \frac{\partial^2 T}{\partial z^2} \tag{5}$$

where the boundary conditions for the stream function are $\psi = 0$ on all solid boundaries.

The set of partial differential equations (4) and (5) form a non-linear coupled system, which together with the corresponding boundary conditions accepts a basic motionless conduction solution. To obtain the complete solution to the non-linear coupled system of partial differential equations (4) and (5) we represent the stream function and temperature in the form

$$\psi = -4\,\tilde{X}\sin\left(\frac{\pi x}{L}\right)\sin(\pi z) \tag{6}$$

$$T = 1 - z + \frac{2\tilde{Y}}{\pi}\cos\left(\frac{\pi x}{L}\right)\sin(\pi z) - \frac{\tilde{Z}}{\pi}\sin(2\pi z) \tag{7}$$

This representation is equivalent to a Galerkin expansion of the solution in both x and z directions, truncated when $i + j = 2$, where i is the Galerkin summation index in the x direction and j is the Galerkin summation index in the z direction. Substituting equations (6) and (7) into the equations (4) and (5), multiplying the equations by the orthogonal eigenfunctions corresponding to equations (6) and (7) and integrating them over the domain, i.e. $\int_0^L \mathrm{d}x \int_0^1 \mathrm{d}z(\bullet)$, yields a set of three ordinary differential equations for the time evolution of the amplitudes (see Vadasz and Olek, 1999a, 2000a).

By using the wave number corresponding to the convection threshold, rescaling the time $\hat{t}$, and introducing the following notation

$$R = \frac{Ra}{4\pi^2}, \quad \alpha = \frac{Va}{2\pi^2}, \quad t = 2\pi^2\hat{t} \tag{8}$$

yields the following set of equations

$$\dot{\tilde{X}} = \alpha \left(R\,\tilde{Y} - \tilde{X} \right) \tag{9}$$

$$\dot{\tilde{Y}} = \tilde{X} - \tilde{Y} - \tilde{X}\,\tilde{Z} \tag{10}$$

$$\dot{\tilde{Z}} = 2 \left(\tilde{X}\,\tilde{Y} - \tilde{Z} \right) \tag{11}$$

The fixed points of the system (9)–(11) are obtained by setting the time derivative to be zero, in the form $\tilde{X}_S = \pm(R-1)^{1/2}$, $\tilde{Y}_S = \pm(R-1)^{1/2}\big/R$ and $\tilde{Z}_S = (R-1)\big/R$. They represent steady state solutions consisting of convection cells moving clockwise or counter-clockwise. These fixed points lose stability in the linear sense at a value of $R = R_o = 25$ (for $\alpha = 5$ pertaining to the present investigation), at which point a sub-critical Hopf bifurcation occurs (see Vadasz, 1999b for details). The bifurcation diagram representing the convective fixed points and the unstable bifurcating oscillatory solutions is presented in Fig. 2.

A rescaling of the variables with respect to these fixed points in the form

$$X = \frac{\tilde{X}}{\sqrt{(R-1)}}, \quad Y = \frac{R\,\tilde{Y}}{\sqrt{(R-1)}}, \quad Z = \frac{R\,\tilde{Z}}{(R-1)} \tag{12}$$

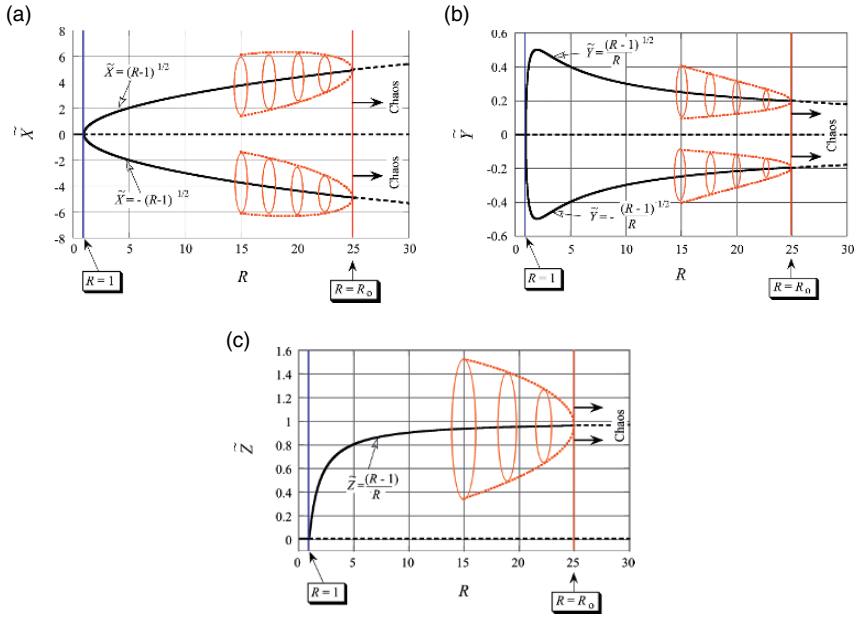

Fig. 2 The bifurcation diagram obtained analytically from equations (9) to (11). (**a**) $\tilde{X}$ versus R, (**b**) $\tilde{Y}$ versus R, (**c**) $\tilde{Z}$ versus R

provides the following set of scaled equations

$$\dot{X} = \alpha\ (Y - X) \tag{13}$$

$$\dot{Y} = R\,X - Y - (R-1)\,X\,Z \tag{14}$$

$$\dot{Z} = 2\ (X\,Y - Z) \tag{15}$$

where the dots ($\dot{}$) denote time derivatives $\mathrm{d}()/dt$. Equations (13), (14) and (15) are equivalent to Lorenz equations (Lorenz, 1963; Sparrow, 1982) although with different coefficients. The demonstration of this equivalence is provided by Vadasz and Olek (1999a). Their convective fixed points are $X_S = Y_S = \pm 1$, $Z_S = 1$ for $R > 1$.

The model is expected to represent qualitatively well the effects related to the overall dynamics of the system. Some wide thermal boundary layers near the top and bottom of the layer can be recovered. However this model excludes the possibility of formation of narrow thermal boundary layers, or of hydrodynamic boundary layers, next to these walls. Note that the formation of hydrodynamic boundary layers near solid walls is not typical for flows in porous media since the non-slip conditions do not apply for the filtration velocity next to these walls. Assumption *(iv)* in Vadasz (2001a) can be tested *aposteriori* by using a relationship obtained via a scale analysis, between the pore scale Reynolds number and the scaled Rayleigh number in the present model. This relationship yields $Re_\Delta = Re\,Da^{1/2} = 4\pi\,(R-1)^{1/2}\,Da^{1/2} X \Big/ \left(M_f\,Pr\right) = 4\pi\,(R-1)^{1/2}\,X\,\phi \Big/ \left(M_f\,Va\,Da^{1/2}\right)$. Then by using typical porous media parameter values and typical values of X from the solutions presented by Vadasz (1999b) and Vadasz and Olek (1999a) we obtain $Re_{\Delta\max} = 61.56\,Da^{1/2}/Pr = 61.56\,\phi/\left(Va\,Da^{1/2}\right)$ for $R \sim 25$. The transition from Darcy to a non-linear Forchheimer regime in porous media occurs at a pore scale Reynolds number of an order of magnitude of 1. Therefore, for fluid Prandtl numbers around 10 the condition for validity of the Darcy regime is $Da^{1/2} << 1$, which is clearly valid. As the value of the fluid Prandtl number decreases the Darcy regime validity condition may be violated by some combinations of solid-fluid materials forming the porous matrix. In such cases the Darcy regime can not be recovered.

3 Analytical Solution

The analytical solution to the problem is evaluated via a weak non-linear analysis by using an expansion around the point where the non-trivial stationary solutions lose stability in the linear sense, i.e. around $R = R_o = 25$. The stationary (fixed) points of the system (13)–(15) are the convection (non-trivial) solutions $X_S = Y_S = \pm 1$, $Z_S = 1$ and the trivial solution $X_S = Y_S = Z_S = 0$. The expansion around the trivial stationary solution yields the familiar results of a pitchfork bifurcation from a motionless state to convection at $R = 1$. We expand now the dependent variables around the non-trivial stationary points in the form

$$[X, Y, Z] = [X_S, Y_S, Z_S] + \varepsilon\,[X_1, Y_1, Z_1] + \varepsilon^2\,[X_2, Y_2, Z_2] + \varepsilon^3\,[X_3, Y_3, Z_3] + \ldots. \tag{16}$$

We also expand R in a finite series of the form $R = R_o\left(1 + \varepsilon^2\right)$ which now defines the small expansion parameter as $\varepsilon^2 = (R - R_o)/R_o$, where R_o is the value of R where the stationary non-trivial solutions lose their stability in the linear sense (see Vadasz and Olek 1999a, 2000a, Vadasz 1999b). Therefore the present weak non-linear analysis is expected to be restricted to initial conditions sufficiently close to *any one* but only one of the non-trivial fixed points. Introducing a long time scale $\tau = \varepsilon^2 t$ and replacing the time derivatives in equations (13)–(15) with $d/dt \rightarrow d/dt + \varepsilon^2 d/d\tau$ yields a hierarchy of ordinary differential equations at the different orders. The solutions to order $O(\varepsilon)$ are:

$$X_1 = a_1 e^{\sigma_r + i\sigma_o t} + a_1^* e^{\sigma_r - i\sigma_o t} + a_{13} e^{\sigma_3 t}, \quad Y_1 = b_1 e^{\sigma_r + i\sigma_o t} + b_1^* e^{\sigma_r - i\sigma_o t} + b_{13} e^{\sigma_3 t}$$
$$Z_1 = c_1 e^{\sigma_r + i\sigma_o t} + c_1^* e^{\sigma_r - i\sigma_o t} + c_{13} e^{\sigma_3 t} \tag{17}$$

where $\sigma_1 = \sigma_r + i\sigma_o$, $\sigma_2 = \sigma_r - i\sigma_o$ and σ_3 are the three eigenvalues of the system (13)–(15) linearized around R_o. It turns out that the first two, σ_1 and σ_2 are a pair of complex conjugate eigenvalues, while the third one is real and negative, i.e. $\sigma_3 < 0$ and real. At marginal stability, i.e. at $R = R_o$, the real part of the complex eigenvalues is zero. Therefore, at order $O(\varepsilon)$ one can set the argument of the exponents in equations (17) to $\sigma_1 = i\sigma_o$ and $\sigma_2 = -i\sigma_o$, by substituting $\sigma_r = 0$. What typically follows when using the weak non-linear method of solution is the neglect of the decaying term $a_{13}\mathrm{e}^{\sigma_3 t}$ from the solution. Clearly this term does not bring any contribution to the post-transient solution. However, while indeed this term vanishes at the post-transient state, its inclusion in the solution becomes essential in order to provide a relationship between the initial conditions in the present analytical solution and the computational one. The coefficients $a_1(\tau)$, $a_1^*(\tau)$, $b_1(\tau)$, $b_1^*(\tau)$, $c_1(\tau)$ and $c_1^*(\tau)$ are allowed to vary over the long time scale τ. By substituting the solutions (17) into the linearized form of equations (13)–(15), that apply at order $O(\varepsilon)$ (see Vadasz 1999b, 2001d for details), one obtains the following relationships between these coefficients

$$b_1 = \frac{(\alpha + i\sigma_o)}{\alpha}\, a_1; \quad b_1^* = \frac{(\alpha - i\sigma_o)}{\alpha}\, a_1^*; \quad b_{13} = \frac{(\sigma_3 + \alpha)}{\alpha}\, a_{13} \tag{18}$$

$$c_1 = \frac{\sigma_o\,[\sigma_o - i\,(\alpha + 1)]}{\alpha\,(R_o - 1)}\, a_1;$$

$$c_1^* = \frac{\sigma_o\,[\sigma_o + i\,(\alpha + 1)]}{\alpha\,(R_o - 1)}\, a_1^*; \quad c_{13} = \frac{-\sigma_3\,[\sigma_3 + \alpha + 1]}{\alpha\,(R_o - 1)}\, a_{13} \tag{19}$$

The values of σ_o, R_o and σ_3 corresponding to $\sigma_r = 0$ are also obtained as

$$R_o = \frac{\alpha\,(\alpha + 4\gamma + 3)}{(\alpha - 4\gamma - 1)}; \quad \sigma_o^2 = \frac{8\alpha\gamma\,(\alpha + 1)}{(\alpha - 4\gamma - 1)}; \quad \sigma_3 = -(\alpha + 4\gamma + 1) \tag{20}$$

The linear stability analysis produces results that are identical to the $O(\varepsilon)$ solutions presented above. Therefore, based on the linear stability analysis the loss of stability of the non-trivial stationary points occurs at a value of $R = R_o$. For $R < R_o$ linear stability predicts a solution that converges to one of the stationary points, while for $R > R_o$ a post-transient chaotic solution is anticipated. In reality, computational, numerical and experimental results show that the transition from the steady solution to chaos occurs at a value of $R = R_t \leq R_o$.

Solving the resulting non-homogeneous equations at order $O\left(\varepsilon^2\right)$ by using the $O(\varepsilon)$ solutions provides the required solution to be used in the equations at order $O\left(\varepsilon^3\right)$. A solvability condition is obtained at order $O\left(\varepsilon^3\right)$ in order to prevent terms of the form $\mathrm{e}^{i\sigma_o t}$ and $\mathrm{e}^{-i\sigma_o t}$ on the right hand side of the $O\left(\varepsilon^3\right)$ equations to resonate the homogeneous operator, hence forcing secular solutions of the form $t\mathrm{e}^{i\sigma_o t}$ and $t\mathrm{e}^{-i\sigma_o t}$ that are not bounded as $t \to \infty$. Hence, the coefficients of these secular terms must vanish, a requirement which provides a constraint on the amplitudes at order $O(\varepsilon)$ in the form of an amplitude equation

$$\frac{\mathrm{d}r}{\mathrm{d}t} = \chi\left[\xi - r^2\right] r, \quad \frac{\mathrm{d}\theta}{\mathrm{d}t} = m_1\,\varepsilon^2 - m_2\,r^2 \tag{21}$$

with $a\,a^* = r^2$, and m_1, m_2 are parameters that depend on α and γ, where the $O(\varepsilon)$ complex amplitude was presented in the form

$$a = \varepsilon\,a_1 = re^{i\theta}, \quad a^* = \varepsilon\,a_1^* = re^{-i\theta} \tag{22}$$

with $\mathrm{d}\theta/\mathrm{d}t = \dot{\theta}$ representing the frequency correction to σ_o (θ being the phase of the amplitude on the complex plane), $\chi = \varphi/\beta$ and

$$\xi = \frac{\varepsilon^2}{\varphi} = \frac{(R - R_o)}{R_o\varphi} \tag{23}$$

where φ and β are parameters that depend on the value of α. For $\alpha = 5$, corresponding to a $Va \cong 98.7$, and consistent with the present study $\varphi = -2.4$, $\beta = 0.403226$, and the following critical values apply $R_o = 25$ and $\sigma_o = \sqrt{60}$. Clearly $\chi < 0$ over all the cases considered, while $\xi > 0$ for $R < R_o$ (sub-critical conditions), $\xi < 0$ for $R > R_o$ (supercritical conditions), and $\xi = 0$ for $R = R_o$ (critical conditions). The post-transient solution to equation (21) yields $r = \pm\sqrt{\xi}$ which produces a real value of r only for $R < R_o$ (because $\varphi < 0$ as indicated above). The Hopf bifurcation at $R = R_o = 25$ is therefore sub-critical and in order to investigate the breakdown of the periodic solution at $R = R_o = 25$ the derivation of the transient solution to equation (21) is undertaken. This transient solution is obtained by direct integration in the form

$$r^2 = \frac{\xi}{\left[1 - \left(1 - \frac{\xi}{r_o^2}\right)\exp\left(-2\xi\,\chi\,t\right)\right]} \text{ for } \xi \neq 0\ (R \neq R_o) \tag{24}$$

$$r^2 = \frac{r_o^2}{\left[1 + 2r_o^2 \chi\, t\right]} \text{ for } \xi = 0\ (R = R_o) \tag{25}$$

where the following initial conditions were introduced: $r = r_o$ at $t = 0$.

Both solutions (24) and (25) are valid at $t = 0$ leading to $r^2 = r_o^2$, which can be recovered by substituting $t = 0$ in equations (24) and (25). The question of what happens at a later time $t > 0$ that causes these solutions to disappear when $R > R_o$, (i.e. when $\xi < 0$) is the focus of this analysis. Vadasz (1999b) has shown that both solutions (24) and (25) become singular, i.e. their denominator vanishes at a value of t, identified as the critical time, expressed by the equation

$$t_{cr} = \frac{1}{2\chi\xi} \ln\left[1 - \frac{\xi}{r_o^2}\right] \tag{26}$$

The existence of this critical time is linked to a condition that the argument of the $\ln(\bullet)$ function in equation (26) is positive and greater or smaller than 1, depending on whether ξ is negative or positive, respectively. The latter requirement comes to impose a positive value of t_{cr}, otherwise no physical significance can be associated with this critical time. This condition exists only for sub-critical values of R, i.e. for $\xi > 0\ (R < R_o)$, and is presented in the form $\xi \big/ r_o^2 < 1$, while for supercritical values of R, i.e. for $\xi < 0\ (R > R_o)$ the critical time exists unconditionally. **The physical interpretation of the existence of a critical time when the limit cycle solution diverges is explained as being the analytical representation of the homoclinic explosion leading to a chaotic solution.** Transforming the condition for this transition to occur, from $r_o^2 > \xi$, to the original physical parameters of the system by substituting the definition of $\xi = \varepsilon^2 \big/ \varphi = (R - R_o) \big/ R_o \varphi$, leads to a value of $R \leq R_o$, say R_t, beyond which the transition occurs, which can be expressed in the form

$$R_t = R_o \left(1 - |\varphi|\ r_o^2\right) \tag{27}$$

where the minus sign and the absolute value of φ appear in order to show explicitly that $\varphi < 0$. If $R < R_t$ the solution decays, spiraling towards the corresponding fixed point, and at $R = R_t$ we expect the limit cycle solution. Beyond this transitional value of R, i.e. $R > R_t$, the solution moves away from this fixed point either (a) towards the other fixed point, or (b) wanders around both fixed points before it stabilizes towards one of them, or (c) yields a chaotic behavior. The present expansion can not provide an answer to select between these three possibilities. However, it is important to stress that for any consistent initial condition r_o^2, which we choose, we can find a value of $R \leq R_o$ which satisfies equation (27). At that value of R we expect to obtain a limit cycle solution and beyond it a possible chaotic solution.

The horizontally average Nusselt number is evaluated based on the technique presented by Vadasz (2001a) resulting in the following relationship

$$\overline{Nu}^{h}\left(\hat{t},z\right)=1+\frac{2\left(R-1\right)}{R}\,Z+\frac{2\left(R-1\right)}{R}\,\left(XY-Z\right)\,\left[1-\cos\left(2\pi\,z\right)\right] \quad (28)$$

Clearly when the post-transient solution is not time dependent and a steady state is reached, $\dot{Z}=0$ and $Z=Z_S=1$, therefore equation (28) yields

$$\overline{Nu}^{h}_{steady\ state}=3-\frac{2}{R} \quad (29)$$

where $\overline{(\bullet)}^{h}=\left(\int_0^W dy\int_0^L dx\,(\bullet)\right)/(W\,L)$ stands for the horizontal averaging operator. A Taylor expansion of equation (29) around $R=1$, corresponding to the neighbourhood of the convection threshold, produces

$$\overline{Nu}^{h}_{steady\ state}=3-\frac{2}{R}=1+2\left(R-1\right)-2\left(R-1\right)^2+\ldots \quad (30)$$

The first two terms in expansion (30) represent the first order approximation as obtained by Braester and Vadasz (1993) via a weak non-linear solution by using an expansion around $R=1$. Nield and Bejan (2006) (based on Elder, 1967) suggested a linear approximation as a good curve fitting of the experimental data in the neighbourhood of the convection threshold. The present model, equation (30), recovers a linear first order approximation as a particular case of the more general expression for the Nusselt number at steady state, as presented by equation (29).

4 Computational and Numerical Solutions

One computational and one numerical method of solution is being used to solve the system (13)–(15). The first, the computational one, is Adomian's decomposition method (Adomian, 1988, 1994; Olek, 1994; Vadasz, 1999a, b, 2000, 2001a, b, c, d; Vadasz and Olek 1998, 1999a, b, 2000a, b). The method provides in principle an analytical solution in the form of an infinite power series for each dependent variable. However, the practical need to evaluate numerical values from the infinite power series, the consequent series truncation, and the practical procedure to accomplish this task transform the otherwise analytical results into a computational solution achieved up to a finite accuracy. The second, referred here as the numerical method, is used to solve the system (13)–(15) numerically to double precision by using the fifth and sixth order Runge-Kutta-Verner method from the IMSL Library (DIVPRK) (IMSL, 1991) up to a desired tolerance for error control specified by the parameter tol. We then compared the Adomian decomposition results (referred thereafter as **"the computational results"**) with the numerical solution (referred thereafter as **"the numerical results"**) by evaluating the difference between the two at all values of t up to $t_{\max}=210$ and plotting this difference in the results as projections of the trajectory of differences on the planes $\Delta Z=0$ ($\Delta Y-\Delta X$ plane), $\Delta Y=0$

($\Delta Z - \Delta X$ plane) and $\Delta X = 0$ ($\Delta Z - \Delta Y$ plane), where $\Delta X = X_{comp.} - X_{num.}$, $\Delta Y = Y_{comp.} - Y_{num.}$ and $\Delta Z = Z_{comp.} - Z_{num.}$. The indices "$comp.$" and "$num.$" stand for representing the computational (Adomian decomposition) and numerical (Runge-Kutta) results, respectively.

5 Compatible Initial Conditions

In order to compare the computational results to the analytical ones obtained via the weak non-linear theory one needs to ensure that the initial conditions for the computations are consistent with the initial conditions corresponding to the weak non-linear solution. The present weak non-linear solution provides the following conditions, which are necessary and sufficient to ensure the consistency of the initial conditions between the weak non-linear and computational solutions. The latter was obtained by Vadasz (2001d) in the form

$$X_o = 1 + 2\, r_o \cos(\theta_o) + a_{30} + O\left(\varepsilon^2\right) \tag{31}$$

$$Y_o = 1 + \frac{2\, r_o}{\alpha}\left[\alpha \cos(\theta_o) - \sigma_o \sin(\theta_o)\right] + \frac{(\sigma_3 + \alpha)}{\alpha} a_{30} + O\left(\varepsilon^2\right) \tag{32}$$

$$Z_o = 1 + \frac{2\, r_o}{\alpha\ (R_o - 1)}\left[\sigma_o^2 \cos(\theta_o) - \sigma_o\,(\alpha + 1)\sin(\theta_o)\right] - \frac{\sigma_3\,(\sigma_3 + \alpha + 1)}{\alpha\ (R_o - 1)} a_{30} + O\left(\varepsilon^2\right) \tag{33}$$

While equations (31)–(33) provide the equivalence relationships for the initial conditions in terms of $[X_o, Y_o, Z_o]$ as a function of $[r_o, \theta_o, a_{3o}]$, it is convenient to obtain a similar inverse relationship explicitly for $[r_o, \theta_o, a_{3o}]$ as a function of $[X_o, Y_o, Z_o]$, in the form

$$\tan(\theta_o) = \frac{\left[\sigma_o^2 + \sigma_3\,(\sigma_3 + \alpha + 1)\right]\left[(\sigma_3 + \alpha)\, x_o - \alpha\, y_o\right] - \sigma_3\left[\sigma_3\,(\sigma_3 + \alpha + 1)\, x_o + \alpha\,(R_o - 1)\, z_o\right]}{\sigma_o\left\{\left[\sigma_3\,(\sigma_3 + \alpha + 1)\, x_o + \alpha\,(R_o - 1)\, z_o\right] - (\alpha + 1)\left[(\sigma_3 + \alpha)\, x_o - \alpha y_o\right]\right\}} \tag{34}$$

where $x_o = X_o - 1$, $y_o = Y_o - 1$ and $z_o = Z_o - 1$. Once the value of θ_o is established from equation (34) one can evaluate the value of r_o by substitution, in the form

$$r_o = \frac{(\sigma_3 + \alpha)\, X_o - \alpha\, Y_o}{2\left[\sigma_3 \cos(\theta_o) + \sigma_o \sin(\theta_o)\right]} \tag{35}$$

Substituting equation (34) and the expression for r_o from equation (35) into equation (31) allows expressing a_{30} in the form

$$a_{30} = x_o - \frac{\left[\sigma_3 x_o + \alpha\,(x_o - y_o)\right]}{\left[\sigma_3 + \sigma_o \tan(\theta_o)\right]} \tag{36}$$

Equations (34), (35) and (36) represent the inverse compatibility relationships between the analytical weak non-linear solution and any computational solutions, the latter being naturally expressed in terms of $[X_o, Y_o, Z_o]$, while the former is expressed in terms of $[r_o, \theta_o, a_{30}]$. One can observe from equation (34) that for any given set of initial conditions in the form of $[X_o, Y_o, Z_o]$ the value of θ_o has a multiplicity greater than 1. Actually the solution for θ_o can be expressed in the form $\theta_o = \theta_{o1} + n\pi$. Values of θ_o greater than 2π are not relevant as then, the sine and cosine functions in equation (35) yield the same results. However, values of $\theta_o = \theta_{o1} + \pi$ are of relevance as they change the sign in front of the expression for r_o in equation (35). Therefore, since values of $\theta_o \in (\pi, 2\pi)$ have no other impact but to reverse the sign in front of r_o we can use this property to extend the definition of r and allow it to include negative values, while on the other hand we limit the variation of θ to be between 0 and π. The same applies therefore, in particular, to r_o and θ_o.

Two particular cases of interest are worth mentioning.

i. $a_{30} = 0$ and $\theta_o = 0$
The first particular case is related to the conditions $a_{30} = 0$ and $\theta_o = 0$ that upon substitution into equations (34), (35) and (36) yield

$$X_o = Y_o = 1 + 2\,r_o\,; \quad Z_o = 1 + \frac{\sigma_o^2}{\alpha\ (R_o - 1)}\ (X_o - 1) = 1 + \frac{2\,\sigma_o^2}{\alpha\ (R_o - 1)}\ r_o$$
$$\text{for } a_{30} = 0 \text{ and } \theta_o = 0 \tag{37}$$

This particular case represents the results presented by Vadasz (1999b) and it can be observed that it limits the possible set of initial conditions only to particular values of X_o, Y_o and Z_o because the inverse transformation does not exist but only for a particular combination of X_o, Y_o and Z_o that satisfies equation (37).

ii. $X_o = Y_o = Z_o$
This particular case yields upon substitution into equations (34), (35) and (36) the following relationships

$$\tan(\theta_o) = \frac{\sigma_3\left[\sigma_o^2 - \alpha\,(R_o - 1)\right]}{\sigma_o\left[\sigma_3^2 + \alpha\,(R_o - 1)\right]} \quad \text{for} \quad X_o = Y_o = Z_o \tag{38}$$

$$r_o = \frac{\sigma_3\ (X_o - 1)}{2\ [\sigma_3 \cos(\theta_o) + \sigma_o \sin(\theta_o)]} \quad \text{for} \quad X_o = Y_o = Z_o \tag{39}$$

$$a_{30} = \frac{\sigma_o \tan(\theta_o)\ (X_o - 1)}{2\ [\sigma_3 + \sigma_o \tan(\theta_o)]} \quad \text{for} \quad X_o = Y_o = Z_o \tag{40}$$

Clearly, from equation (38) one notices that for this particular case the possible values of θ_o are independent of the choice of X_o, Y_o and Z_o (as long as $X_o = Y_o = Z_o$), they will be therefore restricted and dependent only on the problem's parameters

R, α and γ. Furthermore, from equations (39) and (40) one can derive a relationship between a_{30} and r_o, therefore providing an additional constraint on the possible set of initial conditions.

Nevertheless, the compatibility relationships presented in equations (34)–(36) are general and do not restrict or constrain in any way the possible set of initial conditions. Despite this generality one should however realize that these relationships were derived by using the $O(\varepsilon)$ solution of the asymptotic expansion (16), and its corresponding amplitude solution obtained at order $O\left(\varepsilon^3\right)$. When the asymptotic expansion breaks down, or looses accuracy, naturally these relationships break down or loose accuracy as well. Then, including higher order corrections may restore accuracy.

6 Results and Discussion

Before presenting the comparison between the computational and weak non-linear analytical results, a brief sequence of computational results are presented in Fig. 3 to demonstrate the subcritical transition from steady convection to chaos. The results corresponding to initial conditions consistent with $r_o = 0.15$ ($X_o = Y_o = 1.3$ and $Z_o = 1.15$) are presented in Fig. 3, at two values of R, the first (Fig. 3a,b) at $R = 23.632$ just before the transition to chaos occurs, and the second (Fig. 3c,d) just after the transition at $R = 23.633 < R_o$ (note that $R_o = 25$ for $\alpha = 5$ and $\gamma = 0.5$, which are the parameter values considered in this presentation). The decay of the solution corresponding to $R = 23.632$ towards the stationary point $X = 1$ is clearly identified in Fig. 3(a), while Fig. 3b shows the inset of Fig. 3a zooming into the time domain $0 < t < 5$ clearly highlighting the oscillatory nature of the solution. On the other hand, for $R = 23.633$, Fig. 3(c,d) show a typical chaotic result. It is worth emphasizing the fact that the computational results show a transition to chaos at a sub-critical value of R (the critical value is $R_o = 25$). A comparison between Fig. 3(a) and 3(c) shows that the envelope of the function $X(t)$ converges for $R = 23.632$ (Figure 3a) and diverges for $R = 23.633$ (Figure 3c). This suggests that somewhere in-between $R = 23.632$ and $R = 23.633$ the envelope of the function $X(t)$ will neither converge nor diverge, producing a typical limit cycle. Looking for this limit cycle provides the result presented in Fig. 3(e), where it is evident that the envelope of the function $X(t)$ does not converge nor diverge, and the inset presented in Fig. 3(f) demonstrates the periodic behavior of the solution.

The objective in the presentation of the following results is in identifying the transition point, i.e. the value of R_t where the homoclinic explosion occurs and compare the computational and analytical values of R_t, the latter corresponding to equation (27), for different initial conditions that are consistent with the weak non-linear solution.

A sequence of numerous computations was performed in order to evaluate these transitional R values. In all computations the values of $\gamma = 0.5$ and $\alpha = 5$ were used. They yield the following corresponding parameter values $\varphi = -2.4$, $R_o = 25$,

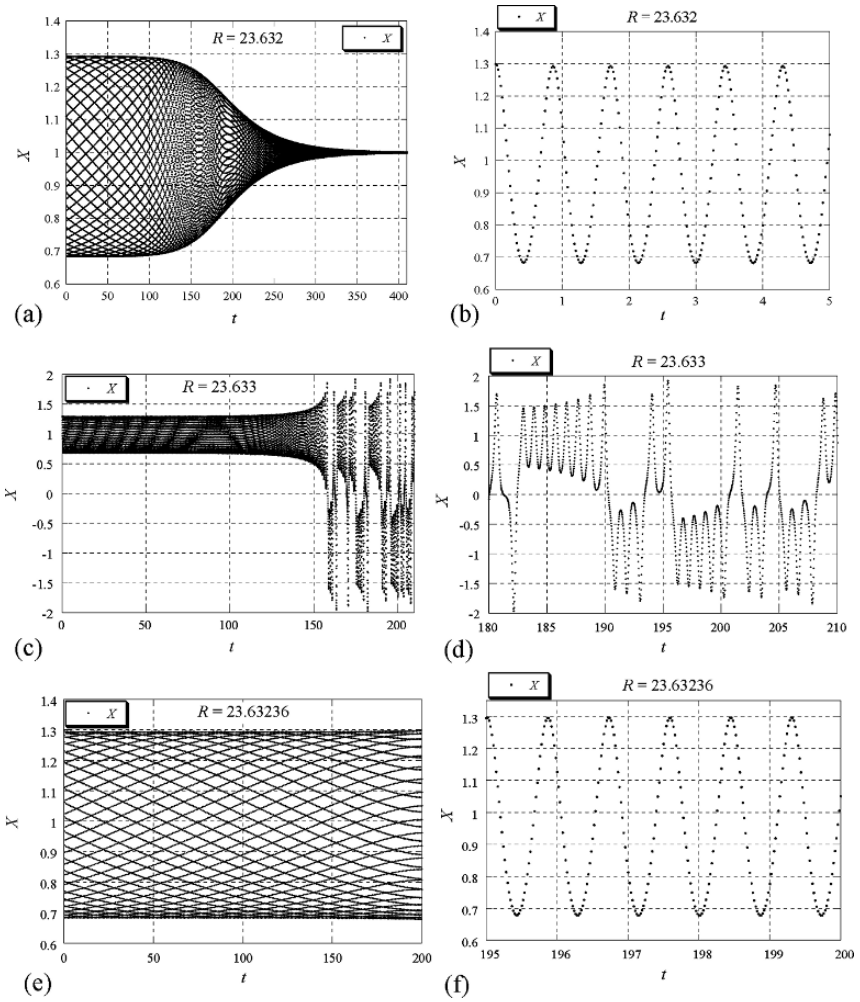

Fig. 3 The computational results for the evolution of $X(t)$ in the time domain for three values of Rayleigh number, in terms of R (data points are not connected). The initial conditions are $X_o = Y_o = 1.3$ and $Z_o = 1.15$ ($r_o = 0.15$). (**a**) X as a function of time for $R = 23.632$; the solution stabilizes to the fixed point. (**b**) the inset of Fig. 3(**a**) detailing the oscillatory decay of the solution. (**c**) X as a function of time for $R = 23.633$; the solution exhibits chaotic behaviour. (**d**) the inset of Fig. 3(**c**) detailing the chaotic solution. (**e**) X as a function of time for $R = 23.63236$; the solution is periodic. (**f**) the inset of Fig. 3(**e**) detailing the periodic solution

$\sigma_o = \sqrt{60}$ and $\sigma_3 = -8$. The computations were divided in three computational sets of results. Computational set "A" corresponds to the particular case when $a_{30} = 0$ and $\theta_o = 0$ (presented by Vadasz 1999b), computational set "B" corresponds to the particular case when $X_o = Y_o = Z_o$, associated with equations (34)–(36), while computational set "C" corresponds to arbitrary initial conditions that do not

belong to any particular case and are therefore general. The results are presented in Fig. 4 where the continuous curve represents the analytical solution expressed by equation (27) while the different markers represent the computational results corresponding to the different computational sets. The very good agreement between the analytical and computational solutions in the neighborhood of the non-trivial fixed point (i.e. $|r_o| << 1$) is evident from Fig. 4. Actually for $|r_o| < 0.2$ the computational and analytical solutions overlap. As the initial conditions move away from the non-trivial fixed point and the value of $|r_o|$ increases the analytical solution departs from the computational results, which reconfirms the validity of the weak non-linear solution in the neighborhood of a non-trivial fixed point and its breakdown far away from this point. In addition, the computational results move apart from each other as well, when $|r_o|$ increases. The reason for this latter departure is the fact that the compatibility of the initial conditions in terms of r_o was also derived based on the weak non-linear solution at order $O(\varepsilon)$. Therefore, as the latter solution looses accuracy when $|r_o|$ increases the compatibility conditions loose accuracy as well. The departure between the computational results and the analytical ones is clearly not symmetrical with respect to $r_o = 0$. While the $O(\varepsilon)$ weak non-linear solution is symmetrical with respect to $r_o = 0$, due to its elliptical shape, there is no reason to expect this symmetry from a computational solution as one moves away from the fixed point (the symmetry is kept for $|r_o| << 1$). Actually in the neighborhood of $|r_o| = 0.5$ one may expect to find the homoclinic orbit. Its shape is by far different than the one of an ellipse (see Vadasz 1999a, Vadasz and Olek 1999b). Both improvement of accuracy and loss of symmetry are expected if higher order

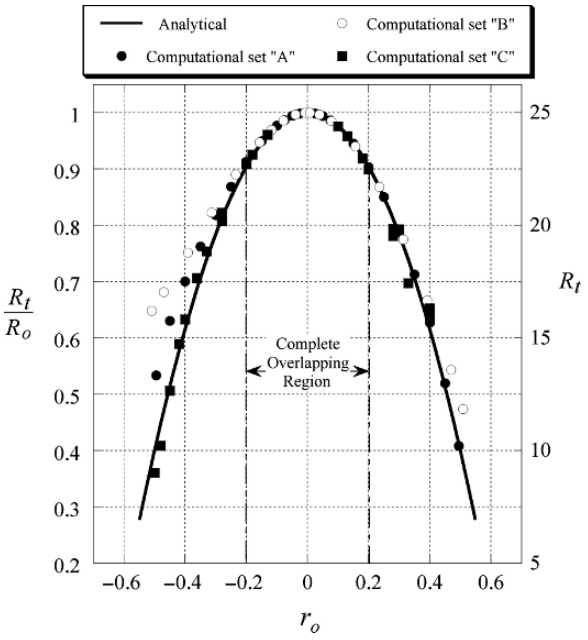

Fig. 4 Transitional sub-critical values of Rayleigh number in terms of R_t/R_o as a function of the initial conditions r_o. A comparison between the weak non-linear solution (— analytical) and the computational results (• computational set "A", ○ computational set "B", ■ computational set "C")

corrections are considered. The relatively easy computational recovery of the limit cycle does not imply that this limit cycle is stable. On the contrary, a slight variation of the initial conditions causes a change in the value of R_t and consequently the limit cycle disappears. It can be recovered again by a further adjustment of the value of R (see equation (27)). From the figure it is evident that as long as the initial conditions are not too far away from the non-trivial fixed point, i.e. $|r_o| << 1$, the computational and analytical solutions are identical. For values of r_o close to the non-trivial fixed point, i.e. in the neighborhood of $r_o \sim 0$, both solutions overlap. However, as r_o moves away from this neighborhood the weak non-linear solution loses accuracy and the analytical results for R_t depart from the accurate computational ones. Higher order corrections of this analytical transition value could improve the accuracy of the analytical results. Nevertheless, it can be anticipated that the actual transition point, R_t, depends not only on r_o as equation (27) suggests, but also on θ_o and a_{30}.

The results of the evaluation of the mean Nusselt number over a wide range of values of R are presented graphically in Fig. 5 based on Vadasz (2001a). The evaluation of this mean Nusselt number was performed for three different cases, as relevant to the impact of the initial conditions on the results. The first case corresponds to *fixed initial conditions* for all values of R considered (the values used correspond to $X^{(o)} = Y^{(o)} = Z^{(o)} = 0.9$), the second case uses the final values of X, Y and Z obtained at the previous, *slightly smaller*, value of R as initial conditions for the current value of R. This case is referred to as the "*forward moving*" case. The third case is similar to the latter however it moves in the opposite R direction, i.e. the initial conditions for the solution at the current value of R are taken from the final values of X, Y and Z obtained at the previous, *slightly larger*, value of R. This case is referred to as the "*backward moving*" case. This procedure was followed for values of R ranging between $1 \leq R \leq 150$, with a step of $\Delta R = 0.1$. It is evident from Fig. 5 that the transition from steady convection to chaos is associated with a sharp decline in heat flux. This can be linked to the solitary limit cycle that appears at this transition, hence the retarding effect that this transition has on the

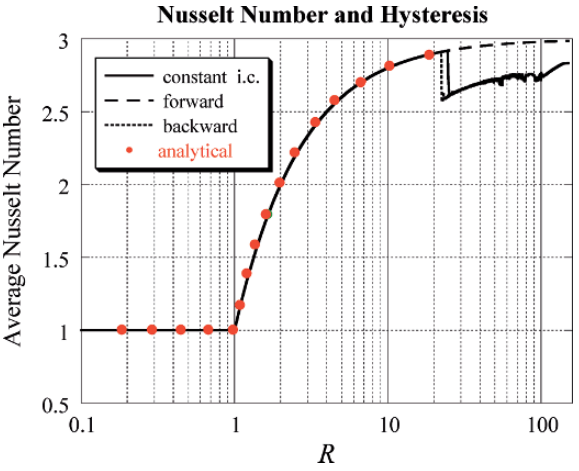

Fig. 5 The variation of the mean Nusselt number as a function of R as obtained computationally, via forward and backward variation of R, and compared with the analytical relationship, equation (29), for sub-transitional values of R, highlighting the transition from steady convection to chaos, and the corresponding Hysteresis effect

heat flux is due to the oscillatory nature of the transition point, rather than the chaotic (weak-turbulent) nature of the solution beyond this transition point. Furthermore, it is evident that the weak-turbulent regime following the transition point contributes to a recovery from this sharp reduction in heat flux. An additional impressive result evident from Fig. 5 is the effect of Hysteresis linked to the transition from steady to weak-turbulent convection. While the solution corresponding to constant initial conditions experiences the transition (observed by the jump in the value of the mean Nusselt number) at a value of R close to $R = R_o = 25$ (actually slightly below it) the transition for the "backward moving" case occurs at a value of R substantially below $R_o = 25$, as indeed anticipated from the analytical results and the discussion on Hysteresis presented in Sec. 3 and equation (27). The computational results confirm the analytical upper bound for the average Nusselt number

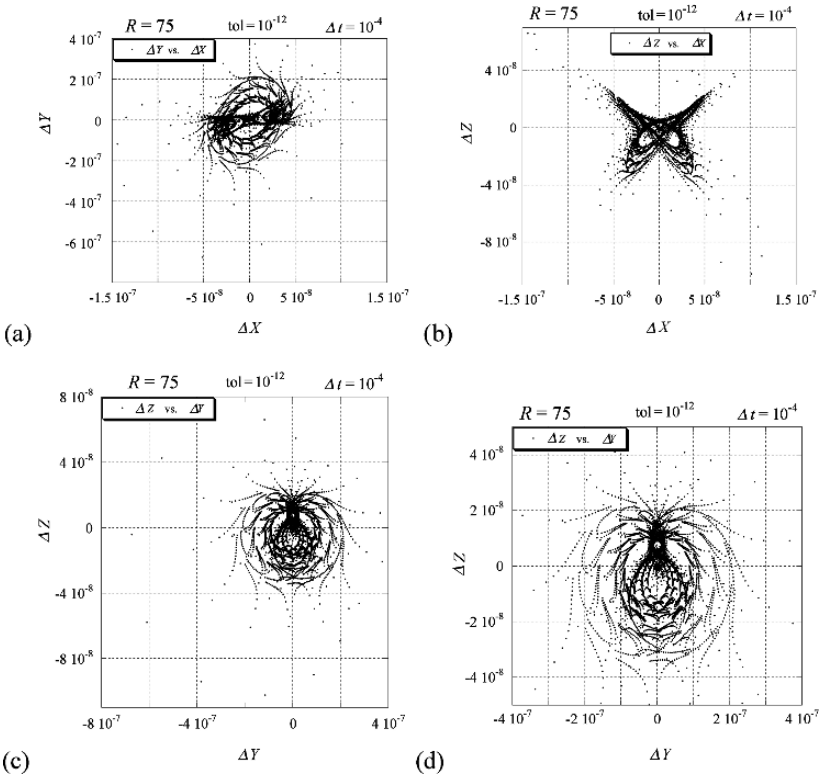

Fig. 6 Trajectory of differences between the computational (Adomian decomposition) and numerical (Runge-Kutta) solutions corresponding to $\Delta t = 10^{-4}$ in the computational solution, $tol = 10^{-12}$ in the numerical solution, and $R = 75$. (**a**) projection of trajectory's data points on the plane $\Delta Z = 0$, (**b**) projection of trajectory's data points on the plane $\Delta Y = 0$, (**c**) projection of trajectory's data points on the plane $\Delta X = 0$, (**d**) inset of the projection of trajectory's data points on the plane $\Delta X = 0$. (Data points are not connected)

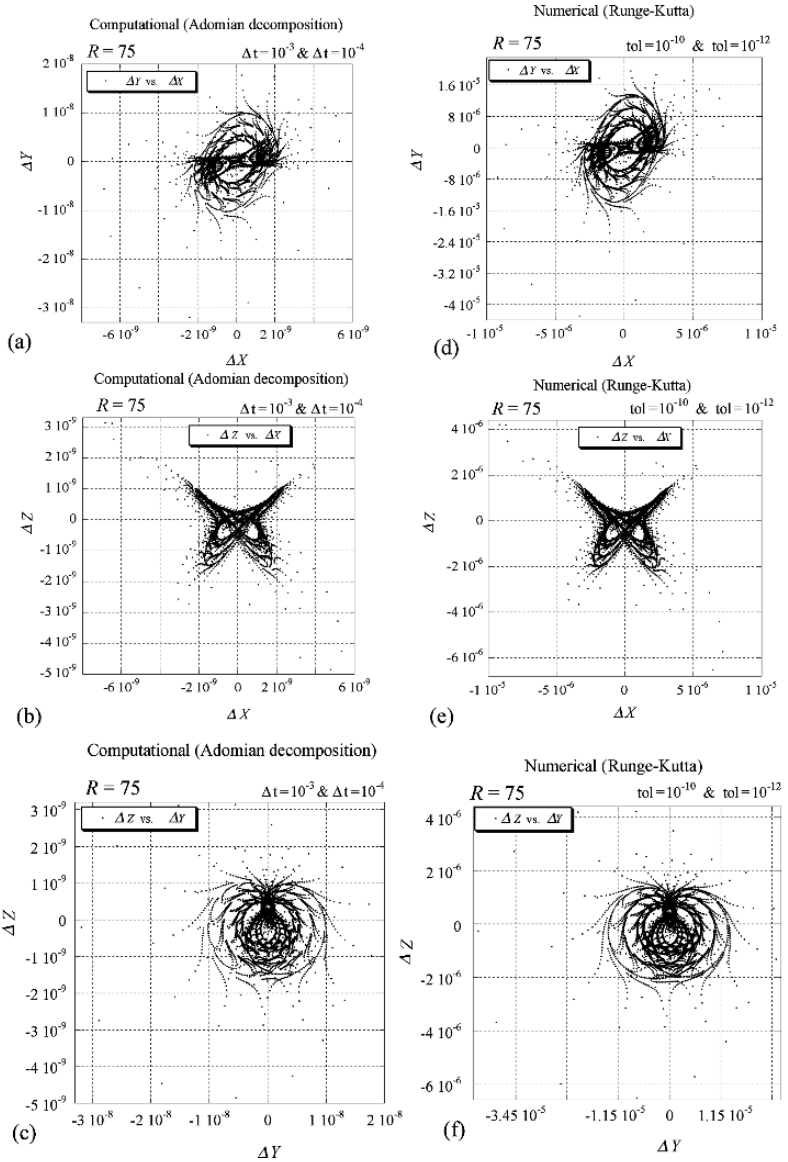

Fig. 7 Trajectory of differences between the computational (Adomian decomposition) results corresponding to $\Delta t = 10^{-3}$ and $\Delta t = 10^{-4}$ for $R = 75$ (**a**) projection of trajectory's data points on the plane $\Delta Z = 0$, (**b**) projection of trajectory's data points on the plane $\Delta Y = 0$, (**c**) projection of trajectory's data points on the plane $\Delta X = 0$. Trajectory of differences between the numerical (Runge-Kutta) results corresponding to $tol = 10^{-10}$ and $tol = 10^{-12}$ for $R = 75$ (**d**) projection of trajectory's data points on the plane $\Delta Z = 0$, (**e**) projection of trajectory's data points on the plane $\Delta Y = 0$, (**f**) projection of trajectory's data points on the plane $\Delta X = 0$. (Data points are not connected)

represented by equation (30) and in particular the value of $\overline{Nu}_{o,\infty}^{h\infty} = 3$ for the limit as $R \to \infty$.

To investigate the accuracy of the results we evaluated the differences between the computational and numerical solutions, $\Delta X, \Delta Y$ and ΔZ at $R = 75$ as presented in Fig. 6(a,b,c) in terms of projections of trajectories data points on the planes $\Delta Z = 0$, $\Delta Y = 0$ and $\Delta X = 0$. It can be observed from the figures that the maximum difference between the two solutions is of the order of magnitude of 10^{-7}. In addition the detail of the trajectory of differences projected on the plane $\Delta X = 0$ is presented as the inset of Fig. 6(c) in Fig. 6(d) where a better description of the shape of the trajectory can be observed.

An additional interesting result was obtained by evaluating the differences between two consecutive computational solutions corresponding to $\Delta t = 10^{-3}$ and $\Delta t = 10^{-4}$, respectively, and two consecutive numerical solutions corresponding to $tol = 10^{-10}$ and $tol = 10^{-12}$, respectively. The differences between the two computational solutions are presented in Fig. 7(a,b,c) and the differences between the numerical solutions are presented in Fig. 7(d,e,f). As the maximum difference in the computational solution is of the order of magnitude $O\left(10^{-9}\right)$ while the maximum difference in the numerical solution is of the order of magnitude $O\left(10^{-5}\right)$, it is evident from Fig. 7 that the shape of the trajectory of differences is kept similar under the scale reduction and magnification suggesting that the results represent a fractal shape.

7 Conclusions

The analytical derivation of the transition point from steady to chaotic solutions in Lorenz equations was presented by using the weak non-linear theory. The analytical results are accurate within the validity domain of the weak non-linear method of solution. A comparison between the analytical prediction and computational results show an excellent fit as long as the analytical solution is within the validity domain. Gradual loss of accuracy of the analytical solution produces gradual loss of accuracy of the analytical prediction for the transition point. Both the analytical and computational results confirmed the transition from steady convection to chaos via a limit cycle at a sub-critical value of the Rayleigh number.

References

Adomian, G. 1988 A Review of the Decomposition Method in Applied Mathematics. *J. Math. Anal. Appl.* **135**, 501–544.

Adomian, G. 1994 *Solving Frontier Problems in Physics: The Decomposition Method*. Kluwer Academic Publishers, Dordrecht.

Bhadauria, B.S. 2007 Double Diffusive Convection in a Porous Medium with Modulated Temperature on the Boundaries, *Transport in Porous Media*, (in press, DOI 10.1007/s11242-006-9095-y).

Bejan, A. 1995, *Convection Heat Transfer*, 2nd edition, Wiley, New York.

Braester, C., and Vadasz, P. 1993 The Effect of a Weak Heterogeneity of the Porous Medium on the Natural Convection, *J. Fluid Mech.* **254**, pp. 345–362.

Bau, H. H. 1994 An Engineer's Perspective on Chaos, in *Chaos in Heat Transfer and Fluid Dynamics*, ed. Arpacci, Hussain, Paollucci and Watts, **HTD-Vol.298**, pp. 1–7.

Elder, J.W. 1967 Steady Free Convection in a Porous Medium Heated from Below, *J. Fluid Mech.* **27**, pp. 609–623.

Govender, S. 2003 Coriolis Effect on the Linear Stability of Convection in a Porous Layer Placed Far Away from the Axis of Rotation, *Transp. Porous. Med.* **51**, 315–326.

Govender, S. 2006a Stability of Gravity Driven Convection in a Cylindrical Porous Layer Subject to Vibration, *Transp. Porous Media* **63**, 489–502.

Govender, S. 2006b Effect of Darcy-Prandtl number on the Stability of Solutal Convection in Solidifying Binary Alloy Systems, *J. Porous Med.* **9** (6), 523–539.

IMSL Library, 1991 *Fortran Subroutines for Mathematical Applications*, Version 2, Houston.

Lorenz, E.N. 1963 Deterministic Non-Periodic Flows. *J. Atmos. Sci.* **20**, 130–141.

Lombardo, S. and Mulone, G. 2002 Necessary and Sufficient Stability Conditions of Global Nonlinear Stability for Rotating Double Diffusive Convection in a Porous Medium, *Continuum Mech. Thermodyn.* **14**, 527–540.

Mulone, G., and Straughan, B. 2006 An Operative Method to Obtain Necessary and Sufficient Stability Conditions for Double Diffusive Convection in Porous Media, *Z. Angew. Math. Mech.* **86** (7), 507–520.

Nield, D.A., and Bejan, A. 2006 *Convection in Porous Media*, 3rd ed., Springer Verlag, New York.

Olek, S. 1994 An Accurate Solution to the Multispecies Lotka-Volterra Equations. *SIAM Revi.* **36**, 480–488.

Sheu, L.J. 2006 An Autonomous System for Chaotic Convection in a Porous Medium Using a Thermal Non-Equilibrium Model, *Chaos, Soliton. Fract* **30** (3) 672–689.

Sparrow, C. 1982 *The Lorenz Equations: Bifurcations, Chaos, and Strange Attractors*. Springer-Verlag, New York.

Straughan, B. 2001 A Sharp Nonlinear Stability Threshold in Rotating Porous Convection. *Proc. R. Soc. Lond. A* **457**, 87–93.

Straughan, B. 2004 Resonant Porous Penetrative Convection. *Proc. R. Soc. Lond. A* **460**, 2913–2927.

Vadasz, P. 1998 Coriolis Effect on Gravity Driven Convection in a Rotating Porous Layer Heated from Below. *J Fluid Mech.* **376**, 351–375.

Vadasz, P. 1999a On the Homoclinic Orbit for Convection in a Fluid Layer Heated from Below. *International J. Heat and Mass Transfer* **42** (19), 3557–3561.

Vadasz, P. 1999b Local and Global Transitions to Chaos and Hysteresis in a Porous Layer Heated from Below. *Transport in Porous Media* **37** (2), 213–245.

Vadasz, P. 2000 Subcritical Transitions to Chaos and Hysteresis in a Fluid Layer Heated from Below. *International J. Heat and Mass Transf.* **43** (5), 705–724.

Vadasz, P. 2001a Heat Transfer Regimes and Hysteresis in Porous Media Convection. *ASME J. Heat Transf.* **123**, 145–156.

Vadasz, P. 2001b The Effect of Thermal Expansion on Porous Media Convection – Part 1: Thermal Expansion Solution. *Transp Porous Media* **44** (3), 421–443.

Vadasz, P. 2001c The Effect of Thermal Expansion on Porous Media Convection – Part 2: Thermal Convection Solution. *Transp Porous Media* **44** (3), 445–463.

Vadasz, P. 2001d Equivalent Initial Conditions for Compatibility between Analytical and Computational Solutions of Convection in Porous Media. *Int. J. Non Linear Mech.* **36** (2), 197–208.

Vadasz, P. 2006 Chaotic Dynamics and Hysteresis in Thermal Convection, *Proc. ImechE Part C J. Mechanical Engineering Science* **220**, 309–323.

Vadasz, P., and Braester, C., 1992 The Effect of Imperfectly Insulated Sidewalls on Natural Convection in Porous Media, Acta Mechanica, **91** (3–4), 215–233.

Vadasz, P., Olek, S. 1998 Transitions and Chaos for Free Convection in a Rotating Porous Layer. *Int. J. Heat Mass Transf.* **14** (11), 1417–1435.

Vadasz, P., Olek, S. 1999a Weak Turbulence and Chaos for Low Prandtl Number Gravity Driven Convection in Porous Media. *Transp. Porous Media* **37** (1), 69–91.

Vadasz, P., Olek, S. 1999b Computational Recovery of the Homoclinic Orbit in Porous Media Convection. *Int. J. NonLinear Mech.* **34** (6), 89–93.

Vadasz, P., Olek, S. 2000a Route to Chaos for Moderate Prandtl Number Convection in a Porous Layer Heated from Below. *Transp. Porous Media* **41** (2), 211–239.

Vadasz, P., Olek, S. 2000b Convergence and Accuracy of Adomian's Decomposition Method for the Solution of Lorenz Equations. *Int. J. Heat and Mass Transf.* **43** (10), 1715–1734.

Natural Convection in Gravity-Modulated Porous Layers

Saneshan Govender

Abstract We analyze natural convection in porous layers subjected to gravity modulation. In particular a linear stability analysis and weak non-linear analysis is presented for both synchronous and subharmonic solutions and the exact point for the transition from synchronous to subharmonic solutions is computed. It is demonstrated that increasing the excitation frequency rapidly stabilizes the convection up to the transition point from synchronous to subharmonic convection. Beyond the transition point, the effect of increasing the frequency is to slowly destabilize the convection.The weak-non-linear results show that increasing the excitation frequency rapidly decays the convection amplitude. An analogy between the inverted pendulum with an oscillating pivot point and the gravity modulated porous layer is developed and it is shown that the convection cell wavelength is related to the length of the pendulum.

1 Introduction

The classical Rayleigh–Benard problem has been extensively studied for both pure fluids and porous domains, with and without rotation. In both pure fluids and porous media, the density gradient becomes unstable and fluid motion results when a critical temperature difference, measured by means of the Rayleigh number, is exceeded. Comprehensive reviews are provided by Chandrasekar (1961) for pure fluids whilst Bejan (1995) provides a review of the fundamentals of heat convection in porous media.

The classical stability analysis no longer applies if the Rayleigh number (or the temperature difference) is time dependant. Time dependant body forces may occur in systems, with density gradients, subjected to vibrations. The influence of vibrations on thermal convection depends on the orientation of the time dependant acceleration with respect to the thermal stratification. Much work has been done for pure fluids for a vertically modulated fluid layer with constant vertical

S. Govender
University of Kwa-Zulu Natal, Durban, South Africa
e-mail: govenders65@ukzn.ac.za

P. Vadász (ed.), *Emerging Topics in Heat and Mass Transfer in Porous Media*,

© Springer Science+Business Media B.V. 2008

stratification, i.e. modulated Rayleigh–Benard convection. Comprehensive analyses by Gresho & Sani (1970), Wadih & Roux (1988), Christov & Homsy (2001) and Hirata et al. (2001) are available for flow and heat transfer in a pure fluid layer subjected to gravity modulation. Alex & Patil (2002a, b), Bardan and Mojtabi (2000) and Bardan et al. (2004) provide the good references of work dealing with the effects of vibration on flow and heat transfer in porous media. In the latter two studies however, an averaging technique is used whereby the vibration body force is split into a steady and time dependant portion. It is also mentioned that with this method of solution, the subharmonic modes are never captured. Govender (2004, 2005a) utilises a direct method of solution and the resulting governing equation is cast into the canonical form of the much publicized Mathieu equation. The author then analyses the problem and recovers both the synchronous and subharmonic solutions in the parameter domain. In addition Govender (2005b) provides a comprehensive weak-nonlinear analysis for high frequency vibration. Also, Govender (2005c) provides an analysis for stability analyses for gravity modulation with heating from below whilst Govender (2005d) provides a stability analysis of low frequency vibration.

2 Problem Formulation

A shallow horizontal fluid saturated porous layer subject to vibration is presented in Fig. 1. The porous medium is constrained by rigid horizontal plates, spaced a distance H_* apart, and oscillates parallel to the gravitational field in the vertical direction. In addition the Darcy law is extended to include the time derivative while the Boussinesq approximation is applied to account for the effects of the density variations.

Subject to these conditions, the following dimensional set of governing equations for continuity, Darcy and energy, is proposed:

$$\nabla_* \cdot \boldsymbol{V}_* = 0, \tag{1}$$

$$\boldsymbol{V}_* = \frac{\boldsymbol{k}_*}{\mu_*}\left[-\nabla_* p_* - (\rho_* - \rho_{c^*})\left(g_* + b_*\omega_* \sin(\omega_* t_*)\right)\hat{e}_z - \frac{\rho_{c^*}}{\phi}\frac{\partial \boldsymbol{V}_*}{\partial t_*}\right], \tag{2}$$

$$\frac{\partial T_*}{\partial t_*} + \boldsymbol{V}_* \cdot \nabla_* T_* = \lambda_* \nabla_*^2 T_*. \tag{3}$$

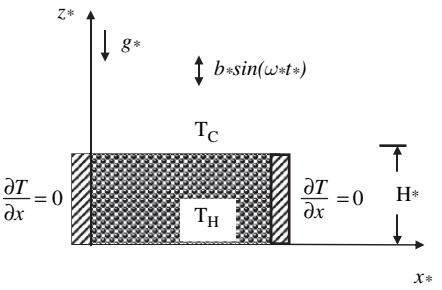

Fig. 1 Differentially heated porous layer subjected to vibration

It should be borne in mind that if the temperature effects are removed from Eq. (2), we obtain in the frequency domain a frequency dependant and complex valued permeability whose real and imaginary parts show a behaviour that resembles the Biot seepage law. The values λ_* / H_* , $\mu_* \lambda_* / k_{c^*}$ and $\Delta T_c = (T_H - T_C)$ are used to scale the filtration velocity components (u_*, v_*, w_*), reduced pressure (p_*), and temperature variations ($T_* - T_C$), respectively, where λ_* is the effective thermal diffusivity including the effect of the ratio between the heat capacity of the fluid and the effective heat capacity of the porous domain, μ_* is the fluid's viscosity and k_{c^*} is a characteristic permeability associated with the porous matrix. The height of the layer H_* is used for scaling the variables x_*, y_*, and z_*. Accordingly, $x = x_* / H_*$, $y = y_* / H_*$, and $z = z_* / H_*$. The time variable is scaled using H_*^2 / λ_* , hence $t = t_* \lambda_* / H_*^2$. In the current study a linear approximation was assumed for the relationship between the density and temperature, in the form $\rho_* = \rho_{c*} (1 - \beta_* \Delta T_c T)$ where β_* is the thermal expansion coefficient. Subject to the dimensional analysis, the following system of dimensionless equations result:

$$\nabla \cdot \boldsymbol{V} = 0, \tag{4}$$

$$\left(\frac{1}{Va} \frac{\partial}{\partial t} + 1 \right) \boldsymbol{V} = -\nabla p - R \left[1 + \delta \sin(\Omega t) \right] T \hat{e}_z, \tag{5}$$

$$\frac{\partial T}{\partial t} + \boldsymbol{V} \cdot \nabla T = \nabla^2 T. \tag{6}$$

The symbols $\boldsymbol{V}$, T and p represent the dimensionless filtration velocity vector, temperature and reduced pressure, respectively, and $\hat{e}_z$ is a unit vector in the z-direction. In Eq. (5), Ω is the scaled frequency, defined as $\Omega = \omega_* H_*^2 / \lambda_*$, whilst the non-dimensional amplitude δ is defined as $\delta = \kappa Fr \Omega^2$, where $\kappa = b_* / H_*$ and Fr is the modified Froude number defined as $Fr = \lambda_*^2 / (g_* H_*^3)$. The parameter Va is the Vadasz number, as pointed out by Straughan (2000), and includes the Prandtl and Darcy numbers as well as the porosity of the porous domain and is defined as

$$Va = \frac{\phi \, \mathrm{Pr}}{Da}. \tag{7}$$

In Eq. (7) $Pr = \nu_* / \lambda_*$ is the Prandtl number, $Da = k_{c^*} / H_*^2$ is the Darcy number, ϕ is the porosity and ν_* stands for the kinematic viscosity of the fluid. It is only through this combined dimensionless group that the Prandtl number affects the flow in the porous media, see Vadasz (1998) for a full discussion on the numerical values that Pr can assume in a typical porous medium. In Eq. (5) one also observes the Rayleigh number, R; defined as $R = \beta_* \Delta T_C g_* k_{c^*} H_* / \nu_* \lambda_*$. As all boundaries are rigid, the solution must follow the impermeability conditions there, i.e. $\boldsymbol{V} \cdot \hat{e}_n = 0$ on the boundaries, where $\hat{e}_n$ is a unit vector normal to the boundary. The temperature boundary conditions are: $T = 1$ *at* $z = 0$, $T = 0$ *at* $z = 1$ and $\nabla T \cdot \hat{e}_n = 0$ on all other walls representing the insulation condition on these walls. The partial differential equations (4–6) forms a non-linear coupled system which together with the corresponding boundary conditions accepts a basic motionless solution with a

parabolic pressure distribution. The solutions for the basic temperature and flow field is given as, $T_B = 1 - z$ and $\boldsymbol{V_B} = 0$. To provide a non-trivial solution to the system it is convenient to apply the curl operator $(\nabla\times)$ twice on Eq. (5) and consider the z-component, to obtain,

$$\left(\frac{1}{Va}\frac{\partial}{\partial t} + 1\right)\nabla^2 \boldsymbol{V} + R\left[1 + \delta\sin(\Omega t)\right]\nabla_H^2 T\hat{e}_z = 0, \tag{8}$$

for a solenoidal velocity field, Eq. (4). The Laplacian operator in Eq. (8) is defined as $\nabla_H^2 \equiv \partial^2/\partial x^2 + \partial^2/\partial y^2$ for cartesian co-ordinates.

3 Linear Stability Analysis

The basic motionless solution is $\boldsymbol{V_B} = 0$ and $T_B = 1 - z$. Assuming small perturbations around the basic solution in the form $\boldsymbol{V} = \boldsymbol{V}_B + \boldsymbol{V}'$ and $T = T_B + T'$, and linearising equations (6) and (8) yields the following linear system,

$$\left(\frac{1}{Va}\frac{\partial}{\partial t} + 1\right)\nabla^2 \boldsymbol{V}' + R\left[1 + \delta\sin(\Omega t)\right]\left[\frac{\partial^2 T'}{\partial x\partial z}\hat{e}_x + \frac{\partial^2 T'}{\partial y\partial z}\hat{e}_y - \nabla_H^2 T'\hat{e}_z\right] = 0, \tag{9}$$

$$\left[\frac{\partial}{\partial t} - \nabla^2\right]T' - w' = 0, \tag{10}$$

where w' is the perturbation to the vertical component of the filtration velocity. The boundary conditions in the $z-$direction required for solving Eqs. (9) and (10) are $w' = T' = 0$ at $z = 0$ and $z = 1$. In the x-direction $\partial T/\partial x = 0$ at $x = 0$ and $x = L$. The coupling between Eqs. (9) and (10) can be removed by considering the vertical component of Eq. (9) and eliminating w' to provide one equation for the temperature perturbation in the form

$$\left(\frac{1}{Va}\frac{\partial}{\partial t} + 1\right)\nabla^2\left[\frac{\partial}{\partial t} - \nabla^2\right]T' - R\left[1 + \delta\sin(\Omega t)\right]\nabla_H^2 T' = 0. \tag{11}$$

Assuming an expansion into normal modes in the x- and y-directions, and a time-dependant amplitude $\theta(t)$ of the form,

$$T' = \theta(t)\exp\left[i\left(s_x y + s_y z\right)\right]\sin(\pi z) + c.c, \tag{12}$$

where $c.c.$ stands for the complex conjugate terms and $s^2 = s_x^2 + s_y^2$. Substituting Eq. (12) into the Eq. (11) provides an ordinary differential equation for the amplitude $\theta(t)$,

$$\frac{d^2\theta}{dt^2} + 2p\frac{d\theta}{dt} - F(\alpha)\gamma\left[\left(\tilde{R} - \tilde{R}_o\right) + \tilde{R}\delta\sin(\Omega t)\right]\theta = 0, \tag{13}$$

where $\alpha = s^2/\pi^2$, $\gamma = Va/\pi^2$ and $\tilde{R} = R/\pi^2$. In Eq. (13), $2p = \pi^2(\alpha + 1 + Va)$, $F(\alpha) = \pi^4\alpha/(\alpha + 1)$ and $\tilde{R}_o$ is the un-modulated Rayleigh number defined as $\tilde{R}_o = (\alpha + 1)^2/\alpha$. Using the transformation $t = (\pi/2 + 2\tau)/\Omega$, equation (13) may be cast into the canonical form of the Mathieu equation, as outlined by McLachlan (1964), and is given as

$$\frac{d^2X}{d\tau^2} + [a + 2q\cos(2\tau)]\,X = 0. \tag{14}$$

The solution to Eq. (14) follows the form $X = G(\tau)\,e^{\sigma\tau}$ where $G(\tau)$ is a periodic function with a period of π or 2π and σ is a characteristic exponent which is a complex number and is a function of a and q respectively. In this chapter the definitions for a, q and σ are obtained upon transforming Eq. (13) to the canonical form and is defined as,

$$\frac{2}{\sqrt{-a}} = \frac{\Omega}{\left[F(\alpha)\,\gamma\left(\tilde{R} - \eta\right)\right]^{1/2}}, \tag{15}$$

$$\frac{1}{2}q = \frac{F(\alpha)\,\gamma\tilde{R}\delta}{\Omega^2} = F(\alpha)\,\gamma\tilde{R}\kappa Fr, \tag{16}$$

$$\sigma = -2p/\Omega, \tag{17}$$

where η is a parameter defined as,

$$\eta = -\tilde{R}_o\frac{(\alpha + 1 - \gamma)^2}{4\gamma(\alpha + 1)}. \tag{18}$$

When $\sigma = \sigma_r = 0$, the solution to Eq. (14) is defined in terms of Mathieu functions, c_n and d_m, such that for each Mathieu function, c_n and d_m, there exists a relation between a and q. This relationship is shown in Fig. 2 for the Mathieu functions d_0, c_1 and d_1 for small values of q.

It is observed from Fig. 2 that d_0, c_1 and d_1 separates the stable and unstable solutions. If the other Mathieu functions (viz. c_n and d_m where $n = 2, 3, 4..N$ and $m = 2, 3, 4, ..M$) are superimposed on Fig. 2 one would observe that the regions separated by the Mathieu functions in the a–q plane are alternately stable and unstable. For our analysis we consider only small values of q, so the analysis around the Mathieu functions d_0, c_1 and d_1 is sufficient. Upon examining Fig. 2, one is able to note that the region below curve d_0, and the region enclosed between curves c_1 and d_1 correspond to the unstable zones. The narrow region between curves d_0 and c_1 represent the stable zones. In principle the regions enclosed by even indices of d_m (i.e. $m = 0, 2, 4, 6..$) yields synchronous solutions whilst those regions enclosed by odd indices of d_m (i.e. $m = 1, 3, 5, 7..$) yields subharmonic solutions thus implying that the a–q plane consists of alternating regions of synchronous and subharmonic solutions. In the stable regions of Mathieu's equation, σ is complex with a negative real part. Since σ is a function of a and q, which are dependant on γ, $\tilde{R}$, α, δ and Ω,

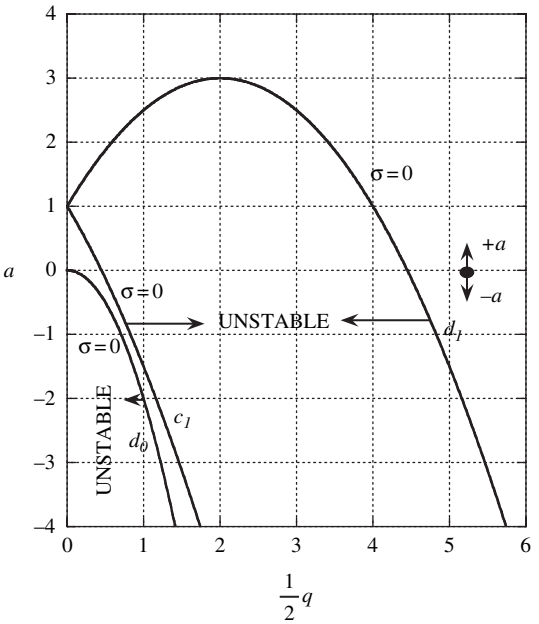

Fig. 2 Mathieu chart clearly demarcating the stable and unstable zones

the stability porous layer is also seen to depend on these variables as well. In addition there are solutions to Eq. (14) for $a > 0$ and $a < 0$; also, q may be replaced by $-q$ with no effect on the solution. In this study for a porous medium heated from below the numerical values for a are less than zero and are defined by Eq. (15). In the case of liquid metals, as found during the solidification of binary alloys, see Pillay & Govender (2005), we may propose for a Lead-Antimony (Pb-Sn) system, $\lambda_* = 1.08 \times 10^{-5}\,\mathrm{m^2/s}$, $\nu_* = 2.47 \times 10^{-7}\,\mathrm{m^2/s}$, and $Pr = 2.3 \times 10^{-2}$. For a characteristic height $H_* = 0.1\,m$, we find that the corresponding value for the Froude number, Fr, is $Fr = 1.1 \times 10^{-3}$. If the vibration amplitude to characteristic height ratio κ is $\kappa = 10^{-2}$, then the parameter $(\kappa Fr) = O\left(10^{-5}\right)$. As a result we note that q assumes very small values for the above property values. For the low Prandtl number liquid melt, we follow Vadasz (1998) and propose that $Va = O(1)$, thereby allowing for the retention of the time derivative in the Darcy equation. In the current study we propose the following definition for the modified characteristic exponent: $\xi = \sigma/\sqrt{-a}$. A chart of $1/2q$ versus $2/\sqrt{-a}$, for various values of ξ, is shown in Fig. 3 for small values of q, see McLachlan (1964). In Fig. 3, $\xi = 0$ refers to the Mathieu function solution depicted by the curves for d_0, c_1 and d_1 in Fig. 3. We may now present a relation for the characteristic Rayleigh number in terms of the newly defined parameter ξ, by substituting $\xi = \sigma/\sqrt{-a}$ in Eq. (15), and rearranging yields,

$$\tilde{R} = \eta + \frac{\left(\tilde{R}_o - \eta\right)}{\xi^2}. \tag{19}$$

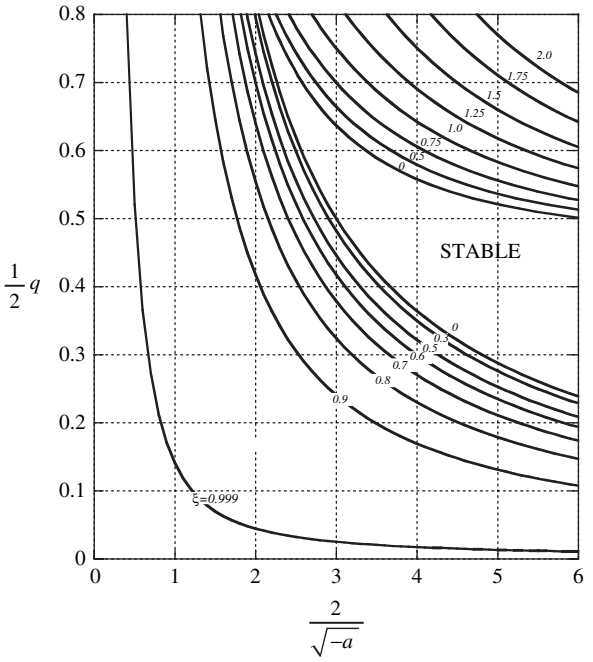

Fig. 3 Mathieu chart for the synchronous and sub-harmonic zones

Figure 3 together with Eqs. (15)–(19) may be used to evaluate the critical Rayleigh number and wavenumber ($\alpha_{cr} = \left(\alpha_x + \alpha_y\right)_{cr}$) in terms of the frequency Ω, the parameters (κFr) and γ.

We proceed by first evaluating the characteristic Rayleigh number versus the frequency for $\gamma \approx O(3)$ and $(\kappa Fr) = O\left(10^{-5}\right)$ and selected values of the wavenumber according to the following method: (a) select a value of ξ, (b) evaluate $\tilde{R}$ using Eq. (19), (c) compute the value for $1/2q$ using Eq. (16), (d) read $2/(-a)^{1/2}$ from Fig. 2, and (e) evaluate the frequency from Eq. (15). A series of curves of the critical Rayleigh number versus the frequency may be plotted for various wavenumbers and an example of such a curve is shown in Fig. 4 for $\alpha = 0.3$. Using Fig. 4 we evaluate the critical wavenumber and Rayleigh number corresponding to each wavenumber across the frequency range. The critical Rayleigh number and wavenumber as a function of the frequency is shown in Fig. 5, and shows that gravity modulation stabilizes the convection for the region of synchronous response but slowly destabilizes convection for the region of subharmonic response.

The stabilizing effect of vibration is small at low frequencies, but becomes significant for larger frequencies. Figure 5 also shows that close to $\Omega_t \cong 1225$, the Rayleigh number curve changes from a rapidly increasing trend to a slowly decreasing trend. The critical wavenumber is also seen to decrease with increasing frequencies, for both the regions of synchronous and subharmonic response. It is notable that upon transition from synchronous to subharmonic solutions there is a rapid increase in the critical wavenumber.

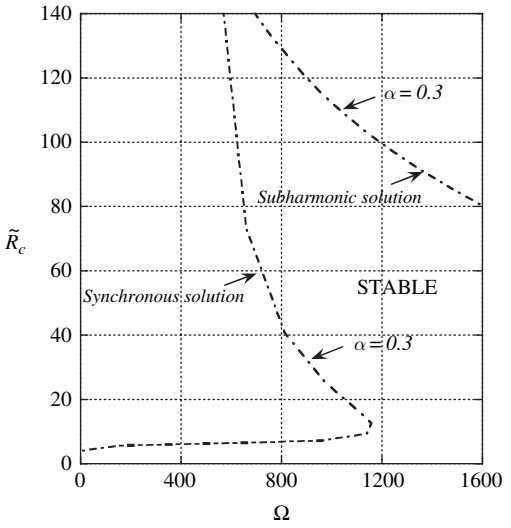

Fig. 4 Characteristic Rayleigh and wave number versus frequency

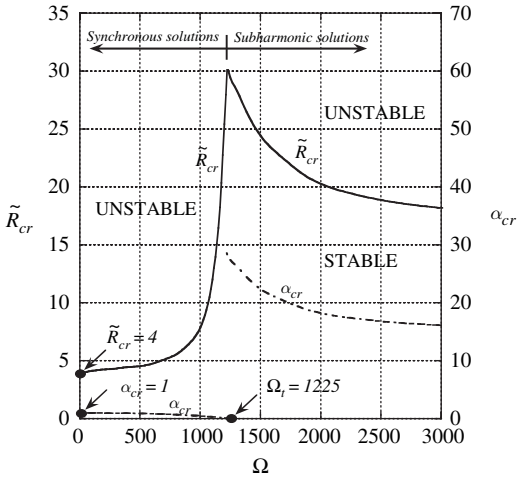

Fig. 5 Critical Rayleigh and wave number versus frequency

4 Weak Non-linear Anlaysis

Govender (2005b) provides a weak non-linear analysis in order to determine quantitatively the amplitude of convection. It is convenient to use the definition of the stream function in the form $u = \partial\psi/\partial z$; $w = -\partial\psi/\partial x$, and Govender (2005b) presents Eqs. (1–3) in terms of the stream function and temperature as follows for slow time scale variations,

$$\left(\frac{1}{Va}\frac{\partial}{\partial t} + 1\right)\nabla^2\psi + Ra\,(1 + \delta\sin(\Omega t))\,\frac{\partial T}{\partial x} = 0, \tag{20}$$

$$\frac{\partial T}{\partial t} + \frac{\partial \psi}{\partial z}\frac{\partial T}{\partial x} - \frac{\partial \psi}{\partial x}\frac{\partial T}{\partial z} = \nabla^2 T, \tag{21}$$

where the definition of the Laplacian operator is given as $\nabla^2 = \partial^2/\partial x^2 + \partial^2/\partial z^2$. The stream function, temperature and amplitude δ may be expanded in terms of a small parameter ε, defined as $\varepsilon = \left[Ra/Ra_{cr} - 1\right]^{1/2}$, as follows:

$$[\psi, T] = [\psi_B, T_B] + \varepsilon\,[\psi_1, T_1] + \varepsilon^2\,[\psi_2, T_2] + \varepsilon^3\,[\psi_3, T_3] + O(\varepsilon^4), \tag{22}$$

$$\delta = \delta_0 + \varepsilon\delta_1 + \varepsilon^2\delta_2 + . \tag{23}$$

The expansion (23) is consistent with the basic solution ($T_B = 1 - z$ and $\boldsymbol{V_B} = 0$) provided that δ_0 vanishes at the lowest order. In addition, unless δ_1 vanishes, the equations obtained at order ε and ε^2 present a singularity in the solution. These observations indicate that the effects of vibration should be introduced at the lowest possible order i.e., $\delta \approx \varepsilon^2\delta_1$, thereby enabling consistency. By using the definition for ε given above, the Rayleigh number may be expanded as $Ra = Ra_{cr}(1 + \varepsilon^2)$, where $Ra_{cr} = 4\pi^2$ is the critical Rayleigh number for a porous layer heated from below and subjected to gravity only. In addition we allow time variations only at the slow time scale $\tau = \varepsilon^2 t$ in order to prevent exponential growth and reaching finite values for the amplitude at the steady state. Substituting the expansion (22), as well as the slow time scale, just defined, into the system (20), (21) and equating like powers of ε produces a hierarchy of linear partial differential equations to each order.

$$\left(\frac{\varepsilon^2}{Va}\frac{\partial}{\partial \tau} + 1\right)\nabla^2\psi_m + Ra_{cr}\,(1 + \delta\sin(\Omega_0\tau))\,\frac{\partial T_m}{\partial x} = H_m, \tag{24}$$

$$\varepsilon^2\frac{\partial T_m}{\partial \tau} + \frac{\partial \psi_m}{\partial z}\frac{\partial T_m}{\partial x} - \frac{\partial \psi_m}{\partial x}\frac{\partial T_m}{\partial z} - \nabla^2 T_m = J_m, \tag{25}$$

where $\Omega_0 = \Omega/\varepsilon^2$ represents the large frequency scaling. To order, ε, $H_1 = J_1 = 0$ and the solution at order ε is given by

$$\psi_1 = A_1\sin(sx)\sin(\pi z),\ T_1 = B_1\cos(sx)\sin(\pi z). \tag{26}$$

The relationship between the amplitudes is obtained by substituting Eq. (26) in the system (24), (25) and is found to be

$$A_1 = -\pi\frac{(\alpha + 1)}{\sqrt{\alpha}}B_1. \tag{27}$$

The amplitude A_1 remains undetermined at this stage, and will be determined from a solvability condition of the order $O(\varepsilon^3)$ equations at order ε^3. The critical Rayleigh number and wavenumber to the leading order are found to be $R_{cr} = 4$ and $\alpha_{cr} = 1$. The equations to order ε^3 yields a solvability condition which constrains the amplitude

of the solution at order ε and enables its determination. The solvability condition is obtained by decoupling the governing equation at order ε^3 to yield a single non-homogenous partial differential equation for T_3 with corresponding forcing functions which include the $O(\varepsilon)$, and $O\left(\varepsilon^2\right)$ solutions (Govender 2005b) as follows,

$$\nabla^4 T_3 + Ra_{cr}\frac{\partial^2 T_3}{\partial x^2} = \frac{\partial H_3}{\partial x} + \nabla^2 J_3, \tag{28}$$

$$\text{where } H_3 = -\left(Ra_{cr}(t)\frac{\partial T_1}{\partial x} + \frac{1}{Va}\frac{\partial \nabla^2 \psi_1}{\partial \tau}\right), \tag{29}$$

$$\text{and, } J_3 = \frac{\partial T_1}{\partial \tau} + \frac{\partial \psi_1}{\partial z}\frac{\partial T_2}{\partial x} + \frac{\partial \psi_2}{\partial z}\frac{\partial T_1}{\partial x} - \frac{\partial \psi_1}{\partial x}\frac{\partial T_2}{\partial z} - \frac{\partial \psi_2}{\partial x}\frac{\partial T_1}{\partial z}. \tag{30}$$

Setting the coefficients of the secular terms in Eq. (28) to zero, yields the following Ginzburg–Landau equation for the leading order $O(\varepsilon)$ amplitude,

$$\frac{dB}{dt} = \mu_0\left(1 + \delta_1 \sin(\Omega t)\right)B - \chi B^3, \tag{31}$$

where $B = \varepsilon B_1$. The following notation is used in Eq. (31),

$$\mu_0 = \chi\xi, \quad \chi = \frac{\pi^4\gamma(\alpha+1)^2}{4(\alpha+1+\gamma)}, \xi = \frac{4R_{cr}\alpha}{\pi^2(\alpha+1)^3}\varepsilon^2. \tag{32}$$

Equation (31) is in the form of Bernoulli's differential equation and the solution to this type of equation is of the form,

$$B = \frac{e^{\mu_0\left(t-\delta_1/\Omega\cos(\Omega t)\right)}}{\left[2\chi\int e^{\mu_0\left(t-\delta_1/\Omega\cos(\Omega t)\right)}dt + C_1\right]}, \tag{33}$$

where $B(0) = b_0$ and C_1 is an integration constant. When $\delta_2 \to 0$, the analytical solution to Eq. (33) is given as ,

$$B = \frac{b_0\xi^{1/2}e^{\mu_0 t}}{\left[\xi - b_0^2\left(1 - e^{2\mu_0 t}\right)\right]^{1/2}}. \tag{34}$$

When $t \to \infty$, the classic steady state solution is found to be $B = 0$ or $B = b_0\left/|b_0|\xi^{1/2}\right.$. If $\delta_2 \neq 0$, we observe that the integral in Eq. (34) cannot be evaluated to obtain a closed form solution, and it is for this reason that we resort to a numerical solution of Eq. (34) by adopting the Runge–Kutte method. For a time step of 0.079 it was shown by Govender (2005b) that the analytical and numerical solutions were in perfect agreement for the case of no vibration ($\delta_2 = 0$). A time step of 0.079, will be retained for simulations corresponding to $\delta_2 \neq 0$. Figure 6 shows the amplitude B versus time for $\Omega = 0$, $\Omega = 100$ and $\Omega = 250$.

It can be clearly seen that increasing the frequency from $\Omega = 0$ to $\Omega = 100$ reduces the convection amplitude B. For $\Omega = 250$, it can be observed that for $t > \approx 7.5$, the conduction solution ($B = 0$) is stable. Figure 7 shows the amplitude B versus time for $\Omega = 0$, $\Omega = 300$ and $\Omega = 350$.

It can be seen for $\Omega = 300$ that beyond $t \approx 20$ the conduction solution is stable, whilst for $\Omega = 350$, the conduction solution sets in as the stable mode as early as $t \approx 2.5$. Figure 8 shows the amplitude B versus time for $\Omega = 0$, $\Omega = 370$ and $\Omega = 450$. Figure 8 shows that the conduction solution is stable beyond $t \approx 5$ for $\Omega = 370$ and $\Omega = 450$. Further simulations were performed for $\Omega = 500$, $\Omega = 750$, $\Omega = 1500$ and $\Omega = 3000$, and it was discovered that the basic solution

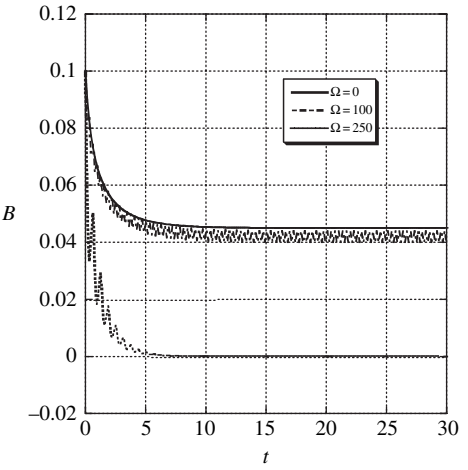

Fig. 6 Convection amplitude B versus time t for $\Omega = 0, 100, 250$

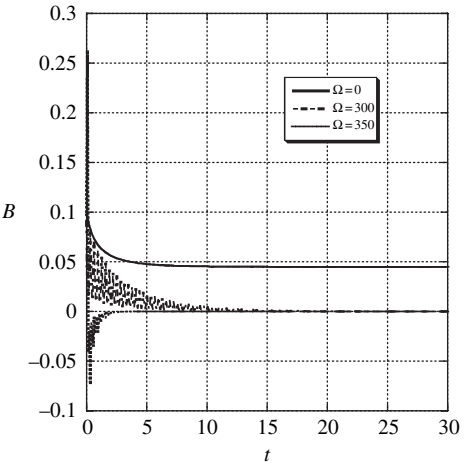

Fig. 7 Convection amplitude B versus time t for $\Omega = 0, 300, 350$

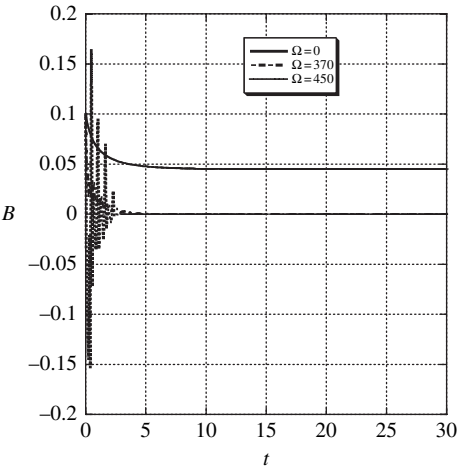

Fig. 8 Convection amplitude B versus time t for $\Omega = 0, 370, 450$

($B = 0$) is the only possible solution. The results depicted in Figs. 6–8 clearly indicate that increasing the vibration frequency stabilizes the convection by causing the convection amplitude to approach zero.

5 Pendulum Analogy

Govender (2006) demonstrated that the temperature in a porous layer heated from below may be likened to the motion of an inverted pendulum with an oscillating pivot point. Figure 9 below shows the inverted pendulum that will be considered. With reference to Fig. 9, one may write the net velocity as,

$$\vartheta^2 = (L\dot{\varphi})^2 + \dot{y}^2 - 2L\dot{\varphi}\dot{y}\sin\varphi. \tag{35}$$

Using the above definition we may write the equations for the kinetic, damping and potential energies respectively:

$$\text{Kinetic energy} : KE = \frac{1}{2}m\left((L\dot{\varphi})^2 + \dot{y}^2 - 2L\dot{\varphi}\dot{y}\sin\varphi\right), \tag{36}$$

$$\text{Damping energy} : DE = \frac{1}{2}c\left((L\dot{\varphi})^2 + \dot{y}^2 - 2L\dot{\varphi}\dot{y}\sin\varphi\right), \tag{37}$$

$$\text{Potential energy} : PE = -\left(mgL\left(1 - \cos\varphi\right) + mgy\right). \tag{38}$$

Substituting in Lagranges equation,

$$\frac{d}{dt}\left(\frac{\partial KE}{\partial\dot{\varphi}}\right) - \frac{\partial KE}{\partial\varphi} + \frac{\partial PE}{\partial\varphi} + \frac{\partial DE}{\partial\varphi} = 0, \tag{39}$$

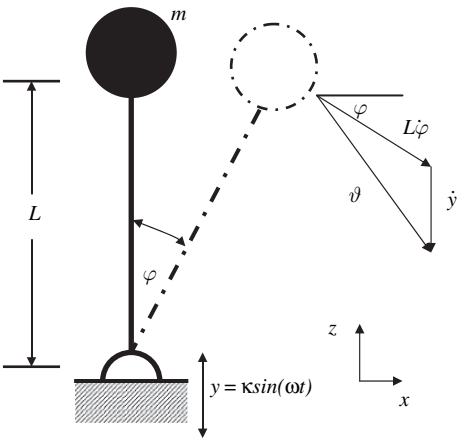

Fig. 9 The inverted pendulum with an oscillating pivot point

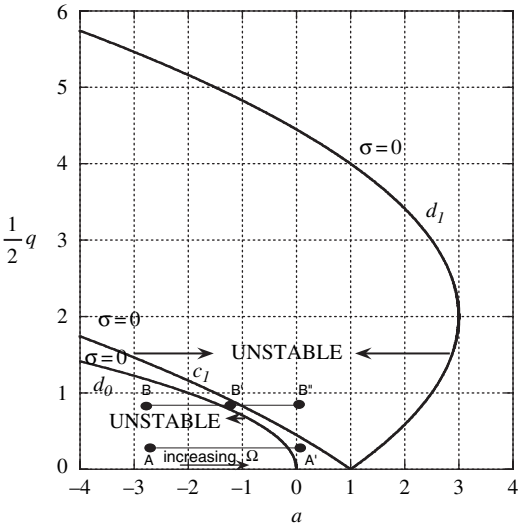

Fig. 10 Mathieu chart showing the stability of an inverted pendulum

and simplifying the result yields,

$$\frac{d^2\varphi}{dt^2} + 2\lambda\Omega_n \frac{d\varphi}{dt} - \left[\Omega_n^2 + 2\lambda\Omega_n\Omega\frac{\kappa}{L}\cos(\Omega t) - \Omega^2\frac{\kappa}{L}\sin(\Omega t)\right]\varphi = 0, \qquad (40)$$

which represents the equation for the motion of the inverted pendulum of length L with an oscillating pivot point, where the vertical motion of the pivot is given as $\kappa \sin(\Omega t)$. The above equation for the pendulum motion is valid for planar motion at small angles φ from the vertical. Also the un-damped natural frequency is given as $\Omega_n = \sqrt{g_*/L}$,

and the damping ratio is defined as $\xi_0 = c/2m\Omega_n$. Both Eqs. (13) and (40) may be cast into the canonical form of the Mathieu equation, as outlined by McLachlan (1964), and is given as

$$\frac{d^2X}{d\tau^2} + [a + 2q\cos(2\tau)]\,X = 0. \tag{41}$$

The solution to Eq. (41) follows the form $X = \theta(\tau)\,e^{\sigma\tau}$ where $\theta(\tau)$ is a periodic function with a period of π or 2π and σ is a characteristic exponent which is a complex number and is a function of a and q respectively. Incidentally the damping terms in Eqs. (13) and (40) has a stabilizing effect on the solutions and the exponential behavior is no longer of the form $e^{\sigma t}$. Following McLachlan (1964): for the pendulum, the argument of the exponential factor is $\left(1/2\cdot\sigma\cdot\Omega/\Omega_n - \xi_0\right)\Omega_0 t$, whilst for the gravity modulated porous layer heated from below, the argument of the exponential factor is $\left(1/2\cdot\sigma\Omega - p\right)t$. The stability criterion for the inverted pendulum is of the form $\xi_0 \geq 1/2\cdot\sigma\cdot\Omega/\Omega_n$ whilst for the gravity modulated porous layer $p \geq 1/2\cdot\sigma\Omega$. For the inverted pendulum with an oscillating pivot point:

$$\frac{2}{\sqrt{-a}} = \frac{1}{\left(\frac{\Omega_n}{\Omega}\right)\left(1+\xi_0^2\right)^{1/2}},\ \frac{1}{2}q = \frac{\delta}{L},\quad \sigma = 2\Omega_n/\Omega. \tag{42}$$

Equating the relations for $1/2q$ for both the oscillating porous layer and the pendulum, and noting that $\Delta T_C = \Delta\rho/\rho << 1$ yields, $1/2\ q = \kappa/L = F(\alpha)\,\gamma\tilde{R}\kappa Fr = F(\alpha)\cdot\kappa\cdot\phi_*/\pi^4\cdot\beta_*\Delta T_C$, which implies that the roll cell behaves like a very long pendulum with an effective dimensionless length of $L = 1/\left(F(\alpha)\cdot\kappa\cdot\phi_*/\pi^4\cdot\beta_*\Delta T_C\right)$. Rewriting Eq. (11) as, $a = -4\left(\Omega_n/\Omega\right)\left(1+\xi_0^2\right)^{1/2}$, one clearly observes that as Ω is increased, the absolute value for a gets smaller and smaller, up to a point when a is identically zero, at which point the frequency $\Omega \to \infty$. Choosing some exploratory value for δ/L (or $1/2q$) in Fig. 10, we may observe, by means of reference plane $A - A'$ which straddles the unstable and stable zones, the effects of frequency of oscillation Ω. Point A is incidentally in the unstable zone whilst point A' is in the stable zone. Increasing the frequency from some small/moderate value at point A in the unstable zone allows a shift towards point A' in the stable zone. This clearly shows that a, statically unstable, inverted pendulum may be stabilized by oscillating the pivot point in the vertical plane at some frequency Ω. However if some larger value of δ/L (or $1/2q$) is selected, say $\delta/L = 1$, we observe by means of reference plane $B - B' - B''$,which straddles the unstable; stable; and unstable zones respectively, that although increasing the frequency stabilizes the inverted pendulum up to point B', very large pivot frequencies tends to destabilize the inverted pendulum. In essence we have observed via the second case that for larger values of $1/2q$ a transition from synchronous to subharmonic solutions may occur as observed by Govender (2005a, b) for the gravity modulated porous layer heated from below.

The following analogy is thus evident: The temperature in a gravity modulated porous layer heated from below ($R > 0$, "top heavy"-unstable) is similar to the motion of a simple pendulum with an oscillating pivot point (inverted – unstable).

6 Conclusion

The author presents results dealing with the investigation of the effect of gravity modulation on the stability of convection in a differentially heated porous layer with particular focus on the transition from synchronous to subharmonic solutions. In addition a weak non linear analysis is also presented together with the development of an analogy between the oscillating porous layer and a pendulum. The linear stability analysis is performed with the aid of the Mathieu stability charts and it is discovered that gravity modulation stabilizes the convection for the region of synchronous solutions but slowly destabilizes convection for the region of subharmonic solutions. The transition point from synchronous to subharmonic solutions is found to be $\Omega_t \cong 1225$. It is proposed that the results of the current work may be extended for use in the investigation of the stability of solutal convection in solidifying mushy layers, with a view to preventing the onset of freckle formation in binary alloys, Pillay & Govender (2005)

Analytical results are also presented for the weak non-linear analysis which included an extended Darcy equation formulation. The numerical results revealed that increasing the frequency of vibration causes the amplitude of convection to approach zero, i.e. vibration stabilizes the convection.

Finally the author also showed that an analogy exits between the gravity modulated porous layer heated from below and the inverted pendulum with an oscillating pivot point. It is shown that the temperature in a gravity modulated porous layer subjected to vibration ($R > 0$-"top heavy" unstable) may be likened to the motion of a pendulum (inverted-unstable). In addition it was also pointed out that the roll cell behaves similar to a very long pendulum.

Acknowledgments The author would like to dedicate this exposition to his daughter Miss Sumithra Govender, who was born on 11 August 2006.

References

Alex, S.M. & Patil, R.: (2002a), Effect of variable gravity field on thermal instability in a porous medium with inclined temperature gradient and vertical throughflow, *J. Porous Media* **5**, 137–147.

Alex, S.M. and Patil, R.: (2002b), Effect of variable gravity field on convection in an anisotropic porous medium with internal heat source and inclined temperature gradient, *ASME J. Heat Transfer* **124**, 144–150.

Bardan, G and Mojtabi, A. (2000) On the Horton–Rogers–Lapwood convective instability with vertical vibration: onset of convection, *Phys. Fluids* **12**, 2723–2731.

Bardan, G, Razi, Y.P. & Mojtabi, A. (2004) Comments on the mean flow averaged model, *Phys. Fluids* **16**, 4535–4538.

Bejan, A.: (1995), *Convection Heat Transfer*, 2nd ed., Wiley, New York.
Chandrasekar, S.: (1961), *Hydrodynamic and Hydromagnetic Stability*, Oxford University Press, Oxford.
Christov, C.I. & Homsy, G.M.: (2001), Nonlinear dynamics of two-dimensional convection in a vertically stratified slot with and without gravity modulation, *J. Fluid Mech* **430**, 335–360.
Govender, S.: (2004), Stability of convection in a gravity modulated porous layer heated from below, *Trans. Porous Media* **57** (2), 113–123.
Govender S.: (2005a), Linear stability and convection in a gravity modulated porous layer heated from below: Transition from synchronous to subharmonic solutions, *Trans. Porous Media* **59** (2), 227–238.
Govender S.: (2005b), Weak non-linear analysis of convection in a gravity modulated porous layer, *Trans. Porous Media* **60** (1), 33–42.
Govender S.: (2005c), Destabilising a fluid saturated gravity modulated porous layer heated from above, *Trans. Porous Media* **59** (2), 215–225.
Govender S.: (2005d), Stability analysis of a porous layer heated from below and subjected to low frequency vibration: Frozen time analysis, *Trans. Porous Media* **59** (2), 239–247.
Govender S.: (2006), An analogy between a gravity modulated porous layer heated from below and the inverted pendulum with an oscillating pivot point, *Trans. Porous Media*, In Press.
Gresho, P.M. & Sani, R.L.: (1970), The effects of gravity modulation on the stability of a heated fluid layer, *J. Fluid Mech.* **40**, 783–806.
Hirata, K., Sasaki, T. & Tanigawa, H.: (2001), Vibrational effect on convection in a square cavity at zero gravity, *J. Fluid Mech.* **455**, 327–344.
McLachlan, N.W.: (1964), *Theory and Application of Mathieu Functions*, Dover, New York.
Pillay S.K. & Govender S.: (2005), Stability of convection in a gravity modulated mushy layer during the solidification of binary alloys, *Trans. Porous Media* **60** (2), 183–197.
Straughan, B.: (2000), A sharp nonlinear stability threshold in rotating porous convection, *Proc. R. Soc. Lond. A* **457**, 87–93.
Vadasz, P.: 1998, Coriolis effect on gravity-driven convection in a rotating porous layer heated from below, *J. Fluid Mech* **376**, 351–375.
Wadih, M. & Roux, B.: (1988), Natural convection in a long vertical cylinder under gravity modulation, *J. Fluid Mech* **193**, 391–415.

Thermal Vibrational Convection in a Porous Medium Saturated by a Pure or Binary Fluid

Yazdan Pedramrazi, Marie-Catherine Charrier-Mojtabi and Abdelkader Mojtabi

1 Introduction

1.1 What is Thermal Vibration?

The importance of mechanical vibration, as a source of pattern generating mechanism on the surface of a container filled with liquid, was recognized as early as the beginning of the 19th century by Faraday (1831). However, its importance as a mechanism controlling the convective motion has only been recognized during the 20th century.

Originally, mechanical vibration was used in mathematical modeling aimed at increasing the stability threshold of thermo-fluid system (Gershuni et al. 1970, Gresho and Sani 1970). The space exploration and especially the benefits expected from material production in space stations accelerated its development (Alexander 1994).

Formally, the thermo-vibrational convection studies concern the form of a mean flow in a confined cavity filled with a fluid presenting temperature non-homogeneities. Compared to the gravity-induced convection, this type of convection presents the advantage that it may exist under weightlessness condition.

Under micro-gravity conditions, the gravitational force is reduced drastically. However this situation may cause other forces, which under earth conditions are of minor importance, to be more significant.

Y. Pedramrazi
Reservoir Engineering Research Institute (RERI), Palo Alto, CA, USA

M.-C. Charrier-Mojtabi
Université Paul Sabatier, Toulouse cedex, France
e-mail: cmojtabi@cict.fr

A. Mojtabi
Université Paul Sabatier, Toulouse cedex, France

P. Vadász (ed.), *Emerging Topics in Heat and Mass Transfer in Porous Media*,

© Springer Science+Business Media B.V. 2008

1.2 A Brief History of Thermal Vibration in Porous Media: Suppression of Motion and Generation of Motion

The theory of thermo-vibrational convection in the fluid medium is summarized by Gershuni and Lyubimov (1998) which mainly covers Russian studies in this field. Contrary to the thermo-vibrational problems in fluid media, studies of the vibrational counterpart in porous media are quite recent.

Most of the studies concerning thermo-vibrational convection in porous media are theoretical and are focused on the linear stability analysis. The preferred method is the time-averaged method (see Simonenko and Zenkovskaya (1966) for details). In this method the time dependent acceleration does not appear explicitly in the governing equations. Furthermore, this method provides us with closed form solution by which it is possible to obtain the stability threshold. Given the fact that thermal vibration problems generally depend on many parameters, the existence of some closed form relation are quite beneficial in understanding these problems. For porous media saturated by pure fluid, Zenkovskaya (1992) studies the effect of vertical vibration (parallel to the temperature gradient) on the thermal stability of the conductive solution. The geometry considered is an infinite horizontal porous layer. Zenkovskaya and Rogovenko (1999) consider the same problem with variable direction of vibration. The results of their linear stability analysis show that only the vertical vibration always has a stabilizing effect. These authors find that, for other directions of vibration, depending on the vibrational parameter and the angle of vibration, stabilizing and destabilizing effects are possible.

Malashetty and Padmavathi (1997) consider the same geometry with finite frequency. They use the Brinkman–Forcheimer model in their momentum equation. It has been found that the low frequency g-jitter has a significant effect on the stability of the system and that the effect of gravity modulation can be used to stabilize the conductive solution.

In a confined porous cavity heated from below, Bardan and Mojtabi (2000) consider the effect of vertical vibration. The vibration is in the limiting range of high frequency and small amplitude, which justifies their use of the time averaged method. The transient Darcy model is used in their momentum equation. It is shown that vibration reduces the number of convective rolls. Their results show that, in order to apply the time-averaged formulation effectively, the transient Darcy model should be kept. Further, they find that vibration increases the stability threshold. They also perform a weakly nonlinear stability analysis which indicates that primary bifurcations are of a special type of symmetry-breaking pitch fork bifurcation.

Pedramrazi et al. (2002) and Charrier-Mojtabi et al. (2003) discuss the validity of the time-averaged formulation in the Horton–Rogers–Lapwood problem using two different approaches; the time-averaged and the direct method. They also explain, from a physical point of view, the necessary assumptions for performing the time-averaged method. They further study the stability of the conductive solution via the Mathieu equation. Charrier-Mojtabi et al. (2006) revisited the horizontal layer and confined cavity and found a relation between stability analysis of these two problems via Mathieu equation. Bardan et al. (2004) revisited the effect of

vertical vibration on confined cavity and they argued to obtain well-interpreted physical results, vibrational Rayleigh number should be redefined. Pedramrazi (2004) emphasized the restrictions of time-averaged method and showed the importance of sub-harmonic solutions. Govender studied the effect of vertical vibration on a horizontal porous layer (Pedramrazi 2004, Govender 2004, 2005a,b, 2006a,b, Pedramrazi et al. 2005). His results are in agreement with Palm et al. (1972).

2 The Effect of Vibration in Horizontal Porous Layer Saturated by a Pure Fluid

2.1 Infinite Horizontal Porous Layer

2.1.1 Mathematical Formulation

The problem of the onset of thermal instability in an infinite horizontal porous layer heated from below is well suited to illustrate mathematical and physical nature of thermo-vibrational problem.

The geometry of the problem consists of two horizontal parallel plates having lateral infinite extension (Fig. 1). The two rigid and impermeable plates are kept at two constant but different temperatures T_1 and T_2. The two plates are placed in a distant H apart. The porosity and permeability of the porous mesh forming the layer are ε and K respectively.

The porous medium is considered homogenous and isotropic. The porous layer and its boundaries are subjected to a harmonic vibration. As the objective is to study the onset of convection, the Darcy model can be used in the momentum equation. The fluid saturating porous media is assumed to be Newtonian and to satisfy the Oberbeck–Boussinesq approximation. The thermophysical properties are considered constant except for the density of fluid in the buoyancy term which depends linearly on the local temperature:

$$\rho(T) = \rho_0 \left[1 - \beta_T (T - T_2)\right]. \tag{1}$$

where T_2 is taken as the reference state, and the coefficient of volumetric expansion β_T is assumed constant ($\beta_T > 0$). In a coordinate system linked to the layer, the gravitational field is replaced by the sum of the gravitational and vibrational accelerations

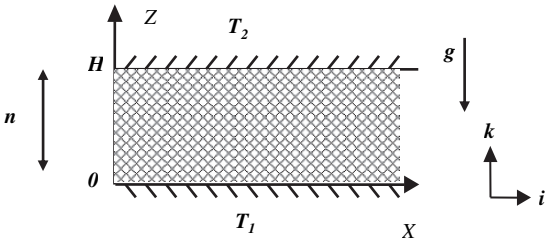

Fig. 1 Problem definition sketch

$\boldsymbol{g} \rightarrow -g\boldsymbol{k} + b\omega^2 \sin(\omega t)\boldsymbol{n}$. In this transformation $\boldsymbol{n}$ is the unit vector along the axis of vibration, b is the displacement amplitude and ω is the angular frequency of vibration. After making standard assumptions (local thermal equilibrium, negligible viscous heating dissipations. . .), the governing equations may be written as:

$$\begin{aligned} &\nabla \cdot \mathbf{V} = 0, \\ &\frac{\rho_0}{\varepsilon}\frac{\partial \mathbf{V}}{\partial t} = -\nabla P + \rho_0 \left[\beta_T (T - T_2)\right] \left(-g\,\mathbf{k} + b\omega^2 \sin \omega t\, \mathbf{n}\right) - \frac{\mu_f}{K}\mathbf{V}, \\ &(\rho c)_* \frac{\partial T}{\partial t} + (\rho c)_f \mathbf{V} \cdot \nabla T = \lambda_* \nabla^2 T. \end{aligned} \tag{2}$$

The boundary conditions corresponding to this system are written as:

$$\begin{aligned} &\mathrm{V}_z(x, z = 0) = 0, \quad T(x, z = 0) = T_1, \\ &\mathrm{V}_z(x, z = H) = 0, \quad T(x, z = H) = T_2. \end{aligned} \tag{3}$$

In (2), μ_f is the dynamic viscosity of fluid, $(\rho c)_*$ represents the effective volumic heat capacity, $(\rho c)_f$ is the volumic heat capacity of fluid and λ_* is the effective thermal conductivity of saturated porous media.

2.1.2 Time-Averaged Formulation

In order to study the mean behavior of mathematical system (1–2), the time-averaged method is used. This method is adopted under the condition of high-frequency and small-amplitude of vibration. Under these conditions, it is shown that two different time scales exist, which make it possible to subdivide the fields into two different parts. The first part varies slowly with time (i.e. the characteristic time is large with respect to vibration period) while the second part varies rapidly with time and is periodic with period $\tau = 2\pi/\omega$. Simonenko and Zenkovskaya (1966) used this procedure in thermo-vibrational problem in a horizontal fluid layer under the action of vertical vibration. So we may write:

$$\begin{aligned} \mathbf{V}(M, t) &= \bar{\mathbf{V}}(M, t) + \mathbf{V}'(M, \omega t), \\ T(M, t) &= \bar{T}(M, t) + T'(M, \omega t), \\ P(M, t) &= \bar{P}(M, t) + P'(M, \omega t). \end{aligned} \tag{4}$$

In the above transformations $(\bar{\mathbf{V}}, \bar{T}, \bar{P})$ represent the averaged fields (for a given function f(M, t), the average is defined as $\bar{f}(M, t) = \frac{1}{\tau}\int_{t-\tau/2}^{t+\tau/2} f(M, s)\, \mathrm{d}s$).

On replacing (4) in (2), we obtain two coupled systems of equations, one for the mean flow and the other for oscillatory one.

By making some assumption, we may express the oscillating fields in terms of the averaged ones. This procedure is detailed elsewhere (Mc Lachlan 1964).

Governing Time-Averaged Equations

By introducing the reference parameter, $T_1 - T_2$ for temperature, H for height, $\sigma H^2/a_*$ for time, ($a_* = \lambda_*/(\rho c)_f$ is the effective thermal diffusivity), a_*/H for velocity, $\beta_T \Delta T$ for $\mathbf{W}$ and $\mu a_*/K$ for pressure, we obtain dimensionless governing equation :

$$\begin{aligned}
&\nabla \cdot \bar{\mathbf{V}}^* = 0,\\
&B\frac{\partial \bar{\mathbf{V}}^*}{\partial t} = -\nabla \bar{P}^* + Ra_T \bar{T}^* \mathbf{k} + Ra_v (\mathbf{W} \cdot \nabla)\bar{T}^* \mathbf{n} - \bar{\mathbf{V}}^*,\\
&\frac{\partial \bar{T}^*}{\partial t} + \bar{\mathbf{V}}^* \cdot \nabla \bar{T}^* = \nabla^2 \bar{T}^*,\\
&\nabla \cdot \mathbf{W}^* = 0,\\
&\nabla \times \mathbf{W}^* = \nabla \bar{T}^* \times \mathbf{n}
\end{aligned} \tag{5}$$

The corresponding boundary conditions for the mathematical problem can be written as:

$$\begin{aligned}
&\forall x^*, \quad \text{for } z^* = 0, \quad \bar{\mathrm{V}}_z^* = 0, \quad \bar{T}^* = 1, \quad \mathrm{W}_z^* = 0,\\
&\forall x^*, \quad \text{for } z^* = 1, \quad \bar{\mathrm{V}}_z^* = 0, \quad \bar{T}^* = 0, \quad \mathrm{W}_z^* = 0.
\end{aligned} \tag{6}$$

where:

$$Ra_T = \frac{\mathrm{K} g \beta_T \Delta T H}{\nu a_*}, \quad Ra_v = \frac{(\delta^* Fr_F Ra_T \omega^*)^2}{2B},$$
$$\left(\delta^* = \frac{b}{H},\ Fr_F = \frac{a_*^2}{gH^3\sigma^2},\ \omega^* = \omega\frac{\sigma H^2}{a_*},\ B = \frac{a_* \mathrm{K}}{\varepsilon \nu \sigma H^2} = \frac{\tau_{hyd}}{\tau_{ther}}\right)$$

In the above relations Ra_T is the thermal Rayleigh number, Ra_v is the vibrational Rayleigh number ω^* is the dimensionless pulsation, B is the transient coefficient, Fr_F is the filtration Froude number and δ^* is the dimensionless amplitude. It should be added that these parameters (Fr, δ^*) are originally used in a horizontal fluid layer under vertical vibration in the pioneering work of Gresho and Sani (1970).

It should be noted that $\mathbf{W}$ is solenoidal field resulting from the Helmholtz decomposition (($\bar{T} - T_2)\mathbf{n} = \mathbf{W} + \nabla\varphi$., $\mathbf{W}$ and $\nabla\phi$ are soloneidal and irrotational parts).

Linear Stability Analysis of the Time-Averaged System of Equations (Case of Vertical Vibration)

In the presence of vertical vibration ($\mathbf{n} = \mathbf{k}$), mechanical equilibrium is possible. In order to find the necessary condition for thermal stability of the problem, we set the velocity field equal to zero in (4). Then the steady-state distribution of fields are sought.

The equilibrium state corresponds to:

$$\bar{T}_0^* = 1 - z^*, \qquad \mathbf{W}_\mathbf{0}^* = 0. \tag{7}$$

For stability analysis, the fields are perturbed around the equilibrium state (for simplicity bars are omitted):

$$\mathbf{V}^* = 0 + \mathbf{v}',\ T^* = T_0^* + T',\ P^* = P_0^* + p',\ \mathbf{W}^* = \mathbf{W}_\mathbf{0}^* + \mathbf{w}'.$$

Replacing the above equations in system (4) and (5), and after eliminating the nonlinear terms we obtain:

$$\begin{aligned}
\nabla \cdot \mathbf{v}' &= 0,\\
B\frac{\partial \mathbf{v}'}{\partial t^*} &= -\nabla p' + Ra_T T'\mathbf{k} + Ra_v(\mathbf{w}' \cdot \nabla T_0^* + \mathbf{W}_\mathbf{0}^* \cdot \nabla T')\mathbf{k} - \mathbf{v}',\\
\frac{\partial T'}{\partial t^*} + \mathbf{v}' \cdot \nabla T_0^* &= \nabla^2 T',\\
\nabla \cdot \mathbf{w}' &= 0,\\
\nabla \times \mathbf{w}' &= \nabla T' \times \mathbf{k}.
\end{aligned} \tag{8}$$

with corresponding boundary conditions:

$$\begin{aligned}
&\mathrm{v}'_z(x^*, z^* = 0) = 0,\ T'(x^*, z^* = 0) = 0,\ \mathrm{w}'_z(x^*, z^* = 0) = 0,\\
&\mathrm{v}'_z(x^*, z^* = 1) = 0,\ T'(x^*, z^* = 1) = 0,\ \mathrm{w}'_z(x^*, z^* = 1) = 0.
\end{aligned} \tag{9}$$

Introducing the stream functions Ψ, F, one can write:

$$\mathrm{v}'_x = \frac{\partial \psi}{\partial z^*},\ \mathrm{v}'_z = -\frac{\partial \psi}{\partial x^*},\ \mathrm{w}'_x = \frac{\partial F}{\partial z^*},\ \mathrm{w}'_z = -\frac{\partial F}{\partial x^*}. \tag{10}$$

On considering the 2D disturbances which are developed in normal modes:

$$(\psi,\ T',\ F) = (\phi(z^*),\ \theta(z^*),\ f(z^*))\exp(-\lambda t^* + ikx^*) \tag{11}$$

in which k is the wave number in the horizontal direction 0x. Replacing (10) in (8) and (9), and eliminating pressure leads one to:

$$\begin{aligned}
&(-\lambda B + 1)\left(\frac{d^2\phi(z^*)}{dz^{*2}} - k^2\phi(z^*)\right) = -ikRa_T\theta(z^*) + k^2Ra_v f(z^*),\\
&-\lambda\theta(z^*) + ik\phi(z^*) = \frac{d^2\theta(z^*)}{dz^{*2}} - k^2\theta(z^*),\\
&-k^2 f(z^*) + \frac{d^2 f(z^*)}{dz^{*2}} = -ik\theta(z^*).
\end{aligned} \tag{12}$$

System (12) is a spectral amplitude problem where λ is the eigenvalue of the system, which depends on:

$$\lambda = \lambda(Ra_T, Ra_v, k, B)$$

Generally, λ is a complex number ($\lambda = \lambda_r + i\lambda_i$).

The mathematical system (21), admits exact solutions of the form:

$$(\phi(z^*),\ \theta(z^*),\ f(z^*)) = (\phi, \theta, f)\sin n\pi\, z^* \tag{13}$$

By substituting (13) in (12), the necessary condition for obtaining marginal stability ($\lambda = 0$):

$$Ra_T = \frac{(\pi^2 + k^2)^2}{k^2} + Ra_v \frac{k^2}{\pi^2 + k^2}. \quad (n = 1) \tag{14}$$

One can understand from the above equation that, under micro-gravity ($Ra_T = 0$), the system is always stable.

Under the condition of vibration in presence of gravity, we can replace Ra_v with $(\delta^* Fr_F \omega^* Ra_T)^2/2B$. From (13), we get:

$$Ra_T = \frac{B}{\delta^{*2} Fr_F^2 \omega^{*2}} \frac{k^2}{k^2 + \pi^2} \left[1 - \sqrt{1 - 2\frac{\delta^{*2} Fr_F^2 \omega^{*2}}{B}(k^2 + \pi^2)} \right]. \tag{15}$$

Another interesting feature of this equation is that it gives additional information:

$$\omega^*_{\max} = \frac{\sqrt{B/2}}{\delta^* Fr_F \pi}. \qquad (k \to 0) \tag{16}$$

Relation (16) gives a possible maximum frequency for achieving absolute stabilization for high-frequency and small-amplitude vibration.

Weakly Non-linear Stability Analysis of the Time-Averaged System of Equations

In order to determine the characteristics of the solutions near the bifurcation point, the normal form of amplitude equation is sought.

The weakly nonlinear stability analysis of the time-averaged equations is expressed in terms of (ψ, θ, F) as follows:

$$\frac{\partial}{\partial t}\begin{bmatrix} B\nabla^2\psi \\ \theta \\ 0 \end{bmatrix} = \underbrace{\begin{bmatrix} -\nabla^2 & -Ra_T \frac{\partial}{\partial x^*} & -Ra_v \frac{\partial^2}{\partial x^{*2}} \\ -\frac{\partial}{\partial x^*} & \nabla^2 & 0 \\ 0 & \frac{\partial}{\partial x^*} & \nabla^2 \end{bmatrix}}_{L} \begin{bmatrix} \psi \\ \theta \\ F \end{bmatrix} + \begin{bmatrix} N_1 \\ N_2 \\ 0 \end{bmatrix} \tag{17}$$

in which $\mathbf{L}$ represents a linear operator whereas N_1 and N_2 are nonlinear operators:

$$\begin{aligned} N_1 &= -Ra_v \left[\frac{\partial^2\theta}{\partial x^{*2}} \frac{\partial F}{\partial z^*} + \frac{\partial\theta}{\partial x^*} \frac{\partial^2 F}{\partial x^* \partial z^*} - \frac{\partial^2 F}{\partial x^{*2}} \frac{\partial\theta}{\partial z^*} - \frac{\partial F}{\partial x^*} \frac{\partial^2\theta}{\partial x^* \partial z^*} \right], \\ N_2 &= \frac{\partial\psi}{\partial x^*} \frac{\partial\theta}{\partial z^*} - \frac{\partial\psi}{\partial z^*} \frac{\partial\theta}{\partial x^*}. \end{aligned} \tag{18}$$

In order to study the onset of thermo-vibrational convection near the critical thermal Rayleigh number, the linear operator and the solution are expanded into power series of the positive small parameter η, defined by:

$$Ra_T = Ra_{Tc} + \eta\, Ra_{T1} + \eta^2\, Ra_{T2} + \cdots \tag{19}$$

Thus:

$$\begin{aligned} &[\psi, \theta, F] = \eta\,[\psi_1, \theta_1, F_1] + \eta^2\,[\,\psi_2, \theta_2, F_2] + \cdots \\ &\mathbf{L} = \mathbf{L}_0 + \eta\mathbf{L}_1 + \eta^2\mathbf{L}_2 + \cdots \end{aligned} \tag{20}$$

($\mathbf{L}_0$ is the operator which governs the linear stability). It should be noted that, in the operators, Ra_v is also expanded:

$$Ra_v = \frac{(\delta^* Fr_F \omega^*)^2}{2B}\left[Ra_{Tc}^2 + 2\eta Ra_{T1} Ra_{Tc} + \eta^2(2Ra_{Tc}Ra_{T2} + Ra_{T1}^2) + \cdots\right] \tag{21}$$

By replacing (19–21) in (17), and after introducing time transformation:

$$\frac{\partial}{\partial t^*} = \eta\frac{\partial}{\partial t_1^*} + \eta^2\frac{\partial}{\partial t_2^*} + \cdots$$

By equating the same power of η we obtain a sequential system of equations.

At each order of η, a linear eigenvalue problem is found. At the first order (η) the perturbation is written in the following form:

$$\begin{bmatrix} \psi_1 \\ \theta_1 \\ F_1 \end{bmatrix} = A(t_1^*, t_2^*, ...) \begin{bmatrix} (\pi^2 + k^2)/k^2 \ \sin \pi z^* \sin kx^* \\ -(\pi^2 + k^2)/k \sin \pi z^* \cos kx^* \\ \sin \pi z^* \sin kx^* \end{bmatrix}. \tag{22}$$

The amplitude A depends on slow time evolutions $(t_1^*, t_2^*, \ldots)$.

At the second order η^2, the existence of a convective solution requires that the solvability lemma be satisfied, in other words there must be a non-zero solution for the adjoint of $\mathbf{L}_0$ associated with identical boundary conditions. From the adjoint operator, we obtain:

$$Ra_{Tc}^* = Ra_{Tc}.$$

Also, we find $Ra_{T1} = 0$ and amplitude A does not depend on time scale ${t_1}^*$.

At the third order η^3 by invoking the solvability condition and the Fredholm alternative we obtain the amplitude equation:

$$\frac{dA}{dt_2^*} = \alpha(A - \beta A^3).$$

in which α and β are defined as:

$$\alpha = \frac{k^2}{(k^2+\pi^2)^2}\left[(k^2+\pi^2) - \frac{(\delta^* Fr_F \omega^*)^2}{B} k^2 Ra_{Tc}\right] Ra_{T2},$$
$$\beta = \frac{(\pi^2+k^2)^2\left[1 - \dfrac{k^4(\delta^* Fr_F\omega^*)^2}{B(\pi^2+k^2)^3} Ra_{Tc}^2\right]}{8Ra_{T2}\left[(\pi^2+k^2) - \dfrac{(\delta^* Fr_F\omega^*)^2}{B} k^2 Ra_{Tc}\right]}. \tag{23}$$

In α and β, Ra_{T2} is defined as $Ra_{T2} = (Ra_T - Ra_{Tc})/\eta^2$ which is the control parameter.

When there is no vibrational effect, we find that the amplitude of thermo-convective flow near the bifurcation point is proportional to:

$$A \approx \sqrt{Ra_T - Ra_{Tc}}$$

which is in agreement with Palm et al. (1972). Under the effect of vibration α and β are both positive, which results in a supercritical pitchfork bifurcation.

2.1.3 Linear Stability Analysis from Direct Formulation

In this section, we study the stability of the solution corresponding to governing equations where the time dependent buoyancy term appears explicitly. As was stated before, when the direction of vibration is parallel to gravitational acceleration, mechanical stability is possible. This equilibrium is characterized by a linear temperature and parabolic pressure distribution. In order to study linear stability, the field variables are infinitesimally perturbed around the motionless equilibrium state. The perturbed system of equation becomes:

$$\begin{aligned}
&\nabla\cdot\tilde{\mathbf{v}} = 0,\\
&\frac{\rho_0}{\varepsilon}\frac{\partial\tilde{\mathbf{v}}}{\partial t} = -\nabla\tilde{p} + \rho_0\beta_T\tilde{\theta}(g + b\omega^2\sin\omega t)\,\mathbf{k} - \tfrac{\mu}{\mathrm{K}}\tilde{\mathbf{v}},\\
&\sigma\frac{\partial\tilde{\theta}}{\partial t} + \tilde{\mathbf{v}}\cdot\nabla T_0 = a_*\nabla^2\tilde{\theta}.
\end{aligned} \tag{24}$$

By eliminating the pressure in the momentum equation and by substituting the normal modes as:

$$\tilde{\mathrm{v}}_z = X(t)\,e^{ik\frac{x}{H}}\sin\frac{z}{H}\pi,\ \tilde{\theta} = h(t)e^{ik\frac{x}{H}}\sin\frac{z}{H}\pi. \tag{25}$$

in the resulting equations, we get:

$$\begin{aligned}
&\frac{d^2h}{dt^2} + \left[\frac{a_*}{\sigma H^2}(k^2+\pi^2) + \frac{\varepsilon\nu}{K}\right]\frac{dh}{dt} +\\
&\left[\frac{\varepsilon\nu a_*}{KH^2\sigma}(k^2+\pi^2) - \frac{\varepsilon\beta_T\Delta T}{\sigma H}\frac{k^2}{k^2+\pi^2}(g + b\omega^2\sin\omega t)\right]h = 0.
\end{aligned} \tag{26}$$

The above equation is similar to a mechanical pendulum with oscillating support:

$$\ddot{Y} + 2\xi\omega_n \dot{Y} \pm (\omega_n{}^2 - \omega^2 \frac{\delta}{\ell} \sin \omega t)\, Y = 0. \tag{27}$$

in which ω_n represents the natural frequency, ξ damping ratio, ω vibrational frequency, ℓ pendulum length and finally δ the amplitude of vibration. The plus sign in (27) corresponds to a normal hanging pendulum while the negative sign corresponds to an inverted pendulum. Equalizing the vibrational effect in the two systems gives:

$$\ell_{eff} \approx \frac{H}{\frac{\varepsilon}{\sigma}\beta_T \Delta T}. \tag{28}$$

which is the effective length of the equivalent system. In addition it is clear that this effective length is quite long ($\beta_T \Delta T << 1$).

Equation (26) can be written in dimensionless form:

$$B\frac{d^2h^*}{dt^{*2}} + \left[B(k^2+\pi^2)+1\right]\frac{dh^*}{dt^*} + \left[(k^2+\pi^2) - Ra_T \frac{k^2}{k^2+\pi^2}(1 + R\sin\omega^* t^*)\right] h^* = 0. \tag{29}$$

where B, Ra_T, ω^* are defined as in the previous section. Also we can define R as $\delta^* Fr_F \omega^{*2}$. For the above equation two different cases are distinguished:

(i) $B\omega^* << 1$

In this case, the governing equation is written as:

$$\frac{dh^*}{dt^*} + \left[(\pi^2+k^2) - Ra_T \frac{k^2}{k^2+\pi^2}(\,1 + \delta^* Fr_F \omega^{*2} \sin\omega^* t^*)\right] h^* = 0. \tag{30}$$

The solution of this first order differential equation with periodic coefficient is:

$$h^* = h_0^* \exp - \left[(\pi^2+k^2) - \frac{k^2}{k^2+\pi^2} Ra_T\right] t^* \cdot \exp\left(2\delta^* Fr_F \omega^* \frac{k^2}{k^2+\pi^2} Ra_T \sin^2 \omega^* t^*\right),$$
$$h^*(0) = h_0^*. \tag{31}$$

When there is no vibration ($\delta^* Fr_F \omega^* = 0$), from (30) the classical result of $Ra_{Tc} = 4\pi^2$ for marginal stability may be deduced. In the presence of vibration, if the layer is heated from above the solution is always stable. This is true because, in this situation, the arguments in exponential functions (31) are always positive. When the layer is heated from below, the solution is composed of two parts, see (30) the second part of which can be considered as a positive bounded periodic function. Therefore, for marginal stability, the first part is important and gives $\mathrm{Ra_T} = 4\pi^2$. In other words, vibration has no effect on stability threshold. Physically from the mechanical analogy, this case corresponds to a pendulum in which the viscous damping is much larger than angular acceleration. Strong damping is able to destroy the oscillatory movements.

(ii) $B\omega^* >> 1$

Using transformation $h^*(t^*) = e^{-mt^*}M(t^*)$ equation (29) is cast into Mathieu's equation (m being $(\pi^2 + k^2 + 1/B)/2$):

$$\frac{d^2M(\tau)}{d\tau^2} + (A - 2Q\cos 2\tau)M(\tau) = 0, \quad \left(\omega^* t^* = 2\tau - \frac{\pi}{2}\right) \tag{32}$$

in which A and Q are:

$$A = \frac{\pi^2 + k^2}{B} - m^2 - \frac{k^2}{B(\pi^2 + k^2)}Ra_T, \qquad Q = \frac{2k^2}{B(\pi^2 + k^2)}\delta^* Fr_F Ra_T. \tag{33}$$

Detailed analysis of the stable regions for this equation can be found elsewhere (Mc Lachlan 1964, Cunningham 1958, Jordan and Smith 1987). They divide the domain into alternate stable and unstable regions. In order to solve (32), the Floquet theory is used, which considers the solution as:

$$M = R(\tau)e^{\mu\tau}.$$

in which $R(\tau)$ is a periodic function having period π or 2π, the parameter μ is the Floquet exponent and the marginal stability condition is $m = \mu\omega^*/2$. The details of this method can be found elsewhere Aniss et al. (2000).

To obtain the critical thermal Rayleigh and wave numbers for marginal stability, all the working parameters ($B, \omega^*, \delta^*, Fr_F$) are fixed except Ra_T and k. Then we search for the minimum Ra_T vs k. It can be concluded that, for given dimensionless amplitude δ^* and dimensionless frequency of vibration ω^*, there are two modes of convection onset, namely harmonic (with dimensionless frequency ω^*) and sub-harmonic (with dimensionless frequency: $\omega^*/2$) (Fig. 2)

For heating from below ($Ra_T > 0$, which corresponds to $A < 0$), two different behaviors for harmonic and sub-harmonic modes are distinguished: for harmonic mode with increasing ω^*, thermal Rayleigh number Ra_T increases. This means that vibration has a stabilizing effect which depends significantly on dimensionless amplitude δ^*. On decreasing δ^*, the stable region with harmonic response widens. If the frequency is increased, the critical wave number for this mode decreases. For the sub-harmonic mode we have a different scenario, the vibration has a destabilizing effect, in other words Ra_{Tc} decreases and ultimately reaches a limiting value. The critical wave number in this mode increases with increasing dimensionless frequency. It should be noted that the intersection of harmonic and sub-harmonic modes corresponds to different values of wave number. For other heating condition, one may consult Cunningham (1958).

2.1.4 Comparison of the Two Methods

The objective of this section is to compare the two approaches of stability analysis in the thermo-vibrational problem, namely the time-averaged and the so-called direct methods. The time-averaged method under high frequency and small amplitude

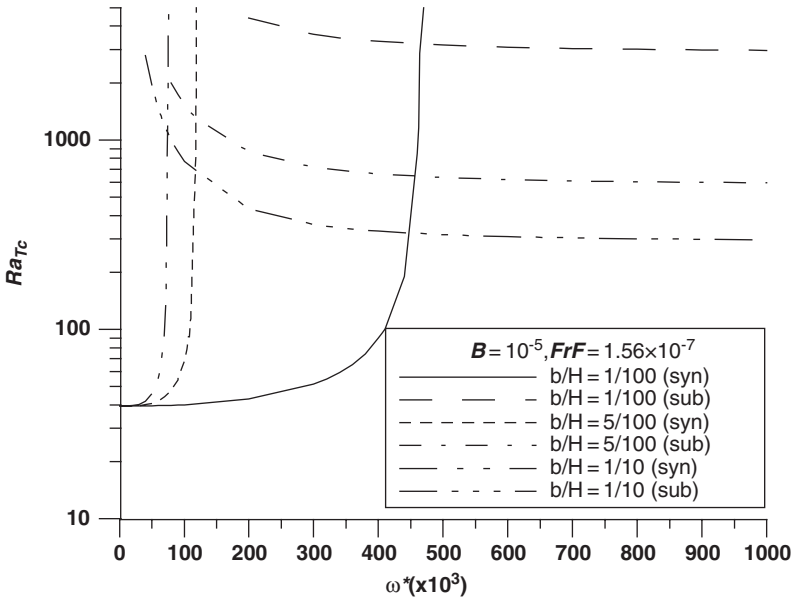

Fig. 2 The effect of vibrational frequency on the critical Rayleigh Number Ra_{Tc}, for different values of b/H: harmonic response (syn) and sub-harmonic response (sub)

vibration is considered in the previous section. As has been stated before, this limiting case permits us to subdivide the fields (temperature, velocity and pressure) into two parts. The question is under which condition we can find this characteristic of solution (subdivision of fields) if we adopt the direct method. Let us examine what will happen if we apply the assumptions needed for finding the criteria of high frequency and small amplitude to the coefficients of Mathieu's equation. We write Mathieu's equation and its coefficients A and Q as:

$$\frac{d^2M(\tau)}{d\tau^2} + (A - 2Q\cos 2\tau)M(\tau) = 0, \tag{34}$$

$$A = -\left[\frac{a_*}{\sigma H^2\omega}\left(k^2+\pi^2\right) + \frac{\varepsilon\nu}{K\omega}\right]^2 + 4\left(\frac{\varepsilon\nu}{K\omega}\right)\left(\frac{a_*}{\omega\sigma H^2}\right)\left(k^2+\pi^2\right) - 4\left(\frac{\varepsilon\beta_T\Delta T g}{\sigma H\omega^2}\right)\frac{k^2}{k^2+\pi^2},$$

$$Q = 2\left(\frac{\varepsilon}{\sigma}\beta_T\Delta T\frac{b}{H}\right)\frac{k^2}{k^2+\pi^2}.$$

Let us examine A and Q closely:

The first and second terms in A involve the ratios of vibrational time scale to conductive and viscous time scales. The third term in A involves the ratio of vibrational time scale to pseudo buoyancy time scale.

Q involves a kind of amplitude ratio. Based on hypothesis of high-frequency and small amplitude all these terms are very small (vibration time scale is the smallest time scale and amplitude of temperature oscillation should be also small) so A and Q tend to zero. A regular perturbation method in which Q is considered as a small parameter may be used:

$$\begin{aligned} M(\tau) &= M_0(\tau) + QM_1(\tau) + Q^2M_2(\tau) + \cdots \\ A &= A_0 + QA_1 + Q^2A_2 + \cdots \end{aligned} \tag{35}$$

Replacing the above expansions in Mathieu's equation and invoking solvability condition results:

$$A = -\frac{Q^2}{2}, \tag{36}$$

$$M = a_0 - \frac{a_0}{2}\cos 2\tau. \tag{37}$$

(a_0 is an arbitrary constant)

On replacing A and Q in the (36) and using the fact that $\mu = [a_*(k^2 + \pi^2)/\sigma H^2\omega + \varepsilon\nu/K\omega)] = 0$, we find:

$$Ra_{T_c} = \frac{(\pi^2 + k^2)^2}{k^2} + Ra_v\frac{k^2}{k^2 + \pi^2}. \quad (Ra_v = \frac{(\delta^* Fr_F\omega^* Ra_T)^2}{2B}) \tag{38}$$

Which means that imposing the assumptions needed for the averaging method on Mathieu's equation gives identical results to the time-averaged formulation. The most interesting thing about this fact is that the time-averaged method gives only harmonic (with dimensionless frequency ω^*) mode and is not able to give subharmonic mode.

2.1.5 Effect of the Direction of Vibration

Zenkovskaya and Rogovenko (1999) study the effect of the direction of vibration on the onset of convection. They use the time-averaged formulation and discuss several physical situations. When the direction of vibration is not parallel to the temperature gradient, there exists a quasi-equilibrium; i.e. the mean velocity is zero but the oscillating velocity is not zero. The equilibrium solution is characterized by:

$$\mathbf{V_0} = \mathbf{0}, T_0 = 1 - z \quad \text{and} \quad W_{0x} = (\frac{1}{2} - z)\cos(\alpha) \tag{39}$$

where α is the angle between the vibration direction and the horizontal direction.

We study different physical situations:

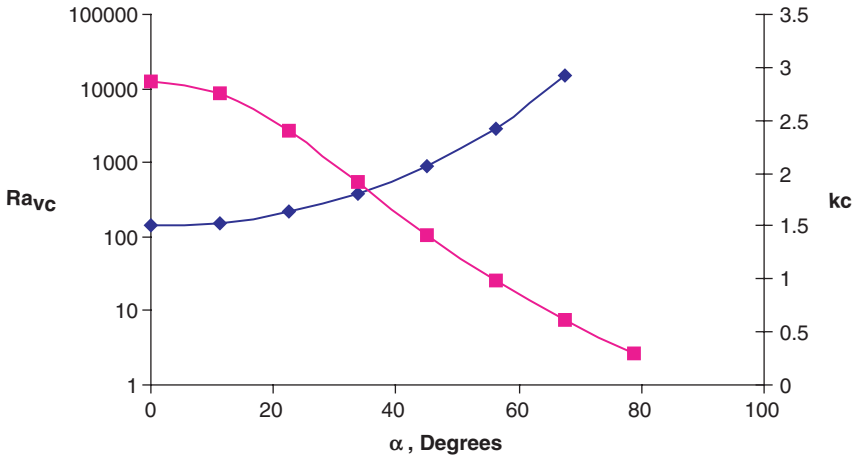

Fig. 3 Influence of the direction of the vibration on the values of the vibrational critical Rayleih number Ra_{vc} (*left*) and the critical wave number kc (*right*)

The Onset of Convection Under Micro-gravity ($Ra_T = 0$)

One of the most interesting results reported in Zenkovskaya and Rogovenko (1999) is that, if the direction of vibration is not parallel to the temperature gradient, there is a possibility of convective motion under micro-gravity conditions. In this situation, only vibrational controlling force is operational. Figure 3 shows the critical values of the vibrational Rayleigh number (Ra_V) and the critical values of wave number (k_c) as a function of α (the direction of vibration with respect to the heated plate). It can be observed that, with increasing direction of vibration α, the domain of stability increases. At the same time, the wave number decreases with increasing direction of vibration. It should be emphasized that for $\alpha = \pi/2$, i.e. the vertical vibration, the equilibrium solution is infinitely linearly stable.

The Onset of Thermo-Vibrational Convection in the Presence of Gravity ($Ra_T \neq 0 \; and \; R \neq 0$)

In this case, the two controlling mechanisms, namely the vibrational and gravitational, are present. For the direction of vibrations $5\pi/16 < \alpha < \pi/2$, there are some values of R for which maximum stability may be obtained. Another interesting feature of the effect of direction of vibration is that for the layer heated from above, we may obtain convective motions. This is in severe contrast to the classical Horton–Rogers–Lapwood problem in which, for the case of the layer heated from above, the layer is infinitely stable. A detailed summary of the effect of direction of vibration can be found elsewhere (Cunningham 1958).

2.2 Confined Cavity

2.2.1 Introduction

From few studies devoted to confined geometries under the effect of vibration, we may mention Bardan and Mojtabi (2000). A numerical and an analytical study of convective motion in a rectangular porous cavity saturated by a pure fluid and subjected to a high-frequency and small-amplitude vibration is presented in Bardan and Mojtabi (2000). The transient Darcy formulation is adopted in the momentum equation. As vibration has high frequency and small amplitude, the relevant equations are solved by the time-averaged method. The same problem under arbitrary frequency of vibration has been studied recently by Charrier-Mojtabi et al. (2006). They conclude that the results found from stability analysis of infinite porous layer can be used to calculate the onset of convection in a confined cavity.

2.2.2 Stability Analysis

Linear Stability Analysis

In the study (Bardan and Mojtabi 2000), the case of vertical vibration, i.e. $\alpha = \pi/2$ has been considered. For this situation mechanical equilibrium is possible. To perform linear stability analysis, the field variables are infinitesimally perturbed around the motionless equilibrium state. By eliminating the pressure in the momentum equation and introducing the perturbed field as:

$$\tilde{v}_z = \sum_{n=1}^{p}\sum_{m=1}^{q} X_{nm}(t)\sin n\pi z \sin\frac{m\pi x}{A_L}, \tilde{\theta} = \sum_{n=1}^{p}\sum_{m=1}^{q} h_{nm}(t)\sin n\pi z \sin\frac{m\pi x}{A_L}. \quad (40)$$

m and n are integer numbers and represent number of rolls in the x and z directions respectively.

By defining $Y = (X_{mn}(t), h_{mn}(t))$ with components as explained in (40), we obtain the following equation:

$$\frac{dY}{dt} = M_0 Y + N_0 Y \sin\omega t \quad (41)$$

with M_0 and N_0 defined as:

$$M_0 = \begin{bmatrix} -\frac{1}{B} & \frac{Ra_T}{B}\dfrac{\left(\frac{m\pi}{A_L}\right)^2}{\left(\frac{m\pi}{A_L}\right)^2 + (n\pi)^2} \\ 1 & -\left(\left(\frac{m\pi}{A_L}\right)^2 + (n\pi)^2\right) \end{bmatrix}, \quad N_0 = \begin{bmatrix} 0 & -\frac{Ra_T}{B}\delta Fr\omega^2\dfrac{\left(\frac{m\pi}{A_L}\right)^2}{\left(\frac{m\pi}{A_L}\right)^2 + (n\pi)^2} \\ 0 & 0 \end{bmatrix} \quad (42a)$$

Elimination of $X_{mn}(t)$ in (40) and setting $h_{mn} = h$, leads us to a damped Mathieu equation:

$$B\frac{\mathrm{d}^2\mathrm{h}}{\mathrm{dt}^2} + \left[B\left(\left(\frac{m\pi}{\mathrm{A_L}}\right)^2 + (\mathrm{n}\pi)^2\right) + 1\right]\frac{\mathrm{dh}}{\mathrm{dt}} + \left[\left(\left(\frac{\mathrm{m}\pi}{\mathrm{A_L}}\right)^2 + (\mathrm{n}\pi^2)\right) - \mathrm{Ra_T}\frac{\left(\frac{\mathrm{m}\pi}{\mathrm{A_L}}\right)^2}{\left(\frac{\mathrm{m}\pi}{\mathrm{A_L}}\right)^2 + (\mathrm{n}\pi)^2}(1 - \delta\mathrm{Fr_F}\omega^2\sin\omega\mathrm{t})\right]\mathrm{h} = 0. \tag{42b}$$

Dividing by B and using the transformation $h(t) = e^{-\lambda t}M(t)$, the above equation is cast into Mathieu's equation (λ being $[(m\pi/A_L)^2 + (n\pi)^2 + 1/B]/2$:

$$\frac{d^2M}{d\tau^2} + (A - 2Q\cos 2\tau)M = 0 \qquad (\omega t = 2\tau - \pi/2) \tag{43}$$

in which A and Q are defined as:

$$A = \frac{4}{B\omega^2}\left[\left(\frac{m\pi}{A_L}\right)^2 + (n\pi)^2\right] - \frac{\left(\frac{m\pi}{A_L}\right)^2}{\left(\frac{m\pi}{A_L}\right)^2 + (n\pi)^2}\frac{Ra_T}{B\omega^2},$$
$$Q = \frac{2\left(\frac{m\pi}{A_L}\right)^2}{\left(\frac{m\pi}{A_L}\right)^2 + (n\pi)^2}\frac{Ra_T\tilde{R}}{B\omega^2} \tag{44}$$

If we compare (43) and (44) with the coefficients of the Mathieu equation obtained from the linear stability analysis of an infinite horizontal layer of previous section, we observe an interesting analogy between these two equations. It means that one should set: $m\pi/A_L = k$ (k being the wave number in the infinite direction (Ox) of the layer). Thus we obtain:

$$Ra_T = \frac{\left[\left(\frac{m\pi}{A_L}\right)^2 + (n\pi)^2\right]^2}{\left(\frac{m\pi}{A_L}\right)^2} + \frac{\left(\frac{m\pi}{A_L}\right)^2}{\left[\left(\frac{m\pi}{A_L}\right)^2 + (n\pi)^2\right]}Ra_V \tag{45}$$

with $Ra_v = Ra_T^2R^2$ and $R_v^2 = \dfrac{(\delta\,\mathrm{Fr_F}\,w)^2}{2\,B}$

The critical values of Ra_{Tc} and $m\pi/A_L = k_c$ are given as:

$$Ra_{Tc} = \frac{\left(2\pi^2 - k_c^2\right)\left(\pi^2 + k_c^2\right)^2}{\pi^2 k_c^2} \quad \text{(a)}$$
$$R_v^2 = \frac{\pi^2\left(\pi^2 - k_c^2\right)}{\left(2\pi^2 - k_c^2\right)^2\left(\pi^2 + k_c^2\right)} \quad \text{(b)} \tag{46}$$

In order to find the critical value of the thermal Rayleigh number, we should simultaneously solve (46a) and (46b) for given values of A_L and m.

Weakly Non-linear Stability Analysis

In order to obtain the normal form of the amplitude equation and to determine the characteristics of solutions (stream function and temperature) near the bifurcation point, a weakly non-linear analysis is carried out in Bardan and Mojtabi (2000). This analysis is based on the multi-scale approach. The procedure is the same as in previous section and will not be repeated. The amplitude equation can be written as:

$$a\frac{\partial K}{\partial t} = bK(\mu + cK^2) \tag{47}$$

where $\mu = (Ra - Ra_c)/\eta^2$ is the bifurcation parameter.

The sign of these coefficients (a, b, and c) are functions of Ra_v and A_L. We distinguish two different cases:

$C > 0$ and $-b\mu/a < 0 \Rightarrow$ bifurcation is stable supercritical pitch-fork
$C < 0$ and $-b\mu/a > 0 \Rightarrow$ bifurcation is unstable sub-critical pitch-fork

2.2.3 2D Numerical Simulations

The time-averaged equations are solved using a collocation spectral method.

The time discretization is a second order Adams–Bashforth–Euler backward scheme (Sovran et al. 2002). The influence of the vibrational Rayleigh number Ra_v (B is fixed to 10^{-5}), is investigated for a cavity of aspect ratio $A_L = 3$. The spatial resolution is 63×27 collocation points along the horizontal and vertical axes respectively.

For $A_L = 3$, we deduce from the results of the stability analysis (46) that for $Ra_{Tc} = 4\pi^2$ and $Ra_v = 0, m = 3$ and $n = 1$, the onset of the convection corresponds to a three rolls motion in the horizontal direction. We also obtain, for $Ra_{Tc} = 72.09$ and $Ra_v = 82.94$, the transition from the convective motion characterized by three rolls to the two rolls motion ($m = 2, n = 1$).It should be observed that, as the problem depends on two control parameters , Ra_T and Ra_v, the results are expressed as function of the couple (Ra_T, Ra_v).

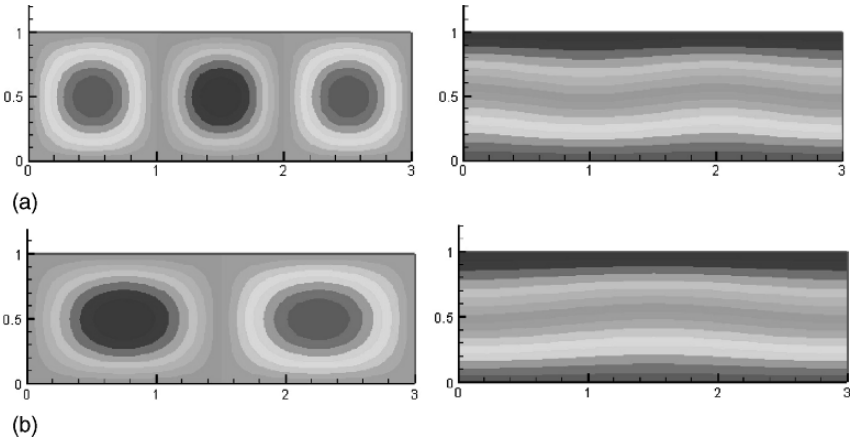

Fig. 4 Streamlines and isotherms for: (**a**) $A_L = 3.$, $Ra_{Tcnum} = 41$ and $Ra_{vnum} = 0$, (**b**) $A_L = 3$, $Ra_{Tcnum} = 73$ and $Ra_{vnum} = 84$

For the onset of stationary convection, the numerical results are presented as the streamlines and the isotherms associated to the mean field for $Ra_{Tcnum} = 41$ and $Ra_{vnum} = 0$ (Fig. 4a).We can observe three rolls as predicted by the linear stability theory. For the set of parameters: $Ra_{Tcnum} = 73$ and $Ra_{vnum} = 84$, the streamlines and isotherms are shown in Fig. 4b. We can observe the existence of two rolls which is in good agreement with our theoretical results.

For the aspect ratio $A_L = 4$, the stability analysis indicates that the onset of convection for $m = 4$ and $n = 1$ corresponding to four rolls is obtained for $Ra_{Tc} = 4\pi^2$ and $Ra_v = 0$ .We also obtain for $Ra_{Tc} = 61.58$ and $Ra_v = 52.06$, the transition from the convective motion characterized by four rolls to the three rolls motion. The numerical results obtained for the onset of convection for the solution with four rolls are $Ra_{Tcnum} = 39.6$ and $Ra_{vnum} = 0$ (global Nusselt number, Nu $= 1.0061$). For the onset of the solution with three rolls, we obtain: $Ra_{Tcnum} = 62.5$ and $Ra_{vnum} = 54$ (global Nusselt number, Nu $= 1.0187$).

For all the numerical cases studied, the global Nusselt number, Nu, is close to one which indicates that we are close to the threshold of convection. In conclusion for these two aspect ratios the numerical results corroborate the theoretical ones.

2.3 Some Key Results

The stability analysis of a porous layer under the effect of mechanical vibration is presented. The layer can be heated uniformly from below or from above. It is shown that vibration can change the onset of convective motion in porous media. The change of threshold depends on direction, amplitude and frequency of vibration. For the case of mechanical vibration parallel to the temperature gradient (vertical vibration), mechanical equilibrium is possible. For this case, under different heating conditions (heating from above or below), there is a possibility of convective

motion that largely depends on the chosen values of amplitude and frequency of vibration. The response of the system shows harmonic or sub-harmonic behavior. For heating from below, the harmonic mode exhibits a stabilizing behavior whereas the sub-harmonic mode exhibits a destabilizing one. For heating from below the results indicate that, under the condition of high-frequency and small amplitude of vibration, the harmonic part shows a strong stabilizing effect. Under this limiting situation, the time-averaged formulation can be adopted. A weakly nonlinear stability analysis is performed for this averaged system revealing that bifurcation is of supercritical pitch-fork type. For the case of other directions of vibration ($\alpha \neq \pi/2$) under high-frequency and small amplitude, it is shown that, in the presence of gravitational acceleration for the layer heated from below, vibration may produce stabilizing or destabilizing effects. These depend largely on the choice of vibrational parameter and the direction of vibration. For the layer heated from above, decreasing the direction of vibration from $\alpha = \pi/2$ to $\alpha = 0$ reduces the stability domain (Ra_{T_c} decreases). For the case of convection under micro-gravity conditions, it is shown that there is a possibility of thermo-vibrational convection for all directions of vibration except vertical vibration ($\alpha \neq \pi/2$).

A simple procedure for obtaining the critical Rayleigh number in a confined cavity is proposed through an analogy with the linear stability analysis results in an infinite porous layer.

3 Influence of Mechanical Vibration on a Porous Media Saturated by a Binary Mixture

In this section, we study the effect of vibrational mechanism on coupled dissipative phenomena, namely, the Soret driven convective motion in a porous medium saturated by a binary mixture. Under the Soret effect, a concentration gradient is established as a result of the temperature gradient (De Groot and Mazur 1984). This problem in the context of vibration in fluid media was studied in an infinite horizontal layer (Gershuni et al. 1997, 1999). The limiting case of high-frequency and small amplitude vibration was studied which enabled the time-averaged method to be used. It is found that vibration could drastically change the stable zones in the stability diagram. Generally, vertical vibration (parallel to the temperature gradient) increases the stability of the conductive mode. Smorodin et al. (2002) studied the same problem under finite frequency. They also showed that, in synchronous mode, vibration has a stabilizing effect.

On existing vibrational thermosolutal convection, we may mention Jounet and Bardan (2001) and Charrier-Mojtabi et al. (2004). In Jounet and Bardan (2001) the solutal and temperature differences are imposed while in Sovran et al. (2002) and Charrier-Mojtabi et al. (2004) the temperature gradient generates mass flux (Soret effect).

It should be noted that the study of thermosolutal problem provides us with more interesting instability mechanisms and pattern generating phenomena, which are normally absent in single component fluid.

3.1 Problem Description

The geometry consists of a rectangular cavity filled with a porous medium saturated by a binary mixture. The aspect ratio is defined as $A = L/H$ where H is the height and L is the length of the cavity. The boundaries of the cavity are rigid and impermeable; the horizontal ones can be heated from below or above. The lateral boundaries are thermally insulated and impermeable (Fig. 5). The governing equations are written in a reference frame linked to the cavity. The case with high frequency and small amplitude vibration is considered.

The direction of vibrations is defined in this Section 3 by:

$$\mathbf{e} = \cos(\alpha)\mathbf{i} + \sin(\alpha)\mathbf{j} \qquad \text{with} \quad g = -g\mathbf{j}$$

Under the Boussinesq approximation the dimensionless governing equations for the mean flow averaged over the vibration period can be written as:

$$\begin{aligned}
&\nabla \cdot \mathbf{V} = 0 \\
&B\tfrac{\partial \mathbf{V}}{\partial t} + \mathbf{V} = -\nabla P + Ra(T + \psi C)\mathbf{j} + Rv(\mathbf{W}_T + \psi \mathbf{W}_c)\cdot \\
&\nabla(T + \tfrac{\psi}{\varepsilon^*}C)(\cos\alpha\,\mathbf{i} + \sin\alpha\,\mathbf{j}) \\
&\frac{\partial T}{\partial t} + \vec{\mathbf{V}} \cdot \nabla T = \Delta T, \\
&\varepsilon^* \frac{\partial C}{\partial t} + \vec{\mathbf{V}} \cdot \nabla C = \tfrac{1}{Le}(\Delta C - \Delta T) \\
&\nabla \cdot \mathbf{W}_T = 0, \quad \nabla \cdot \mathbf{W}_c = 0 \\
&T\,\mathbf{e} = \mathbf{W}_T + \nabla \xi_T, \quad C\mathbf{e} = \mathbf{W}_c + \nabla \xi_c
\end{aligned} \tag{48}$$

Where $\mathbf{V}$, T, C are velocity, temperature and mass fraction fields and $\mathbf{W_T}$ and $\mathbf{W_c}$ are solenoidal vectors corresponding to the temperature and concentration fields respectively.

The corresponding boundary conditions are:

$$\begin{aligned}
&\mathbf{W}_T \cdot \mathbf{n} = \mathbf{W}_c \cdot \mathbf{n} = 0 \\
&y = 0 : T = T_1, \quad \mathbf{J_m}\cdot\mathbf{n} = 0 \\
&y = 1 : T = T_2, \quad \mathbf{J_m}\cdot\mathbf{n} = 0 \\
&x = 0,\ A : \frac{\partial T}{\partial x} = \frac{\partial C}{\partial x} = 0
\end{aligned} \tag{49}$$

Mathematical system (48) depends on eight parameters; the thermal Rayleigh number $Ra = Kg\beta\Delta TH/\nu a^*$, the vibrational Rayleigh number

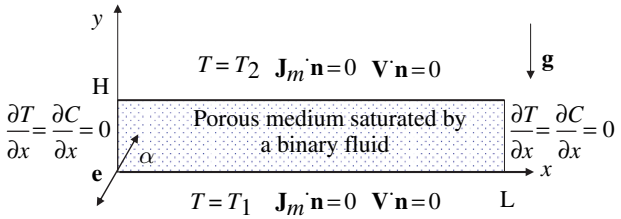

Fig. 5 Geometry and boundary conditions: case of a porous medium saturated by a binary fluid

$Rv = (\tilde{R}^2 Ra^2 B)/2(B^2\omega^2 + 1) = R^2 Ra^2(\tilde{R} = b\varpi^2/g)$, the separation factor $\psi = -C_i(1 - C_i)(\beta_c/\beta_T)D_T/D^*$, the normalized porosity ε^* ($\varepsilon^* = \varepsilon/\sigma$,), the Lewis number Le ($Le = a^*/D^*$ in which a^* is the effective thermal diffusivity and D^* is the effective mass difusivity), the coefficient of the unsteady Darcy term in the momentum equation $B = Da/(\sigma\varepsilon Pr^*)$ (in porous media $B \approx 10^{-5}$ and Da represents the Darcy number $Da = K/H^2$), and finally α the direction of vibration with respect to the heated boundary.

3.2 Linear Stability Analysis

For the direction of vibration parallel to the temperature gradient ($\alpha = \pi/2$), there exists a mechanical equilibrium (for both an infinite horizontal layer and a confined cavity), which is characterized by:

$$\mathbf{V}_0 = 0, \quad T_0 = 1 - y, \quad C_0 = cst - y, \quad \mathbf{W}_{T0} = 0, \quad \mathbf{W}_{C0} = 0 \tag{50}$$

However, for other directions of vibration, we may obtain quasi-equilibrium solution only for the infinite horizontal layer. This is characterized by:

$$\begin{aligned} &\mathbf{V}_0 = 0, \quad T_0 = 1 - y, \quad C_0 = c_1 - y, \quad \mathbf{W}_{T0_x} = c_2 - y\cos\alpha; \quad \mathbf{W}_{T0_y} = 0, \\ &\mathbf{W}_{C0_x} = c_3 - y\cos\alpha, \quad \mathbf{W}_{C0_y} = 0 \end{aligned} \tag{51}$$

It should be noted that, for a confined cavity, there is no equilibrium solution under the horizontal vibration ($\alpha = 0$).

3.2.1 Infinite Horizontal Porous Layer

In order to investigate the stability of the conductive solution, the fields are perturbed around the equilibrium state. Then after linearization, the disturbances are developed in the form of normal modes. We introduce the stream function perturbation ϕ, the temperature perturbation θ and the mass fraction perturbation c. Also we designate the stream function perturbations ϕ_θ and ϕ_c for corresponding solenoidal fields $\mathbf{W_T}$ and $\mathbf{W_c}$. In order to facilitate our study, we use the transformations $\eta = c - \theta$ and $\varphi_\eta = \varphi_c - \varphi_\theta$. We may write:

$$\begin{aligned} \varphi &= \sum_{i=1}^{N} \mathrm{a_i} \sin(i\pi y)\exp(\sigma t + Ikx); \theta = \sum_{i=1}^{N} \mathrm{b}_i \sin(i\pi y)\exp(\sigma t + Ikx); \\ \eta &= \sum_{i=0}^{N-1} \mathrm{c_i} \cos(i\pi y)\exp(\sigma t + Ikx) \\ \varphi_\theta &= \sum_{i=1}^{N} \mathrm{d}_i \sin(i\pi y)\exp(\sigma t + Ikx); \quad \varphi_\eta = \sum_{i=1}^{N} \mathrm{g}_i \sin(i\pi y)\exp(\sigma t + Ikx) \end{aligned} \tag{52}$$

in which k is the wave number in the infinite horizontal direction Ox and $I^2 = -1$.

The corresponding linear stability problem is solved using the Galerkin method.

Vertical Vibration ($\alpha = \pi/2$)

For different sets of parameters $0 < Rv < 100$, $2 < Le < 100$ and $\varepsilon^* = 0.5, 0.7$, the numerical simulations are carried out. The results of linear stability analysis for $Le = 2$, $\psi = -0.2$ and $\varepsilon^* = 0.5$ are presented in Table 1. It should be noted that, in the range of Lewis numbers studied, the results are qualitatively the same. As can be observed from Table 1, we may distinguish two types of bifurcations; namely stationary and Hopf bifurcations. For the stationary bifurcation, we assume that the principle of the exchange of stability is valid (i.e. $\sigma \in \Re$). From this the marginal state is determined ($\sigma = 0$). For the Hopf bifurcation ($\sigma = \sigma_r + I\omega_0$); the marginal state corresponds to $\sigma_r = 0$. It should be added that the Hopf bifurcation is present only for negative separation factors and, for the layer heated from below, it can be formed before the stationary bifurcation ($Ra_{co} < Ra_{cs}$). The effects of vibration on the Hopf bifurcation for $\psi = -0.2$, $\varepsilon^* = 0.5$ and $Le = 2$ are represented in Table 1. We conclude from Table 1 that vibration has a stabilizing effect; it increases the critical value of thermal Rayleigh number for the onset of convection. This is true for both the stationary and the Hopf bifurcation. It should be mentioned that vibration reduces the critical wave number (k_{cs}, k_{co}) and the Hopf frequency (ω_o).

Here after, we present the evolution of the critical Rayleigh number (Ra_{cs}) (Fig. 6a) and the critical wave-number (k_{cs}) (Fig. 6b) versus the separation factor Ψ for different values of the vibrational Rayleigh number Rv in the case $Le = 10$ and $\epsilon^* = 0.5$ and for stationary bifurcations.

One can observe that for $\Psi > 0$, when Rv increases, the value Ψ_1 of the separation ratio beyond which the critical wave number vanishes (i.e $k_{cs} = 0$) decreases. We show that for $\Psi > \Psi_1$ and for vertical vibrations:

$$Ra_{cs} = \frac{12}{Le\psi}; \forall R_v \tag{53}$$

Horizontal Vibration ($\alpha = 0$)

The stability domain for different vibrational parameters in the (Ra, Ψ) stability diagram has been determined.This diagram is characterized by stationary and

Table 1 Effect of vertical vibrations on stationary and Hopf bifurcations ($Le = 2$, $\Psi = -0.2$ and $\varepsilon^* = 0.5$)

Rv	Ra_{cs}	k_{cs}	Ra_{co}	k_{co}	ω_o
0	153.19	4.75	95.43	2.59	10.78
10	157.53	4.73	97.78	2.56	10.75
50	173.63	4.65	107.1	2.41	10.50
100	193.60	4.54	117.8	2.26	10.26

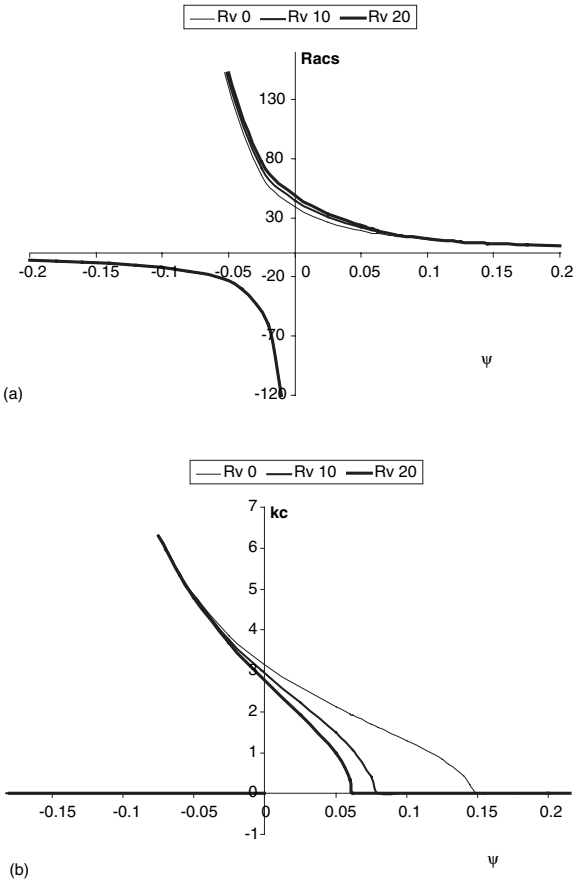

Fig. 6 (**a**) $Ra_{cs} = f(\Psi)$, $Le = 10$, $\varepsilon^* = 0.5$ (stationary bifurcations) and ($\alpha = \pi/2$), (**b**) $k_{cs} = f(\Psi)$, $Le = 10$, $\varepsilon^* = 0.5$ (stationary bifurcations) and ($\alpha = \pi/2$)

oscillatory bifurcations. For $\Psi > 0$ the bifurcation is always of the stationary type while for $\Psi < 0$, we may obtain oscillatory or stationary bifurcations. The computations are performed for $\varepsilon^* = 0.3$, $B = 10^{-6}$ (usual values used in porous media) and $Le = 2, 10, 100$. The results show that horizontal vibrations have a destabilizing effect on both stationary and Hopf bifurcations while vertical vibrations have stabilizing effect.

As for the case of vertical vibrations, we note the existence of long-wave-mode instability (i.e. $k_{cs} = 0$) for $\Psi > 0$. A regular perturbation method with the wave number as small parameter has been performed and the following relation:

$$Ra_{cs} + R_v(1+\psi)\frac{\psi}{\epsilon^*} = \frac{12}{Le\psi} \quad (\alpha = 0) \tag{54}$$

has been obtained. From (54), for fixed values of Rv, Le, Ψ and ϵ^*, we can calculate the value of the critical Rayleigh number $\mathrm{Ra_{cs}}$, corresponding to the onset of a monocellular flow, for $\alpha = 0$.

3.3 Numerical Simulations in a Confined Cavity ($A = 1$ and $A = 10$)

The numerical simulations for a confined cavity are performed for vertical and horizontal vibrations. The calculations are made for different aspect ratios $A = 1$ and $A = 10$. The 27*27 collocation points are used for $A = 1$ while 63*27 collocation points are used for $A = 10$.

3.3.1 Vertical Vibration ($\alpha = \pi/2$)

In this section we provide a qualitative representation of the flow and thermal fields to complete the results of our stability analysis. In order to study the effect of vibrations on the convective pattern, we set $Le = 2$, $\psi = 0.4$, $A = 1$ and $Ra = 30$ and we changed the value of the vibrational Rayleigh number R_v. To study the importance of the normalized porosity, computations have been performed, for $\varepsilon^* = 0.5$ and 0.7, with an increasing Rv, in order to determine the value of Rv, note Rvc, below which the conductive state appears (the global Nusselt number, defined as follows, $Nu = \frac{1}{A}\int_0^A \frac{\partial T}{\partial y}\Big)_{y=1} \mathrm{d}x$, is equal to one). The results are presented in Table 2 and Figs. 7a and 7b.

Thus these results illustrate clearly the stabilizing effect of vertical vibrations and the importance of the normalized porosity. When ϵ^* increases, for a fixed value of the thermal Rayleigh number, the value of Rv for which the conductive regime appears increases. In addition, for the combination of Rv, ψ and ε^*, there exists an interesting relation $Rv_c(1 + \psi/\varepsilon^*) = cst$. In our case this constant is equal to 31.5.

On Fig. 8a and b, we illustrate the modification of the convective structure due to vibrations for $A = 10$, $Le = 10$, $\epsilon^* = 0.5$, $\Psi = 0.1$ and $Ra = 12.5$.

For this set of parameters and $Rv = 0$ (Fig. 8a), we obtain five cells and the iso-concentrations are deformed. For $Rv = 10$ (Fig. 8b), a monocellular motion takes place and induces a separation of the binary fluid components.

Table 2 Evolution of the global Nusselt number, Nu, versus Rv for $\varepsilon^* = 0.5$ and 0.7. ($\alpha = \pi/2$)

$\varepsilon^* = 0.5$ *Rv*	$\varepsilon^* = 0.5$ *Nu*	$\varepsilon^* = 0.7$ *Rv*	$\varepsilon^* = 0.7$ *Nu*
5	1.2047	5	1.2057
10	1.1483	10	1.1528
15	1.0789	15	1.0942
16	1.0604	17	1.0669
17	1.0358	18	1.0514
17.5	1.0124	19	1.0329
17.53	1.0084	19.5	1.0208
		19.7	1.0156
		20.02	1.0036

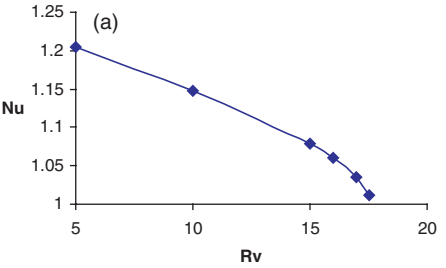

Fig. 7a Effect of mechanical vibration on the global Nusselt number for $A = 1$, $\alpha = \pi/2$, $Le = 2$, $\varepsilon^* = 0.5$, $\psi = 0.4$ and $Ra = 30$

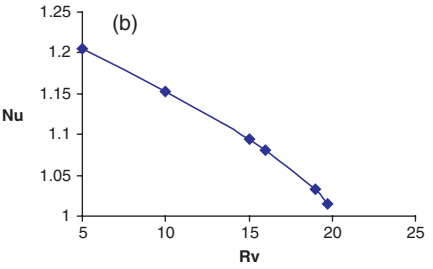

Fig. 7b Effect of mechanical vibration on the global Nusselt number for $A = 1$, $\alpha = \pi/2$, $Le = 2$, $\varepsilon^* = 0.7$, $\psi = 0.4$ and $Ra = 30$

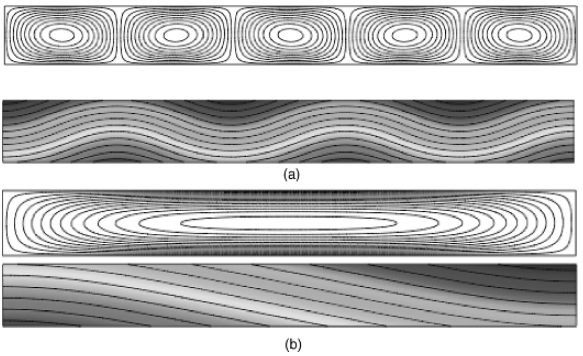

Fig. 8 Streamlines and iso-concentrations for: (**a**) $Le = 10$, $\varepsilon^* = 0.5$, $\Psi = 0.1$ and $Ra = 12.5$ for $Rv = 0(\alpha = \pi/2)$, (**b**): $Le = 10$, $\varepsilon^* = 0.5$, $\Psi = 0.1$ and $Ra = 12.5$ for $Rv = 10(\alpha = \pi/2)$

3.3.2 Horizontal Vibrations ($\alpha = 0$)

To illustrate the influence of horizontal vibrations, we consider the case $A = 1$, $Le = 2$, $\varepsilon^* = 0.5$, $\psi = 0.2$, $R = 0.3$. For a confined cavity, there is no equilibrium solution under horizontal vibrations. However, we study the different convective structures obtained when the thermal Rayleigh number increases for a fixed value of R. Note that for $Le = 2$, $\varepsilon^* = 0.5$, $\psi = 0.2$, $R = 0.3$ and for an infinite layer, the critical value of the Rayleigh number corresponding to the onset of convection is $\mathrm{Ra}_{cs} = 14.06$.

Firstly we set the value of Ra to the previous value so that only the vibrational mechanism is in action. For $Ra = 6$, Figs. 9 and 10 show the corresponding fluid

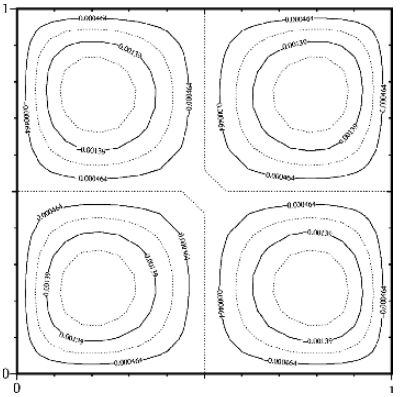

Fig. 9 Stream functions for $A = 1$, Le $= 2$, $\varepsilon^* = 0.5$, $\psi = 0.2$, Ra $= 6$, $R = 0.3$ and $\alpha = 0$

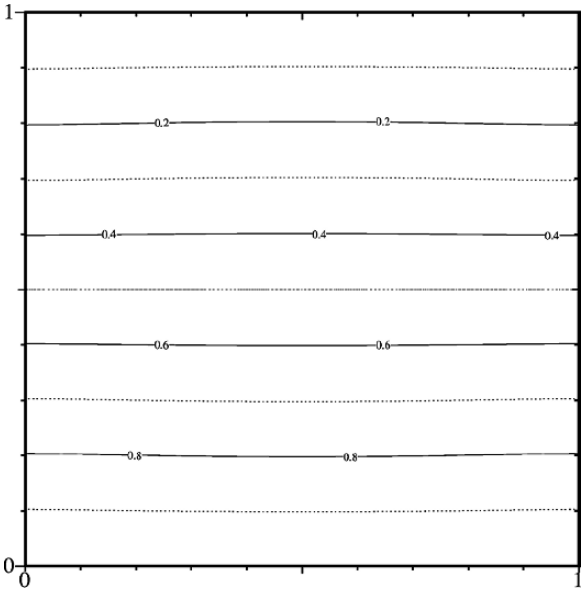

Fig. 10 Isotherms for $A = 1$, Le $= 2$, $\varepsilon^* = 0.5$, $\psi = 0.2$, Ra $= 6$, $R = 0.3$ and $\alpha = 0$

flow structure and temperature distribution; the stream functions are characterized by symmetrical four-vortex rolls. This structure is a typical example of an imperfect bifurcation. The sum of stream functions is zero in this case.

Secondly the thermal Rayleigh number is increased further to $Ra = 13.15$, the gravitational acceleration will be in action. The intensity of convective motion will be accordingly increased. The sum of stream functions at all points in the domain is a good criterion for the intensity of convective motion. This case is shown in Figs. 11 and 12 . As can be seen from the figures, we obtain a symmetry breaking structure. This is explained by coalescence of the two rolls with the same sign in the diagonal direction and the existence of two separate off-diagonal rolls with weaker intensity.

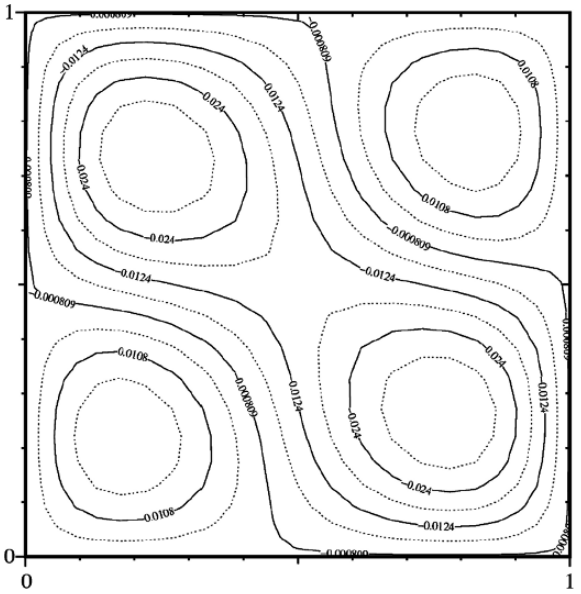

Fig. 11 Stream functions for $A = 1$, $Le = 2$, $\varepsilon^* = 0.5$, $\psi = 0.2$, $Ra = 13.15$, $R = 0.3$ and $\alpha = 0$

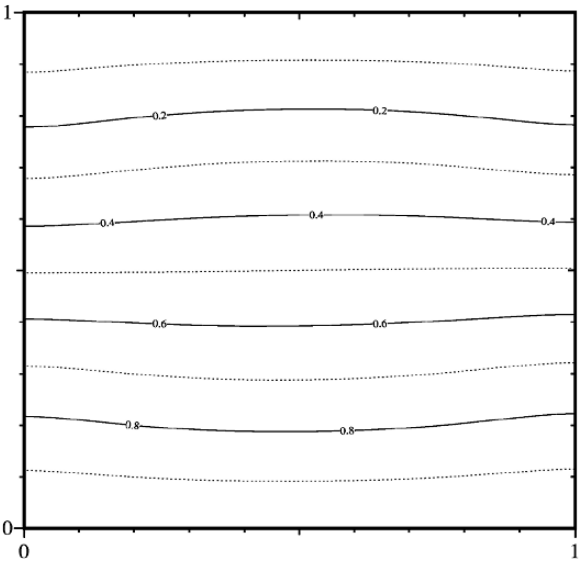

Fig. 12 Isotherms for $A = 1$, $Le = 2$, $\varepsilon^* = 0.5$, $\psi = 0.2$, $Ra = 13.15$, $R = 0.3$ and $\alpha = 0$

Then we increase further the thermal Rayleigh number to $Ra = 15$, we find a single convective roll, which means that the gravitational effect is more important than the vibrational effect, Figs. 13 and 14.

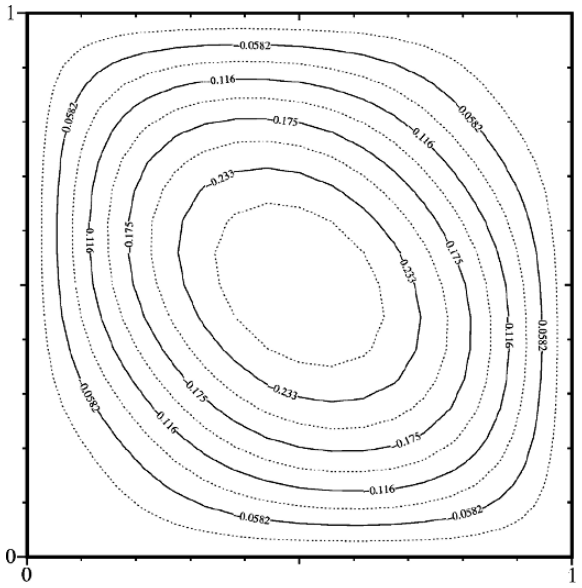

Fig. 13 Stream functions for $A = 1$, $Le = 2$, $\varepsilon^* = 0.5$, $\psi = 0.2$, $Ra = 15$, $R = 0.3$ and $\alpha = 0$

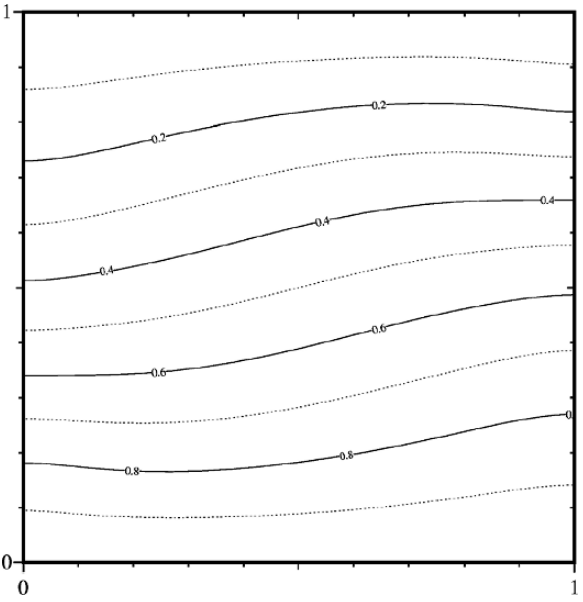

Fig. 14 Isotherms for $A = 1$, $Le = 2$, $\varepsilon^* = 0.5$, $\psi = 0.2$, $Ra = 15$, $R = 0.3$ and $\alpha = 0$

3.4 Conclusions

In this section, we studied two-dimensional thermo-solutal convection under mechanical vibration analytically and numerically. The vibration is in the limiting range of high frequency and small amplitude. Linear stability analyses of equilibrium

and quasi-equilibrium states are performed for infinite horizontal layer. It is found that when the direction of vibration is parallel to the temperature gradient, vibration has a stabilizing effect for both the stationary and the Hopf bifurcation. The action of vibration reduces the number of convective rolls and the Hopf frequency. However, when the direction of vibration is perpendicular to the temperature gradient, vibration has a destabilizing effect. The numerical simulation shows that the vertical vibration can reduce the number of convective rolls. The effect of vibration on reducing the Nusselt number is presented. In this respect, the importance of the group $(Rv_c(1 + \psi/\varepsilon^*))$ is emphasized. For the cases in which mechanical equilibrium is impossible the fluid flow structures are sought. For a fixed value of vibrational Rayleigh number, we increase the Rayleigh number from a value much less than the critical value corresponding to the onset of convection in an infinite layer. We observe first a symmetrical four-vortex structure, then a diagonal dominant symmetry breaking structure and finally a mono-cellular structure. These results are similar to the results obtained in a cavity filled with pure fluid under the action of vibration in weightlessness (Bardan et al. 2000). The interesting result of this study is that, by appropriate use of residual acceleration in micro-gravity environment, we may obtain significant enhancement in heat and mass transfer rates.

NOMENCLATURE

Roman Letters

a	effective thermal diffusivity, $\mathrm{m}^2.\mathrm{s}^{-1}$
b	vibration amplitude, m
C_i	initial mass fraction
C′	dimensional mass fraction
C	perturbation of concentration
D^*	mass diffusion coefficient
D_T	thermodiffusion coefficient
Da	Darcy number
$\boldsymbol{e}$	direction of vibration
$\boldsymbol{g}$	gravitational acceleration, $\mathrm{m.s}^{-2}$
H	height, m
$\boldsymbol{j}$	unit vector in y direction
k	wave number
K	permeability, m^2
Le	Lewis number (a/D^*)
P	pressure, $\mathrm{N.m}^{-2}$
Pr	Prandtl number (v/a)
R	acceleration ratio
R_v	vibrational parameter
Ra	Rayleigh number

Ra_v vibrational Rayleigh number
T temperature, K
T' dimensional temperature
t' dimensional time
$\boldsymbol{V}$ velocity, m.s^{-1}
$\boldsymbol{W}$ solenoidal vector

Greek Letters

β_C coefficient of mass expansion
β_T coefficient of thermal expansion
ε porosity
ε^* normalized porosity
θ perturbation of temperature
λ^* effective thermal conductivity
ν kinematic viscosity, m^2.s^{-1}
ρ density, kg.m^{-3}
$(\rho c)^*$ volumic heat capacity of medium
τ vibration period
ψ separation ratio
φ steam function perturbation
ϖ pulsation
ω dimensionless pulsation
α angle of vibration
σ^* dimensionless volumic heat capacity ratio
$\Delta T = T_1 - T_2$

References

Alexander J.I.D. (1994) Residual gravity jitter effects on fluid processes. Microgravity Sci. Tech. vol. 7, pp. 131–136.

Aniss A., Souhar M. and Belhaq M. (2000) Asymptotic study of the convective parametric instability in Hele–Shaw cell. Phys. Fluids vol. 12, pp. 262–268.

Bardan G. and Mojtabi A. (2000) On the Horton–Rogers–Lapwood convective instability with vertical vibration. Phys. Fluids vol. 12, pp. 1–9.

Bardan G., Mojtabi A. and Souhar (2000) Numerical investigation of vibrational high frequency field upon double diffusive convection in microgravity. Q. Micrograv., vol. 1, No. 2, pp. 1–9.

Bardan G., Pedramrazi Y., Mojtabi A. (2004) Phys. Fluids vol. 16, pp. 1–4.

Charrier-Mojtabi M.C., Maliwan K., Pedramrazi Y., Bardan G. and Mojtabi A. (2003) Contrôle des écoulements thermoconvectifs par vibration. Journal de Mécanique et Industrie, vol. 4, No. 5, pp. 545–554.

Charrier-Mojtabi M.C., Pedramrazi Y., Maliwan K. and Mojtabi A. (2004) Influence of vibration on Soret-driven convection in porous media. Num. Heat Transfer Part A vol. 46, pp. 1–13.

Charrier-Mojtabi M.C., Pedramrazi Y. and Mojtabi A. (2006) The influence of mechanical vibration on convective motion in a confined porous cavity with emphasis on harmonic and subharmonic responses. Proceedings (CD Rom) of the 13th international heat transfer conference. IHTC13, Sydney, Australia.

Cunningham W.J. (1958) Introduction to nonlinear analysis. McGraw-Hill, New York.
De Groot S.R. and Mazur P. (1984) Non equilibrium thermodynamics. Dover, New York.
Faraday M. (1831) Phil. Trans. R. Soc. Lond. vol. 121, pp. 299.
Gershuni G.Z., Zhukhovitskiy E.M. and Iurkov S. (1970) On convective stability in the presence of periodically varying parameter. J. Appl. Math. Mech 34: pp. 470–480.
Gershuni G.Z. and Lyubimov D.U. (1998). Thermal vibrational convection Willey, New york.
Gershuni G.Z., Kolesnikov A.K., Legros J.C. and Myznikova B.I. (1997) On the vibrational convective instability of a horizontal binary mixture layer with Soret effect. J. Fluid Mech. vol. 330, pp. 251–269.
Gershuni G.Z., Kolesnikov A.K., Legros J.C. and Myznikova B.I. (1999) On the convective instability of a horizontal binary mixture layer with Soret effect under transversal high frequency vibration. Int. J. Heat Mass Transfer vol. 42, pp. 547–553.
Govender S. (2004) Stability of convection in a gravity modulated porous layer heated from below. Trans. Porous Media, vol. 7, pp. 113–123.
Govender S. (2005a) Stability analysis of a porous layer heated from below and subjected to low frequency vibration. Trans. Porous Media vol. 59, pp. 239–247.
Govender S. (2005b)Weak non linear analysis of convection in a gravity modulated porous layer. Trans. Porous Media vol. 60, pp. 33–42.
Govender S. (2006a) An analogy between a gravity modulated porous layer heated from below and the inverted pendulum with an oscillating pivot point, accepted for publication in Transport in Porous Media 2006.
Govender S. (2006b) Stability of gravity driven convection in a cylindrical porous layer subjected to vibration. Trans. Porous Media vol. 63, pp. 489–502.
Gresho P.M. and Sani R.L. (1970) The effects of gravity modulation on the stability of heated fluid layer. J. Fluid Mech. vol. 40, pp. 783–806.
Jordan D.W. and Smith P. (1987) Transport phenomena in porous media. Oxford University Press, New York.
Jounet A. and Bardan G. (2001) Onset of thermohaline convection in a rectangular porous cavity in the presence of vertical vibration. Phys. Fluids vol. 13, pp. 1–13.
Malashetty M.S. and Padmavathi V. (1997) Effect of gravity modulation on the onset of convection in a fluid and porous layer. Int. J. Eng. Sci. vol. 35, pp. 829–840.
Mc Lachlan N.W. (1964) Theory and application of Mathieu functions. Dover, New York.
Palm E., Weber J.E. and Kvernvold O. (1972) On steady convection in a porous medium. J. Fluid Mech. Vol. 54, pp. 153–161.
Pedramrazi Y. (2004) Ph.D thesis, Fluid Mechanical Institute, IMFT and University Paul Sabatier, Toulouse III.
Pedramrazi Y., Maliwan K. and Mojtabi A. (2002) Two different approaches for studying the stability of the Horton–Rogers–Lapwood problem under the effect of vertical vibration. Proceedings of the first international conference in applications of porous media. Jerba , Tunisia, pp. 489–497.
Pedramrazi Y., Maliwan K., Charrier-Mojtabi M.C. and Mojtabi A. (2005) Influence of vibration on the onset of thermoconvection in porous medium. Handbook of porous media. Marcel Dekker, New York, pp. 321–370.
Simonenko I.B. and Zenkovskaya S.M. (1966) On the effect of high frequency vibration on the origin of convection. Izv. Akad. Nauk SSSR, Mekh. Zhidk. Gaza vol. 5, pp. 51.
Smorodin B.L., Myznikova B.I. and Keller I.O. (2002) On the Soret-driven thermosolutal convection in vibrational field of arbitrary frequency, in: Thermal Non-equilibrium Phenomena in Fluid Mixtures, Lectures, Lecture Notes in Physics, 584, pp. 372–388.
Sovran O., Charrier Mojtabi M.C., Azaiez M. and Mojtabi A. (2002) Onset of Soret driven convection in porous medium under vertical vibration. Proccedings of the 12th international heat transfer conference. IHTC12, Grenoble pp. 839–844.
Zenkovskaya S.M. (1992) Action of high-frequency vibration on filtration convection. J. Appl. Mech. Tech. Phys. vol. 32, pp. 83–86.
Zenkovskaya S.M. and Rogovenko T.N. (1999) Filtration convection in a high-frequency vibration field. J. Appl. Mech. Tech. Phys. vol. 40, pp. 379–385.

New Developments in Bioconvection in Porous Media: Bioconvection Plumes, Bio-Thermal Convection, and Effects of Vertical Vibration

A.V. Kuznetsov

Abstract This chapter reviews new developments in bioconvection in a fluid saturated porous medium caused by either gyrotactic or oxytactic microorganisms. Bioconvection arises as a result of an unstable density stratification caused by upswimming microorganisms. This unstable density stratification occurs when the microorganisms, heavier than water, accumulate in the upper regions of the fluid. This hydrodynamic instability may lead to the development of bioconvection plumes, which in case of oxytactic microorganisms transport cells and oxygen from the upper fluid region to the lower fluid regions. The presented modeling is limited to the situation when the average pore size is much larger than the size of a microorganism; therefore, local vorticity generated by flow through the pores does not affect the ability of microorganisms to reorient.

The chapter introduces bio-thermal convection, which, contrary to traditional bioconvection, has two destabilizing mechanisms that contribute to creating the unstable density stratification. The utilization of the Galerkin method to solve a linear stability problem leads to a correlation between the critical value of the bioconvection Rayleigh number and the traditional "thermal" Rayleigh number. The chapter also investigates the potential of utilizing the vertical vibration for controlling bioconvection. The linear stability analysis indicates that vertical vibration has a stabilizing effect on the suspension.

1 Introduction

Bioconvection is an area of fluid mechanics that considers suspensions of self-propelled microorganisms. This is different from traditional multiphase flows, where particles are not self-propelled; they are just carried by the flow. Bioconvection

A.V. Kuznetsov
North Carolina State University, Mechanical & Aerospace Engineering, Raleigh, NC, USA
e-mail: avkuznet@eos.ncsu.edu

P. Vadász (ed.), *Emerging Topics in Heat and Mass Transfer in Porous Media*,

© Springer Science+Business Media B.V. 2008

occurs because of unstable density stratification that arises when upswimming microbiological organisms that are denser than their surrounding fluid gather at regions near the upper surface. The accumulation of these organisms causes the upper layer to be denser than the region below and instability is introduced, which in turn leads to the development of various flow patterns (Harashima et al., 1988; Kessler, 1985; Kessler et al., 1997, 2000; Bees and Hill, 1997; Ghorai and Hill, 1999, 2000).

Bioconvection is a phenomenon in which physical laws that govern smaller scales lead to a phenomenon visible on a larger scale. While superfluidity and superconductivity are quantum phenomena visible at the macroscale, bioconvection is a mesoscale phenomenon, in which the motion of motile microorganisms induces a macroscopic motion in the fluid.

When it is considered helpful to dampen the convective effects brought on by bioconvection, a porous medium (such as gauze) may be introduced as shown in Kessler (1986). Such a medium should be sufficiently porous to allow the swimming and falling cells to penetrate through it. The stability analysis reported in Kuznetsov and Avramenko (2003) and Kuznetsov (2005c) suggests that if the permeability of a porous medium is larger than critical, bioconvection instability will develop in a porous medium as well.

One potential application of bioconvection is to enhance mass transfer. Bioconvection provides a method for manipulating mass transfer and inducing mixing in fluid microvolumes. This has potential pharmaceutical and bio-technological applications (the importance of mixing in microfluidics is reviewed in Burghelea et al., 2004). A possible biomedical link is using bioconvection for faster dissolving of solid particles. Effects of bioconvection on sedimentation of large solid particles (bioconvective sedimentation) are investigated in Geng and Kuznetsov (2006, 2007).

The effect of small solid particles on the stability of bioconvection is investigated in Kuznetsov and Avramenko (2004), Kuznetsov and Geng (2005), and Geng and Kuznetsov (2005). It is shown that the presence of small solid particles increases the critical Rayleigh number (makes the suspension more stable). Since both microorganisms and particles are heavier than water, the upswimming of microorganisms leads to an increase of bulk density in the upper part of the fluid layer (causes an unstable density stratification), but the settling of small particles partly compensates for this unstable density stratification caused by microorganisms and leads to an increase of bulk density at the bottom of the layer. According to Einstein's relation that determines the diffusivity of small particles due to the Brownian motion, the diffusivity is inversely proportional to the particles' radius, which means that larger particles have smaller diffusivity. This means that larger particles will stabilize the suspension better than very small particles (nanoparticles). This is because nanoparticles with large diffusivity have almost uniform distribution across the layer, but larger particles will concentrate near the bottom of the layer creating a more stable density stratification. All this is applicable only to the case when particles are small, so that gravitational settling and diffusion compete.

Another possible application of bioconvection theory is microbial-enhanced oil recovery, when microorganisms and nutrients are injected in oil-bearing layers to

correct permeability variation (Stewart and Fogler, 2001; Kim and Fogler, 2000). Swimming microbial species have the advantage of having favorable transport properties through porous formations.

All models presented in this chapter assume a dilute suspension. It is assumed that the porous matrix does not absorb microorganisms. The presented modeling is limited to the situation when the average pore size is much larger than the size of a microorganism; therefore, local vorticity generated by flow through the pores does not affect the ability of microorganisms to reorient; thus, oxytactic or gyrotactic behaviors of microorganisms are not affected by the presence of the porous matrix. If porosity is small (or pore sizes are small), the suspension would not reach sufficiently high concentrations for bioconvection to occur (Hill and Pedley, 2005). This conclusion is supported by the stability analysis presented in Kuznetsov and Avramenko (2003) who concluded that bioconvection can occur only in a porous media with a high porosity (however, there is sufficient number of examples of such highly permeable media). Similar to bioconvection in clear (of porous obstacles) fluids, a carefully designed lab experiment would be required to observe bioconvection in porous media.

2 Numerical Modeling of a Falling Plume in a Suspension of Oxytactic Microorganisms

2.1 Problem Description

Here the microorganisms are assumed to be the oxytactic bacteria *Bacillus subtilis,* as in Kessler (1989), Hillesdon et al. (1995), Hillesdon and Pedley (1996), and Metcalfe and Pedley (1998, 2001). These bacteria are oxygen consumers and thus they tend to swim from lower to higher oxygen concentrations. Oxygen diffuses from the free surface into the regions below, therefore the bacteria tend to migrate to regions just below the free surface where the oxygen concentration is the highest. As these plumes begin to form, cells are drawn from the cell-rich upper fluid layer. Although the cell-rich upper layer would eventually be depleted of cells, plume formation and development occurs in a much shorter time so the falling plumes may be assumed to be steady or at least quasi-steady. The plumes are also assumed to be axisymmetric. A schematic of a bioconvection plume is provided in Fig. 1.

As the cells are transported away from the surface, they continue to consume oxygen, and try to migrate towards higher oxygen concentrations. Although at regions far below the surface oxygen consumption by the cells depletes the fluid of oxygen to such an extent that the cells become inactive, this research focuses on the regions where all the bacteria are still active.

Metcalfe and Pedley (2001) describes the falling plumes using a similarity solution. Kuznetsov et al. (2004) and Becker et al. (2004) expand on Metcalfe and Pedley's work by finding a similarity solution of the plumes in a porous medium.

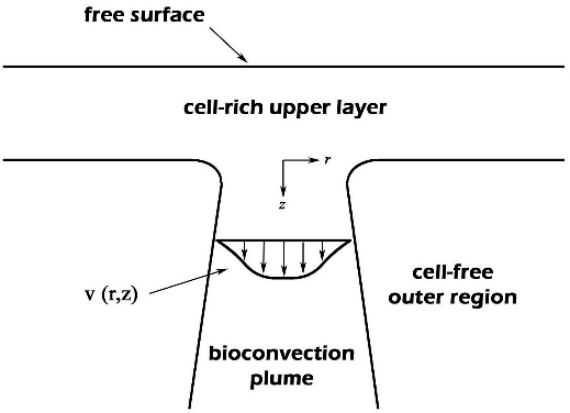

Fig. 1 Schematic diagram of the bioconvection plume

2.2 Governing Equations

A numerical solution for a steady-state axisymmetric falling bioconvection plume is obtained in Becker et al. (2004) by solving the following governing equations, expressing oxygen conservation, microorganisms conservation, momentum conservation, and mass conservation, respectively:

$$-\nabla \cdot (C\mathbf{U} - D_c \nabla C) - \gamma_0 n = 0 \tag{1}$$

$$\nabla \cdot (n\mathbf{U} + n\mathbf{V} - D_n \nabla n) = 0 \tag{2}$$

$$-\nabla p - \frac{\mu}{K}\mathbf{V} + n\theta \Delta\rho \boldsymbol{g} = 0 \tag{3}$$

$$\nabla \cdot \mathbf{U} = 0 \tag{4}$$

where $\mathbf{U}$ is the bulk fluid filtration velocity, D_C refers to the effective diffusivity of oxygen in the porous medium, n represents the concentration of cells, $-\gamma_0 n$ describes the consumption of oxygen by the cells, the parameter γ_0 is an effective constant characterizing the oxygen consumption rate in the porous medium, p is the excess pressure (above hydrostatic), μ is the fluid dynamic viscosity (assumed to be the same as that of water), K is the permeability of the porous medium, and the term $D_n \nabla n$ in equation (2) accounts for random non-directional cell swimming. The last term in equation (3), $n\theta\Delta\rho\boldsymbol{g}$, is a buoyancy term and while the suspension is unstable, it acts as a driving force for the falling motion caused by the density gradient; θ is the cell volume; $\Delta\rho$ is the difference between cell density and the fluid (assumed to be water); and $\mathbf{g}$ is the gravity vector. The dimensionless oxygen concentration in equation (1) is defined as:

$$C = \frac{\tilde{C} - \tilde{C}_{min}}{\tilde{C}_0 - \tilde{C}_{min}} \tag{5}$$

where $\tilde{C}_0$ is the concentration of oxygen at the free surface (assumed to be the same as the initial oxygen concentration), and $\tilde{C}_{\min}$ is a minimum concentration of oxygen required for the bacteria to be active. This model assumes that the cells always have enough oxygen to remain active, i.e. $C > 0$.

The term $\nabla \cdot (n\mathbf{V})$ in equation (2) describes the contribution of the cell swimming along the oxygen gradient. The cell swimming velocity $\mathbf{V}$ is represented as:

$$\mathbf{V} = bW_c \nabla C \tag{6}$$

where $b\mathrm{W}_c$ is a constant that refers to the directional aspect of cell swimming along the oxygen gradient.

Equations (1)–(4) are simplified in Becker et al. (2004) by using the boundary layer approximation and solved subject to the following boundary conditions. Utilizing symmetry about $r = 0$, the following boundary conditions are imposed in the center of the plume, at $r = 0$:

$$\frac{\partial n}{\partial r} = 0, \quad \frac{\partial C}{\partial r} = 0, \quad u = 0, \quad \frac{\partial \mathrm{v}}{\partial r} = 0 \tag{7}$$

where r is the radial coordinate, u is the radial filtration velocity, and v is the streamwise filtration velocity (see Fig. 1).

At $r \to \infty$ the following boundary conditions are imposed:

$$n \to 0, \quad \frac{\partial C}{\partial r} \to 0, \quad \mathrm{v} \to 0 \tag{8}$$

In addition, the following inlet conditions are imposed. Axial velocity and cell concentration are uniform inside the plume and zero outside the plume:

$$z = 0, \quad r \le R_0 : \quad \mathrm{v} = \mathrm{v}_0 \quad n = n_0 \tag{9}$$

$$z = 0, \quad r \ge R_0 : \quad \mathrm{v} = 0 \quad n = 0 \tag{10}$$

where z is the streamwise coordinate (see Fig. 1).

The radial velocity at $z = 0$ is zero:

$$z = 0 : \quad u = 0 \tag{11}$$

The terms R_0, n_0, and v_0 represent inlet values of plume radius, cell concentration, and axial velocity, respectively.

2.3 Numerical Results

In Becker et al. (2004) the governing equations are discretized by using a conservative finite-difference scheme. The following dimensionless variables are utilized:

$$\bar{u} = \frac{u}{\mathrm{v}_0},\ \bar{\mathrm{v}} = \frac{\mathrm{v}}{\mathrm{v}_0},\ \bar{r} = \frac{r}{R_0},\ \bar{z} = \frac{z}{R_0},\ \bar{n} = \frac{n}{n_0}$$
$$\mathrm{Pe} = \frac{\mathrm{W}_c b}{D_n},\ \mathrm{Pe}_0 = \frac{\mathrm{v}_0 R_0}{D_c},\ \mathrm{Pe}_\mathrm{n} = \frac{\mathrm{v}_0 R_0}{D_n},\ \alpha = \frac{\theta\ \Delta\rho\ g n_0 K}{\mu\ \mathrm{v}_0},\ \bar{\gamma} = \frac{\gamma_0 R_0^2}{D_c}\frac{n_0}{\Delta C} \tag{12}$$

A fully implicit scheme is used to obtain the steady state solutions of cell and oxygen concentrations and of the axial velocity profile. An iterative line-by-line tridiagonal matrix algorithm is used to solve the nonlinear discretized equations.

Figure 2a shows the dimensionless cell concentrations and axial velocity profiles at different depths. Cell concentrations are highest at the center. The velocities and cell concentrations at the center of the plume decrease with depth. Conversely the plume width increases with depth. Figure 2b shows the oxygen concentrations at various depths. Due to oxygen consumption, the oxygen concentrations inside the plume decrease with depth. The location of lowest oxygen concentration corresponds with the location of the highest cell concentration, which occurs at the center of the plume. Figure 2c shows the dimensionless radial velocity at various depths. The magnitudes of the radial velocity are much smaller than corresponding axial velocities inside the plume. Radial velocities are positive inside the plume (the plume spreads and axial velocities are decreasing with depth) and negative outside the plume (the fluid outside the plume is drawn into the plume).

The oxygen consumption term, $\bar{\gamma}$, represents the strength of oxygen consumption by the cells. Obviously as this term is increased, the oxygen concentration should decrease. The computational results of the effect of changing $\bar{\gamma}$ on oxygen concentration are depicted in Fig. 3b. As expected, higher values of $\bar{\gamma}$ result in lower oxygen concentrations throughout the plume. Figure 3a shows the effect of this term on the plume profile at $\bar{z} = 12$. For small magnitudes of the cell consumption term, the effect on the plume profile is negligible. The wider profile for large $\bar{\gamma}$ reflects cell swimming along the radial oxygen gradient that results from very strong oxygen consumption by the cells. In Fig. 3c the radial cell swimming is reflected in an outward shift of the dimensionless radial velocity curve for large $\bar{\gamma}$.

3 The Onset of Bio-thermal Convection in a Porous Medium

This section investigates the interaction between bioconvection caused by motile microorganisms and natural convection caused by heating from below in a horizontal layer occupied by a fluid saturated porous medium. This problem may be relevant to a number of geophysical and engineering applications. One example is modeling the behavior of motile thermophilic microorganisms that live in hot springs. The stability of bio-thermal convection in a suspension of gyrotactic microorganisms in a clear fluid layer (with no porous obstacles) is investigated in Kuznetsov (2005a) while a stability problem in a suspension of oxytactic bacteria is solved in Kuznetsov (2005b). Corresponding stability problems in a

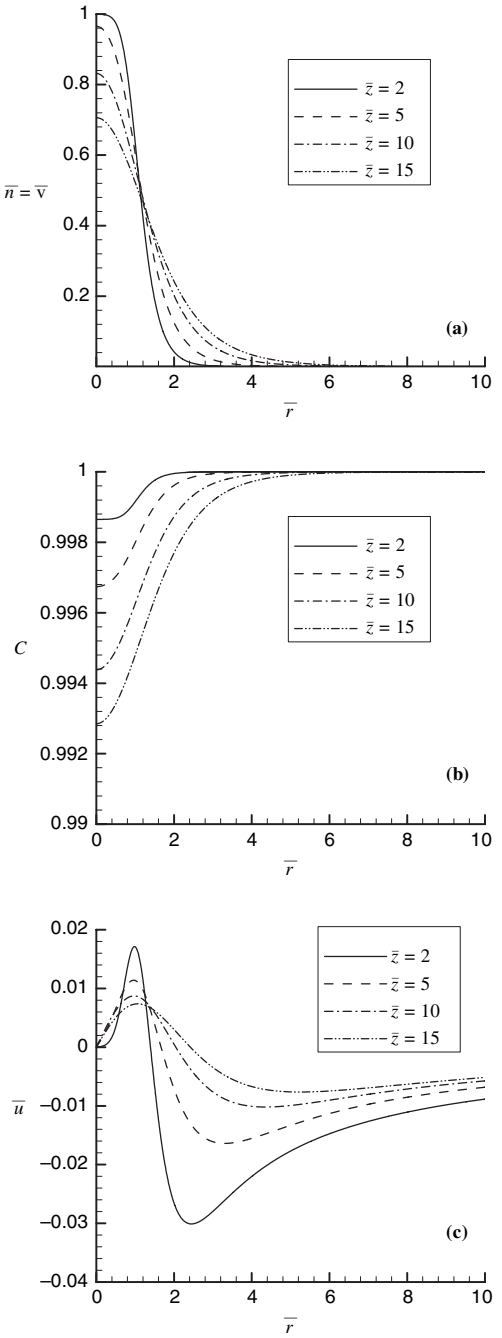

Fig. 2 Depth effects: (**a**) Dimensionless cell concentration, $\bar{n}$, dimensionless axial velocity, $\bar{v}$; (**b**) Dimensionless oxygen concentration, C; (**c**) Dimensionless radial velocity, $\bar{u}$; $Pe = 10$, $Pe_n = Pe_0 = 57.5$, $\bar{\gamma} = 0.04$

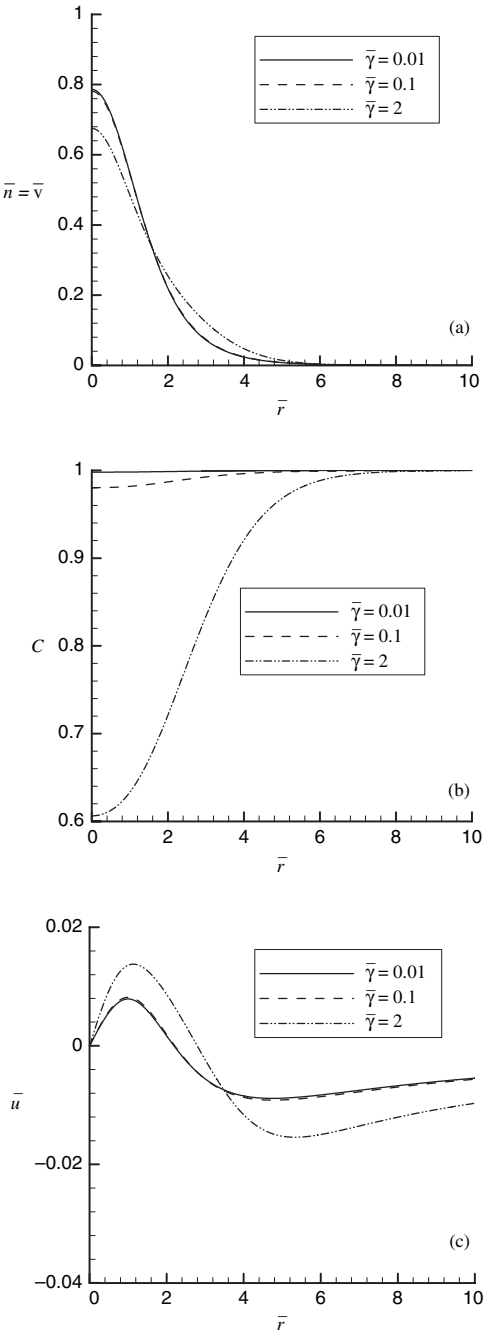

Fig. 3 Effects of oxygen consumption term, $\bar{\gamma}$: (**a**) Dimensionless cell concentration, $\bar{n}$, dimensionless axial velocity, $\bar{v}$; (**b**) Dimensionless oxygen concentration, C; (**c**) Dimensionless radial velocity, $\bar{u}$; $\bar{z} = 12$, $Pe_n = Pe_0 = 57.5$, $Pe = 10$

porous layer are investigated in Kuznetsov (2006a) for gyrotactic microorganisms and in Kuznetsov (2006b) for oxytactic microorganisms. Oscillatory bio-thermal convection in a fluid layer with cooling from below is investigated in Nield and Kuznetsov (2006).

3.1 The Onset of Bio-thermal Convection in a Suspension of Gyrotactic Microorganisms

Gyrotactic microorganisms, such as *Dunaliella, Chlamydomonas*, *Volvox*, and *Peridinium* (Pedley et al., 1988), swim in a particular direction due to the balance of gravitational and viscous torques. It is assumed that heating from below is sufficiently weak, so that it does not kill microorganisms and does not affect their gyrotactic behavior.

3.1.1 Governing Equations

The model presented here is based on a continuum model of a suspension of gyrotactic microorganisms developed in Pedley et al. (1988), which is supplemented by an energy equation and a buoyancy term in the momentum equation that results from the temperature variation across the layer. Governing equations for a porous medium are obtained by volume averaging these equations. The volume averaging procedure is described in detail in Whitaker (1999). This procedure results in the replacement of the Laplacian viscous terms with the Darcian terms that describe viscous resistance in a porous medium (Nield and Bejan, 2006). Also, the Boussinesq approximation is utilized. The resulting governing equations are:

$$c_a \rho_w \frac{\partial \boldsymbol{U}}{\partial t} = -\nabla p - \frac{\mu}{K}\boldsymbol{U} + n\theta \Delta\rho \boldsymbol{g} - \rho_w \beta (T - T_0)\boldsymbol{g} \tag{13}$$

$$\nabla \cdot \boldsymbol{U} = 0 \tag{14}$$

$$\varphi \frac{\partial n}{\partial t} = -\mathrm{div}(\boldsymbol{j}) \tag{15}$$

$$c_p \rho_w \left(\frac{\partial T}{\partial t} + \boldsymbol{U} \cdot \nabla T \right) = k \nabla^2 T \tag{16}$$

where

$$\boldsymbol{j} = n\boldsymbol{U} + n W_c \hat{\boldsymbol{p}} - D \nabla n \tag{17}$$

where c_a is the acceleration coefficient introduced by Nield and Bejan (2006), it depends on the geometry of the porous medium and is determined mainly by the nature of the pore channels of the largest cross sections (in narrow pore channels

the transients decay more rapidly); c_p is the specific heat of water, D is the effective diffusivity of microorganisms in the porous medium (this assumes that all random motions of microorganisms can be approximated by a diffusive process); $\mathbf{j}$ is the flux of microorganisms; k is the effective thermal conductivity of the porous medium; n the number density of motile microorganisms; $\hat{\boldsymbol{p}}$ is the unit vector indicating the direction of swimming of microorganisms; t is the time; T is the temperature; $\boldsymbol{U}$ is the fluid filtration velocity vector, (u, v, w); $W_c\,\hat{\boldsymbol{p}}$ is the vector of average swimming velocity relative to the fluid in the porous medium (W_c is assumed to be constant); x, y, and z are the Cartesian coordinates (z is the vertical coordinate); β is the volume expansion coefficient of water at constant pressure; ρ_w is the density of water; and φ is the porosity.

Porosity φ is involved in the first term on the left-hand side of equation (15) because in the porous medium, the concentration of cells (unlike the heat) is advected/convected with the intrinsic velocity (not the Darcy filtration velocity) since the cells cannot pass through the solid phase. An extra factor φ has been incorporated into the effective transport coefficients for the porous medium, D and W_c, in equation (17).

3.1.2 Boundary Conditions

A horizontal porous medium of depth H is considered (Fig. 4). Cartesian axes with the z-axis vertical are utilized, so that the layer is confined between $z = 0$ and $z = H$. It is assumed that the layer is unbounded in the x and y directions.

At the bottom of the layer (assumed to be rigid) the following conditions are satisfied:

$$\text{At } z = 0: \; w = 0, \qquad T = T_0 + \Delta T, \; \boldsymbol{j} \cdot \hat{\boldsymbol{k}} = 0 \tag{18}$$

where $\hat{\boldsymbol{k}}$ is the vertically-upward unit vector.

At the upper surface of the layer (assumed to be rigid as well) the following conditions are satisfied:

$$\text{At } z = H: \; w = 0, \quad T = T_0, \qquad \boldsymbol{j} \cdot \hat{\boldsymbol{k}} = 0 \tag{19}$$

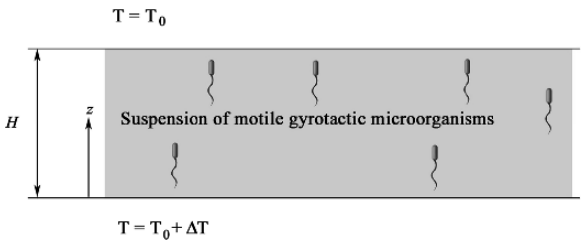

Fig. 4 Schematic diagram for the onset of bio-thermal convection in a porous layer saturated by a dilute suspension of gyrotactic microorganisms

3.1.3 Basic State

The equation of continuity admits a steady-state solution where the fluid is motionless and n_b, the number density of the microorganisms in the basic state, p_b, the pressure in the basic state, and T_b, the temperature in the basic state, are functions of z only.

In this case equations (15) and (17) reduce to

$$n_b W_c = D\frac{\partial n_b}{\partial z}. \tag{20}$$

The solution of this equation is

$$n_b(z) = \nu \exp\left(\frac{W_c z}{D}\right). \tag{21}$$

The integration constant ν, which represents the value of the basic number density at the bottom of the layer, is related to the average concentration $\bar{n}$ by

$$\bar{n} = \frac{1}{H}\int_0^H n_b(z)\,dz = \frac{\nu}{H}\int_0^H \exp\left(\frac{W_c z}{D}\right)dz, \tag{22}$$

and so is given by

$$\nu = \frac{\bar{n}\mathrm{Q}}{\exp(\mathrm{Q}) - 1}, \tag{23}$$

where the bioconvection Péclet number Q is defined by

$$Q = \frac{W_c H}{D}. \tag{24}$$

From equations (16), (18), and (19) the temperature distribution in the basic state is

$$T_b = T_0 + \Delta T\left(1 - \frac{z}{H}\right) \tag{25}$$

Finally, from equation (13), assuming that $p = p_0$ at $z = H$, the pressure distribution in the basic state is found to be

$$p_b = p_0 + \nu\theta\Delta\rho g\frac{D}{W_c}\left[\exp(Q) - \exp\left(\frac{W_c z}{D}\right)\right] - \rho_w g\beta\Delta T\left(H - z - \frac{1}{2H}\left(H^2 - z^2\right)\right) \tag{26}$$

3.1.4 Linear Stability Analysis

The perturbations for n, $\boldsymbol{U}$, p, T, and $\hat{\boldsymbol{p}}$ are introduced as (for example):

$$n(t, x, y, z) = n_b(z) + \varepsilon n^*(t, x, y, z) \tag{27}$$

where asterisk denotes a perturbation quantity and ε is the small perturbation amplitude. Substituting equation (27) and analogous equations for $\boldsymbol{U}$, p, T, and $\hat{\boldsymbol{p}}$ into equations (13)–(16), linearizing, and eliminating u^*, v^*, and p^* (for details see Kuznetsov, 2006a) results in the following equations for perturbations:

$$c_p \rho_w \left(\frac{\partial T^*}{\partial t} - w^* \frac{\Delta T}{H} \right) = k \left(\frac{\partial^2 T^*}{\partial x^2} + \frac{\partial^2 T^*}{\partial y^2} + \frac{\partial^2 T^*}{\partial z^2} \right) \tag{28}$$

$$\begin{aligned} & c_a \rho_w \frac{\partial}{\partial t} \left(\frac{\partial^2 w^*}{\partial x^2} + \frac{\partial^2 w^*}{\partial y^2} + \frac{\partial^2 w^*}{\partial z^2} \right) \\ & = -\theta \Delta\rho g \left(\frac{\partial^2 n^*}{\partial x^2} + \frac{\partial^2 n^*}{\partial y^2} \right) + \rho_w g \beta \left(\frac{\partial^2 T^*}{\partial x^2} + \frac{\partial^2 T^*}{\partial y^2} \right) \\ & \quad - \frac{\mu}{K} \left(\frac{\partial^2 w^*}{\partial x^2} + \frac{\partial^2 w^*}{\partial y^2} + \frac{\partial^2 w^*}{\partial z^2} \right) \end{aligned} \tag{29}$$

$$\begin{aligned} & \varphi \frac{\partial n^*}{\partial t} = -w^* \frac{\partial n_b}{\partial z} - W_c \frac{\partial n^*}{\partial z} \\ & + W_c B n_b \left((1 - \alpha_0) \left(\frac{\partial^2 w^*}{\partial x^2} + \frac{\partial^2 w^*}{\partial y^2} \right) + (1 + \alpha_0) \frac{\partial^2 w^*}{\partial z^2} \right) + D \nabla^2 n^* \end{aligned} \tag{30}$$

where

$$\alpha_0 = \frac{a^2 - b^2}{a^2 + b^2} \tag{31}$$

$$B = \frac{\alpha_\perp \mu}{2 h \rho_0 g}, \tag{32}$$

a and b being the semi-major and -minor axes of the spheroidal cell, so α_0 is related to cell eccentricity; B is the "gyrotactic orientation parameter" which was introduced by Pedley and Kessler (1987) and which has dimensions of time; $\alpha_\perp$ being a dimensionless constant relating viscous torque to the relative angular velocity of the cell; while h is the displacement of the center of mass of the cell from the center of buoyancy.

A normal mode expansion is introduced in the following form:

$$[w^*, n^*, T^*] = [W(z), N(z), \Theta(z)] f(x, y) \exp(\sigma t) \tag{33}$$

Function $f(x, y)$ satisfies the following equation:

$$\frac{\partial^2 f}{\partial x^2} + \frac{\partial^2 f}{\partial y^2} = -m^2 f, \tag{34}$$

where m is the horizontal wavenumber (used as a separation constant).

Substituting equation (33) into equations (28)–(30), and accounting for equation (34), the following equations for the amplitudes W, Θ, and N are obtained:

$$\theta \Delta \rho g m^2 N + \left(\frac{\mu}{K} - c_a \rho\, \sigma\right) m^2 W - \rho_w g \beta m^2 \Theta - \left(\frac{\mu}{K} - c_a \rho\, \sigma\right) W'' = 0, \tag{35}$$

$$- c_p \Delta T \rho_w W + H\left[\left(k m^2 + c_p \rho_w \sigma\right)\Theta - k\Theta''\right] = 0, \tag{36}$$

$$D\left(D m^2 + \sigma\varphi\right) N + D(W_c N' - D N'')$$

$$- \exp\left(\frac{W_c z}{D}\right) W_c \nu\left[-\left(1 + BDm^2\left(1 - \alpha_0\right)\right) W + BD\left(1 + \alpha_0\right) W''\right] = 0. \tag{37}$$

It is now convenient to put equations (35)–(37) in non-dimensional form. The following scalings are introduced:

$$\bar{z} = \frac{z}{H}, \bar{m} = mH, \bar{W} = \left(\frac{\nu\theta H}{a}\right) W, \bar{N} = N\theta, \bar{\Theta} = \left(\frac{\nu\theta}{\Delta T}\right)\Theta \tag{38}$$

The dimensionless parameters are defined by

$$Ra = \frac{g\beta\Delta T H^3 \rho_w^2 c_p}{\mu k}, Rb = \frac{\Delta\rho g \nu\theta H^3}{\mu D}, Da = \frac{K}{H^2}, G = \frac{DB}{H^2}, Le = \frac{a}{D} \tag{39}$$

where *Ra* is the Rayleigh number, *Rb* is the bioconvection Rayleigh number, *Da* is the Darcy number, *G* is the gyrotaxis number, and *Le* is the Lewis number.

The utilization of the principal of exchange of stabilities (Chandrasekhar, 1961) is warranted for a porous layer heated from below. Although there are two agencies affecting the density in this case (gyrotactic upswimming of microorganisms and heating from below), both of these agencies are destabilizing; therefore, overstability in this system is not possible unless there is cooling of the fluid layer from below (this situation is investigated in Nield and Kuznetsov, 2006). Therefore, σ is set to zero in equations (35)–(37). Transforming everything to dimensionless variables and also setting σ to zero, equations (35)–(37) are recast as:

$$\hat{R}b\,\bar{m}^2\bar{N} + \bar{m}^2\hat{W} - \hat{R}a\,\bar{m}^2\hat{\Theta} - \hat{W}'' = 0 \tag{40}$$

$$-\hat{W} + \bar{m}^2\hat{\Theta} - \hat{\Theta}'' = 0 \tag{41}$$

$$Q^{-1}\bar{m}^2\bar{N} + \bar{N}' - Q^{-1}\bar{N}'' - \exp\left(Q\,\bar{z}\right)\left[-\left(1 + G\,\bar{m}^2\left(1 - \alpha_0\right)\right)\hat{W} + G\left(1 + \alpha_0\right)\hat{W}''\right] = 0 \tag{42}$$

where $\hat{W} = Le\,\bar{W}$, $\hat{\Theta} = Le\,\bar{\Theta}$, and the Raleigh–Darcy numbers (traditional and bioconvection) are defined as:

$$\hat{R}a = Da\,Ra \text{ and } \hat{R}b = Da\,Rb \tag{43}$$

Since both the lower and upper boundaries are assumed rigid, equations (40)–(42) are solved subject to the following boundary conditions:

$$\text{At } \bar{z} = 0 : \hat{W} = 0, \hat{\Theta} = 0, Q\bar{N} = \frac{d\bar{N}}{d\bar{z}} \tag{44}$$

$$\text{At } \bar{z} = 1 : \hat{W} = 0, \hat{\Theta} = 0, Q\bar{N} = \frac{d\bar{N}}{d\bar{z}} \tag{45}$$

For the solution of this system, a simple Galerkin method is employed. Suitable trial functions, satisfying the boundary conditions given by equations (44) and (45), are:

$$W_1 = \bar{z} - \bar{z}^2, \quad \Theta_1 = \bar{z} - \bar{z}^2, \quad N_1 = 2 - Q(1 - 2\bar{z}) - Q^2\left(\bar{z} - \bar{z}^2\right) \tag{46}$$

The utilization of a standard Galerkin procedure (Finlayson, 1972), which involves substituting the trial functions given by equation (46) into equations (40)–(42), calculating the residuals, and making the residuals orthogonal to the relevant trial functions, results in the following equation for the critical Rayleigh number:

$$\begin{aligned}\hat{R}b_{cr} = \min_{\bar{m}} -\Big\{ & Q^2\left(10Q^4 + \bar{m}^2\left(120 - 10Q^2 + Q^4\right)\right)\left(\left(10 + \bar{m}^2\right)^2 - \bar{m}^2\hat{R}a\right)\Big\}\Big/ \\ & \left[30\bar{m}^2\left(10 + \bar{m}^2\right)\left(-10 + Q^2\right)\left\{(4+Q)^2 - G\left(\bar{m}^2(4+Q)^2(-1+\alpha_0) + 4Q^2(1+\alpha_0)\right)\right.\right. \\ & \left.\left. + e^Q\left(-(-4+Q)^2 + G\left(\bar{m}^2(-4+Q)^2(-1+\alpha_0) + 4Q^2(1+\alpha_0)\right)\right)\right\}\right]\end{aligned} \tag{47}$$

3.1.5 Validation

As Q tends to zero, for the case of $\hat{R}a = 0$ and $G = 0$ from equation (47) follows that $Q\,\hat{R}b_{cr} \to 12$ and the corresponding critical wavenumber tends to zero. This coincides exactly with the value given in Table 6.1 of Nield and Bejan (2006) which lists values of critical Rayleigh numbers for various cases. Another test is the case of $\hat{R}b = 0$ (the microorganisms are buoyancy-neutral). In this case equation (47) predicts that $\hat{R}a_{cr} = 40$ at $\bar{m}_{cr} = 3.16$. This is within 1.27% of the exact result of $\hat{R}a_{cr} = 39.49$ and $\bar{m}_{cr} = 3.14$ that follows from Table 6.1 of Nield and Bejan (2006).

3.1.6 Numerical Results

Numerical results are presented for the following representative parameter values. $\alpha_0 = 0.2$, $G = 1$, and $Q = 1$ are adopted for the basic case, and then values of Q and G are varied around unity in Figs. 5 and 6.

Figures 5 and 6 display the effect of the Rayleigh number, $\hat{R}a$, on the critical value of the bioconvection Rayleigh number, $\hat{R}b_{cr}$, and on the critical wavenumber, $\bar{m}_{cr}$. Figure 5 is computed for various fixed values of the bioconvection Péclet number, Q, and Fig. 6 is computed for various fixed values of the gyrotaxis number, G. The decrease of $\hat{R}b_{cr}$ with increase of $\hat{R}a$ means that increasing the temperature variation across the porous layer destabilizes the suspension and helps the development of bioconvection.

As expected, the curves in Figs. 5a and 6a intersect at the point $\left(\hat{R}a, \hat{R}b\right) = (40, 0)$. The curves in Figs. 5b and 6b intersect at the point $\left(\hat{R}a, \bar{m}\right) = (40, 3.16)$. When $\hat{R}a$ exceeds 40, convection develops even in a suspension of buoyancy-neutral microorganisms because of the unstable density stratification caused by heating the porous layer from below. Since physically $\hat{R}b < 0$ is not possible, the region $40 < \hat{R}a \leq 50$ in Figs. 5 and 6 should be considered as that displaying mathematical features of the solution given by equation (47) only.

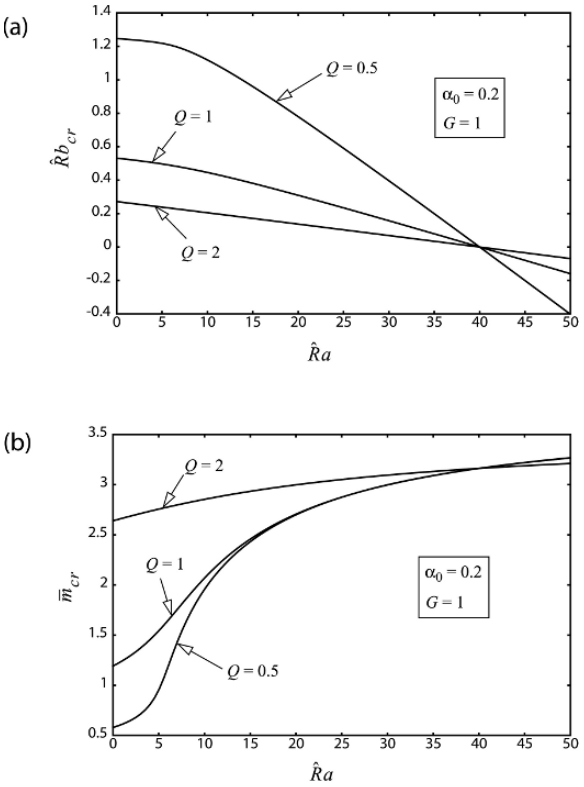

Fig. 5 Effect of the Rayleigh number, $\hat{R}a$, on the critical value of the bioconvection Rayleigh number, $\hat{R}b_{cr}$ (**a**) and on the critical wavenumber, $\bar{m}_{cr}$ (**b**). Different curves correspond to different fixed values of the bioconvection Péclet number, Q

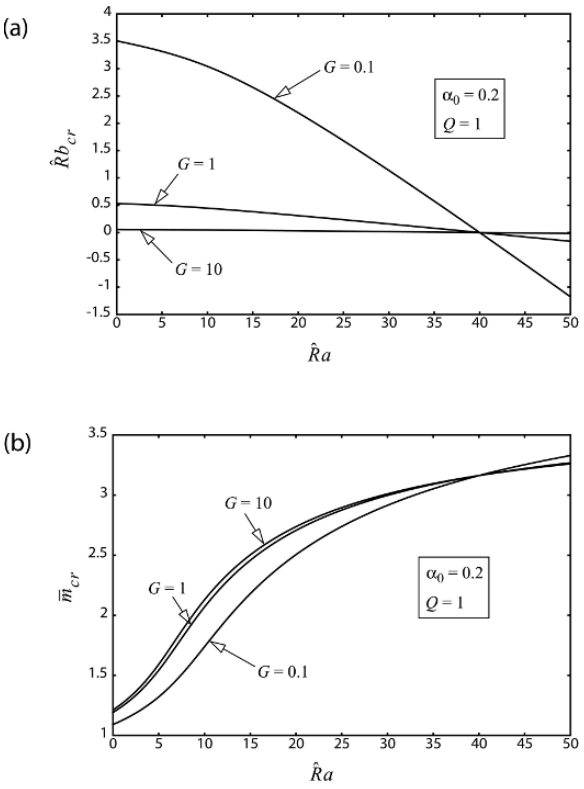

Fig. 6 Effect of the Rayleigh number, $\hat{R}a$, on the critical value of the bioconvection Rayleigh number, $\hat{R}b_{cr}$ (**a**) and on the critical wavenumber, $\bar{m}_{cr}$ (**b**). Different curves correspond to different fixed values of the gyrotaxis number, G

The bioconvection Péclet number, Q, defined by equation (24), characterizes the ratio of the cell swimming speed to the speed of bulk fluid motions. Figure 5a shows that as long as $\hat{R}b > 0$ (which means that microorganisms are heavier than water), and, therefore, their upswimming contributes to creating an unstable density stratification, the increase of Q decreases $\hat{R}b_{cr}$, which means it makes the system less stable. Since larger Q corresponds to faster species of microorganisms, this means that a suspension containing faster swimmers is less stable than a suspension containing slower swimmers.

The gyrotaxis number, G, characterizes the deviation of the cell swimming direction from strictly vertical. If $G = 0$, there is no gyrotaxis and the microorganisms swim vertically upwards (exhibit negative geotaxis). Childress et al. (1975) established that an infinite uniform suspension of negatively geotactic microorganisms ($G = 0$) is stable in the absence of cell concentration stratification. Pedley et al. (1988) have shown that under the same conditions a suspension of gyrotactic microorganisms ($G > 0$) is unstable. Hence, gyrotaxis helps the development of

convection instability. Figure 6a shows that as long as $\hat{R}b > 0$ (microorganisms are heavier than water), the increase of G (the utilization of "more gyrotactic" species of microorganisms) decreases $\hat{R}b_{cr}$, which means it makes the system more unstable.

3.2 The Onset of Bio-thermal Convection in a Suspension of Oxytactic Microorganisms

3.2.1 Governing Equations

The governing equations describing the onset of bio-thermal convection in a suspension of oxytactic bacteria, such as *Bacillus subtilis,* in a porous medium layer are based on a continuum model of a suspension of oxytactic microorganisms developed in Hillesdon and Pedley (1996). This model is supplemented by an energy equation and a buoyancy term in the momentum equation that results from the temperature variation across the layer. The Boussinesq approximation is utilized and the suspension is assumed dilute.

Figure 7 displays a schematic diagram of the problem. A horizontal fluid saturated porous layer of depth H confined between $\tilde{z} = 0$ (the top surface) and $\tilde{z} = H$ (the bottom surface) and unbounded in the $\tilde{x}$ and $\tilde{y}$ directions is considered, where $\tilde{z}$ is positively oriented downward. The layer is heated from below and both top and bottom surfaces are assumed to be at uniform temperatures, $\tilde{T}_0$ and $\tilde{T}_0 + \Delta T$, respectively. Heating from below is expected to enhance instability by adding a second destabilizing mechanism to that already existing in a suspension of oxytactic bacteria: bacteria, which are heavier than water, tend to migrate to the regions just below the top surface where the oxygen concentration is the highest, thus creating an unstable density stratification with the maximum density at the top surface. The resulting momentum, continuity, cell conservation, thermal energy, and oxygen conservation equations are:

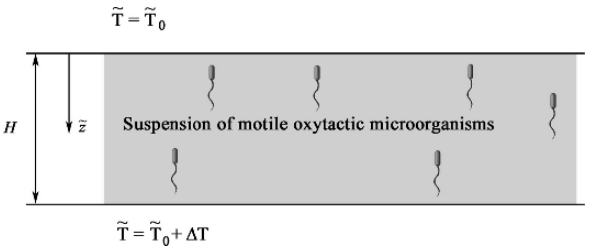

Fig. 7 Schematic diagram for the onset of bio-thermal convection in a porous layer saturated by a dilute suspension of oxytactic microorganisms

$$c_a \rho_w \frac{\partial \tilde{\boldsymbol{U}}}{\partial \tilde{t}} = -\tilde{\nabla} \tilde{p} - \frac{\mu}{K} \tilde{\boldsymbol{U}} + \tilde{n} \theta \Delta \rho \boldsymbol{g} - \rho_w \hat{\beta} \left(\tilde{T} - \tilde{T}_0 \right) \boldsymbol{g} \tag{48}$$

$$\tilde{\nabla} \cdot \tilde{\boldsymbol{U}} = 0 \tag{49}$$

$$\varphi \frac{\partial \tilde{n}}{\partial \tilde{t}} = -\text{div}(\tilde{\boldsymbol{j}}) \tag{50}$$

$$c_p \rho_w \left(\frac{\partial \tilde{T}}{\partial \tilde{t}} + \tilde{\boldsymbol{U}} \cdot \tilde{\nabla} \tilde{T} \right) = k \tilde{\nabla}^2 \tilde{T} \tag{51}$$

$$\varphi \frac{\partial C}{\partial \tilde{t}} + \tilde{\boldsymbol{U}} \cdot \tilde{\nabla} C = D_C \tilde{\nabla}^2 C - \frac{\gamma \tilde{n}}{\Delta \tilde{C}} \tag{52}$$

where

$$\tilde{\boldsymbol{j}} = \tilde{n} \tilde{\boldsymbol{U}} + \tilde{n} \tilde{\boldsymbol{V}} - D_n \tilde{\nabla} \tilde{n} \tag{53}$$

is the flux of microorganisms. D_n in equation (53) is the diffusivity of the microorganisms, $\tilde{n}$ is the number density of motile microorganisms, $\tilde{p}$ is the excess pressure (above hydrostatic); $\tilde{t}$ is the time, $\tilde{\boldsymbol{U}} = (\tilde{u}, \tilde{v}, \tilde{w})$ is the fluid filtration velocity, $\hat{\beta}$ is the volume expansion coefficient of water at constant pressure, $\tilde{T}$ is the temperature, $\tilde{\nabla}^2$ is the Laplacian operator, $-\gamma \tilde{n} / \Delta \tilde{C}$ describes the consumption of oxygen by the microorganisms in the fluid, $\Delta \tilde{C}$ equals $\tilde{C}_0 - \tilde{C}_{\min}$, $\tilde{C}_0$ is the free-surface oxygen concentration, and $\tilde{C}_{\min}$ is the minimum oxygen concentration that microorganisms need in order to be active; tildes denote dimensional variables.

The average directional swimming velocity of a microorganism is approximated as (Hillesdon and Pedley, 1996):

$$\tilde{\boldsymbol{V}} = b W_c \hat{H}(C) \tilde{\nabla} C \tag{54}$$

where b is the chemotaxis constant [m] and W_c is the maximum cell swimming speed [m/s] (the product bW_c is assumed to be constant). The dimensionless oxygen concentration, C, in equation (52) is defined as:

$$C = \frac{\tilde{C} - \tilde{C}_{\min}}{\Delta \tilde{C}} \tag{55}$$

where $\tilde{C}$ is the dimensional oxygen concentration. Since for the shallow layer C is greater than zero throughout the layer thickness, the Heaviside step function, $\hat{H}(C)$, in equation (54) is equal to unity.

3.2.2 Boundary Conditions

In accordance with Fig. 7, the following boundary conditions are imposed at the top surface:

$$\text{At } \tilde{z} = 0 : \tilde{w} = 0, C = 1, \tilde{T} = \tilde{T}_0, \tilde{\mathbf{j}} \cdot \hat{\mathbf{k}} = 0 \tag{56}$$

where $\hat{\mathbf{k}}$ is the vertically-downward unit vector.

At the bottom of the layer (assumed to be rigid) the following conditions are satisfied:

$$\text{At } \tilde{z} = H : \tilde{w} = 0, \frac{\partial C}{\partial \tilde{z}} = 0, \tilde{T} = \tilde{T}_0 + \Delta T, \tilde{\mathbf{j}} \cdot \hat{\mathbf{k}} = 0 \tag{57}$$

where ΔT is positive when heating from below is considered.

3.2.3 Basic State

Dimensionless variables and operators are introduced as follows:

$$n = \tilde{n}/\tilde{n}_0, \quad [x, y, z] = [\tilde{x}, \tilde{y}, \tilde{z}]/H, \quad t = \left(\frac{D_n}{H^2}\right)\tilde{t}, \quad \boldsymbol{U} = \left(\frac{H}{D_n}\right)\tilde{\boldsymbol{U}}, \quad p = \left(\frac{H^2}{\mu D_n}\right)\tilde{p},$$

$$T = \frac{\tilde{T} - \tilde{T}_0}{\Delta T}, \quad \nabla^2 = H^2\tilde{\nabla}^2, \quad \nabla = H^2\tilde{\nabla} \tag{58}$$

where $\tilde{n}_0$ is the average number density of the microorganisms (number density of the microorganisms in a well-stirred suspension) and $\boldsymbol{U} = (u, v, w)$ is the dimensionless fluid filtration velocity.

Dimensionless constants are defined as

$$\delta = D_C/D_n, \quad Pe = bW_c/D_n, \quad \beta = \left(\gamma\, \tilde{n}_0 H^2\right)/\left(D_C \Delta\tilde{C}\right), \quad Le = \frac{D_C c_p \rho_w}{k},$$

$$Sc = \mu/\left(\rho_w D_n\right), \quad Ra = \frac{g\hat{\beta}\Delta T H^3 \rho_w^2 c_p}{\mu\, k}, \quad Rb = \frac{\Delta\rho\theta\tilde{n}_0 g}{\mu D_n} H^3, \quad Da = \frac{K}{H^2} \tag{59}$$

where Da is the Darcy number, Le is the Lewis number, Ra is the traditional Rayleigh number, Rb is the bioconvection Rayleigh number, and Sc is the Schmidt number. β characterizes the ratio of the rate of oxygen consumption to the rate of oxygen diffusion, it can be regarded as a depth parameter. Pe can be regarded as a ratio of two characteristic velocities; one due to oxytactic swimming and the other due to random, diffusive swimming (Hillesdon and Pedley, 1996).

In the basic state the fluid is motionless and cell and oxygen concentrations change in the z-direction only. The solutions for $C_b(z)$ and $n_b(z)$ follow from

Hillesdon and Pedley (1996) and the solution for $T_b(z)$ and $p_b(z)$ are obtained by integrating equations (51) and (48), respectively, with boundary conditions (56) and (57):

$$C_b(z) = 1 - \frac{2}{\mathrm{Pe}} \ln\left(\frac{\cos\{A_1(1-z)/2\}}{\cos\{A_1/2\}}\right), \tag{60}$$

$$n_b(z) = \frac{A_1^2}{2\mathrm{Pe}\beta} \sec^2\left(\frac{A_1}{2}(1-z)\right), \tag{61}$$

$$T_b(z) = z \tag{62}$$

$$p_b(z) = p_0 + Rb\frac{A_1}{\mathrm{Pe}\beta}\left[\tan\left(\frac{A_1}{2}\right) - \tan\left(\frac{A_1}{2}(1-z)\right)\right] - Ra\,\frac{\delta}{Le}\frac{z^2}{2} \tag{63}$$

where $p_0 = H^2\tilde{p}_0/(\mu D_n)$ is the dimensionless pressure at the top surface, $\tilde{p}_0$ is the pressure at the top surface, and the constant A_1 is found from the transcendental equation

$$\tan(A_1/2) = \mathrm{Pe}\beta/A_1 \tag{64}$$

The solution for the basic state given by equations (60)–(63) is valid as long as the dimensionless oxygen concentration is positive throughout the chamber. In Hillesdon and Pedley (1996) it is shown that this condition holds as long as

$$\beta \le \frac{2\phi}{\mathrm{Pe}} \tan^{-1}\phi \tag{65}$$

where

$$\phi^2 = \exp(\mathrm{Pe}) - 1 \tag{66}$$

Since β is proportional to H^2, equation (65) determines the largest layer depth for which the layer can be treated as shallow.

3.2.4 Linear Stability Analysis

The perturbations for n, $\boldsymbol{U}$, p, T, and C are introduced similar to equation (27) (for details see Kuznetsov, 2006b). Substituting these equations into equations (48)–(52), linearizing, and eliminating u^*, v^*, and p^* results in the following equations for perturbations:

$$\varphi\frac{\partial n^*}{\partial t} + w^*\frac{\partial n_b(z)}{\partial z} + Pe\frac{\partial C^*}{\partial z}\frac{\partial n_b(z)}{\partial z} + Pe\frac{\partial C_b(z)}{\partial z}\frac{\partial n^*}{\partial z} + Pe\,n^*(z)\frac{\partial^2 C_b(z)}{\partial z^2} + Pe\,n_b(z)\nabla^2 C^* = \nabla^2 n^* \tag{67}$$

$$\frac{\partial T^*}{\partial t} + w^* = \frac{\delta}{Le}\nabla^2 T^* \tag{68}$$

$$\varphi\frac{\partial C^*}{\partial t} + w^*\frac{\partial C_b(z)}{\partial z} = \delta\nabla^2 C^* - \beta\delta n^* \tag{69}$$

$$\begin{aligned}&\frac{c_a}{Sc}\frac{\partial}{\partial t}\left(\frac{\partial^2 w^*}{\partial x^2} + \frac{\partial^2 w^*}{\partial y^2} + \frac{\partial^2 w^*}{\partial z^2}\right)\\ &= Rb\left(\frac{\partial^2 n^*}{\partial x^2} + \frac{\partial^2 n^*}{\partial y^2}\right) - Ra\frac{\delta}{Le}\left(\frac{\partial^2 T^*}{\partial x^2} + \frac{\partial^2 T^*}{\partial y^2}\right)\\ &-\frac{1}{Da}\left(\frac{\partial^2 w^*}{\partial x^2} + \frac{\partial^2 w^*}{\partial y^2} + \frac{\partial^2 w^*}{\partial z^2}\right)\end{aligned} \tag{70}$$

A normal mode expansion is introduced in the form:

$$[w^*, n^*, T^*, C^*] = [W(z), N(z), \Theta(z), \Xi(z)] f(x, y)\exp(\sigma t) \tag{71}$$

The function $f(x, y)$ satisfies the following equation:

$$\frac{\partial^2 f}{\partial x^2} + \frac{\partial^2 f}{\partial y^2} = -m^2 f \tag{72}$$

where m is the horizontal wavenumber.

Substituting equation (71) into equations (67)–(70), and accounting for equation (72), the following equations for the amplitudes W, Θ, N, and Ξ are obtained:

$$m^2 Da\, Le\, Rb\, Sc\, N - m^2 Le\,(Sc + c_a Da\,\sigma)\, W - m^2 Da\, Ra\, Sc\delta\Theta + Le\,(Sc + c_a Da\,\sigma)\, W'' = 0 \tag{73}$$

$$Le\, W + \left(m^2\delta + Le\sigma\right)\Theta - \delta\,\Theta'' = 0 \tag{74}$$

$$\begin{aligned}&2A_1 Pe\,\beta\tan\left[\frac{1}{2}A_1(z-1)\right]N'(z) + A_1^3\sec^2\left[\frac{1}{2}A_1(z-1)\right]\tan\left[\frac{1}{2}A_1(z-1)\right]\left(W + Pe\,\Xi'\right)\\ &+ 2Pe\beta\left(\left(m^2 + \sigma\varphi\right)N - N''\right) + A_1^2 Pe\sec^2\left[\frac{1}{2}A_1(z-1)\right]\left(\beta N - m^2\Xi + \Xi''\right) = 0\end{aligned} \tag{75}$$

$$Pe\,\beta\,\delta\, N - A_1\tan\left[\frac{1}{2}A_1(1-z)\right]W + Pe\left(m^2\delta + \sigma\varphi\right)\Xi - Pe\delta\,\Xi'' = 0 \tag{76}$$

The utilization of the principal of exchange of stabilities (Chandrasekhar, 1961) is again warranted for a fluid layer heated from below. Although there are two agencies affecting the density in this case (oxytactic upswimming of microorganisms and heating from below), both of these agencies are destabilizing; therefore, overstability in this system is not possible unless there is cooling of the fluid layer from below. Therefore, σ is set to zero in equations (73)–(76). This makes these equations independent of the Schmidt number, Sc. Also, by letting $\Xi \to \beta\bar{\Xi}$, the system (76)–(79) depends on the product $\varpi = Pe\beta$ rather than Pe and β individually. Finally, by letting $\Theta \to Le\bar{\Theta}$, the system (73)–(76) becomes independent of Le. Also, new Rayleigh–Darcy numbers (traditional and bioconvection) are introduced as:

$$\hat{R}a = Da\,Ra \text{ and } \hat{R}b = Da\,Rb \tag{77}$$

Rescaling Ξ and Θ, equations (73)–(76) are recast as:

$$m^2\hat{R}b\,N - m^2 W - m^2\hat{R}a\,\delta\bar{\Theta} + W'' = 0 \tag{78}$$

$$W + m^2\delta\bar{\Theta} - \delta\bar{\Theta}'' = 0 \tag{79}$$

$$2A_1\varpi\tan\left[\frac{1}{2}A_1(z-1)\right]N'(z) + A_1^3\sec^2\left[\frac{1}{2}A_1(z-1)\right]\tan\left[\frac{1}{2}A_1(z-1)\right]\left(W + \varpi\bar{\Xi}'\right)$$
$$+ 2\varpi\left(m^2N - N''\right) + A_1^2\varpi\sec^2\left[\frac{1}{2}A_1(z-1)\right]\left(N - m^2\Xi + \Xi''\right) = 0 \tag{80}$$

$$\varpi\delta N - A_1\tan\left[\frac{1}{2}A_1(1-z)\right]W + \varpi\,m^2\delta\bar{\Xi} - \varpi\delta\bar{\Xi}'' = 0 \tag{81}$$

Equations (78)–(81) are solved subject to the following boundary conditions:

$$\text{At } z = 0: W = 0, \bar{\Xi} = 0, \bar{\Theta} = 0, \varpi\left(n_b|_{z=0}\frac{d\bar{\Xi}}{dz} + \frac{1}{\beta}\frac{dC_b}{dz}\bigg|_{z=0}N\right) - \frac{\partial N}{\partial z} = 0 \tag{82}$$

$$\text{At } z = 1: W = 0, \frac{d\bar{\Xi}}{dz} = 0, \bar{\Theta} = 0, \frac{dN}{dz} = 0 \tag{83}$$

It should be noted that the term $\beta^{-1}dC_b/dz$ in the last equation of (82) depends on ϖ, but does not depend on Pe and β individually.

For the solution of this system, a single term Galerkin method is employed. Suitable trial functions, which satisfy the boundary conditions given by equations (82) and (83), are:

$$W_1 = z - z^2, \quad \bar{\Theta}_1 = z - z^2, \quad N_1 = 1 + \alpha\left(z - \frac{1}{2}z^2\right), \quad \bar{\Xi}_1 = z - \frac{1}{2}z^2 \tag{84}$$

where

$$\alpha = \frac{A_1(A_1 - \sin A_1)}{(1 + \cos A_1)} \tag{85}$$

The utilization of a standard Galerkin procedure (Finlayson, 1972), results in the following equation for the critical bioconvection Rayleigh number:

$$\hat{R}b_{cr} = \min_m\left\{16\varpi\delta\left[\left(10 + m^2\right)^2 - m^2\hat{R}a\right]\right.$$
$$\left.\times\left\{-\frac{\left(2I_3 + m^2A_1^2I_4\varpi\right)\left(5 + 2A_1^2 + 5\cos(A_1) - 2A_1\sin(A_1)\right)}{1 + \cos(A_1)}\right.\right.$$

$$+2\left(5+2m^2\right)\left[I_2+\frac{1}{60}m^2\varpi\sec^4\left(\frac{A_1}{2}\right)\left(45+22A_1^2+4A_1^4+20\left(3+A_1^2\right)\cos\left(A_1\right)\right.\right.$$
$$\left.\left.+\left(15-2A_1^2\right)\cos\left(2A_1\right)-4A_1\left(5+2A_1^2+5\cos\left(A_1\right)\right)\sin\left(A_1\right)\right]\right\}/$$
$$\left\{m^2\left(10+m^2\right)\left[15I_1\left(2I_3+m^2A_1^2I_4\varpi\right)-4\left(5+2m^2\right)I_5\varpi\delta\right]\right.$$
$$\left.\times\left(40+7A_1\sec^2\left(\frac{A_1}{2}\right)\left(A_1-\sin\left(A_1\right)\right)\right)\right\} \tag{86}$$

where the integrals I_1–I_5 (all of which are functions of ϖ only) are given by the following equations:

$$I_1(\varpi)=A_1\int_0^1(2-z)\,(-1+z)\,z^2\tan\left(\frac{1}{2}A_1(1-z)\right)dz \tag{87}$$

$$I_2(\varpi)=\frac{1}{4}A_1\varpi\int_0^1 F(z,\varpi)$$
$$\times\left[A_1\sec^2\left(\frac{A_1}{2}\right)\sec^2\left(\frac{1}{2}A_1(-1+z)\right)\left(2-A_1^2(-2+z)\,z+2\cos\left(A_1\right)+A_1(-2+z)\,z\sin\left(A_1\right)\right)\right.$$
$$\left.+\frac{8\left(A_1-\sin\left(A_1\right)\right)\left(1-A_1(-1+z)\tan\left(\frac{1}{2}A_1(-1+z)\right)\right)}{1+\cos\left(A_1\right)}\right]dz \tag{88}$$

$$I_3(\varpi)=A_1^2\varpi\int_0^1\sec^2\left(\frac{1}{2}A_1(-1+z)\right)F(z,\varpi)\left(-1-A_1(-1+z)\tan\left(\frac{1}{2}A_1(-1+z)\right)\right)dz \tag{89}$$

$$I_4(\varpi)=\int_0^1(-2+z)\,z\,\sec^2\left(\frac{1}{2}A_1(-1+z)\right)F(z,\varpi)\,dz \tag{90}$$

$$I_5(\varpi)=-A_1^3\int_0^1(-1+z)\,z\,\sec^2\left(\frac{1}{2}A_1(-1+z)\right)\left(1+\frac{A_1\left(z-0.5z^2\right)\left(A_1-\sin\left(A_1\right)\right)}{1+\cos\left(A_1\right)}\right)$$
$$\times\tan\left(\frac{1}{2}A_1(-1+z)\right)dz \tag{91}$$

where

$$F(z,\varpi)=1+\frac{1}{4}A_1(-2+z)\,z\,\sec^2\left(\frac{A_1}{2}\right)\left(-A_1+\sin\left(A_1\right)\right) \tag{92}$$

3.2.5 Validation

For the case of $\hat{R}b=0$ (the microorganisms are buoyancy-neutral), equation (86) predicts that $\hat{R}a_{cr}=40$ at $m_{cr}=3.16$. This is within 1.27% of the exact result of $\hat{R}a_{cr}=39.48$ and $m_{cr}=3.14$ that follows from Table 6.1 of Nield and Bejan (2006).

3.2.6 Numerical Results

For computations, $\varpi = Pe\beta = 1$ and $\delta = 1$ are adopted for the basic case, and then values of ϖ and δ are varied around unity in Figs. 8 and 9.

Figure 8 displays the effect of the Rayleigh number, $\hat{R}a$, on the critical value of the bioconvection Rayleigh number, $\hat{R}b_{cr}$, and on the critical wavenumber, m_{cr}. Figure 8 is computed for three fixed values of ϖ: 0.1, 1, and 10. The decrease of $\hat{R}b_{cr}$ with increase of $\hat{R}a$ means that increasing the temperature variation across the porous layer destabilizes the suspension and helps the development of bioconvection. As expected, the curves in Fig. 8a intersect at the point $\left(\hat{R}a, \hat{R}b\right) = (40, 0)$. The curves in Fig. 8b intersect at the point $\left(\hat{R}a, m\right) = (40,\ 3.16)$. When $\hat{R}a$ exceeds 40, convection develops even in a suspension of buoyancy-neutral microorganisms because of the unstable density stratification caused by heating the porous layer from below.

Hillesdon and Pedley (1996) interpreted ϖ as a depth parameter; larger values of ϖ correspond to a steeper free-surface density gradient in the basic state. It is

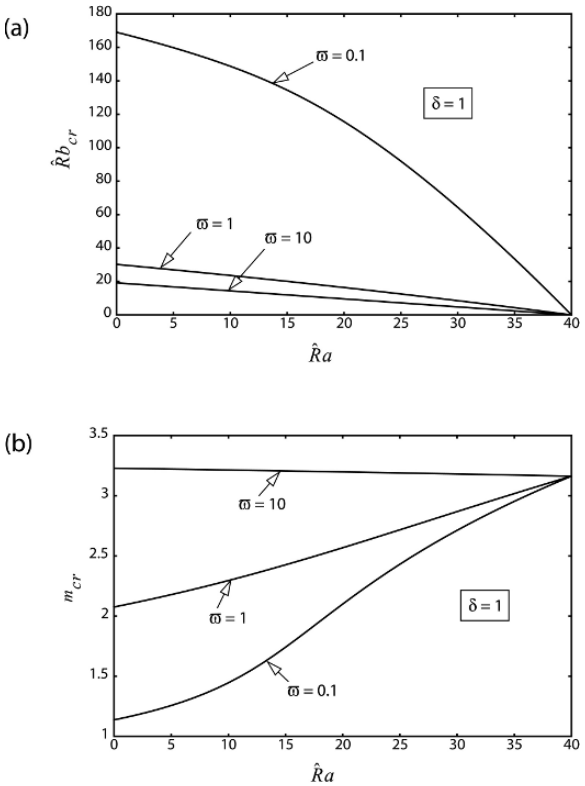

Fig. 8 Effect of the traditional "thermal" Rayleigh number, $\hat{R}a$, on the critical value of the bioconvection Rayleigh number, $\hat{R}b_{cr}$ (**a**) and on the critical horizontal wavenumber, m_{cr} (**b**). Different curves correspond to different fixed values of ϖ

expected that a steeper free-surface density gradient leads to a more unstable system, which explains the decrease of $\hat{R}b_{cr}$ with the increase of ϖ, as observed in Fig. 8a.

Figures 9 displays the effect of δ on $\hat{R}b_{cr}$ and m_{cr}. This figure is computed for five fixed values of $\hat{R}a$: 0, 10, 20, 30, and 40. δ characterizes the ratio of oxygen diffusivity to that of microorganisms (the diffusivity of microorganisms is mostly due to the random component in their swimming). From Fig. 9a it is clear that $\hat{R}b_{cr}$ first increases rapidly as δ increases, but then approaches an asymptotic limit. It should be noted that in a shallow chamber (considered here) the oxygen and cell concentrations in the basic state (given by equations (60) and (61) respectively) depend on ϖ but do not depend on δ. The increase of $\hat{R}b_{cr}$ when increasing δ is consistent with the findings of Hillesdon and Pedley (1996) for small values of δ (see Fig. 7(a) in Hillesdon and Pedley, (1996)); however, the maximum that the dependence $\hat{R}b_{cr}(\delta)$ takes on at a certain value of δ is not observed in Fig. 9a; this may be due to what the porous medium brings to the problem.

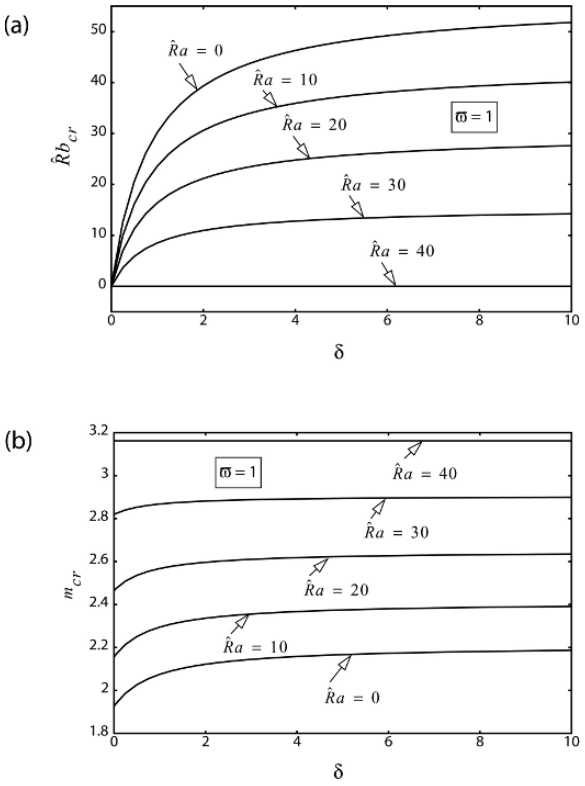

Fig. 9 Effect of δ on the critical value of the bioconvection Rayleigh number, $\hat{R}b_{cr}$ (**a**) and on the critical wavenumber, m_{cr} (**b**). Different curves correspond to different fixed values of $\hat{R}a$

4 Effect of Vertical Vibration on the Onset of Bioconvection in a Horizontal Porous Layer of Finite Depth

4.1 Problem Description

A capability to control bioconvection may be important in certain bioengineering and pharmaceutical applications as well as in lab experiments. Recent investigations (Cisse et al., 2004; Bardan and Mojtabi, 2000; Bardan et al., 2001, 2004; Mojtabi et al., 2004) indicate that vibration is an effective way of controlling the stability of thermal and thermo-solutal convection. This section analyses the potential of using vibration for controlling the stability of bioconvection. Since there is no experimental research on the effect of vibration on oxytactic behavior of microorganisms, it is assumed that vertical vibration imposed on the system changes neither the oxytactic behavior of microorganisms nor their average swimming speed. This assumption is reasonable because the vibration considered in this research is assumed to be high-frequency and low-amplitude.

Effects of high-frequency vibration on the stability of suspensions of negatively geotactic and oxytactic microorganisms in a fluid layer of final depth are investigated in Kuznetsov (2005d, 2006c), respectively. Kuznetsov (2006d) investigated the effect of vibration on stability of a fluid saturated porous layer that contains oxytactic bacteria.

4.2 Governing Equations

Governing equations for this problem are obtained by volume averaging equations developed in Hillesdon and Pedley (1996) and extending the resulting governing equations to account for gravity modulation. The momentum, continuity, cell conservation, and oxygen conservation equations are

$$c_a \rho_w \frac{\partial \tilde{\boldsymbol{U}}}{\partial \tilde{t}} = -\tilde{\nabla}\tilde{p} - \frac{\mu}{K}\tilde{\boldsymbol{U}} + \boldsymbol{g}'\tilde{n}\theta\Delta\rho \tag{93}$$

$$\tilde{\nabla}\cdot\tilde{\boldsymbol{U}} = 0 \tag{94}$$

$$\varphi\frac{\partial \tilde{n}}{\partial \tilde{t}} = -\mathrm{div}(\tilde{\boldsymbol{j}}) \tag{95}$$

$$\varphi\frac{\partial C}{\partial \tilde{t}} + \tilde{\boldsymbol{U}}\cdot\tilde{\nabla}C = D_C\tilde{\nabla}^2 C - \frac{\gamma\tilde{n}}{\Delta\tilde{C}} \tag{96}$$

where

$$\boldsymbol{g}' = \boldsymbol{g} + \left(\hat{b}\Omega^2\cos\Omega\tilde{t}\right)\boldsymbol{k} \tag{97}$$

$\hat{b}$ is the vibration amplitude, $\boldsymbol{K}$ is the vertically-downward unit vector in the $\tilde{z}$-direction, $\tilde{\boldsymbol{U}}$ is the fluid convection velocity vector (induced by bioconvection and vibration), and Ω is the angular frequency of vibration. Tildes on variables

indicate dimensional quantities. $\tilde{\boldsymbol{j}}$ and $\tilde{\boldsymbol{V}}$ are defined by equations (53) and (54), respectively.

For the case of high-frequency vibration the governing equations can be dramatically simplified by utilizing the averaging method described in Gershuni and Lyubimov (1998). This method allows obtaining the equations for the mean flow; it is valid if the following assumptions are satisfied (Bardan et al., 2001): (i) the frequency is sufficiently high (but not acoustic), so that the vibration period is small compared to all the characteristic hydrodynamic times; (ii) the vibration amplitude is small so that the inertial terms involving the *rapidly varying* velocity component can be neglected. Mathematical justification of the averaging method is given in Simonenko (1972).

Utilizing the averaging method, solutions of equations (93)–(96) are decomposed into two components (the first component varies slowly with time and the second component varies rapidly with time), as follows:

$$\tilde{\boldsymbol{U}} = \bar{\boldsymbol{U}}\left(\tilde{t}\right) + \boldsymbol{U}'\left(\Omega\tilde{t}\right), \tilde{p} = \bar{p}\left(\tilde{t}\right) + p'\left(\Omega\tilde{t}\right), \tilde{n} = \bar{n}\left(\tilde{t}\right) + n'\left(\Omega\tilde{t}\right), C = \bar{C}\left(\tilde{t}\right) + C'\left(\Omega\tilde{t}\right) \tag{98}$$

where overbar denotes the mean, or average, component and prime denotes the pulsating component.

Utilizing the procedure described in Gershuni and Lyubimov (1998), the following dimensionless averaged equations for the mean components are obtained:

$$\frac{c_a}{Sc}\frac{\partial \boldsymbol{U}}{\partial t} = -\nabla p - \frac{1}{Da}\boldsymbol{U} + \boldsymbol{k}Rbn + Rv\left(\boldsymbol{w}\cdot\nabla\right)\left(n\boldsymbol{k} - \boldsymbol{w}\right) \tag{99}$$

$$\nabla\cdot\boldsymbol{U} = 0 \tag{100}$$

$$\varphi\frac{\partial n}{\partial t} = -\mathrm{div}(n\boldsymbol{U} + nPe\nabla\bar{C} - \nabla n) \tag{101}$$

$$\varphi\frac{\partial \bar{C}}{\partial t} + \boldsymbol{U}\cdot\nabla\bar{C} = \Gamma\nabla^2\bar{C} - \beta\Gamma n \tag{102}$$

$$\mathrm{div}\,\boldsymbol{w} = 0 \tag{103}$$

$$\mathrm{curl}\,\boldsymbol{w} = \nabla n\times\boldsymbol{k} \tag{104}$$

where dimensionless variables and operators are introduced as follows:

$$n = \bar{n}/\tilde{n}_0, \quad [x, y, z] = [\tilde{x}, \tilde{y}, \tilde{z}]/H, \quad t = \left(\frac{D_n}{H^2}\right)\tilde{t}, \quad \boldsymbol{U} = \left(\frac{H}{D_n}\right)\bar{\boldsymbol{U}},$$
$$p = \left(\frac{H^2}{\mu D_n}\right)\bar{p},$$
$$\boldsymbol{w} = \bar{\boldsymbol{w}}/\tilde{n}_0, \quad \nabla^2 = H^2\,\tilde{\nabla}^2, \quad \nabla = H\,\tilde{\nabla} \tag{105}$$

and dimensionless constants are defined as

$$\Gamma = D_C/D_n,\ Pe = bW_c/D_n,\ \beta = \left(\gamma \tilde{n}_0 H^2\right)/\left(D_C \Delta C\right),\ Rv = \frac{\rho_w H^2 n_0^2}{\mu D_n}\hat{\delta},$$

$$Sc = \mu/\left(\rho_w D_n\right),\ Rb = \frac{\Delta\rho\theta\tilde{n}_0 g}{\mu D_n}H^3,\ Da = K/H^2 \tag{106}$$

where Da is the Darcy number, Rv is the vibration Rayleigh number, Rb is the bioconvection Rayleigh number, and Sc is the Schmidt number. β characterizes the ratio of the rate of oxygen consumption to the rate of oxygen diffusion, it can be regarded as a depth parameter. Pe can be regarded as a ratio of two characteristic velocities; one due to oxytactic swimming and the other due to random, diffusive swimming (Hillesdon and Pedley (1996).

4.3 Boundary Conditions

A horizontal fluid layer of depth H is considered. Cartesian axes with the $\tilde{z}$-axis directed vertically downward are utilized (see Fig. 10), so that the layer is confined between $\tilde{z} = 0$ (top of the layer) and $\tilde{z} = H$ (bottom of the layer). It is assumed that the layer is unbounded in the $\tilde{x}$ and $\tilde{y}$ directions.

At the bottom of the layer the following conditions are satisfied:

$$\text{At } \tilde{z} = H:\ \bar{\boldsymbol{U}} \cdot \boldsymbol{k} = 0,\ \boldsymbol{j} \cdot \boldsymbol{k} = 0,\ \frac{\partial \bar{C}}{\partial \tilde{z}} = 0,\ \bar{\boldsymbol{w}} \cdot \boldsymbol{k} = 0 \tag{107}$$

At the top of the layer the following conditions are satisfied:

$$\text{At } \tilde{z} = 0:\ \bar{\boldsymbol{U}} \cdot \boldsymbol{k} = 0,\ \boldsymbol{j} \cdot \boldsymbol{k} = 0,\ \frac{\partial \bar{C}}{\partial \tilde{z}} = 0,\ \bar{\boldsymbol{w}} \cdot \boldsymbol{k} = 0 \tag{108}$$

The last equation in (107) and (108) follows from the requirement that the solenoidal part of the contribution of the cell concentration to the gravity force, $\bar{\boldsymbol{w}}$, must satisfy the impermeable boundary condition at the upper and lower surfaces of the domain.

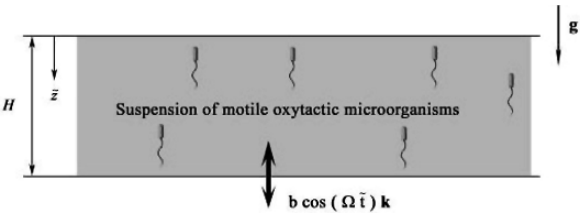

Fig. 10 Schematic diagram for the onset of bioconvection in a porous layer saturated by a suspension of oxytactic microorganisms subjected to low-amplitude high-frequency vertical vibration

4.4 Basic State

The governing equations admit the following steady-state solution where the fluid is motionless, $\boldsymbol{w}_b = 0$, and n_b, $\bar{C}_b$ and p_b are functions of z only. The solutions for $\bar{C}_b$ and n_b follow from Hillesdon and Pedley (1996) and are given by equations (60) and (61), respectively.

The pressure distribution is given by:

$$p_b(z) = p_0 + Rb\frac{A_1}{Pe\beta}\left[\tan\left(\frac{A_1}{2}\right) - \tan\left(\frac{A_1}{2}(1-z)\right)\right] \tag{109}$$

4.5 Linear Stability Analysis

The perturbations for $\bar{C}$, n, $\boldsymbol{U}$, $\boldsymbol{w}$, and p are introduced similar to equation (27) (for details see Kuznetsov, 2006d). Substituting these equations into equations (99)–(104), linearizing, and eliminating p^*, u_x^*, u_y^*, w_x^*, and w_y^* results in the following equations for perturbations:

$$Rb\left(\frac{\partial^2 n^*}{\partial x^2} + \frac{\partial^2 n^*}{\partial y^2}\right) - \frac{1}{Da}\nabla^2 u_z^* + Rv\frac{\partial n_b}{\partial z}\left(\frac{\partial^2 w_z^*}{\partial x^2} + \frac{\partial^2 w_z^*}{\partial y^2}\right) = \frac{c_a}{Sc}\frac{\partial}{\partial t}\nabla^2 u_z^* \tag{110}$$

$$\nabla^2 w_z^* = \frac{\partial^2 n^*}{\partial x^2} + \frac{\partial^2 n^*}{\partial y^2} \tag{111}$$

$$\varphi\frac{\partial \bar{C}^*}{\partial t} + u_z^*\frac{\partial \bar{C}_b(z)}{\partial z} = \Gamma\nabla^2 C^* - \beta\Gamma n^* \tag{112}$$

$$\varphi\frac{\partial n^*}{\partial t} + u_z^*\frac{\partial n_b(z)}{\partial z} + Pe\frac{\partial \bar{C}^*}{\partial z}\frac{\partial n_b(z)}{\partial z} + Pe\frac{\partial \bar{C}_b(z)}{\partial z}\frac{\partial n^*}{\partial z} + Pen^*(z)\frac{\partial^2 \bar{C}_b(z)}{\partial z^2} + Pen_b(z)\nabla^2\bar{C}^* = \nabla^2 n^* \tag{113}$$

The following normal mode expansion is used in equations (110)–(113):

$$[u_z^*, n^*, w_z^*, \bar{C}^*] = [U(z), N(z), W(z), \Xi(z)]f(x, y)\exp(\sigma t) \tag{114}$$

The function $f(x, y)$ satisfies equation (72) where the symbol for the horizontal wavenumber, m, is now replaced by a.

This results in the following equations for amplitudes:

$$a^2 A_1^3 Da\, Rv\, Sc \sec^2\left(\frac{1}{2}A_1(z-1)\right)\tan\left(\frac{1}{2}A_1(z-1)\right)W$$

$$-2Pe\beta\left(-a^2 Rb\, Da\, Sc\, N + (Sc + c_a\, Da\sigma)(a^2 U - U'')\right) = 0 \tag{115}$$

$$a^2(N - W) + W'' = 0 \tag{116}$$

$$2A_1 Pe\,\beta\tan\left[\frac{1}{2}A_1(z-1)\right]N'(z) + A_1^3\sec^2\left[\frac{1}{2}A_1(z-1)\right]\tan\left[\frac{1}{2}A_1(z-1)\right]\left(U + Pe\Xi'\right)$$

$$+2Pe\beta\left(\left(a^2+\sigma\varphi\right)N - N''\right) + A_1^2 Pe\sec^2\left[\frac{1}{2}A_1(z-1)\right]\left(\beta N - a^2\Xi + \Xi''\right) = 0 \tag{117}$$

$$Pe\,\beta\,\Gamma N - A_1\tan\left[\frac{1}{2}A_1(1-z)\right]U + Pe\left(a^2\Gamma + \varphi\sigma\right)\Xi - Pe\Gamma\Xi'' = 0 \tag{118}$$

If the principal of exchange of stabilities (Chandrasekhar, 1961) is assumed valid (this hypothesis is supported by computational results presented in Bardan and Mojtabi (2000) and Gershuni and Lyubimov (1998)), equations (115)–(118) can be simplified by setting σ to zero. In this case, equations (115)–(118) can be additionally simplified by setting $\Xi \to \beta\bar{\Xi}$; after this transformation the resulting equations depend on the product $\varpi = Pe\,\beta$ rather than Pe and β individually:

$$a^2 A_1^3 \hat{R}v\sec^2\left(\frac{1}{2}A_1(z-1)\right)\tan\left(\frac{1}{2}A_1(z-1)\right)W + 2a^2\hat{R}bN - 2a^2 U + 2U'' = 0 \tag{119}$$

$$a^2(N - W) + W'' = 0 \tag{120}$$

$$2A_1\varpi\tan\left[\frac{1}{2}A_1(z-1)\right]N'(z) + A_1^3\sec^2\left[\frac{1}{2}A_1(z-1)\right]\tan\left[\frac{1}{2}A_1(z-1)\right]\left(U + \varpi\,\bar{\Xi}'\right)$$

$$+2\varpi\left(a^2 N - N''\right) + A_1^2\varpi\sec^2\left[\frac{1}{2}A_1(z-1)\right]\left(N - a^2\bar{\Xi} + \bar{\Xi}''\right) = 0 \tag{121}$$

$$\varpi\Gamma N - A_1\tan\left[\frac{1}{2}A_1(1-z)\right]U + \varpi a^2\Gamma\bar{\Xi} - \varpi\Gamma\bar{\Xi}'' = 0 \tag{122}$$

where

$$\hat{R}v = \frac{Rv\,Da}{Pe\beta}\ \text{and}\ \hat{R}b = Rb\,Da \tag{123}$$

are the modified vibration and bioconvection Rayleigh numbers, respectively.

Equations (119)–(122) are solved subject to the following boundary conditions:

$$\text{At } z = 0 : U = 0, \bar{\Xi} = 0, W = 0, \varpi \left(n_b|_{z=0} \frac{d\bar{\Xi}}{dz} + \frac{1}{\beta} \frac{dC_b}{dz}\bigg|_{z=0} N \right) - \frac{\partial N}{\partial z} = 0 \tag{124}$$

$$\text{At } z = 1 : U = 0, \frac{d\bar{\Xi}}{dz} = 0, W = 0, \frac{dN}{dz} = 0 \tag{125}$$

For the solution of this system, a single term Galerkin method is employed. Suitable trial functions, which satisfy the boundary conditions given by equations (124) and (125), are:

$$U_1 = z - z^2, W_1 = z - z^2, N_1 = 1 + \alpha \left(z - \frac{1}{2} z^2 \right), \Xi_1 = z - \frac{1}{2} z^2 \tag{126}$$

where

$$\alpha = \frac{A_1 \left(A_1 - \sin A_1 \right)}{\left(1 + \cos A_1 \right)} \tag{127}$$

The utilization of a standard Galerkin procedure (Finlayson, 1972) results in the following equation for the critical bioconvection Rayleigh number:

$$\begin{aligned} Rb_{cr} = \min_a \Bigg\{ \Bigg[& \cos^2 \left(\frac{A_1}{2} \right) \Big\{ -16 \left(10 + a^2 \right)^2 \left(5 + 2a^2 \right) \left(I_3 + 2a^2 I_4 \right) \Gamma \varpi \\ & - \frac{450 a^4 A_1^4 I_1 \left(2I_5 + a^2 A_1^2 I_6 \right) I_7 \hat{R} v \left(20 + 7A_1^2 + 20 \cos \left(A_1 \right) - 7A_1 \sin \left(A_1 \right) \right)}{1 + \cos \left(A_1 \right)} \\ & - \frac{60 a^4 \left(5 + 2a^2 \right) A_1^6 I_1 I_2 \hat{R} v \Gamma \left(20 + 7A_1^2 + 20 \cos \left(A_1 \right) - 7A_1 \sin \left(A_1 \right) \right)}{1 + \cos \left(A_1 \right)} \\ & + 4 \left(10 + a^2 \right)^2 \left(2I_5 + a^2 A_1^2 I_6 \right) \Gamma \varpi \sec^2 \left(\frac{A_1}{2} \right) \left(5 + 2A_1^2 + 5 \cos \left(A_1 \right) - 2A_1 \sin \left(A_1 \right) \right) \Big\} \Bigg] \Big/ \\ & \Big\{ a^2 \left(10 + a^2 \right) A_1 \left(30 I_5 I_7 + A_1^2 \left(10 I_2 \Gamma + a^2 \left(15 I_6 I_7 + 4 I_2 \Gamma \right) \right) \right) \\ & \times \left(-20 - 7A_1^2 - 20 \cos \left(A_1 \right) + 7A_1 \sin \left(A_1 \right) \right) \Big\} \end{aligned} \tag{128}$$

where the integrals I_1–I_7 (all of which are functions of ϖ only) are

$$I_1 \left(\varpi \right) = \int_0^1 (-1 + z) z \left(z - z^2 \right) \sec^2 \left(\frac{1}{2} A_1 \left(-1 + z \right) \right) \tan \left(\frac{1}{2} A_1 \left(-1 + z \right) \right) dz \tag{129}$$

$$I_2 \left(\varpi \right) = \int_0^1 (-1 + z) z \sec^2 \left(\frac{1}{2} A_1 \left(-1 + z \right) \right) \tan \left(\frac{1}{2} A_1 \left(-1 + z \right) \right) \left(1 + \alpha \left(z - \frac{z^2}{2} \right) \right) dz \tag{130}$$

$$I_3(\varpi) = \int_0^1 \left[A_1^2 \sec^2\left(\frac{1}{2}A_1(-1+z)\right) + \frac{2A_1(A_1 - \sin(A_1))}{1+\cos(A_1)} \right.$$
$$+ \frac{1}{4}A_1^3(-2+z)\,z\sec^2\left(\frac{A_1}{2}\right)\sec^2\left(\frac{1}{2}A_1(-1+z)\right)(-A_1+\sin(A_1))$$
$$\left. + A_1^2(-1+z)\sec^2\left(\frac{A_1}{2}\right)(-A_1+\sin(A_1))\tan\left(\frac{1}{2}A_1(-1+z)\right)\right]$$
$$\times\left(1+\alpha\left(z-\frac{z^2}{2}\right)\right)dz \tag{131}$$

$$I_4(\varpi) = \int_0^1 \left[1+\frac{1}{4}A_1(-2+z)\,z\sec^2\left(\frac{A_1}{2}\right)(-A_1+\sin(A_1))\right]\left(1+\alpha\left(z-\frac{z^2}{2}\right)\right)dz \tag{132}$$

$$I_5(\varpi) = \int_0^1 [-A_1^2\sec^2\left(\frac{1}{2}A_1(-1+z)\right)$$
$$-A_1^3(-1+z)\sec^2\left(\frac{1}{2}A_1(-1+z)\right)\tan\left(\frac{1}{2}A_1(-1+z)\right)\Big]$$
$$\times\left(1+\alpha\left(z-\frac{z^2}{2}\right)\right)dz \tag{133}$$

$$I_6(\varpi) = \int_0^1 (-2+z)\,z\,\sec^2\left(\frac{1}{2}A_1(-1+z)\right)\left(1+\alpha\left(z-\frac{z^2}{2}\right)\right)dz \tag{134}$$

$$I_7(\varpi) = \int_0^1 (-1+z)z\left(z-\frac{z^2}{2}\right)\tan\left(\frac{1}{2}A_1(1-z)\right)dz \tag{135}$$

4.6 Numerical Results

Typical values of the dimensionless parameters for the soil bacterium *Bacillus subtilis* are estimated in Hillesdon and Pedley (1996) as follows: $Pe = 15H$, $\beta = 7H^2$, and $\Gamma = 16$, where the layer depth, H, must be given in mm. A typical depth of a shallow layer in experiments described in Hillesdon et al. (1995) was 2.5 mm; this gives a value of $\varpi = 1640$. Using parameter values given in Hillesdon and Pedley (1996), for $\Omega = 1000$ Hz, $\hat{b} = 10\,\mu$m, $\tilde{n}_0 = 10^{15}$ cell/m^3, and $Da = 0.01$, $\hat{R}b$ is estimated as 1.2×10^3; also, $\hat{R}v$ is estimated as 8.9×10^{-11}. Since $\hat{R}v$ is proportional to Ω^2 and $\hat{b}^2$, its value can be controlled by varying the frequency and the amplitude of vibration.

Figures 11a and 11b are computed for $\Gamma = 16$ for three fixed values of $\hat{R}v$: 8.9×10^{-11}, 5, and 10. Figure 11a displays the effect of $\varpi = Pe\beta$ on the critical value of the bioconvection Rayleigh number, $\hat{R}b_{cr}$, while Fig. 11b displays the effect of ϖ on the corresponding critical horizontal wavenumber, a_{cr}. Figure 11a shows

that when ϖ is small, $\hat{R}b_{cr}$ decreases as ϖ increases; this trend is consistent with findings of Hillesdon and Pedley (1996) for small values of the product $Pe\beta$ (see Fig. 6a in Hillesdon and Pedley, 1996).

Hillesdon and Pedley (1996) interpreted ϖ as a depth parameter; larger values of ϖ correspond to a steeper free-surface density gradient in the basic state. It is expected that a steeper free-surface density gradient leads to a more unstable system, which explains the decrease of $\hat{R}b_{cr}$ with the increase of ϖ. When ϖ exceeds the value of approximately two, the trend of the dependence of $\hat{R}b_{cr}$ on ϖ reverses and $\hat{R}b_{cr}$ increases as ϖ increases. The trend in Fig. 11a agrees well with the trend observed in Fig. 6a of Hillesdon and Pedley (1996) for $\varpi > 10$. Hillesdon and Pedley (1996) explained this trend by noting that $\hat{R}b$ may not be the most appropriate measure of the ratio between the buoyancy forces that drive bioconvection and viscous forces which slow it down. The difference between the value of ϖ at which the minimum of $\hat{R}b_{cr}$ occurs (approximately two in this chapter and approximately ten in Hillesdon and Pedley, 1996) can be explained by the effect of the porous medium,

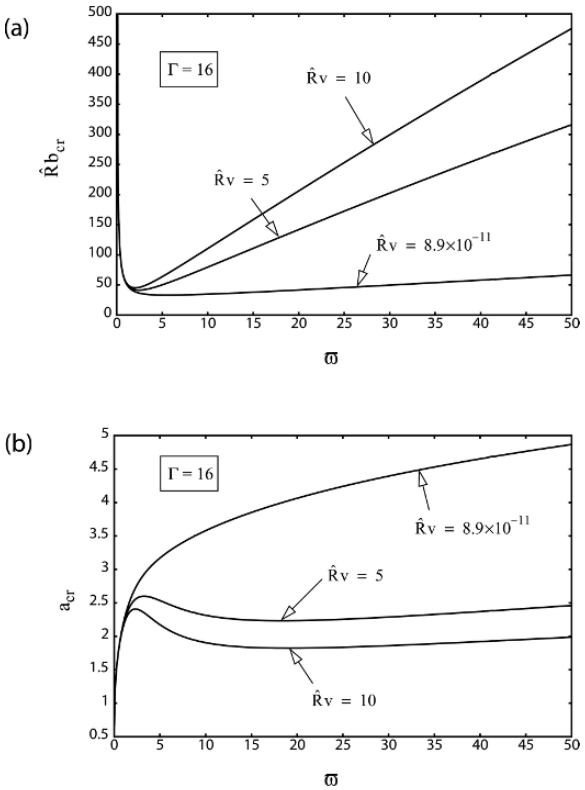

Fig. 11 Effect of ϖ on the critical value of the bioconvection Rayleigh number, $\hat{R}b_{cr}$ (**a**) and on the critical horizontal wavenumber, a_{cr} (**b**). Different curves correspond to different fixed values of $\hat{R}v$

since the chapter of Hillesdon and Pedley (1996) addresses bioconvection in a clear (of porous material) fluid.

The dependence of a_{cr} on ϖ, displayed in Fig. 11b, is quite complex: a_{cr} first increases, takes on a maximum value, and then decreases. The value of ϖ at which the maximum value of a_{cr} occurs increases as $\hat{R}v$ decreases; for $\hat{R}v = 10$ the maximum of a_{cr} occurs at approximately $\varpi = 2$. This trend is also in agreement with results displayed in Fig. 6b of Hillesdon and Pedley (1996).

Figures 12a and 12b display the dependence of $\hat{R}b_{cr}$ and a_{cr} on $\hat{R}v$ for three fixed values of ϖ: 500, 1640, 3000. Figure 12a shows that $\hat{R}b_{cr}$ increases as $\hat{R}v$ increases. This means that high-frequency low-amplitude vibration makes the system more stable. This conclusion is in agreement with the results obtained in Mojtabi et al. (2004), who considered two-dimensional thermosolutal natural convection and discovered that vertical vibration has a stabilizing effect on the system. The stabilizing effect of vertical vibration can be explained by considering the direction of the effective vibration force represented by the last term on the

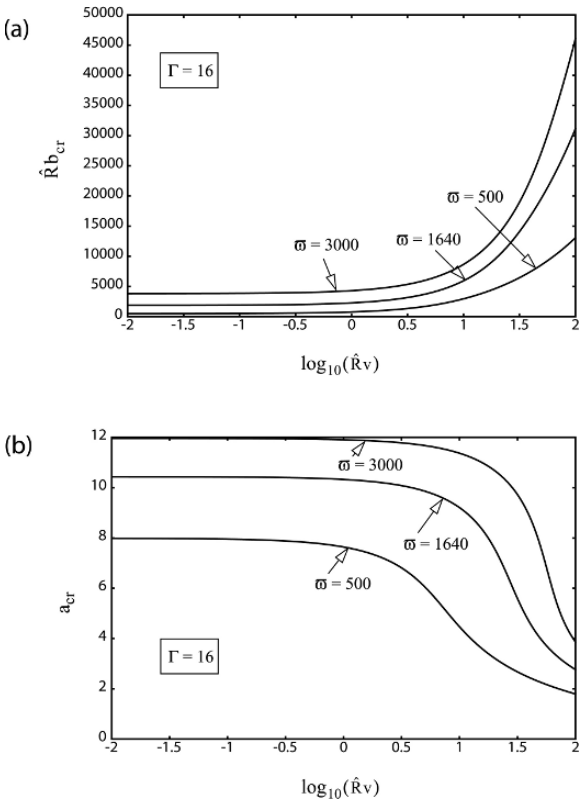

Fig. 12 Effect of the vibration Rayleigh number, $\hat{R}v$, on the critical value of the bioconvection Rayleigh number, $\hat{R}b_{cr}$ (**a**) and on the critical wavenumber, a_{cr} (**b**). Different curves correspond to different fixed values of ϖ

right-hand side of the averaged momentum equation (99). As shown in Gershuni and Lyubimov (1998), this force, with represents the average effect of vertical vibrations on the fluid, causes the fluid to flow along gradients of density inhomogeneities. Bardan et al. (2001) analyzed the direction of this effective vibration force and have shown that, in the case of vertical vibration, the vibration-induced flow (caused by the effective vibration force) is opposite to the flow induced by buoyancy forces (in this case, to the flow induced by bioconvection). Therefore, increasing $\hat{R}v$ reduces the overall circulation and stabilizes the system. A full numerical solution, which would include the investigation of possible overstability regimes, is needed to further understand the effect of vertical vibration. Figure 12b shows that a_{cr} decreases as $\hat{R}v$ increases, which means that stronger vibrations correspond to smaller critical wavenumbers.

Acknowledgments The author gratefully acknowledges the grant # NAG3-2706 awarded to him by NASA Office of Biological and Physical Research, Physical Sciences Division.

References

Bardan G, Mojtabi A (2000) On the Horton–Rogers–Lapwood convective instability with vertical vibration: Onset of convection. Physics of Fluids 12: 2723–2731

Bardan G, Knobloch E, Mojtabi A, Khallouf H (2001) Natural doubly diffusive convection with vibration. Fluid Dynamics Research 28: 159–187

Bardan G, Razi YP, Mojtabi A (2004) Comments on the mean flow averaged model. Physics of Fluids 16: 4535–4538

Becker SM, Kuznetsov AV, Avramenko AA (2004) Numerical modeling of a falling bioconvection plume in a porous medium. Fluid Dynamics Research 33: 323–339

Bees MA, Hill NA (1997) Wavelength of bioconvection patterns. Journal of Experimental Biology 200: 1515–1526

Burghelea T, Segre E, Bar-Joseph I, Groisman A, Steinberg V (2004) Chaotic flow and efficient mixing in a microchannel with a polymer solution. Physical Review E 69: #066305

Chandrasekhar S (1961) Hydrodynamic and Hydromagnetic Stability. Oxford University Press, Oxford

Childress S, Levandowsky M, Spiegel EA (1975) Pattern formation in a suspension of swimming micro-organisms: Equations and stability theory. Journal of Fluid Mechanics 63: 591–613

Cisse I, Bardan G, Mojtabi A (2004) Rayleigh Bénard instability of a fluid under high-frequency vibration. International Journal of Heat and Mass Transfer 47: 4101–4112

Finlayson BA (1972) The Method of Weighted Residuals and Variational Principles. Academic Press, New York, Chapter 6

Geng P, Kuznetsov AV (2005) Settling of bidispersed small solid particles in a dilute suspension containing gyrotactic micro-organisms. International Journal of Engineering Science 43: 992–1010

Geng P, Kuznetsov AV (2006) Direct numerical simulation of settling of a large solid particle during bioconvection. International Journal for Numerical Methods in Fluids 51: 511–530

Geng P, Kuznetsov AV (2007) Dynamics of large solid particles in bioconvective sedimentation. International Journal for Numerical Methods in Fluids, 53:713–733

Gershuni GZ, Lyubimov DV (1998) Thermal Vibrational Convection. Wiley, New York

Ghorai S, Hill NA (1999) Development and stability of gyrotactic plumes in bioconvection. Journal of Fluid Mechanics 400:1–31

Ghorai S, Hill NA (2000) Periodic arrays of gyrotactic plumes in bioconvection. Physics of Fluids 12:5–22

Harashima A, Watanabe M, Fujishiro I (1988) Evolution of bioconvection patterns in a culture of motile flagellates. Physics of Fluids 31, 764–775

Hill NA, Pedley TJ (2005) Bioconvection. Fluid Dynamics Research 37: 1–20

Hillesdon AJ, Pedley TJ (1996) Bioconvection in suspensions of oxytactic bacteria: Linear theory. Journal of Fluid Mechanics 324: 223–259

Hillesdon AJ, Pedley TJ, Kessler JO (1995) The development of concentration gradients in a suspension of chemotactic bacteria. Bulletin of Mathematical Biology 57: 299–344

Kessler JO (1985) Cooperative and concentrative phenomena of swimming microorganisms. The Contemporary Physics 26:147–166

Kessler JO (1986) The external dynamics of swimming micro-organisms. Progress in Phycological Research 4, Biopress, Bristol, pp 257–307

Kessler JO (1989) Path and pattern – the mutual dynamics of swimming cells and their environment. Comments Theor. Biol. 1:85–108

Kessler JO, Burnett GD, Remrick KE (2000) Mutual dynamics of swimming microorganisms and their fluid habitat. In: Christiansen PL, Sorensen MP, Scott AC (eds) Nonlinear Science at the Dawn of the 21st Century. Springer, New York, pp 409–426

Kessler JO, Wiseley DA, Remrick KE, Marthaler DE (1997) Individual and collective dynamics of swimming bacteria. In: Schreckenburg M, Wolf DE (eds) Proceedings of the Workshop "Traffic and Granular Flow '97", Springer, New York, pp 37–51

Kim D-S, Fogler HS (2000) Biomass evolution in porous media and its effects on permeability under starvation conditions. Biotechnology and Bioengineering 69: 47–56

Kuznetsov AV (2005a) The onset of bioconvection in a suspension of gyrotactic microorganisms in a fluid layer of finite depth heated from below. International Communications in Heat and Mass Transfer 32: 574–582

Kuznetsov AV (2005b) Investigation of the onset of thermo-bioconvection in a suspension of oxytactic microorganisms in a shallow fluid layer heated from below. Theoretical and Computational Fluid Dynamics 19: 287–299

Kuznetsov AV (2005c) Modeling bioconvection in porous media. In: Vafai K (ed) Handbook of Porous Media. 2nd ed., Taylor & Francis, New York, pp 645–686

Kuznetsov AV (2005d) The onset of bioconvection in a suspension of negatively geotactic microorganisms with high-frequency vertical vibration. International Communications in Heat and Mass Transfer 32: 1119–1127

Kuznetsov AV (2006a) Thermo-bio-convection in porous media. Journal of Porous Media 9:581–589

Kuznetsov AV (2006b) The onset of thermo-bioconvection in a shallow fluid saturated porous layer heated from below in a suspension of oxytactic microorganisms. European Journal of Mechanics B/Fluids 25: 223–233

Kuznetsov AV (2006c) Investigation of the onset of bioconvection in a suspension of oxytactic microorganisms subjected to high- frequency vertical vibration. Theoretical and Computational Fluid Dynamics 20: 73–87

Kuznetsov AV (2006d) Linear stability analysis of the effect of vertical vibration on bioconvection in a horizontal porous layer of finite depth. Journal of Porous Media 9:597–608

Kuznetsov AV, Avramenko AA (2003) Analysis of stability of bioconvection of motile oxytactic bacteria in a horizontal fluid saturated porous layer. International Communications in Heat and Mass Transfer 30: 593–602

Kuznetsov AV, Avramenko AA (2004) Effect of small particles on the stability of bioconvection in a suspension of gyrotactic microorganisms in a layer of finite depth. International Communications in Heat and Mass Transfer 31: 1–10

Kuznetsov AV, Avramenko AA, Geng P (2004) Analytical investigation of a falling plume caused by bioconvection of oxytactic bacteria in a fluid saturated porous medium. International Journal of Engineering Science 42:557–569

Kuznetsov AV, Geng P (2005) The interaction of bioconvection caused by gyrotactic microorganisms and settling of small solid particles. International Journal of Numerical Methods in Heat and Fluid Flow 15: 328–347

Metcalfe M, Pedley TJ (1998) Bacterial biocovection: weakly nonlinear theory for pattern selection. J. Fluid Mech. 370:249–270

Metcalfe M, Pedley TJ (2001) Falling plumes in bacterial bioconvection. Journal of Fluid Mechanics 445:121–149

Mojtabi MCC, Razi YP, Maliwan K, Mojtabi A (2004) Influence of vibration on Soret-driven convection in porous media. Numerical Heat Transfer A 46: 981–993

Nield DA, Bejan A (2006) Convection in Porous Media. 3nd ed., Springer, New York

Nield DA, Kuznetsov AV (2006) The onset of bio-thermal convection in a suspension of gyrotactic microorganisms in a fluid layer: Oscillatory convection. International Journal of Thermal Sciences 45: 990–997

Pedley TJ, Kessler JO (1987) The orientation of spheroidal micro-organisms swimming in a flow field. Proceedings of the Royal Society of London. Series B231: 47–70

Pedley TJ, Hill NA, Kessler JO (1988) The growth of bioconveciton patterns in a uniform suspension of gyrotactic microorganisms. Journal of Fluid Mechanics 195: 223–237

Simonenko IB (1972) A justification of the averaging method for a problem of convection in a field rapidly oscillating forces and other parabolic equations. Matematicheskii Sbornik 129(2): 245–263

Stewart TL, Fogler HS (2001) Biomass plug development and propagation in porous media. Biotechnology and Bioengineering 72: 353–363

Whitaker S (1999) The Method of Volume Averaging. Kluwer, Dordrecht

Macromolecular Transport in Arterial Walls: Current and Future Directions

K. Khanafer and K. Vafai

Abstract Relevant mathematical models associated with the transport of macromolecules in the blood stream and in the arterial walls are reviewed in this work. A robust four-layer model (endothelium, intima, internal elastic lamina and media) based on porous media concept and accounting for selective permeability of each porous layer to certain solutes is presented to describe the transport of macromolecules in the arterial wall coupled with the transport in the lumen. The variances in the current models are analyzed and discussed. Future direction in developing a rigorous mathematical model for transport in arterial walls using porous media theory and fluid-structure interaction approach is outlined in this study.

1 Introduction

Atherosclerosis, which comes from the Greek words athero (meaning gruel or paste) and sclerosis (hardness), is a form of vascular disease that is commonly located in the large- and medium-size arteries. Atherosclerosis is a slow, progressive disease that may start in childhood. It can affect the arteries of the brain, heart, kidneys, and the arms and legs. It is caused by the slow buildup of fatty substances, cholesterol, cellular waste products, calcium and other substances found in the blood within the arterial walls. This buildup is called plaque. It has been suggested that the transport of the low-density lipoprotein (LDL) from the blood into the arterial wall and its accumulation within the wall play an important role in the process of atherogenesis (Ross 1993, Hoff et al. 1975, Schwenke et al. 1993, Newby and Zaltsman 2000). This transport process is termed "arterial mass transport" and is influenced by blood flow in the lumen and transmural flow in the arterial wall.

Several mathematical models have been developed to model the transport of macromolecules, such as low density lipoproteins (LDLs), from the arterial lumen to the

K. Khanafer
University of Michigan, Ann Arbor, MI, USA

K. Vafai
University of California, Riverside, CA, USA
e-mail: vafai@engr.ucr.edu

P. Vadász (ed.), *Emerging Topics in Heat and Mass Transfer in Porous Media*,

© Springer Science+Business Media B.V. 2008

arterial walls and their accumulation in the wall (Fry 1985, Huang and Tarbell 1997, Stangeby and Ethier 2002a,b, Karner et al. 2001, Karner and Perktold 2000, Ai and Vafai 2006, Yang and Vafai 2006). Prosi et al. (2005) have classified these models in three major categories. The simplest model is referred to as wall-free model in which the arterial wall is described by simplified boundary conditions (Back et al. 1977, Ehrlich and Friedman 1977, Rappitsch and Perktold 1996, Ethier 2002, Wada and Karino 1999, 2000, 2002, Qui and Tarbell 2000). This model has been used to investigate oxygen and LDL transport in idealized and physiological arterial models. This model has the advantage of being computationally expedient and provides qualitative information on mass transfer in the blood lumen. However, the main drawback of this model is its limitation in computing concentration profiles within the arterial wall. A more realistic approach is named lumen-wall models which approximate the complex structure of the arterial wall by a simple homogeneous layer. Such models, originally proposed by Moore and Ethier (1997), have been used to study the mass transport of LDL within the arterial wall by Stangeby and Ethier (2002a,b). They used a model that coupled transmural fluid flow to the motion of the flowing blood in the arterial lumen. The most realistic models are multilayer models, which break the arterial wall down into several layers, precisely the endothelium, intima, internal elastic lamina and media, and model the transport within the wall, either at the microscopic (Yuan et al. 1991, Huang et al. 1994, Huang and Tarbell 1997, Tada and Tarbell 2004) or macroscopic (Fry 1985, 1987, Karner et al. 2001, Prosi et al. 2005, Ai and Vafai 2006, Yang and Vafai 2006) levels. The multilayer model was found to provide the most realistic information on the dynamics of chemicals (especially macromolecules) within the wall.

2 Mathematical Models

2.1 Wall-Free Model

Rappitsch and Perktold (1996) and Rappitsch et al. (1997) presented a numerical study for the simulation of blood flow and transport processes in large arteries. Blood flow in the arterial lumen was described by incompressible Navier-Stokes equations for Newtonian fluids, while the solute transport was modeled by the diffusion-advection equation. The resistance of the arterial wall to transmural transport is described by a shear-dependent wall permeability model. At the wall-lumen interface, two different transport models for the diffusive flux q_w were assumed. The first model assumed constant wall permeability as follows:

$$q_w = -D \left.\frac{\partial c}{\partial n}\right|_{wall} = \alpha\, c_w \tag{1}$$

where α is a constant wall permeability (Rappitsch and Perktold 1996) and c_w is the wall concentration. In the second model, the permeability of the arterial wall was assumed to be linearly dependent on the local wall-shear stress magnitude$|\tau_w|$:

$$q_w = -D \left.\frac{\partial c}{\partial n}\right|_{wall} = \alpha\, c_w = f\left(|\tau_w|\right) c_w = \beta\, |\tau_w|\, c_w \tag{2}$$

where β is constant.

A more physical boundary condition, which is a function of blood-side solute concentration at the wall and an endothelial permeability parameter, was used by Wada and Karino (1999, 2002) and Ethier (2002) at the blood-wall interface which states that the amount of LDL passing into the vessel wall is determined as the difference between the amount carried to the arterial wall by a filtration flow and the amount which diffuses back to the mainstream. Mathematically, this takes the form:

$$c_w u_w - D \left.\frac{\partial c}{\partial n}\right|_{wall} = \kappa\, c_w \tag{3}$$

where u_w is the filtration velocity at the vessel wall (transmural velocity) which was assumed to be 4×10^{-5} mm/s for a natural artery (Tedgui and Lever 1984, Wilens and McCluskey 1952). The permeability coefficient of LDL (κ) at the arterial wall was about 2×10^{-7} mm/s as reported by Truskey et al. (1992). Qui and Tarbell (2000) analyzed numerically oxygen mass transfer in a compliant curved tube model of a coronary artery using a finite element method. They showed that oxygen can be transported from the lumen to the vessel wall by convective-diffusive mechanism which depends on the fluid phase mass transfer coefficient (h_m) as follows:

$$-D \left.\frac{\partial c}{\partial n}\right|_{wall} = h_m \left(c_b - c_w\right) \Rightarrow h_m = \frac{-D \left.\frac{\partial c}{\partial n}\right|_{wall}}{\left(c_b - c_w\right)} \tag{4}$$

where c_b and c_w are bulk concentration of oxygen in lumen and the wall concentration, respectively.

2.2 Fluid-Wall Model

Fluid-wall model is a single-layer formulation which models the arterial wall as one single layer of porous medium with homogeneous transport properties. As such, it takes into account transport processes within the arterial wall without excessive computational expense (Moore and Ethier 1997, Stangeby and Ethier 2002a,b, Sun et al. 2006). Either (2002), Stangeby and Ethier (2002a,b) developed a mathematical model to study the transport of macromolecules, such as low density lipoproteins (LDLs), across the artery wall and their accumulation in the wall as related to atherosclerosis. Coupled analysis of lumenal blood flow and transmural fluid flow was achieved through the solution of Brinkman's model. The authors assumed that the concentration field of LDL species does not affect the velocity field in the artery and therefore, the Navier–Stokes and continuity equations for the lumen can be written for an incompressible flow of a Newtonian fluid as follows:

$$\nabla \cdot \vec{V} = 0 \tag{5}$$

$$\frac{\partial \vec{V}}{\partial t} + \vec{V} \cdot \nabla \vec{V} = -\frac{1}{\rho} \nabla P + \nu \nabla^2 \vec{V} \tag{6}$$

The velocity field in the porous wall region is computed using Brinkman's model which is a limiting case of the generalized equation in porous media (Vafai and Tien 1980, 1981, Khanafer et al. 2003, Khanafer and Vafai 2006, Khaled and Vafai 2003) and can be expressed as:

$$\frac{\partial \vec{V}}{\partial t} + \vec{V} \cdot \nabla \vec{V} = -\frac{1}{\rho} \nabla P + \nu \nabla^2 \vec{V} - \frac{\nu \vec{V}}{K} \tag{7}$$

where K is the Darcian permeability of the porous medium. Assuming constant diffusivity, the concentration field is computed via the solution of the mass transport equations as:

$$\frac{\partial c}{\partial t} + \vec{V} \cdot \nabla c = D \nabla^2 c + r \tag{8}$$

Where D is the diffusivity of the species of interest in blood, c is the concentration of the species, and r is the reaction term. A suitable boundary condition must be applied at the blood-wall interface. Ethier (2002) assumed that the amount of the species passing into the wall was determined as the difference between the amount carried to the wall by transmural filtration and the amount that diffuses back to the mainstream:

$$c_w u_w - D \frac{\partial c}{\partial n} = \kappa \, c_w \tag{3}$$

Sun et al. (2006) utilized the fluid-wall model to treat the arterial wall as a single-layer of porous medium assuming shear-dependent endothelial transport properties to study the effects of wall shear stress on the transport of LDL and oxygen from blood to and within the wall in an idealized model of a stenosed artery. The transmural flow in the arterial wall was modeled by Darcy's Law:

$$u_w - \nabla \cdot \left(\frac{K}{\mu_p} p_w \right) = 0 \tag{9}$$

Where u_w is the velocity of transmural flow, p_w is the pressure in the arterial wall and μ_p is the viscosity of the blood plasma. Mass transfer in the arterial wall is coupled with the transmural flow and modeled by the convection-diffusion reaction equation as follows:

$$\nabla \cdot (-D_w \nabla c_w + K_{sl} c_w \boldsymbol{u}_w) = k_w c_w \tag{10}$$

Where D_w is the solute diffusivity in the arterial wall, K_{sl} is the solute lag coefficient, and k_w is the consumption rate constant. Transport processes in the arterial wall were coupled with the blood flow in the lumen by Kedem and Katchalsky (1958) equations:

$$J_v = L_p\,(\Delta p - \sigma_d \Delta\pi) \tag{11}$$

$$J_s = P\Delta c + (1 - \sigma_f) J_v \bar{c} \tag{12}$$

Where J_v is the transmural velocity, J_s is the solute flux, L_p is the hydraulic conductivity of the endothelium, Δc is the solute concentration difference across the endothelium, Δp is the pressure across the endothelium, $\Delta\pi$ is the osmotic pressure differential, σ_d and σ_f are the Staverman filtration and osmotic reflection (which accounts for the selective permeability of the biological membranes to certain solutes) coefficients respectively, and $\bar{c}$ is the mean endothelial concentration. Shear-dependent hydraulic conductivity was assumed by Sun et al. (2006) for LDL and oxygen transport, respectively, as follows:

$$L_p\,(|\tau_w|) = 0.392 \times 10^{-12} \ln(|\tau_w| + 0.015) + 2.7931 \times 10^{-12} \tag{13}$$

From the above, it is noted that the fluid–wall model approximates the wall structure by a simple homogeneous layer. It is better than the wall-free model. However, it is still quite inaccurate as it ignores the major wall components which are crucial to atherosclerosis (Stangeby and Ethier 2002a,b).

2.3 Multi-Layers Model

Karner and Perktold (2000) and Karner et al. (2001) developed a mathematical model for the description of the mass transport process in the arterial wall coupled with the mass transport in the arterial lumen. Volume-averaged stationary convection-diffusion equation with a reaction term describing metabolic process was used for the description of the mass transport processes in the intima and media. The filtration velocity in the intima and media was calculated using Darcy's law. Kedem—Katchalsky equations, which describe the convective and diffusive flux across the endothelium and internal elastic lamina (IEL) were utilized to couple the transport equations in the lumen, intima, and media. The physical parameters of the intima and media were obtained from fiber matrix models (Curry 1984, Huang et al. 1992, Huang and Tarbell 1997). Pore theory equations (Curry 1984, Crone and Levitt 1984) were utilized to determine the transport parameters of the endothelium and IEL. The filtration velocity in the wall layer was determined using Darcy's law. The description of the mass transport processes in the intima and media uses the volume-averaged stationary convection-diffusion-reaction equation:

$$\nabla \cdot (-D_w \nabla c_w + K_{sl} c_w \boldsymbol{u}_w) = k_w c_w \tag{10}$$

The transport parameters in the above equation (D_w, K_{sl}, k_w) were calculated using an appropriate fiber matrix model (Curry 1984, Huang and Tarbell 1997, Huang et al. 1992). The transport processes in the lumen, intima and media were coupled by the flux across the endothelium and IEL which was mathematically modeled using the Kedem—Katchalsky equations. The continuity of convective-diffusive flux at the interfaces between lumen, endothelium, intima, IEL, and media was assumed as follows:

$$-D\frac{\partial c}{\partial n} + \mathrm{v}c = J_s = -D_w\frac{\partial c_w}{\partial n} + u_w c_w \tag{14}$$

2.4 Other Models

Several analytical and numerical works have explored the mechanism of transport of macromolecules within the artery wall. Huang and Tarbell (1997) studied the transport and reaction processes for ATP (Adenosine triphasphate) and LDL in the media, which they modeled as a heterogeneous material consisting of a continuous interstitial porous media phase and an array of cylindrical SMCs embedded in the interstitial phase. They did not consider the entrance effects associated with the distribution of material in the media through fenestral pores in the internal elastic lamina (IEL). Tada and Tarbell (2004) developed a two-dimensional numerical model to analyze the effect of the IEL on convective-diffusive transport of macromolecules in the media. The IEL was modeled as an impermeable barrier to both water and solute except for the fenestral pores that were assumed to be uniformly distributed over the IEL. The media was modeled as a heterogeneous medium composed of an array of smooth muscle cells (SMCs) embedded in a continuous porous medium representing the interstitial proteoglycan and collagen fiber matrix (Fig. 1).

The governing equation for the fluid flow in the media is the Brinkman's equation:

$$\nabla P = \mu\nabla^2\boldsymbol{u} - \frac{\mu\boldsymbol{u}}{K_p} \tag{15}$$

and the continuity equation

$$\nabla\cdot\boldsymbol{u} = 0 \tag{16}$$

where K is the Darcian permeability of the extracellular matrix. Solute transport through the extracellular matrix is described by a convective-diffusion equation

$$K_{cf}\boldsymbol{u}\cdot\nabla c = D_f\nabla^2 c \tag{17}$$

where K_{cf} is the lag coefficient for convective transport in the fiber matrix, c is the interstitial macromolecule concentration, and D_f is the effective diffusivity of solutes in the fiber matrix. The boundary condition on the surface of a smooth muscle cell (SMC) is

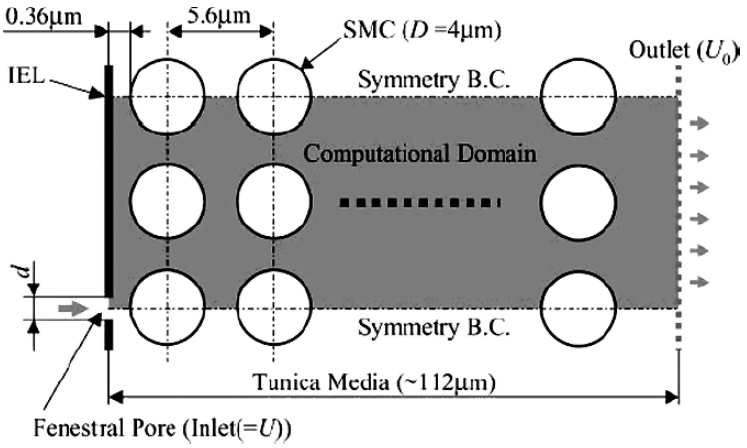

Fig. 1 Schematic illustration of the arterial media underneath the subendothelial layer. Internal elastic lamina (IEL) has a single fenestral pore (Tada and Tarbell 2004)

$$k_r c = D_f \nabla c \tag{18}$$

where k_r is the rate constant associated with the rate of disappearance of solute by surface reaction or cell permeation. In modeling solute uptake by SMCs, Adenosine triphosphate (ATP) and LDL were chosen as substances representing a broad range of molecular size. The degradation of ATP (hydrolysis of ATP to ADP: adenosine diphosphate) on the surface of SMC can be modeled using Michaelis-Menten kinetics with a rate

$$V = \frac{V_{\max} C_s}{k_m + C_s} \tag{19}$$

where $V_{\max}$ is the maximum rate, c_s is the surface concentration, and k_m is the Michaelis constant. For pseudo-first order reaction rate ($c_s << k_m$), the above equation reduces to

$$V = \frac{V_{\max} C_s}{k_m + C_s} \cong \frac{V_{\max}}{k_m} C_s = k_r C_s \tag{20}$$

The effective reaction rate coefficient for ATP was taken as $k_r = 1.25 \times 10^{-4}$ cm/s based on experimental data for $V_{\max}$ and k_m (Gordon et al. 1989) and the effective diffusivity (D_f) was set at $D_f = 2.36 \times 10^{-6}$ cm^2/s (Gordon et al. 1989).

3 Physiological Parameters

The physiological parameters of the various wall layers used in the transport equations were calculated using pore and fiber matrix models, in vivo and in vitro experiments.

3.1 Endothelium and Internal Elastic Lamina

Traditionally, transport characterization across the endothelium and IEL is represented by the Staverman-Kedem–Katchalsky membrane transport equations given as

$$J_v = \frac{K'}{\mu}\left(\Delta p - \sigma_d \Delta\pi\right) = L_p\left(\Delta p - \sigma_d \Delta\pi\right) \tag{21}$$

$$J_s = D'_e \Delta c + (1-\sigma_f) J_v \bar{c} = P\Delta c + (1-\sigma_f) J_v \bar{c} \tag{22}$$

where D'_e is the effective diffusivity per unit length and K' is the permeability per unit length. Using pore theory, some researchers (Prosi et al. 2005, Karner et al. 2001) have derived $L_{p,endothelium} = 3 \times 10^{-9}\,\mathrm{mm^2\,s/g}$, $L_{p,IEL} = 3.05 \times 10^{-7}\,\mathrm{mm^2\,s/g}$, $D'_{e,endothelium} = 3 \times 10^{-10}\,\mathrm{mm/s}$, and $D'_{IEL} = 1.59 \times 10^{-6}\,\mathrm{mm/s}$ for LDL.

3.2 Intima and Media

The subendothelial intima was modeled as an extracellular matrix of randomly distributed fibers (proteoglycan and collagen). Curry (1984) demonstrated that the partition coefficient ϕ_f (space available to the solute relative to the space available to water) was given by:

$$\phi_f = \exp\left[-(1-\varepsilon)\left(\frac{2\,r_{sol}}{r_f} + \frac{r_{sol}^2}{r_f^2}\right)\right] \tag{23}$$

Where ε is the porosity defined as:

$$\varepsilon = 1 - \pi r_f^2\, l_t \tag{24}$$

Where r_f, r_{sol} are the radii of fiber and solute respectively, and l_t is the total length of fibers per unit volume. The Staverman reflection coefficients σ_f and σ_d for the convective transport in the fiber matrix can be expressed as (Curry 1984):

$$\sigma_f = \sigma_d = \left(1-\phi_f\right)^2 \tag{25}$$

The diffusivity coefficient in the intimal extracellular fiber matrix was calculated as follows (Ogston et al. 1973):

$$D_f = D\exp\left[-(1-\varepsilon)^{0.5}\left(1 + \frac{r_{sol}}{r_f}\right)\right] \tag{26}$$

The Darcy permeability K was given as (Vafai and Tien 1980, 1981, Vafai 1984, Huang et al. 1992):

$$K = \frac{r_f^2 \varepsilon^3}{4G\,(1-\varepsilon)^2} \tag{27}$$

Where G is the Kozeny constant. Similar to the intima, media was modeled as a medium composed of smooth muscle cells (porosity $= \varepsilon_{SMC}$) and an extracellular fluid phase with fibers (porosity $= \varepsilon$). Therefore, the porosity of the media is given by

$$\varepsilon_m = \varepsilon\,(1-\varepsilon_{SMC}) \tag{28}$$

4 Mathematical Model of Macromolecule Transport within the Arterial Wall

Multilayer model is the most complex model which takes into account the heterogeneous properties of the layers constituting the wall. Due to its complexity, a larger number of parameters are required to characterize the physical properties of each layer (Fry 1985, Karner et al. 2001). Most of the previous multilayer models were based on the assumption that the physical properties of the porous wall can be identified by the pore theory. However, this approach does not provide logical estimations. Prosi et al. (2005) proposed a new methodology which starts from a set of data that can be more easily determined by experimental measurements. However, some of the assumptions made in this model give substantial errors. For example, the Kedem–Katchalsky equations used for endothelium and IEL do not take into account the boundary effects associated with the flow across these two layers. In fact, these effects are large due to the thinness of these two layers. Also, they take into account the effects of the reaction inside the media layer by approximating the loss of mass flux upstream of the layer. This simplification can lead to an over or underestimation of the influence of the chemical reaction

Yang and Vafai (2006, 2008), Ai and Vafai (2006), and Khakpour and Vafai (2008a, b) developed a new fundamental four-layer model for the description of the mass transport in the arterial wall coupled with the mass transport in the arterial lumen. The endothelium, intima, internal elastic lamina (IEL) and media layers were all treated as macroscopically homogeneous porous media and mathematically modeled using proper types of the volume averaged porous media equations with the Staverman filtration and osmotic reflection coefficients employed to account for selective permeability of each porous layer to certain solutes. The typical anatomical structure of an arterial wall is shown schematically in Fig. 2.

4.1 Lumen

Blood flow in the arterial lumen was described by the Navier–Stokes and continuity equations assuming incompressible Newtonian fluid as follows:

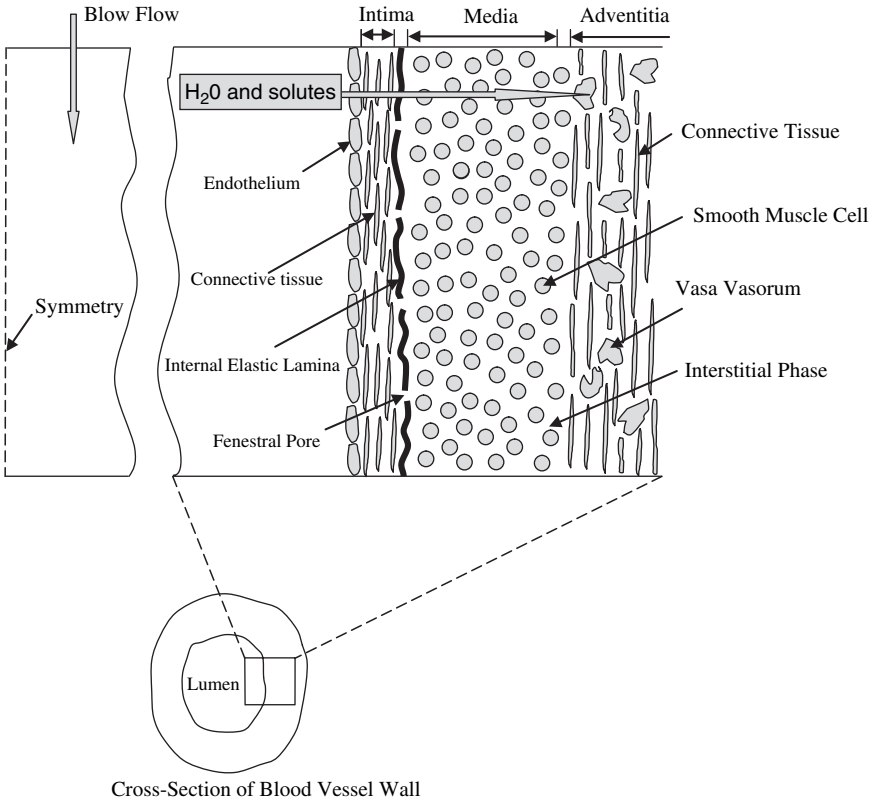

Fig. 2 Schematic illustration of the geometric artery wall

$$\nabla \cdot \vec{V} = 0 \tag{5}$$

$$\frac{\partial \vec{V}}{\partial t} + \vec{V} \cdot \nabla \vec{V} = -\frac{1}{\rho} \nabla P + \nu \nabla^2 \vec{V} \tag{6}$$

The concentration field in the arterial lumen is computed using the mass transport equation:

$$\frac{\partial c}{\partial t} + \vec{V} \cdot \nabla c = D \nabla^2 c \tag{29}$$

4.2 Endothelium and Internal Elastic Lamina

The endothelium and internal elastic lamina (IEL) were modeled as biological porous membranes (Ai and Vafai 2006, Yang and Vafai 2006). The Staverman fil-

tration and osmotic reflection coefficients were employed to account for selective rejection of species by the membranes and for the effects of osmotic pressure. The volume averaged governing equations were given by:

$$\nabla \cdot < \vec{V} > = 0 \tag{30}$$

$$\frac{\rho}{\varepsilon}\frac{\partial < \vec{V} >}{\partial t} = -\nabla < p >^f + \frac{\mu}{\varepsilon}\nabla^2 < \vec{V} > - \frac{\mu < \vec{V} >}{K} + R_u T \sigma_d \nabla < c > \tag{31}$$

$$\frac{\partial < c >}{\partial t} + (1 - \sigma_f) < \vec{V} > \cdot \nabla < c > = D_e \nabla^2 < c > \tag{32}$$

where K is the permeability, and D_e is the effective LDL diffusivity in the medium. The parameters σ_f and σ_d are the Staverman filtration and osmotic reflection coefficients (to account for selective permeability of biological membrane to certain solutes), respectively, T is the absolute temperature of the medium, and R_u is the universal gas constant. The symbol $< >$ denotes the local volume average of a quantity (Vafai and Tien 1980, 1981), and the superscript f refers to the local volume average inside the fluid.

4.3 Intima and Media

The intima and media were also modeled as macroscopically homogeneous porous media. Since the porous media are selectively permeable to certain species such as LDL, the Staverman filtration reflection coefficient has to be introduced to account for this effect. The osmotic effect in the transport modeling is not included in this part since the maximum osmotic pressure gradient in the medial layer is far below the hydraulic pressure gradient (Huang and Tarbell 1997). Therefore, the volume averaged governing equations of the intima and media layers are (Alazmi and Vafai 2000, 2001)

$$\nabla \cdot < \vec{V} > = 0 \tag{30}$$

$$\frac{\rho}{\varepsilon}\frac{\partial < \vec{V} >}{\partial t} = -\nabla < p >^f + \frac{\mu}{\varepsilon}\nabla^2 < \vec{V} > - \frac{\mu < \vec{V} >}{K} \tag{31}$$

$$\frac{\partial < c >}{\partial t} + (1 - \sigma_f) < \vec{V} > \cdot \nabla < c > = D_e \nabla^2 < c > + k(c) \tag{32}$$

where k is the effective volumetric first-order reaction rate coefficient. To verify the results obtained using this model, a comparison between the numerical result for species profiles in the media and an exact solution was carried out by Yang and Vafai (2006). This comparison is displayed in Fig. 3. The exact solution was derived based on an assumption that the LDL transport in the media is one-dimensional, with constant filtration velocity. It can be seen from Fig. 3 that the results of porous model results are in excellent agreement with the exact solutions.

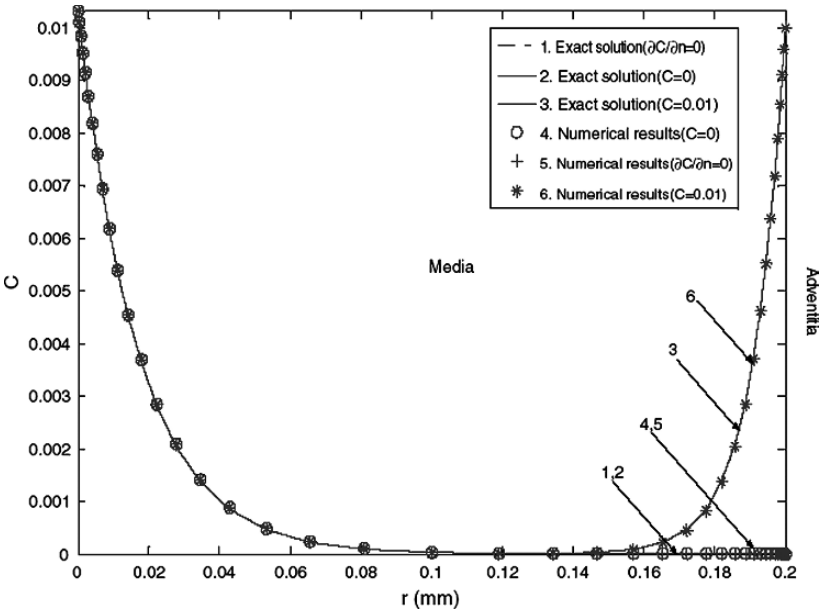

Fig. 3 Comparison between the numerical dimensionless LDL profiles in the media for three different types of concentration boundary conditions at the media adventitia interface and the exact solutions

An additional check on the accuracy of their model, Table 1 illustrates a comparison between the values of the filtration velocity and species concentration taken from literature and the results obtained using porous medium approach. The numerical species concentrations at each interface were found close to the experimental data by Meyer et al. (1996) and numerical results by Prosi et al. (2005).

Tables 2 and 3 show a summary of different boundary conditions used at the interface between the lumen and the arterial wall as well as various momentum equations used in modeling the flow in the arterial wall.

Table 1 Comparison between the values of the filtration velocity and species concentration taken from literature and the porous model (Nang and Vafai , 2006)

	Meyer et al. (1996)	Prosi et al. (2005) $C = 0$	Porous Model $C = 0$
Filtration velocity (mm/s)	1.78×10^{-5}	1.76×10^{-5}	2.31×10^{-2}
Species Concentration			
Lumen-endothelium interface	1.026	1.0262	1.0246
Intima-IEL interface	N/A	2.716×10^{-2}	3.983×10^{-2}
IEL-media interface	1.00×10^{-2}	8.58×10^{-3}	1.033×10^{-2}
Media (r = 3.214 mm)	2.5×10^{-3}	2.23×10^{-3}	2.687×10^{-5}
Media-adventitia interface	1.00×10^{-2}	0.00	0.00

Table 2 Summary of the mass interface boundary conditions between lumen and arterial wall

Model	Remarks
$-D\ \frac{\partial c}{\partial n}\big\vert_{wall} = \alpha\, c_w$	-wall free model -constant wall permeability
$-D\ \frac{\partial c}{\partial n}\big\vert_{wall} = \alpha\, c_w = f\,(\vert\tau_w\vert)\, c_w = \beta\,\vert\tau_w\vert\, c_w$	-wall free model -permeability is linearly dependent on the local shear stress magnitude
$c_w u_w - D\ \frac{\partial c}{\partial n}\big\vert_{wall} = \kappa\, c_w$	-wall free model and fluid-wall model -more realistic -depends on the blood-side solute concentration at the wall, endothelial permeability parameter, and the filtration velocity
$-D\ \frac{\partial c}{\partial n}\big\vert_{wall} = h_m\,(c_b - c_w)$	-wall free model -depends on the bulk concentration in the lumen and the arterial wall concentration

*w: interface between the lumen and the arterial wall

Table 3 Summary of the momentum equation used in the arterial wall

Model	Remarks
$u_w - \nabla\cdot\left(\frac{K}{\mu_\rho}\, p_w\right) = 0$	-fluid-wall model -arterial wall modeled as single-layer porous medium -Darcy model -constant permeability
$\frac{\partial \vec{V}}{\partial t} + \vec{V}\cdot\nabla\vec{V} = -\frac{1}{\rho}\nabla P + \nu\,\nabla^2\vec{V} - \frac{\nu\,\vec{V}}{K}$	-fluid-wall model -arterial wall modeled as single-layer porous medium -Brinkman's model -constant permeability
$\frac{\rho}{\varepsilon}\frac{\partial <\vec{V}>}{\partial t} = -\nabla <p>^f + \frac{\mu}{\varepsilon}\nabla^2 <\vec{V}> - \frac{\mu <\vec{V}>}{K} + R_u T \sigma_d \nabla <c>$	-endothelium and internal elastic lamina -more realistic -The Staverman filtration and osmotic reflection coefficients were employed to account for selective rejection of species by the membranes and for the effects of osmotic pressure
$\frac{\rho}{\varepsilon}\frac{\partial <\vec{V}>}{\partial t} = -\nabla <p>^f + \frac{\mu}{\varepsilon}\nabla^2 <\vec{V}> - \frac{\mu <\vec{V}>}{K}$	-intima and media -more realistic -accounts for Staverman filtration reflection coefficient -neglects the osmotic effect in the transport modeling

5 Future Directions

In the cardiovascular system, blood flow is under constant interaction with arterial walls. The interactions between blood flow and wall deformation can involve a wide range of fluid- mechanical phenomena. When blood flows through the lumen, the forces associated with the flow may deform the arterial walls and consequently alter the properties of the wall which in turn affect the flow structure in the lumen as well as the transport process of macromolecules from the lumen to the arterial walls. This will have an impact on the development of many diseases such as atherosclerosis. Most previous studies have been carried out under different simplifying assumptions such as steady flow, rigid boundary, Newtonian fluid, etc. The comparison between the simulations considering rigid arteries and deformable arteries have shown a substantial increase in the wall shear stresses for a rigid artery. This indicates that as the artery becomes more rigid, its wall shear stress increases leading to atherosclerosis. Hence, simultaneous fluid-structure interactions (FSIs) should be considered when studying the hemodynamics, flow structure, and the transport of macromolecules from the lumen to the arterial walls. Transient FSI simulations may provide physical insight to the mechanisms of the atherosclerosis. The solution of fluid-structure interaction problems, coupling computational fluid dynamics analysis with finite element stress analysis, is now becoming tractable through the accessibility of high performance computing.

There is a need for an FSI approach in studying the transport of macromolecules in the arterial walls under pulsatile flow condition and utilizing a porous media approach to analyze the arterial walls. Since the wall of the artery is deformable, a complex coupling exists between the flow in the lumen and the arterial wall. Thus, the variations in the porosity and permeability of the deformable arterial wall should be considered in such analysis. In addition, the variations in the physical properties of the arterial walls such as Young modulus and Poisson's ratio should be considered in any future studies since the materials of the walls are nonlinear, non-homogeneous, and anisotropic.

Nomenclature

D diffusion coefficient
D'_e effective diffusivity per unit length
c concentration
c_b bulk concentration
c_s surface concentration
c_w wall concentration (at the interface between lumen and the arterial wall)
$\bar{c}$ mean endothelial concentration
h_m fluid phase mass transfer coefficient
J_s solute flux

k_m Michaelis constant
k_w consumption rate constant
K Darcian permeability
K_{sl} solute lag coefficient
L_p hydraulic conductivity of the endothelium
p_w pressure in the arterial wall
q_w diffusive wall flux
r reaction term
u_w transmural velocity
$V_{\max}$ maximum rate

Greek Symbols

α constant wall permeability
β proportionality factor (shear-dependent wall permeability model)
$\Delta\pi$ osmotic pressure differential
κ The permeability coefficient at the arterial wall
μ_p viscosity of the blood plasma
ε porosity
σ_d Staverman filtration
σ_f osmotic reflection

References

Ai L, Vafai K (2006) A coupling model for macromolecule transport in a stenosed arterial wall, Int. J. Heat Mass Transf. 49: 1568–1591.

Alazmi B, Vafai K (2001) Analysis of fluid flow and heat transfer interfacial conditions between a porous medium and a fluid layer. Int. J. Heat Mass Transf. 44: 1735–1749.

Alazmi B, Vafai K (2000) Analysis of variants within the porous media transport models. ASME J. Heat Transfer 122: 303–326.

Back L, Radbill J, Crawford D (1977) Analysis of oxygen transport from pulsatile, viscous blood flow to diseased coronary artery of man. J. Biomech. 10: 763–774.

Crone C, Levitt DG (1984) Capillary permeability to small solutes. In: Handbook of Physiology. Microcirculation. The Cardiovascular System, Section 2, Vol. IV, Pt. 1, American Physiological Society, Bethesda, MD, pp. 411–466 (Chapter 8).

Curry FE (1984) Mechanics and thermodynamics of transcapillary exchange. In: Handbook of Physiology. Microcirculation. The Cardiovascular System, Section. 2, Vol. IV, Pt. 1, American Physiological Society, Bethesda, MD, pp. 309–374 (Chapter 8).

Ehrlich L, Friedman M (1977) Steady convective diffusion in a bifurcation. IEEE Trans. Biomed. Eng. 24: 12–18.

Ethier CR (2002) Computational modeling of mass transfer and links to atherosclerosis, Ann. Biomed. Eng. 30: 461–471.

Fry DL (1985) Mathematical models of arterial transmural transport. Am. J. Physiol. 248: H240–H263.

Fry DL (1987), Mass transport, atherogenesis and risk, Arteriosclerosis 7: 88–100.
Gordon EL, Pearson JD, Dickinson ES, Moreau E, Slakey L (1989) The hydrolysis of extraceller adenine nucleotides by arterial smooth muscle cells. J. Biol. Chem. 15: 18986–18992.
Hoff HF, Heideman CL, Jackson RL, Bayardo RJ, Kim HS, and Gotto AMJ (1975) Localization patterns of plasma apolipoproteins in human atherosclerotic lesions. Circ. Res. 37: 72–79.
Huang ZJ, Tarbell JM (1997) Numerical simulation of mass transfer in porous media of blood vessel walls, Am. J. Physiol. 273: H464–H477.
Huang Y, Rumschitzki D, Chien S, Weinbaum S (1994) A fiber matrix model for the growth of macromolecular leakage spots in the arterial intima, J. Biomech. Eng. 116: 430–445.
Huang Y, Weinbaum S, Rumschitzki D, Chien S (1992) A fiber matrix model for the growth of macromolecular leakage spots in the arterial intima. In: Advances in Biological Heat and Mass Transfer, HTD-Vol. 231. ASME, New York, pp. 81–92.
Karner G, Perktold K (2000) Effect of endothelial injury and increased blood pressure on albumin accumulation in the arterial wall: a numerical study. J. Biomech. 33: 709–715.
Karner G, Perktold K, Zehentner HP (2001) Computational modeling of macromolecule transport in the arterial wall, Comput. Meth. Biomech. Biomed. Eng. 4: 491–504.
Kedem O, Katchalsky A (1958) Thermodynamic analysis of the permeaility of biological membranes to non-electrolytes. Biochem. Biophys. Acta. 27: 229–246.
Khakpour M, Vafai K (2008a) A critical assessment of arterial transport models. Int. J. Heat Mass Transfer 51: 807–822.
Khakpour M, Vafai K (2008b) A compelete analytical solution for mass transport within a multilayer arterial wall. In press for Int. J. Heat Mass Transfer.
Khaled A-RA, Vafai K (2003) The role of porous media in modeling flow and heat transfer in biological tissues. Int. J. Heat Mass Transfer 46: 4989–5003.
Khanafer K, Vafai K (2006) The role of porous media in biomedical engineering as related to magnetic resonance imaging and drug delivery, Heat Mass Trans. 42: 939–953.
Khanafer K, Vafai K, Kangarlu A (2003) Computational modeling of cerebral diffusion-application to stroke imaging. Magn. Reson. Imag. 21: 651–661.
Meyer G, Merval R, Tedgui A (1996) Effects of pressure-induced stretch and convection on low-density lipoprotein and albumin uptake in the rabbit aortic wall, Circ. Res. 79: 532–540.
Moore JA, Ethier CR (1997) Oxygen mass transfer calculations in large arteries. ASME J. Biomech. Eng. 119: 469–475.
Newby AC, Zaltsman AB (2000) Molecular mechanisms in intimal hyperplasia. J. Pathol. 190: 300–309.
Ogston AG, Preston BN, and Wells JD (1973) On the transport of compact particles through solutions of chain polymer, Proc. R. Soc. London Ser. A 333: 297–316.
Prosi M, Zunino P, Perktold K, and Quarteroni A (2005) Mathematical and numerical models for transfer of low-density lipoproteins through the arterial walls: a new methodology for the model set up with applications to the study of disturbed luminal flow. J. Biomech. 38: 903–917.
Qui YC, Tarbell JM (2000) Numerical simulation of oxygen mass transfer in a compliant curved tube model of a coronary artery, Ann. Biomed. Eng. 28: 26–38.
Rappitsch G, Perktold K (1996) Pulsatile albumin transport in large arteries: a numerical simulation study. ASME J. Biomech. Eng. 118: 511–519.
Rappitsch G, Perktold K, Pernkopf E (1997) Numerical modeling of shear dependent mass transfer in large arteries. Int. J. Numer. Methods Fluids 25: 847–857.
Ross R(1993) Atherosclerosis: a defense mechanism gone awry. Am. J. Pathol. 143: 987–1002.
Schwenke DC, St. Clair RW (1993) Influx, efflux, and accumulation of LDL in normal arterial areas and atherosclerotic lesions of white Carneau pigeons with naturally occurring and cholesterol-aggravated aortic atherosclerosis. Arterioscler. Thromb. Vasc. Biol. 13: 1368–1381.
Stangeby DK, Ethier CR (2002a) Coupled computational analysis of arterial LDL transport-effects of hypertension, Comput. Meth. Biomech. Biomed. Eng. 5: 233–241.
Stangeby DK, Ethier CR (2002b) Computational analysis of coupled blood-wall arterial LDL transport, J. Biomech. Eng. 124: 1–8.

Sun N, Wood NB, Hughes AD, Thom AS, Xu XY (2006) Fluid-Wall modelling of mass transfer in an axisymmetric stenosis. Ann. Biomed. Eng. 34: 1119–1128.
Tada S, Tarbell JM (2004) Internal elastic lamina affects the distribution of macromolecules in the arterial wall: a computational study, Am. J. Physiol. 287: H905–H913.
Tedgui A, Lever MJ (1984) Filtration through damaged and undamaged rabbit thoracic aorta. Am. J. Physiol. 247: H784–H791.
Truskey GA, Roberts WL, Herrmann RA, Malinauskas RA (1992) Measurement of endothelial permeability to 125I-low density lipoproteins in rabbit arteries by use of enface preparations. Circ. Res. 71: 883–897.
Vafai K (1984) Convective flow and heat transfer in variable porosity media J. Fluid Mech. 147: 233–259.
Vafai K, Tien CL (1980) Boundary and inertia effects on flow and heat transfer in porous media. Int. J. Heat Mass Transf. 24: 195–203.
Vafai K, Tien C L (1981) Boundary and inertia effects on convective mass transfer in porous media. Int. J. Heat Mass Transf. 25: 1183–1190.
Wada S, Karino T (1999) Theoretical study on flow-dependent concentration polarization of low density lipoproteins at the luminal surface of a straight artery, Biorheology 36: 207–223.
Wada S, Karino T (2000) Computational studyon LDL transfer from flowing blood to arterial walls. In: Yamaguchi, T. (Ed.), Clinical Application of Computational Mechanics to the Cardiovascular System. Springer, Berlin, 157–173.
Wada S, Karino T (2002) Theoretical prediction of low-density lipoproteins concentration at the luminal surface of an artery with a multiple bend, Ann. Biomed. Eng. 30: 778–791.
Wilens SL, McCluskey RT (1952) The comparative filtration properties of excised arteries and veins. Am. J. Med. 224: 540–547.
Yuan F, Chien S, Weinbaum S (1991) A new view of convective–diffusive transport processes in the arterial intima, J. Biomech. Eng. 133: 314–329.
Yang N, Vafai K (2006) Modeling of low-density lipoprotein (LDL) transport in the artery—effects of hypertension, Int. J. Heat Mass Transf. 49: 850–867.
Yang N, Vafai K (2008) Low density lipoprotein (LDL) transport in an artery-A simplified analytical solution. Int. J. Heat Mass Transfer 51: 497–505.

Flow and Heat Transfer in Biological Tissues: Application of Porous Media Theory

Khalil Khanafer, Abdalla AlAmiri, Ioan Pop, and Joseph L. Bull

Abstract The transport phenomena in porous media have generated increasing interest over the past several decades owing to the importance of porous media in diverse fields such as biotechnology, living structures, chemical and environmental engineering, etc. Particularly, significant advances have been achieved in applying porous media theory in modeling biomedical applications. Examples include computational biology, tissue replacement production, drug delivery, advanced medical imaging, porous scaffolds for tissue engineering and effective tissue replacement to alleviate organ shortages, and transport in biological tissues. Another important application of porous media includes diffusion process in the extracellular space (ECS) which is crucial for investigating central nervous system physiology. In this chapter, three applications namely brain aneurysm, flow and heat transfer in biological tissues, and porous scaffolds for tissue engineering are analyzed as related to the advances in porous media theory in biological applications.

1 Brain Aneurysm

1.1 Introduction

A cerebral or brain aneurysm, which is a cerebrovascular disorder, is a balloon-like bulging outward of the wall of an artery in the brain. A common location of cerebral

Khalil Khanafer
University of Michigan, Ann Arbor, MI, USA
e-mail: khanafer@umich.edu

Abdalla AlAmiri
United Arab Emirates University, Al-Ain, UAE
e-mail: alamiri@uaeu.ac.al

Ioan Pop
University of Cluj, Cluj, Romania
e-mail: pop-ioan@yahoo.co.uk; popi@math.ubbcluj.ro

Joseph L. Bull
University of Michigan, Ann Arbor, MI, USA
e-mail: khanafer@umich.edu

P. Vadász (ed.), *Emerging Topics in Heat and Mass Transfer in Porous Media*,

© Springer Science+Business Media B.V. 2008

aneurysms is on the arteries at the base of the brain, known as the Circle of Willis (Hademenos, 1995). The bursting of an aneurysm in a brain artery or blood vessel causes bleeding into the brain or the space closely surrounding the brain called subarachnoid, which leads to a hemorrhagic stroke, brain damage and death. Recently, embolization using coils has been used widely to treat intracranial aneurysms. This endovascular coiling technique (or coil embolization), which involves the deployment of tiny platinum coils into the aneurysm through the catheter, is successfully used in the treatment of brain aneurysms by blocking blood flow into the aneurysm sac and consequently preventing rupture. Coil embolization has been found to have several advantages compared to surgical clipping. It produces significantly better patient results than surgery in terms of survival, free of disability, and a lower risk of death than in surgically-treated patients.

However, coil embolization cannot be used in cases of wide-necked irregular shaped aneurysm due to the difficulties associated with achieving complete filling of the aneurysm sac as well as the risk of coil protrusion into the parent artery (Knuckey et al., 1992). Therefore, intravascular stents have been used across the aneurysm in conjunction with coil embolization to successfully treat surgically challenging aneurysms and to improve the density of coil packing. As such, several advantages of using stents in conjunction with coils were reported in the literature. The placement of an endovascular stent may promote intra-aneurysm stasis and thrombosis (Wakhloo et al., 1994a, 1995, 1998). Further, the stent acts as a rigid endoluminal scaffold that prevents coil protrusion into the parent artery lumen (Wakhloo et al., 1998, Turjman et al., 1994) a problem frequently encountered in wide-necked aneurysms. Thus, the combination stent–coil technique allows for the dense packing of complex large, wide-necked aneurysms that are difficult to treat surgically Fig. 1.

1.2 Clinical and Experimental Studies Associated with the Treatment of Aneurysms Using Stent Implantation and Coil Placement

Experimental studies have been performed to analyze blood flow characteristics of an aneurysm after endovascular treatment using coils and stents (Szikora et al., 1994, Wakhloo et al., 1998, Turjman et al., 1994). Lieber et al. (2002) performed

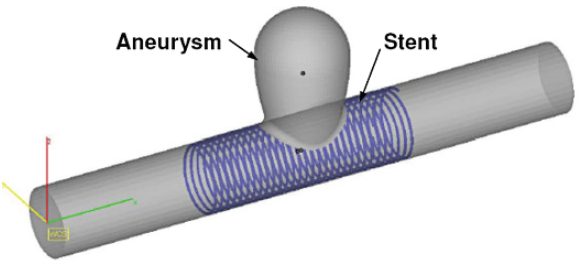

Fig. 1 Schematic diagram of the stent placed across the aneurysm neck

particle image velocimetry (PIV) measurements to study experimentally the influence of the stent filament size and stent porosity on the intra-aneurysmal flow dynamics in a sidewall aneurysm model. Their results showed that stenting significantly reduces both the intra-aneurysmal vorticity and the mean circulation inside the aneurysm. Liou et al. (2004) conducted an experimental study to investigate pulsatile flow fields in a cerebrovascular side-wall aneurysm model using helix and mesh stents. Their results showed that the hemodynamic features inside the aneurysm changed substantially with the shape of the stent. Further, comparison of the results between helix stent and mesh stent revealed that helix mesh is more favorable for endovascular treatment. The influence of aneurysm geometry and stent porosity on velocity and wall shear stress changes inside the aneurysm sac caused by stenting under physiological flow was analyzed experimentally by Rhee et al. (2002). Their results demonstrated that the intra-aneurysmal flow motion and the magnitude and pulsatility of the wall shear rate were significantly reduced in the stented aneurysm models. Canton et al. (2005) conducted an in vitro study to quantify the effect of the stents by measuring the changes in the hemodynamic forces acting on a bifurcating aneurysm model (basilar tip configuration) after the placement of flexible Neuroform stents. A digital particle image velocimetry (DPIV) system was used to measure the pulsatile velocity and shear stress fields within the aneurysm. Their results showed that peak velocity and strength of vortices inside the aneurysm sac were reduced after placing the stents. Gobin et al. (1994) observed reduction of inflow and flow stagnation at the dome with coil insertion in their in vitro model study.

Clinical experiences with stent placement and coil for cerebral aneurysm have also been reported in the literature (See for instance: Marks et al., 1994, Wakhloo et al., 1994b). Lanzino et al. (1998) reported that stent placement within the parent artery across the aneurysm reduced intra-aneurysm flow velocity which led to intra-aneurysm stasis and thrombosis and consequently preventing rupture. Kwon et al. (2006) used a new endovascular technique for treatment of cerebral aneurysms. Eight patients with wide necked aneurysms were successfully treated without complications with detachable coils using the multiple microcatheter technique as shown in Fig. 2.

1.3 Computational Studies Associated with Combined Use of Stents and Coils for the Treatment of Cerebral Aneurysms

Better understanding of the behavior of the blood flow and hemodynamics changes in various organs is a very challenging aspect in medical research. Therefore, computational fluid dynamics is considered an essential tool in the assessment and treatment of cerebral aneurysms using stents and coils. For example, Aenis et al. (1997) used finite element method, pulsatile, Newtonian flows to study the effect of stent placement on a rigid side wall aneurysm. Their results illustrated a diminished flow activity and pressure inside the stented aneurysm. Stuhne and Steinman (2004) conducted a numerical study to analyze the wall shear stress distribution and flow streamlines near the throat of a stented basilar side-wall aneurysm. The numerical simulations

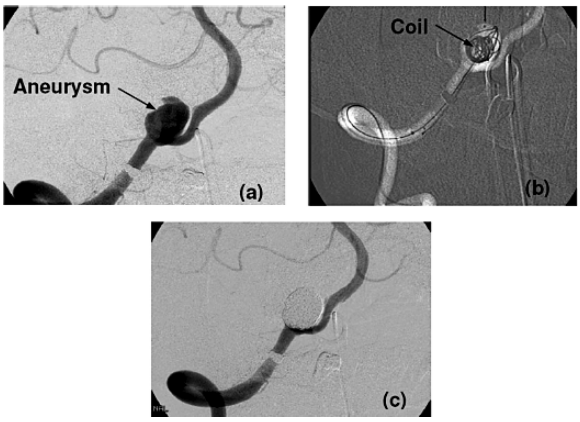

Fig. 2 (**a**) Aneurysmal Configuration visualized in 3D image, (**b**) Coil deployed to aneurismal sac and (**c**) Final angiogram shows complete occlusion of the aneurysm. A total of 333 cm platinum coil was inserted. (Reprinted from Kwon et al. (2006), with permission from Acta Neurochirurgica)

were performed assuming constant pressure at the outflow boundary of the model and specifying either steady or pulsatile flow at the inlet. For pulsatile simulations, wall shear stress (WSS) intensification was most prominent on the sides of the stent wires facing the impinging flow, while WSS reduction was most prominent on the patches of vessel lumen near wire–wire intersections. Ohta et al. (2005) analyzed hemodynamic changes in intracranial aneurysms after stent placement using a finite element modeling approach. Their work illustrated areas with stagnant flow and low shear rates.

Computational modeling of coil embolization technique in the treatment of brain aneurysms has received less attention in the literature due to the irregularly-shaped geometry of the coil. Three-dimensional pulsatile flow simulation before and after endovascular coil embolization of a terminal cerebral aneurysm was investigated by Groden et al. (2001) using in vivo data obtained by computer tomographic angiography. The filling of the aneurysm neck with platinum coils was simulated by a distribution of blocked cells. In essence, the fluid was not allowed to enter these cells. Their results showed that a complete cessation of the inflow through the aneurysm neck was achieved with a 20% filling. It should be pointed out, however, their model represents an approximate approach to determine the effect of filling the aneurysm sac with a coil. Thus, an innovative method for accurately modeling the influence of embedded coils on the flow and pressure conditions in parent vessels and the aneurysm lumen was adopted in this work utilizing a porous substrate approach. The coil embolization was modeled as a porous substrate with direction-dependent permeabilities similar to the study reported by Srinivasan et al. (1994). Srinivasan et al. (1994) developed a model for predicting the friction and heat transfer in spirally fluted tubes using porous media theory. The flute region was modeled as a porous substrate. Recently, Khanafer et al. (2006) developed a mathematical model for determining the flow field under physiological condition within a brain aneurysm filled with

coils using volume-averaged porous media approach. Their results showed that the presence of the coil significantly reduced the velocity and vorticity within the aneurysm sac.

1.4 Mathematical Formulation

The conservation equations for the coil region shown in Fig. 3 are based on the generalized flow model in porous media, which includes the effects of inertia as well as friction caused by the macroscopic shear. The generalized model, which was obtained through local volume averaging and matched asymptotic expansions, is also knows as the Brinkman-Forchheimer-Darcy model and described in rigorous detail by Vafai and Tien (1980, 1981), Nakayama (1995), Vafai and Amiri (1998) and Nield and Bejan (2006). These equations can be summarized as follows:
Continuity equation:

$$\nabla \cdot < \mathbf{v} >= 0 \tag{1}$$

Momentum equation:

$$\frac{\rho_f}{\varepsilon}\left[\frac{\partial < \mathbf{v} >}{\partial t} + < (\mathbf{v}\cdot\nabla)\mathbf{v} >\right] = -\nabla < P >^f + \frac{\mu_f}{\varepsilon}\nabla^2 < \mathbf{v} > \quad -\frac{\mu_f}{K} < \mathbf{v} > \\ -\frac{\rho_f F\varepsilon}{\sqrt{K}}[< \mathbf{v} > . < \mathbf{v} >]J \tag{2}$$

In the above equations ε is the porosity, F is the geometric function, K is the permeability, μ_f is the fluid dynamic viscosity, $\mathbf{J} = \frac{\mathbf{v}_p}{|\mathbf{v}_p|}$ is the unit vector along the pore velocity vector $\mathbf{v}_p$, $< \mathbf{v} >$ is the average velocity vector, and $< P >^f$ is the average readoff pressure. The medium permeability K can be properly modeled (Vafai, 1984, 1986, AlAmiri 2000, 2002, Khanafer et al., 2003a, b).

The porosity of the coil can be used as an index to determine the required density of coil compaction for a patient and consequently reduces the occurrence of rupture during the deployment of the coil. The porosity of the coil depends strongly on the

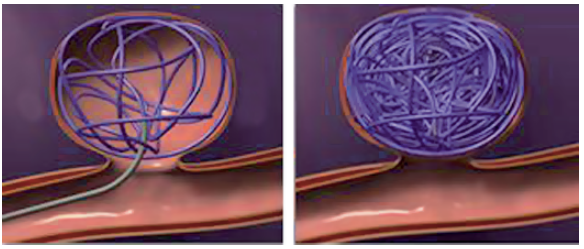

Fig. 3 A schematic diagram of an aneurysm filled with coil (Reprinted with permission from the American Society of Interventional and Therapeutic Neuroradiology)

volume of the aneurismal sac. More experimental studies are necessary to correlate the porosity of the coil to the density of the coil and the volume of the aneurysm sac. An analytical expression of the porosity ε can be easily derived for a helix stent, which is a spring-like in shape for better control of porosity (Fig. 1), as follows.

$$\varepsilon = \frac{L - n \times d}{L} \tag{3}$$

Where L is the length of the stent, n is the number of stent loops (or filaments), and d is the diameter of the wire. The effect of the stent on the inflow into the aneurysm can be characterized by the blocking ratio defined as:

$$C = \frac{n \times d}{L} = 1 - \varepsilon \tag{4}$$

2 Flow and Heat Transfer in Biological Tissues

2.1 Introduction

The development of mathematical models for flow and heat transfer in living tissues has been a topic of interest for various physicians and engineers. The accurate description of the thermal interaction between vasculature and tissues is essential for the advancement of medical technology in treating fetal diseases such as tumor. Currently, mathematical models have been used extensively in the analysis of hyperthermia in treating tumors, cryosurgery, and many other applications. Hyperthermia treatment has been demonstrated effective as cancer therapy in recent years. Its objective is to raise the temperature of pathological tissues above cytotoxic temperatures (41–45 °C) without overexposing healthy tissues (Overgaard et al., 1996, Oleson et al., 1984, Dewhirst and Samulski, 1988, Field and Hand, 1990). The success of hyperthermia treatment strongly depends on the knowledge of the heat transfer processes in blood perfused tissues. As such, accurate thermal modeling is essential for effective treatment by hyperthermia. Khanafer et al. (2007) conducted a numerical study to determine the influence of pulsatile laminar flow and heating protocol on temperature distribution in a single blood vessel and tumor tissue receiving hyperthermia treatment using physiological velocity waveforms. Their results showed that the presence of large vessels has a significant effect on temperature distributions and must be accounted for when planning hyperthermia treatment (Fig. 4). Further, uniform heating scheme was found to exhibit larger temperature distribution than for pulsed heating scheme which may induce areas of overheating (beyond the therapeutic regions) that could damage normal tissues (Fig. 5).

Heat transport in biological tissues, which is usually expressed by the Bioheat Equation, is a complicated process since it involves thermal conduction in tissues, convection and perfusion of blood, and metabolic heat generation. Therefore, several authors have developed mathematical models of bioheat transfer

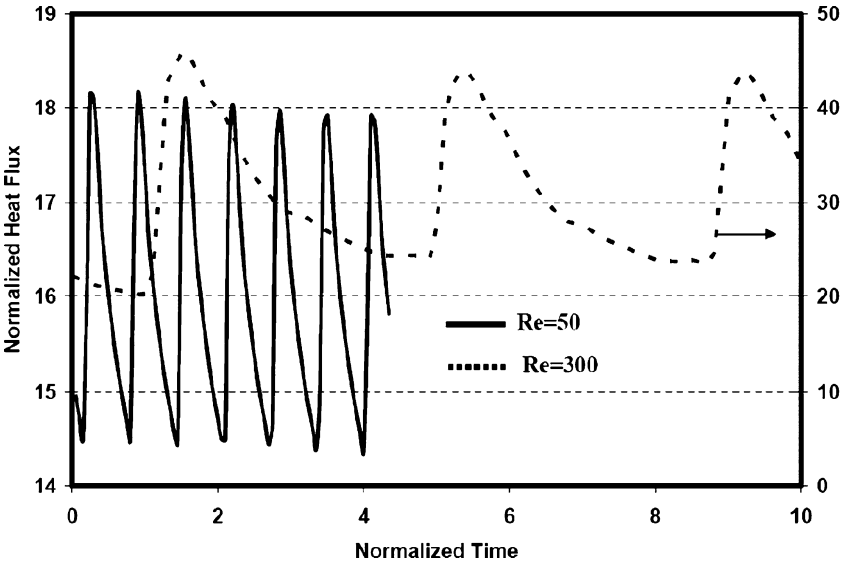

Fig. 4 Temporal variation of the normalized heat flux for different Reynolds numbers

as an extended/modified version of the original work of Pennes (1948) as reported by Charny (1992) and Arkin et al. (1994). Below is a comprehensive summary of different thermal models and their limitations for blood perfused tissues.

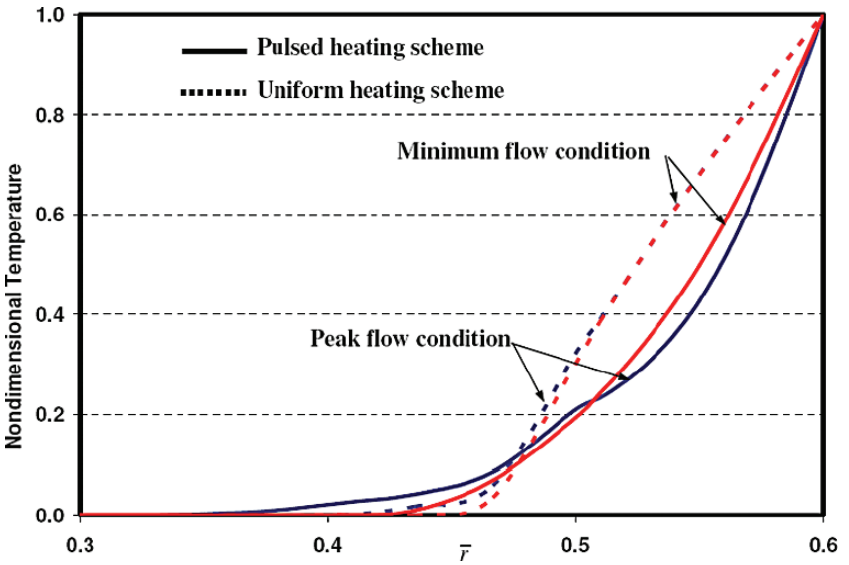

Fig. 5 Influence of the heating protocol on the temperature distribution at various flow conditions (Re = 300)

2.2 Thermal Models for Blood Perfused Tissues

2.2.1 The Pennes Bioheat Equation

The Pennes (1948) model was originally designed for predicting heat transfer in human forearm. Pennes modeled the net heat transfer (q_p) from the blood to the tissue to be proportional to the temperature difference between the arterial blood entering the tissue and the venous blood leaving the tissue as follows:

$$q_p = \omega \rho_b c_b \left(T_b - T\right) \tag{5}$$

where ω is the blood volumetric perfusion rate, ρ_b is the blood density, and c_b is the blood specific heat. Because the perfusion rate (ω) could not be directly measured, Pennes varied this parameter to fit his experimental data. Also, Pennes derivation assumed that the arterial blood temperature T_b is uniform throughout the tissue while he considered the venous temperature to be equal to the tissue temperature which is denoted by T at the same point. The equation that Pennes developed is expressed in its simplest form as:

$$\rho\, c_p \frac{\partial T}{\partial t} = \nabla \cdot (k \nabla T)) + \omega \rho_b c_b \left(T_b - T\right) + q_m \tag{6}$$

where ρ, c_p, k, and q_m are tissue density, tissue specific heat, tissue thermal conductivity, and uniform rate of metabolic heat generation in the tissue layer per unit volume, respectively. Due to the inherent simplicity of Pennes bio-heat transfer model (assume uniform thermal conductivity, perfusion rate, and metabolic heating) Pennes model was implemented in various biological research works such as therapeutic hyperthermia for the treatment of cancer (See for instance: Roemer and Cetas, 1984, Charny and Levin, 1988, 1989).

2.2.2 Wulff Continuum Model

Several investigators have questioned the validity of the fundamental assumptions of Pennes bio-heat equation. Wulff (1974) was one of the first studies that directly criticized the assumptions of Pennes model. Since blood may convect heat in any direction, Wulff (1974) assumed that the heat transfer between flowing blood and tissue should be modeled to be proportional to the temperature difference between these two media rather than between the two blood stream temperatures (temperature of the blood entering and leaving the tissue). Thus, the energy flux at any point in the tissue is expressed by:

$$q = -k \nabla T + \rho_b h_b \mathrm{v}_h \tag{7}$$

where v_h is the local mean blood velocity, and T is the tissue temperature. The specific enthalpy of the blood h_b is given by:

$$h_b = \int_{T_o}^{T_b} c_p(T_b^*)dT_b^* + \frac{P}{\rho_b} + \Delta H_f(1-\phi) \tag{8}$$

Where P is the system pressure, ΔH_f is the specific enthalpy of the metabolic reaction, and ϕ is the extent of reaction, respectively. Thus, the energy balance equation can be written as

$$\rho\, c_p \frac{\partial T}{\partial t} = -\nabla \bullet q = -\nabla \bullet (-k\nabla T + \rho_b h_b \mathrm{v}_h) = \nabla \bullet \left[k\nabla T - \rho_b \mathrm{v}_h \int_{T_o}^{T_b} c_p(T_b^*)dT_b^* + \frac{P}{\rho_b} + \Delta H_f(1-\phi) \right] \tag{9}$$

The above equation can be simplified by neglecting the mechanical work term (P/ρ_b), setting the divergence of the product $(\rho_b \mathrm{v}_h)$ to zero, and assuming constant physical properties as follows:

$$\rho\, c_p \frac{\partial T}{\partial t} = k\nabla^2 T - \rho_b \mathrm{v}_h \left(c_p \nabla T_b - \Delta H_f \nabla \phi \right) \tag{10}$$

Wulff (1974) assumed that T_b is equivalent to the tissue temperature T because blood in the microcirculation is in thermal equilibrium with the surrounding tissue. Therefore, the final form of bio-heat equation that was derived by Wulff (1974) is:

$$\rho\, c_p \frac{\partial T}{\partial t} = k\nabla^2 T - \rho_b \mathrm{v}_h c_p \nabla T + q_m \tag{11}$$

2.2.3 Klinger Continuum Model

Since the effects of non-unidirectional blood flow were neglected in Pennes model, Klinger (1974) emphasized that the convection heat transfer caused by the blood flow inside the tissue should be modeled to take into an account the spatial and temporal variation of the velocity field and heat source. Thus, the general heat transport equation can be written as:

$$\rho\, c \frac{\partial T}{\partial t} + (\rho\, c)\, \mathbf{v}\, \nabla T = k\nabla^2 T + q \tag{12}$$

This model assumed constant physical properties of tissue and incompressible blood flow.

2.2.4 Continuum Model of Chen and Holmes (CH)

In the Chen and Holmes (CH) model (1980), the control volume occupied by the tissue and blood vessels was divided into two separate volumes: one for solid tissue

and the other consisted only of blood in the vascular space within the blood vessels. Using volume-averaged technique, the energy balance equations for both the solid tissue space and vascular spaces can be written as:

Solid Phase:

$$dV_s(\rho\, c)_s \frac{\partial T_s}{\partial\, t} = dQ_{ks} + dQ_{bs} + dQ_m \tag{13}$$

Fluid Phase:

$$dV_b(\rho\, c)_b \frac{\partial T_b}{\partial\, t} = dQ_{kb} - dQ_{bs} + \int_S (\rho\, c)_b T\mathbf{v}d\mathbf{s} \tag{14}$$

Where dV_s is the differential volume of the solid phase, dV_b is the differential volume of the blood in the vascular space, dQ_{ks} is the energy transferred by conduction, dQ_{bs} is the energy transferred gain in the control volume from the blood space, dQ_m is the metabolic heating energy, dQ_{kb} is the energy gain in the vascular space by conduction, and the integral term in Eq. (14) denotes the energy transfer by convection as the blood flows across the surface area S at velocity $\mathbf{v}$. Therefore, the energy balance for the tissue space is derived by the addition of Eqs. (13–14) and division of the result by the total control volume dV yields the following:

$$(\rho\, c)\frac{\partial T_t}{\partial t} = q_k + q_m + q_p \tag{15}$$

Where q_k is the heat transfer by conduction per unit volume, q_m is the metabolic heat per unit volume, and q_p is the perfusion energy per unit volume. Here ρ, c and T_t denote the local mean density, specific heat, and temperature of the tissue based on the volume average as follows:

$$T_t = \frac{1}{\rho\, c}\left[\left(1 - \frac{dV_b}{dV}\right)(\rho\, c)_s T_s + \frac{dV_b}{dV}(\rho\, c)_b T_b\right] \tag{16}$$

$$\rho = \left(1 - \frac{dV_b}{dV}\right)\rho_s + \frac{dV_b}{dV}\rho_b \;\&\; c = \frac{1}{\rho}\left[\left(1 - \frac{dV_b}{dV}\right)(\rho\, c)_s + \frac{dV_b}{dV}(\rho\, c)_b\right] \tag{17}$$

The total heat transfer by conduction per unit volume (q_k) in the tissue control volume is expressed by:

$$q_k = \frac{Q_{ks} + Q_{kb}}{dV} = \nabla \bullet \left(k_{eff}\nabla T_t\right) \tag{18}$$

where k_{eff} is the effective thermal conductivity of the combined tissue and vascular spaces. The effective thermal conductivity is written as:

$$k_{eff} = \varepsilon\, k_b + (1-\varepsilon) k_s \tag{19}$$

Since $\varepsilon = \frac{dV_b}{dV} \sim \frac{dV_b}{dV_s} << 1$ it follows that $k_{eff} \cong k_s$. Therefore, the effective thermal conductivity is equal to the thermal conductivity of the solid tissue medium, k_s.

Chen and Holmes (1980) expressed the perfusion term (or the bulk flow term) q_p as follows:

$$q_p = q_{p(1)} + q_{p(2)} + q_{p(3)} = (\rho\, c)_b \omega^* \left(T_a^* - T_s\right) - (\rho\, c)_b \mathbf{v}_p \bullet \nabla T_s - \nabla \bullet k_p \nabla T_s \tag{20}$$

where $q_{p(1)}$ represents the effect of blood flow on tissue temperature around large vessels, T_s is the temperature of the solid tissue component of the tissue-blood model, ω^* is the total perfusion associated with the blood flow to the tissue only from the vessels, and T_a^* is the temperature of the blood within the largest vessels. $q_{p(2)}$ corresponds to the heat transfer that takes place as a result of the flowing blood, and $\rho_b \mathbf{v}_b$ is the mass flux of the blood through the tissue. Because of the thermal equilibrium, the blood temperature is equal to the solid tissue temperature everywhere in the control volume. $q_{p(3)}$ characterizes the heat transfer due to the small temperature changes and is proportional to the tissue temperature gradient. k_p is the perfusion thermal conductivity. Therefore, the new bio-heat equation for Chen and Holmes (1980) is written as

$$\rho\, c \frac{\partial T_t}{\partial t} = \nabla \bullet k_{eff} \nabla T_t + (\rho\, c)_b \omega^* \left(T_a^* - T_t\right) - (\rho\, c)_b \mathbf{v}_p \bullet \nabla T_t + \nabla \bullet k_p \nabla T_t + q_m \tag{21}$$

where T_s is replaced by the volume-weighted continuum temperature (T_t). This is reasonable as long as $\varepsilon << 1$.

2.2.5 The Weinbaum, Jiji, and Lemons (WJL) Bio-Heat Equation Model

Weinbaum and colleagues (1979, 1984a, b) derived the bio-heat equation based on a hypothesis that small arteries and veins are parallel and the flow direction is countercurrent resulting in counterbalanced heating and cooling effects. Accordingly, they modified the thermal conductivity in the Pennes equation by means of an 'effective conductivity' which is a function exclusively of the blood flow rate and vascular geometry. They also showed that isotropic blood perfusion between the countercurrent vessels can have a significant influence on heat transfer in regions where the countercurrent vessels are under 70 μm diameter. Neglecting axial conduction, the artery and vein energy balances are written as:

$$(\rho\, c)_b \frac{d}{ds}\left(n\pi\, a^2 \bar{u} T_a\right) = -n q_a - (\rho\, c)_b (2\pi\, a\, n\, g) T_a \tag{22}$$

$$(\rho\, c)_b \frac{d}{ds}\left(n\pi\, a^2 \bar{u} T_v\right) = -n q_v - (\rho\, c)_b (2\pi\, a\, n\, g) T_v \tag{23}$$

where q_a denotes the heat loss from the artery by conduction through its wall per unit length and q_{v} is the heat gain by conduction per unit length through the vein wall into the vein. T_a, and T_{v} are the bulk mean temperatures inside the blood vessel, and g is the perfusion bleed-off per unit vessel surface area. For an equal-size artery-vein pair, subtracting Eq. (23) from Eq. (22) yields:

$$(\rho\, c)_b \left[\frac{d}{ds}\left(n\pi\, a^2 \bar{u} T_a\right) - \frac{d}{ds}\left(n\pi\, a^2 \bar{u} T_{\mathrm{v}}\right) \right] = -n(q_a - q_{\mathrm{v}}) - (\rho\, c)_b (2\pi\, a\, n\, g)(T_a - T_{\mathrm{v}}) \tag{24}$$

where the term on the left-hand side represents the total heat exchange blood in the countercurrent vessels and the surrounding tissue. This term can be balanced by conduction and metabolic heating as follows:

$$(\rho\, c)_b \left[\frac{d}{ds}\left(n\pi\, a^2 \bar{u} T_a\right) - \frac{d}{ds}\left(n\pi\, a^2 \bar{u} T_{\mathrm{v}}\right) \right] = \nabla \bullet (k_t \nabla T_t) + q_m \tag{25}$$

The rate of the energy entering and leaving the tissue control volume can be expressed as:

$$q_a - q_{\mathrm{v}} = (\rho\, c)_b (\pi\, a^2 \bar{u}) \frac{d}{ds} \left[T_{\mathrm{v}} - T_{\mathrm{a}} \right] \tag{26}$$

where,

$$q_a = -(\rho\, c)_b (\pi\, a^2\, \bar{u}) \frac{dT_a}{ds} \;\&\; q_{\mathrm{v}} = -(\rho\, c)_b (\pi\, a^2\, \bar{u}) \frac{dT_{\mathrm{v}}}{ds} \tag{27}$$

Thus, Eq. (25) can be written in the final form as:

$$(\rho\, c)_b (n\pi\, a^2 \bar{u}) \frac{d}{ds} \left[T_a - T_{\mathrm{v}} \right] - (\rho\, c)_b (n\, 2\pi\, a\ g)(T_a - T_{\mathrm{v}}) = \nabla \bullet (k_t \nabla T_t) + q_m \tag{28}$$

2.2.6 The Weinbaum and Jiji Bio-Heat Equation Model

Weinbaum and Jiji (1985) derived a simplified, single equation model to study the effect of blood flow on the tissue temperature variations. This is because Eq. (26) cannot be solved for T_t since both T_a and T_{v} are unknowns. Therefore, the mean tissue temperature can be approximated as:

$$T_t \cong \frac{T_a + T_{\mathrm{v}}}{2} \tag{29}$$

Thus, the magnitude of the difference $(q_a - q_{\mathrm{v}})$ is much smaller than the magnitude of either q_a or q_{v}. Moreover, Weinbaum and Jiji (1985) assumed that the tissue around the vessel pair is a pure conduction region such that:

$$q_a \cong q_{\mathrm{v}} = \sigma\, k_t (T_a - T_{\mathrm{v}}) \tag{30}$$

where σ is a geometrical factor given by:

$$\sigma = \frac{\pi}{cosh^{-1}(L_s/a)} \tag{31}$$

The ratio L_s/a denotes the ratio of the vessel spacing to vessel diameter. Equations (27), (29), and (30) are solved to obtain an equation for the artery-vein temperature difference and the tissue temperature gradient:

$$T_a - T_v = -\frac{\pi\, a^2\, \bar{u}\, (\rho\, c)_b}{\sigma\, k_t} \frac{dT_t}{ds} \tag{32}$$

Substituting Eq. (32) in the original model of WJL; Eq. (24), yields a new bioheat equation proposed by Weinbaum and Jiji (1985) as follows:

$$\frac{n\pi^2\, ak_b}{4k_t} Pe \left(\frac{d}{ds} \left[\frac{a\, Pe}{\sigma} \frac{dT_t}{ds} \right] - \frac{2g\, Pe}{\sigma\, \bar{u}} \frac{dT_t}{ds} \right) = -\nabla \bullet k_t \nabla T_t - q_m \tag{33}$$

Where Pe is the Peclet number; which is defined as $Pe = \dfrac{2a(\rho\, c)_b \bar{u}}{k_b}$.

2.2.7 Other Models

Baish (1994) developed a new bioheat transfer model for a perfused tissue based on solving conjugate convection of the blood coupled to the three-dimensional conduction in the extravascular tissue while accounting for a statistical interpretation of the calculated temperature field. He illustrated that Pennes model of bioheat transfer equation accurately determines the mean tissue temperature except when the arteries and veins are in closely spaced pairs. Moreover, Baish (1994) demonstrated the dependence of the temperature distribution on the flow rate and the vascular geometry. Wissler (1987) vigorously criticized the assumptions that used in deriving Weinbaum and Jiji (1985) model. In particular, Wissler (1987) indicated that Weinbaum and Jiji (1985) assumed that the mean temperature in the neighborhood of an artery–vein pair is the arithmetic mean of the arterial and venous blood at the point of entry. Moreover, Wissler (1987) questioned the basis that the temperature gradient is proportional to the temperature difference between the artery–vein pair which was used in the derivation of Weinbaum and Jiji model.

2.3 Mathematical Modeling of Bioheat Equation Using Porous Media Theory

Transport phenomena in porous media have received continuing interest in the past five decades. This interest stems from its importance in many industrial and clinical applications (Bejan et al., 2004, Ingham and Pop, 2002, 2005, Ingham et al., 2004,

Pop and Ingham, 2001, Vafai, 2000, 2005, Khanafer et al., 2003a, b). Moreover, complicated and interesting phenomena can be modeled using porous media concept. Recently, Xuan and Roetzel (1997, 1998) employed porous media concept to model tissue-blood system composed mainly of tissue cells and interconnected voids that contain either arterial or venous blood. The thermal energy exchange between the tissue and blood was modeled using the principle of local thermal non-equilibrium as described in the works of Amiri and Vafai (1994, 1998), Alazmi and Vafai (2002), Khashan et al. (2005, 2006), and Lee and Vafai (1999). Thus, two energy equations were derived for the blood and tissue, respectively:

$$\varepsilon(\rho\, c)_b \left(\frac{\partial < T >^b}{\partial t} + < \mathbf{u} >^b \cdot \nabla < T >^b \right) = \nabla \cdot \left(\mathbf{k}_b^a \cdot \nabla < T >^b \right) + h_{bs} \left[< T >^s - < T >^b \right] \quad (34)$$

$$(1-\varepsilon)(\rho\, c)_s \frac{\partial < T >^s}{\partial t} = \nabla \cdot \left(\mathbf{k}_s^a \cdot \nabla < T >^s \right) - h_{bs} \left[< T >^s - < T >^b \right] + (1-\varepsilon) q_m \quad (35)$$

where $< T >^b$, $< T >^s$, $\mathbf{k}_b^a$, $\mathbf{k}_s^a$, $< \mathbf{u} >^b$ and h_{bs}, and ε are the local volume-averaged arterial blood temperature, local volume-averaged solid tissue temperature, blood effective thermal conductivity tensor, solid tissue effective thermal conductivity tensor, blood velocity vector, and interstitial convective heat transfer coefficient, respectively. For isotropic conduction, the effective thermal conductivity k_b^a of blood and solid tissue k_s^a can be expressed as:

$$k_b^a = \varepsilon\, k_b \text{ and } k_s^a = (1-\varepsilon) k_s \quad (36)$$

The heat exchange between the blood and the tissue is expressed as: $h_{bs} \left[< T >^s - < T >^b \right]$. Further, Xuan and Roetzel (1997, 1998) considered an effective thermal conductivity for the blood to account for blood dispersion. The concept of thermal dispersion is well established in the theory of porous media as presented in the works of Amiri and Vafai (1994, 1998). Due to insufficient knowledge about the thermal and anatomic properties of the tissue, velocity field of the blood, and interstitial convective heat transfer coefficients, the local thermal equilibrium model represents a good approximation for determining the temperature field in applications involving small size blood vessels ($\varepsilon << 1$). This implies that blood flowing in these small vessels will be completely equilibrated with the surrounding tissue. Therefore, Eqs. (34) and (35) reduce to the following equation (Khanafer and Vafai, 2001, Marafie and Vafai, 2001):

$$[(\rho\, c)_b \varepsilon + (1-\varepsilon)(\rho\, c)_s] \frac{\partial < T >}{\partial\, t} + \varepsilon(\rho\, c)_b < \mathbf{u} >^b \cdot \nabla < T > = \nabla \left[\left(\mathbf{k}_s^a + \mathbf{k}_b^a \right) \cdot \nabla < T > \right] + q_m(1-\varepsilon) \quad (37)$$

The second term on the left hand side of the above equation represents the heat transfer due to the blood perfusion. The perfusion source term in Pennes

model was derived based on a uniform blood perfusion assumption and is equal to $(\rho\, c)_b \omega (T_b - T)$. In hyperthermia applications, tissue may absorbs energy from external source such as electromagnetic or ultrasonic radiation and therefore another heat source term should be added to the right side of Eq. (37) as follows:

$$[(\rho\, c)_b \varepsilon + (1-\varepsilon)(\rho\, c)_s] \frac{\partial < T >}{\partial\, t} + \varepsilon (\rho\, c)_b < \mathbf{u} >^b \cdot \nabla < T > = \nabla \left[\left(\mathbf{k}_s^a + \mathbf{k}_b^a \right) \cdot \nabla < T > \right] + q_m (1-\varepsilon) + q_h (1-\varepsilon) \tag{38}$$

From above, one can note that the theory of porous media can be used to develop a more robust bioheat model since it allows including the effect of blood thermal dispersion, porosity variation, effective tissue conductivity, and effective tissue capacitance, and the exact heat transfer exchange between the blood and tissue. However, Pennes equation ignores all these effects. Tables 1 and 2 summarize the previously discussed bioheat transfer models in this work.

3 Tissue Engineering

3.1 Introduction

Tissue engineering is an interdisciplinary field that involves chemical and material engineering, biology, reactor engineering, and medicine to develop viable biological substitutes for the repair or regeneration of human tissue or organ function (Lavik and Langer, 2004, Lanza et al., 2000). Examples of tissue-engineered substitutes that are currently being investigated include skin, cartilage, bone, vascular, heart, breast and liver (Masood et al., 2005). A large number of Americans suffer organ and tissue loss every year from accidents, birth defects, diseases, hereditary disorders, etc. Approximately 72,000 American people were on the waiting list for an organ transplant in 2000. Only 23,000 transplant were performed (Port, 2002).

In order to achieve significant tissue structures, there must be appropriate transport of nutrients to and waste from the cells as they begin to form a tissue or organ (Lavik and Langer, (2004). Various types of bioreactors have been used to culture cells for tissue regeneration or repair such as spinner flask (Sikavitsas et al., (2002), rotating wall vessels (Carrier et al., (1999), and perfusion bioreactors (Bancroft et al., (2002). The aim of the bioreactor is to provide suitable nutrients and oxygen flow and many of the biophysical and biochemical conditions necessary to produce a functional artificial tissue. Thus, bioreactor design is critical for the development of certain tissues (Bancroft et al., 2002).

3.2 Porous Scaffolds for Tissue Engineering

The efficient design and manufacture of a complex scaffold with optimum porosity and interconnectivity is significant for tissue engineering applications. The essential principle of tissue engineering is to combine a scaffold with cells for tissue

Table 1 Summary of bioheat transfer models

Model	Mathematical model
Pennes (1948)	$\rho\, c_p \frac{\partial T}{\partial t} = \nabla \cdot (k \nabla T)) + \omega \rho_b c_b \,(T_b - T) + q_m$
Wulff (1974)	$\rho\, c_p \frac{\partial T}{\partial t} = k \nabla^2 T - \rho_b \mathrm{v}_h c_p \nabla T + q_m$
Klinger (1974)	$(\rho\, c) \frac{\partial T}{\partial t} + (\rho\, c) \mathbf{v}\, \nabla T = k \nabla^2 T + q$
CH (1980)	$\rho\, c \frac{\partial T_t}{\partial t} = \nabla \bullet k_{eff} \nabla T_t + (\rho\, c)_b \omega^* \left(T_a^* - T_t\right) - (\rho\, c)_b \mathbf{v}_p \bullet \nabla T_t - \nabla \bullet k_p \nabla T_t + q_m$
WJL (1979, 1984a, b)	$(\rho\, c)_b (n \pi\, a^2 \bar{u}) \frac{d}{ds} \left[T_a - T_{\mathrm{v}}\right] - (\rho\, c)_b (n 2\pi\, a\, g)(T_a - T_{\mathrm{v}}) = \nabla \bullet (k_t \nabla T_t) + q_m$
WJ (1985)	$\frac{n \pi^2 a k_b}{4 k_t} Pe \left(\frac{d}{ds} \left[\frac{a\, Pe}{\sigma} \frac{dT_t}{ds} \right] - \frac{2 g Pe}{\sigma \bar{u}} \frac{dT_t}{ds} \right) = -\nabla \bullet k_t \nabla T_t - q_m$
Amiri and Vafai (1994, 1998, 2002), Khanafer et al. (2003a,b) Xuan and Roetzel (1997, 1998)	$\varepsilon(\rho\, c)_b \left(\frac{\partial \langle T \rangle^b}{\partial t} + < \mathbf{u} >^b \cdot \nabla < T >^b \right) = \nabla \cdot \left(\mathbf{k}_b^a \cdot \nabla < T >^b \right) + h_{bs} \left[< T >^s - < T >^b \right]$
	$(1 - \varepsilon)(\rho\, c)_s \frac{\partial \langle T \rangle^s}{\partial t} = \nabla \cdot \left(\mathbf{k}_s^a \cdot \nabla < T >^s \right) - h_{bs} \left[< T >^s - < T >^b \right] + (1 - \varepsilon) q_m$
Vafai and co-workers (1994, 1998, 2001, 2002, 2003) Xuan and Roetzel (1997, 1998)	$[(\rho\, c)_b \varepsilon + (1 - \varepsilon)(\rho\, c)_s] \frac{\partial < T >}{\partial t} + \varepsilon (\rho\, c)_b < \mathbf{u} >^b \cdot \nabla < T > = \nabla \left[\left(\mathbf{k}_s^a + \mathbf{k}_b^a \right) \cdot \nabla < T > \right] + q_m (1 - \varepsilon)$

CH: Chen and Holmes, WJ: Weinbaum, Jiji, WJL: Weinbaum, Jiji, and Lemons

Table 2 Summary of bioheat models

Bio-heat model	Main characteristics
Pennes (1948)	• Simple model • Assumed uniform physical properties and metabolic heating • Based on uniform perfusion • Heat transfer between flowing blood and tissue was modeled to be proportional to the temperature difference between the two blood stream temperatures
Wulff (1974)	• Modified version of Pennes model • Assumed thermal equilibrium between flowing blood and surrounding tissue. • Modified perfusion term • Assumed uniform mean blood velocity
Klinger (1974)	• Assumed constant physical properties • Incompressible blood flow • Includes convection heat transfer by blood flow inside the tissue • Assume spatial and temporal variation of the velocity field and heat source
CH (1980)	• Use two separate volumes: one for solid tissue and one for blood • The total heat transfer by conduction relates to heat transfer by conduction in the solid tissue and in the vascular space • The total perfusion term corresponds to: The effect of blood flow on tissue temperature around large vessels, heat transfer that takes place as a result of the flowing blood, and heat transfer due to the small temperature changes • Used solid tissue thermal conductivity for the effective thermal conductivity since the vascular space is much smaller than the tissue volume • Introduced perfusion conductivity tensor in the bio-heat equation

Table 2 (continued)

Bio-heat model	Main characteristics
WJL (1979, 1984)	• Based on a hypothesis that small arteries and veins are parallel and the flow direction is countercurrent resulting in counterbalanced heating and cooling effects • Derived coupled energy equations for artery-vein pair and tissue • Utilizes the effective conductivity which is a function of blood flow rate and vascular geometry • Assume isotropic blood perfusion between the countercurrent vessels
WJ (1985)	• The mean tissue temperature is approximated by an average temperature of the bulk mean temperatures inside the blood vessel • Valid when arteries and veins are close leading to negligible blood perfusion effects • Assumed that the tissue around the vessel pair is a pure conduction region • Utilizes an effective conductivity as function of the perfusion rate
Wissler (1987)	• Avoids assumptions of the Weinbaum and Jiji model
Porous Media Model (Local thermal equilibrium principle) Khanafer and Vafai (2001), Khanafer et al. (2003), Amiri and Vafai (1994, 1998), Xuan and Roetzel (1997, 1998), Marafie and Vafai (2001)	This model modifies Pennes equation by accounting for the following effects: • variable tissue porosity • effective tissue conductivity • effective tissue capacitance • blood dispersion
Porous Media Model (Local thermal non-equilibrium principle) Amiri and Vafai (1994, 1998), Xuan and Roetzel (1997, 1998), Alazmi and Vafai (2002), Khanafer and Vafai (2001)	• This model requires more knowledge about the thermal and anatomic properties of the tissue, velocity field of the blood, and interstitial convective heat transfer coefficients • This model considers the following effect: – variable tissue porosity – blood dispersion – effective tissue conductivity – effective tissue capacitance

replacement or repair. The scaffold provides a temporary biomechanical profile until the cells produce their own matrix proteins and a full tissue (Masood et al., (2005). Masood et al. (2005) addressed the issue of developing an efficient methodology to design and manufacture a scaffold structure using a novel approach based on fused deposition modeling (FDM) rapid prototyping (RP) technology. They derived a theoretical expression for the porosity of one horizontal layer of a cylindrical model created on the FDM process as follows:

$$\varepsilon_{theortical} = \frac{V_{pore,layer}}{V_{part,layer}} = 1 - (1 - \varepsilon_{initial}) \left\{ RW \left[\sum_{n=0}^{n=N_r} W_n \right] N_r + (N_r - 1) RG \times \pi D / N_r \right\} / t$$

$$\varepsilon_{initial} = 1 - W_{\mathrm{mod}\,el} / \left\{ \rho_{material} \times N_L \times t \times RW \left[\sum_{n=0}^{n=N_r} W_n \right] N_r \right\} \tag{39}$$

where D is the diameter, H is the height of the cylindrical model, $\mathrm{W_{model}}$ is the average weight of the model when an RG setting is taken as zero, RG is the raster gap, RW is road width, t is the layer thickness, $\rho_{material}$ is the density of the material, W_n is the width of nth road from the center of the cylindrical layer, N_r and N_L are the number of raster lines and the number of layers, respectively, defined as follows:

$$N_r = (D + RG)/(RW + RG) \;\&\; N_L = H/t \tag{40}$$

Porter et al. (2005) used the Lattice–Boltzmann method to simulate the flow conditions within perfused cell-seeded cylindrical scaffolds. Microcomputed tomography imaging was used to define the scaffold micro-architecture for the simulations, which produced a 3-D fluid velocity field throughout the scaffold porosity. Sucosky et al. (2004) used particle image velocity to determine fluid mechanics of a spinner-flask bioreactor. Coletti et al. (2006) developed a comprehensive mathematical model of convection and diffusion in a perfusion bioreactor, combined with cell growth kinetics. Time-dependent porosity and permeability changes due to the cell density were included in their model. The fluid dynamics of the medium flow inside the bioreactor was described through the Navier–Stokes equations for incompressible fluids while convection through the scaffold was modeled using Brinkman's extension of Darcy's law for porous media. The scaffold porosity $\varepsilon(\mathrm{x_i}, \mathrm{t})$, which decreases from its initial value $\varepsilon_0(\mathrm{x_i}, 0)$ as the cell density increases, was expressed as follows:

$$\varepsilon(x_i, t) = \varepsilon(x_i, 0) - V_{cell}\rho_{cell}(x_i, t) \tag{41}$$

Where V_{cell} is the single cell volume. Tortuosity was modeled as a function of porosity ε as (Perry and Green (1997):

$$\tau = \left(\frac{2 - \varepsilon}{\varepsilon} \right)^2 \tag{42}$$

The functional form of Koponen et al. (1996) was used for permeability K:

$$K = \frac{\varepsilon^3}{q\tau^2 s^2} \tag{43}$$

Where s is the pore surface area per unit volume of porous material and q is a structural scaffold parameter.

References

Aenis M, Stancampiano AP, Wakhloo AK, and Lieber BB (1997) Modeling of flow in a straight stented and nonstented sidewall aneurysm model. ASME J. Biomech. Eng. 119: 206–212.

AlAmiri A (2000) Analysis of momentum and energy transfer in a lid-driven cavity filled with a porous medium. Int. J. Heat Mass Transfer. 43: 3513–3527.

AlAmiri A (2002) Natural convection in porous enclosures: The application of the two-energy equation model. Num. Heat Transfer: Part A. 41(8): 817–834.

Alazmi B and Vafai K (2002) Constant wall heat flux boundary conditions in porous media under local thermal non-equilibrium conditions. Int. J. Heat Mass Transfer 45: 3071–3087.

Amiri A and Vafai K (1994) Analysis of dispersion effects and nonthermal equilibrium, non-Darcian, variable porosity incompressible-flow through porous media. Int. J. Heat Mass Transfer 37: 939–954.

Amiri A and Vafai K (1998) Transient analysis of incompressible flow through a packed bed. Int. J. Heat Mass Transfer 41: 4259–4279.

Arkin H, Xu LX, and Holmes KR (1994) Recent developments in modeling heat transfer in blood perfused tissues. IEEE Trans. Biomed. Eng. 41: 97–107.

Baish JW (1994) Formulation of a statistical-model of heat transfer in perfused tissue. JASME J. Biomech. Eng. 116: 521–527.

Bancroft GN, Sikavitsast VI, Dolder J van den, Sheffield TL, Ambrose CG, Jansen JA, and Mikos AG (2002) Fluid flow increases mineralized matrix deposition in 3D perfusion culture of marrow stromal osteoblasts in a dose-dependent manner. Proc. Natl. Acad. Sci. USA 99:12600–12605

Bejan A, Dincer I, Lorente S, Miguel A, and Reis A (2004) Porous and complex flow structures in modern technologies. Springer-Verlag, NY.

Canton G, Levy DI, and Lasheras JC (2005) Hemodynamic changes due to stent placement in bifurcating intracranial aneurysms. J. Neusurg. 103: 146–155.

Carrier RL, Papadaki M, Rupnick M, Schoen FJ, Bursac N, Langer R, Freed LE, and Vunjak-Novakovic G (1999) Cardiac tissue engineering: cell seeding, cultivation parameters, and tissue construct characterization. Biotechnol Bioeng 64:580–589

Charny CK (1992) Mathematical models of bioheat transfer. Adv. Heat Transfer 22:19–152.

Charny CK and Levin RL (1988) Heat transfer normal to paired arteries and veins embedded in perfused tissue during hyperthermia. Trans. ASME J. Biomech. Eng. 110: 277–282.

Charny CK and Levin RL (1989) Bioheat transfer in a branching countercurrent network during hyperthermia. ASME J. Biomech. Eng. 111: 263–270.

Chen MM and Holmes KR (1980) Microvascular contributions in tissue heat transfer. Ann. NY Acad. Sci. 335: 137–150.

Coletti F, Macchietto S, and Elvassore N (2006) Mathematical modeling of three-dimensional cell cultures in perfusion bioreactors. Ind. Eng. Chem. Res. 45: 8158–8169.

Dewhirst MW and Samulski TV (1988) Hyperthermia in the treatment for cancer. Upjohn, Kalamazoo, MI.

Field SB and Hand JW (1990) An introduction to the practical aspects of hyperthermia. Taylor & Francis, NewYork.

Gobin YP, Counord JL, Flaud P, and Duffaux J (1994) In vitro study of hemodynamics in a giant saccular aneurysm model: Influence of flow dynamics in the parent vessel and effects of coil embolization. Neuroradiology 36: 530–536.

Groden C, Laudan J, Gatchell S, and Zeumer H (2001) Three-dimensional pulsatile flow simulation before and after endovascular coil embolization of a terminal cerebral aneurysm. J. Cerebr. Blood Flow Met. 21:1464–1471.

Hademenos GJ (1995) The physics of cerebral aneurysms. Phys. Today 48: 25–30.

Ingham DB and Pop I (eds.) (2002) Transport phenomena in porous media, vol. II. Pergamon, Oxford.

Ingham DB and I Pop (eds.) (2005) Transport phenomena in porous media, vol. III. Elsevier, Oxford.

Ingham DB, Bejan A, Mamut E, and Pop I (eds.) (2004) Emerging technologies and techniques in porous media. Kluwer, Dordrecht.

Khanafer K and Vafai K (2001) Isothermal surface production and regulation for high heat flux applications utilizing porous inserts. Int. J. Heat Mass Transfer 44: 2933–2947.

Khanafer K, Vafai K, and Kangarlu A (2003a) Computational modeling of cerebral diffusion-application to stroke imaging. Magn. Reson. Imaging 21:651–661.

Khanafer K, Vafai K, and Kangarlu A (2003b) Water diffusion in biomedical systems as related to magnetic resonance imaging. Magn. Reson. Imaging 21: 17–31.

Khanafer K, Sclicht M, Bull JL, and Berguer R (2006) The role of porous media in finite-element modeling of coil compaction in the treatment of cerebral aneurysms, Proceedings of BIO2006, ASME Summer Bioengineering Conference, Amelia Island Plantation, Florida.

Khanafer KM, Bull JL, Pop I, and Berguer R (2007) Influence of pulsatile blood flow and heating scheme on the temperature distribution during hyperthermia treatment. Int. J. Heat Mass Transfer 50: 4883–4890.

Khashan S, AlAmiri A, Pop I (2005) Assessment of the local thermal non-equilibrium condition in developing forced convection flows through fluid-saturated porous tubes, Appl. Thermal Eng. 25: 1429–1445.

Khashan S, AlAmiri A, Pop I (2006) Numerical simulation of natural convection heat transfer in a porous cavity heated from below using a non-Darcian and thermal non-equilibrium model. Int. J. Heat Mass Transfer 49: 1039–1049.

Klinger HG (1974) Heat transfer in perfused tissue-I: General theory. Bull. Math. Biol. 36: 403–415.

Knuckey N, Haas R, Jenkins R, and Epstein M (1992) Thrombosis of difficult aneurysms by the endovascular placement of platinum-dacron microcoils. J. Neurosurg. 77: 43–50.

Koponen A, Kataja M, and Timonen Jv (1996) Tortuous flow in porous media. Phys. ReV. E: Stat. Phys., Plasmas, Fluids, Relat. Interdiscip. Top 54: 406.

Kwon OK, Kim SH, Oh CW, Han MH, Kang HS, Kwon BJ, Kim JH, and Han DH (2006) Embolization of wide-necked aneurysms with using three or more microcatheters. Acta Neurochir (Wien) 148: 1139–1145.

Lanza R, Langer R, Vacanti JP (2000) Principles of tissue engineering, 2nd ed. Academic Press, New York.

Lanzino G, Wakhloo AK, Fessler RD, Mericle RA, Guterman LR, and Hopkins LN (1998) Intravascular stents for intracranial internal carotid and vertebral artery aneurysms: preliminary clinical experience. Neurosurg. Focus 5(4): E3.

Lavik E and Langer R (2004) Tissue engineering: current state and perspectives. Appl. Microbiol. Biotechnol. 65: 1–8.

Lee DY and Vafai K (1999) Analytical characterization and conceptual assessment of solid and fluid temperature differentials in porous media. Int. J. Mass Transfer 42: 423–435.

Lieber RB, Livescu V, Hopkins LN, and Wakhiloo AK (2002) Particle image velocimetry assessment of stent design influence on intra-aneurysmal flow. Ann. Biomed. Eng. 30: 768–777.

Liou TM, Liou SM, and Chu KL (2004) Intra-aneurysmal flow with helix and mesh stent placement across side-wall aneurysm pore of a straight parent vessel. ASME J. Biomech. Eng. 126: 36–43.

Marafie A and Vafai K (2001) Analysis of non-darcian effects on temperature differentials in porous media. Int. J. Heat Mass Transfer 44: 4401–4411.

Marks MP, Dake MD, Steinberg GK, Norbash AM, and Lane B (1994) Stent placement for arterial and venous cerebrovascular disease: Preliminary clinical experience. Radiology 191: 441–446.

Masood SH, Singh JP, and Morsi Y (2005) The design and manufacturing of porous scaffolds for tissue engineering using rapid prototyping. Int. J. Adv. Manuf. Tech. 27: 415–420.
Nakayama A (1995) PC-Aided numerical heat transfer and convective flow. CRC Press, Tokyo.
Nield DA and Bejan A (2006) Convection in porous media, 3rd ed. Springer, New York.
Ohta M, Wetzel SG, Dantan P, Bachelet C, Lovblad KO, Yilmaz H, Flaud P, and Rufenacht DA (2005) Rheological changes after stenting of a cerebral aneurysms: A finite element modeling approach. Cardiovasc. Inter. Rad. 28: 768–772.
Oleson JR, Sim DA, and Manning MR (1984) Analysis of prognostic variables in hyperthermia treatment of 161 patients. Int. J. Radiat. Oncol. Biol. Phys. 10: 2231–2239.
Overgaard J, Gonzales DG, Hulshof MC, Arcangeli G, Dahl O, Mella O, and Bentzen SM (1996) Hyperthermia as an adjuvant to radiation therapy of recurrent or metastatic melanoma: A multicenter randomized trial by the European society for hyperthermic oncology. Int. J. Hyperth. 12: 3–20.
Pennes HH (1948) Analysis of tissue and arterial blood temperature in the resting human forearm. J. Appl. Physiol. 1: 93–122.
Perry RH and Green DW (1997) Perry's chemical engineer handbook, 7th ed. McGraw-Hill, New York.
Pop I and Ingham DB (2001) Convective heat transfer: Mathematical and computational modeling of viscous fluids and porous media. Pergamon, Oxford.
Port F (2002) OPTN/SRTS annual report. Scientific Registry of Transplant Recipients and Organ Procurement Transplantation Network, Washington, D.C.
Porter B, Zauel R, Stockman H, Robert G, and Fyhrie D (2005) 3-D computational modelling of media flow through scaffolds in a perfusion bioreactor. J. Biomech. 38: 543–549.
Rhee K, Han MH, and Cha SH (2002) Changes of flow characteristics by stenting in aneurysm models: Influence of aneurysm geometry and stent porosity. Ann. Biomed. Eng. 30: 894–904.
Roemer RB and Cetas TC (1984) Applications of bioheat transfer simulations in hyperthermia. Cancer Res. 44: 4788–4798.
Sikavitsas VI, Bancroft GN, and Mikos AG (2002) Formation of three dimensional cell/polymer constructs for bone tissue engineering in a spinner flask and a rotating wall vessel bioreactor. J. Biomed. Mater. Res. 62:136–148
Srinivasan V, Vafai K, and Christensen RN (1994) Analysis of heat transfer and fluid flow through a spirally fluted tube using a porous substrate approach. ASME J. Heat Transfer 116: 543–551.
Stuhne GR and Steinman DA (2004) Finite-element modeling of the hemodynamics of stented aneurysm. ASME J. Biomech. Eng. 126: 382–212.
Sucosky P, Osorio DF, Brown JB, Neitzel G (2004) Fluid mechanics of a spinner- flask bioreactor. Biotechnol. Bioeng 85: 34–46.
Szikora I, Guterman LR, Wells KM, et al. (1994) Combined use of stents and coils to treat experimental wide-necked carotid aneurysms: Preliminary results. AJNR 15:1091–1102.
Turjman F, Massoud TF, Ji C, et al. (1994) Combined stent implantation and endosaccular coil placement for treatment of experimental wide-necked aneurysms: A feasibility study in swine. AJNR 12:1087–1090.
Vafai K (1984) Convective flow and heat transfer in variable-porosity media. J. Fluid Mech. 147: 233–259.
Vafai K (1986) Analysis of the channeling effect in variable porosity media. ASME J. Energy Resour. Technol. 108: 131–139.
Vafai K (ed.) (2000) Handbook of porous media. Marcel Dekker, New York.
Vafai K (ed.) (2005) Handbook of porous media, 2nd ed. Taylor & Francis, New York.
Vafai K and Amiri A (1998) Non-Darcian effects in confined forced convective flows, Transport Phenomena in Porous Media. D.B. Ingham and I. Pop (Eds.), 313–329, Pergamon, UK.
Vafai K and Tien CL (1980) Boundary and inertia effects on flow and heat transfer in porous media. Int. J. Heat Mass Transfer 24:195–203.
Vafai K and Tien C L (1981) Boundary and inertia effects on convective mass transfer in porous media. Int. J. Heat Mass Transfer 25:1183–1190.

Wakhloo AK, Schellhammer F, de Vries J, et al. (1994a): Self-expanding and balloon-expandable stents in the treatment of carotid aneurysms: An experimental study in a canine model. AJNR 15: 493–502.

Wakhloo AK, Schellhammer F, Vries JD, Haberstroh J, and Schumacher M (1994b) Self-Expanding and balloon-expandable stents in the treatment of carotid aneurysms: An experimental study in a canine model. AJNR: AM J. Neurosurg. 15: 493–502.

Wakhloo AK, Tio FO, Lieber BB, et al. (1995) Self-expanding nitinol stents in canine vertebral arteries: Hemodynamics and tissue response. AJNR 16:1043–1051.

Wakhloo AK, Lanzino G, Lieber BB, et al. (1998) Stents for intracranial aneurysms: the beginning of a new endovascular era? Neurosurgery 43: 377–379.

Weinbaum S and Jiji LM (1979) A two phase theory for the influence of circulation on the heat transfer in surface tissue. In 1979 Advances in Bioengineering (M.K. Wells, ed.): 179–182, NY.

Weinbaum S, Jiji LM, and Lemons DE (1984a) Theory and experiment for the effect of vascular microstructure on surface tissue heat transfer. Part I. Anatomical foundation and model conceptualization. ASME J. Biomech. Eng.106: 321–330.

Weinbaum S, Jiji LM, and Lemons DE (1984b) Theory and experiment for the effect of vascular microstructure on surface tissue heat transfer. Part II. Model formulation and solution. ASME J. Biomech. Eng. 106: 331–341.

Weinbaum S and Jiji LM (1985) A new simplified equation for the effect of blood flow on local average tissue temperature. ASME J. Biomech. Eng. 107: 131–139.

Wissler EH (1987) Comments on the new bioheat equation proposed by Weinbaum and Jiji. ASME J. Biomech. Eng. 109: 226–232.

Wulff W(1974) The energy conservation equation for living tissues. IEEE Trans. Biomed. Eng. BME 21: 494–495.

Xuan YM and Roetzel W (1997) Bioheat equation of the human thermal system. Chem. Eng. Technol. 20: 268–276.

Xuan YM and Roetzel W (1998) Transfer response of the human limb to an external stimulus. Int. J. Heat Mass Transfer 41: 229–239.

Metal Foams as Passive Thermal Control Systems

Shankar Krishnan, Jayathi Y. Murthy, and Suresh V. Garimella

1 Introduction

Solid–liquid phase change in porous media occurs in many practical applications such as thermal energy storage, freezing of moist soils, and manufacture of metal-matrix composites. Of particular interest in this chapter are thermal energy storage units with thermal conductivity enhancers (e.g., metal foams) for transient thermal control of electronics. Here, the phase change material (PCM) impregnates a metal foam. The latent heat of the PCM serves to absorb the heat generated by the electronics, while the metal foam helps transport heat from the heat source into the volume of the PCM and helps utilize the PCM more effectively. It is important to understand the flow, heat transfer and phase change in these systems to better design phase change energy storage systems for electronics cooling.

Melting and solidification of pure materials coupled with natural convection in the liquid melt has been studied extensively over the years (Sparrow et al., 1977, Gau and Viskanta, 1986, Jany and Bejan, 1988a). A detailed review of the literature on solid–liquid phase change heat transfer is given in Yao and Prusa (1989). Solid/liquid phase change processes in porous media have also received wide attention as they have many practical applications. Beckermann and Viskanta (1988) performed a combined experimental and numerical investigation of phase change occurring in a porous medium. Experiments were performed in a square enclosure with glass beads saturated with gallium. In their mathematical model, they assumed local thermal equilibrium between the glass beads and gallium. Their numerical results, which showed reasonable agreement with experiments, revealed that the solid–liquid interface shape was profoundly influenced by natural convection in the

Shankar Krishnan
Bell Laboratories, Alcatel-Lucent, Dublin-15, Ireland

J.Y. Murthy
Purdue University, West Lafayette, IN, USA
e-mail: jmurthy@ecn.purdue.edu

S.V. Garimella
Purdue University, West Lafayette, IN, USA
e-mail: sureshg@ecn.purdue.edu

P. Vadász (ed.), *Emerging Topics in Heat and Mass Transfer in Porous Media*,

© Springer Science+Business Media B.V. 2008

melt and heat conduction in the solid. Jany and Bejan (1988b) reported a scaling analysis of melting in porous media with local thermal equilibrium between the porous matrix and the PCM; melt convection was also incorporated. They found that the general behavior of the phase change process with a porous medium was similar to that of phase change without the porous medium. The melting phenomenon in porous media was shown to pass through four distinct regimes, each regime being characterized by distinct Nusselt numbers. Bejan (1989) reported an analytical study of melting in a confined porous medium saturated with a PCM. Non-Darcian effects were ignored as was the initial sub-cooling. The local thermal equilibrium assumption was also invoked between the solid and PCM. The liquid Stefan number was found to have a profound effect on the heat transfer and melting rates. Chellaiah and Viskanta (1990a, b) studied numerically and experimentally the melting of ice in a bed of glass and aluminum beads. They assumed local thermal equilibrium for the numerical model and found reasonable agreement with their experimental results. With the aluminum beads, the agreement between the numerical results and experiments was poor at high Rayleigh numbers, and deviation from local thermal equilibrium was suggested as the cause. A review of the literature on phase change heat transfer in porous media is available in Viskanta (1991).

Ellinger and Beckermann (1991) experimentally investigated the heat transfer enhancement in a rectangular domain partially occupied by a porous layer of aluminum beads. They found that the introduction of a porous layer caused the solid–liquid interface to move faster initially during the conduction-dominated regime. However, the overall melting and heat transfer rates were found to be lower with the porous layer present due to low porosity and permeability. They recommended the use of porous media of higher porosity and permeability with higher Rayleigh numbers for enhancement of melting and heat transfer rates. Tong et al. (1996) performed a numerical analysis of the enhancement of melting and heat transfer rates obtained upon incorporating a metal matrix into water, under the assumption of local thermal equilibrium. An order-of-magnitude increase was observed in the heat transfer rate with the metal matrix present. Vesligaj and Amon (1999) investigated the passive thermal control of portable electronics using PCMs with thermal conductivity enhancers under unsteady thermal workloads. An epoxy polymer was used as the PCM. The operational performance of portable electronics was found to improve when such a passive thermal storage device was used. Alawadhi and Amon (2003) reported numerical and experimental studies on the effectiveness of a thermal control unit composed of an organic PCM and a metal matrix. Modeling the metal matrix using modified effective thermophysical properties was found to yield good agreement with the experiments. Harris et al. (2001) presented an approximate theoretical model to analyze the phase change process in a porous medium. Assuming equilibrium melting at the pore scale, a parametric study based on a semi-heuristic conduction model was formulated. The conditions for the existence of local thermal equilibrium were explored. A number of studies have discussed the validity of assuming local thermal equilibrium in porous media saturated by a fluid (egs., Krishnan et al. (2004a), Minkowycz et al. (1999), Nield and Bejan (1992), Vafai and Sozen (1990), and Kaviany (1995)).

The work described in this chapter investigates non-equilibrium thermal transport associated with phase change in metal foams impregnated with organic PCMS for applications in the thermal management of electronics. These materials have also been used in heat exchanger units (Boomsma et al., 2003), thermal storage units (Price, 2003), and others (Ashby et al., 2000). Since the thermal conductivity of the phase change material considered in the present work is two orders of magnitude lower than that of the metal foam, non-equilibrium thermal effects may play a significant role. Flow and heat transfer in the PCM and foam are modeled using a volume-averaged approach. A two-temperature model is developed, with separate energy equations for the metal foam and the PCM, including phase change in the PCM. The interface heat exchange between the PCM and the metal foam and the pressure drop due to the foam are specified through the use of empirical correlations. An alternative approach to modeling these materials is to account for the intricate geometry of the porous structures and to compute the detailed transport through these structures. This approach is computationally expensive if the entire physical domain were to be simulated. Instead, this approach may be used to replace the empiricism in specifying the PCM-foam interaction by considering the detailed flow and heat transfer in a single periodic unit cell. Detailed modeling of pore-scale heat transfer has been used to yield the effective thermal conductivity, permeability, friction factor and local heat transfer coefficient for open-cellular foams Krishnan et al. (2006a, b).

In this chapter, a rectangular enclosure containing a metal foam impregnated with PCM is considered. This work builds on a previous analysis of natural convection in a PCM-foam domain, but in which change of phase was not considered (Krishnan et al., 2004a). Issues investigated and discussed in this work include natural convection in the melt, the effects of Rayleigh, Stefan and interstitial Nusselt numbers on the temporal evolution of the melt front location, heat transfer rate, the temperature differentials between the solid and fluid, and the melting rate under local thermal non-equilibrium. The results are compared with local thermal equilibrium models and the validity of the local thermal equilibrium assumption is discussed.

2 Mathematical Formulation and Numerical Modeling

A schematic of the problem under investigation is shown in Fig. 1. A square domain of height H encloses the porous metal foam which is filled with solid phase change material (PCM). The melting point of the PCM is T_{melt}, and the right wall is maintained at T_C ($< T_{melt}$). The top and bottom walls are adiabatic. Initially, the solid metal foam and the PCM are at equilibrium at temperature T_C. At time $\tau = 0$, the left wall temperature is raised to T_H ($> T_{melt}$) and the PCM is allowed to melt. The thermophysical properties of the solid metal foam and the PCM are assumed to be constant over the range of temperatures considered. In the liquid state, the PCM is assumed to be incompressible, Newtonian, and subject to the Boussinesq approximation. The densities of the solid and liquid PCM are assumed to be equal, i.e., the volume change upon phase change is ignored. Thermal dispersion effects may be important for very high Rayleigh numbers (Amiri and Vafai, 1994), but are

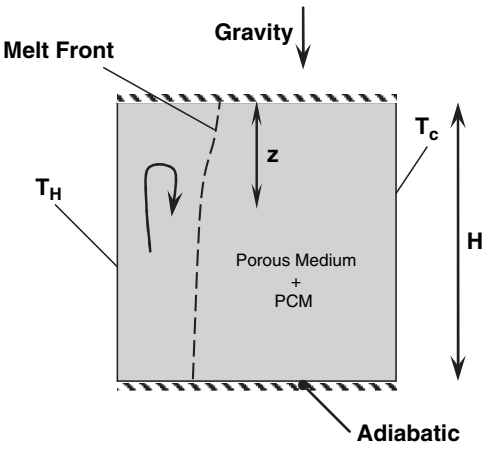

Fig. 1 Schematic illustration of the problem under investigation

neglected in the present work due to the lack of available models for metal foams. The volume-averaged governing mass and momentum equations in dimensionless terms, subject to the above assumptions, are:

$$\nabla.\mathbf{U} = 0 \tag{1}$$

$$\frac{1}{\mathrm{Pr}}\left(\frac{1}{\varphi}\frac{\partial \mathbf{U}}{\partial \tau} + \frac{1}{\varphi^2}(\mathbf{U}.\nabla)\,\mathbf{U}\right) = -\nabla \mathbf{P} + \frac{1}{\varphi}\nabla^2\mathbf{U} - \left(\frac{1}{Da^2} + \frac{F}{\mathrm{Pr}\,.Da}|\mathbf{U}|\right)\mathbf{U} + Ra\,T_f^*\frac{\mathbf{g}}{|\mathbf{g}|} \tag{2}$$

In the above equation, F is the inertial coefficient and φ ($= V_l/V$) is the fraction of liquid PCM in the given volume.

The governing energy equations are written for the metal foam and PCM separately and are closed using an interstitial Nusselt number. Assuming equilibrium melting at the pore scale, i.e. ignoring kinetics effects, the dimensionless energy equations are:

$$(1-\varepsilon)\,\Omega\frac{\partial T_m^*}{\partial \tau} = (1-\varepsilon)\,\lambda\nabla^2 T_m^* - Nu_i\left(T_m^* - T_f^*\right) \tag{3}$$

$$\varepsilon\frac{\partial T_f^*}{\partial \tau} + (\mathbf{U}.\nabla)\,T_f^* = \varepsilon\nabla^2 T_f^* - \frac{\varepsilon}{Ste}\frac{\partial \gamma}{\partial \tau} - Nu_i\left(T_f^* - T_m^*\right) \tag{4}$$

In equation (4), γ ($= V_l/V_f$) is the fraction of liquid in the PCM. As an alternative, if local thermal equilibrium can be assumed, the energy equations (3) and (4) may be replaced by a single energy equation given by

$$(\varepsilon + (1-\varepsilon)\,\Omega)\frac{\partial T^*}{\partial \tau} + (\mathbf{U}.\nabla)\,T^* = (\varepsilon + (1-\varepsilon)\,\lambda)\,\nabla^2 T^* - \frac{\varepsilon}{Ste}\frac{\partial \gamma}{\partial \tau} \tag{5}$$

Equation (5) can be obtained from equation (3) and (4) by setting $T_m^* = T_f^* = T^*$ and adding equation (3) and (4). If no porous medium were present, the governing

mass, momentum and energy equations would be obtained by setting $\varepsilon = 1$ and $\mathrm{Da} = \infty$ in equations (1), (2) and (5). The following dimensionless variables are used in deriving equations (1)–(5):

$$\xi = \frac{x}{H}; \eta = \frac{y}{H}; \tau = \frac{t\alpha_f}{H^2}; U = \frac{uH}{\alpha_f}; \quad P = \frac{pH^2}{\rho_f \upsilon_f \alpha_f}$$
$$T_s^* = \frac{(T_m - T_C)}{(T_H - T_C)}; \quad T_f^* = \frac{\left(T_f - T_C\right)}{(T_H - T_C)}; T^* = \frac{(T - T_C)}{(T_H - T_C)}$$

The relationship between φ, ε and γ in the above equations can be expressed as follows

$$\varphi = \begin{cases} \varepsilon & for \quad T_f^* \geq T_{melt}^* + \Delta T^* \\ \varepsilon \left(\dfrac{T_f^* - T_{melt}^* + \Delta T^*}{2\Delta T^*} \right) & for \quad T_{melt}^* - \Delta T^* < T_f^* < T_{melt}^* + \Delta T^* \\ 0 & for\ T_f^* \leq T_{melt}^* - \Delta T^* \end{cases}$$

Here, phase change is assumed to occur over a small but finite temperature range ΔT^* for numerical stability. For all computations performed in this study a ΔT^* of 0.04 or less was used. In order to model solid–liquid phase change phenomena in the same grid, the third term in equation (2) was used to immobilize the material in the fully solid regime by imposing a small value of permeability K ($= 1 \times 10^{-10}\,\mathrm{m}^2$).

The dimensionless parameters describing the heat and fluid flow processes are

$$\mathrm{Pr} = \frac{\upsilon_f}{\alpha_f}; \; Ra = \frac{g\beta_f H^3 (T_H - T_C)}{\alpha_f \upsilon_f}; \; Da = \frac{\sqrt{K}}{H}$$
$$Nu_i = \frac{h_v H^2}{k_f}; \; Ste = \frac{\left(C_p\right)_f (T_H - T_C)}{\Delta H}$$
$$\lambda = \frac{k_m}{k_f}; \; \lambda_e = \frac{k_{eq}}{k_f} = \varepsilon + (1 - \varepsilon)\lambda; \; \Omega = \frac{\left(\rho C_p\right)_m}{\left(\rho C_p\right)_f}; \; F; \varepsilon$$

The quantity h_v is the volumetric interstitial heat transfer coefficient governing the heat exchange between the PCM and the metal and is specified through the use of empirical correlations. The inertial coefficient, F, for metal foams, is taken to be 0.068 (Hwang et al., 2002). For metal foams, a constant porosity of 0.8 is used for all the computations. The effective conductivity is given by $k_{eq} = \varepsilon k_f + (1 - \varepsilon) k_m$.

The computational domain is discretized into finite volumes using a rectangular mesh. All the variables are stored at the cell centroids. A central-differencing scheme with a deferred correction is used for convective fluxes as discussed in Ferziger and Peric (1995). A central-differencing scheme is used for discretizing diffusive fluxes as well. The transient terms are discretized using a second-order-accurate three-time-level scheme (Ferziger and Peric, 1995). The SIMPLE algorithm is used for obtaining the velocity fields, and the linearized systems of

equations are solved using a strongly implicit procedure (SIP). The calculations are terminated when the dimensionless residual (Ferziger and Peric, 1995) has dropped at least below 10^{-4} for all governing equations. Details of the code validation, grid- and time-independence exercises are available in Krishnan et al.(2004a, 2005).

3 Results and Discussion

The porosity of the metal foam considered is held constant at 0.8 and the pore size (d/H) is 0.0135. The typical ratio of the average ligament diameter (d_m) of the foam to the mean cell size (d) is 0.1875, with the average ligament diameter of 0.36 mm (Hwang et al., 2002). The ratio of the metal foam-to-PCM thermal conductivity (λ) is 1000. The Prandtl number of the PCM is fixed at 50, and is typical of the value for many organic PCMs.

A heat transfer correlation, $Nu_{i,d} = 6(1-\varepsilon)\left[2 + 1.1\,(\mathrm{Re})^{0.6}\,(\mathrm{Pr})^{1/3}\right]$, is available for spherical beads (Wakao and Kaguei, 1982), and covers a wide range of Reynolds number, but a correlation applicable to metal foams is not available. For high Prandtl number fluids undergoing phase change in porous enclosures, the velocities encountered are small (for example, the vertical velocity v (m/s) is $O(10^{-3})$ or less for $\mathrm{RaDa}^2 \leq 10^4$). Also, the heat transfer between the metal foam and the solid PCM is only by conduction during the initial transient. As the system is largely conduction-dominated, it is critical to establish the diffusion limit for the interstitial heat transfer coefficients. Table 1 lists the various models used in the present study for closing the energy equations (3) and (4). Though some of the correlations in Table 1 are for forced convection, they are assumed to be approximately valid for natural convection in the melt as well. The Reynolds number in the equations is interpreted as the local Reynolds number based on the local mean velocity, i.e., $u_{mean}d/\upsilon$. As $\mathrm{Re} \to 0$, some of the equations yield $\mathrm{Nu_{i,d}} = 0$, which does not correctly represent the conduction limit. In the equations listed in Table 1, a_{sf} is the specific surface area of the metal foams and is given by the relation (Calmidi and Mahajan, 2000)

$$a_{sf} = \frac{3\pi d_m}{(0.59d)^2}\left[1 - \exp\left(-\left(\frac{1-\varepsilon}{0.04}\right)\right)\right]$$

In the discussion that follows, the "fluid" phase refers to the PCM, whether solid or melted, while the "solid" phase refers to the metal foam. In order to understand the effect of inter-phase heat transfer on the melting of PCM, the case of zero inter-phase heat transfer ($\mathrm{Nu_i} = 0$) is first considered. Under this condition, there is no thermal interaction between the metal foam and the PCM, and the melt experiences only the flow resistance offered by the porous foam. Figure 2a shows the temporal evolution of the dimensionless solid-to-fluid temperature difference along $\eta = 0.5$ for $\mathrm{Ra} = 10^6$, $\mathrm{Pr} = 50$, $\mathrm{Da} = 10^{-2}$, $\lambda = 10^3$, $\Omega = 1$ and $\mathrm{T_{melt}}^* = 0.3$. The Stefan number for this case is 0.1. Figure 2b shows the PCM and metal foam temperature distributions at the mid-height of the domain. In Fig. 2b and in other similar figures that

Table 1 Interstitial nusselt number

	Interstitial nusselt number, $Nu_{i,d} = \frac{h_v d^2}{k_f}$	Analysis type	Remarks
Wakao and Kaguei (1982)	$6(1-\varepsilon)\left[2 + 1.1\,(\mathrm{Re})^{0.6}\,(\mathrm{Pr})^{1/3}\right]$	Experimental, Analytical	For forced convective flow over spheres ($0 < \mathrm{Re} < 8500,\ \varepsilon \sim 0.4$)
Hwang et al. (2002)	$0.376\,(\mathrm{Re})^{0.644}\,(\mathrm{Pr})^{0.37}$	Experimental	For forced flow across metal foams ($40 < \mathrm{Re} < 200$)
Calmidi and Mahajan (2000)	$\left(a_{sf} d\right) C\mathrm{Re}^{0.5}\mathrm{Pr}^{0.37}$	Experimental	Correlation for forced flow across metal foams ($\mathrm{C} = 0.52,\ 40 < \mathrm{Re} < 1000$). Originally proposed for forced flow across cylinder.
Phanikumar and Mahajan (2002)	$\left(a_{sf} d\right) C\mathrm{Re}^{0.5}\mathrm{Pr}^{0.37}$	Experimental	Correlation for forced flow across metal foams ($\mathrm{C} = 0.52,\ 10^5 < \mathrm{Ra} < 5 \times 10^5$). Originally proposed for forced flow across cylinder.
Kuwahara et al. (2001)	$4(1-\varepsilon)\left[\left(1 + \frac{4(1-\varepsilon)}{\varepsilon}\right) + \frac{1}{2}(1-\varepsilon)^{1/2}\,\mathrm{Re}^{0.6}\mathrm{Pr}^{1/3}\right]$	Numerical	Forced flow across arbitrary geometry ($0 < \mathrm{Re} < 8000,\ 0.2 < \varepsilon < 0.9$)
Morgan (1975)	$\frac{2}{\ln\left(\frac{d_\infty}{d_m}\right)}$	Analytical	For an infinitely long cylinder in an infinite space.
Frankel and Acrivos (1968)	$\frac{2a_{sf} d}{(1.372 + 0.5\ln 2 - 0.5\ln(\mathrm{Re}\cdot\mathrm{Pr}))}$	Analytical	For shear flow across freely suspended cylinders. The derived solution is for $\mathrm{Re.Pr} \to 0$.
Frankel and Acrivos (1968)	$\frac{2}{\ln(\mathrm{Re}\cdot\mathrm{Pr})}$	Analytical	For low Reynolds number flows over cylinders under $\mathrm{Re.Pr} \to 0$.
Resistance analysis	$\frac{a_{sf}}{\left[\frac{d}{2k_f} + \frac{d_m}{2k_m}\right]}$	Analytical	Resistances in series

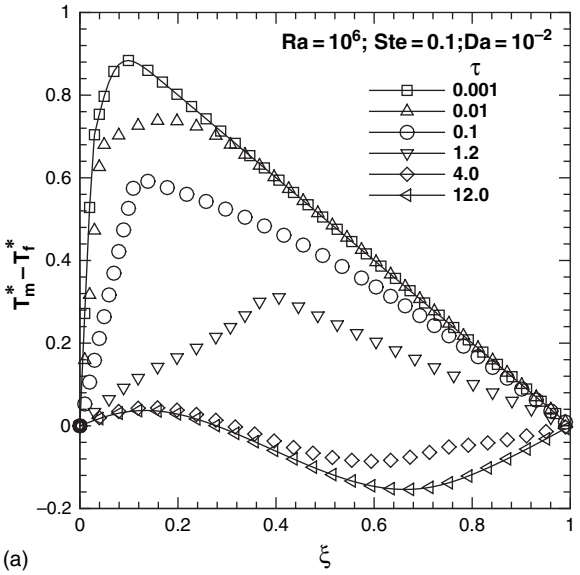

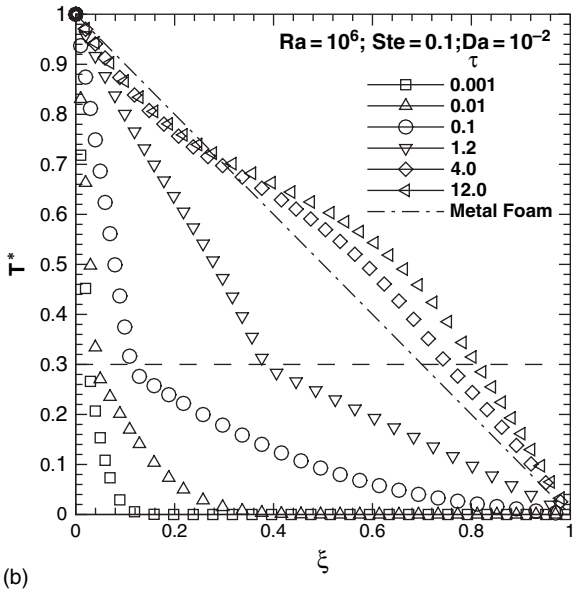

Fig. 2 Predicted temporal evolution of the thermal field for $Ra = 10^6$, $Nu_{i,d} = 0$, $Ste = 0.1$, $Pr = 50$, $Da = 10^{-2}$ at the mid-height of the domain ($\eta = 0.5$): (**a**) Solid-to-fluid temperature difference, and (**b**) Solid and fluid temperature distributions. Also plotted in the figure is the nondimensional melting temperature (horizontal *dashed line*)

follow, the dimensionless metal foam temperature distribution is represented using dot-dashed lines while the PCM is represented using solid lines with open symbols.

Also, the dimensionless melting point is shown as a horizontal dashed line. In the limit of zero inter-phase heat exchange, the metal foam and PCM develop independently and the temperature difference between them is determined by the relative response of the two phases. The metal foam reaches a steady state in a time scale

of order (H^2/α_m), or a dimensionless time scale of $\tau_m \sim \Omega/\lambda$. For low Rayleigh numbers and Ste < 1, the time for the PCM to reach a steady state is governed by the effective inertia associated with phase change. It scales as H^2/α_{ef} where $\alpha_{ef} = k_f/\left(\rho_f C_{p_{ef}}\right)$ and $(C_p)_{ef} = (\Delta H\varepsilon)/\Delta T$. The corresponding dimensionless time scale is $\tau_f \sim \varepsilon/\text{Ste}$. The metal foam is seen to have reached a steady state well before the temperature field in the fluid has started to develop. Thus at early times, the temperature differential in the domain is very large, of O(1). The temperature difference progressively decreases with time, reaching a steady-state value over the PCM time scale. Furthermore, the maximum temperature difference between the metal foam and PCM occurs near the solid/liquid interface. This is expected because the phase-change process constrains the PCM temperature to T^*_{melt} at the interface. The thickness of the warm boundary layer ($\sim [\text{RaDa}^2]^{-0.25}$) near the heated wall ceases to grow at a time of order $\left(\frac{\varepsilon}{Ste\sqrt{RaDa^2}}\right)$ (Jany and Bejan, 1988a). This is the time at which a convective regime in the melt (Jany and Bejan, 1988a) sets in. The time predicted for the onset of the convective regime by Benard et al. (1985) is $\left(\frac{4.59\varepsilon}{Ste\sqrt{RaDa^2}}\right)$.

Figure 3 shows the temporal evolution of melt front location for $Nu_i = 0$, $Ra = 10^6$, $Ste = 0.1$, $Da = 10^{-2}$, $Pr = 50$, $\lambda = 10^3$, $\Omega = 1$ and $T_{melt}^* = 0.3$. Initially, the process is conduction-dominated and the melt front is planar. The horizontal intrusion layer appears in the top half of the domain at a dimensionless time of 0.2, due to the development of natural convection. This denotes the beginning of the convection-plus-conduction regime (Jany and Bejan, 1988a). The vertical height (see Fig. 1) of the upper portion of the domain, z, where convection dominates conduction scales as ($\text{RaDa}^2[\tau_f\ \text{Ste}/\varepsilon]^2$) (Jany and Bejan, 1988a). At a

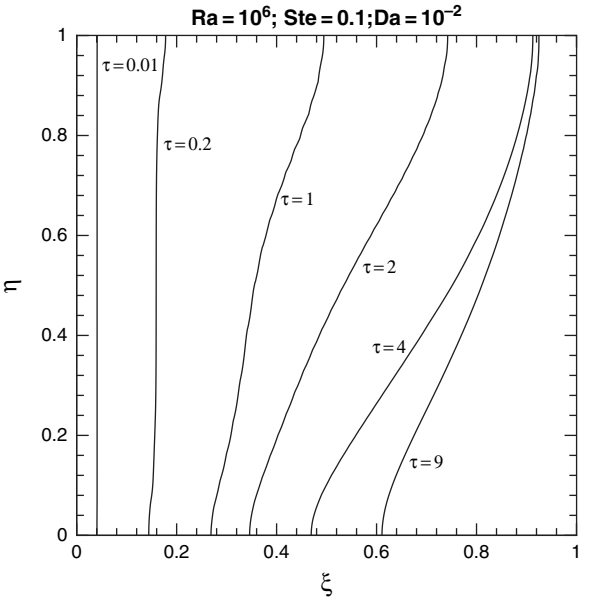

Fig. 3 Predicted temporal evolution of the melt front location for $Ra = 10^6$, $Nu_{i,d} = 0$, $Ste = 0.1$, $Pr = 50$ and $Da = 10^{-2}$

nondimensional time of approximately $\left(\frac{\varepsilon}{Ste\sqrt{RaDa^2}}\right)$, the thermal boundary layer ceases to grow and the quasi-steady regime commences. This can also be seen from Figs. 2a and 2b where the boundary layer thickness is approximately the same after a nondimensional time of 1.2. In this quasi-steady regime, the movement of the melt front is slow enough that the convective process reaches a steady state before the melt front moves to any significant extent.

For all other parameters remaining the same as above, an increase in Stefan number from 0.1 in Fig. 2 to 1.0 expedites the melt front propagation, as expected. As noted previously, the metal foam reaches a steady state over a dimensionless time of Ω/λ and the PCM reaches a steady state over a dimensionless time of ε/Ste. The temporal evolution of the solid and fluid temperature distributions along $\eta = 0.5$ reveal that the temperature distributions are identical for the two different Stefan numbers except for the time to reach steady state (Krishnan et al., 2005). The melt front location for Ste $= 1.0$ is similar to that in Fig. 3 except for the faster evolution of the melt interface, and hence is not shown for brevity. For cases of practical interest, the Stefan number is not large enough to compete with the time scale for the evolution of the solid temperature profile, and the overall behavior described in Figs. 2 and 3 is expected to be typical for $Nu_i = 0$.

The next case considered is one for which the metal foam and PCM exchange energy through inter-phase transfer ($Nu_i \neq 0$). Figure 4a shows the dimensionless solid-to-fluid temperature difference at various times along $\eta = 0.5$, for $Ra = 10^6$, Ste $= 1.0$, $Da = 10^{-2}$, $d/H = 0.0135$, $Pr = 50$, $\lambda = 10^3$, $\Omega = 1$ and $T_m{}^* = 0.3$. The interstitial Nusselt number ($Nu_{i,d}$) based on the pore diameter used for the calculations is 5.9. This Nusselt number was obtained from the expression by Morgan (1975) in Table 1 using a d_∞/d_m ratio of 10^4. Figure 4b shows the dimensionless metal foam and PCM temperature distributions along $\eta = 0.5$ for the same set of parameters. The metal foam-to-PCM temperature difference is determined by the heat exchange between the metal foam and PCM. If the response time for the heat exchange between the PCM and metal foam ($\tau_i \sim \frac{(1-\varepsilon)\Omega}{Nu_i}$) is long compared to the response times of the two phases, the two phases evolve separately, large solid-to-fluid temperature differences exist, and the time to steady state is determined by the slower phase. On the other hand, if the response time for heat exchange is short compared to the response times of the two phases, then the two phases develop together in a coupled manner. For $Nu_i > ((1 - \varepsilon)\lambda)$, the inter-phase exchange time is shorter than the diffusion time for metal foam. For the case in Fig. 4, the inter-phase exchange time is shorter than both the diffusion time for metal foam as well as that for the PCM (i.e. $\tau_i < \tau_m,\ \tau_f$) and hence the metal foam and the PCM develop together in a coupled manner. Initially, the metal foam-to-PCM temperature difference is very high, but it progressively decreases with time and is driven to a value of zero at steady state. It may be noted that a steady state is reached on a time scale of $O(\Omega/\lambda)$. In the earlier case of $Nu_i = 0$, the fluid phase was seen to respond on a time scale of $\tau \sim O(1)$. Here, however, the fluid is seen to evolve faster, on a scale closer to that of the metal foam, as a result of interface exchange. Initially, the metal foam responds faster than the PCM at the hot wall boundary. But since the heat exchange time is shorter than the diffusion

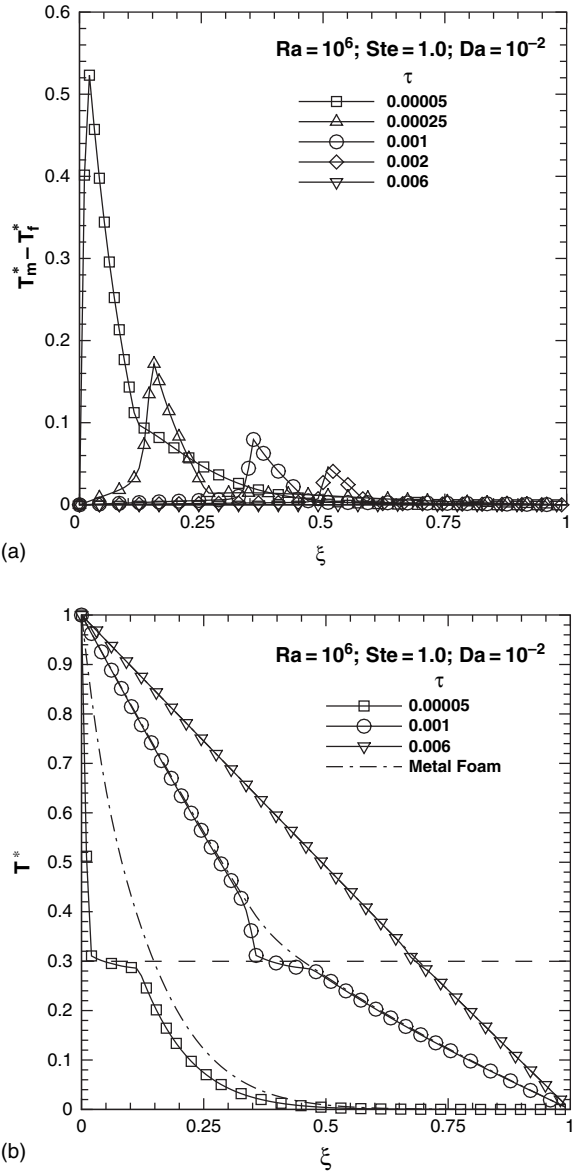

Fig. 4 Predicted temporal evolution of thermal field for $Ra = 10^6$, $Nu_{i,d} = 5.9$, $Ste = 1.0$, $Pr = 50$, $Da = 10^{-2}$ at the mid-height of the domain ($\eta = 0.5$): (**a**) Solid-to-fluid temperature difference, and (**b**) Solid and fluid temperature distributions. Also plotted in the figure is the nondimensional melting temperature (horizontal *dashed line*)

scale (τ_f) for the PCM, heat from the hot boundary travels through the metal and the metal temperature imprints itself on the fluid. Also, as seen in the previous case of $Nu_i = 0$, the maximum solid-to-fluid temperature difference occurs at the interface, which is held at $T_{melt}{}^*$ because of phase change. It may also be noted that the dimensionless solid-to-fluid temperature difference for the uncoupled (Fig. 2) case is not zero at steady state, whereas in the present case, a zero temperature difference is

obtained at steady state. Since the fluid temperature distribution is linear across the domain, the amount of melted PCM is less for $Nu_i \neq 0$ than that of $Nu_i = 0$; this aspect will be discussed in detail later in this Chapter, as will the effect of variations in the interstitial Nusselt number and Stefan number. The temporal evolution of the front location for $Ra = 10^6$, $Nu_{i,d} = 5.9$, $Ste = 1.0$, $Pr = 50$, $Da = 10^{-2}$ was found to be lines parallel (planar) to the two end walls along the ξ-axis due to conduction dominated nature of the flow. Detailed discussion on the melt front propagation can be obtained from Krishnan et al. (2005).

The effect of increasing Rayleigh number on the dimensionless solid-to-fluid temperature difference is discussed next. Figure 5a shows the dimensionless solid-to-fluid temperature difference along $\eta = 0.5$ for $Ra = 10^8$, $Da = 10^{-2}$, $Ste = 1$, $Pr = 50$ and $Nu_{i,d} = 5.9$. Figure 5b shows the dimensionless temperature distributions in the metal foam and PCM along $\eta = 0.5$ for these parameters. The overall behavior is similar to the $Ra = 10^6$ case, albeit with greater convective effects. The solid and fluid temperature profiles are seen to be nearly identical at steady state, and exhibit curvature due to convection. The system is driven to steady state on a time scale $O(\Omega/\lambda)$. The temporal evolution of melt front location for $Ra = 10^8$ is discussed in Krishnan et al. (2005).

A detailed discussion of temperature profiles and melt front shapes for a different Nu_i correlation is outlined in Krishnan et al. (2004b). It is not included here for brevity.

3.1 Melt Volume Fraction

From an engineering standpoint, the melt volume fraction and time-dependent average melt front location are of interest in foam-enhanced PCM units. The effect of interstitial heat transfer coefficient on the melted volume is first discussed.

Figure 6 shows the melt volume fraction ($= \sum_{cells} \gamma \Delta x \Delta y$) as a function of τ for $Ra = 10^6$, $Ste = 1$, $Da = 10^{-2}$, $Pr = 50$ and for different interstitial Nusselt numbers (obtained from various Nu_i relations listed in Table 1 for $\varepsilon = 0.8$). Also plotted in the figure for comparison is the nondimensional time τ_{eq} based on the effective conductivity of the system (foam + PCM). As expected, the higher the interstitial Nusselt number, the faster is the rate at which a steady state is achieved. The time to steady state is dictated by the metal foam response time, as discussed previously. For the parameters considered here, the final steady-state profile for both solid and fluid is a straight line for all $Nu_{i,d}$, and the melt volume fraction is thus the region $T^* > T^*_{melt}$. Consequently, the melt volume fraction is the same for all the different $Nu_{i,d}$ values, with the asymptote being $(1 - T^*_{melt})$. For values of $Nu_{i,d} \geq 1$, little difference in the time to steady state is seen as $Nu_{i,d}$ is increased. For $Nu_{i,d} > 5.9$, the transient response is not distinguishable from that of the equilibrium model ($Nu_{i,d} \to \infty$).

Though not shown here, the melt volume fraction at steady state for $Nu_i = 0$ is 0.8 for the parameter set in this study. For the case when there is no foam, the melt volume fraction is 0.92 at steady state. In the presence of the foam, convective flow in the melt is retarded due to low values of the parameter $RaDa^2$ ($= 100$)

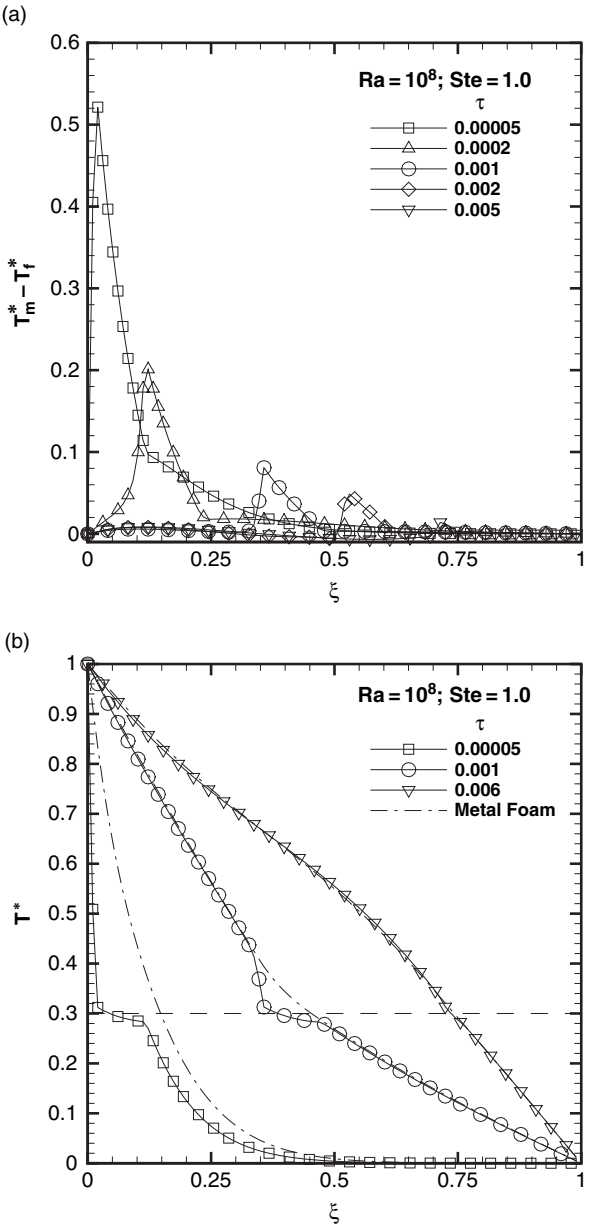

Fig. 5 Predicted temporal evolution of thermal field for $Ra = 10^8$, $Nu_{i,d} = 5.9$, $Ste = 1.0$, $Pr = 50$, $Da = 10^{-2}$ at the mid-height of the domain ($\eta = 0.5$): (**a**) Solid-to-fluid temperature difference, and (**b**) Solid and fluid temperature distributions. Also plotted in the figure is the non-dimensional melting temperature (horizontal *dashed line*)

and conduction-dominated profiles result, limiting the melt volume fraction to $(1 - T^*_{melt})$. But for the uncoupled ($Nu_i = 0$) and the no-foam cases, the fluid temperature distribution is not linear at steady state, and convection in the fluid increases the overall melted volume. However, the response time of the system is

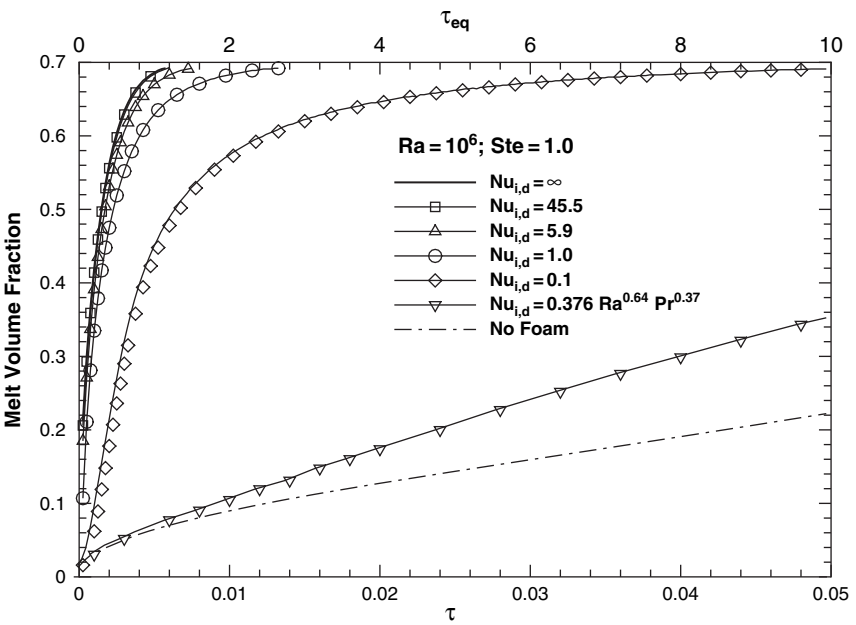

Fig. 6 Predicted melt volume fractions as a function of τ for $\mathrm{Ra} = 10^6$, $\mathrm{Da} = 10^{-2}$, $\mathrm{Ste} = 1.0$ and $\mathrm{Pr} = 50$ for various interstitial Nusselt numbers ($\mathrm{Nu_{i,d}}$). Also shown are the $\tau_{eq}(= \alpha_{eq} t/H^2)$ values for comparison

substantially slower than for the $\mathrm{Nu_{i,d}} > 0$ cases. In practical terms, this means less effective cooling during the transient.

In Fig. 7a, the effect of varying the Rayleigh number on the evolution of the melt volume fraction is shown. Also plotted in Fig. 7 is τ_{eq} as in Fig. 6. As the Rayleigh number increases, the convection contribution increases and the melting rate and the melt volume fraction of the PCM also increase somewhat. In Fig. 7b, the effect of decreasing the Stefan number is examined. A decrease in Stefan number from 1.0 to 0.1 with $\mathrm{Ra} = 10^8$ decreases the rate of melting due to the thermal inertia associated with phase change and the concomitant increase in the latent heat of fusion. Both cases are computed up to a melt volume fraction of 0.74.

3.2 Wall Nusselt Number

In order to compare the performance of the PCM with and without the metal foam, the average Nusselt number at the hot wall for the case without the metal foam case is discussed. The average Nusselt number at the wall is defined as

$$Nu = \frac{hH}{k_f} = (-1) \int_0^1 \left[\frac{\partial T^*}{\partial \xi} \right]_{\xi=0} d\eta$$

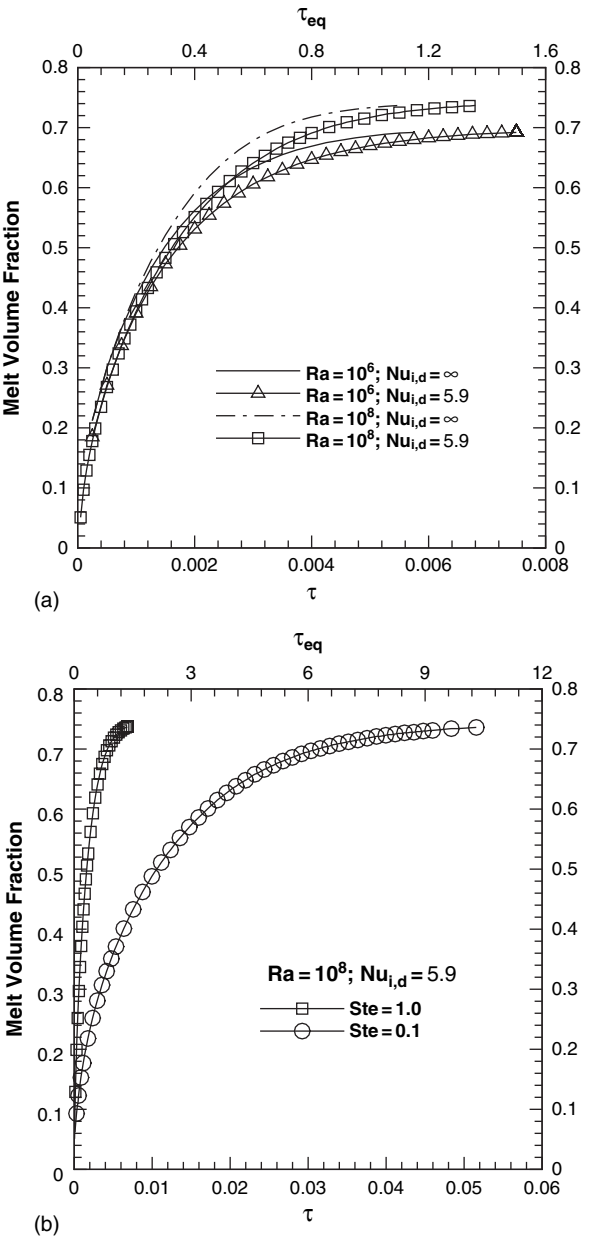

Fig. 7 Predicted melt volume fractions as a function of τ for different Rayleigh, Stefan and interstitial Nusselt numbers. Also shown are the τ_{eq} values for comparison

In the above equation, T^* is the nondimensional PCM temperature. Figure 8 shows the average Nusselt number at the hot wall for two different Rayleigh numbers (10^6 and 10^8) and Ste = 1.0 as a function of dimensionless time. Also plotted in Fig. 8 are the melt front locations for Ra = 10^8 for different flow regimes. Initially,

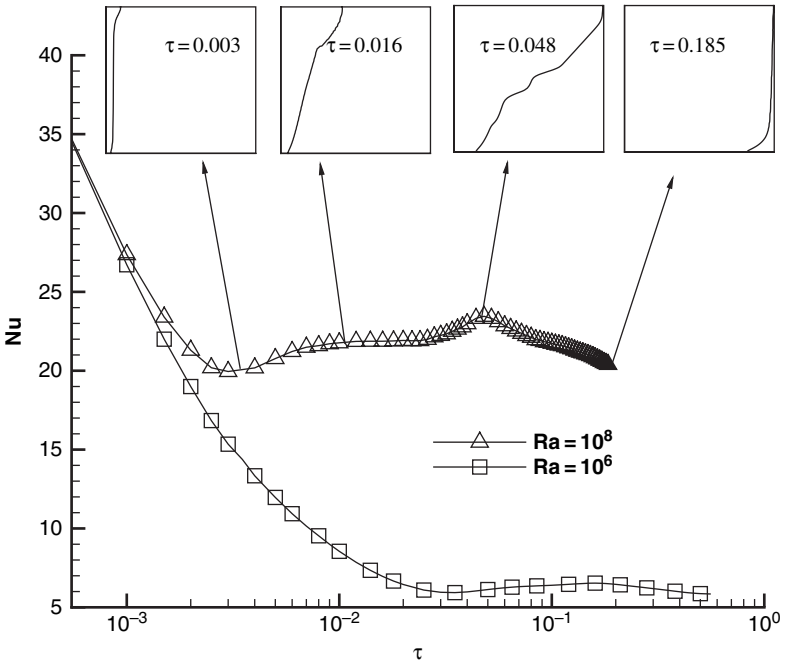

Fig. 8 Predicted hot wall Nusselt number for the no-foam case as a function of τ for Ste = 1 and two different Rayleigh numbers. Also shown are the melt fronts at several critical time instants during flow evolution

at $\tau = 0$, when the left wall temperature is raised to T_H, the heat transfer from the wall to the PCM is large, but the Nusselt number falls rapidly as the PCM heats up. Over a time scale $\tau \sim (1 - T_{melt}^*)^{5/4}\ Ra^{-1/2}$ (Jany and Bejan, 1988a), the Nusselt number reaches a low value corresponding to the pure conduction limit and starts to increase as convection sets in (referred to as conduction-plus-convection regime in Jany and Bejan (1988a)). The increase in Nu ($\sim \tau^{-0.5} + Ra\ (\tau)^{3/2}$ Jany and Bejan (1988a)) in the convection-plus-conduction regime is very small for $Ra = 10^6$. The "quasi-steady" regime or the convection-dominated regime sets in over a time scale $\tau \sim (Ra)^{-1/2}$ (Jany and Bejan, 1988a). The Nusselt number is constant in this regime and is computed to be approximately 22 and 7 for $Ra = 10^8$ and 10^6, respectively. The Nusselt number starts to increase again as the melt front nears the cold wall and peaks when the melt front touches the cold wall on a time scale τ of $O(Ra^{-0.25})$ (Jany and Bejan, 1988a). The Nusselt number drops again when the melt front traverses along the right wall.

The behavior in the presence of the metal foam is markedly different. Figure 9 shows the Nusselt number at the hot wall in this case. The Nusselt number corresponding to the metal foam, Nu_m, and that corresponding to the PCM, Nu_f, are shown. Figure 10 shows the total heat transfer from the hot wall to the system. This Nusselt number is defined as

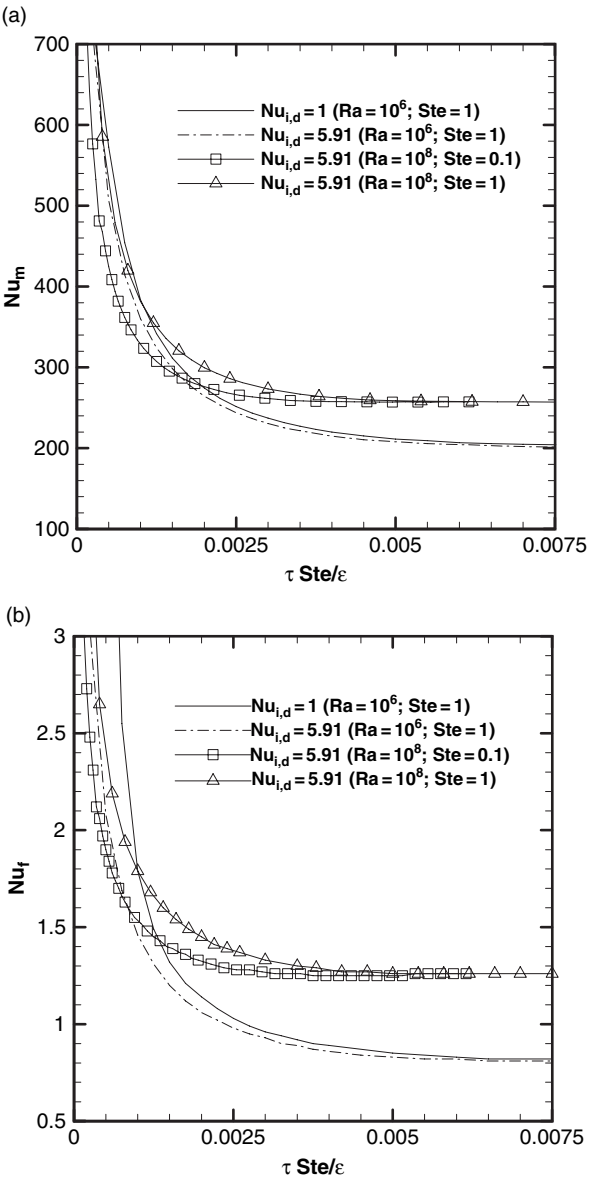

Fig. 9 Predicted hot wall Nusselt number for (**a**) metal foam, and (**b**) PCM for various Rayleigh, Stefan and interstitial Nusselt numbers

$$Nu_{total} = Nu_m + Nu_f = -(1-\varepsilon)\lambda \int_0^1 \left[\frac{\partial T_m^*}{\partial \xi}\right]_{\xi=0} d\eta - \varepsilon \int_0^1 \left[\frac{\partial T_f^*}{\partial \xi}\right]_{\xi=0} d\eta$$

The case of $\mathrm{Ra} = 10^6$, $\mathrm{Da} = 10^{-2}$ and $\mathrm{Ste} = 1$ is considered first. Initially, at $\tau = 0$, the heat transfer from the wall is large, but drops rapidly as both the metal and PCM

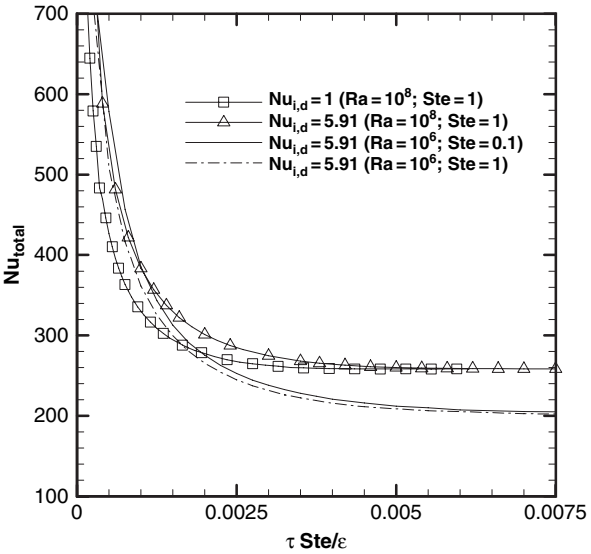

Fig. 10 Predicted total hot wall Nusselt number for various Rayleigh, Stefan and interstitial Nusselt numbers

heat up. In the presence of the foam, heat transfer is conduction- dominated and at steady state, the dimensionless temperature gradient at the wall for both metal foam and PCM is unity. Hence, $\mathrm{Nu}_{\mathrm{total}} \sim \varepsilon + (1-\varepsilon)\lambda$. This is true for both the $\mathrm{Nu}_{\mathrm{i,d}}$ values plotted in Fig. 9. As the Rayleigh number is increased, the Nusselt number at the wall increases due to increased natural convection. The increase in the Nusselt number for metal foam is manifested as a distortion in the metal foam isotherms due to coupling with the PCM (see Fig. 5b). The greatest contribution to sensible heat transfer from the hot wall is due to the metal. The fluid primarily contributes to the phase change heat transfer and heat from the hot wall is conveyed to it by the metal.

4 Summary

A parametric study of the transient melting of PCMs integrated into metal foams for enhanced effective thermal conductivity is presented for the case of a step change in boundary temperature. A number of important results are discussed. For the range of parameters considered, for metal foams with interstitial Nusselt numbers $\mathrm{Nu}_{\mathrm{i,d}} > 5.9$, a single-temperature model is sufficient for analysis. But for smaller $\mathrm{Nu}_{\mathrm{i,d}}$ values, the metal foam and the PCM are sufficiently out of equilibrium that a two-temperature model is necessary. The metal foam is seen to act in two ways. First, it substantially dampens convective flow because of frictional resistance. Second, since the metal responds far faster than the fluid, the linear temperature profile in the metal tends to imprint itself on the fluid, leading to conduction-like temperature profiles for $\mathrm{Ra} \leq 10^6$. Even at $\mathrm{Ra} = 10^8$, only a mild departure from the con-

duction temperature profile is seen. As a result, the melt volume fraction at steady state, which is a measure of the total heat that can be absorbed, is approximately $(1 - T^*_{melt})$. This value may be less than that obtained without the metal foam because of the damping of convective flow. The metal foam acts to substantially decrease the response time of the system, and may thus lead to far less overheating during the transient, despite the smaller melt volume fraction at steady state.

Transients due to a step change in boundary temperature are also explored. In many applications, periodic pulsed heating may be used. The difference in response time between systems with and without metal foam enhancers has important implications for the management of transient energy pulses. If the time scale of the energy pulse is short compared to the response time of the system, local overheating is possible. Since the metal foam response time is typically far faster than typical energy pulse time scales, it would tend to perform far better than systems without metal foams. These aspects are investigated further to gain a clearer understanding of pulsed heating in Krishnan et al. (2007).

Acknowledgments Support for this work from industry members of the Cooling Technologies Research Center, an NSF Industry/University Cooperative Research Center, is gratefully acknowledged.

Nomenclature

a_{sf}	Specific surface area, m^{-1}
C_p	Isobaric specific heat, $Jkg^{-1}K^{-1}$
Da	Darcy number
d	Particle diameter or mean pore diameter, m
F	Inertial coefficient
g	Gravity vector, ms^{-2}
H	Height of the enclosure, m
h_v	Volumetric heat transfer coefficient, $Wm^{-3}K^{-1}$
K	Permeability, m^2
k	Thermal conductivity, $Wm^{-1}K^{-1}$
k_e	Equivalent thermal conductivity, $Wm^{-1}K^{-1}$
Nu	Nusselt number based on the porous foam height
Nu_i	Interstitial Nusselt number $(h_v H^2/k_f)$
$Nu_{i,d}$	Interstitial Nusselt number based on pore diameter $(h_v d^2/k_f)$
P	Pressure, Nm^{-2}
Pr	Prandtl number
Ra	Rayleigh number
Re	Reynolds number
Ste	Stefan number
T	Temperature, K
t	Time, s
U	Velocity vector, ms^{-1}

V Total Volume (metal foam and PCM), m^3
V_f Total PCM volume, m^3
V_l Volume occupied by liquid PCM, m^3
u,v Velocity in x and y directions, ms^{-1}
x,y Cartesian coordinates

Greek Symbols

α Thermal diffusivity, m^2s^{-1}
β Coefficient of thermal expansion, K^{-1}
ΔH Enthalpy of freezing/melting, Jkg^{-1}
ΔT Mushy zone thickness, K^{-1}
ε Porosity
γ Fraction of liquid melt in the PCM
η Dimensionless y-coordinate
φ Fraction of liquid PCM ($= \varepsilon\gamma$)
λ Ratio of thermal conductivities of metal foam and fluid
λ_e Ratio of equivalent thermal conductivity to fluid thermal conductivity
μ Dynamic viscosity, Nsm^{-2}
υ Kinematic viscosity, m^2s^{-1}
ρ Density, kgm^{-3}
τ Dimensionless time
ξ Dimensionless x-coordinate
Ω Ratio of volumetric heat capacities of metal foam and fluid

Subscripts

C Cold
d Diameter
ef Effective fluid property
eq Equivalent
f Fluid (PCM)
H Hot/Height of enclosure
l Liquid
p Pore or particle
m Metal foam
s Solid (PCM)

Superscripts

* Dimensionless quantity

References

Alawadhi, E. M. and Amon, C. H., 2003, "PCM thermal control unit for portable electronic devices: Experimental and numerical studies," *IEEE Trans. Comp. and Pack. Tech*., 26, 116–125.

Amiri, A., and Vafai, K., 1994, "Analysis of dispersion effects and non-thermal equilibrium, non-Darcian, variable porosity incompressible flow through porous media," *Int. J. Heat Mass Transfer*, 37, 939–954.

Ashby, M. F., Evans, A., Fleck, N. A., Gibson, L. J., Hutchinson, J. W., and Wadley, H. J. G., 2000, *Metal Foams: A Design Guide*, Butterworth-Heinemann, Oxford.

Beckermann, C. and Viskanta, R., 1988, "Natural convection solid/liquid phase change in porous media," *Int. J. Heat Mass Transfer*, 31, 35–46.

Bejan, A., 1989, "Theory of melting with natural convection in an enclosed porous medium," *ASME J. Heat Transfer*, 111, 407–415.

Benard, C., Gobin, C., and Martinez, F., 1985, "Melting in rectangular enclosures: experiments and numerical simulations," *ASME J. Heat Transfer*, 107, 794–803.

Boomsma, K., Poulikakos, D., and Zwick, F., 2003, "Metal foams as compact high performance heat exchangers," *Mech. Matls*., 35, 1161–1176.

Calmidi, V. V., and Mahajan, R. L., 2000, "Forced convection in high porosity metal foams," *ASME J. Heat Transfer*, 122, 557–565.

Chellaiah, S. and Viskanta, R., 1990a, "Natural convection melting of a frozen porous medium," *Int. J. Heat Mass Transfer*, 33, 887–899.

Chellaiah, S. and Viskanta, R., 1990b, "Melting of ice-aluminum balls systems," *Exp. Thermal Fluid Sci*., 3, 222–231.

Ellinger, E. A. and Beckermann, C., 1991, "On the effect of porous layers on melting heat transfer in an enclosure," *Exp. Thermal Fluid Sci*., 4, 619–629.

Ferziger, J. H. and Peric, M., 1995, *Computational Methods for Fluid Dynamics*, Springer-Verlag, New York.

Frankel, N. A., and Acrivos, A., 1968, "Heat and mass transfer from small spheres and cylinders freely suspended in shear flow," *Phys. Fluids*, 11, 1913–1918.

Gau, C. and Viskanta, R., 1986, "Melting and solidification of a pure metal on a vertical wall," *ASME J. Heat Transfer*, 108, 174–181.

Harris, K. T., Haji-Sheikh, A., and Agwu Nnanna, A. G., 2001, "Phase-change phenomena in porous media – a non-local thermal equilibrium model," *Int. J. Heat Mass Transfer*, 44, 1619–1625.

Hwang, J. J., Hwang, G. J., Yeh, R. H., and Chao, C. H., 2002, "Measument of interstitial convective heat transfer coefficient and frictional drag for flow across metal foams," *J. Heat Transfer*, 124, 120–129.

Jany, P. and Bejan, A., 1988a, "Scaling theory of melting with natural convection in an enclosure," *Int. J. Heat Mass Transfer*, 31, 1221–1235.

Jany, P. and Bejan, A., 1988b, "Scales of melting in the presence of natural convection in a rectangular cavity filled with porous medium," *ASME J. Heat Transfer*, 110, 526–529.

Kaviany, M., 1995, *Principles of Heat Transfer in Porous Media*, Springer-Verlag, New York.

Krishnan, S., Garimella, S. V., and Murthy, J. Y., 2008, "Simulation of thermal transport in open-cell metal foams: effect of periodic unit cell structure," *ASME J. Heat Transfer,* 130, 024503.

Krishnan, S., Murthy, J. Y., and Garimella, S. V., 2004a, "A two-temperature model for analysis of passive thermal control systems," *ASME J. Heat Transfer*, 126, 628–637.

Krishnan, S., Murthy, J. Y., and Garimella, S. V., 2004b, "A two-temperature model for solid/liquid phase change in metal foams," *Proc. ASME Heat Transfer/Fluids Engg. Summer Conf*., HT-FED2004–56337.

Krishnan, S., Murthy, J. Y., and Garimella, S. V., 2005, "A two-temperature model for solid-liquid phase change in metal foams," *J. Heat Transfer*, 127, 995–1004.

Krishnan, S., Murthy, J. Y., and Garimella, S. V., 2006a, "Direct simulation of transport in open-cell metal foams," *ASME J. Heat Transfer*, 128, 793–799.

Krishnan, S., Murthy, J. Y., and Garimella, S. V., 2007, "Analysis of solid–liquid phase change under periodic pulse heating," *ASME J. Heat Transfer*, 129, 395–400.

Kuwahara, F., Shirota, M., and Nakayama, A., 2001, "A numerical study of interfacial convective heat transfer coefficient in two-energy equation model for convection in porous media," *Int. J. Heat Mass Transfer*, 44, 1153–1159.

Minkowycz, W. J., Haji-Sheikh, A., and Vafai, K., 1999, "On departure from local thermal equilibrium in porous media due to a rapidly changing heat source: the Sparrow number," *Int. J. Heat Mass Transfer*, 42, 3373–3385.

Morgan, V. T., 1975, "The overall convective heat transfer from smooth circular cylinders," *Adv. Heat Transfer*, 11, 199–264.

Nield, D. A. and Bejan, A., 1992, *Convection in Porous Media*, Springer-Verlag, New York.

Phanikumar, M. S., and Mahajan, R. L., 2002, "Non-Darcy natural convection in high porosity metal foams," *Int. J. Heat Mass Transfer*, 45, 3781–3793.

Price D. C., 2003, "A review of selected thermal management solutions for military electronic systems," *IEEE Trans. Comp. Pack. Tech*., 26, 26–39.

Sparrow, E. M., Patankar, S. V., and Ramadhyani, S., 1977, "Analysis of melting in the presence of natural convection in the melt region," *ASME J. Heat Transfer*, 99, 520–526.

Tong, X., Khan, J. A., and Amin, M. R., 1996, "Enhancement of heat transfer by inserting a metal matrix into a phase change material," *Num. Heat Transfer: Part A*, 30, 125–141.

Vafai, K., and Sozen, M., 1990, "An investigation of a latent heat storage porous bed and condensing flow through it," *ASME J. Heat Transfer*, 112, 1014–1022.

Vesligaj, M. J. and Amon, C. H., 1999, "Transient thermal management of temperature fluctuations during time varying workloads on portable electronics," *IEEE Trans. Comp. Pack. Tech*., 22, 541–550.

Viskanta, R., 1991, "Phase change heat transfer in porous media," *Proc. 3rd Int. Symposium Cold Region Heat Transfer*, Fairbanks, 1–24.

Wakao, N., and Kaguei, S., 1982, *Heat and Mass Transfer in Packed Beds*, Gordon and Breach, London.

Yao, L. S. and Prusa, J., 1989, "Melting and freezing," *Adv. Heat Transfer*, 19, 1–95.

Nanofluid Suspensions and Bi-composite Media as Derivatives of Interface Heat Transfer Modeling in Porous Media

Peter Vadász

Abstract Spectacular heat transfer enhancement has been measured in nanofluid suspensions. Attempts in explaining these experimental results did not yield yet a definite answer. Modelling the heat conduction process in nanofluid suspensions is being shown to be a special case of heat conduction in porous media subject to Lack of Local thermal equilibrium (LaLotheq). Similarly, the modelling of heat conduction in bi-composite systems is also equivalent to the applicable process in porous media. The chapter reviews the topic of heat conduction in porous media subject to Lack of Local thermal equilibrium (LaLotheq), introduces one of the most accurate methods of measuring the thermal conductivity, the transient hot wire method, and discusses its possible application to dual-phase systems. Maxwell's concept of effective thermal conductivity is then introduced and theoretical results applicable for nanofluid suspensions are compared with published experimental data.

1 Introduction

The reported breakthrough in substantially increasing the thermal conductivity of fluids by adding very small amounts of suspended metallic or metallic oxide nanoparticles (Cu, CuO, Al_2O_3) to the fluid (Eastman *et al*. 2001, Lee *et al*. 1999), or alternatively using nanotube suspensions (Choi *et al*. 2001, Xuan and Li 2000) conflicts with the classical theories (Maxwell 1891, Batchelor 1972, Batchelor and Green 1972, Hamilton and Crosser 1962, Jeffrey 1973, Davis 1986, Lu and Lin 1996, Bonnecaze and Brady 1990, 1991) of estimating the effective thermal conductivity of suspensions. A very small amount (less than 1% in terms of volume fraction) of copper nanoparticles was reported to improve the measured thermal conductivity of the suspension by 40% (Eastman *et al*. 2001, Lee *et al*. 1999), while over a 150% improvement of the effective thermal conductivity at a volume fraction of 1% was reported by Choi *et al*. (2001) for multiwalled carbon nanotubes suspended in oil.

P. Vadász
Northern Arizona University, Flagstaff, AZ, USA
e-mail: peter.vadasz@nau.edu

P. Vadász (ed.), *Emerging Topics in Heat and Mass Transfer in Porous Media*,

© Springer Science+Business Media B.V. 2008

The objective of this chapter is to introduce the topic of nanofluids heat conduction, showing that it is essentially a particular case of heat conduction in porous media subject to Lack of Local thermal equilibrium (LaLotheq), accounting for the inter-phase (or interface) heat transfer and presenting results as well as challenges arising from such modelling. The topic of heat conduction modelling in porous media subject to a Lack of Local thermal equilibrium (LaLotheq) is introduced first while presenting also the resolution of a paradox (introduced by Vadasz 2005a) arising from the attempt at solving such a model via the elimination method (Vadasz 2007a). The said paradox arises for a combination of Dirichlet and insulation boundary conditions. Previous work on porous media heat transfer subject to Lack of Local Thermal Equilibrium (LaLotheq) was undertaken among others by Nield (1998, 2002), Minkowycz et al. (1999), Banu and Rees (2002), Baytas and Pop (2002), Kim and Jang (2002), Rees (2002), Alazmi and Vafai (2002), Lage (1999), Nield et al. (2002), and Vadasz and Nield (2007). In particular Nield (1998) shows that for uniform thermal conductivities the steady state conduction leads to Local Thermal Equilibrium (Lotheq) if the temperature or its normal derivative on the boundary are identical for both phases.

Tzou (1995, 1997) refers to experimental results in porous media heat conduction identifying thermal oscillations and overshooting, and explains them by applying the Dual-Phase-Lagging (DuPhlag) model. In particular Minkowycz et al. (1999) link the La Lotheq model with the DuPhlag model in a similar manner to Tzou (1995, 1997) however they do not claim the possibility of oscillations. Vadasz (2004, 2005b, 2006a) proved that such oscillations are not possible.

Vadasz (2005a) showed that, for a fluid saturated porous layer subject to heat conduction (transient as well as steady state) and any combination of imposed temperatures and insulation on the boundary, the dual-phase thermal conduction leads apparently back to Lotheq conditions and to a very particular case of identical effective thermal diffusivities for both phases. This paradox was resolved by Vadasz (2007a). While Vadasz (2005a) introduced the apparent paradox in terms of a three-dimensional general domain the present chapter uses Vadasz (2007a) results and deals with a two-dimensional rectangular domain and the generalization to any three-dimensional domain is discussed. While this first part of the chapter is particularly aimed at the conditions applicable to a porous medium Vadasz (2006a, b) showed that similar results and conclusions are applicable to suspensions of solid particles in fluids, or to bi-composite media (a combination of two different solid phases).

This theoretical background is followed by a brief review of the concepts and methods applicable to the experimental measurement of thermal conductivity and its application to dual-phase systems, such as porous media, nanofluids suspensions, bi-composite media, via the introduction of Maxwell's (1891) effective thermal conductivity.

The application of the latter concepts and methods to heat conduction in nanofluid suspensions in an attempt to explain the spectacular heat transfer enhancement obtained experimentally finalizes the presentation.

In the present chapter a *contextual notation* is introduced to distinguish between dimensional and dimensionless variables and parameters. The *contextual notation* implies that an asterisk subscript is used to identify dimensional variables and parameters

only when ambiguity may arise when the asterisk subscript is not used. For example x_* is the dimensional horizontal coordinate, while x is its corresponding dimensionless counterpart. However k_s is the effective solid phase thermal conductivity, a dimensional parameter that appears without an asterisk subscript without causing ambiguity.

2 Problem Formulation and the Apparent Paradox

Let us consider the heat conduction in a rectangular two-dimensional fluid saturated porous domain that is exposed to different constant temperatures on the vertical walls and to insulation conditions on the horizontal walls as presented in Fig. 1. Heat conduction in porous media subject to Lack of Local Thermal Equilibrium (LaLotheq) is governed at the macro-level by the following equations that represent averages over each phase within an REV (Representative Elementary Volume)

$$\gamma_s \frac{\partial T_s}{\partial t_*} = k_s \nabla_*^2 T_s - h\left(T_s - T_f\right) \tag{1}$$

$$\gamma_f \frac{\partial T_f}{\partial t_*} = k_f \nabla_*^2 T_f + h\left(T_s - T_f\right) \tag{2}$$

where $Q_{sf} = h\left(T_s - T_f\right)$ represents the rate of heat generation in the fluid phase within the REV due to the heat transferred over the fluid–solid interface, and where $\gamma_s = (1-\varphi)\,\rho_s c_s$ and $\gamma_f = \varphi\,\rho_f\, c_{p,f}$ are the solid phase and fluid phase effective heat capacities, respectively, φ is the porosity, $k_s = (1-\varphi)\,\tilde{k}_s$ and $k_f = \varphi\,\tilde{k}_f$ are the effective thermal conductivities of the solid and fluid phases, respectively. The

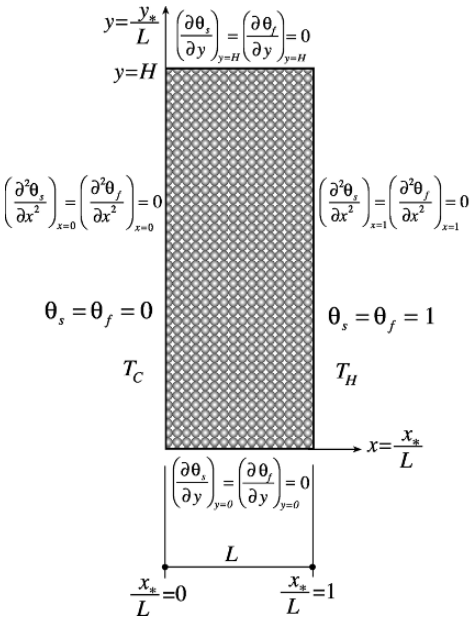

Fig. 1 Problem formulation – heat conduction in a two dimensional rectangular domain subject to Lack of Local thermal equilibrium (LaLotheq)

coefficient $h > 0$, carrying units of $\mathrm{W\,m^{-3}\,K^{-1}}$, is a macro-level integral heat transfer coefficient for the heat conduction at the fluid–solid interface (averaged over the REV) that is assumed independent of the phases' temperatures and independent of time. Note that this coefficient is conceptually distinct from the convection heat transfer coefficient and is anticipated to depend on the thermal conductivities of both phases as well as on the surface area to volume ratio (specific area) of the medium (Vadasz 2006b).

Equations (1)–(2) are linearly coupled and represent the traditional form of expressing the process of heat conduction in porous media subject to LaLotheq (Nield and Bejan 2006, Nield 1998). When the value of the interface heat transfer coefficient vanishes, $h = 0$ (physically representing an interface that is an ideal insulator, e.g. the solid–fluid interface is coated with a highly insulating material), eqs. (1) and (2) uncouple and the solution for the temperature of each phase is independent of the other phase, the phase having the highest thermal diffusivity producing a temperature that equilibrates faster to its steady state value. Very large values of h on the other hand lead to Local Thermal Equilibrium (Lotheq) as observed by dividing eqs. (1) and (2) by h and looking for the limit as $h \to \infty$ that produces (at least at the leading order) $T_s = T_f$. The latter occurs because despite the fact that one phase (the slow one) diffuses heat at a slower pace a perfect compensation occurs due to the interface heat transfer, i.e. the change in temperature in the faster phase is instantly converted into an identical temperature change in the slower phase via the heat transferred through the interface without any resistance because $h \to \infty$. Similar results may be obtained with a finite interface heat transfer coefficient, h, if the thermal diffusivities of both phases are identical, i.e. $\alpha_s = \left(k_s/\gamma_s\right) = \left(k_f/\gamma_f\right) = \alpha_f$. Then, both phases will diffuse heat at the same pace leading naturally to $T_s = T_f$ and a vanishing heat transfer over the interface $h\left(T_s - T_f\right) = 0$ irrespective of the value of h.

For the two-dimensional system considered here (see Fig. 1) the Laplacian operator ∇_*^2 is defined in the form $\nabla_*^2 = \partial^2/\partial x_*^2 + \partial^2/\partial y_*^2$.

The boundary conditions applicable to the problem at hand are constant temperature at the vertical walls and insulation at the top and bottom horizontal walls

$$x_* = 0: \; T_s = T_f = T_C \tag{3}$$

$$x_* = L: \; T_s = T_f = T_H \tag{4}$$

$$y_* = 0 \;\&\; y_* = H_*: \; \left(\frac{\partial T_s}{\partial y_*}\right)_{y_*=0,H_*} = \left(\frac{\partial T_f}{\partial y_*}\right)_{y_*=0,H_*} = 0 \tag{5}$$

The initial conditions are related to the initial physical conditions of having the porous medium in thermal equilibrium with its surroundings leading to the same uniform constant temperature for both phases, i.e.

$$t_* = 0: \; (T_s)_{t_*=0} = \left(T_f\right)_{t_*=0} = T_o = \text{constant} \tag{6}$$

Two methods are in principle available to solving the problem (1)–(2) analytically subject to the boundary conditions (3)–(5) and initial conditions (6). The first method ("the eigenvectors method") is linked to evaluating the eigenvalues and eigenvectors

directly from system (1)–(2). The second method ("the elimination method") is related to deriving an equivalent equation that is second order in time and fourth order in space via elimination of the dependent variables T_s and T_f. The first step in this chapter is to present the paradox that was introduced by Vadasz (2005a), then the solution is presented via both methods listed above and their results compared.

The stated paradox appears when attempting to solve the problem via "the elimination method". The elimination of the dependent variables T_s and T_f (one at a time or simultaneously) is accomplished via one of the two methods presented by Vadasz (2004, 2005a, b, 2006a, b) leading to two independent equations for each phase in the form

$$\tau_q \frac{\partial^2 T_i}{\partial t_*^2} + \frac{\partial T_i}{\partial t_*} = \alpha_e \left[\nabla_*^2 T_i + \tau_T \nabla_*^2 \left(\frac{\partial T_i}{\partial t_*} \right) - \beta_e \nabla_*^4 T_i \right] \quad \forall i = s, f \tag{7}$$

where the index i can take the values s representing the solid phase or f standing for the fluid phase and where the following notation was used

$$\tau_q = \frac{\gamma_s \gamma_f}{h\left(\gamma_s + \gamma_f\right)};\ \alpha_e = \frac{\left(k_s + k_f\right)}{\left(\gamma_s + \gamma_f\right)};\ \tau_T = \frac{\left(\gamma_s k_f + \gamma_f k_s\right)}{h\left(k_s + k_f\right)};\ \beta_e = \frac{k_s k_f}{h\left(k_s + k_f\right)} \tag{8}$$

(Note: the present definition of β_e is different than in Vadasz 2005a). Equation (7) is a linear equation that applies to each phase, while its parameters are effective coefficients common to both phases. By imposing the combination of Dirichlet (constant temperatures) and insulation boundary conditions expressed by eqs. (3)–(5) and assuming uniform and identical initial conditions for both phases expressed by eq. (6) provides two boundary conditions in each direction and one initial condition for each phase. However, eq. (7) is fourth order in space and second order in time, requiring therefore two additional boundary conditions in each direction and one additional initial condition. The latter conditions can be derived from the original ones (3)–(5) and (6) by using the original equations (1) and (2), which govern the heat conduction at all times (including $t_* = 0$) and over the whole physical domain including the boundaries. The derived boundary and initial conditions to be used in connection with the solution to eq. (7) are

$$x_* = 0:\ T_i = T_C\ ;\left(\partial^2 T_i \Big/ \partial x_*^2\right)_{x_*=0} = 0 \forall\ i = s, f \tag{a}$$

$$x_* = L:\ T_i = T_H\ ;\left(\partial^2 T_i \Big/ \partial x_*^2\right)_{x_*=L} = 0 \forall\ i = s, f \tag{b}$$

$$y_* = 0,\ H_*:\left(\partial T_i \Big/ \partial y_*\right)_{y_*=0,H_*} = 0;\left(\partial^3 T_i \Big/ \partial y_*^3\right)_{y_*=0,H_*} = 0\ \forall\ i = s, f \tag{c}$$

$$t_* = 0:\left(T_i\right)_{t_*=0} = T_o = \text{constant}\ ;\left(\partial T_i \Big/ \partial t_*\right)_{t_*=0} = 0\ \forall\ i = s, f \tag{10}$$

Equation (7) that is identical for both phases, shares common effective parameters for both phases, solved subject to identical boundary and initial conditions for each phase, eqs. (9) and (10) produces therefore a solution that is expected to be identical for both phases, i.e.

$$T_s\left(t_*, \mathbf{x}_*\right) = T_f\left(t_*, \mathbf{x}_*\right) \forall\ \left(t_* \geq 0, x_* \in [0, L]\,, y_* \in [0, H_*]\right) \tag{11}$$

where $\mathbf{x}_* = (x_*, y_*)$ represents the spatial variables. Equation (11) is identified as the requirement for Local thermal equilibrium (Lotheq) in porous media conduction causing the heat generation due to the heat transfer at the fluid–solid interface $Q_{sf} = h\left(T_s - T_f\right)$ to vanish. It was obtained accurately from the original system of eqs. (1)–(2) subject to the specified boundary and initial conditions and other than that no other imposed restrictions. This result is quite astonishing and intriguing because it suggests that *Local thermal equilibrium (Lotheq) exists naturally in any porous domain subject to heat conduction and a combination of constant temperature and insulation boundary conditions*. However, this conclusion needs further investigation. Substituting eq. (11) into eqs. (1) and (2) yields

$$\frac{\partial T_s}{\partial t_*} = \alpha_s \nabla_*^2 T_s \tag{12}$$

$$\frac{\partial T_f}{\partial t_*} = \alpha_f \nabla_*^2 T_f \tag{13}$$

where $\alpha_s = k_s \big/ \gamma_s$ and $\alpha_f = k_f \big/ \gamma_f$. The solution to eqs. (12) and (13) subject to the same boundary and initial conditions as indicated in eqs. (3)–(5) and (6) has to be identical to the corresponding solutions of eq. (7) subject to the equivalent boundary and initial conditions (9) and (10) respectively. This means that eqs. (12) and (13) are expected to produce an identical solution $T_s\left(t_*, \mathbf{x}_*\right) = T_f\left(t_*, \mathbf{x}_*\right) \forall \left(t_* \geq 0,\ x_* \in [0, L],\ y_* \in [0, H_*]\right)$ despite the fact that in general their respective thermal diffusivities may vary substantially. The latter cannot be accomplished unless $\alpha_s = \alpha_f$, leading to the inevitable conclusion that consistency requires the effective thermal diffusivities of both phases to be identical. The latter condition was not explicitly imposed a priori, nor implied in any of the subsequent derivations. Nevertheless, it was obtained as a result that is linked to the consequences of eq. (11). However, the effective thermal diffusivities of both phases are based on material properties and therefore this limitation cannot generally be applicable. We must therefore insist that $\alpha_s \neq \alpha_f$ in which case eqs. (12) and (13) subject to the boundary and initial conditions (3)–(5) and (6) will produce distinct solutions $T_s\left(t_*, \mathbf{x}_*\right) \neq T_f\left(t_*, \mathbf{x}_*\right)$ leading back to eqs. (1) and (2) with non-vanishing inter-phase heat transfer $Q_{sf} = h\left(T_s - T_f\right) \neq 0$ and the whole process cycles indefinitely introducing the paradox.

3 Solution by the Eigenvectors Method

The system of eqs. (1) and (2) with its corresponding boundary and initial conditions are rendered dimensionless by using L to scale the space variables x_* and y_*, in the form $x = x_* \big/ L$, $y = y_* \big/ L$, $L^2 \big/ \alpha_e$ to scale time, that is, $t = t_* \alpha_e \big/ L^2$ and introducing the dimensionless temperature $\theta_i = \left(T_i - T_C\right) \big/ \left(T_H - T_C\right)$, $\forall\, i = s, f$, leading to the following dimensionless form of eqs. (1) and (2)

$$Fh_s \frac{\partial \theta_s}{\partial t} = \frac{1}{Ni_s} \nabla^2 \theta_s - \left(\theta_s - \theta_f\right) \tag{14}$$

$$Fh_f \frac{\partial \theta_f}{\partial t} = \frac{1}{Ni_f} \nabla^2 \theta_f + \left(\theta_s - \theta_f\right) \tag{15}$$

where the following dimensionless groups listing the solid phase and fluid phase Nield numbers Ni_s Ni_f, respectively, and additional dimensionless groups that emerged (some of them will be used later)

$$Bh = \frac{\beta_e}{L^2};\ Ni_f = \frac{hL^2}{k_f};\ Ni_s = \frac{hL^2}{k_s};\ Fh_f = \frac{\left(\gamma_s + \gamma_f\right)}{\gamma_s} Fo_q = \frac{\alpha_e \gamma_f}{hL^2};$$
$$Fh_s = \frac{\left(\gamma_s + \gamma_f\right)}{\gamma_f} Fo_q = \frac{\alpha_e \gamma_s}{hL^2};\ Fo_q = \frac{\alpha_e \tau_q}{L^2};\ Fo_T = \frac{\alpha_e \tau_T}{L^2}; \tag{16}$$

The dimensionless form of the boundary and initial conditions (3), (4), (5) and (6) are

$$x = 0:\ \theta_i = 0 \qquad \forall\, i = s,\, f \text{ (a)}$$
$$x = 1:\ \theta_i = 1 \qquad \forall\, i = s,\, f \text{ (b)}$$
$$y = 0, H:\ \left(\partial \theta_i \big/ \partial y\right)_{y=0,H} = 0 \qquad \forall\, i = s,\, f \text{ (c)} \tag{17}$$
$$t = 0:\ (\theta_i)_{t=0} = \theta_o = \text{constant} \qquad \forall\, i = s,\, f \tag{18}$$

The solution to eqs. (14) and (15) is separated into steady state $\theta_{i,sts}$ and transient $\theta_{i,tr}$ parts in the form $\theta_i = \theta_{i,sts} + \theta_{i,tr}$. The steady state for both phases $i = s,\, f$ is satisfied by the linear solution $\theta_{i,sts} = x$, which satisfies the boundary conditions (17). It is sensible to assume for $\theta_{i,tr}$ to be independent of the y coordinate and this assumption satisfies the boundary conditions (17c) at $y = 0, H$. As a result, the equations governing the transient have the form

$$Fh_s \frac{\partial \theta_{s,tr}}{\partial t} = \frac{1}{Ni_s} \frac{\partial^2 \theta_{s,tr}}{\partial x^2} - \left(\theta_{s,tr} - \theta_{f,tr}\right) \tag{19}$$

$$Fh_f \frac{\partial \theta_{f,tr}}{\partial t} = \frac{1}{Ni_f} \frac{\partial^2 \theta_{f,tr}}{\partial x^2} + \left(\theta_{s,tr} - \theta_{f,tr}\right) \tag{20}$$

subject to boundary and initial conditions that are obtained following the substitution of $\theta_i = x + \theta_{i,tr}$ into eqs. (17) and (18) leading to

$$x = 0, 1:\ \theta_{i,tr} = 0\ \forall\, i = s,\, f \tag{21}$$

$$t = 0:\ \left(\theta_{i,tr}\right)_{t=0} = \theta_o - x\ \forall\, i = s,\, f \tag{22}$$

The solutions to eqs. (19) and (20) subject to the boundary and initial conditions (21) and (22) are obtained via separation of variables in the form of two equations for each phase in the form $\theta_{i,tr} = \phi_{in}(t)\, u_n(x)$ where the functions $u_n(x)$ are identical for both phases because they satisfy the same equations and the same boundary conditions. The latter statement about the fact that both phases share the same eigenfunctions $u_n(x)$ can be proven in detail, a step that is skipped here for brevity of the presentation. The

resulting equation is $d^2u_n/dx^2 + \kappa_n^2 u_n = 0$. The solution to this equation subject to the homogeneous boundary conditions derived from eq. (21) $(u_n)_{x=0,1} = 0$ and $\left(\mathrm{d}^2 u_n/\mathrm{d}x^2\right)_{x=0,1} = 0$ at $x = 0, 1$, is $u_n = \sin(\kappa_n x)$, and the resulting eigenvalues are $\kappa_n = n\pi \; \forall \, n = 1, 2, 3, \ldots$. Substituting this eigenfunction solution into eqs. (19) and (20) yields the following set of ordinary differential equations for the eigenfunctions in the time domain $\phi_{sn}(t)$ and $\phi_{fn}(t)$

$$\begin{cases} \dfrac{\mathrm{d}\phi_{sn}}{\mathrm{d}t} = a_n\phi_{sn} + b\phi_{fn} & (a) \\ \dfrac{\mathrm{d}\phi_{fn}}{\mathrm{d}t} = c\phi_{sn} + d_n\phi_{fn} & (b) \end{cases} \tag{23}$$

where the definition of the coefficients that emerged from the substitution is

$$a_n = -\frac{\left(n^2\pi^2 + Ni_s\right)}{Ni_s Fh_s};\; d_n = -\frac{\left(n^2\pi^2 + Ni_f\right)}{Ni_f Fh_f};\; b = Fh_s^{-1};\; c = Fh_f^{-1} \tag{24}$$

The general solution has therefore the form

$$\theta_i = x + \sum_{n=1}^{\infty} \phi_{in}(t)\sin(n\pi x) \quad \forall \, i = s, f \tag{25}$$

where $\phi_{in}(t)$ are the solutions to the system of eq. (23). However the system (23) needs initial conditions in terms of $\phi_{sn}(0)$ and $\phi_{fn}(0)$. The latter may be obtained from the initial conditions of θ_s and θ_f, eq. (18), applied to eq. (25) in the form

$$(\theta_i)_{t=0} \equiv x + \sum_{n=1}^{\infty} \phi_{in}(0)\sin(n\pi x) = \theta_o \qquad \forall \, i = s, f \tag{26}$$

Multiplying eq. (26) by $\sin(j\pi x)$, integrating the result over the whole domain, i.e. $\int_0^1 (\cdot)\mathrm{d}x$, and using the orthogonality conditions yields an identical initial condition for both phases, $\phi_{in}(0)$, in the form

$$\phi_{sn}(0) = \phi_{fn}(0) = \phi_{no} = \frac{2\left\{(-1)^n + \left[1 - (-1)^n\right]\theta_o\right\}}{n\pi} \tag{27}$$

The eigenvalues and eigenvectors are obtained from eq. (23) to yield

$$\lambda_{1,2n} = \frac{1}{2}\left[(a_n + d_n) \pm \sqrt{(a_n + d_n)^2 - 4(a_n d_n - bc)}\right] \tag{28}$$

$$\mathbf{V_{1n}} = \left[1,\; (\lambda_{1n} - a_n)/b\right]^T = \left[1,\; c/(\lambda_{1n} - d_n)\right]^T \tag{29}$$

$$\mathbf{V_{2n}} = \left[1,\; (\lambda_{2n} - a_n)/b\right]^T = \left[1,\; c/(\lambda_{2n} - d_n)\right]^T \tag{30}$$

and the solution in terms of these eigenvectors has the form

$$\phi_{\mathbf{n}} = C_1 \mathbf{V_{1n}} e^{\lambda_{1n} t} + C_2 \mathbf{V_{2n}} e^{\lambda_{2n} t} \tag{31}$$

where $\phi_{\mathbf{n}} = \left[\phi_{sn},\ \phi_{fn}\right]^T$.

The following relationships obtained from eqs. (28), (29) and (30) are useful in the following analysis. From eq. (28) one may obtain (see Vadasz 2007a for details)

$$(\lambda_{1n} - d_n) = -(\lambda_{2n} - a_n) \text{ or } (\lambda_{1n} - a_n) = -(\lambda_{2n} - d_n) \tag{32}$$

From eqs. (30) and (31) one gets

$$(\lambda_{1n} - a_n)(\lambda_{1n} - d_n) = b\,c, \text{ and } (\lambda_{2n} - a_n)(\lambda_{2n} - d_n) = b\,c \tag{33}$$

respectively. The following identities that are obtained from eqs. (14) and (6) are useful to demonstrate the next point

$$\left(Ni_s Ni_f Fh_s Fh_f\right)^{-1} = Bh/Fo_q = Bf; \left(Ni_s + Ni_f\right)\left(Ni_s Ni_f Fh_s Fh_f\right)^{-1} = Fo_q^{-1} \tag{34}$$

By substituting eq. (24) and the definitions (16) and (8) yields (introducing the notation of ν_n and ω_n^2)

$$\nu_n = -(a_n + d_n) = \left[n^2\pi^2 \frac{\left(\alpha_s + \alpha_f\right)}{\alpha_e} + \frac{1}{Fo_q}\right] \tag{35}$$

and using also eq. (34) leads to

$$\begin{aligned} \omega_n^2 = (a_n d_n - bc) &= \frac{n^4\pi^4}{Ni_s Ni_f Fh_s Fh_f} + \frac{\left(Ni_s + Ni_f\right)}{Ni_s Ni_f Fh_s Fh_f} n^2\pi^2 \\ &= \left(\frac{Bh}{Fo_q}\right) n^4\pi^4 + \frac{n^2\pi^2}{Fo_q} \end{aligned} \tag{36}$$

By using the initial conditions (25) into eq. (29) and evaluating the coefficients C_1 and C_2 produces the solutions in the time domain $\phi_{in}(t)$ needed in the general solution (23), in the form

$$\begin{aligned} \phi_{sn} &= \frac{[\lambda_{2n} - (a_n + b)]\,\phi_{no}}{(\lambda_{2n} - \lambda_{1n})} e^{\lambda_{1n} t} - \frac{[\lambda_{1n} - (a_n + b)]\,\phi_{no}}{(\lambda_{2n} - \lambda_{1n})} e^{\lambda_{2n} t} \\ \phi_{fn} &= \frac{(\lambda_{1n} - a_n)\,[\lambda_{2n} - (a_n + b)]\,\phi_{no}}{b\,(\lambda_{2n} - \lambda_{1n})} e^{\lambda_{1n} t} - \frac{(\lambda_{2n} - a_n)\,[\lambda_{1n} - (a_n + b)]\,\phi_{no}}{b\,(\lambda_{2n} - \lambda_{1n})} e^{\lambda_{2n} t} \end{aligned} \tag{37}$$

By using now eq. (30) followed by using eq. (31) yields

$$\phi_{fn} = \frac{[\lambda_{2n} - (d_n + c)]\,\phi_{no}}{(\lambda_{2n} - \lambda_{1n})} e^{\lambda_{1n} t} - \frac{[\lambda_{1n} - (d_n + c)]\,\phi_{no}}{(\lambda_{2n} - \lambda_{1n})} e^{\lambda_{2n} t} \tag{38}$$

where ϕ_{no} is defined in eq. (27), λ_{1n} and λ_{2n} are defined in eq. (28), and a_n, b, c, d_n are defined in eq. (24). Substituting eqs. (37) and (38) into (25) produces the general solution obtained via the eigenvectors method in the form

$$\theta_s = x + \sum_{n=1}^{\infty} \left\{ \frac{[\lambda_{2n} - (a_n + b)]\,\phi_{no}}{(\lambda_{2n} - \lambda_{1n})} e^{\lambda_{1n} t} - \frac{[\lambda_{1n} - (a_n + b)]\,\phi_{no}}{(\lambda_{2n} - \lambda_{1n})} e^{\lambda_{2n} t} \right\} \sin(n\pi x) \tag{39}$$

$$\theta_f = x + \sum_{n=1}^{\infty} \left\{ \frac{[\lambda_{2n} - (d_n + c)]\,\phi_{no}}{(\lambda_{2n} - \lambda_{1n})} e^{\lambda_{1n} t} - \frac{[\lambda_{1n} - (d_n + c)]\,\phi_{no}}{(\lambda_{2n} - \lambda_{1n})} e^{\lambda_{2n} t} \right\} \sin(n\pi x) \tag{40}$$

4 Solution by the Elimination Method

Equation (7) and its corresponding boundary and initial conditions are converted into a dimensionless form by using the same scales introduced in the previous section, leading to the following dimensionless form of eq. (7)

$$Fo_q \frac{\partial^2 \theta_i}{\partial t^2} + \frac{\partial \theta_i}{\partial t} = \nabla^2 \theta_i + Fo_T \nabla^2 \left(\frac{\partial \theta_i}{\partial t} \right) - Bh \nabla^4 \theta_i \quad \forall\, i = s, f \tag{41}$$

where the two Fourier numbers, Fo_q, Fo_T, and one additional dimensionless group (the Bi-harmonic number, Bh) that were defined in eq. (16) emerged. The dimensionless form of the boundary and initial conditions (9) and (10) that are required for the solution of eq. (41) are

$$x = 0 :\ \theta_i = 0\ ; \left(\partial^2 \theta_i / \partial x^2\right)_{x=0} = 0 \qquad \forall\, i = s, f \text{(a)}$$

$$x = 1 :\ \theta_i = 1\ ; \left(\partial^2 \theta_i / \partial x^2\right)_{x=1} = 0 \qquad \forall\, i = s, f \text{(b)}$$

$$y = 0, H :\ \left(\partial \theta_i / \partial y\right)_{y=0,H} = 0; \left(\partial^3 \theta_i / \partial y^3\right)_{y=0,H} = 0 \quad \forall\, i = s, f \text{(c)} \tag{42}$$

$$t = 0 : (\theta_i)_{t=0} = \theta_o = \text{constant}\ ; \left(\partial \theta_i / \partial t\right)_{t=0} = 0 \qquad \forall\, i = s, f \tag{43}$$

The solution to eq. (41) is separated into steady state $\theta_{i,sts}$ and transient $\theta_{i,tr}$ parts in the form $\theta_i = \theta_{i,sts} + \theta_{i,tr}$. The steady state for both phases $i = s, f$ is satisfied by the linear solution $\theta_{i,sts} = x$, which satisfies the boundary conditions (42). In addition, it is a sensible assumption for the transient part $\theta_{i,tr}$ to be considered independent of the y coordinate and this assumption satisfies the boundary conditions (42c) at $y = 0, H$. As a result, the equation governing the transient has the form

$$Fo_q \frac{\partial^2 \theta_{i,tr}}{\partial t^2} + \frac{\partial \theta_{i,tr}}{\partial t} = \frac{\partial^2 \theta_{i,tr}}{\partial x^2} + Fo_T \frac{\partial^3 \theta_{i,tr}}{\partial t \partial x^2} - Bh \frac{\partial^4 \theta_{i,tr}}{\partial x^4} \quad \forall\, i = s, f \tag{44}$$

subject to boundary and initial conditions that are obtained following the substitution of $\theta_i = x + \theta_{i,tr}\ \forall i = s,\ f$ into eqs. (42) and (43) leading to

$$\begin{aligned} &x = 0:\ \theta_{i,tr} = 0\,;\left(\partial^2\theta_{i,tr}\big/\partial x^2\right)_{x=0} = 0 \qquad \forall\, i = s,\ f \qquad \text{(a)} \\ &x = 1:\ \theta_{i,tr} = 0\,;\left(\partial^2\theta_{i,tr}\big/\partial x^2\right)_{x=1} = 0 \qquad \forall\, i = s,\ f \qquad \text{(b)} \end{aligned} \tag{45}$$

$$t = 0:\left(\theta_{i,tr}\right)_{t=0} = \theta_o - x\ ;\ \left(\partial\theta_{i,tr}\big/\partial t\right)_{t=0} = 0 \qquad \forall\, i = s,\ f \tag{46}$$

The solution to eq (44) subject to the boundary and initial conditions (45) and (46) is obtained via separation of variables in the form of two equations for each phase as $\theta_{i,tr} = \phi_{in}(t)\,u_n(x)$ where the function $u_n(x)$ is identical for both phases because it satisfies the same equations and the same boundary conditions. The equation for the common eigenfunction $u_n(x)$ is identical to the one obtained in the previous section and is subject to the same homogeneous boundary conditions $(u_n)_{x=0,1} = 0$ leading inevitably to the same eigenfunction solution $u_n(x) = \sin(n\pi x)$. The equations for the eigenfunctions in the time domain is

$$Fo_q\frac{d^2\phi_{in}}{dt^2} + \left(1 + Fo_T\kappa_n^2\right)\frac{d\phi_{in}}{dt} + \kappa_n^2\left(1 + \kappa_n^2 Bh\right)\phi_{in} = 0 \quad \forall i = s,\ f \tag{47}$$

Equation (47) is identical to a linear damped oscillator (mechanical mass-spring-damper $m - K - c$, or electrical L-R-C circuit). A more convenient form of eq. (47) is obtained after dividing it by Fo_q to yield

$$\frac{d^2\phi_{in}}{dt^2} + \nu_n\frac{d\phi_{in}}{dt} + \omega_n^2\phi_{in} = 0 \quad \forall i = s,\ f \tag{48}$$

where the specific damping coefficient ν_n and natural frequency ω_n are the parameters defined in eqs. (35) and (36), respectively.

The dimensionless group that emerged from the definition of ω_n^2 in eq. (36) as a combination of the bi-harmonic number Bh and the heat flux Fourier number Fo_q is $Bf = Bh\big/Fo_q = \alpha_s\alpha_f\big/\alpha_e^2$, where $\alpha_s = k_s\big/\gamma_s$ and $\alpha_f = k_f\big/\gamma_f$. In addition, the dimensionless group that emerged from the definition of ν_n in eq. (35) as a combination of the heat flux and temperature gradient related Fourier numbers Fo_q and Fo_T, respectively, is $\psi = Fo_T\big/Fo_q = \tau_T\big/\tau_q = 1 + Bf + \left(\eta_\gamma - \eta_k\right)^2\Big/\left[\eta_\gamma\eta_k\left(1+\eta_k\right)\left(1+\eta_k^{-1}\right)\right] \geq 1 + Bf > 1$, where $\eta_\gamma = \gamma_f\big/\gamma_s$ and $\eta_k = k_f\big/k_s$. Despite the similarity of eq. (48) to a linear damped oscillator, physical constraints allow only over-damped solutions to exist in this particular application as demonstrated by Vadasz (2004, 2005b, 2006a).

From eq. (48), the equation for the eigenvalues has the form $\lambda_n^2 + \nu_n\lambda_n + \omega_n^2 = 0$, leading to the eigenvalues solutions

$$\lambda_{1n} = -\frac{\nu_n}{2}\left[1 + \sqrt{1 - 4\frac{\omega_n^2}{\nu_n^2}}\right]\ \&\ \lambda_{2n} = -\frac{\nu_n}{2}\left[1 - \sqrt{1 - 4\frac{\omega_n^2}{\nu_n^2}}\right] \tag{49}$$

and the eigenfunctions ϕ_{in} are the superposition of $\exp[\lambda_{1n}t]$ and $\exp[\lambda_{2n}t]$

$$\phi_{in}(t) = A_{in}e^{\lambda_{1n}t} + B_{in}e^{\lambda_{2n}t} \quad \forall\, i = s,\, f \tag{50}$$

leading to the solution for $\theta_{i,tr}$ expressed in the form

$$\theta_{i,tr} = \sum_{n=1}^{\infty} \phi_{in}(t) \sin(n\pi x) \qquad \forall\, i = s,\, f \tag{51}$$

The solution (51) includes two sequences of coefficients presented in eq. (50) that need to be established from the two initial conditions (46) at $t = 0$. The first initial condition produces

$$\left(\theta_{i,tr}\right)_{t=0} \equiv \sum_{n=1}^{\infty} \phi_{in}(0) \sin(n\pi x) = \theta_o - x \qquad \forall\, i = s,\, f \tag{52}$$

A relationship between A_{in} and B_{in} in eq. (50) is obtained by multiplying eq. (52) by $\sin(j\pi x)$, integrating the results over the whole domain, i.e. $\int_0^1 (\cdot)\mathrm{d}x$ and using orthogonality conditions to yield

$$A_{in} + B_{in} = \phi_{no} \qquad \forall\, i = s,\, f \tag{53}$$

where

$$\phi_{sn}(0) = \phi_{fn}(0) = \phi_{no} = \frac{2\left[\theta_o + (1-\theta_o)(-1)^n\right]}{n\pi} \tag{54}$$

and from eq. (53) the relationship between the coefficients A_{in} and B_{in} is

$$B_{in} = \phi_{no} - A_{in} \qquad \forall\, i = s,\, f \tag{55}$$

which upon substitution into eq. (50) and then into eq. (51) yields

$$\theta_{i,tr} = \sum_{n=1}^{\infty} \left[A_{in}e^{\lambda_{1n}t} + (\phi_{no} - A_{in})\, e^{\lambda_{2n}t}\right] \sin(n\pi x) \qquad \forall\, i = s,\, f \tag{56}$$

Using now the second initial condition from eq. (44) into eq. (54) produces the equation

$$\left(\frac{\partial \theta_i}{\partial t}\right)_{t=0} \equiv \sum_{n=1}^{\infty} \left[A_{in}\lambda_{1n} + (\phi_{no} - A_{in})\,\lambda_{2n}\right] \sin(n\pi x) = 0 \qquad \forall\, i = s,\, f \tag{57}$$

The values of the coefficients A_{in} are finally obtained from eq. (57) to yield

$$A_{in} = \frac{\lambda_{2n}\phi_{no}}{(\lambda_{2n} - \lambda_{1n})} \qquad \forall\, i = s,\, f \tag{58}$$

Equation (58) indicates that the coefficients for both phases are identical, i.e. $A_{sn} = A_{fn}$, a fact that causes the solutions for both phases to be identical too. The complete solution is obtained from eq. (56) by substituting eq. (58) and the steady state solution leading to

$$\theta_i = x + \sum_{n=1}^{\infty}\left[\frac{\lambda_{2n}\phi_{no}}{(\lambda_{2n} - \lambda_{1n})}e^{\lambda_{1n}t} - \frac{\lambda_{1n}\phi_{no}}{(\lambda_{2n} - \lambda_{1n})}e^{\lambda_{2n}t}\right]\sin(n\pi x) \quad \forall\, i = s,\, f \tag{59}$$

and is perfectly consistent with the conclusion reached in Section 2, eq. (11), indicating that the temperature of both phases are identical leading to Lotheq and consequently to the stated paradox.

5 Resolution of the Paradox

While the eigenvalues obtained via both the elimination and the eigenvectors methods are identical leading to identical final forms of the solution let us compare the final coefficients in these solutions obtained via the two different methods. Comparing the coefficients of the $e^{\lambda_{1n}t}$ term in eqs. (39) and (40) with the corresponding coefficients to the same term in eq. (59) shows that the first part of the coefficients is identical but the second part is missing in eq. (59). Similarly for the coefficients to the $e^{\lambda_{2n}t}$ term, their second part is missing in eq. (59).

What is therefore the reason that the elimination method produces an incorrect result? The first part of the answer to this question can be obtained by observing that both methods produce identical solutions up to the point where we imposed the second initial condition on the elimination method solution, eq. (56). Only after imposing the initial condition (57) specifying a vanishing initial temperature derivative in time, i.e. $\left(\partial\theta_i \big/ \partial t\right)_{t=0} = 0\ \forall\ i = s,\, f$ the two solutions obtained via the two different methods diverged producing the apparent paradox. Then, the second part of the answer should be related to the question of why a perfectly correct initial condition obtained correctly from the analysis preceding eqs. (9) and (10) produces an incorrect solution. The answer to this second part of the question is related to the way the coefficients were evaluated from the Fourier series in eq. (57) by using this derivative initial condition. The implied assumption when doing so is that any constant (including the 0) can be expanded into a Fourier series. It is however naïve to expect the existence of a Fourier expansion to the 0 constant as eq. (57) implies. The coefficients obtained this way are therefore incorrect, although the initial condition $\left(\partial\theta_i \big/ \partial t\right)_{t=0} = 0\ \forall i = s,\, f$ is indeed correct. In order to correct this evaluation of the coefficients via the elimination method let us check what do we need to do instead of using the initial condition $\left(\partial\theta_i \big/ \partial t\right)_{t=0} = 0\ \forall i = s,\, f$. We still need derivative initial conditions for $\phi_{in}(t)$, i.e. $\left(\mathrm{d}\phi_{in} \big/ \mathrm{d}t\right)_{t=0}\ \forall i = s,\, f$ in order to establish the value of the coefficients $A_{in}\ \forall i =$

s, f. However, as distinct from $\left(\partial\theta_i \big/ \partial t\right)_{t=0}$ which needs the full system of partial differential equations (14) and (15) to extract its value, the values of $\left(\mathrm{d}\phi_{in} \big/ \mathrm{d}t\right)_{t=0}$ can be obtained from the system of ordinary differential equations (23a,b) by using the known values of $\phi_{sn}(0) = \phi_{fn}(0) = \phi_{no}$ that were evaluated and presented in eq. (54). Substituting these values for $t = 0$ in eq. (23) yields

$$\begin{aligned} \left(\frac{d\phi_{sn}}{dt}\right)_{t=0} &= a_n\phi_{sn}(0) + b\phi_{fn}(0) = (a_n + b)\,\phi_{no} \quad (a) \\ \left(\frac{d\phi_{fn}}{dt}\right)_{t=0} &= c\phi_{sn}(0) + d_n\phi_{fn}(0) = (c + d_n)\,\phi_{no} \quad (b) \end{aligned} \tag{60}$$

Now, from eq. (56) we evaluated $\phi_{in}(t)$ up to the yet unknown value of the constants A_{in}, in the form

$$\phi_{in}(t) = A_{in}e^{\lambda_{1n}t} + (\phi_{no} - A_{in})\,e^{\lambda_{2n}t} \qquad \forall i = s,\, f \tag{61}$$

From eq. (61) one can take the time derivative to yield

$$\frac{d\phi_{in}}{dt} = \lambda_{1n}A_{in}e^{\lambda_{1n}t} + \lambda_{2n}(\phi_{no} - A_{in})\,e^{\lambda_{2n}t} \qquad \forall i = s,\, f \tag{62}$$

and evaluating eq. (62) at $t = 0$ produces

$$\left(\frac{d\phi_{in}}{dt}\right)_{t=0} = \lambda_{1n}A_{in} + \lambda_{2n}(\phi_{no} - A_{in}) \tag{63}$$

Substituting now the initial conditions (60) into (63) leads to the result

$$\lambda_{1n}A_{sn} + \lambda_{2n}(\phi_{no} - A_{sn}) = (a_n + b)\,\phi_{no} \tag{64}$$

$$\lambda_{1n}A_{fn} + \lambda_{2n}\left(\phi_{no} - A_{fn}\right) = (c + d_n)\,\phi_{no} \tag{65}$$

The values of the coefficients A_{sn} and A_{fn} can now be evaluated from eqs. (64) and (65) in the form

$$A_{sn} = \frac{[\lambda_{2n} - (a_n + b)]\,\phi_{no}}{(\lambda_{2n} - \lambda_{1n})} \tag{66}$$

$$A_{fn} = \frac{[\lambda_{2n} - (d_n + c)]\,\phi_{no}}{(\lambda_{2n} - \lambda_{1n})} \tag{67}$$

Substituting eqs. (66), (67) into (56) and adding the steady part yields

$$\theta_s = x + \sum_{n=1}^{\infty}\left[\frac{[\lambda_{2n} - (a_n + b)]\,\phi_{no}}{(\lambda_{2n} - \lambda_{1n})}e^{\lambda_{1n}t} - \frac{[\lambda_{1n} - (a_n + b)]\,\phi_{no}}{(\lambda_{2n} - \lambda_{1n})}e^{\lambda_{2n}t}\right]\sin(n\pi x) \tag{68}$$

$$\theta_f = x + \sum_{n=1}^{\infty}\left[\frac{[\lambda_{2n} - (d_n + c)]\,\phi_{no}}{(\lambda_{2n} - \lambda_{1n})}e^{\lambda_{1n}t} - \frac{[\lambda_{1n} - (d_n + c)]\,\phi_{no}}{(\lambda_{2n} - \lambda_{1n})}e^{\lambda_{2n}t}\right]\sin(n\pi x) \tag{69}$$

The first observation from the solutions (68) and (69) is that these solutions are not anymore identical, i.e. now we obtained LaLotheq conditions i.e. $\theta_s \neq \theta_f$ as we did via the eigenvector method. Comparing now these solutions obtained via the elimination method (68) and (69) with the solutions (39) and (40), respectively, obtained via the eigenvectors method by looking at the coefficients of the terms $e^{\lambda_{1n}t}$ and $e^{\lambda_{2n}t}$, brings us to the conclusion that both methods yield identical solutions, i.e. eq. (39) is identical to eqs. (68) and (40) is identical to eq. (69). The latter conclusion resolves therefore the paradox.

However, now that we have obtained identical solutions via both methods and resolved the paradox, it is interesting to observe how the initial temperature derivative with respect to time $\left(\partial\theta_i \big/ \partial t\right)_{t=0}$ as evaluated from these solutions looks like, and whether it indeed vanishes as expected. Taking the time derivative of the solutions (39) and (40), or (68) and (69), and evaluating it at $t = 0$ leads to

$$\left(\frac{\partial\theta_s}{\partial t}\right)_{t=0} = \sum_{n=1}^{\infty}\phi_{no}\,(a_n + b)\sin(n\pi x) \tag{70}$$

$$\left(\frac{\partial\theta_f}{\partial t}\right)_{t=0} = \sum_{n=1}^{\infty}\phi_{no}\,(d_n + c)\sin(n\pi x) \tag{71}$$

Substituting the definitions of a_n, b, d_n and$c$ from eq. (24) and by using eq. (16) yields

$$a_n + b = -\frac{n^2\pi^2}{Ni_sFh_s} = -\frac{\alpha_s}{\alpha_e}n^2\pi^2 \tag{72}$$

$$d_n + c = -\frac{n^2\pi^2}{Ni_fFh_f} = -\frac{\alpha_f}{\alpha_e}n^2\pi^2 \tag{73}$$

where $\alpha_s = k_s \big/ \gamma_s$, $\alpha_f = k_f \big/ \gamma_f$ and α_e is defined in eq. (8). Substituting eqs. (72) and (73) as well as the value of ϕ_{no} from eq. (54) into (70) and (71) yields

$$\left(\frac{\partial\theta_s}{\partial t}\right)_{t=0} = -\frac{2\alpha_s\pi}{\alpha_e}\sum_{n=1}^{\infty}n\left[\theta_o + (1-\theta_o)(-1)^n\right]\sin(n\pi x) \tag{74}$$

$$\left(\frac{\partial\theta_f}{\partial t}\right)_{t=0} = -\frac{2\alpha_f\pi}{\alpha_e}\sum_{n=1}^{\infty}n\left[\theta_o + (1-\theta_o)(-1)^n\right]\sin(n\pi x) \tag{75}$$

The simplest case is obtained for $\theta_o = 0$ when eqs. (74) and (75) become

$$\left(\frac{\partial \theta_s}{\partial t}\right)_{t=0} = -\frac{2\alpha_s \pi}{\alpha_e} \sum_{n=1}^{\infty} (-1)^n \, n \quad \sin(n\pi x) \tag{76}$$

$$\left(\frac{\partial \theta_f}{\partial t}\right)_{t=0} = -\frac{2\alpha_f \pi}{\alpha_e} \sum_{n=1}^{\infty} (-1)^n \, n \quad \sin(n\pi x) \tag{77}$$

For a value of $x = 0.5$ these alternating series have the form $\sum_{n=1}^{\infty} (-1)^n \, n = -1 + 2 - 3 + 4 - 5 + 6 - \ldots$. The sum of any two consecutive terms is either 1 or -1, depending on the choice of grouping the terms. In both cases the sum becomes $\sum_{n=1}^{\infty} (-1)^n \, n = \sum_{n=1}^{\infty} \pm 1 \to \pm\infty$, hence we conclude that the series in eqs. (76) and (77) diverge and we cannot estimate $\left(\partial\theta_i \big/ \partial t\right)_{t=0}$ analytically from the solutions. Actually the funny part of this result is that according to eqs. (76) and (77) the initial temperature derivatives $\left(\partial\theta_i \big/ \partial t\right)_{t=0}$ are identically zero on the boundaries, at $x = 0, 1$, where we could have anticipated the singularity because of the temperature step change there. Yet the results show that $\left(\partial\theta_i \big/ \partial t\right)_{t=0}$ is identically zero on the boundaries and diverges elsewhere. This particular anomaly should be the subject of further investigation.

The analytical series solution obtained via both methods was evaluated and plotted in order to visualize the behaviour of the solutions for both phases during the transient, evaluate the temperature differences between the phases and verify the analytical conclusions drawn.

The initial temperature value was taken as $\theta_o = 0.5$, implying $T_o = (T_H + T_C)\big/2$. The values of the parameters used were $Ni_f = 1$, $Ni_s = 0.5$ and $Fh_f = Fh_s = 1.5$. The results are presented graphically in Fig. 2 in terms of θ_s and θ_f as a function of time at constant values of x. Figure 2a presents the results for $x = 0.1,\ 0.2,\ 0.3$, and 0.4, while Fig. 2b presents the results for $x = 0.6,\ 0.7,\ 0.8$, and 0.9. It is obvious from these results that the temperatures of the phases are distinct, they start initially at $t = 0$ being identical, i.e. $(\theta_s)_{t=0} = \left(\theta_f\right)_{t=0} = \theta_o = 0.5$ and they end-up being identical at steady state, i.e. $(\theta_s)_{t\to\infty} = \left(\theta_f\right)_{t\to\infty} = x$, but during the transient $\theta_s \neq \theta_f$.

These results were plotted again in Fig. 3 in more detail while zooming into the initial time domain $t \in [0,\ 0.002]$ in order to check the initial time derivative of temperature $\left(\partial\theta_s \big/ \partial t\right)_{t=0}$ and $\left(\partial\theta_f \big/ \partial t\right)_{t=0}$. It is observed as anticipated that the temperature values overlap showing no variation in time except for the neighbourhood of the boundaries, i.e. for $x = 0.1$ and $x = 0.9$. Even for this neighbourhood it may be observed that there is an initial time domain $t \in [0,\ 0.0005]$ where temperature variations in time seem nonexistent reinforcing the analytical conclusion that $\left(\partial\theta_s \big/ \partial t\right)_{t=0} = \left(\partial\theta_f \big/ \partial t\right)_{t=0} = 0$. The numerical values (not shown here) confirm this result to machine precision.

The temperature difference between the phases in terms of $\Delta\theta = \left(\theta_s - \theta_f\right)$ as a function of time at selected constant values of x is presented in Fig. 4 clearly identifying the variation of the temperature difference between the phases with time, starting from and ending with identical values.

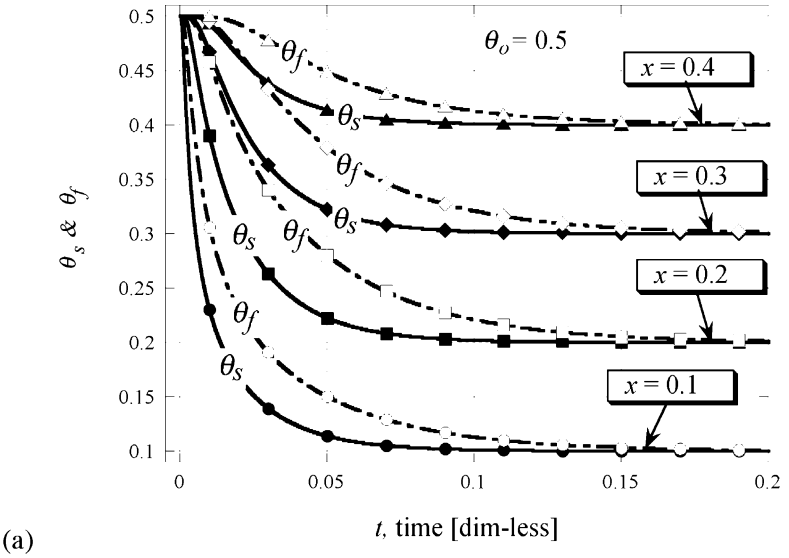

(a)

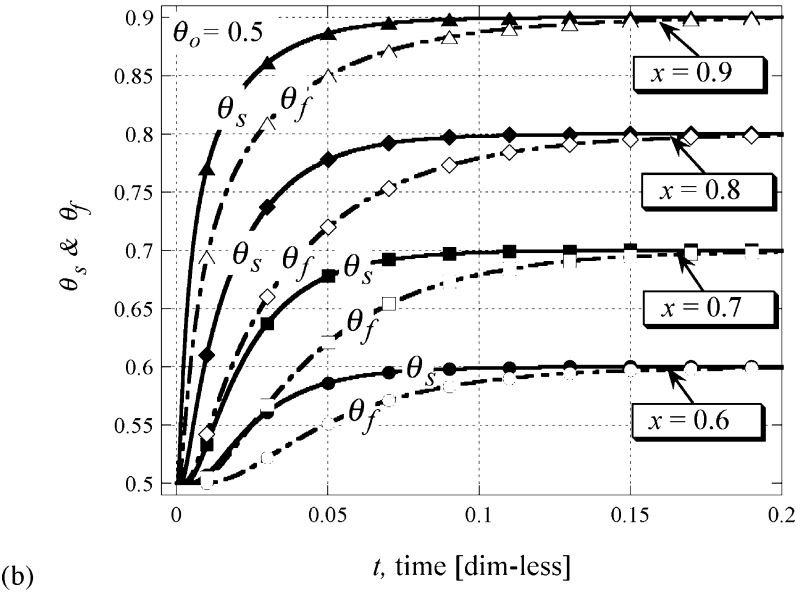

(b)

Fig. 2 Results of the analytical solution for the temperature of both phases as a function of time at selected locations. (**a**) at values of $x = 0.1,\ 0.2,\ 0.3$, and 0.4; (**b**) at values of $x = 0.6,\ 0.7,\ 0.8$, and 0.9

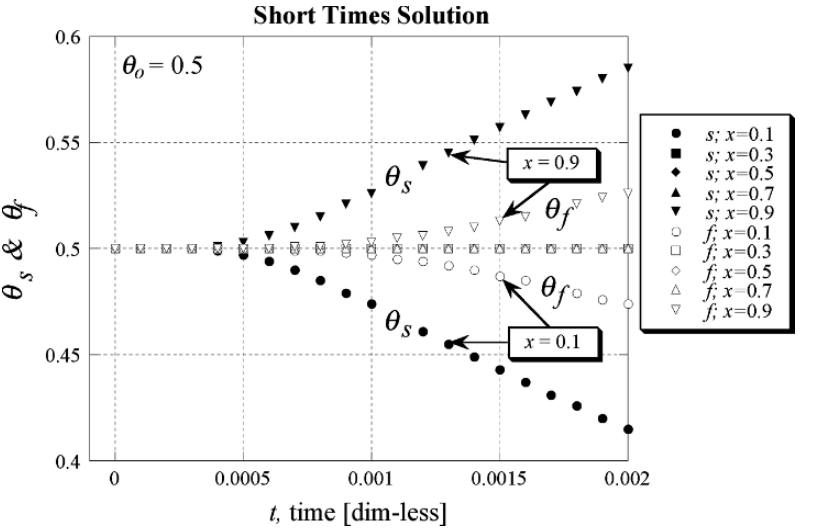

Fig. 3 Results of (**a**) the temperature solutions for short times by zooming into the initial time domain $t \in [0,\ 0.002]$ in order to check the initial time derivative of the temperature $\left(\partial \theta_s / \partial t\right)_{t=0}$ and $\left(\partial \theta_f / \partial t\right)_{t=0}$

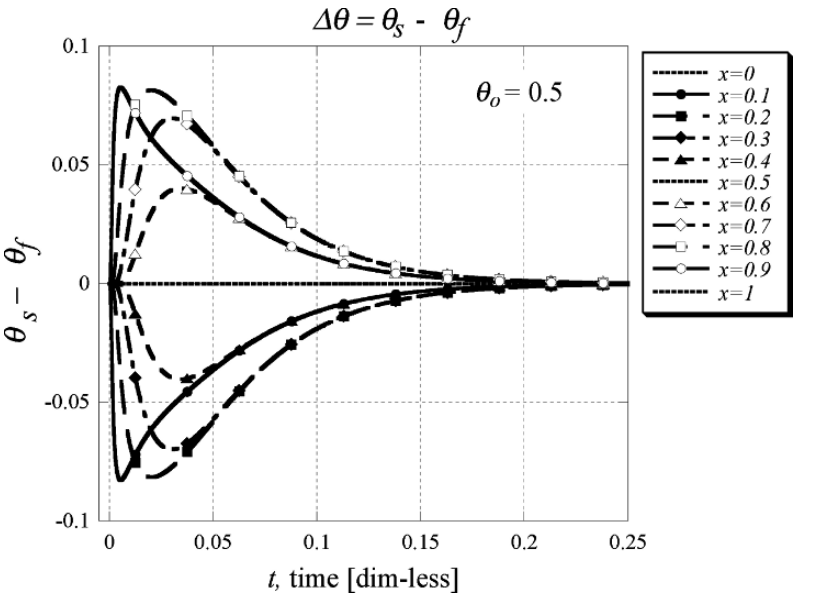

Fig. 4 Results of the temperature difference between the phases in terms of $\Delta\theta = \left(\theta_s - \theta_f\right)$ as a function of time at selected constant values of x

6 Experimental Measurement of the Effective Thermal Conductivity of a Porous Medium via the Transient Hot Wire (THW) Method

6.1 Background

The application of the Transient Hot Wire (THW) experimental method for the measurement of thermal conductivity of materials is presently limited to homogeneous and single phase materials because its simple and elegant theoretical expression on which it is based cannot be extended without associated corrections to porous media systems. Corrections to the THW method in the form presented by Vadasz (2006b) are not sufficiently simple because they are expressed in terms of a ratio of infinite power series rather than a simple expression as in the single-phase case. The Dual-Phase systems that benefit from these results are nanofluid suspensions, metal foams (porous media), insulating foams (porous media), two immiscible liquids, bi-composite solids (not a two-phase system but the method will nevertheless be applicable to such systems too).

6.2 Concepts and Methods

Inherent assumptions for the existence of an effective thermal conductivity for dual-phase systems such as porous insulating foams (Coquard and Bailis 2006, Coquard *et al*. 2006) having properties that are similar to homogeneous materials are being made even without mentioning them. The practice of using the terminology "effective thermal conductivity" over the years yielded a "tradition" of not even challenging its existence – a natural internalization but rather incorrect. A direct result of this practice is the obvious application of single-phase measurements methods to porous media.

6.2.1 Measuring Temperature in a Dual-Phase System via the Transient Hot Wire Method

Homogeneous Fluids and Solids

The THW method is well established as the most accurate, reliable and robust technique (Hammerschmidt and Sabuga 2000) for evaluating the thermal conductivity of fluids (De Groot *et al*. 1974, Healy *et al*. 1976, Kestin and Wakeham 1978) and solids (Assael *et al*. 2002). It replaced the steady state methods primarily because of the difficulty to determine that steady state conditions haven indeed been established and for fluids the difficulty in preventing the occurrence of natural convection and consequently the difficulty in eliminating the effects of natural convection on the heat flux. The THW method consists in principle of determining the thermal conductivity of a selected material/fluid by observing the rate at which the temperature of a very thin platinum (or alternatively tantalum) wire (5–80 μm in diameter) increases with time after a step change in voltage has been applied to it. The platinum (tantalum) wire is embedded vertically in the selected material/fluid (see Fig. 5) and serves as

a heat source as well as a thermometer. The temperature of the wire is established by measuring its electrical resistance, the latter being related to the temperature via a relationship of the form (Bentley 1984)

$$R_w = R_o \left[1 + \beta \left(T - T_o\right)\right] \tag{78}$$

A quadratic term is usually included too in eq. (78) but the linear part is already very accurate and the quadratic term ads only 0.4% to the resistance value over a wide temperature change of 100 °C and 0.004% over a temperature change of 10 °C (Bentley 1984). The requirement for a very thin (5–80 μm in diameter) platinum/tantalum wire is due to the need to obtain a uniform temperature across the cross section of the wire in a time scale that is substantially shorter than the time scale of thermal diffusion to the neighboring fluid. For platinum having a thermal diffusivity of $\alpha_{Pt} = 2.6 \times 10^{-5} \mathrm{m}^2/\mathrm{s}$ (Martinsons *et al.* 2001) and a micrometer size wire radius (4.81×10^{-5} m) the transient within the wire will disappear within $\sim$ 0.1 ms, and therefore the readings that are being taken at times that are much longer than 0.1 ms ($t >> 0.1$ ms) correspond to a uniform temperature over the wire's cross section.

A Wheatstone bridge is used to measure the electrical resistance R_w of the wire (see Fig. 5). The electrical resistance of a potentiometer R_3 is adjusted until the reading of the galvanometer G shows zero current. When the bridge is balanced as indicated by a zero current reading on the galvanometer G, the value of R_w can be established from

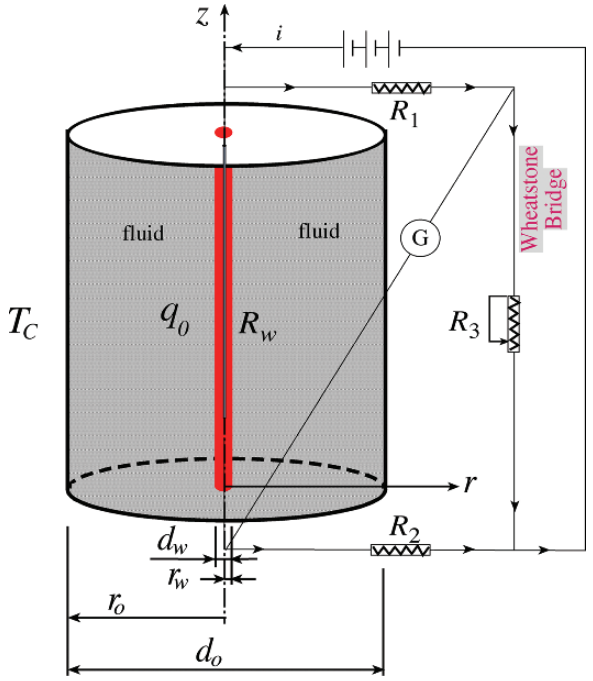

Fig. 5 Typical schematic setup for a Transient Hot Wire experiment in a pure fluid

the known electrical resistances R_1, R_2 and R_3 by using the balanced Wheatstone bridge relationship $R_w = R_1 R_2 \big/ R_3$.

While the application of the method to solids and gases is straightforward its corresponding application to electrically conducting liquids needs further attention. The experiments conducted in nano-fluid suspensions for example (Eastman *et al*. 2001, Lee *et al*. 1999, Choi *et al*. 2001, Xuan and Li 2000) used a thin electrical insulation coating layer to cover the platinum wire instead of using the bare metallic wire, a technique developed by Nagasaka and Nagashima (1981). The latter is aimed at preventing problems such as electrical current flow through the liquid causing ambiguity of the heat generation in the wire. Alternatively, Assael et al. (2004) used tantalum wires, which were anodized in situ to form a coating layer of tantalum pentoxide (Ta_2O_5), which is an electrical insulator. Because of the very small diameter (micrometer size) and high thermal conductivity of the platinum wire the latter can be regarded as a line source in an otherwise infinite cylindrical medium (Fig. 6).

The rate of heat generated per unit length (l) of platinum wire is therefore $\dot{q}_l = iV \big/ l \ \mathrm{W} \cdot \mathrm{m}^{-1}$, where i is the electric current flowing through the wire and V is the voltage drop across the wire. In this sub-section the contextual notation refers to r, r_w, t and t_o as dimensional quantities, as we do not introduce yet dimensionless ones. Solving for the radial heat conduction due to this line heat source leads to a temperature solution in the following closed form that can be expanded in an infinite series as follows

$$T = \frac{\dot{q}_l}{4\pi k} Ei\left(\frac{r^2}{4\alpha t}\right) = \frac{\dot{q}_l}{4\pi k}\left[-\gamma_{Eu} + \ln\left(\frac{4\alpha t}{r^2}\right) + \frac{r^2}{4\alpha t} - \frac{r^4}{64\alpha^2 t_2} + \frac{r^6}{1152\alpha^3 t_3} - \ldots.\right] \tag{79}$$

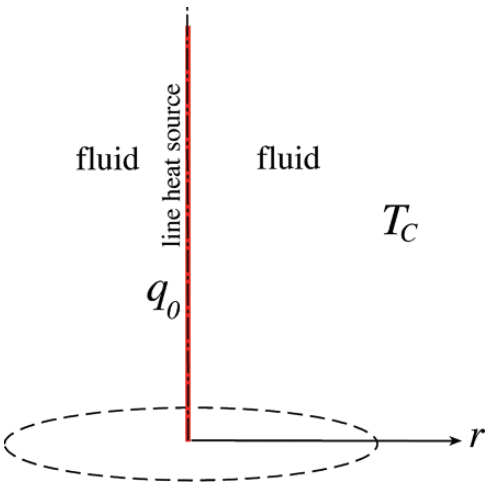

Fig. 6 The line heat source analytical problem underlying the Transient Hot Wire method

where $Ei(\bullet)$ represents the exponential integral function, and $\gamma_{Eu} = \ln(\sigma_{Eu}) = 0.5772156649$ is Euler's constant. For a line heat source embedded in a cylindrical cell of infinite radial extent and filled with the test fluid one can use the approximation $r^2/4\alpha t << 1$ in eq. (79) to truncate the infinite series and yield

$$T \approx \frac{\dot{q}_l}{4\pi k}\left[-\gamma_{Eu} + \ln\left(\frac{4\alpha t}{r^2}\right) + O\left(\frac{r^2}{4\alpha t}\right)\right] \tag{80}$$

Equation (80) reveals a linear relationship, on a logarithmic time scale, between the temperature and time. Therefore, one way of evaluating the thermal conductivity is from the slope of this relationship evaluated at $r = r_w$, for example, r_w being the radius of the platinum wire. However the latter needs the knowledge of the thermal diffusivity, α, of the fluid. Alternatively one may evaluate k by using any two readings of temperature T_1 and T_2 recorded at times t_1 and t_2 respectively. The temperature difference $(T_2 - T_1)$ can then be approximated by using eq. (80), in the form

$$(T_2 - T_1) \approx \frac{iV}{4\pi kl}\left[\ln\left(\frac{t_2}{t_1}\right)\right] \tag{81}$$

where we replaced the heat source with its explicit dependence on i, V and l, i.e. $\dot{q}_l = iV/l$. From eq. (81) one can express the thermal conductivity k explicitly in the form

$$k \approx \frac{iV}{4\pi\,(T_2 - T_1)\,l}\left[\ln\left(\frac{t_2}{t_1}\right)\right] \tag{82}$$

For $r = r_w$ the condition for the series truncation $r_w^2/4\alpha t << 1$ can be expressed in the following equivalent form that provides the validity condition of the approximation in the form

$$t >> t_o = \frac{r_w^2}{4\alpha} \tag{83}$$

The value of $t_o = r_w^2/4\alpha$ provides a validity condition of the experimental readings, i.e. $t >> t_o$.

Equation (82) is a very accurate way of estimating the thermal conductivity as long as the validity conditions for appropriateness of the problem derivations used above are fulfilled. A finite length of the platinum (tantalum) wire, the finite size of the cylindrical container, the heat capacity of the platinum (tantalum) wire, and possibly natural convection effects are examples of possible deviations of any realistic system from the one used in deriving eq. (82). De Groot *et al.* (1974), Healy *et al.* (1976), and Kestin and Wakeham (1978) introduce an assessment of these deviations and possible corrections to the THW readings to improve the accuracy of the results. In general all the deviations indicated above could be eliminated via the proposed corrections provided the validity condition listed in eq. (83) is enforced as well as an additional condition that ensures that natural convection is absent. The validity condition (83) implies the application of

eq. (82) for long times only. Nevertheless, when evaluating this condition (83) to data used in the nano-fluid suspensions experiments one obtains explicitly the following values. For a 76.2 μm diameter of platinum wire used by Eastman *et al*. (2001), Lee *et al*. (1999), and Choi *et al*. (2001) and an electrical insulation coating thickness of 10 μm, the wire radius is $r_w = 4.81 \times 10^{-5}$ m leading to $t_o = r_w^2/4\alpha = 13.7$ ms for ethylene glycol and $t_o = r_w^2/4\alpha = 7.2$ ms for oil, leading to the validity condition $t >> 13.7$ ms for ethylene glycol and $t >> 7.2$ ms for oil. The long times beyond which the solution (82) can be used reliably are therefore of the order of hundreds of milliseconds, not so long in the actual practical sense. These values also correspond to the ones needed for the assumption of a wire temperature that is uniform over the wire's cross section a condition that developed following eq. (78) above. On the other hand the experimental time range is limited from above as well in order to ensure the lack of natural convection that develops at longer time scales. Xuan and Li (2000) estimate this upper limit for the time that an experiment may last before natural convection develops as about 5 s. They indicate that "An experiment lasts about 5 s. If the time is longer, the temperature difference between the hot-wire and the sample fluid increases and free convection takes place, which may result in errors". Lee *et al*. (1999) while using the THW method and providing experimental data in the time range of 1–10 s, indicate in their Fig. 3 the "valid range of data reduction" to be between 3 and 6 s. Our estimations evaluated above confirm these lower limits as a very safe constraint and we assume that the upper limits listed by Xuan and Li (2000) and Lee *et al*. (1999) are also good estimates. Within this time range the experimental results should produce a linear relationship, on a logarithmic time scale, between the temperature and time.

Fluid-Saturated Porous Media

The first major problem when attempting to apply the THW method to porous media is focused in the question "What temperature precisely is the wire exposed to?". Obviously, the wire is exposed partly to the solid-phase and partly to the fluid phase that constitutes the porous medium. There is no justification to assume that local thermal equilibrium between the solid and fluid phases occurs generally (especially when a heat flux boundary condition is applied, as in the THW case). On the contrary, it is sensible to assume that the average temperature of the fluid differs from that of the solid. Then the wire being in contact with both phases will "feel" the fluid temperature on parts of its surface and the solid temperature on other parts of its surface. How to integrate these two effects in terms of its overall lumped effect on the total electrical resistance of the wire is not a simple averaging procedure. It forms one of the objectives of continued research. The following derivations demonstrate the direction one intends adopting in resolving this problem. Obviously we need to separate between two extreme cases. One is related to the one extreme possibility when the pores near the wire form complete rings around the wire, i.e. at any point along the wire's length, the complete circumference of the wire is exposed either completely to the fluid or completely to the solid. In such a case one may look to this configuration as small electrical resistors connected in series along the wire's length.

A macroscopic experimental testing of this concept is presented in Fig. 7 where a two-phase system consisting of two different immiscible liquids is being used with the Transient Hot Wire system to check the following derivations. Consider the two immiscible stationary liquids, a lighter one on top of a heavier one as presented in Fig. 7. The total height of the container H is occupied partly, H_d, by the heavy liquid on the down-section and partly, H_u, by the lighter liquid on the upper section. We define the relative height of the interface between the two fluids as $\varphi = H_d \big/ H$, which is identical to the ratio between the volume of the heavier liquid and the total volume occupied by both liquids. This is equivalent to the porosity in porous media. Obviously, the following relationship holds $(1-\varphi) = 1 - H_d \big/ H = H_u \big/ H$. Neglecting the tiny region in the neighborhood of the interface where sharp temperature gradients are being expected we can assume far away from the interface radial temperatures of the form that were presented for a single fluid in eq. (79)

$$T_d \approx \frac{\dot{q}_l}{4\pi k_d}\left[-\gamma_{Eu} + \ln\left(\frac{4\alpha_d t}{r_w^2}\right)\right], T_u \approx \frac{\dot{q}_l}{4\pi k_u}\left[-\gamma_{Eu} + \ln\left(\frac{4\alpha_u t}{r_w^2}\right)\right] \tag{84}$$

leading to relationships of the form presented in eq. (82), i.e. the thermal conductivities of each liquid is approximately given by

$$k_d \approx \frac{i\,V}{4\pi\,(T_{d2} - T_{d1})\,H}\left[\ln\left(\frac{t_2}{t_1}\right)\right], k_u \approx \frac{i\,V}{4\pi\,(T_{u2} - T_{u1})\,H}\left[\ln\left(\frac{t_2}{t_1}\right)\right] \tag{85}$$

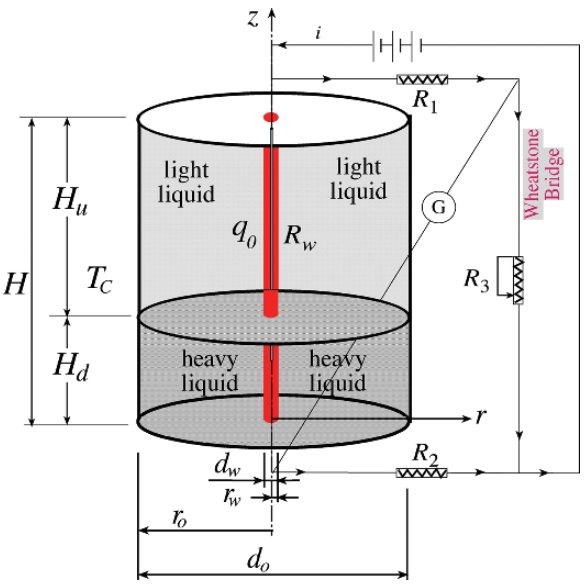

Fig. 7 Schematic setup for a Transient Hot Wire experiment in two immiscible fluids

However, we do not measure separately the temperatures T_d and T_u but rather the wire's electrical resistance due to the lumped effect of both T_d and T_u. The resistance of the wire is directly proportional to the wire's length and therefore the contribution of the lower and upper sections can be expressed in the form

$$R_w = \varphi R_{wd} + (1-\varphi) R_{wu} \tag{86}$$

where

$$R_{wd} = R_o \left[1 + \beta \left(T_d - T_o\right)\right] \text{ and } R_{wu} = R_o \left[1 + \beta \left(T_u - T_o\right)\right] \tag{87}$$

Combining eq. (87) with eq. (86) yields

$$R_w = R_o \left\{1 + \beta \left[\varphi T_d + (1-\varphi) T_u - T_o\right]\right\} = R_o \left[1 + \beta \left(T_{eff} - T_o\right)\right] \tag{88}$$

where an effective temperature in the form

$$T_{eff} = \varphi T_d + (1-\varphi) T_u \tag{89}$$

appears and represents the average temperature "felt" by the wire in the sense of its impact on the wire's electrical resistance. We can now express this effective temperature by using the individual temperatures eq. (84) into (89) leading to

$$T_{eff} \approx \frac{\dot{q}_l}{4\pi} \left[-\gamma_{Eu} \left(\frac{\varphi}{k_d} + \frac{(1-\varphi)}{k_u} \right) + \frac{\varphi}{k_d} \ln\left(\frac{4\alpha_d t}{r_w^2} \right) + \frac{(1-\varphi)}{k_u} \ln\left(\frac{4\alpha_u t}{r_w^2} \right) \right] \tag{90}$$

Evaluating eq. (90) at two instances of time t_1 and t_2 and evaluating the difference yields

$$\left(T_{eff,2} - T_{eff,1}\right) \approx \frac{\dot{q}_l}{4\pi} \left[\frac{\varphi}{k_d} + \frac{(1-\varphi)}{k_u} \right] \ln\left(\frac{t_2}{t_1} \right) \tag{91}$$

where an effective thermal conductivity emerged (not necessarily the typical "effective" value), in the form of thermal resistances $\left(1/k_i \;\forall\; i = d, u\right)$ connected in series

$$\frac{1}{k_{eff}} = \frac{\varphi}{k_d} + \frac{(1-\varphi)}{k_u} \tag{92}$$

This result is still not satisfactory because our aim is to measure k_u and k_d separately and not their lumped effect on the wire. To overcome this problem we need to run the experiment twice, with different values of the interface location, i.e. φ_1 and φ_2. Then, from the known effective values of $k_{eff,1}$ and $k_{eff,2}$ obtained by the method presented above one may solve the system of two equations

$$\varphi_1 R_d + (1-\varphi_1) R_u = R_{eff,1} \; ; \quad \varphi_2 R_d + (1-\varphi_2) R_u = R_{eff,2} \tag{93}$$

where $R_d = 1/k_d$, $R_u = 1/k_u$ and $R_{eff,i} = 1/k_{eff,j}\ \forall\ j = 1, 2$ leading to

$$k_d = \frac{(\varphi_1 - \varphi_2)}{\left[(1-\varphi_1)\,R_{eff,1} - (1-\varphi_2)\,R_{eff,2}\right]};\ k_u = \frac{(\varphi_1 - \varphi_2)}{\left[\varphi_1 R_{eff,2} - \varphi_2 R_{eff,1}\right]} \tag{94}$$

Alternatively, one may use a second wire located far away (in the sense of the thermal impact of the heating from the wire, approximately $>> 100\ \mu m$ apart) from the first one and embedded only in the upper liquid, hence evaluating k_u independently and then substituting it into eq. (92) to obtain the value of k_d. More difficult is the other extreme when we assume that the wire is exposed partly to the fluid and partly to the solid but this separation is along the wire, i.e. part of circumference of any cross section, say $0 < \theta < \theta_1$, is exposed to one fluid and the other part, $\theta_1 < \theta < 2\pi$, is exposed to the other fluid, where two partitions located at $\theta = 0$ and $\theta = \theta_1$ separate the two fluids. (Here given the contextual notation θ represents the angular coordinate.) In this case the cross section will not have a uniform temperature and while this configuration represents electrical resistances connected in parallel the very dependence of the temperature solution within the wire on r and θ makes the application of the electrical resistance – temperature relationship questionable. It may very well be that there is a need to solve a simplified version of the electromagnetic Maxwell's equations to find an answer to the latter question and be certain of the applicability of the electrical resistance – temperature relationship for this case. The realistic porous media outcome is expected to be in between these two limits and will depend on the areal-porosity of the porous medium and its distribution around and along the wire. More work will be needed to find precisely how to characterize a porous medium in a way that these parameters will be established independently and could then be used with confidence with the Transient Hot Wire method.

6.2.2 Maxwell's "Effective" Thermal Conductivity

Maxwell (1891) showed that an "effective" thermal conductivity of a bi-composite system (dual-phase, or single-phase heterogeneous) exists in the sense of an equivalent single-phase homogeneous system transferring and identical heat flux. He considered a configuration similar to that presented in Fig. 8 below, where spherical materials "b" are distributed uniformly within a different material "a". These may be spherical solid particles of material "b" suspended in a fluid "a", or spherical inserts of solid particles "b" within another solid "a", an example of an unusual composite solid. The spherical particles are assumed to be distributed uniformly but far away from each other such that the temperature and heat fluxes in the neighborhood of one solid particle is not affected by the presence of other solid particles. Therefore the applicability of Maxwell's model for the evaluation of the effective thermal conductivity of a porous medium is questionable, because not only that the solid particles are not far away from each other in a porous medium but they rather touch each other, violating the basic assumption made in the derivation. Nevertheless, the concept of Maxwell's effective

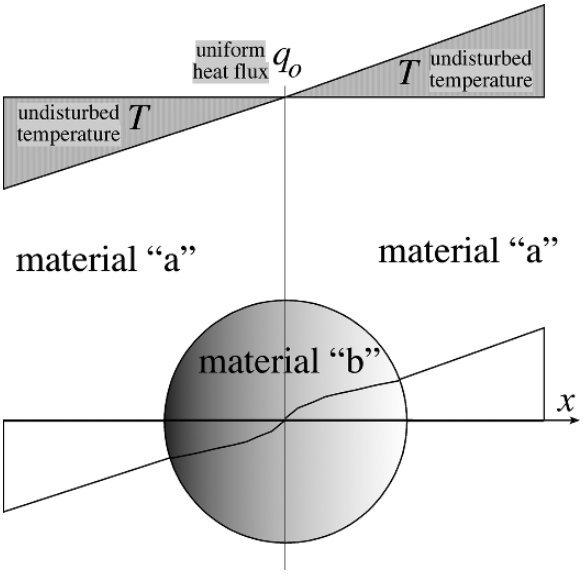

Fig. 8 Maxwell's effective thermal conductivity; problem formulation

thermal conductivity is introduced here for two reasons. The first is that in terms of heat conduction Vadasz (2006b) showed that solid suspensions in a fluid follow the same conceptual governing equations as the porous media equations with vanishing effective thermal conductivity over the solid phase. Second, it might be possible to use the conceptual thinking of Maxwell in attempting to derive an equivalent expression for a porous medium. Therefore, we continue by considering the Maxwell derivation for far away particles of one material embedded in a second material. A uniform heat flux $q_o = \text{const.}$ is applied across material "a" leading to a linear undisturbed temperature profile far away from the spherical particle "b", in the form $T = \left(q_o / k_a\right) x$. The objective is to find first the temperature distribution considering the presence of the spherical particle "b", and then attempt to find an effective thermal conductivity for the composite medium that transfers an identical heat flux q_o, and express this effective thermal conductivity in terms of the thermal conductivities of materials "a" and "b". Towards this end one needs first to convert the problem and the heat flux which is uniform in the x direction into the spherical coordinates r, θ, ϕ, given the shape of the particle.

This transformation yields at steady state, after separation of variables, $T = R_n(r) M_n(\mu)$ with $\mu = \cos(\theta)$, two equations for the temperature components in the r and θ directions in the form

$$\frac{d^2 R_n}{dr^2} + \frac{2}{r}\frac{dR_n}{dr} - \frac{n(n+1)}{r^2} R_n = 0; \tag{95}$$

$$\frac{d}{d\mu}\left[\left(1-\mu^2\right)\frac{dM_n}{d\mu}\right]+n\left(n+1\right)M_n=0 \tag{96}$$

Equation (95) is the Euler–Cauchy differential equation and eq. (96) is Legendre's differential equation producing solutions of the form

$$R_n\left(r\right)=a_{1n}r^n+a_{2n}r^{-(n+1)};\quad M_n\left(\mu\right)=c_{1n}P_n\left(\mu\right)+c_{2n}Q_n\left(\mu\right) \tag{97}$$

where $P_n\left(\mu\right)$ and $Q_n\left(\mu\right)$ are Legendre functions of degree n, of the first and second kind, respectively. After imposing the boundary condition of the applied heat flux in the form $\lim_{r\to\infty} q_r=-k\left(\partial T\big/\partial r\right)_{r\to\infty}=q_o\cos\theta=q_o\mu$ yields the temperature solution in the form

$$T=\left(a_{21}r^{-2}-\frac{q_o}{k}r\right)\cos\left(\theta\right) \tag{98}$$

The additional undefined integration constant a_{21} will be established by using the interface boundary condition at $r=r_o$, where r_o is the particle's radius. By using the solution (98) and introducing the existence of a number of j uniformly distributed identical spherical particles far away from each other defining the solid fraction (or phase b fraction) in the form $\varepsilon=V_b\big/V_{tot}$, where $V_{tot}=V_a+V_b$, we obtain a temperature solution (eq. (99) below) that may be shown to be identical to the one that is obtained by using an "effective thermal conductivity" for the whole medium. As a result it is simple to demonstrate that an "effective" thermal conductivity, k_e, exists and is found to have the form as follows

$$T=\frac{q_o}{k_a}\left[\frac{jr_o^3\left(k_b-k_a\right)}{\left(k_b+2k_a\right)}r^{-2}-r\right]\cos\left(\theta\right) \tag{99}$$

$$k_e=\frac{\left[k_b+2k_a+2\varepsilon\left(k_b-k_a\right)\right]}{\left[k_b+2k_a-\varepsilon\left(k_b-k_a\right)\right]}k_a \tag{100}$$

Equation (100) is the familiar Maxwell's expression for the "effective" thermal conductivity (Maxwell 1891). The derivations above demonstrate that it was obtained at steady state. The existence of such an effective thermal conductivity at transients is by no means obvious. Therefore, since this equivalence applies to steady state only and Maxwell (1891) did not show that the same result applies for transients too, it appeals indeed to extend these derivations as well as their extensions (Batchelor 1972, Batchelor and Green 1972, Hamilton and Crosser 1962, Jeffrey 1973, Davis 1986, Lu and Lin 1996, Bonnecaze and Brady 1990, 1991) for the transient. Why shouldn't the "effective thermal conductivity" apply to transients? The answer to this question is the fact that the "effective thermal conductivity" of a dual-phase system is not a property of a new material. If it happens that an accurate representation of its "effective" impact in terms of an identical heat flux exists, one needs reassurance that this effective behavior applies to transients too.

6.2.3 Interface Heat Transfer Coefficient in Porous Media and Fluid Suspensions

In addition to the important question raised above, and to compensate for the possibility that such an accurate representation of the "effective thermal conductivity" has its limitations, the averaging concept can be applied by defining a Representative Elementary Volume (REV) and averaging the dependent variables over this REV. The resulting effect in addition to the heat transferred within each phase is the heat conduction over the interface separating the two phases (inter-phase heat transfer). Evaluating this heat transfer is possible for regular geometries, like the spherical one used by Maxwell (1891), however it becomes increasingly more difficult as the geometry becomes more complicated. Heat conduction in porous media subject to Lack of Local Thermal Equilibrium (LaLotheq) is governed at the macro-level by the following equations that represent averages over each phase within an REV (Representative Elementary Volume)

$$\gamma_s \frac{\partial T_s}{\partial t_*} = k_s \nabla_*^2 T_s - Q_{sf} \tag{101}$$

$$\gamma_f \frac{\partial T_f}{\partial t_*} = k_f \nabla_*^2 T_f + Q_{sf} \tag{102}$$

where Q_{sf} represents the rate of heat generation in the fluid phase within the REV due to the heat transferred over the fluid-solid interface, and where the other parameters were defined in Section 2. The traditional formulation of the rate of heat generation in the fluid phase within the REV due to the heat transferred over the fluid-solid interface uses a linear relationship between Q_{sf} and the average temperature difference between the phases in the form $Q_{sf} = h(T_s - T_f)$. In this discussion one assumed that h is an independent property while in reality h depends on the thermal conductivities and heat capacities of both phases, on the interface heat transfer area A_{sf}, and on other factors. Then, a change in h will occur due to changes in A_{sf}, k_f, k_s, γ_f and γ_s.

The lack of macroscopic level conduction mechanism in fluid suspensions (with $\varepsilon = (1 - \varphi)$) i.e. the heat transfer within the solid phase which is expressed by the fact that the solid particles represent the dispersed phase in the fluid suspension and therefore the solid particles can conduct heat between themselves only via the neighboring fluid, leads to setting $k_s = 0$ in eq. (101). The latter yields from eqs. (101) and (102) the averaged equations applicable to fluid suspensions. When steady state is accomplished in fluid suspensions $\partial T_s / \partial t_* = \partial T_f / \partial t_* = 0$ leading to local thermal equilibrium between the solid and fluid phases, i.e. $T_s(\mathbf{r}) = T_f(\mathbf{r})$, a condition that does not necessarily apply in porous media. By using eqs. (101) and (102) for a line heat source as needed for the application of the THW method and introducing the following dimensionless variables $t = t_* h / \gamma_f$, $r^2 = r_*^2 h / k_f$, $\theta_s = (T_s - T_o) / \left(\dot{q}_l / 2\pi k_f\right)$, $\theta_f = \left(T_f - T_o\right) / \left(\dot{q}_l / 2\pi k_f\right)$ renders these equations into their corresponding dimensionless form

$$\frac{1}{\chi}\frac{\partial \theta_s}{\partial t} = \frac{1}{\sigma r}\frac{\partial}{\partial r}\left(r\frac{\partial \theta_s}{\partial r}\right) - \left(\theta_s - \theta_f\right) \tag{103}$$

$$\frac{\partial \theta_f}{\partial t} = \frac{1}{r}\frac{\partial}{\partial r}\left(r\frac{\partial \theta_f}{\partial r}\right) + \left(\theta_s - \theta_f\right) \tag{104}$$

where $\chi = \gamma_f/\gamma_s$, $\sigma = k_f/k_s$, and $\kappa = \alpha_f/\alpha_s = \sigma/\chi$ represent the heat capacities, thermal conductivities and thermal diffusivities ratios, respectively. Introducing a Boltzmann transformation in the form

$$\eta = \frac{r^2}{4t} = \frac{r_*^2}{4\alpha_f t_*} \tag{105}$$

transforms eqs. (103) and (104) into the following equivalent, but not self-similar, form

$$t\frac{\partial \theta_s}{\partial t} = \kappa^{-1}\frac{\partial}{\partial \eta}\left(\eta\frac{\partial \theta_s}{\partial \eta}\right) + \eta\frac{\partial \theta_s}{\partial \eta} - \chi t\left(\theta_s - \theta_f\right) \tag{106}$$

$$t\frac{\partial \theta_f}{\partial t} = \frac{\partial}{\partial \eta}\left(\eta\frac{\partial \theta_s}{\partial \eta}\right) + \eta\frac{\partial \theta_s}{\partial \eta} + t\left(\theta_s - \theta_f\right) \tag{107}$$

The corresponding single-phase equation is self-similar, a result of utmost importance because it is this self-similarity that produces the simple solution expressed by eq. (79) and makes the application of the THW method possible. Nevertheless, eqs. (106) and (107) produce interesting self-similar solutions for short times $t << 1$ (and we will see that these are precisely the times that the THW method is focused on), by using the following short times expansion

$$\theta_i = \theta_i^{(0)} + t\theta_i^{(1)} + t^2\theta_i^{(2)} + O\left(t^3\right) \forall i = s, f \tag{108}$$

Then the equations at leading order decouple and take the form

$$\kappa^{-1}\frac{d}{d\eta}\left(\eta\frac{\partial \theta_s^{(0)}}{\partial \eta}\right) + \eta\frac{d\theta_s^{(0)}}{d\eta} = 0 \tag{109}$$

$$\frac{d}{d\eta}\left(\eta\frac{\partial \theta_f^{(0)}}{\partial \eta}\right) + \eta\frac{d\theta_f^{(0)}}{d\eta} = 0 \tag{110}$$

hence restoring at leading order the single-phase self-similarity at short times despite the dual-phase nature of the problem. The solution to eqs. (109) and (110) subject to the hot wire boundary conditions is presented below after converting it back to dimensional form

$$\left(T_s^{(0)} - T_o\right) = \frac{\dot{q}_{l*}}{4\pi k_s} Ei\left(\frac{r_*^2}{4\alpha_s t_*}\right) = \frac{\dot{q}_{l*}}{4\pi k_s}\left[-\gamma_{Eu} + \ln\left(\frac{4\alpha_s t_*}{r_*^2}\right) + O\left(\frac{r_*^2}{4\alpha_s t_*}\right)\right] \tag{111}$$

$$\left(T_f^{(0)} - T_o\right) = \frac{\dot{q}_{l*}}{4\pi k_f} Ei\left(\frac{r_*^2}{4\alpha_f t_*}\right) = \frac{\dot{q}_{l*}}{4\pi k_f}\left[-\gamma_{Eu} + \ln\left(\frac{4\alpha_f t_*}{r_*^2}\right) + O\left(\frac{r_*^2}{4\alpha_f t_*}\right)\right] \tag{112}$$

These solutions can be used to evaluate the effective thermal conductivity of the solid and fluid phases respectively for any pairs of two temperature readings $\left(T_{f1}^{(0)},\ T_{s1}^{(0)}\right)$ and $\left(T_{f2}^{(0)},\ T_{s2}^{(0)}\right)$ taken at subsequent times t_{1*} and t_{2*}, respectively, in the form

$$k_s \approx \frac{\dot{q}_{l*}}{4\pi\left(T_{s2}^{(0)} - T_{s1}^{(0)}\right)}\left[\ln\left(\frac{t_{2*}}{t_{1*}}\right)\right]; \quad k_f \approx \frac{\dot{q}_{l*}}{4\pi\left(T_{f2}^{(0)} - T_{f1}^{(0)}\right)}\left[\ln\left(\frac{t_{2*}}{t_{1*}}\right)\right] \tag{113}$$

These results are quite promising because they indicate that the THW method may be applied with some higher order corrections in porous media too, however we need to check the conditions under which the latter applies. Clearly a condition similar to eq. (83), which is applicable to single-phase, applies here too as the truncation of eqs. (111) and (112) requires $t_* >> t_o$, where the value of the minimum time is $t_o = \max\left[\left(r_{w*}^2/4\alpha_f\right), \left(r_{w*}^2/4\alpha_s\right)\right]$. In addition, the leading order solutions (111) and (112) apply for dimensionless short times only, i.e. for $t = t_* h/\gamma_f << 1$. Note also that an inherent, but reasonable, assumption was included in the derivation of the leading order eqs. (109) and (110), implying that $\eta_\gamma = \gamma_f/\gamma_s = O(1)$, i.e. $\gamma_f \sim \gamma_s$ at least in their order of magnitude. Therefore the condition $t = t_* h/\gamma_f << 1$ implies $t_* << \gamma_f/h$ or similarly $t_* << \gamma_s/h$. These conditions specify the range of short times that are needed for the approximated solutions (111) and (112) leading to eq. (113) to be valid. Combining the two conditions above produces

$$t_o << t_* << t_m \tag{114}$$

where
$t_o = \max\left[\left(r_{w*}^2/4\alpha_f\right), \left(r_{w*}^2/4\alpha_s\right)\right]$; $t_m = \min\left[\left(\gamma_f/h\right), \left(\gamma_s/h\right)\right]$. The requirement that $t_m >> t_o$, is necessary and sufficient for such a time interval to exist and makes the THW experimental method applicable to dual-phase systems. This requirement implies $\gamma_f/h >> r_{w*}^2/4\alpha_f$ (assuming $\eta_\gamma = \gamma_f/\gamma_s = O(1)$), leading to

$$h << \frac{4k_f}{r_{w*}^2} \tag{115}$$

This condition is the requirement for the existence of a time interval (method validity window) over which the THW method may produce reliable results in Dual-Phase applications. It reveals the significant impact that the interface heat transfer coefficient h has on the applicability of the THW method to dual-phase systems.

In fluid suspensions like in porous media, the parameter h, carrying units of $\mathrm{W}\cdot\mathrm{m}^{-3}\cdot\mathrm{K}^{-1}$, represents an integral heat transfer coefficient for the heat conduction at the solid-fluid interface within an REV. Its general relationship to the surface-area-to-volume ratio (specific area) was derived by Vadasz (2006b) by using relationships that are available for the respective coefficient in fluid saturated porous media (Quintard and Whitaker 1995, Alazmi and Vafai 2002, Amiri and Vafai 1994, Wakao et al. 1979, Wakao and Kaguei 1982, Kuwahara, Shirota and Nakayama 2001). Most of the reported evaluations of h in porous media listed above were derived with a particular focus on convection rather than conduction heat transfer. Their applicability and accuracy for conduction are therefore questionable. The implication of the derived relationship presented by Vadasz (2006b) is that the heat transfer coefficient is related to the particle size by the inversely quadratic relationship $h = [k_f / d_p^2] s\left(\varepsilon,\ k_f / k_s\right)$. While the particular form of the function $s\left(\varepsilon,\ k_f / k_s\right)$ and its possible further dependence on the particle size d_p as well, especially if the particle size is reduced to nano-scale levels, is not established for the case of suspensions, the general dependence of the heat transfer coefficient on the particle size is evident. This dependence of the heat transfer coefficient on the particle size introduces the effect of the surface-area-to-volume ratio (specific area) that was claimed by Eastman *et al*. (2001) to be missing in the classical models of evaluating the effective thermal conductivity of the suspension. One should however bear in mind that further dependence on particle size is anticipated as the particle size is reduced to the nano-scale level predominantly when the ballistic rather than diffusive nature of heat transfer becomes dominant (Chen 1996, 2000, 2001) and hence reducing the rate of heat transfer, implying a consequential reduction of the value of h to somewhat compensate for the otherwise substantial increase of h as the particle size is reduced. In addition one may anticipate an increase of h due to Brownian motion induced nanoconvection Jang and Choi (2004), Prasher et al. (2005) or a decrease due to the exceptionally small interface thermal conductance Huxtable *et al*. (2003).

Summarizing the topic of experimental methods one may state that an attempt has been made to render the Transient Hot Wire Experimental method to porous media applications. However, substantial more work is however necessary to complete this process and produce clear validity criteria for such applications. The latter criteria can then be used to develop reliable experimental procedures within these validity limits.

7 Application of the Heat Conduction in Porous Media to Nanofluid Suspensions

The impressive heat transfer enhancement revealed experimentally in nanofluid suspensions by Eastman *et al*. (2001), Lee *et al*. (1999) as presented in Fig. 9a below, and

by Choi *et al*. (2001) as presented in Fig. 9b below, conflicts apparently with Maxwell's (1891) classical theory of estimating the effective thermal conductivity of suspensions discussed in the previous section, including higher order corrections and other than spherical particle geometries developed by Hamilton and Crosser (1962), Jeffrey (1973), Davis (1986), Lu and Lin (1996), and Bonnecaze and Brady (1990, 1991).

Vadasz (2006b) derived theoretically a model for the heat conduction mechanisms of nanofluid suspensions including the effect of the surface area-to-volume ratio of the suspended nanoparticles/nanotubes on the heat transfer. The theoretical model is based on the concept of inter-phase heat transfer that is widely used in porous media. It is essentially a special case of the porous media heat conduction equations subject to Lack of Local thermal equilibrium (LaLotheq). This model was shown to provide apparently a viable explanation for the excessive values of the effective thermal conductivity obtained experimentally by Eastman *et al*. (2001), Lee *et al*. (1999), and Choi *et al*. (2001). The explanation is based on the fact that the Transient Hot Wire (THW) experimental method used in all nanofluid suspensions experiments listed above needs a major correction factor when applied to non-homogeneous systems. This time dependent correction factor is of the same order of magnitude as the claimed enhancement of the effective thermal conductivity. However no direct comparison to experiments was possible because the authors (Eastman *et al*. 2001, Lee *et al*. 1999, Choi *et al*. 2001) did not report so far their temperature readings as a function of time, which is the base upon which the effective thermal conductivity is being evaluated. Nevertheless, in a recent chapter Liu *et al*. (2006) reveal three important new results that allow the comparison of the theoretical model with experiments. The first important new result presented by Liu *et al*. (2006) is reflected in the fact that the value of "effective thermal conductivity" revealed experimentally by using the THW method is time dependent. The second new result is that the authors present graphically their time dependent "effective thermal conductivity" for three specimen and therefore allow the comparison of their results with our theoretical predictions showing a very good fit as presented in the present section. The third new result is that their time dependent

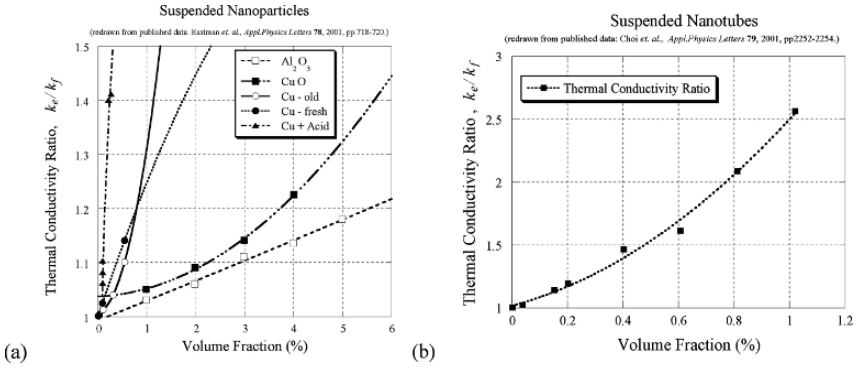

Fig. 9 Thermal conductivity enhancement in systems consisting of (**a**) nanoparticles suspended in ethylene glycol as reported by Eastman *et al*. 2001; (**b**) multiwalled carbon nanotubes suspended in oil, as reported by Choi *et al*. 2001 (here redrawn from published data)

"effective thermal conductivity" converges at steady state to values that according to our calculations confirm the validity of the classical Maxwell's theory (Maxwell 1891) and its extensions Hamilton and Crosser (1962), Jeffrey (1973), Davis (1986), Lu and Lin (1996), and Bonnecaze and Brady (1990, 1991).

A variety of possible reasons for the excessive values of the effective thermal conductivity have been investigated but only few succeeded to show a viable explanation. Prasher et al. (2005) show that convection due to Brownian motion may explain the enhancement of the effective thermal conductivity. Alternatively, Vadasz et al. (2005) showed that hyperbolic heat conduction also provides a viable explanation for the latter, although more recent results exclude this possibility. While recent experimental results of Li and Peterson (2006) confirm the substantial enhancement of the effective thermal conductivity in nanofluid suspensions, other experiments conducted via a different experimental method (an optical beam deflection technique) by Putnam *et al*. (2006) show that the results do not produce the "anomalous enhancements of the thermal conductivity that have been reported in previous studies in nanofluids".

7.1 Problem Formulation

The theoretical model derived by Vadasz (2006b) to investigate the transient heat conduction in a fluid containing suspended solid particles by considering phase-averaged equations will be presented only briefly without including the details. The phased-averaged equations are

$$\gamma_s \frac{\partial T_s}{\partial t_*} = h\left(T_f - T_s\right) \tag{116}$$

$$\gamma_f \frac{\partial T_f}{\partial t_*} = k_e \nabla_*^2 T_f - h\left(T_f - T_s\right) \tag{117}$$

where t_* is time, $T_f\left(\mathbf{r}_*, t_*\right)$, $T_s\left(\mathbf{r}_*, t_*\right)$ are temperature values for the fluid and solid phases respectively, averaged over a Representative Elementary Volume (REV) that is large enough to be statistically valid but sufficiently small compared to the size of the domain, and where $\mathbf{r}_*$ are the coordinates of the centroid of the REV. In eqs. (1) and (2) $\gamma_s = \varepsilon\, \rho_s c_s$ and $\gamma_f = (1-\varepsilon)\, \rho_f c_p$ represent the effective heat capacity of the solid and fluid phases, respectively, with ρ_s and ρ_f being the density of the solid and fluid phases, respectively, c_s and c_p being the specific heat of the solid and fluid phases, respectively, and ε being the volumetric solid fraction of the suspension. Similarly, k_e is the effective thermal conductivity of the fluid. The parameter h, carrying units of $\mathrm{W} \cdot \mathrm{m}^{-3} \cdot \mathrm{K}^{-1}$, represents an integral heat transfer coefficient for the contribution of the heat conduction at the solid-fluid interface as a volumetric heat source/sink within an REV. It is assumed to be independent of time and its general relationship to the surface-area-to-volume ratio (specific area) was derived in Vadasz (2006b). The lack of macroscopic level conduction mechanism in fluid suspensions i.e. the heat transfer within the solid phase which is expressed by the fact that the solid particles

represent the dispersed phase in the fluid suspension and therefore the solid particles can conduct heat between themselves only via the neighboring fluid, leads to setting $k_s = 0$ in the governing equations.

For the case of a thin hot wire embedded in a cylindrical container insulated on its top and bottom one can assume that the heat is transferred in the radial direction only, r_*, and eventually rendering the two equations (116) and (117) that each depends on both T_s and T_f into separate equations for T_s and T_f, respectively, in the form

$$\tau_q \frac{\partial^2 T_i}{\partial t_*^2} + \frac{\partial T_i}{\partial t_*} = \alpha_e \left[\frac{1}{r_*} \frac{\partial}{\partial r_*} \left(r_* \frac{\partial T_i}{\partial r_*} \right) + \frac{\tau_T}{r_*} \frac{\partial}{\partial r_*} \left(r_* \frac{\partial^2 T_i}{\partial r_* \partial t_*} \right) \right] \qquad \forall \quad i = s, f \tag{118}$$

where the following notation was used

$$\tau_q = \frac{\gamma_s \gamma_f}{h\left(\gamma_s + \gamma_f\right)}; \alpha_e = \frac{k_e}{\left(\gamma_s + \gamma_f\right)}; \; \tau_T = \frac{\gamma_s k_e}{h\left(\gamma_s + \gamma_f\right)\alpha_e} = \frac{\gamma_s}{h} \tag{119}$$

In eq. (119) τ_q and τ_T are the heat flux and temperature related time lags linked to Dual-Phase-Lagging (DuPhlag), while α_e is the effective thermal diffusivity of the suspension. The boundary and initial conditions applicable to eq. (118) are an initial ambient constant temperature, T_C, within the whole domain, an ambient constant temperature, T_C, at the outer radius of the container and a constant heat flux, q_{o^*}, over the fluid–platinum–wire interface that is related to the Joule heating of the platinum wire in the form $q_{o^*} = i\,V \big/ (2\pi r_{w^*} l)$, where r_{w^*} and l are the diameter and the length of the platinum wire respectively, i is the electric current and V is the voltage drop across the wire. Vadasz (2006b) assumed that eq. (118) applies for an effective temperature of the medium rather than the average temperatures of the phases. The impact of this assumption on the results will be discussed later.

An essential component in the application of the Transient Hot Wire (THW) method for estimating experimentally the effective thermal conductivity of the nanofluid suspension is the assumption that the nanofluid suspension behaves basically like an homogeneous material following Fourier law for the bulk. According to the Transient Hot Wire method the effective thermal conductivity, when applied directly to the two-phase system without the corrections suggested in Section 4 produces the following equation that was discussed in Section 4.2.1 above

$$k \approx \frac{i\,V}{4\pi\left(T_2 - T_1\right) l} \left[\ln\left(\frac{t_2}{t_1} \right) \right] \tag{120}$$

Equation (120) is a very accurate way of estimating the thermal conductivity as long as the validity condition is fulfilled. The validity condition implies the application of eq. (120) for long times only, $t >> t_o = r_w^2 \big/ 4\alpha$. However, when evaluating this condition to data used in the nanofluid suspensions experiments one obtains that $t_o \sim$ 7–14 ms and the time beyond which the solution (120) can be used reliably is therefore of the order of hundreds of milliseconds, not so long in the actual practical sense.

7.2 Solution and Correction of the THW Results

The analytical solution to the problem is obtained following the transformation of the equations into a dimensionless form by introducing the following dimensionless variables $\mathbf{q} = \mathbf{q}_* / q_{o^*}$, $\theta = (T - T_C) k_e / q_{o^*} r_{o^*}$, $r = r_* / r_{o^*}$, $t = \alpha_e t_* / r_{o^*}^2$, where the following two dimensionless groups representing a heat flux Fourier number, $Fo_q = \alpha_e \tau_q / r_{o^*}^2$, and a temperature Fourier number, $Fo_T = \alpha_e \tau_T / r_{o^*}^2$, emerged, and the ratio between them is identical to the ratio between the time lags, i.e. $Fo_T / Fo_q = \tau_T / \tau_q$.

When evaluating the thermal conductivity by applying the Transient-Hot-Wire method and using Fourier Law one obtains for the effective thermal conductivity the following relationship (Vadasz 2006b)

$$k_{app} = \frac{q_{o^*} r_{o^*}}{[T_w(t) - T_C]} [-r_w \ln(r_w) + f(t)] \tag{121}$$

where the temperature difference $[T_w(t) - T_C]$ is represented by the recorded experimental data and the value of the heat flux at the fluid–platinum–wire interface q_{o^*} is evaluated from the Joule heating of the hot wire. In eq. (7) $f(t) = \sum_{n=1}^{\infty} C_n \exp\left(-\kappa_n^2 t\right)$, where the coefficient C_n and the eigenvalues κ_n are defined in Vadasz (2006b) (see also Özisik 1993). The results obtained from the application of eq. (121) to homogeneous materials fit extremely well the approximation used by the THW method via eq. (120) within the validity limits of the approximation eq. (120). Therefore, the THW method is extremely accurate for homogeneous materials.

On the other hand, for non-homogeneous materials, by using the solution to the dimensionless version of eq. (118) applicable to fluid suspensions one obtains for the effective thermal conductivity (Vadasz 2006b)

$$k_{act} = \frac{q_{o^*} r_{o^*}}{[T_{w^*} - T_{C^*}]} [-r_w \ln(r_w) + g(t)] \tag{122}$$

where k_{act} is the actual effective thermal conductivity and the function $g(t)$ in equation (122) obtained from the solution is defined in the form $g(t) = \sum_{n=1}^{\infty} B_n \left[\lambda_{n2} \exp(\lambda_{n1} t) - \lambda_{n1} \exp(\lambda_{n2} t)\right]$. The coefficient B_n is related to C_n by the following relationship $B_n = C_n / (\lambda_{n2} - \lambda_{n1})$ where λ_{n1} and λ_{n2} are the eignevalues for the solution in the time domain and are defined in Vadasz (2006b).

When using the Fourier solution (121) or (120) for homogeneous materials to evaluate the effective thermal conductivity of non-homogeneous materials like nanofluid suspensions instead of using eq. (122) one obtains a value that differs from the actual one by a factor of

$$\sigma = \frac{k_{app}}{k_{act}} = \frac{[-r_w \ln(r_w) + f(t)]}{[-r_w \ln(r_w) + g(t)]} \tag{123}$$

where k_{app} is the apparent effective thermal conductivity obtained from the Fourier conduction solution while k_{act} is the actual effective thermal conductivity that

corresponds to data that follow a Dual-Phase-Lagging conduction following the derivations presented here as well as in Vadasz (2006b). The ratio between the two provides a correction factor for the deviation of the apparent effective thermal conductivity from the actual one. This correction factor when multiplied by the ratio k_{act}/k_f produces the results for $\sigma\left(k_{act}/k_f\right) = k_{app}/k_f$, where k_f is the thermal conductivity of the base fluid without the suspended particles and k_{act} is the effective thermal conductivity evaluated by using Maxwell's (1891) theory. Then, these results of k_{app}/k_f can be compared with the experimental results presented by Liu *et al*. (2006).

7.3 Results, Discussion and Conclusions

Liu *et al*. (2006) used a very similar THW experimental method as the one used by Eastman *et al*. (2001), Lee *et al*. (1999), and Choi *et al*. (2001) with the major distinction being in the method of producing the nanoparticles and a cylindrical container of different dimensions. They used water as the base fluid and Cu nanoparticles as the suspended elements at volumetric solid fractions of 0.1% and 0.2%. Their data that are relevant to our present discussion were digitized from their Fig. 3 and used in the following presentation to compare our theoretical results. Three specimen data are presented in Fig. 3 (Liu *et al*. 2006) resulting in extensive overlap of the various curves and therefore in some digitizing error which is difficult to estimate when using only this figure to capture the data.

The comparison between the theoretical results presented here and in Vadasz (2006b) with the experimental data (Liu *et al*. 2006) is presented in Figs. 10–12.

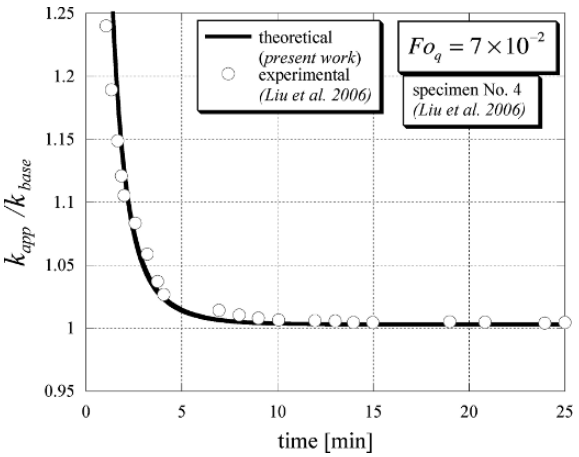

Fig. 10 Comparison of the present theory with experimental data of Liu *et al*. (2006) (here redrawn from published data) of the effective thermal conductivity ratio for conditions compatible with specimen No. 4, leading to a Fourier number of $Fo_q = 7 \times 10^{-2}$

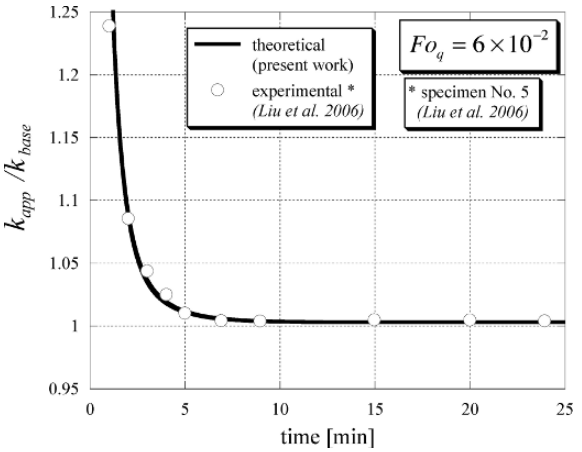

Fig. 11 Comparison of the present theory with experimental data of Liu *et al*. (2006) (here redrawn from published data) of the effective thermal conductivity ratio for conditions compatible with specimen No. 5, leading to a Fourier number of $Fo_q = 6 \times 10^{-2}$

The separation of these results into three different figures aims to better distinguish between the different curves and avoid overlapping as well as presenting the results on their appropriate scales. Figure 10 presents the results that are applicable to specimen No. 4 in Liu *et al*. (2006) and corresponding to a value of $Fo_q = 7 \cdot 10^{-2}$ in the theoretical model. Maxwell's (1891) effective thermal conductivity can be summarized in the form

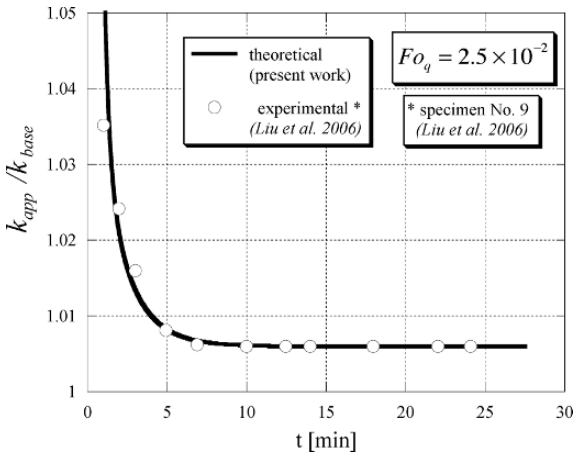

Fig. 12 Comparison of the present theory with experimental data of Liu *et al*. (2006) (here redrawn from published data) of the effective thermal conductivity ratio for conditions compatible with specimen No. 9, leading to a Fourier number of $Fo_q = 2.5 \times 10^{-2}$

$$\frac{k_e}{k_f} = 1 + \frac{3\varepsilon\,(\kappa - 1)}{(\kappa + 2) - \varepsilon\,(\kappa - 1)} \tag{124}$$

where k_e is Maxwell's effective thermal conductivity, $\kappa = k_s/k_f$ is the ratio between the thermal conductivity of the solid phase and the thermal conductivity of the base fluid, and ε is the volumetric solid fraction of the suspension. Evaluating Maxwell's (1891) effective thermal conductivity for specimen No. 4 leads to a value of 0.6018 W/m K, which is by 0.3% higher than that of the base fluid (water), i.e. $k_e/k_f = 1.003$. From the figure it is evident that the theoretical results match very well the digitized experimental data. Furthermore, the steady state result for the ratio between the effective thermal conductivity and that of the base fluid was estimated from the digitized data to be $k_{act}/k_f = 1.003 \pm 0.001$ clearly validating Maxwell's (1891) predicted value. The results applicable to specimen No. 5 in Liu *et al*. (2006) and corresponding to a value of $Fo_q = 6 \cdot 10^{-2}$ in the theoretical model are presented in Fig. 11. The very good match between the theory and the digitized experimental data is again evident. In addition, the ratio between the effective thermal conductivity and that of the base fluid was estimated from the digitized data to be $k_{act}/k_f = 1.004 \pm 0.001$ again validating Maxwell's (1891) predicted value of $k_e/k_f = 1.003$. The last result is presented in Fig. 12, which corresponds to specimen No. 9 in Liu *et al*. (2006) and to a value of $Fo_q = 2.5 \cdot 10^{-2}$ in the theoretical model. The results are presented on an appropriately scaled vertical axis and show again a very good match between the theory presented here and in Vadasz (2006b), and the experimental data as digitized from Liu *et al*. (2006). Since the volumetric solid fraction for this specimen was 0.2% its corresponding Maxwell's (1891) effective thermal conductivity for this specimen leads to a value of 0.6036 W/m K, which is by 0.6% higher than that of the base fluid (water), i.e. $k_e/k_f = 1.006$. The steady state result for the ratio between the effective thermal conductivity and that of the base fluid was estimated from the digitized data to be $k_{act}/k_f = 1.0059 \pm 0.002$ validating again Maxwell's (1891) predicted value.

It should be mentioned that Liu *et al*. (2006) explain their time dependent effective thermal conductivity by claiming that it was caused by nanoparticle agglomeration.

While the present results reinforce the explanation provided by Vadasz (2006b) for the excessively high effective thermal conductivity in nanofluids suspensions they are ignoring a subtle but essential point (Vadasz 2007b). The evaluated temperature based on which the two-phase correction eq. (122) was introduced was assumed to be an effective temperature of the two-phase medium, where in reality eq. (118) and its equivalent dimensionless version represent equations for each phase temperature T_s and T_f.

The solution that was used in deriving eq. (122) was obtained via the elimination method and suffers from similar "paradoxical" problems as presented in Section 2 for a general two-phase system. As distinct from Section 2, where the elimination method yielded originally incorrect results, in the present case it may be shown that the results are correct, but apply to only one of the phases, while the other phase follows a different solution. By applying the paradox resolution method described in

Section 5 to the present problem it is concluded that the results presented here apply to the solid phase, while the fluid phase behaves approximately as the Fourier solution. Therefore, one may conclude that unless the hot wire was excessively exposed to the solid nanoparticles/nanotubes the results presented above cannot explain the enhanced thermal conductivity captured experimentally, nor indicate an apparent rather than a real measurement. However, if substantial agglomeration occurred at the hot wire surface (about 50% in volume) then the presented explanation reverts back to become relevant. Agglomeration at the wire's surface may occur as a result of electrophoresis. Although, the results at this stage are still not conclusive and substantial more work is required in order to understand how to render the Transient Hot Wire experimental method to dual-phase applications, the present review shows quite an extensive volume of theoretical as well as experimental consideration that need to be accounted for in future research.

The presentation of the spectacular heat transfer enhancement that was measured in nanofluid suspensions has been introduced. Modelling the heat conduction process in nanofluid suspensions was shown to be a special case of heat conduction in porous media subject to Lack of Local thermal equilibrium (LaLotheq). Reviewing the topic of heat conduction in porous media subject to Lack of Local thermal equilibrium (LaLotheq) introduced one of the most accurate methods of measuring the thermal conductivity, the transient hot wire method, and its rendering to possible application to dual-phase systems was discussed.

Nomenclature

Latin Symbols

Fh_s = dimensionless group defined in eq. (16).
Fh_f = dimensionless group defined in eq. (16).
Fo_q = heat flux related Fourier number, equals $\alpha_e \tau_q / L^2$.
Fo_T = temperature gradient related, Fourier number, equals $\alpha_e \tau_T / L^2$.
Bh = bi-harmonic dimensionless group, equals β_e / L^2
Bf = dimensionless group, equals $Bh / Fo_q = \alpha_s \alpha_f / \alpha_e^2$
h = integral heat transfer coefficient for the heat conduction at the solid-fluid interface (dimensional).
i = electric current (dimensional).
k_s = effective thermal conductivity of the solid phase, equals $(1-\varphi)\tilde{k}_s$ (dimensional).
$\tilde{k}_s$ = thermal conductivity of the solid phase, (dimensional).
k_f = effective thermal conductivity of the fluid phase, equals $\varphi \tilde{k}_f$ (dimensional).
$\tilde{k}_f$ = thermal conductivity of the fluid phase, (dimensional).
L = the length of the porous slab (dimensional).
Ni_s = solid phase Nield number, eq. (16).
Ni_f = fluid phase Nield number, eq. (16).
$\boldsymbol{q}_*$ = heat flux vector (dimensional).

r_* = radial co-ordinate (dimensional).
R = electrical resistance (dimensional). t_* = time (dimensional).
T = temperature, (dimensional).
T_C = coldest wall temperature (dimensional).
T_H = hottest wall temperature (dimensional).
V = electric voltage (dimensional).
x_* = horizontal co-ordinate (dimensional).
$\boldsymbol{x}_*$ = spatial variables vector, (dimensional), equals (x_*, y_*, z_*).

Greek Symbols

α_e = effective thermal diffusivity, defined in eq. (8), (dimensional).
α_s = solid phase effective thermal diffusivity, equals $k_s \big/ \gamma_s$ (dimensional).
α_f = fluid phase effective thermal diffusivity, equals $k_f \big/ \gamma_f$ (dimensional).
β_e = bi-harmonic coefficient, defined in eq. (8), (dimensional).
γ_s = solid phase effective heat capacity, equals $(1 - \varphi)\, \rho_s c_s$ (dimensional).
γ_f = fluid phase effective heat capacity, equals $\varphi\ \rho_f c_{p,f}$ (dimensional).
ε = volumetric solid fraction of the suspension (dimensional).
η_γ = heat capacities ratio, equals $\gamma_f \big/ \gamma_s$.
η_k = thermal conductivity ratio, equals $k_f \big/ k_s$.
θ_i = dimensionless temperature, equals $(T_i - T_C)/(T_H - T_C)$ for $i = s,\ f$.
θ = angular co-ordinate.
ρ_s = solid phase density.
ρ_f = fluid phase density.
τ_q = time lag associated with the heat flux, defined in eq. (8), (dimensional).
τ_T = time lag associated with the temperature gradient, defined in eq. (8), (dimensional).
φ = porosity.
ψ = dimensionless group, equals $Fo_T \big/ Fo_q = \tau_T \big/ \tau_q$

Subscripts

$*$ = corresponding to dimensional values (in the context, see contextual notation).
s = related to the solid phase.
f = related to the fluid phase.

References

Alazmi, B. and Vafai, K. 2002 Constant wall heat flux boundary conditions in porous media under local thermal non-equilibrium conditions, *Int. J. Heat Mass Transfer* **45**, 3071–3087.

Amiri, A. and Vafai, K. 1994 Analysis of dispersion effects and non-thermal equilibrium, non-Darcian, variable porosity incompressible flow through porous media, *Int. J. Heat Mass Transfer* **37**, 934–954.

Assael, M.J., Dix, M., Gialou, K., Vozar, L., and Wakeham, W.A. 2002 Application of the transient hot-wire technique to the measurement of the thermal conductivity of solids, *Int. J. Thermophys*. **23**, 615–633.

Assael, M.J., Chen, C.-F., Metaxa, I., and Wakeham, W.A. 2004 Thermal conductivity of suspensions of carbon nanotubes in water, *Int. J. Thermophys*. **25**, 971–985.

Banu, N. and Rees, D.A.S. 2002 Onset of Darcy–Benard convection using a thermal non-equilibrium model, *Int. J. Heat Mass Transfer* **45**, 2221–2238.

Batchelor, G.K. 1972 Sedimentation in a dilute dispersion of spheres, *J. Fluid Mech*. **52**, 45–268.

Batchelor, G.K. and Green, J.T. 1972 The hydrodynamic interaction of two small freely-moving spheres in a linear flow field, *J. Fluid Mech*. **56**, 375–400.

Baytas, A.C. and Pop, I. 2002 Free convection in a square porous cavity using a thermal nonequilibrium model, *Int. J. Thermal Sci*. **41**, 861–870.

Bentley, J.P. 1984 Temperature sensor characteristics and measurement system design, *J. Phys. E: Sci. Instrum*. **17**, 430–439.

Bonnecaze, R.T. and Brady, J.F. 1990 A method for determining the effective conductivity of dispersions of particles, *Proc. R. Soc. Lond. A*, **430**, 285–313.

Bonnecaze, R.T. and Brady, J.F. 1991 The effective conductivity of random suspensions of spherical particles, *Proc. R. Soc. Lond. A*, **432**, 445–465.

Chen, G. 1996 Nonlocal and nonequilibrium heat conduction in the vicinity of nanoparticles, *J. Heat Transfer* **118**, 539–545.

Chen, G., 2000 Particularities of heat conduction in nanostructures, *J. Nanoparticle Res*. **2**, 199–204.

Chen, G. 2001 Balistic-diffusive heat-conduction equations, *Phys. Rev. Lett*. **86** (11), 2297–2300.

Choi, S.U.S., Zhang, Z.G., Yu, W., Lockwood, F.E., and Grulke, E.A. 2001 Anomalous thermal conductivity enhancement in nanotube suspensions, *Appl. Phys. Lett*., **79**, 2252–2254.

Coquard, R., Bailis, D. 2006 Modeling of heat transfer in low-denisty EPS foams, *J. Heat Transfer* **128**, 538–549.

Coquard, R., Bailis, D., and Quenard, D. 2006 Experimental and theoretical study of the hot-wire method applied to low-density thermal insulators, *Int. J. Heat Mass Transfer* **49**, 4511–4524.

Davis, R.H. 1986 The effective thermal conductivity of a composite material with spherical inclusions, *Int. J. Thermophys*. **7**, 609–620.

De Groot, J.J., Kestin, J., and Sookiazian, H. 1974 Instrument to measure the thermal conductivity of gases, *Physica* **75**, 454–482.

Eastman, J.A., Choi, S.U.S., Li, S., Yu, W., and Thompson, L.J. 2001 Anomalously increased effective thermal conductivities of ethylene glycol-based nanofluids containing copper nanoparticles, *Appl. Phys. Lett*. **78**, 718–720.

Hamilton, R.L. and Crosser, O.K. 1962 Thermal conductivity of heterogeneous two-component systems, *I&EC Fundamentals* **1**, 187–191.

Hammerschmidt, U. and Sabuga, W., 2000 Transient hot wire (THW) method: Uncertainty assessment, *Int. J. Thermophys*. **21**, 1255–1278.

Healy, J.J., de Groot, J.J. and Kestin, J. 1976 The theory of the transient hot-wire method for measuring thermal conductivity, *Physica* **82C**, 392–408.

Huxtable, S.T., Cahill, D.G., Shenogin, S., Xue, L., Ozisik, R., Barone, P., Usrey, M., Strano, M.S., Siddons, G., Shim, M., and Keblinski, P. 2003 Interfacial heat flow in carbon nanotube suspensions, *Nat. Mater*. **2**, 731–734.

Jang, S.P., and Choi, S.U.-S. 2004 Role of Brownian motion in the enhanced thermal conductivity of nanofluids, *Appl. Phys. Lett*. **84** (21), 4316–4318.

Jeffrey, D.J., 1973 Conduction through a random suspension of spheres, *Proc. R. Soc. Lond. A*, **335**, 355–367.

Kestin, J. and Wakeham, W.A. 1978 A contribution to the theory of the transient hot-wire technique for thermal conductivity measurements, *Physica* **92A**, 102–116.

Kim, S.J. and Jang, S.P. 2002 Effects of Darcy number, the Prandtl number, and the Reynolds number on local thermal non-equilibrium, *Int. J. Heat Mass Transfer* **45**, 3885–3896.

Kuwahara, F., Shirota, M. and Nakayama, A. 2001 A numerical study of interfacial convective heat transfer coefficient in two-energy equation model for convection in porous media, *Int. J. Heat Mass Transfer* **44**, 1153–1159.

Lage, J.L. 1999 The implications of the thermal equilibrium assumption for surrounding-driven steady conduction within a saturated porous medium layer, *Int. J. Heat Mass Transfer* **42**, 477–485.

Lee, S. Choi, S.U.-S. Li, S. and Eastman, J.A. 1999 Measuring thermal conductivity of fluids containing oxide nanoparticles, *J. Heat Transfer* **121**, 280–289.

Li, C.H. and Peterson, G.P. 2006 Experimental investigation of temperature and volume fraction variations on the effective thermal conductivity of nanoparticle suspensions (nanofluids), *J. Appl. Phys*. **99**, p. 084314.

Liu, M.S., Lin, M.C.C., Tsai, C.Y. and Wang, C.C. 2006 Enhancement of thermal conductivity with Cu for nanofluids using chemical reduction method, *Int. J. Heat Mass Transfer* **49**, 3028–3033.

Lu, S. and Lin, H. 1996 Effective conductivity of composites containing aligned spheroidal inclusions of finite conductivity, *J. Appl. Physics* **79**, 6761–6769.

Martinsons, C., Levick, A., and Edwards, G. 2001 Precise measurements of thermal diffusivity by photothermal radiometry for semi-infinite targets using accurately determined boundary conditions, *Anal. Sci*. **17**, 114–117.

Maxwell, J.C. 1891 *A Treatise on Electricity and Magnetism*, 3rd edition, Clarendon Press, 1954 reprint, Dover, NY, pp. 435–441.

Minkowycz, W.J., Haji-Shiekh, A., and Vafai, K. 1999 On departure from local thermal equilibrium in porous media due to a rapidly changing heat source: The sparrow number, *Int. J. Heat Mass Transfer* **42**, 3373–3385.

Nagasaka, Y. and Nagashima, A. 1981 Absolute measurement of the thermal conductivity of electrically conducting liquids by the transient hot-wire method, *J. Phys. E: Sci. Instrum*. **14**, 1435–1440.

Nield, D.A., and Bejan, A. 2006 *Convection in Porous Media*, 3rd Edition, Springer-Verlag, New-York.

Nield, D.A. 1998 Effects of local thermal nonequilibrium in steady convective processes in a saturated porous medium: Forced convection in a channel, *J. Porous Media* **1**, 181–186.

Nield, D.A. 2002 A note on the modeling of local thermal non-equilibrium in a structured porous medium, *Int. J. Heat Mass Transfer* **45**, 4367–4368.

Nield, D.A., Kuznetsov, A.V. and Xiong, M. 2002 Effect of local thermal non-equilibrium on thermally developing forced convection in a porous medium, *Int. J. Heat Mass Transfer* **45**, 4949–4955.

Özisik, M.N. 1993 *Heat Conduction*. 2nd edition, John Wiley & Sons, Inc., New York.

Prasher, R. Bhattacharya, P., and Phelan, P.E. 2005 Thermal conductivity of nanoscale colloidal solutions (Nanofluids), *Phys. Rev. Lett*. **94**, p. 025901.

Putnam, S.A., Cahill, D.G., Braun, P.V., Ge, Z., and Shimmin, R.G 2006 Thermal conductivity of nanoparticle suspensions, *J. Appl. Phys*. **99**, p. 084308.

Quintard, M. and Whitaker, S. 1995 Local thermal equilibrium for transient heat conduction: Theory and comparison with numerical experiments, *Int. J. Heat Mass Transfer* **38**, 2779–2796.

Rees, D.A.S. 2002 Vertical free convective boundary-layer flow in a porous medium using a thermal nonequilibrium model: Elliptical effects, *Zeitchrift fur angewandte Mathematik und Physik ZAMP* **53**, 1–12.

Tzou, D.Y. 1997 *Macro-to-Microscale Heat Transfer, The Lagging Behavior*, Taylor & Francis, Washington, DC.

Tzou, D.Y. 1995 A unified field approach for heat conduction from macro-to-micro-scales, J. *Heat Transfer* **117**, 8–16.

Vadasz, P. 2004 Absence of oscillations and resonance in porous media Dual–Phase–Lagging Fourier heat conduction, *J. Heat Transfer* **127**, 307–314.

Vadasz, P. 2005a Explicit conditions for local thermal equilibrium in porous media heat conduction, *Trans. Porous Media* **59**, 341–355.

Vadasz, P. 2005b Lack of oscillations in Dual–Phase–Lagging heat conduction for a porous slab subject to imposed heat flux and temperature, *Int. J. Heat Mass Transfer* **48**, 2822–2828.

Vadasz, P. 2006a Exclusion of oscillations in heterogeneous and bi-composite media thermal conduction, *Int. J. Heat Mass Transfer* **49**, 4886–4892.

Vadasz, P. 2006b Heat conduction in nanofluid suspensions, *J. Heat Transfer* **128**, 465–477.

Vadasz, P. 2007a On the paradox of heat conduction in porous media subject to lack of local thermal equilibrium, *Int. J. Heat Mass Transfer***50**, 4131–4140.

Vadasz, P. 2007b Nanofluid suspensions: Possibility for heat transfer enhancement, *in preparation*.

Vadasz, J.J., Govender, S., and Vadasz, P. 2005 Heat transfer enhancement in nanofluids suspensions: possible mechanisms and explanations, *Int. J. Heat Mass Transfer* **48**, 2673–2683.

Vadasz, P. and Nield, D.A. 2007 Extending the Duhamel theorem to dual phase applications, *Int. J. Heat Mass Transfer*, in press, doi:10.1016/j.ijheatmasstransfer.2007.03.054

Wakao, N., Kaguei, S. and Funazkri, T. 1979 Effect of fluid dispersion coefficients on particle-to-fluid heat transfer coefficients in packed beds, *Chem. Engng. Sci*. **34**, 325–336.

Wakao, N. and Kaguei, S. 1982 Effect of fluid dispersion coefficients on particle-to-fluid heat transfer coefficients in packed beds, *Heat and Mass Transfer in Packed Beds*, Gordon and Breach, New York.

Xuan, Y. and Li, Q. 2000 Heat transfer enhancement of nanofluids, *Int. J. Heat Mass Transfer* **21**, 58–64.

Index

Theory and Applications of Transport in Porous Media

Series Editor:
Jacob Bear, *Technion – Israel Institute of Technology, Haifa, Israel*

1. H.I. Ene and D. Polisševski: *Thermal Flow in Porous Media*. 1987 ISBN 90-277-2225-0
2. J. Bear and A. Verruijt: *Modeling Groundwater Flow and Pollution*. With Computer Programs for Sample Cases. 1987 ISBN 1-55608-014-X; Pb 1-55608-015-8
3. G.I. Barenblatt, V.M. Entov and V.M. Ryzhik: *Theory of Fluid Flows Through Natural Rocks*. 1990 ISBN 0-7923-0167-6
4. J. Bear and Y. Bachmat: *Introduction to Modeling of Transport Phenomena in Porous Media*. 1990 ISBN 0-7923-0557-4; Pb (1991) 0-7923-1106-X
5. J. Bear and J-M. Buchlin (eds.): *Modelling and Applications of Transport Phenomena in Porous Media*. 1991 ISBN 0-7923-1443-3
6. Ne-Zheng Sun: *Inverse Problems in Groundwater Modeling*. 1994 ISBN 0-7923-2987-2
7. A. Verruijt: *Computational Geomechanics*. 1995 ISBN 0-7923-3407-8
8. V.N. Nikolaevskiy: *Geomechanics and Fluidodynamics*. With Applications to Reservoir Engineering. 1996 ISBN 0-7923-3793-X
9. V.I. Selyakov and V.V. Kadet: *Percolation Models for Transport in Porous Media*. With Applications to Reservoir Engineering. 1996 ISBN 0-7923-4322-0
10. J.H. Cushman: *The Physics of Fluids in Hierarchical Porous Media: Angstroms to Miles*. 1997 ISBN 0-7923-4742-0
11. J.M. Crolet and M. El Hatri (eds.): *Recent Advances in Problems of Flow and Transport in Porous Media*. 1998 ISBN 0-7923-4938-5
12. K.C. Khilar and H.S. Fogler: *Migration of Fines in Porous Media*. 1998 ISBN 0-7923-5284-X
13. S. Whitaker: *The Method of Volume Averaging*. 1999 ISBN 0-7923-5486-9
14. J. Bear, A.H.-D. Cheng, S. Sorek, D. Ouazar and I. Herrera (eds.): *Seawater Intrusion in Coastal Aquifers. Concepts, Methods and Practices*. 1999 ISBN 0-7923-5573-3
15. P.M. Adler and J.-F. Thovert: *Fractures and Fracture Networks*. 1999 ISBN 0-7923-5647-0
16. M. Panfilov: *Macroscale Models of Flow Through Highly Heterogeneous Porous Media*. 2000 ISBN 0-7923-6176-8
17. J.M. Crolet (ed.): *Computational Methods for Flow and Transport in Porous Media*. 2000 ISBN 0-7923-6263-2
18. R. de Boer: *Trends in Continuum Mechanics of Porous Media*. 2005 ISBN 1-4020-3143-2
19. R.J. Schotting, H.(C.J.) van Duijn and A. Verruijt (eds.): *Soil Mechanics and Transport in Porous Media*. Selected Works of G. de Josselin de Jong. 2006 ISBN 1-4020-3536-5
20. C. Ho and S. Webb (eds.): *Gas Transport in Porous Media*. 2006 ISBN 1-4020-3961-1
21. To be published
22. P. Vadász (ed.): *Emerging Topics in Heat and Mass Transfer in Porous Media.* From Bioengineering and Microelectronics to Nanotechnology. 2008 ISBN 978-1-4020-8177-4